
Seismic Analysis, Behavior, And Design of Unbonded Post-Tensioned Hybrid Coupled Wall Structures

Qiang Shen

Publication Date

15-01-2007

License

This work is made available under a All Rights Reserved license and should only be used in accordance with that license.

Citation for this work (American Psychological Association 7th edition)

Shen, Q. (2007). *Seismic Analysis, Behavior, And Design of Unbonded Post-Tensioned Hybrid Coupled Wall Structures* (Version 1). University of Notre Dame. <https://doi.org/10.7274/rr171v55z5p>

This work was downloaded from CurateND, the University of Notre Dame's institutional repository.

For more information about this work, to report or an issue, or to preserve and share your original work, please contact the CurateND team for assistance at curate@nd.edu.

SEISMIC ANALYSIS, BEHAVIOR, AND DESIGN OF UNBONDED
POST-TENSIONED HYBRID COUPLED WALL STRUCTURES

VOLUME II

A Dissertation

Submitted to the Graduate School
of the University of Notre Dame
in Partial Fulfillment of the Requirements
for the Degree of

Doctor of Philosophy

by

Qiang Shen, B.S., M.S.

Yahya C. Kurama, Director

Graduate Program in Civil Engineering and Geological Sciences

Notre Dame, Indiana

December 2006

CONTENTS

VOLUME II

CHAPTER 11 PERFORMANCE-BASED SEISMIC DESIGN APPROACH	381
11.1 Overview	381
11.2 Performance (Damage) Levels	383
11.2.1 Immediate Occupancy Performance Level	384
11.2.2 Life Safety Performance Level	384
11.2.3 Collapse Prevention Performance Level	385
11.3 Structure Limit States and Capacities	385
11.3.1 Steel Coupling Beam Limit States	386
11.3.2 Concrete Wall Pier Limit States	387
11.4 Seismic Demand Levels	390
11.5 Structure Demands	391
11.6 Relationships between Performance Levels and Limit States	392
11.6.1 Steel Coupling Beams	392
11.6.2 Cast-in-Place Concrete Wall Piers	394
11.6.3 Precast Concrete Wall Piers	394
11.7 Design Objectives	395
11.7.1 Coupling Beams	395
11.7.2 Systems with Cast-in-Place Concrete Wall Piers	396
11.7.3 Systems with Precast Concrete Wall Piers	396
11.8 Seismic Design Criteria	397
11.9 Design Acceleration Response Spectra	397
11.9.1 Design Spectra for the Survival-Level Demand	397
11.9.2 Design Spectra for the Design-Level Demand	399
11.10 Equivalent Nonlinear SDOF Representation	400
11.10.1 Transformation from MDOF System to SDOF System	401
11.10.2 Equivalent Nonlinear SDOF Model	407
11.10.3 Application of Equivalent SDOF BP Model	408
11.10.4 Evaluation of Equivalent SDOF BP Model	415
11.11 Seismic Displacement Demand Relationships	419
11.11.1 Previous Research	420
11.11.2 Displacement Demand Relationships for SDOF BP Model	425
11.12 Nonlinear Static Procedure	431
11.12.1 Coupled Wall Design Base Shear Demand, Q_{wd}	431
11.12.2 Vertical Distribution of Seismic Lateral Forces	434
11.12.3 Horizontal Distribution of Story Forces	435

11.12.4 Load Combinations	437
11.13 Maximum Base Shear Demand	438
11.14 Chapter Summary	442
 CHAPTER 12 DESIGN OF PROTOTYPE STRUCTURES	 445
12.1 Design Overview	445
12.1.1 Design Material Properties	448
12.1.2 Selection of Initial Dimensions for Structural Members	449
12.1.3 Design Gravity Loads and Seismic Weight	450
12.1.4 Design Load Combination and Capacity Reduction Factors	452
12.1.5 Design Scope and Limitations	453
12.2 Performance-Based Seismic Design Parameters	453
12.2.1 Allowable Target Roof Drift Demands	454
12.2.2 Allowable Inter-story Drift Demands	454
12.2.3 Acceleration Response Spectra Used in Design	455
12.3 Linear-Elastic Structure Properties	457
12.3.1 Linear Elastic Stiffness	457
12.3.2 Period, Mode Shape, and Effective Mass	458
12.4 Design Base Shear Demand	459
12.4.1 Displacement Demand Relationships	459
12.4.2 Strength Ratios	461
12.4.3 Building Design Base Shear Demands	462
12.4.4 Coupled Wall Design Base Shear Demands	463
12.5 Preliminary Design Checks	463
12.5.1 Peak Roof Drift Demands	464
12.5.2 Peak Inter-story Drift Demands	465
12.5.3 Diagonal Tension at Wall Pier Bases	466
12.6 Design of Steel Coupling Beams	468
12.6.1 Design Coupling Beam Shear Force Demand	468
12.6.2 Angle and Post-Tensioning Contributions to Coupling Resistance	470
12.6.3 Coupling Beam Cross Section	475
12.6.4 Beam Post-Tensioning	476
12.6.5 Top and Seat Angles and Connections	481
12.6.6 Coupling Beam Shear Force versus Rotation Behavior	485
12.6.7 Coupling Beam Rotation Demands	486
12.6.8 Yielding of Beam Post-Tensioning Tendons	488
12.6.9 Fracture of Top and Seat Angles	489
12.6.10 Shear Slip at Beam-to-Wall Interfaces	491
12.6.11 Wall-Contact Regions	493
12.7 Design of Wall Piers in Structure P1-CWUPT	496
12.7.1 Wall Pier Flexural Reinforcement	498
12.7.2 Concrete Confinement at Wall Pier Bases	502
12.7.3 Diagonal Tension at Wall Pier Bases	505

12.7.4 Shear Slip at Coupled Wall Base	507
12.8 Design of Wall Piers in Structure P2-PWUPT	509
12.8.1 Wall Pier Post-Tensioning Steel Reinforcement	509
12.8.2 Yielding of Wall Pier Post-Tensioning Steel	513
12.8.3 Concrete Confinement at Wall Pier Bases	515
12.8.4 Diagonal Tension at Wall Pier Bases	518
12.8.5 Shear Slip at Coupled Wall Base	520
12.9 Summary of Design and Final Checks	524
12.9.1 Lateral Load versus Deformation Relationships	524
12.9.2 Design Criteria	526

CHAPTER 13 BEHAVIOR OF PROTOTYPE STRUCTURES UNDER STATIC

LATERAL LOADING	532
13.1 Introduction	532
13.2 Behavior under Monotonic Loading	534
13.2.1 Coupled Wall Base Shear Force versus Roof Drift Behaviors	535
13.2.2 Wall Pier Base Flexural Steel Strains and Stresses	541
13.2.3 Wall Pier Base Axial Forces	546
13.2.4 Wall Pier Base Shear Forces	549
13.2.5 Wall Pier Base Moments	553
13.2.6 Degree of Coupling	555
13.2.7 Wall Pier Base Concrete Strains	557
13.2.8 Coupling Beam Shear Force versus Chord Rotation Behaviors	560
13.2.9 Coupling Beam Axial Forces and Post-Tensioning Forces	561
13.2.10 Coupling Beam End Strains	566
13.2.11 Tension Angle Force versus Deformation Behaviors	569
13.3 Behavior under Reversed Cyclic Loading	574
13.3.1 Coupled Wall Base Shear Force versus Roof Drift Behaviors	575
13.3.2 Wall Pier Post-Tensioning Forces in Structure P2-PWUPT	577
13.3.3 Wall Pier Base Axial Forces	579
13.3.4 Wall Pier Base Shear Forces	582
13.3.5 Wall Pier Base Moments	583
13.3.6 Degree of Coupling	586
13.3.7 Wall Pier Base Concrete Strains	588
13.3.8 Coupling Beam Shear Force versus Chord Rotation Behaviors	591
13.3.9 Coupling Beam Axial Forces and Post-Tensioning Forces	591
13.3.10 Coupling Beam End Strains	597
13.3.11 Angle Force versus Deformation Behaviors	597
13.4 Structure with Embedded Steel Coupling Beams	604
13.4.1 Behaviors under Monotonic and Cyclic Loading	605
13.5 Chapter Summary	607

CHAPTER 14 GROUND MOTION RECORDS FOR DYNAMIC ANALYSES	608
14.1 Overview	608
14.2 Design-Level Ground Motion Records	611
14.3 Survival-Level Ground Motion Records	615
CHAPTER 15 BEHAVIOR OF PROTOTYPE STRUCTURES UNDER EARTHQUAKE LOADING	621
15.1 Analytical Model for Dynamic Analyses	621
15.1.1 Building Mass	622
15.1.2 Viscous Damping	622
15.1.3 Time Step	624
15.2 Structure P1-CWUPT	625
15.2.1 Floor/Roof Drifts	625
15.2.2 Inter-Story Drifts	628
15.2.3 Floor/Roof Accelerations	634
15.2.4 Wall Base Axial Forces	636
15.2.5 Wall Base Shear Forces	642
15.2.6 Wall Base Diagonal Tension and Shear Slip Failure	652
15.2.7 Wall Base Moments	653
15.2.8 Wall Base Strains	660
15.2.9 Coupling Beam Chord Rotations	664
15.2.10 Coupling Beam Axial Forces	670
15.2.11 Coupling Beam Post-Tensioning Forces	675
15.2.12 Coupling Beam Shear Forces	677
15.2.13 Coupling Beam Shear Slip Failure	684
15.2.14 Angle Deformations	690
15.3 Structure P2-PWUPT	692
15.3.1 Floor/Roof Drifts	695
15.3.2 Inter-Story Drifts	699
15.3.3 Floor/Roof Accelerations	704
15.3.4 Wall Post-Tensioning Forces	706
15.3.5 Wall Base Axial Forces	714
15.3.6 Wall Base Shear Forces	718
15.3.7 Wall Base Diagonal Tension and Shear Slip Failure	730
15.3.8 Wall Base Moments	736
15.3.9 Wall Base Strains	743
15.3.10 Coupling Beam Chord Rotations	749
15.3.11 Coupling Beam Axial Forces	752
15.3.12 Coupling Beam Post-Tensioning Forces	756
15.3.13 Coupling Beam Shear Forces	763
15.3.14 Coupling Beam Shear Slip Failure	768
15.3.15 Angle Deformations	771
15.4 Uncoupled Concrete Wall Systems	778
15.5 Chapter Summary	781

CHAPTER 16 SUMMARY, CONCLUSIONS AND FUTURE WORK	783
16.1 Summary	783
16.2 Conclusions	788
16.3 Future Work	798
REFERENCES	799

FIGURES

VOLUME II

CHAPTER 11

Fig. 11.1 Outline of the proposed performance-based seismic design approach (adapted from Kurama 1997)	384
Fig. 11.2 Limit states, performance levels, and design objectives: (a) steel coupling beam; (b) coupled wall system with cast-in-place concrete wall piers; (c) coupled wall system with precast concrete wall piers.....	393
Fig. 11.3 Design acceleration response spectra	399
Fig. 11.4 First mode component of roof-displacement time-history	403
Fig. 11.5 BP hysteresis model with $\beta_s=\beta_r<1$ (adapted from Farrow and Kurama 2003)	407
Fig. 11.6 Idealized base shear force versus roof displacement relationships: (a) CIP-UPT system; (b) PRE-UPT system	409
Fig. 11.7 Equivalent SDOF representation of CIP-UPT system: (a) smooth MDOF hysteresis; (b) MDOF BP model; (c) hysteretic energy dissipation; (d) equivalent SDOF BP model.....	413
Fig. 11.8 Equivalent SDOF representation of PRE-UPT system: (a) smooth MDOF hysteresis; (b) MDOF BP model; (c) hysteretic energy dissipation; (d) equivalent SDOF BP model.....	415
Fig. 11.9 Peak SDOF versus MDOF displacements: (a) CIP-UPT system; (b) PRE-UPT system	417
Fig. 11.10a SDOF and MDOF roof-displacement time-histories for CIP-UPT system (SAC LA21-LA30)	418
Fig. 11.10b SDOF and MDOF roof-displacement time-histories for CIP-UPT system (SAC LA31-LA40)	419

Fig. 11.11a SDOF and MDOF roof-displacement time-histories for PRE-UPT system (SAC LA21-LA30)	420
Fig. 11.11b SDOF and MDOF roof-displacement time-histories for PRE-UPT system (SAC LA31-LA40)	421
Fig. 11.12 Definitions of R_μ and μ (from Farrow and Kurama 2003)	423
Fig. 11.13 Distribution of inertial forces: (a) $H=0.67h_w$; (b) $H=0.3h_w$; (c) bending moment diagrams (adapted from Paulay and Priestley 1992)	440
 CHAPTER 12	
Fig. 12.1 Plan view of prototype buildings	446
Fig. 12.2 Design-level and survival-level acceleration response spectra	456
Fig. 12.3 Design coupling beam shear force demand	469
Fig. 12.4 Angle strength ratio, β_{ar} : (a) $\beta_{ar}=0.66$; (b) $\beta_{ar}=0.91$; (c) $\beta_{ar}=1.27$	473
Fig. 12.5 Post-tensioning contribution to coupling resistance: (a) preliminary; (b) revised	475
Fig. 12.6 Coupling beam and post-tensioning details: (a) Structure P1-CWUPT; (b) Structure P2-PWUPT	478
Fig. 12.7 Angle contribution to coupling resistance	482
Fig. 12.8 Top and seat angle and connection details: (a) Structure P1-CWUPT; (b) Structure P2-PWUPT	484
Fig. 12.9 Coupling beam shear force versus chord rotation ($V_b-\theta_b$) relationships: (a) Structure P1-CWUPT; (b) Structure P2-PWUPT	487
Fig. 12.10 Coupled wall idealized displaced shape	488
Fig. 12.11 Tension angle deformation	490
Fig. 12.12 Wall contact region stresses: (a) side view; (b) beam end view	495
Fig. 12.13 Wall-contact region concrete confinement	497

Fig. 12.14 Wall pier flexural reinforcement: (a) trial section 1; (b) trial section 2; (c) flexural steel area versus base shear resistance; (d) final wall cross section	500
Fig. 12.15 Concrete confinement at wall pier bases	504
Fig. 12.16 Wall pier post-tensioning steel reinforcement.....	512
Fig. 12.17 Concrete confinement at wall pier bases	517
Fig. 12.18 Prestress losses in wall pier post-tensioning bars	521
Fig. 12.19 Coupled wall base shear force versus roof drift ($F-\Delta$) relationships: (a) Structure P1-CWUPT; (b) Structure P2-PWUPT.....	525
CHAPTER 13	
Fig. 13.1 Coupled wall base shear force versus roof drift behaviors: (a) Structure P1-CWUPT; (b) Structure P2-PWUPT	536
Fig. 13.2 Wall pier flexural mild steel stresses at base of Structure P1-CWUPT: (a) tension-side wall; (b) compression-side wall.....	541
Fig. 13.3a Wall pier post-tensioning bar stresses in Structure P2-PWUPT: tension-side wall; (b) compression-side wall	542
Fig. 13.3b Wall pier post-tensioning bar stresses in Structure P2-PWUPT: compression-side wall	543
Fig. 13.4a Wall pier post-tensioning bar stress-strain behaviors for Structure P2-PWUPT: tension-side wall	544
Fig. 13.4b Wall pier post-tensioning bar stress-strain behaviors for Structure P2-PWUPT: compression-side wall.....	545
Fig. 13.5 Wall pier base axial forces: (a) Structure P1-CWUPT; (b) Structure P2-PWUPT	547
Fig. 13.6 Components of wall pier base axial forces: (a) Structure P1-CWUPT; (b) Structure P2-PWUPT.....	548
Fig. 13.7 Wall base shear forces: (a) Structure P1-CWUPT; (b) Structure P2-PWUPT	550

Fig. 13.8 Ratio of compression-side wall base shear force to total coupled wall base shear forces: (a) Structure P1-CWUPT; (b) Structure P2-PWUPT	552
Fig. 13.9 Wall base moments: (a) Structure P1-CWUPT; (b) Structure P2-PWUPT	554
Fig. 13.10 Degree of coupling: (a) Structure P1-CWUPT; (b) Structure P2-PWUPT	556
Fig. 13.11 Wall pier base neutral axis (i.e., contact) depths: (a) Structure P1-CWUPT; (b) Structure P2-PWUPT	558
Fig. 13.12 Wall pier base extreme confined concrete compression strains: (a) Structure P1-CWUPT; (b) Structure P2-PWUPT	559
Fig. 13.13 Coupling beam shear force versus chord rotation behaviors for Structure P1-CWUPT	562
Fig. 13.14 Coupling beam shear force versus chord rotation behaviors for Structure P2-PWUPT	563
Fig. 13.15 Coupling beam axial forces and post-tensioning forces in Structure P1-CWUPT	564
Fig. 13.16 Coupling beam axial forces and post-tensioning forces in Structure P2-PWUPT	565
Fig. 13.17 Coupling beam end neutral axis (i.e., contact) depths for Structure P1-CWUPT	567
Fig. 13.18 Coupling beam end neutral axis (i.e., contact) depths for Structure P2-PWUPT	568
Fig. 13.19 Coupling beam end extreme steel compression strains for Structure P1-CWUPT	570
Fig. 13.20 Coupling beam end extreme steel compression strains for Structure P2-PWUPT	571
Fig. 13.21 Coupling beam tension angle force-deformation behaviors for Structure P1-CWUPT	572
Fig. 13.22 Coupling beam tension angle force-deformation behaviors for Structure P2-PWUPT	573

Fig. 13.23 Cyclic coupled wall base shear force versus roof drift behaviors: (a) Structure P1-CWUPT; (b) Structure P2-PWUPT	576
Fig. 13.24 Cyclic wall post-tensioning forces for Structure P2-PWUPT: (a) left-side wall pier; (b) right-side wall pier; (c) total coupled wall	578
Fig. 13.25 Cyclic wall base axial forces for Structure P1-CWUPT: (a) left-side wall pier; (b) right-side wall pier; (c) total coupled wall	580
Fig. 13.26 Cyclic wall base axial forces for Structure P2-PWUPT: (a) left-side wall pier; (b) right-side wall pier; (c) total coupled wall	581
Fig. 13.27 Cyclic wall pier base shear forces for Structure P1-CWUPT: (a) left-side wall pier; (b) right-side wall pier	582
Fig. 13.28 Cyclic wall pier base shear forces for Structure P2-PWUPT: (a) left-side wall pier; (b) right-side wall pier	583
Fig. 13.29 Cyclic wall base moments for Structure P1-CWUPT: (a) left-side wall pier base moment; (b) right-side wall pier base moment; (c) coupling base moment; (d) total coupled wall base moment.....	584
Fig. 13.30 Cyclic wall base moments for Structure P2-PWUPT: (a) left-side wall pier base moment; (b) right-side wall pier base moment; (c) coupling base moment; (d) total coupled wall base moment.....	585
Fig. 13.31 Degree of coupling: (a) Structure P1-CWUPT; (b) Structure P2-PWUPT	587
Fig. 13.32 Cyclic wall pier base neutral axis (i.e., contact) depths and extreme confined concrete compression strains for Structure P1-CWUPT: (a) left-side wall pier contact depth; (b) right-side wall pier contact depth; (c) left-side wall pier concrete strains; (d) right-side wall pier concrete strains	589
Fig. 13.33 Cyclic wall pier base neutral axis (i.e., contact) depths and extreme confined concrete compression strains for Structure P2-CWUPT: (a) left-side wall pier contact depth; (b) right-side wall pier contact depth; (c) left-side wall pier concrete strains; (d) right-side wall pier concrete strains	590
Fig. 13.34 Cyclic coupling beam shear force versus chord rotation behaviors for Structure P1-CWUPT	592
Fig. 13.35 Cyclic coupling beam shear force versus chord rotation behaviors for Structure P2-PWUPT	593

Fig. 13.36 Cyclic coupling beam axial forces and post-tensioning forces in Structure P1-CWUPT	594
Fig. 13.37 Cyclic coupling beam axial forces and post-tensioning forces in Structure P2-PWUPT	595
Fig. 13.38 Cyclic coupling beam end neutral axis (i.e., contact) depths for Structure P1-CWUPT	598
Fig. 13.39 Cyclic coupling beam end neutral axis (i.e., contact) depths for Structure P2-PWUPT	599
Fig. 13.40 Cyclic coupling beam end extreme steel compression strains for Structure P1-CWUPT	600
Fig. 13.41 Cyclic coupling beam end extreme steel compression strains for Structure P2-PWUPT	601
Fig. 13.42 Cyclic coupling beam angle force versus deformation behaviors for Structure P1-CWUPT	602
Fig. 13.43 Cyclic coupling beam angle force versus deformation behaviors for Structure P2-PWUPT	603
Fig. 13.44 Coupled wall base shear force versus roof drift behavior of Structure P3-CWEMB: (a) monotonic loading; (b) cyclic loading	606

CHAPTER 14

Fig. 14.1a Acceleration time-histories of the SAC design-level ground motions (LA01-LA10)	611
Fig. 14.1b Acceleration time-histories of the SAC design-level ground motions (LA11-LA20)	612
Fig. 14.2a 5%-damped linear-elastic pseudo-acceleration response spectra of the SAC design-level ground motions (LA01-LA10)	613
Fig. 14.2b 5%-damped linear-elastic pseudo-acceleration response spectra of the SAC design-level ground motions (LA11-LA20)	614

Fig. 14.3a Acceleration time-histories of the SAC survival-level ground motions (LA21-LA30).....	616
Fig. 14.3b Acceleration time-histories of the SAC survival-level ground motions (LA31-LA40).....	617
Fig. 14.4a 5%-damped linear-elastic pseudo-acceleration response spectra of the SAC survival-level ground motions (LA21-LA30).....	618
Fig. 14.4b 5%-damped linear-elastic pseudo-acceleration response spectra of the SAC survival-level ground motions (LA31-LA40).....	619
 CHAPTER 15	
Fig. 15.1 Roof drift time history for Structure P1-CWUPT	627
Fig. 15.2 Peak roof drift demands for Structure P1-CWUPT: (a) survival level; (b) design level.....	630
Fig. 15.3 Inter-story drift time histories for Structure P1-CWUPT	632
Fig. 15.4 Peak inter-story drift demands for Structure P1-CWUPT: (a) survival level; (b) design level	633
Fig. 15.5 Floor/roof acceleration time histories for Structure P1-CWUPT	637
Fig. 15.6 Peak floor/roof acceleration demands for Structure P1-CWUPT: (a) survival level; (b) design level.....	638
Fig. 15.7 Wall pier base axial force time histories for Structure P1-CWUPT: (a) left-side wall; (b) right-side wall.....	641
Fig. 15.8 Wall pier base axial force time histories for Structure P1-CWUPT: (a) left-side wall; (b) right-side wall.....	641
Fig. 15.9 Peak wall pier base axial force demands for Structure P1-CWUPT: (a) survival level; (b) design level.....	643
Fig. 15.10 Coupled wall base shear force time history for Structure P1-CWUPT	646
Fig. 15.11 Peak coupled wall base shear force demands for Structure P1-CWUPT: (a) survival level; (b) design level.....	647

Fig. 15.12 Wall pier base shear force time histories for Structure P1-CWUPT: (a) left-side wall; (b) right-side wall	650
Fig. 15.13 Peak wall pier base shear force demands for Structure P1-CWUPT: (a) survival level; (b) design level.....	651
Fig. 15.14 Wall pier base moment time histories for Structure P1-CWUPT: (a) left-side wall; (b) right-side wall.....	656
Fig. 15.15 Peak wall pier base moment demands for Structure P1-CWUPT: (a) survival level; (b) design level.....	657
Fig. 15.16 Coupled wall base moment time history for Structure P1-CWUPT	660
Fig. 15.17 Peak coupled wall base moment demands for Structure P1-CWUPT: (a) survival level; (b) design level.....	661
Fig. 15.18 Wall pier base extreme confined concrete compression strain time histories for Structure P1-CWUPT: (a) left-side wall; (b) right-side wall.....	664
Fig. 15.19 Peak wall base confined concrete compression strain demands for Structure P1-CWUPT: (a) survival level; (b) design level.....	665
Fig. 15.20 Coupling beam chord rotation time histories for Structure P1-CWUPT.....	668
Fig. 15.21 Peak coupling beam chord rotation demands for Structure P1-CWUPT: (a) survival level; (b) design level.....	669
Fig. 15.22 Coupling beam midspan axial force time histories for Structure P1-CWUPT.....	673
Fig. 15.23 Peak coupling beam midspan axial force demands for Structure P1-CWUPT: (a) survival level; (b) design level	674
Fig. 15.24 Coupling beam post-tensioning force time histories for Structure P1-CWUPT ..	678
Fig. 15.25 Peak coupling beam post-tensioning force demands for Structure P1-CWUPT: (a) survival level; (b) design level	679
Fig. 15.26 Coupling beam shear force time histories for Structure P1-CWUPT	682
Fig. 15.27 Peak coupling beam shear force demands for Structure P1-CWUPT: (a) survival level; (b) design level.....	683

Fig. 15.28 Coupling beam shear slip capacity and shear force demand time histories for Structure P1-CWUPT	688
Fig. 15.29 Minimum coupling beam shear slip capacity to shear force demand ratios for Structure P1-CWUPT: (a) survival level; (b) design level	689
Fig. 15.30 Coupling beam connection angle deformation time histories for Structure P1-CWUPT	693
Fig. 15.31 Peak coupling beam connection angle tensile deformation demands for Structure P1-CWUPT: (a) survival level; (b) design level	694
Fig. 15.32 Roof drift time history for Structure P2-PWUPT	695
Fig. 15.33 Peak roof drift demands for Structure P2-PWUPT: (a) survival level; (b) design level	698
Fig. 15.34 Inter-story drift time histories for Structure P2-PWUPT	702
Fig. 15.35 Peak inter-story drift demands for Structure P2-PWUPT: (a) survival level; (b) design level	703
Fig. 15.36 Floor/roof acceleration time histories for Structure P2-PWUPT	707
Fig. 15.37 Peak floor/roof acceleration demands for Structure P2-PWUPT: (a) survival level; (b) design level	708
Fig. 15.38 Total coupled wall post-tensioning force time histories for Structure P2-PWUPT: (a) LA38; (b) LA33	712
Fig. 15.39 Minimum and maximum total coupled wall post-tensioning forces for Structure P2-PWUPT: (a) survival level; (b) design level	713
Fig. 15.40 Wall pier base axial force time histories for Structure P2-PWUPT: (a) left-side wall; (b) right-side wall	719
Fig. 15.41 Wall pier base axial force time histories for Structure P2-PWUPT: (a) left-side wall; (b) right-side wall	719
Fig. 15.42 Peak wall pier base axial force demands for Structure P2-PWUPT: (a) survival level; (b) design level	720
Fig. 15.43 Coupled wall base shear force time history for Structure P2-PWUPT	723

Fig. 15.44 Peak coupled wall base shear force demands for Structure P2-PWUPT: (a) survival level; (b) design level.....	725
Fig. 15.45 Wall pier base shear force time histories for Structure P2-PWUPT: (a) left-side wall; (b) right-side wall.....	727
Fig. 15.46 Peak wall pier base shear force demands for Structure P2-PWUPT: (a) survival level; (b) design level.....	729
Fig. 15.47 Coupled wall base shear slip capacity and base shear force demand time histories for Structure P2-PWUPT.....	734
Fig. 15.48 Minimum coupled wall base shear slip capacity to base shear force demand ratio for Structure P2-PWUPT: (a) survival level; (b) design level.....	735
Fig. 15.49 Wall pier base moment time histories for Structure P2-PWUPT: (a) left-side wall; (b) right-side wall.....	738
Fig. 15.50 Peak wall pier base moment demands for Structure P2-PWUPT: (a) survival level; (b) design level.....	740
Fig. 15.51 Coupled wall base moment time history for Structure P2-PWUPT	743
Fig. 15.52 Peak coupled wall base moment demands for Structure P2-PWUPT: (a) survival level; (b) design level.....	744
Fig. 15.53 Wall pier base extreme confined concrete compression strain time histories for Structure P2-PWUPT: (a) left-side wall; (b) right-side wall	747
Fig. 15.54 Peak wall base confined concrete compression strain demands for Structure P2-PWUPT: (a) survival level; (b) design level	748
Fig. 15.55 Coupling beam chord rotation time histories for Structure P2-PWUPT	751
Fig. 15.56 Peak coupling beam chord rotation demands for Structure P2-PWUPT: (a) survival level; (b) design level.....	753
Fig. 15.57 Coupling beam midspan axial force time histories for Structure P2-PWUPT	757
Fig. 15.58 Peak coupling beam midspan axial force demands for Structure P2-PWUPT: (a) survival level; (b) design level	758

Fig. 15.59 Coupling beam post-tensioning force time histories for Structure P2-PWUPT...	761
Fig. 15.60 Peak coupling beam post-tensioning force demands for Structure P2-PWUPT: (a) survival level; (b) design level	762
Fig. 15.61 Coupling beam shear force time histories for Structure P2-PWUPT	766
Fig. 15.62 Peak coupling beam shear force demands for Structure P2-PWUPT: (a) survival level; (b) design level.....	767
Fig. 15.63 Coupling beam shear slip capacity and shear force demand time histories for Structure P2-PWUPT	772
Fig. 15.64 Minimum coupling beam shear slip capacity to shear force demand ratios for Structure P2-PWUPT: (a) survival level; (b) design level.....	773
Fig. 15.65 Coupling beam connection angle deformation time histories for Structure P2- PWUPT	776
Fig. 15.66 Peak coupling beam connection angle tensile deformation demands for Structure P2-PWUPT: (a) survival level; (b) design level.....	777
Fig. 15.67 Peak roof drift demand for uncoupled wall systems: (a) Structure P4-CWUNC; (b) Structure P5-PWUNC	780

TABLES

VOLUME II

CHAPTER 11

Table 11.1 MDOF System Properties.....	410
Table 11.2 Idealized MDOF BP Model Properties.....	412
Table 11.3 Equivalent SDOF BP Model Properties	414
Table 11.4 Regression coefficients a and b for BP models (based on IND spectra)	427
Table 11.5 Regression coefficients a and b for BP models (based on DES spectra)	429

CHAPTER 12

Table 12.1 General properties of the prototype structures.....	447
Table 12.2 Seismic weights and gravity loads.....	452
Table 12.3 Acceleration response spectra.....	455
Table 12.4 Linear-elastic stiffnesses.....	458
Table 12.5 Linear-elastic modal analysis results	459
Table 12.6 Displacement demand relationships	460
Table 12.7 Displacement ductility demands and strength ratios	461
Table 12.8 Design base shear demands	462
Table 12.9 Peak roof drift demands.....	464
Table 12.10 Peak inter-story drift demands.....	465

Table 12.11 Diagonal tension at wall pier bases.....	467
Table 12.12 Design coupling beam shear force demands.....	470
Table 12.13 Effect of β_{ar} on coupling beam behavior	474
Table 12.14 Components of coupling beam design forces	474
Table 12.15 Beam post-tensioning	479
Table 12.16 Top and seat angles.....	483
Table 12.17 Coupling beam shear force versus rotation relationships	485
Table 12.18 Coupling beam rotation demands	486
Table 12.19 Tension angle deformation demands	490
Table 12.20 Shear slip at beam-to-wall interfaces.....	493
Table 12.21 Wall-contact regions.....	496
Table 12.22 Wall pier flexural reinforcement.....	501
Table 12.23 Concrete confinement at wall pier bases	505
Table 12.24 Diagonal tension at wall pier bases.....	507
Table 12.25 Shear slip at coupled wall base.....	508
Table 12.26 Wall pier post-tensioning steel reinforcement.....	512
Table 12.27 Yielding of wall pier post-tensioning steel	514
Table 12.28 Concrete confinement at wall pier bases	517
Table 12.29 Diagonal tension at wall pier bases.....	519
Table 12.30 Shear slip at coupled wall base.....	523
Table 12.31 Idealized F- Δ behaviors for Structures P1-CWUPT and P2-PWUPT	526
Table 12.32 Seismic design criteria for Structures P1-CWUPT and P2-PWUPT.....	528

CHAPTER 13

Table 13.1 Wall pier gravity loads in Structures P1-CWUPT and P2-PWUPT	534
--	-----

Table 13.2 Comparisons between estimation and analytical results	540
--	-----

CHAPTER 14

Table 14.1 SAC design-level ground motions records LA01-LA20	615
--	-----

Table 14.2 SAC Survival-level ground motions records LA21-LA40	620
--	-----

CHAPTER 15

Table 15.1 Period and damping ratios for the first eight modes of the prototype structures	624
--	-----

Table 15.2 Peak roof drift demands for Structure P1-CWUPT under survival level ground motions	626
---	-----

Table 15.3 Peak roof drift demands for Structure P1-CWUPT under design level ground motions	626
---	-----

Table 15.4 Peak inter-story drift demands for Structure P1-CWUPT under survival level ground motions	629
--	-----

Table 15.5 Peak inter-story drift demands for Structure P1-CWUPT under design level ground motions	629
--	-----

Table 15.6 Peak floor/roof acceleration demands for Structure P1-CWUPT under survival level ground motions	634
--	-----

Table 15.7 Peak floor/roof acceleration demands for Structure P1-CWUPT under design level ground motions	635
--	-----

Table 15.8 Peak wall pier base tensile axial force demands for Structure P1-CWUPT under survival level ground motions	636
---	-----

Table 15.9 Peak wall pier base tensile axial force demands for Structure P1-CWUPT under design level ground motions	639
---	-----

Table 15.10 Peak wall pier base compressive axial force demands for Structure P1-CWUPT under survival level ground motions.....	639
Table 15.11 Peak wall pier base compressive axial force demands for Structure P1-CWUPT under design level ground motions.....	640
Table 15.12 Peak coupled wall base shear force demands for Structure P1-CWUPT under survival level ground motions.....	644
Table 15.13 Peak coupled wall base shear force demands for Structure P1-CWUPT under design level ground motions	644
Table 15.14 Peak wall pier base shear force demands for Structure P1-CWUPT under survival level ground motions.....	648
Table 15.15 Peak wall pier base shear force demands for Structure P1-CWUPT under design level ground motions	649
Table 15.16 Peak wall pier base shear force distribution ratios for Structure P1-CWUPT under survival level ground motions.....	652
Table 15.17 Peak wall pier shear force distribution ratios for Structure P1-CWUPT under design level ground motions	653
Table 15.18 Peak wall pier base moment demands for Structure P1-CWUPT under survival level ground motions.....	654
Table 15.19 Peak wall pier base moment demands for Structure P1-CWUPT under design level ground motions.....	654
Table 15.20 Peak coupled wall base moment demands for Structure P1-CWUPT under survival level ground motions.....	658
Table 15.21 Peak coupled wall base moment demands for Structure P1-CWUPT under design level ground motions	658
Table 15.22 Peak wall pier base confined concrete compression strain demands for Structure P1-CWUPT under survival level ground motions	662
Table 15.23 Peak wall pier base confined concrete compression strain demands for Structure P1-CWUPT under design level ground motions.....	662
Table 15.24 Peak coupling beam chord rotation demands for Structure P1-CWUPT under survival level ground motions.....	666

Table 15.25 Peak coupling beam chord rotation demands for Structure P1-CWUPT under design level ground motions	666
Table 15.26 Peak coupling beam midspan axial force demands for Structure P1-CWUPT under survival level ground motions.....	670
Table 15.27 Peak coupling beam midspan axial force demands for Structure P1-CWUPT under design level ground motions	671
Table 15.28 Peak coupling beam post-tensioning force demands for Structure P1-CWUPT under survival level ground motions.....	675
Table 15.29 Peak coupling beam post-tensioning force demands for Structure P1-CWUPT under design level ground motions	676
Table 15.30 Peak coupling beam shear force demands for Structure P1-CWUPT under survival level ground motions.....	680
Table 15.31 Peak coupling beam shear force demands for Structure P1-CWUPT under design level ground motions	680
Table 15.32 Minimum coupling beam shear slip capacity-demand ratios for Structure P1-CWUPT under survival level ground motions.....	685
Table 15.33 Minimum coupling beam slip capacity-demand ratios for Structure P1-CWUPT under design level ground motions	685
Table 15.34 Peak angle tensile deformation demands for Structure P1-CWUPT under survival level ground motions.....	690
Table 15.35 Peak angle tensile deformation demands for Structure P1-CWUPT under design level ground motions	691
Table 15.36 Peak roof drift for Structure P2-PWUPT under survival level ground motions	696
Table 15.37 Peak roof drift for Structure P2-PWUPT under design level ground motions ..	696
Table 15.38 Peak inter-story drift for Structure P2-PWUPT under survival level ground motions.....	699

Table 15.39 Peak inter-story drift for Structure P2-PWUPT under design level ground motions.....	700
Table 15.40 Peak floor/roof acceleration for Structure P2-PWUPT under survival level ground motions	704
Table 15.41 Peak floor/roof acceleration for Structure P2-PWUPT under design level ground motions	705
Table 15.42 Minimum total coupled wall post-tensioning forces for Structure P2-PWUPT under survival level ground motions.....	709
Table 15.43 Minimum total coupled wall post-tensioning forces for Structure P2-PWUPT under design level ground motions	709
Table 15.44 Maximum total coupled wall post-tensioning forces for Structure P2-PWUPT under survival level ground motions.....	710
Table 15.45 Maximum total coupled wall post-tensioning forces for Structure P2-PWUPT under design level ground motions	710
Table 15.46 Minimum wall pier base compression axial force demands for Structure P2-PWUPT under survival level ground motions.....	715
Table 15.47 Minimum wall pier base compression axial force demands for Structure P2-PWUPT under design level ground motions	716
Table 15.48 Maximum wall pier base compression axial force demands for Structure P2-PWUPT under survival level ground motions.....	716
Table 15.49 Maximum wall pier base compression axial force demands for Structure P2-PWUPT under design level ground motions	717
Table 15.50 Peak coupled wall base shear force demands for Structure P2-PWUPT under survival level ground motions.....	721
Table 15.51 Peak coupled wall base shear force demands for Structure P2-PWUPT under design level ground motions	721
Table 15.52 Peak wall pier base shear force demands for Structure P2-PWUPT under survival level ground motions.....	726
Table 15.53 Peak wall pier base shear force demands for Structure P2-PWUPT under design level ground motions	726

Table 15.54 Peak wall pier base shear force distribution ratios for Structure P2-PWUPT under survival level ground motions.....	730
Table 15.55 Peak wall pier base shear force distribution ratios for Structure P2-PWUPT under design level ground motions.....	730
Table 15.56 Minimum coupled wall base shear slip capacity-demand ratios for Structure P2-PWUPT under survival level ground motions	733
Table 15.57 Minimum coupled wall base shear slip capacity-demand ratios for Structure P2-PWUPT under design level ground motions.....	733
Table 15.58 Peak wall pier base moment demands for Structure P2-PWUPT under survival level ground motions.....	736
Table 15.59 Peak wall pier base moment demands for Structure P2-PWUPT under design level ground motions.....	737
Table 15.60 Peak coupled wall base moment demands for Structure P2-PWUPT under survival level ground motions.....	741
Table 15.61 Peak coupled wall base moment demands for Structure P2-PWUPT under design level ground motions	741
Table 15.62 Peak wall pier base confined concrete compression strain demands for Structure P2-PWUPT under survival level ground motions.....	745
Table 15.63 Peak wall pier base confined concrete compression strain demands for Structure P2-PWUPT under design level ground motions	745
Table 15.64 Peak coupling beam chord rotation demands for Structure P2-PWUPT under survival level ground motions.....	749
Table 15.65 Peak coupling beam chord rotation demands for Structure P2-PWUPT under design level ground motions	750
Table 15.66 Peak coupling beam midspan axial forces demands for Structure P2-PWUPT under survival level ground motion	754
Table 15.67 Peak coupling beam midspan axial force demands for Structure P2-PWUPT under design level ground motions	754

Table 15.68 Peak coupling beam post-tensioning force demands for Structure P2-PWUPT under survival level ground motions	759
Table 15.69 Peak coupling beam post-tensioning force demands for Structure P2-PWUPT under design level ground motions	759
Table 15.70 Peak coupling beam shear force demands for Structure P2-PWUPT under survival level ground motions	763
Table 15.71 Peak coupling beam shear force demands for Structure P2-PWUPT under design level ground motions	764
Table 15.72 Minimum coupling beam shear slip capacity-demand ratios for Structure P2-PWUPT under survival level ground motions	769
Table 15.73 Minimum coupling beam slip capacity-demand ratios for Structure P2-PWUPT under design level ground motions	769
Table 15.74 Peak angle tensile deformation demands for Structure P2-PWUPT under survival level ground motions	774
Table 15.75 Peak angle tensile deformation in Structure P2-PWUPT under design level ground motions	774
Table 15.76 Peak roof drift demands for Structure P4-CWUNC under survival level ground motions	779
Table 15.77 Peak roof drift demands for Structure P5-PWUNC under survival level ground motions	779

CHAPTER 11

PERFORMANCE-BASED SEISMIC DESIGN APPROACH

This chapter proposes a performance-based seismic design approach for multi-story unbonded post-tensioned hybrid coupled wall structures. The chapter is divided into the following sections: (1) overview; (2) performance (damage) levels; (3) structure limit states and capacities; (4) seismic demand levels; (5) structure demands; (6) relationships between performance levels and limit states; (7) design objectives; (8) seismic design criteria; (9) ground motion response spectra; (10) equivalent nonlinear SDOF representation; (11) seismic displacement demand relationships; (12) nonlinear static procedure; and (13) maximum base shear demand. The design of two prototype structures using the proposed design approach is presented in Chapter 12.

11.1 Overview

Performance-based seismic design refers to a noble concept that aims to allow the designer to specify and predict, with reasonable accuracy, the performance (degree of damage) of a structure for a specified level of ground motion intensity. Over the last three decades following the 1971 San Fernando Earthquake in California, the need for performance-based seismic design has been recognized. For example, greater emphasis has been given to damage control by controlling drift, and the concept of an “importance factor” has been introduced for critical structures that should remain functional after a

ground motion. It has also been well recognized that increasing the lateral strength of a structure alone may not necessarily enhance safety nor reduce damage. For example, in the seismic design of a frame building, ensuring a “weak beam/strong column” yield mechanism is much more important than increasing the total lateral strength of the structure.

Over the past 10-15 years, significant research has been conducted on performance-based seismic engineering. Two of the more recent developments in this area are as follows:

(1) Recognizing the importance of limiting the nonlinear lateral displacements of a structure during an earthquake, there is a gradual shift from “force-based” design approaches to “displacement-based” approaches.

(2) The use of nonlinear pushover analyses in seismic design is becoming more standard practice, especially, for unusual or “complex” structures, or structures of higher “importance.”

Even though the idea of performance-based engineering is not new and significant progress has been made in recent years, the application of performance-based seismic design concepts in model U.S. building codes is limited, primarily, because of lack of reliable methods to assess seismic demands and structure capacities with reasonable certainty. The FEMA-356 (ASCE 2000) prestandard and commentary applies some of the latest methodologies in performance-based seismic engineering to achieve various levels of seismic performance in the seismic rehabilitation of existing buildings.

The performance-based seismic design and evaluation guidelines in FEMA-356 are comprised of three basic components: (1) performance objectives categorized by four

discrete structural performance levels and two intermediate structural performance ranges; (2) seismic demand prediction using one of four alternative analysis procedures; and (3) acceptance criteria using force and/or deformation limits that are meant to satisfy the desired performance objective(s).

The seismic design approach proposed in this dissertation for unbonded post-tensioned hybrid coupled wall structures utilizes similar concepts as the provisions in FEMA-356, focusing on a displacement-based procedure. The components used in this seismic design approach are shown in Fig. 11.1 (Kurama et al. 1997) as: (1) performance (damage) levels; (2) structure limit states and capacities; (3) seismic demand levels; and (4) structure demands. The performance levels are related to the seismic demand levels through “design objectives” and the structure capacities are related to the structure demands through “design criteria” as described below.

11.2 Performance (Damage) Levels

Performance-based seismic design requires the identification of specific seismic performance levels. A performance level is defined in terms of the damage expected in various structural and non-structural members during a ground motion. In general, less damage corresponds to better performance. The proposed design approach uses three performance levels in order of increasing damage as: (1) Immediate Occupancy; (2) Life Safety; and (3) Collapse Prevention. These performance levels are described below.

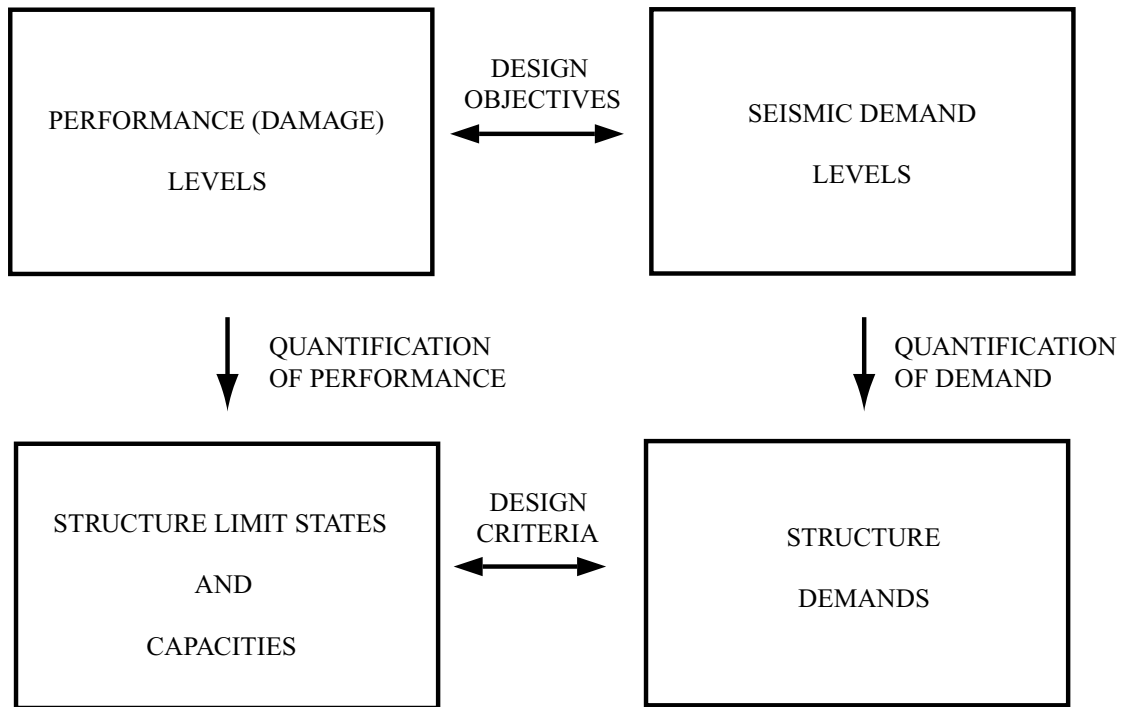


Fig. 11.1 Outline of the proposed performance-based seismic design approach (adapted from Kurama 1997)

11.2.1 Immediate Occupancy Performance Level

The Immediate Occupancy performance level refers to a post-earthquake damage state in which only very limited structural damage has occurred. The basic vertical- and lateral-force-resisting systems of the building retain nearly all of their pre-earthquake strengths and stiffnesses. Although some minor structural repairs may be appropriate, these would generally not be required prior to re-occupancy. The risk of life-threatening injury as a result of structural damage is very low.

11.2.2 Life Safety Performance Level

The Life Safety performance level refers to a post-earthquake damage state in which significant damage to the structure has occurred but an adequate margin against

either total or partial collapse remains. Some structural members and components may be severely damaged, but this does not result in large falling debris hazards, either inside or outside the building. Injuries may occur during the earthquake; however, the overall risk of life-threatening injury as a result of structural damage is low. It would be possible to repair the structure. While the damaged structure is not an imminent collapse risk, it would be prudent to implement structural repairs or install temporary bracing prior to re-occupancy.

11.2.3 Collapse Prevention Performance Level

The collapse prevention performance level refers to a post-earthquake damage state in which the structure is on the verge of partial or total collapse. Substantial damage to the structure has occurred, potentially including significant degradation in the stiffness and resistance of the lateral-force system. Degradation in the vertical load capacity of the structure is possible; however, all major components of the gravity-load system continue to carry their gravity load demands. Significant risk of injury due to falling hazards from structural debris may exist. The structure may not be practical to repair and may not be safe for reoccupancy, as aftershock activity could induce collapse.

11.3 Structure Limit States and Capacities

Performance-based seismic design requires the identification of limit states to describe and quantify the damage in various members or components of the structure. For each limit state, a force or deformation limit is defined as the corresponding capacity. The structure limit states and capacities depend on the type of structure. For example, the

limit states for a steel frame structure may include yielding, buckling, and fracture of the beam and column members, whereas the limit states for a reinforced concrete frame may include yielding of the reinforcement and crushing of the concrete. The limit states and capacities that are considered in the seismic design of unbonded post-tensioned hybrid coupled wall structures are given below.

It is assumed that the lateral load behavior of the coupled wall structure is governed by the axial-flexural behavior of the walls and gap opening behavior at the beam-to-wall joints. The desired failure mode of the structure occurs through the crushing of the confined concrete at the wall base after the yielding of the wall flexural reinforcement. The following undesirable limit states should be prevented by design: (1) shear failure of the walls, including diagonal tension failure and shear slip at the base; (2) local and/or global instability of the walls or the coupling beams; (3) failure of the concrete wall-contact regions adjacent to the coupling beams; (4) fracture or anchorage failure of the wall reinforcement; (5) fracture of the top and seat angles at the beam-to-wall connections; (6) slip of the beams with respect to the walls; (7) failure of the angle-to-beam or angle-to-wall connections; and (8) failure of the post-tensioning anchorages or fracture of the post-tensioning steel.

11.3.1 Steel Coupling Beam Limit States

As described in Chapters 4 and 5, the following limit states are identified for properly-designed unbonded post-tensioned steel coupling beams:

- (1) Decompression (i.e., initiation of gap opening) at the beam-to-wall interfaces.
- (2) Yielding of the top and seat angles in tension.

- (3) Yielding of the beam flange cover plates (if any) in compression.
- (4) Yielding of the beam flanges in compression.
- (5) Yielding of the beam post-tensioning tendons.

The following two states are used to identify an idealized bilinear lateral force versus deformation relationship for the beams (see Chapters 5 and 10):

Beam Softening State – This state identifies a significant reduction in the lateral stiffness of the beam due to, primarily, a combined effect of increased gap opening and yielding of the angles in tension. The beam end moment and chord rotation at the softening state are referred to as $M_{b,sof}$ and $\theta_{b,sof}$, respectively.

Beam PT-Yielding State – This state corresponds to the yielding of the beam post-tensioning tendons. It is assumed that at the beam PT-yielding state, the maximum strain in the beam post-tensioning tendons is equal to the linear limit strain of the post-tensioning strand stress-strain relationship. The beam end moment and chord rotation at the PT-yielding state are referred to as $M_{b,pty}$ and $\theta_{b,pty}$, respectively.

11.3.2 Concrete Wall Pier Limit States

As described in Chapters 7 and 8, both monolithic cast-in-place reinforced concrete wall piers and precast concrete wall piers are considered in this dissertation.

Cast-in-place Concrete Wall Piers

The limit states identified for a properly-designed cast-in-place reinforced concrete wall are:

(1) Cracking of concrete at the base of the tension-side wall (i.e., left side wall for lateral loads applied from left to right).

(2) Spalling of unconfined (i.e., cover) concrete at the base of the compression-side wall (i.e., right side wall for lateral loads applied from left to right).

(3) Softening of the tension-side wall. This state is defined as the state when the neutral axis at the base of the tension-side wall reaches the centerline of the wall.

(4) Softening of the compression-side wall. This state is defined as the state when the neutral axis at the base of the compression-side wall reaches the centerline of the wall.

(5) Yielding of the flexural mild steel reinforcement at the base of the tension-side wall.

(6) Crushing of the confined concrete at the base of the compression-side wall.

The following two states are used to identify an idealized bilinear lateral load versus displacement relationship for coupled wall structures with cast-in-place concrete walls (see Chapter 8):

Coupled Wall Softening State – This state corresponds to a significant reduction in the lateral stiffness of the coupled wall system. It is assumed that at the coupled wall softening state, all of the coupling beams have reached their softening states (see above for the definition of the beam softening state), the extreme flexural mild steel reinforcement in the tension-side wall has reached the yield strain, and the neutral axis at the base of compression-side wall is at the centerline of the wall (i.e., the compression side wall has softened). The coupled wall base shear force and roof drift at the wall softening state are referred to as F_{ws} and Δ_{ws} , respectively.

Coupled Wall Ultimate State – This state corresponds to the crushing of the confined concrete at the base of the compression-side wall. It is assumed that at the coupled wall ultimate state, the maximum compression strain in the confined concrete at the base of the compression-side wall is equal to the ultimate strain of the confined concrete. The coupled wall base shear force and roof drift at the wall ultimate state are referred to as F_{wu} and Δ_{wu} , respectively.

Precast Concrete Wall Piers

The limit states identified for a properly-designed precast concrete wall are:

- (1) Decompression at the base of the tension-side wall (i.e., left side wall for lateral loads applied from left to right).
- (2) Spalling of unconfined (i.e., cover) concrete at the base of the compression-side wall (i.e., right side wall for lateral loads applied from left to right).
- (3) Softening of the tension-side wall. This state is defined as the state when the neutral axis at the base of the tension-side wall reaches the centerline of the wall.
- (4) Softening of the compression-side wall. This state is defined as the state when the neutral axis at the base of the compression-side wall reaches the centerline of the wall.
- (5) Yielding of the post-tensioning steel in the tension-side wall.
- (6) Crushing of the confined concrete at the base of the compression-side wall.

The following three states are used to identify an idealized tri-linear lateral force versus displacement relationship for coupled wall structures with precast concrete walls (see Chapter 8):

Coupled Wall Softening State – This state corresponds to a significant reduction in the lateral stiffness of the coupled wall system. It is assumed that at the coupled wall softening state, all of the coupling beams have reached their softening states (see above for the definition of the beam softening state), the maximum concrete compression stress at the base of the tension-side wall is equal to the linear limit stress of the confined concrete, and the neutral axis at the base of compression-side wall is at the centerline of the wall (i.e., the compression-side wall has softened). The coupled wall base shear force and roof drift at the wall softening state are referred to as F_{ws} and Δ_{ws} , respectively.

Coupled Wall PT-Yielding State – This state corresponds to the yielding of the wall post-tensioning steel. It is assumed that at the coupled wall PT-yielding state, the maximum strain in the wall post-tensioning bars (which occurs in the tension-side wall) is equal to the linear limit strain of the post-tensioning bar stress-strain relationship. The coupled wall base shear force and roof drift at the wall PT-yielding state are referred to as F_{wy} and Δ_{wy} , respectively.

Coupled Wall Ultimate State – This state corresponds to the crushing of the confined concrete at the base of the compression-side wall. It is assumed that at the coupled wall ultimate state, the maximum compression strain in the confined concrete at the base of the compression-side wall is equal to the ultimate strain of the confined concrete. The coupled wall base shear force and roof drift at the wall ultimate state are referred to as F_{wu} and Δ_{wu} , respectively.

11.4 Seismic Demand Levels

In addition to performance levels and structure limit states and capacities, performance-based seismic design requires a set of seismic demand levels. These seismic

demand levels are generally defined in terms of selected levels of ground motion (with selected return periods) for a given site. Two seismic demand levels are considered in this dissertation using a “design” level ground motion and a “survival” level ground motion.

The survival level ground motion is the same as the “maximum considered earthquake” level in IBC 2000 (ICC 2000), which has a 2% probability of being exceeded in 50 years, approximately corresponding to a 2500-year return period. The acceleration response spectrum for the design-level ground motion is determined by multiplying the spectrum for the survival-level ground motion by a factor of 2/3 [referred to as the “seismic margin” in the NEHRP provisions (BSSC 1998)]. This demand level roughly corresponds to an earthquake with a 10% probability of being exceeded in 50 years, or a return period of approximately 500 years, for coastal California and a lower probability of occurrence (a return period of approximately 1400 years) for the eastern United States (BSSC 1998).

11.5 Structure Demands

Structure demands quantify lateral displacement (e.g., roof drift) and force (e.g., base shear) requirements of a structure for the selected seismic demand levels. The structure demands considered in the design of an unbonded post-tensioned hybrid coupled wall system include:

- (1) The survival-level coupled wall roof drift demand, Δ_s .
- (2) The design-level coupled wall roof drift demand, Δ_d .
- (3) The survival-level coupling beam chord rotation demand, θ_s .
- (4) The design-level coupling beam chord rotation demand, θ_d .

(5) The coupled wall design base shear force demand, Q_{wd} , as determined from a design ground motion acceleration spectrum based on the first mode response of the structure.

(6) The maximum coupled wall base shear force demand, $Q_{w,max}$, including the effect of higher modes.

The estimation of these structure demands is discussed in detail later in this chapter.

11.6 Relationships Between Performance Levels And Limit States

Performance-based design requires the development of relationships between the target performance levels and the structure limit states. These relationships are necessary to determine when the structure reaches a specified performance level. The following relationships are used in the design of unbonded post-tensioned hybrid coupled wall structures.

11.6.1 Steel Coupling Beams

Immediate Occupancy performance level—This performance level is assumed to be reached when the beam softening state is reached (i.e., at $M_{b,sof}$, $\theta_{b,sof}$).

Life Safety performance level—This performance level is assumed to be reached when the beam chord rotation reaches 2/3 times the rotation at the beam PT-yielding state (i.e., at $2\theta_{b,pty}/3$).

Collapse Prevention performance level—This performance level is assumed to be reached when the beam PT-yielding state is reached (i.e., at $M_{b,pty}$, $\theta_{b,pty}$).

These three performance levels are shown on the typical idealized end moment versus chord rotation (M_b - θ_b) relationship of an unbonded post-tensioned steel coupling beam in Fig. 11.2a.

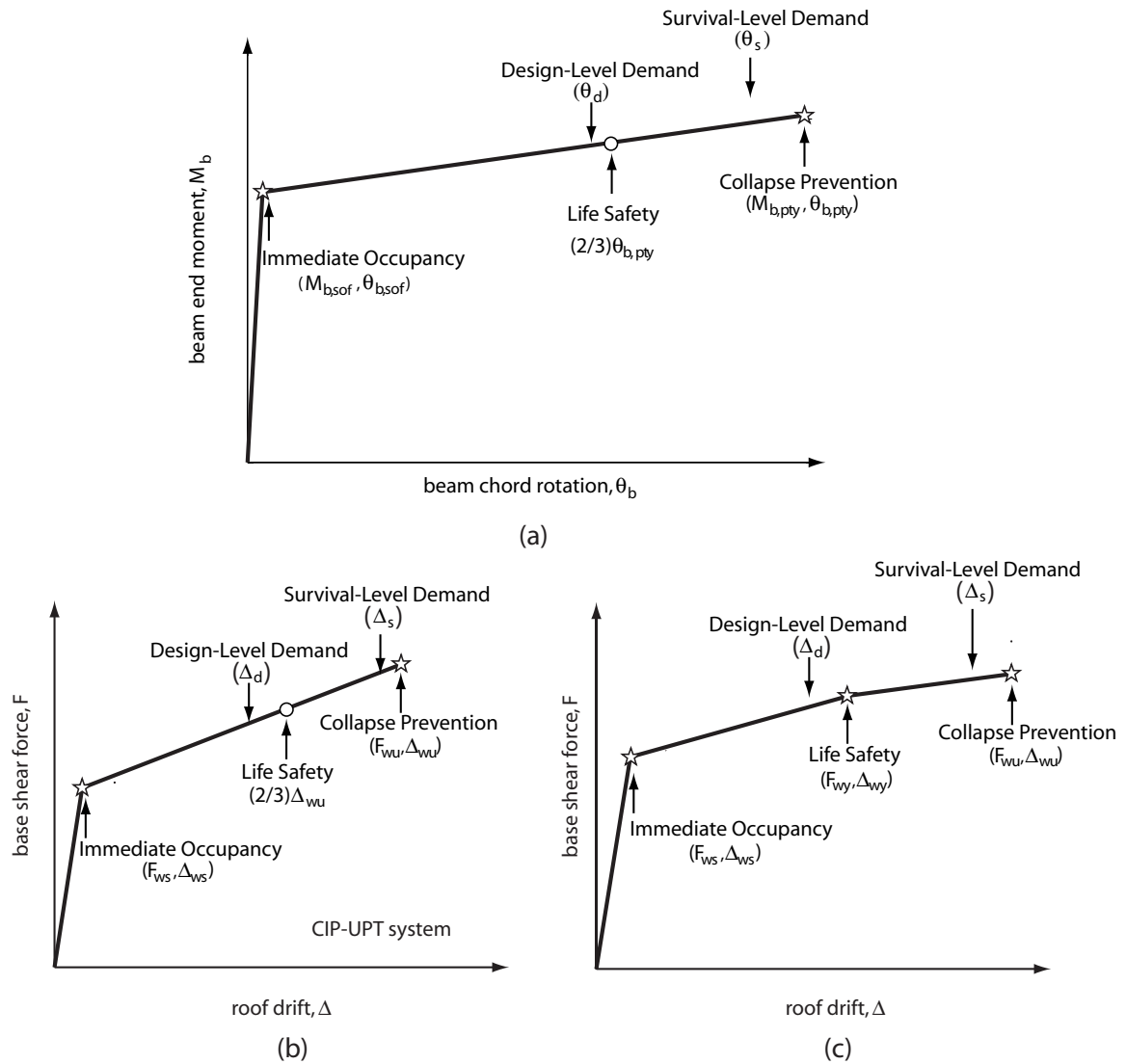


Fig. 11.2 Limit states, performance levels, and design objectives: (a) steel coupling beam; (b) coupled wall system with cast-in-place concrete wall piers; (c) coupled wall system with precast concrete wall piers

11.6.2 Cast-in-Place Concrete Wall Piers

Immediate Occupancy performance level—This performance level is assumed to be reached when the coupled wall softening state is reached (i.e., at F_{ws} , Δ_{ws}).

Life Safety performance level—This performance level is assumed to be reached when the wall roof drift reaches 2/3 times the roof drift at the coupled wall ultimate state (i.e., at $2\Delta_{wu}/3$).

Collapse Prevention performance level—This performance level is assumed to be reached when the coupled wall ultimate state is reached (i.e., at F_{wu} , Δ_{wu}).

These three performance levels are shown on the typical idealized base shear force versus roof drift (F- Δ) relationship of an unbonded post-tensioned hybrid coupled wall system with cast-in-place concrete wall piers in Fig. 11.2b.

11.6.3 Precast Concrete Wall Piers

Immediate Occupancy performance level—This performance level is assumed to be reached when the coupled wall softening state is reached (i.e., at F_{ws} , Δ_{ws}).

Life Safety performance level—This performance level is assumed to be reached when the coupled wall PT-yielding state is reached (i.e., at F_{wy} , Δ_{wy}).

Collapse Prevention performance level—This performance level is assumed to be reached when the coupled wall ultimate state is reached (i.e., at F_{wu} , Δ_{wu}).

These three performance levels are shown on the typical idealized base shear force versus roof drift (F- Δ) relationship of an unbonded post-tensioned hybrid coupled wall system with precast concrete wall piers in Fig. 11.2c.

11.7 Design Objectives

Design objectives relate the target performance levels to the seismic demand levels as shown in Fig. 11.1. The design approach developed in this dissertation has two objectives as follows:

(Design Objective 1) To achieve the Collapse Prevention performance level under the survival demand level; and

(Design Objective 2) To achieve the Life Safety performance level under the design demand level.

11.7.1 Coupling Beams

As shown in Fig. 11.2a, the design objectives for the coupling beams are assumed to be achieved if the following conditions are met:

(1) The coupling beam chord rotation capacity at the beam PT-yielding state is larger than the survival-level chord rotation demand \rightarrow Design Objective 1. Thus,

$$\theta_{b,pty} > \theta_s \quad (11.1)$$

(2) 2/3 times the coupling beam chord rotation capacity at the beam PT-yielding state is larger than the design-level chord rotation demand \rightarrow Design Objective 2. Thus,

$$\frac{2}{3}\theta_{b,pty} > \theta_d \quad (11.2)$$

(3) All other failure modes (e.g., shear failure, instability, fracture of top and seat angles) are prevented.

11.7.2 Systems with Cast-in-Place Concrete Wall Piers

As shown in Fig. 11.2b, the design objectives for the cast-in-place concrete wall piers are assumed to be achieved if the following conditions are met:

(1) The coupled wall roof drift capacity at the wall ultimate state is larger than the survival-level wall roof drift demand → Design Objective 1. Thus,

$$\Delta_{wu} > \Delta_s \quad (11.3)$$

(2) 2/3 times the coupled wall roof drift capacity at the wall ultimate state is larger than the design-level wall roof drift demand → Design Objective 2. Thus,

$$\frac{2}{3} \Delta_{wu} > \Delta_d \quad (11.4)$$

(3) All other failure modes (e.g., diagonal tension failure, shear slip) are prevented.

11.7.3 Systems with Precast Concrete Wall Piers

As shown in Fig. 11.2c, the design objectives for the precast concrete wall piers can be achieved if the following conditions are met:

(1) The coupled wall roof drift capacity at the wall ultimate state is larger than the survival-level wall roof drift demand → Design Objective 1. Thus,

$$\Delta_{wu} > \Delta_s \quad (11.5)$$

(2) The coupled wall roof drift capacity at the wall PT-yielding state is larger than the design-level wall roof drift demand → Design Objective 2. Thus,

$$\Delta_{wy} > \Delta_d \quad (11.6)$$

(3) All other failure modes (e.g., diagonal tension failure, shear slip) are prevented.

11.8 Seismic Design Criteria

As indicated in Fig. 11.1, seismic design criteria (or acceptance criteria) specify required comparisons between structure capacities and structure demands. If the structure capacities are larger than the structure demands, then, the design objectives are expected to be achieved. If the capacities are smaller than the demands, the structure has to be redesigned.

The seismic design of a coupled wall structure involves establishing structure demands and providing structure capacities until all of the design criteria are satisfied. Equations (11.1)-(11.6) represent six of the design criteria used the proposed design approach. The other required design criteria used in the dissertation are provided in Chapter 12.

11.9 Design Acceleration Response Spectra

This section describes the design acceleration response spectra for the survival-level and design-level seismic demands used in the proposed design approach.

11.9.1 Design Spectra for the Survival-Level Demand

As described earlier, the survival-level ground motion is the same as the maximum considered ground motion in IBC 2000 (ICC 2000), which has a 2% probability of being exceeded in 50 years (corresponding to a return period of approximately 2500 years). The design acceleration response spectrum for the survival-level ground motion is determined as follows.

According to IBC 2000, the maximum considered earthquake spectral response acceleration at short periods, S_{MS} , and at 1 second period, S_{M1} , are found as:

$$S_{MS} = F_a S_S \quad (11.7)$$

$$S_{M1} = F_v S_1 \quad (11.8)$$

where, F_a and F_v are site coefficients given in IBC 2000, and S_S and S_1 are mapped spectral response acceleration values at short periods and at 1 second period, respectively, obtained from Maps 1 through 24 in IBC 2000, from contour maps published by the Federal Emergency Management Agency (BSSC 1998), or from the United States Geological Survey (USGS 1996).

The general response spectrum for the survival-level ground motion, S_{as} is plotted using S_{MS} and S_{M1} (see Fig. 11.3). For periods less than or equal to T_0 , the spectral response acceleration, S_{as} , is given as:

$$S_{as} = 0.6 \frac{S_{MS}}{T_0} T + 0.4 S_{MS} \quad (11.9)$$

where, T is the period and $T_0 = 0.2 S_{M1} / S_{MS}$.

For periods between T_0 and $T_s = S_{M1} / S_{MS}$, the spectral response acceleration is taken as equal to S_{MS} .

For periods greater than T_s , the spectral response acceleration is determined as:

$$S_{as} = \frac{S_{M1}}{T} \quad (11.10)$$

The peak acceleration of the survival-level ground motion, PGA_s can be obtained by substituting $T=0$ into Equation (11.9) as:

$$PGA_s = 0.4 S_{MS} \quad (11.11)$$

Note that IBC 2000 requires a site-specific geotechnical investigation and dynamic site response analyses for certain sites with soft soil characteristics.

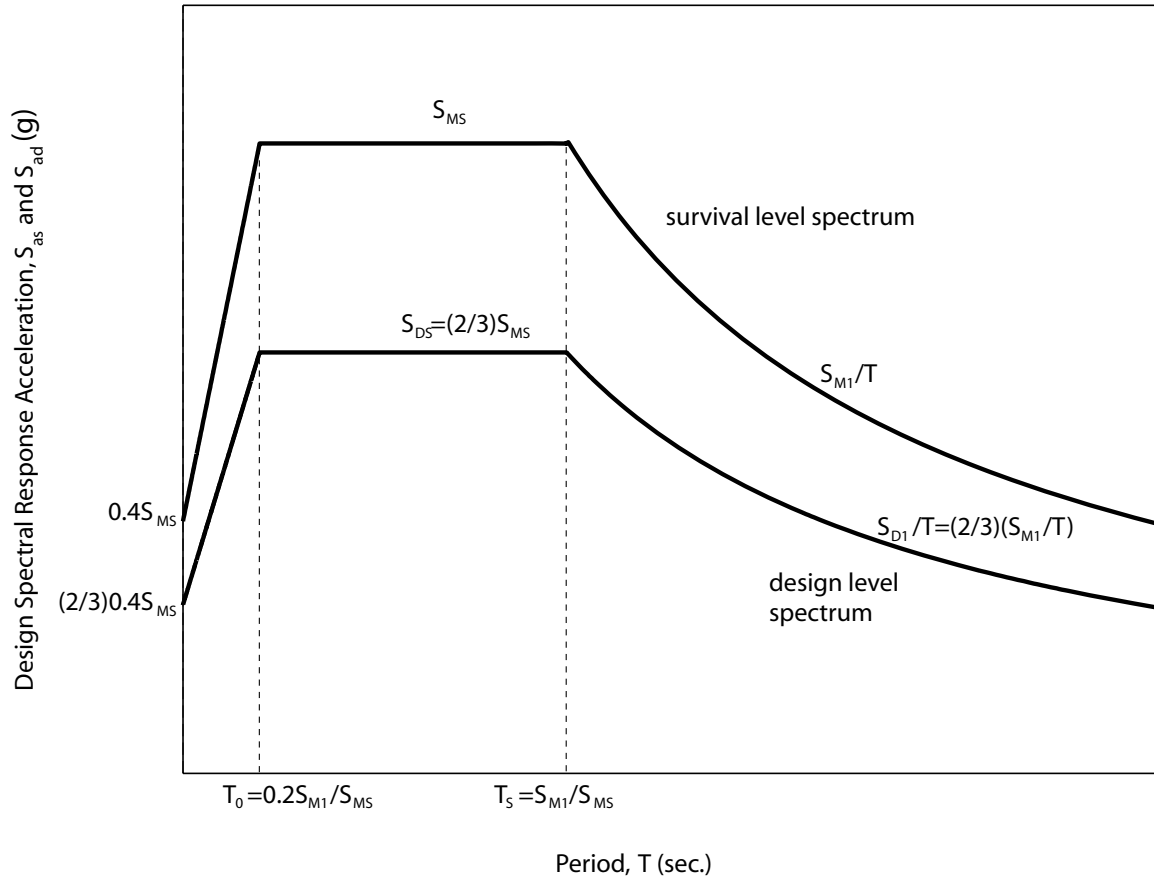


Fig. 11.3 Design acceleration response spectra

11.9.2 Design Spectra for the Design-Level Demand

According to IBC 2000, the design-level ground motion spectrum, S_{ad} is determined by multiplying the spectrum for the maximum considered earthquake by a factor of 2/3 (referred to as the “seismic margin”). Thus,

$$S_{ad} = \frac{2}{3} S_{as} \quad (11.12)$$

The peak acceleration of the design-level ground motion PGA_d can be calculated as:

$$PGA_d = (2/3)0.4S_{MS} \quad (11.13)$$

11.10 Equivalent Nonlinear SDOF Representation

The proposed seismic design approach requires the estimation of the nonlinear displacement demands of a coupled wall structure under design-level and survival-level ground motions. The most accurate analytical method to estimate the seismic demands of a structure is to conduct nonlinear multi-degree-of-freedom (MDOF) dynamic time-history analyses. However, since this procedure is time-consuming and is usually not employed in practice for most regular structures, the proposed design approach uses a nonlinear static procedure (NSP).

The nonlinear static procedure is based, in part, on the assumption that the lateral displacement response of a building during an earthquake can be related to the response of an equivalent single-degree-of-freedom (SDOF) system following simplifying assumptions for mode shapes and mass participation (SEAOC 1996). This implies that the displacement response of the structure is controlled by a single mode (often the first mode), and that the shape of this mode remains essentially constant throughout the nonlinear response history. Previous studies (Saiidi and Sozen 1981; Fajfar and Fischinger 1988; Qi and Moehle 1991; Miranda 1991; Lawson et al. 1994) have indicated that these assumptions lead to reasonable predictions of the peak seismic displacements of MDOF buildings provided that the response is dominated by the first mode.

An equivalent nonlinear SDOF model that can be used to represent the nonlinear lateral displacement response of MDOF unbonded post-tensioned hybrid coupled wall

structures is presented below. It is assumed that there are no significant plan or vertical discontinuities/irregularities (e.g., set-backs) in the structure and that the building is not excessively tall (e.g., not taller than 240 ft or, approximately, 18 stories as described in IBC 2000).

11.10.1 Transformation from MDOF System to SDOF System

Multistory buildings can be represented as MDOF systems with masses lumped at the floor and roof levels. For structures responding linear-elastically to a base excitation $\ddot{u}_g(t)$, the MDOF equation of motion can be expressed as:

$$[M]\{\ddot{U}(t)\} + [C]\{\dot{U}(t)\} + [K]\{U(t)\} = -[M]\{R\}\ddot{u}_g(t) \quad (11.14)$$

where: $[M]$ is the lumped diagonal mass matrix of the system;

$[C]$ is the damping matrix of the system;

$[K]$ is the stiffness matrix of the system;

$\ddot{u}_g(t)$ is the horizontal ground acceleration time-history;

$\{R\}$ is a vector of rigid body displacements in the horizontal direction
($\{R\}=\{1\}$ considering horizontal degrees of freedom only); and

$\{U(t)\}$ is the relative lateral displacement vector of the MDOF system at the floor and roof levels, with $\{\dot{U}(t)\}$ and $\{\ddot{U}(t)\}$ representing the first and second time derivatives (i.e., velocity and acceleration), respectively.

First Mode Displacements

The vector $\{U(t)\}$ can be decomposed using mass-orthogonal mode shapes as:

$$\{U\} = \{\phi_1\}Y_1 + \{\phi_2\}Y_2 + \cdots + \{\phi_n\}Y_n = \sum_{i=1}^n \{\phi_i\}Y_i = [\Phi]\{Y\} \quad (11.15)$$

where, $\{\phi_i\}$ is the i^{th} linear-elastic vibration mode-shape of the MDOF system, n is the number of modes, $[\Phi]$ is a matrix containing the n mode shapes, Y_i is the i^{th} modal amplitude, and $\{Y\}$ is the modal amplitude vector. The orthogonality property of the mode shapes leads to

$$\{\phi_i\}^T [M] \{U\} = \{\phi_i\}^T [M] \{\phi_i\} Y_i \quad (11.16)$$

Let $u(t)$ be equal to the roof displacement of the MDOF system. The first mode component of the roof-displacement time-history, u_1 can be calculated as:

$$u_1 = Y_1 = \frac{\{\phi_1\}^T [M] \{U\}}{\{\phi_1\}^T [M] \{\phi_1\}} = \frac{\{\phi_1\}^T [M] \{U\}}{M_{eq}} \quad (11.17)$$

where, Y_1 is the amplitude of the first mode, $\{\phi_1\}$ is the first linear-elastic mode-shape of the structure normalized with respect to the roof, and M_{eq} is the “generalized mass” for the first mode.

The first mode representation of the nonlinear lateral displacement response of unbonded post-tensioned hybrid coupled wall structures is demonstrated using nonlinear dynamic time-history analyses of the CIP-UPT system described in Chapters 6, 7, and 8. The fiber element model in Chapter 6 is used to conduct the analyses, with the wall-contact elements removed to reduce the computation time. The structure is assumed to have a viscous damping ratio of $\xi=3\%$ in the first and third modes using Rayleigh damping.

The solid line in Fig. 11.4 shows the roof-displacement time-history of the CIP-UPT system under the LA22 ground motion from the SAC Steel Project (Somerville et al. 1997). The dashed line represents the first mode component of the roof-displacement time-history, u_1 as calculated using Equation (11.17). Comparison between the solid and dashed lines in Fig. 11.4 shows that u_1 is very close to the total roof-displacement, u indicating that the lateral displacement response of the structure can be estimated based on the first mode as:

$$\{U(t)\} = \{\varphi_1\}Y_1(t) = \{\varphi_1\}u_1(t) \quad (11.18)$$

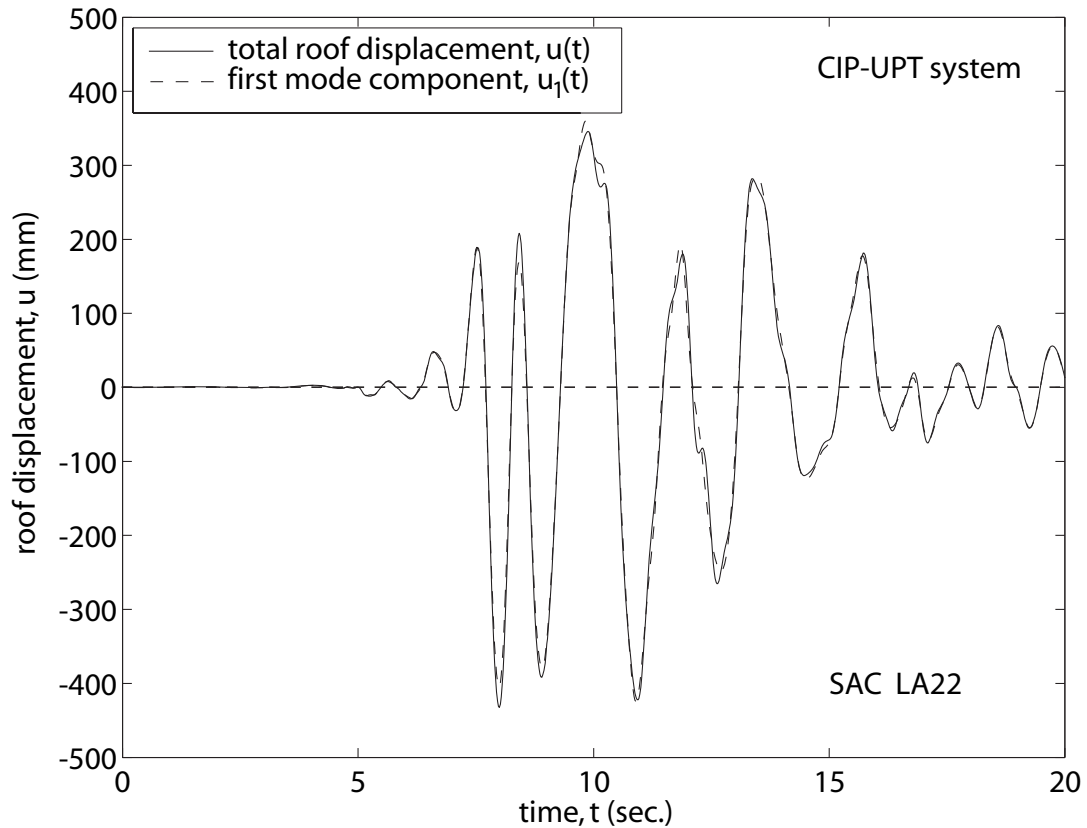


Fig. 11.4 First mode component of roof-displacement time-history

Equivalent SDOF System

Pre-multiplying both sides of Equation (11.14) by the transpose of the first mode shape vector $\{\phi_1\}^T$, and substituting Equation (11.18)

$$M_{eq}\ddot{u}_1(t) + C_{eq}\dot{u}_1(t) + K_{eq}u_1(t) = -L_{eq}\ddot{u}_g(t) \quad (11.19)$$

$$\ddot{u}_1(t) + 2\xi_{eq}\omega_{eq}\dot{u}_1(t) + \omega_{eq}^2u_1(t) = -\frac{L_{eq}}{M_{eq}}\ddot{u}_g(t) \quad (11.20)$$

where,

$$M_{eq} = \{\phi_1\}^T [M] \{\phi_1\}, \quad (11.21)$$

$$C_{eq} = \{\phi_1\}^T [C] \{\phi_1\}, \quad (11.22)$$

$$K_{eq} = \{\phi_1\}^T [K] \{\phi_1\}, \quad (11.23)$$

$$\omega_{eq}^2 = K_{eq}/M_{eq} \quad (11.24)$$

$$2\xi_{eq}\omega_{eq} = C_{eq}/M_{eq} \quad (11.25)$$

$$L_{eq} = \{\phi_1\}^T [M] \{1\} \quad (11.26)$$

The scalars M_{eq} , C_{eq} , and K_{eq} represent the generalized mass, damping, and stiffness for the first mode, respectively. The scalar L_{eq} is often referred to as the earthquake excitation factor and represents the extent to which the ground motion tends to excite response in the first mode of vibration.

Equation (11.20) is the equation of motion of a unit mass SDOF system subjected to a factored earthquake, where the factor, given by $\Gamma = L_{eq}/M_{eq}$, is generally known as the participation factor. Multiplying Equation (11.20) by M_{eq}/L_{eq} , a new displacement coordinate is defined as:

$$u_{eq}(t) = \frac{M_{eq}}{L_{eq}}u_1(t) = \frac{u_1(t)}{\Gamma} \quad (11.27)$$

and Equation (11.20) can be rewritten as:

$$\ddot{u}_{eq}(t) + 2\xi_{eq}\omega_{eq}\dot{u}_{eq}(t) + \omega_{eq}^2 u_{eq}(t) = -\ddot{u}_g(t) \quad (11.28)$$

Equation (11.28) describes the displacement response of an equivalent unit mass SDOF system under the original earthquake acceleration record. Here, u_{eq} is the displacement of the equivalent SDOF system and the product $\omega_{eq}^2 u_{eq}$ is the force per unit of mass acting on the equivalent system.

The period of the equivalent SDOF system, T_{eq} , is equal to

$$T_{eq} = \frac{2\pi}{\omega_{eq}} = \frac{2\pi}{\sqrt{\frac{K_{eq}}{M_{eq}}}} = 2\pi \sqrt{\frac{M_{eq}}{K_{eq}}} \quad (11.29)$$

Using the undamped first mode free vibration equation of motion as:

$$[K]\{\phi_1\} = \omega_1^2 [M]\{\phi_1\} \quad (11.30)$$

and multiplying both sides of the equation by $\{\phi_1\}^T$, it can be shown that ω_{eq} and T_{eq} of the equivalent SDOF system are equal to the first mode frequency ω_1 and period T_1 of the MDOF system, respectively.

Relationships Between MDOF and SDOF Displacements and Forces

Based on the above equivalent SDOF formulation, the roof displacement $u(t)$ of the MDOF system can be estimated as:

$$u(t) = u_1(t) = \Gamma u_{eq}(t) \quad (11.31)$$

and the displacements, $\{U(t)\}$ of the structure over the height are given as:

$$\{U(t)\} = \{\phi_1\} u_1(t) = \{\phi_1\} \Gamma u_{eq}(t) \quad (11.32)$$

The base shear, $F(t)$ of the MDOF system can be obtained as:

$$F(t) = \{1\}^T \{f(t)\} \quad (11.33)$$

where, $\{f(t)\}$ is a vector containing the resisting forces at the floor and roof levels. This vector of forces can be expressed as the product of the stiffness matrix, $[K]$, and the displacement vector, $\{U(t)\}$, resulting in

$$F(t) = \{1\}^T [K] \{\phi_1\} \Gamma u_{eq}(t) \quad (11.34)$$

Substituting Equations (11.26), (11.30), and $\Gamma = L_{eq}/M_{eq}$

$$F(t) = \frac{L_{eq}^2}{M_{eq}} \omega_{eq}^2 u_{eq} \quad (11.35)$$

where the term $\frac{L_{eq}^2}{M_{eq}}$ is often referred to as the effective first mode mass, M_{eff} .

Note that Equation (11.28) can also be written for an equivalent SDOF system with mass equal to the effective first mode mass, M_{eff} as:

$$M_{eff} \ddot{u}_{eq}(t) + M_{eff} 2\xi_{eq} \omega_{eq} \dot{u}_{eq}(t) + M_{eff} \omega_{eq}^2 u_{eq}(t) = -M_{eff} \ddot{u}_g(t) \quad (11.36)$$

The corresponding SDOF force can be written as:

$$F_{eq}(t) = M_{eff} \omega_{eq}^2 u_{eq} = \frac{L_{eq}^2}{M_{eq}} \omega_{eq}^2 u_{eq} = F(t) \quad (11.37)$$

and thus, the resisting force of the SDOF system with mass equal to M_{eff} is the same as the base shear force of the MDOF system.

11.10.2 Equivalent Nonlinear SDOF Model

The objective of developing an equivalent SDOF system is to provide a tool to estimate the nonlinear lateral displacement response of a MDOF system without the need for MDOF dynamic time-history analyses. This section presents a hysteretic SDOF model for unbonded post-tensioned hybrid coupled wall structures. For design purposes, the smooth nonlinear lateral load versus displacement relationship of the structure is idealized using a multi-linear relationship.

The lateral load versus displacement behavior of unbonded post-tensioned hybrid coupled wall systems possesses hysteretic characteristics similar to the bilinear-elastic/elasto-plastic (BP) model developed by Farrow and Kurama (2001, 2003, 2004). As shown in Fig. 11.5, the BP hysteresis model is constructed by placing a bilinear-elastic (BE) hysteresis model in parallel with an elastic-perfectly-plastic (EP) hysteresis model. The BE model represents the self-centering capability of the structure provided by the post-tensioning force and the EP model represents the energy dissipation capability provided by the top and seat angles and yielding of the mild steel reinforcement at the bases of the cast-in-place concrete walls.

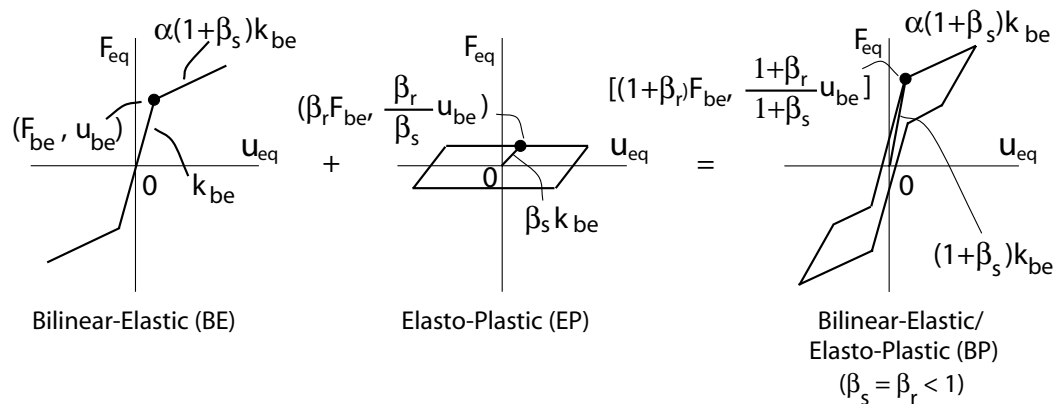


Fig. 11.5 BP hysteresis model with $\beta_s = \beta_r < 1$ (adapted from Farrow and Kurama 2003)

As shown in Fig. 11.5 the relationships between the lateral stiffnesses and strengths of the BE and EP hysteresis models that make up a BP model are:

$$k_{ep} = \beta_s k_{be} \quad (11.38)$$

$$F_{ep} = \beta_r F_{be} \quad (11.39)$$

where, k_{be} and k_{ep} are the linear-elastic stiffnesses, and F_{be} and F_{ep} are the yield strengths of the BE and EP models, respectively, and β_s and β_r are the BP model stiffness and strength ratios, respectively.

Note that BP models with only one yield point are used in this dissertation as illustrated in Fig. 11.4. In this case, β_s must be equal to β_r . More information on the BP hysteresis model can be found in Farrow and Kurama (2001, 2003, 2004).

11.10.3 Application of Equivalent SDOF BP Model

This section describes the use of the equivalent SDOF BP hysteresis model to represent the nonlinear lateral displacement response of multi-story unbonded post-tensioned hybrid coupled wall structures. The procedure is demonstrated using the CIP-UPT and PRE-UPT coupled wall structures from Chapters 6, 7, and 8. Note that the structure properties given below are for one coupled wall system only, and not for the entire building, which consists of four identical coupled wall systems in the E-W direction.

First, idealized base shear force versus roof displacement (F - u) relationships of the CIP-UPT and PRE-UPT structures are developed using the procedures described in Chapter 8. The idealized relationships give the base shear force and roof displacement

values corresponding to the coupled wall softening, PT-yielding, and ultimate states. Figs. 11.6a and 11.6b show comparisons between the idealized relationships (dashed lines) and the smooth relationships from static push-over analyses of the two structures using the fiber element model described in Chapter 6 (solid lines). A reasonable representation of the behavior of the coupled wall systems is observed.

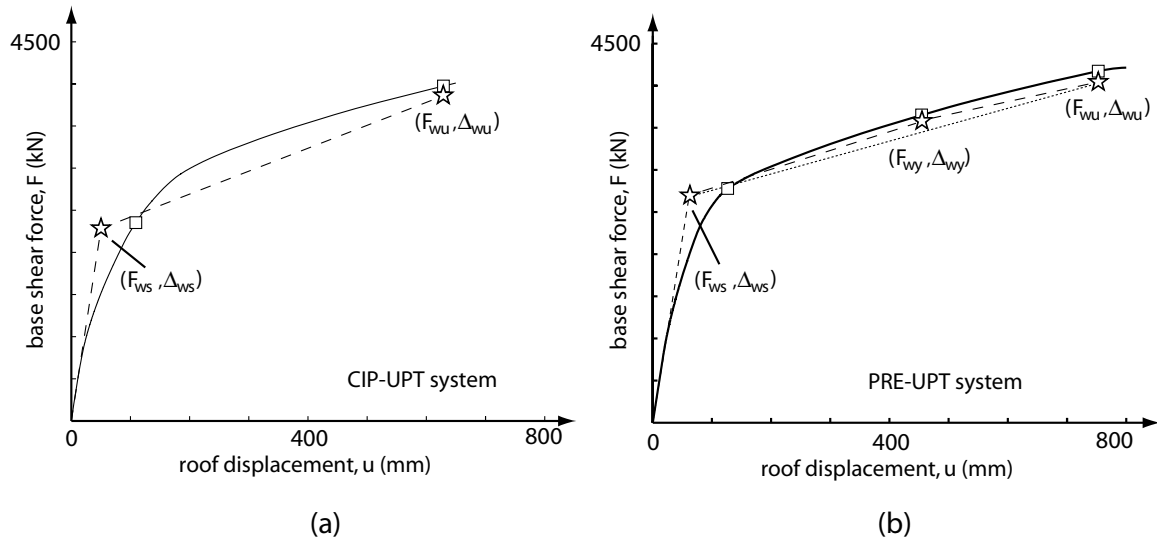


Fig. 11.6 Idealized base shear force versus roof displacement relationships:
(a) CIP-UPT system; (b) PRE-UPT system

Note that a trilinear idealized relationship is described in Chapter 8 and shown in Fig. 11.6b for the PRE-UPT structure; however, the SDOF BP model uses a bilinear relationship. Thus, the procedure demonstrated below utilizes only the coupled wall softening and ultimate states for the structures, and the PT-yielding state for the PRE-UPT system is ignored (dotted line in Fig. 11.6b). The results from the idealized MDOF base shear force versus roof displacement relationships, as well as the results from a linear-elastic modal analysis of the MDOF structures are given in Table 11.1 below.

TABLE 11.1
MDOF SYSTEM PROPERTIES

Structure	Wall Softening State		Wall Ultimate State		T_1 (sec.)	ξ_1	Γ	m_{eff} (kg)
	F_{ws} kN (kips)	u_{ws} mm (in.)	F_{wu} kN (kips)	u_{wu} mm (in.)				
CIP-UPT	2282(513)	50 (1.98)	3856 (867)	630 (24.8)	0.83	3%	1.42	1137000
PRE-UPT	2700(607)	62 (2.43)	4052 (911)	752 (29.6)	0.85	3%	1.42	1142000

where, m_{eff} is the effective first mode mass assigned to the coupled wall system (assumed to be equal to the total building effective first mode mass, M_{eff} divided by the number of coupled wall systems, n_w).

Then, the idealized MDOF base shear force versus roof displacement (F-u) relationships are used to determine BP models to represent the hysteretic characteristics of the structures. There are four independent unknowns for each BP model, F_{be} , u_{be} , α , and β_r , which can be combined with Equations (11.38) and (11.39) to determine the BE and EP components assuming $\beta_s = \beta_r$. Referring to Fig. 11.5, the four independent unknowns for a BP model are calculated using the following four relationships.

(1) The yield strength of the BP model is the same as the base shear capacity of the MDOF system at the coupled wall softening state. Thus,

$$F_{be}(1 + \beta_r) = F_{ws} \quad (11.40)$$

(2) The yield displacement of the BP model is the same as the roof displacement capacity of the MDOF system at the coupled wall softening state. Thus,

$$u_{be} = u_{ep} = u_{ws} \quad (11.41)$$

(3) The post-yield stiffness of the BP model is the same as the lateral stiffness of the MDOF system between the coupled wall softening and ultimate states. Thus,

$$\alpha(1 + \beta_r) \frac{F_{be}}{u_{be}} = \frac{F_{wu} - F_{ws}}{u_{wu} - u_{ws}} \quad (11.42)$$

Note that α represents the post-yield stiffness ratio of the combined BP model.

(4) The hysteretic energy dissipation of the BP model during a selected displacement cycle is the same as the energy dissipation from the smooth base shear force versus roof displacement relationship of the MDOF system during the same displacement cycle.

Let the hysteretic energy dissipation from the smooth MDOF base shear force versus roof displacement relationship during a roof displacement cycle to $\pm u_c$, measured by the area inside the hysteresis loop, be equal to E_{hc} . Then, it can be shown that,

$$4\beta_r F_{be}(u_c - u_{be}) = E_{hc} \quad (11.43)$$

Substituting Equations (11.40) and (11.41) into Equation (11.43), it can be shown that,

$$\beta_r = \frac{E_{hc}}{4F_{ws}(u_c - u_{ws}) - E_{hc}} \quad (11.44)$$

Note that an exact application of Equation (11.44) requires a smooth cyclic base shear force versus roof displacement relationship for the MDOF structure (to determine E_{hc}), which may not be available for design. In practical design applications, the use of an assumed value of β_r (based on the expected hysteretic characteristics of the structure) is typically adequate because of the relatively small effect of β_r on the seismic demands (Farrow and Kurama 2003, 2004). This is demonstrated in Chapter 12.

The properties of the idealized MDOF BP models for the CIP-UPT and PRE-UPT structures are determined using Equations (11.40), (11.41), (11.42) and (11.44) and presented in Table 11.2. As an example, Fig. 11.7a shows the cyclic base shear force versus roof displacement (F-u) relationship of the CIP-UPT structure using the fiber element model described in Chapter 6. The structure is subjected to roof displacements of $u=\pm 163$ mm, ± 245 mm, ± 326 mm, ± 408 mm, ± 489 mm, ± 571 mm, ± 652 mm, ± 734 mm, and ± 815 mm (corresponding to roof drift values of $\Delta=\pm 0.5\%$, $\pm 0.75\%$, $\pm 1.0\%$, $\pm 1.25\%$, $\pm 1.5\%$, $\pm 1.75\%$, $\pm 2.0\%$, $\pm 2.25\%$, and $\pm 2.5\%$, respectively). The displacement cycle to $u_c=\pm 489$ mm (thick lines in Fig. 11.7a) is used in Equation (11.44) above.

TABLE 11.2
IDEALIZED MDOF BP MODEL PROPERTIES

Structure	BE component			EP component		Combined BP model			
	F_{be} kN (kips)	u_{be} mm (in.)	$\alpha(1+\beta_r)$	F_{ep} kN (kips)	u_{ep} mm (in.)	F_{bp} kN (kips)	u_{bp} mm (in.)	β_r	α
CIP-UPT	1557 (350)	50 (1.98)	0.088	729 (164)	50 (1.98)	2282 (513)	50 (1.98)	0.47	0.060
PRE-UPT	2139 (481)	62 (2.43)	0.056	556 (125)	62 (2.43)	2700 (607)	62 (2.43)	0.26	0.045

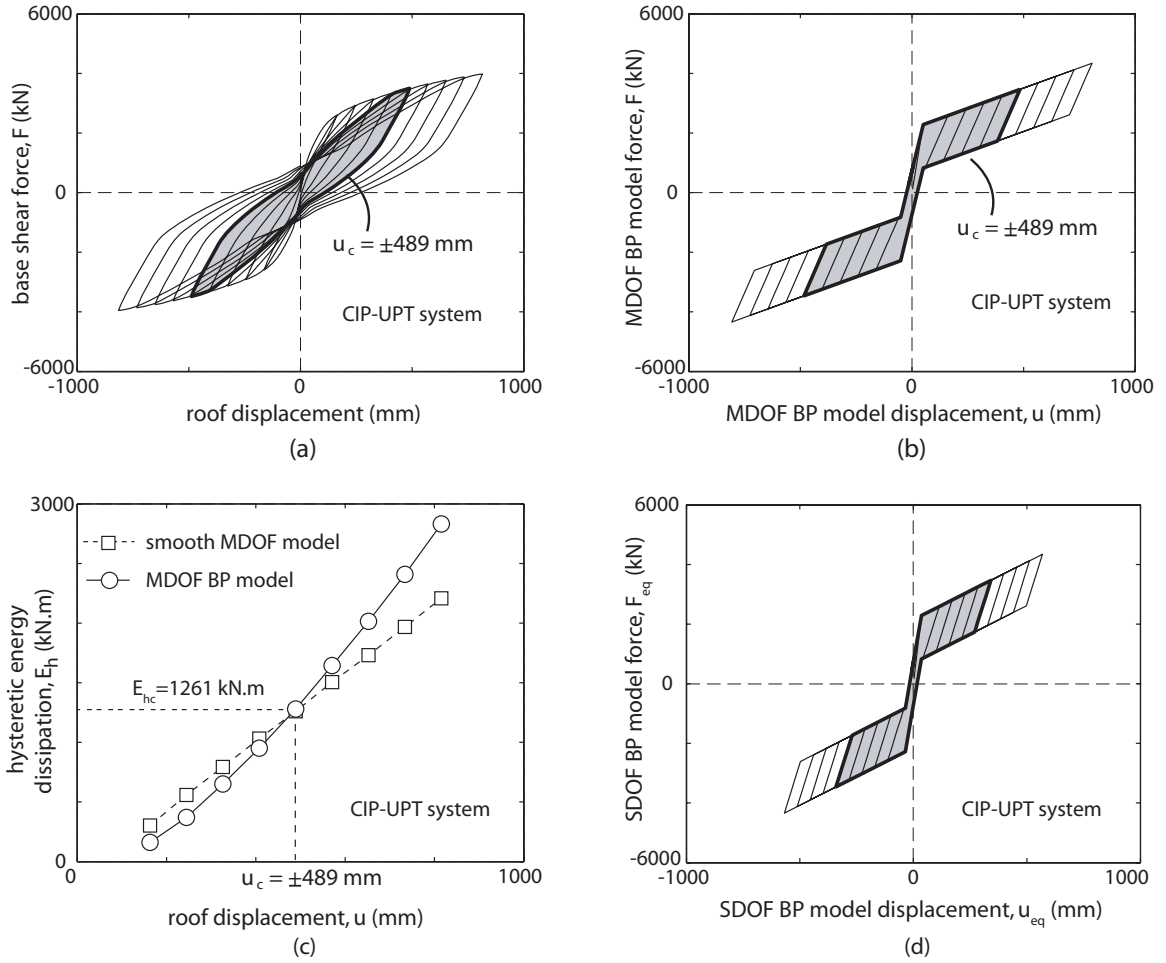


Fig. 11.7 Equivalent SDOF representation of CIP-UPT system: (a) smooth MDOF behavior; (b) MDOF BP model; (c) hysteretic energy dissipation; (d) equivalent SDOF BP model

Fig. 11.7b shows the cyclic force versus displacement (F - u) behavior of the idealized MDOF BP model. The thick lines indicate the selected roof displacement cycle to $u_c = \pm 489$ mm. The dashed and solid lines in Fig. 11.7c show the hysteretic energy, E_h dissipated by the smooth and idealized relationships (calculated as the area enclosed by each hysteresis loop) in Figs. 11.7a and 11.7b, respectively. The energy dissipations during $u_c = \pm 489$ mm are the same because of Equation (11.44). The energy dissipation of the idealized MDOF BP model is smaller than the energy dissipation of the smooth

model during smaller displacement cycles and larger than the energy dissipation of the smooth model during larger displacement cycles.

Finally, the properties of the equivalent SDOF BP model are determined by dividing the displacements of the MDOF BP model with the roof displacement participation factor, Γ as shown in Fig. 11.7d.

Similarly, Fig. 11.8 shows the development of an equivalent SDOF BP model for the PRE-UPT structure. Table 11.3 lists the equivalent SDOF BP model properties for the CIP-UPT and PRE-UPT structures.

TABLE 11.3
EQUIVALENT SDOF BP MODEL PROPERTIES

Structure	BE component			EP component		Combined BP model			
	F_{be} kN (kips)	u_{be} mm (in.)	$\alpha(1+\beta_r)$	F_{ep} kN (kips)	u_{ep} mm (in.)	F_{bp} kN (kips)	u_{bp} mm (in.)	β_r	α
CIP-UPT	1557 (350)	35 (1.39)	0.088	729 (164)	35 (1.39)	2282 (513)	35 (1.39)	0.47	0.060
PRE-UPT	2139 (481)	43 (1.71)	0.056	556 (125)	43 (1.71)	2700 (607)	43 (1.71)	0.26	0.045

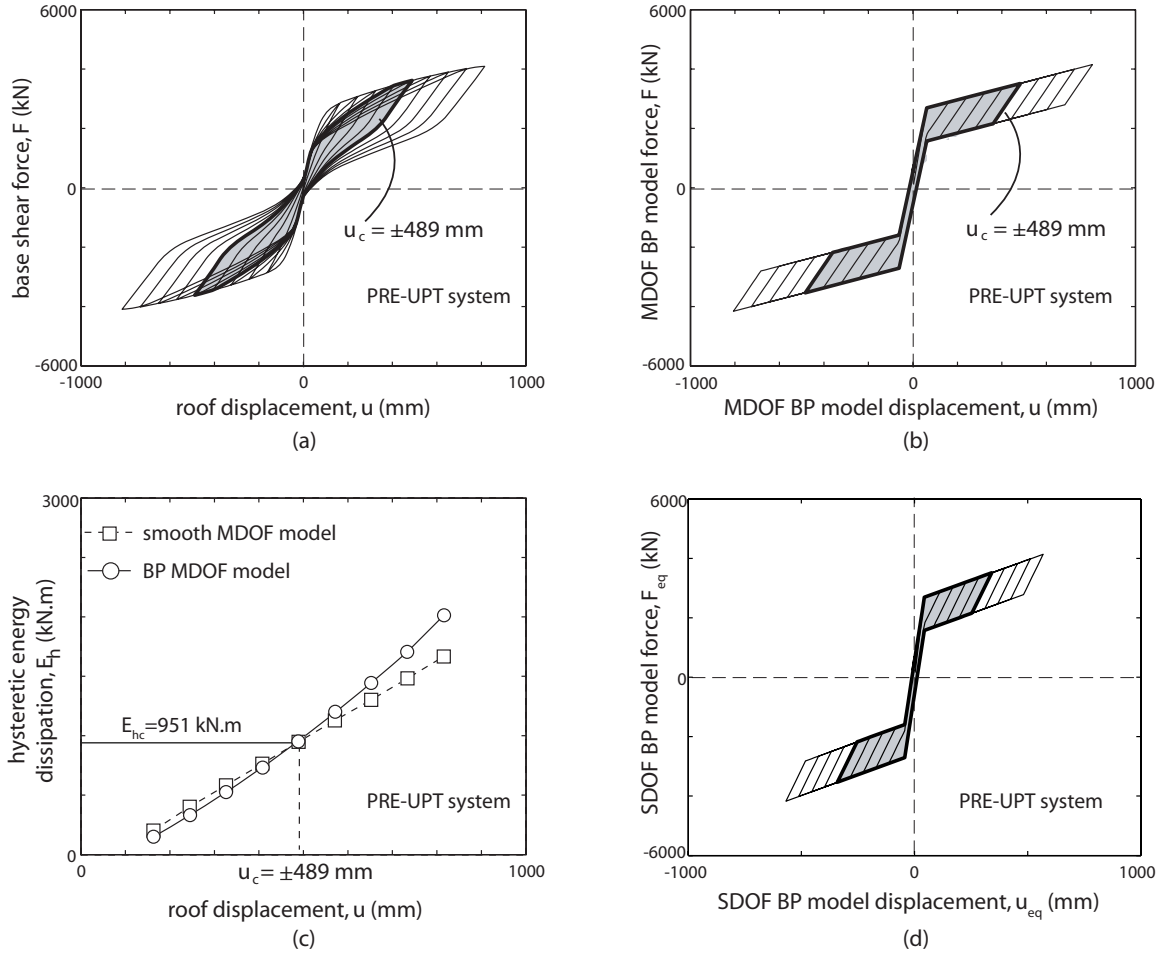


Fig. 11.8 Equivalent SDOF representation of PRE-UPT system: (a) smooth MDOF behavior; (b) MDOF BP model; (c) hysteretic energy dissipation; (d) equivalent SDOF BP model

11.10.4 Evaluation of Equivalent SDOF BP Model

In order to evaluate the capability of the SDOF BP hysteresis model to capture the nonlinear displacement response characteristics of unbonded post-tensioned hybrid coupled wall structures, nonlinear dynamic time-history analyses of the smooth MDOF and equivalent SDOF BP models for the CIP-UPT and PRE-UPT structures were conducted under 20 ground motion records (LA21-LA40) from the SAC Steel Project

(Somerville et al. 1997). More information on these ground motion records can be found in Chapter 14.

The equivalent SDOF analyses were conducted using the BP models given in Table 11.3 and shown in Figs. 11.7d and 11.8d for the CIP-UPT and PRE-UPT systems, respectively. The other dynamic properties of the equivalent SDOF systems are as follows:

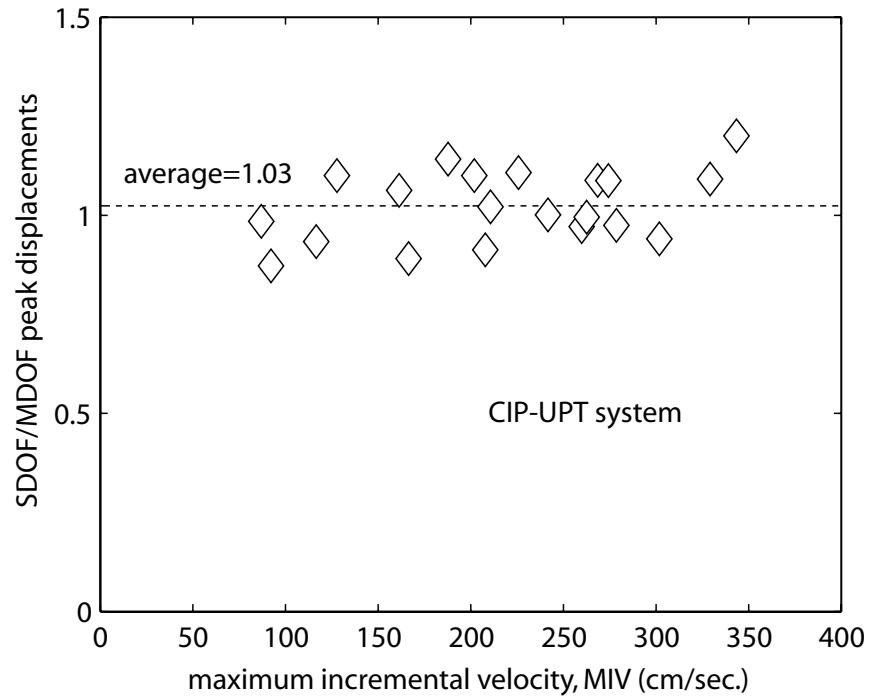
Equivalent BP model period = T_1 (see Table 11.1)

Equivalent BP model mass = m_{eff} (see Table 11.1)

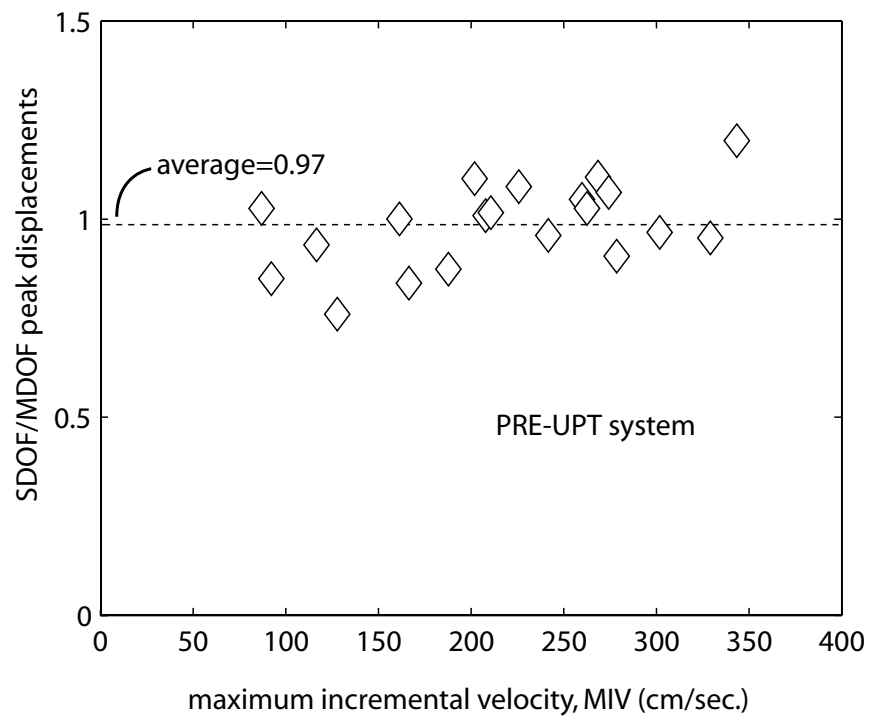
Equivalent BP model damping ratio = $\xi_1 = 3\%$ of critical damping (see Table 11.1).

Similarly, the MDOF analyses were conducted with a viscous damping ratio of 3% in the first and third modes (i.e., $\xi_1 = \xi_3 = 3\%$) using Rayleigh damping. The damping coefficients were calculated based on the linear-elastic properties of each structure and were kept constant during the nonlinear dynamic time-history analyses.

Figs. 11.9a and 11.9b show the ratios between the peak displacements from the SDOF and MDOF analyses of the CIP-UPT and PRE-UPT structures, respectively. Note that the displacements from the SDOF analyses are multiplied by the roof displacement participation factor, Γ . The results are plotted against the maximum incremental velocities (MIV) of the SAC ground motion records (LA21-LA40), where MIV for a ground motion is calculated as the maximum area under the acceleration time history of the record between two successive zero acceleration crossings. On average (dashed lines), the ratio between the peak displacements of the SDOF and MDOF systems is close to 1.0, with little scatter in the results from the 20 ground motions.



(a)



(b)

Fig. 11.9 Peak SDOF versus MDOF displacements:
(a) CIP-UPT system; (b) PRE-UPT system

Similarly, Figs. 11.10 and 11.11 show comparisons between the SDOF and MDOF roof-displacement time-histories for the CIP-UPT and PRE-UPT systems, respectively, under the 20 SAC ground motions (LA21-LA40). It is concluded that the nonlinear equivalent SDOF BP model is capable of predicting not only the peak roof displacements but also the roof-displacement time-histories of the structures reasonably well.

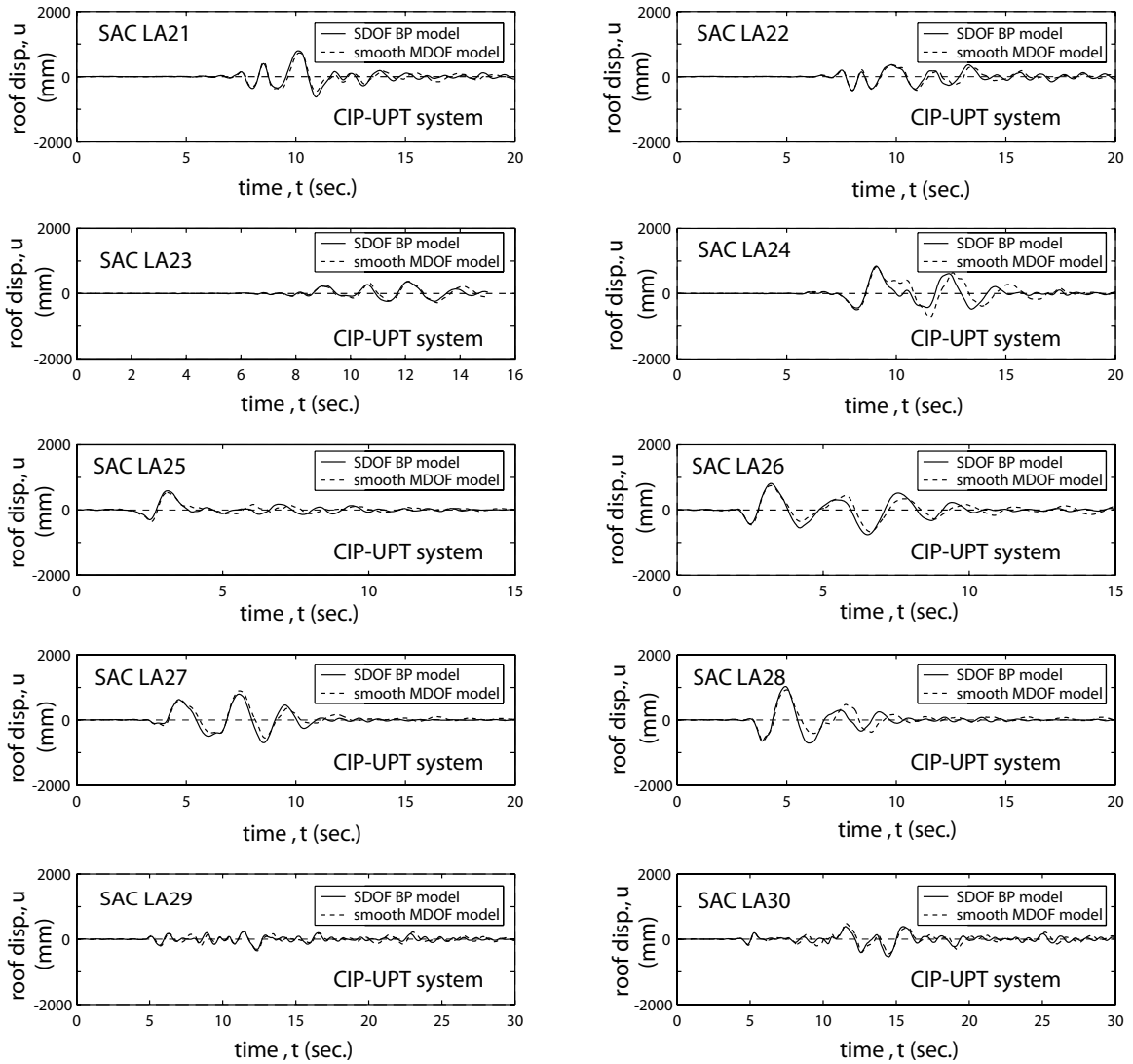


Fig. 11.10a SDOF and MDOF roof-displacement time-histories for CIP-UPT system (SAC LA21-LA30)

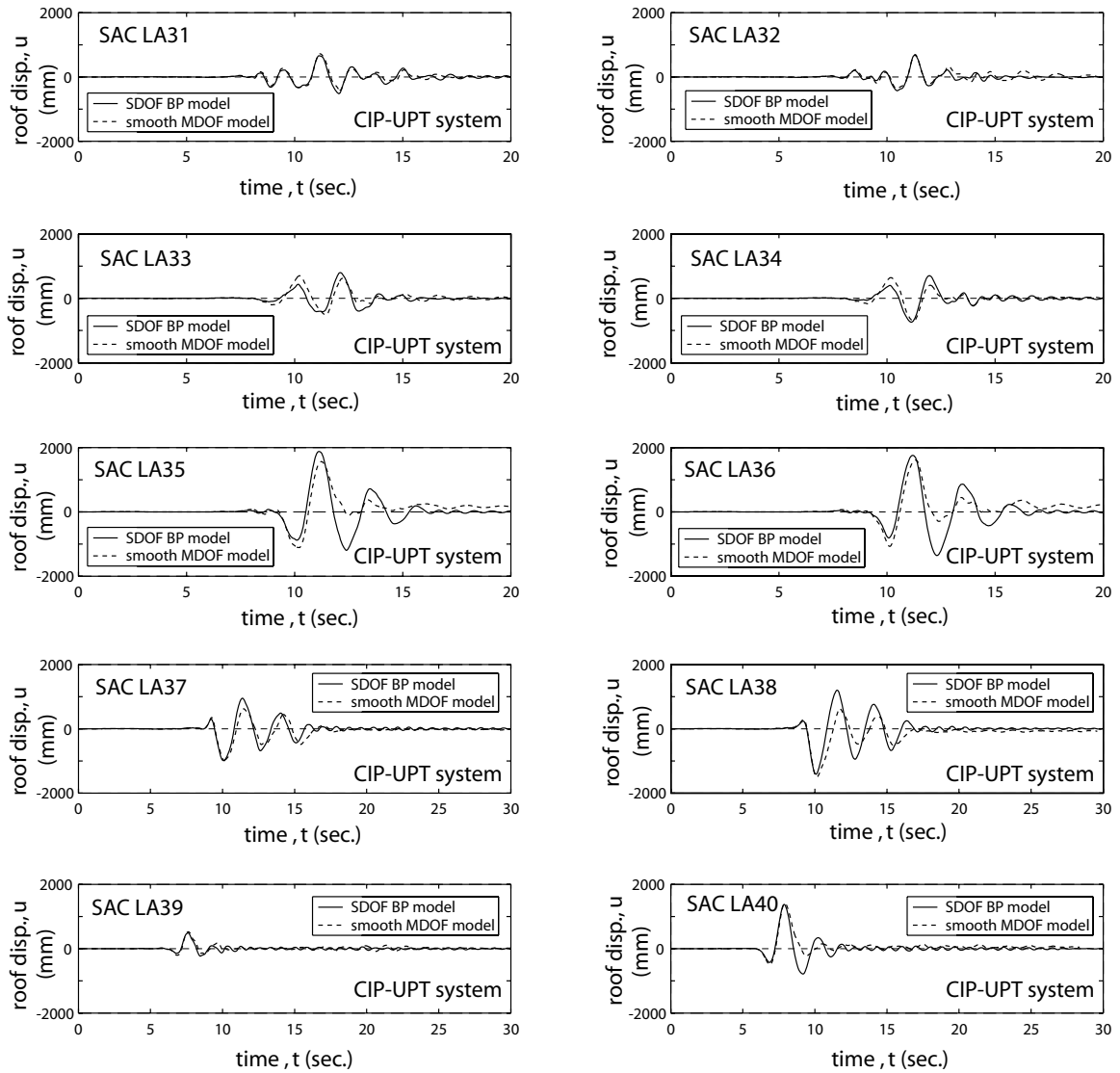


Fig. 11.10b SDOF and MDOF roof-displacement time-histories for CIP-UPT system (SAC LA31-LA40)

11.11 Seismic Displacement Demand Relationships

This section describes design relationships between the lateral strength and the mean peak lateral displacements of BP type SDOF models. These relationships are used to establish design demands for MDOF unbonded post-tensioned hybrid coupled wall structures, in lieu of conducting nonlinear dynamic time-history analyses.

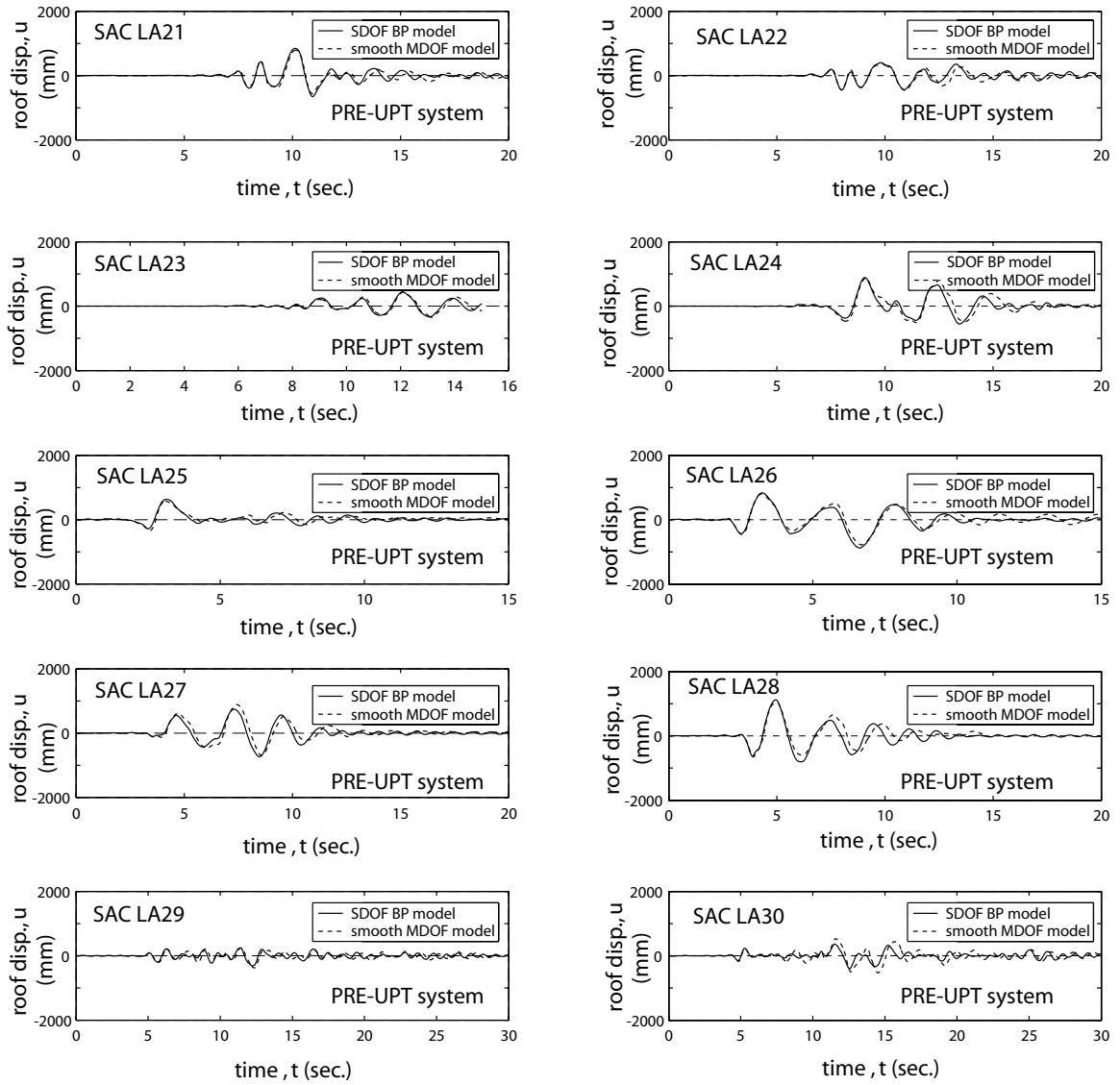


Fig. 11.11a SDOF and MDOF roof-displacement time-histories for PRE-UPT system (SAC LA21-LA30)

11.11.1 Previous Research

Peak nonlinear displacement demands for different types of hysteretic SDOF systems have been studied by many researchers (e.g., Newmark and Hall 1973; Newmark and Riddell 1980; Al-Sulaimani and Roessett 1985; Lin and Mahin 1985; Elghadamsi

and Mohraz 1987; Nassar and Krawinkler 1991; Miranda 1993; Priestley and Tao 1993; Rahn timer and Krawinkler 1993; Hall et al. 1995; Naeim 1995; Shome et al. 1998; Kwan and Billington 1999; Borzi and Elnashai 2000; Christopoulos et al. 2002; Farrow and Kurama 2001, 2003, 2004). These studies show that the SDOF peak displacement demand depends on structure (e.g., lateral strength, period, hysteretic behavior), site (e.g., soil type), and ground motion characteristics.

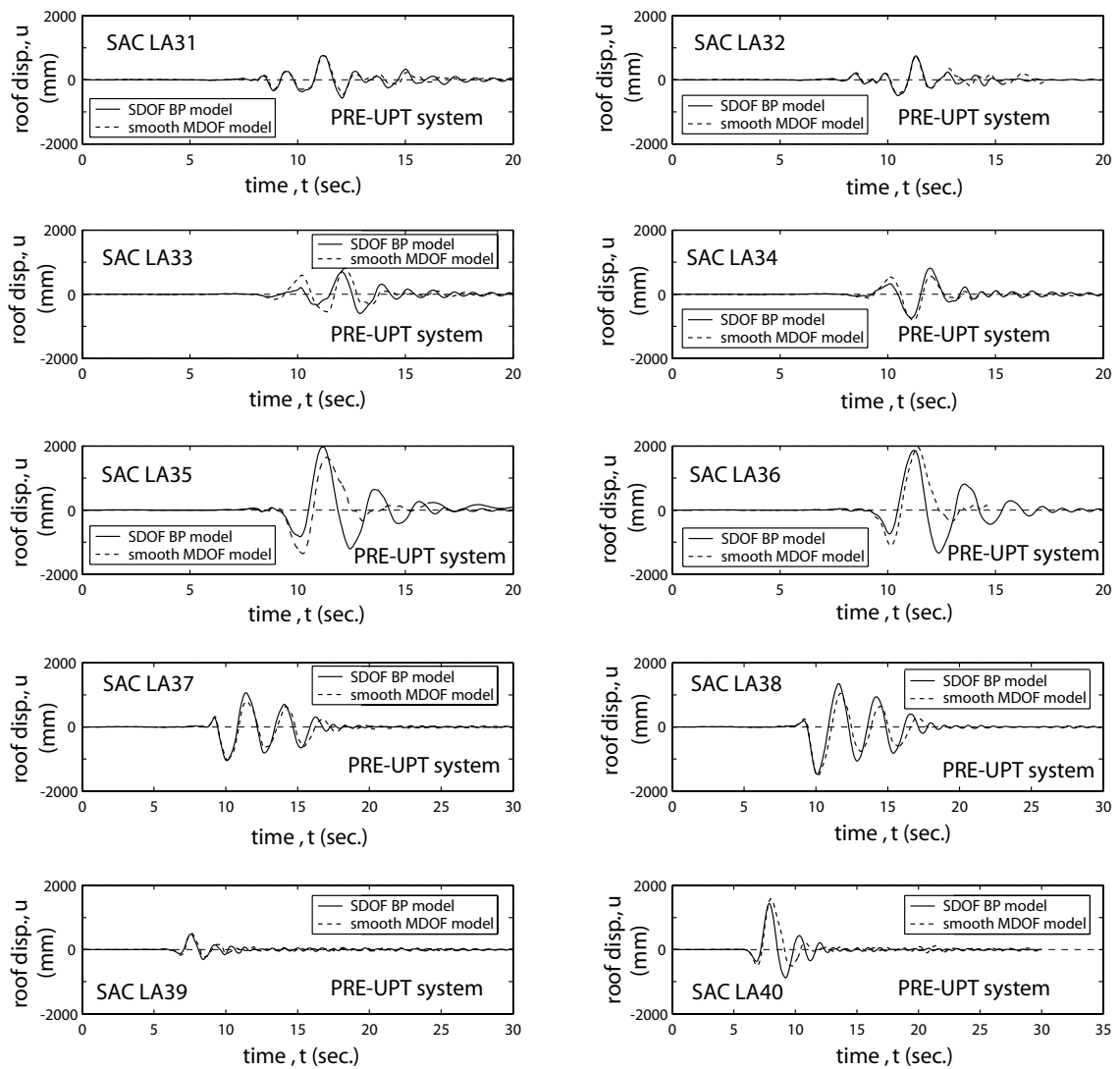


Fig. 11.11b SDOF and MDOF roof-displacement time-histories for PRE-UPT system (SAC LA31-LA40)

For medium and long period systems (i.e., $T \geq 0.5$ sec.) with no strength degradation, it has been shown that the peak displacement demand does not depend strongly on the lateral strength. In other words, for a given ground motion, a nonlinear system has approximately the same peak displacement demand as a corresponding linear-elastic system with the same period. For shorter periods (i.e., $T < 0.5$ sec.), the peak displacements tend to increase as the lateral strength of a structure decreases.

Previous studies on the development of relationships between the lateral strength, period, and peak displacement demands of SDOF systems have primarily considered models with significant hysteretic energy dissipation. These systems include bilinear elasto-plastic models and stiffness degrading models. An idealized bilinear lateral force-displacement relationship (Fig. 11.12) is often used with the yield strength, F_y , quantified with respect to the strength required to keep the structure linear-elastic during an earthquake (i.e., the linear-elastic force demand), F_{elas} , using the strength ratio, R_μ . The ductility demand, μ , provides an estimate of the peak nonlinear displacement demand of the structure, u_{nlin} and is usually presented in relationship to R_μ .

The hysteretic energy dissipation of unbonded post-tensioned hybrid coupled wall structures is typically smaller than bilinear elasto-plastic systems and stiffness degrading systems. As part of a comprehensive statistical investigation of SDOF demand index relationships for performance-based seismic design, Farrow and Kurama (2001, 2003, 2004) developed design relationships for the peak displacement demands of SDOF BP type models. These relationships relate the strength reduction factor R_μ to the peak displacement ductility demand μ and the SDOF period of vibration T using a two-step

nonlinear regression analysis scheme and the form of the regression equations from Nassar and Krawinkler (1991) as:

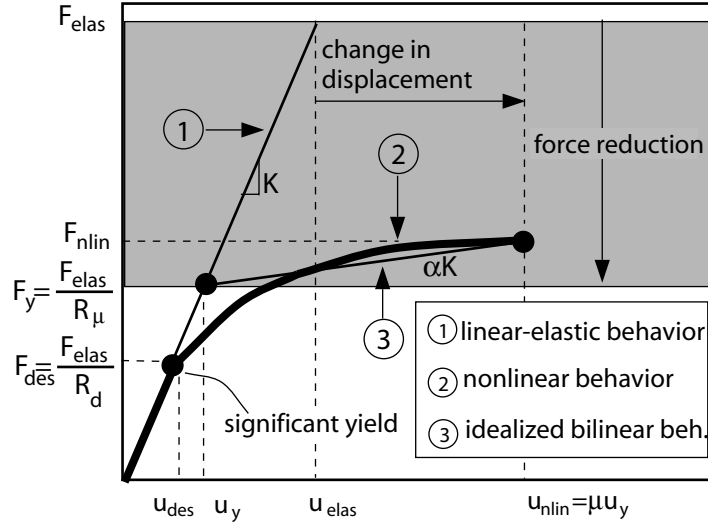


Fig. 11.12 Definitions of R_μ and μ (from Farrow and Kurama 2003)

$$R_\mu(\mu, T, \alpha) = [c(\mu - 1) + 1]^{1/c} \quad (11.45)$$

with,

$$R_\mu = \frac{F_{elas}}{F_y}, \quad \mu = \frac{u_{nlin}}{u_y} \quad (11.46)$$

$$c(T, \alpha) = \frac{T^a}{T^a + 1} + \frac{b}{T} \quad (11.47)$$

where, α is the post-yield stiffness ratio, μ is the displacement ductility demand, and a and b are regression coefficients determined from a statistical evaluation of SDOF nonlinear dynamic time-history analyses using the BP system.

The form of the regression relationship given by Equations (11.45-11.47) is based on a previous relationship proposed by Osteraas and Krawinkler (1990). The first step

regression is carried out in the R_μ - μ domain to relate the period, T and other parameter dependencies (i.e., hysteresis type and site conditions) to the c coefficient. The second step regression is carried out in the c - T domain to relate the parameter dependencies to the a and b coefficients. More information on the regression procedure to determine the design R_μ - μ - T relationships can be found in Farrow and Kurama (2001, 2003, 2004).

Note that the definition of R_μ in the proposed design approach is based on a point of “global yield” for the structure (i.e., F_y , u_y), which is different from the definition of the strength ratio in current U.S. seismic design provisions (referred to as the response modification factor, R_d) based on a point of “significant yield” in the lateral load system (i.e., F_{des} , u_{des} in Fig. 11.12). The definition based on the global yield point takes into account the over-strength in the structure, and thus, is expected to result in better measures of the seismic demands through u_y , instead of u_{des} .

Note also that the strength ratio R_μ in this research is used to quantify the structure yield strength. Current U.S. seismic design provisions (ICBO 1997, BSSC 1998, ICC 2000) are “force-based” and, in this context, provide prescribed R_d values to specify the required design strength of a structure. These force-based approaches may be replaced with displacement-based and performance-based approaches in future design provisions. In accordance with this transition, the use of R_μ in this dissertation is from a “displacement-based” perspective, where the problem of interest is the estimation of the required structure strength for a given target peak displacement ductility demand, μ_t . In this context, R_μ is used to quantify the yield strength F_y of the structure with respect to the linear-elastic force demand F_{elas} , and is considered as a ground-motion-dependent structure property, not as a code-specified constant.

11.11.2 Displacement Demand Relationships for SDOF BP Model

This section describes the development of peak seismic displacement demand (i.e., R_{μ} - μ - T) relationships for SDOF BP systems. A MATLAB (2000) algorithm, CDSPEC (Capacity-Demand SPECTra), was developed by Farrow and Kurama (2001a,b, 2003, 2004) to determine R_{μ} - μ - T relationships for various types of SDOF models, including BP type models. Ground motion ensembles from the SAC Steel Project (Somerville et al. 1997) were used and augmented by records generated at the University of Notre Dame to conduct statistical analyses of SDOF demands for selected seismic design conditions, including site soil type, site seismicity, and seismic demand level.

The CDSPEC program was used in this dissertation to develop R_{μ} - μ - T relationships [in the form of Equations (11.45), (11.46), (11.47)] for BP models considering a wider range of seismic design conditions than originally studied by Farrow and Kurama (2001, 2003, 2004). Farrow and Kurama (2004) used three different “reference” linear-elastic acceleration response spectra to calculate the linear-elastic force demand, F_{elas} for use in Equation (11.46) as follows: (1) individual (IND) response spectra of the ground motions used in each ensemble; (2) average (AVG) spectra of each ground motion ensemble; and (3) smooth design (DES) response spectra from model building seismic design provisions.

In the case of the IND spectra, F_{elas} is calculated as the structure mass times the spectral acceleration (at the structure period) from each ground motion in an ensemble. Thus, the structure lateral strength is recalculated for each ground motion in the ensemble. As described in Farrow and Kurama (2004), most of the previous research efforts on the development of peak SDOF displacement demand relationships are based on this method.

In the case of the AVG spectra, F_{elas} is calculated as the structure mass times the average spectral acceleration (at the structure period) from the ground motion ensemble. Thus, the same structure lateral strength is used for all of the ground motions in an ensemble. The AVG spectra provide an overall representation, in an average sense, of the ground motion characteristics in each ensemble.

In the case of the DES spectra, F_{elas} is calculated as the structure mass times the spectral acceleration (at the structure period) from a smooth design response spectrum. Thus, the structure lateral strength does not vary with the individual ground motions used in an ensemble, similar to the use of the AVG spectra described above.

The previous research on seismic displacement demand relationships has mostly used IND spectra to determine the structure lateral strength. In comparison, Farrow and Kurama (2001, 2004) argue that R_{μ} - μ - T relationships developed based on smooth DES spectra from current design codes (e.g., IBC 2000) are more suitable for use in seismic design. This is because, in practical seismic design applications, the lateral strength of a structure does not vary with the individual ground motions considered in an ensemble. R_{μ} - μ - T relationships from DES spectra utilize the design spectra used in the determination of the design base shear demand for the structure. Thus, the resulting seismic displacement demand estimates are compatible with the lateral strength of the structure.

Tables 11.4 and 11.5 show the a and b regression coefficients, corresponding to IND spectra and DES spectra respectively, for the R_{μ} - μ - T relationships developed as part of the proposed seismic design approach in this dissertation. Displacement demand relationships for the following seismic design conditions are developed:

TABLE 11.4
REGRESSION COEFFICIENTS A AND B FOR BP MODELS
(BASED ON IND SPECTRA)

Hysteresis Model	Site Seismicity	Demand Level	Site Soil Class	Regression Coefficient	
				a	b
BP ($\beta_r=1/3$, $\alpha=0.10$)	Los Angeles	Design	D	3.82	0.87
			E	0.65	1.02
		Survival	D	1.1*	0.89*
			E	-	-
	Seattle	Design	D	2.39	0.64
			E	0.61	0.68
		Survival	D	1.33	0.63
			E	-	-
	Boston	Design	D	0.92	0.61
			E	0.43	0.59
		Survival	D	0.93	0.62
			E	-	-
BP ($\beta_r=1/2$, $\alpha=0.10$)	Los Angeles	Design	D	3.52	0.84
			E	0.55	0.99
		Survival	D	0.96*	0.87*
			E	-	-
	Seattle	Design	D	2.15	0.61
			E	0.50	0.65
		Survival	D	1.21	0.60
			E	-	-
	Boston	Design	D	0.83	0.59
			E	0.34	0.56
		Survival	D	0.83	0.59
			E	-	-

Note: these a and b regression coefficients are also reported by Farrow and Kurama (2001, 2003).

- 1) Two types of BP models with $\beta_r=1/3$ and $\beta_r=1/2$.
- 2) One post-yield stiffness ratio, $\alpha=0.10$.
- 3) Three site seismicities – low seismicity (Boston), medium seismicity (Seattle), and high seismicity (Los Angeles).

4) Two seismic demand levels – design-level and survival-level. The design and survival seismic demand levels correspond to the “design-level” ground motion (with a 10% probability of exceedance in 50 years) and the “maximum considered earthquake” ground motion (with a 2% probability of exceedance in 50 years) in IBC 2000 (ICC 2000), respectively.

5) Two types of site soil characteristics – “stiff” soil and “soft” soil. The stiff and soft soil characteristics correspond to Site Classes D and E in IBC 2000 (ICC 2000), respectively.

The design-level and survival-level DES spectra used in the development of the regression coefficients in Table 11.5, and the spectral acceleration coefficients (S_{MS} , S_{M1} , S_{DS} , and S_{D1}) that define the DES spectra can be found in Farrow and Kurama (2001, 2004). The IND spectra used in the development of the regression coefficients in Table 11.4 are also given in Farrow and Kurama (2001, 2004).

TABLE 11.5
REGRESSION COEFFICIENTS *A* AND *B* FOR BP MODELS
(BASED ON DES SPECTRA)

Hysteresis Model	Site Seismicity	Demand Level	Site Soil Class	Regression Coefficient	
				<i>a</i>	<i>b</i>
BP ($\beta_r=1/3$, $\alpha=0.10$)	Los Angeles	Design	<i>D</i>	1.17	0.59
			<i>E</i>	0.93	0.96
		Survival	<i>D</i>	2.84*	0.88*
			<i>E</i>	-	-
	Seattle	Design	<i>D</i>	-1.03	0.29
			<i>E</i>	-3.12	0.32
		Survival	<i>D</i>	0.14	0.68
			<i>E</i>	-	-
	Boston	Design	<i>D</i>	-4.92	0.027
			<i>E</i>	-5.80	0.039
		Survival	<i>D</i>	-0.25	0.67
			<i>E</i>	-	-
BP ($\beta_r=1/2$, $\alpha=0.10$)	Los Angeles	Design	<i>D</i>	1.07	0.55
			<i>E</i>	0.84	0.94
		Survival	<i>D</i>	2.66	0.85
			<i>E</i>	-	-
	Seattle	Design	<i>D</i>	-1.19	0.24
			<i>E</i>	-3.44	0.27
		Survival	<i>D</i>	0.038	0.65
			<i>E</i>	-	-
	Boston	Design	<i>D</i>	-5.23	-0.012
			<i>E</i>	-6.09	-0.0029
		Survival	<i>D</i>	-0.35	0.64
			<i>E</i>	-	-

Note: these *a* and *b* regression coefficients are also reported by Farrow and Kurama (2001, 2004).

The dynamic analyses to determine the regression coefficients in Tables 11.4 and 11.5 were conducted following the procedure described in Farrow and Kurama (2001, 2003, 2004) using a viscous damping ratio of $\xi=5\%$, five strength ratios of $R_\mu=1$ (linear-elastic), 2, 4, 6, and 8, and thirty structure periods, exponentially spaced, between $T=0.1$ to 3.0 sec. A total of nine “far-field” ground motion ensembles were used (see Farrow

and Kurama 2001, 2003, 2004), corresponding to the site seismicities, seismic demand levels, and soil classes listed above. Each ensemble contains 20 ground motion records, resulting in a total of 180 records used in the SDOF dynamic time-history analyses. Note that regression coefficients were not developed for sites with a soft soil type under the survival demand level (blank cells in Tables 11.4 and 11.5), since IBC 2000 requires a site-specific geotechnical investigation and dynamic site response analyses for this condition.

The SDOF dynamic time-history analyses were conducted for selected values of R_μ , with the objective of determining the μ demands from each analysis. This approach is referred to as the “constant- R_μ ” approach in Farrow and Kurama (2001, 2004). In Nassar and Krawinkler (1991), the “constant- μ ” approach was used, where the objective is to determine the R_μ values required to limit the μ demand to pre-selected values. Unlike the constant- R_μ approach, for each pre-selected μ demand in the constant- μ approach, a series of nonlinear dynamic time-history analyses are conducted based on an initial value of R_μ , until the desired μ demand is obtained. Farrow and Kurama (2001, 2004) show that the constant- R_μ approach results in more conservative peak displacement demand relationships than the constant- μ approach.

The use of the displacement demand relationships developed above is demonstrated in the design of two prototype unbonded post-tensioned hybrid coupled wall structures in Chapter 12. Note that, as demonstrated by Farrow and Kurama (2001, 2003, 2004), the effect of structure hysteretic characteristics (e.g., α and β_r) on the peak displacement demands is small as compared with the effects of site seismicity, demand level, and soil type. Thus, the use of assumed values for α and β_r (based on the expected hysteretic

characteristics of the structure) is typically adequate for seismic design as shown in Chapter 12.

11.12 Nonlinear Static Procedure

This section describes the main steps of the nonlinear static procedure (NSP) used in the proposed seismic design approach.

11.12.1 Coupled Wall Design Base Shear Demand, Q_{wd}

The determination of the coupled wall design base shear demand, Q_{wd} requires that trial values are selected for the number, n_w and gross dimensions of the coupled wall systems in a building. Then, a linear-elastic modal analysis of the structure is conducted to determine the first (i.e., fundamental) mode shape, $\{\phi_1\}$ and period, T_1 . Alternatively, $\{\phi_1\}$ and T_1 may be estimated using approximate procedures [e.g., as described in the Equivalent Lateral Load procedure of IBC 2000 (ICC 2000)].

The coupled wall design base shear demand, Q_{wd} is determined by distributing the total design base shear demand, Q_{sd} for the entire building vertically over the height and horizontally to the lateral load resisting members in the plan of the structure as described in the Equivalent Lateral Force Procedure of IBC 2000. The total building design base shear demand, Q_{sd} is calculated as:

$$Q_{sd} = \max(Q_{ds}, Q_{dd}) = \max\left(\frac{M_{eff} f_{\xi} S_{as}}{R_{\mu s}}, \frac{M_{eff} f_{\xi} S_{ad}}{R_{\mu d}}\right) \quad (11.48)$$

where, Q_{ds} and Q_{dd} are the survival-level and design-level total building base shear demands, $M_{eff} = L_{eq}^2 / M_{eq}$ is the design effective linear-elastic first mode mass of the building (with $L_{eq} = \{\phi_1\}^T [M] \{1\}$ and $M_{eq} = \{\phi_1\}^T [M] \{\phi_1\}$ as described previously), f_ξ is a damping adjustment coefficient, S_{as} and S_{ad} are the site-adjusted linear-elastic design spectral response accelerations (based on $T_{eq} = T_1$) for the survival-level and design-level ground motions used in design (as determined from IBC 2000), and $R_{\mu s}$ and $R_{\mu d}$ are the survival-level and design-level strength ratios calculated based on an equivalent SDOF BP system used to represent the structure.

The damping adjustment coefficient f_ξ accounts for the difference (if any) in the assumed viscous damping ratio, ξ_1 for the structure being designed and the viscous damping ratio, ξ_o corresponding to the $S_{as}/R_{\mu s}$ and $S_{ad}/R_{\mu d}$ values used in design. For example, a value of $\xi_1 = 3\%$ is often assumed for dry-jointed precast concrete structures whereas the $S_{as}/R_{\mu s}$ and $S_{ad}/R_{\mu d}$ values from IBC 2000 are based on $\xi_o = 5\%$. The damping adjustment coefficient accounts for the difference between ξ_1 and ξ_o , and can be calculated as (AIJ 1993):

$$f_\xi = \sqrt{\frac{(1 + 25\xi_o)}{(1 + 25\xi_1)}} \quad (11.49)$$

For $\xi_o = 5\%$ and $\xi_1 = 3\%$, f_ξ is equal to 1.13. Note that this value is similar to the damping adjustment coefficients given in the FEMA 356 Prestandard and Commentary for the Seismic Rehabilitation of Buildings (FEMA 2000).

In accordance with the general principles of a displacement-based design approach, the strength ratios $R_{\mu s}$ and $R_{\mu d}$ are used to determine the required base shear strengths, Q_{ds} and Q_{dd} to limit the peak roof drift demands of the structure to below selected allowable

target roof drift values, Δ_{ts} and Δ_{td} for the survival and design seismic demand levels, respectively. This requires an iterative procedure for each selected allowable target roof drift as follows:

- 1) Assume survival-level and design-level displacement ductility demands, μ_{ts} and μ_{td} , corresponding to Δ_{ts} and Δ_{td} , respectively.
- 2) Determine $R_{\mu s}$ and $R_{\mu d}$ (corresponding to μ_{ts} and μ_{td}) from Equations (11.45)-(11.47) for the equivalent SDOF BP system assumed to represent the structure.
- 3) Determine the total building design base shear demand, Q_{sd} from Equation (11.48).
- 4) If Q_{ds} governs Q_{sd} in Step 3, then, calculate a revised $R_{\mu d} = (R_{\mu d} \text{ from Step 2})(Q_{dd}/Q_{sd})$ and determine the corresponding revised μ_{td} . If Q_{dd} governs Q_{sd} , then revise $R_{\mu s}$ instead.
- 5) Determine the coupled wall design base shear demand, Q_{wd} by distributing Q_{sd} vertically over the height and horizontally to the lateral load resisting members in the plan of the structure.
- 6) Estimate the nonlinear survival-level and design-level peak roof drift demands Δ_s and Δ_d of the structure as:

$$\Delta_s = \mu_{ts} \frac{Q_{wd}}{h_w K_{wi}} \quad (11.50)$$

$$\Delta_d = \mu_{td} \frac{Q_{wd}}{h_w K_{wi}} \quad (11.51)$$

where, h_w is the structure height and K_{wi} is the linear-elastic lateral stiffness of a coupled wall system.

- 7) Compare the estimated nonlinear roof drift demands Δ_s and Δ_d with the allowable drifts Δ_{ts} and Δ_{td} , respectively. Repeat Steps (1-6) if any of the allowable drifts, Δ_{ts} or Δ_{td} , is exceeded or if both Δ_s and Δ_d are significantly smaller than Δ_{ts} and Δ_{td} indicating an over-design. If the design objectives cannot be achieved, the trial wall and beam dimensions (e.g., wall length, l_w , and thickness, t_w) and/or the number of coupled wall systems, n_w in the structure may need to be revised.

The application of this iterative procedure to the design of two prototype coupled wall structures is presented in Chapter 12.

11.12.2 Vertical Distribution of Seismic Lateral Forces

This section describes the distribution of the total building design base shear force, Q_{sd} as lateral forces applied at the floor and roof levels over the height of the structure. The first linear-elastic mode shape of the structure, $\{\phi_1\}$ is used to determine the lateral force f_x applied at level x as follows:

$$f_x = C_{vx} Q_{sd} \quad (11.52)$$

with

$$C_{vx} = \frac{M_x \phi_{1x}}{L_{eq}} \quad (11.53)$$

where,

C_{vx} =vertical distribution factor

M_x = portion of the building seismic mass assigned to level x

ϕ_{1x} =coordinate of $\{\phi_1\}$ at level x

$$L_{eq} = \{\phi_1\}^T [M] \{\phi_1\}$$

$[M]$ =diagonal lumped mass matrix of the structure.

Alternatively, the Equivalent Lateral Force procedure described in IBC 2000 (ICC 2000) can be used to distribute the base shear force over the height of the structure.

11.12.3 Horizontal Distribution of Story Forces

Once the total building design base shear force is distributed over the structure height, then, the total design story shear force and story moment demands can be determined from the floor/roof lateral forces using equilibrium. The horizontal (i.e., in the plan of the structure) distribution of the design story shear and moment demands between the lateral load resisting systems in the structure depends on the in-plane stiffness of the floor/roof diaphragms. This dissertation focuses on the design of buildings that can be assumed to have “rigid” diaphragms (in the plane of the diaphragms). Thus, the horizontal distribution of the story forces is based only on the distribution of story mass and stiffness in the plan of the structure.

The horizontal distribution of the story forces should consider “applied” torsional moments resulting from the difference (if any) in the locations of the center of mass and center of stiffness at each floor or roof level under consideration. The center of mass (CM) is the location where the inertial forces generated at a floor/roof level are assumed to be concentrated and the center of stiffness (CS) represents the point where the application of a lateral force would cause only relative floor/roof translations without twist. Since the inertial forces act through CM rather CS, relative floor rotations (twist) as well as floor translations occur if CM and CS differ. For regular structures, CM and CS are at the same location over the height of the structure.

In addition, an “accidental” torsion may be introduced during the seismic response of a structure because of differences between the estimated and actual stiffnesses of the lateral load resisting members, different amounts of stiffness degradation in the lateral load resisting members during nonlinear response, differences between assumed and actual distributions and values for the floor and roof masses, etc. For this reason, allowance is made in IBC 2000 (ICC 2000) for an accidental torsional moment caused by an assumed re-location of the center of mass (in each orthogonal direction of the building) from its actual location by a distance equal to 5% of the dimension of the building perpendicular to the direction of the applied forces.

The portion of the building design story shear force resisted by one coupled wall system is given as:

$$Q_{wd} = vQ_{sd} \quad (11.54)$$

The distribution factor v can be expressed as:

$$v = v' + v'' \quad (11.55)$$

where, v' represents the effect of story translations and v'' represents the effect of story twist from applied and accidental eccentricities, $e = e_{app} + e_{acc}$. Since regular structures with no “applied” torsion are considered in this dissertation, $e_{app} = 0$ and $e = e_{acc}$ (equal to 5% of the dimension of the building perpendicular to the direction of the applied forces).

Based on the assumption of rigid floor and roof diaphragms, it can be shown that,

$$v' = \frac{K_{wi}}{K_{si}} \quad (11.56)$$

and

$$v'' = \frac{es_w K_{wi}}{\sum (s_l^2 K_{li})} \quad (11.57)$$

where, K_{wi} and K_{si} are the initial linear elastic lateral stiffnesses of the coupled wall system being designed and of the entire building, respectively, in the direction considered, s_w is the distance (in the perpendicular direction) of the shear center of the coupled wall system from the center of story stiffness (CS), and s_i and K_{ii} represent similar quantities to s_w and K_{wi} for all of the lateral load resisting systems in the plan of the structure (including the coupled wall systems and any other lateral load systems in both directions of the building). In determining v , the stiffnesses of the lateral load resisting systems in their weak (i.e., transverse) direction are ignored.

11.12.4 Load Combinations

The IBC 2000 (ICC 2000) provisions specify two load combinations (lc1 and lc2 below) for seismic design. In lc1, the effects of gravity loads and seismic loads are additive, and in lc2, the effects of gravity loads counteract the seismic load effects as follows:

$$\begin{aligned} \text{lc1: } & 1.2D+1.0E+0.5L+0.2S, \text{ where } E=\rho Q_E+0.2S_{DS}D, \text{ resulting in} \\ & (1.2+0.2S_{DS})D+\rho Q_E+0.5L+0.2S \end{aligned} \quad (11.58)$$

$$\begin{aligned} \text{lc2: } & 0.9D+1.0E, \text{ where } E=\rho Q_E-0.2S_{DS}D, \text{ resulting in} \\ & (0.9-0.2S_{DS})D+\rho Q_E \end{aligned} \quad (11.59)$$

where,

D = effect of dead load;

E = combined effect of horizontal and vertical seismic forces;

Q_E = effect of horizontal seismic forces;

S_{DS} = site-adjusted design-level spectral acceleration at short periods,
 $S_{DS}=(2/3)S_{MS}$;

ρ = reliability factor based on system redundancy as described in IBC 2000;

L = effect of live loads; and

S = effect of snow loads.

11.13 Maximum Base Shear Demand

The displacement-based seismic design procedure described in this chapter assumes that the nonlinear response of the structure is governed by the first (i.e., fundamental) linear elastic mode of vibration. While this assumption has been shown to provide reasonable estimates for the maximum displacement demands of most regular structures, the maximum base shear demands under earthquake loading may be grossly underestimated due to the effects of higher modes of vibration, especially in wall structures (e.g., Ghosh and Markevicius 1990; Aoyama 1993; Eberhard and Sozen 1993; Kabeyasawa 1993; Otani et al. 1994).

During a predominantly first-mode response of a wall structure under earthquake loading, the distribution of inertial forces is similar to the one shown in Fig. 11.13a. The force pattern is similar to that of standard code-specified equivalent lateral forces, with a resultant force located near $H=0.67h_w$ above the base (for regular structures). At some instants during the nonlinear vibrations of the structure, the response accelerations may be strongly influenced by the higher modes (especially the second and third modes), resulting in inertial force distributions similar to the one in Fig. 11.13b, with a resultant force located much closer to the wall base (as low as $H=0.3h_w$). For a flexural wall (i.e., a

wall with nonlinear behavior dominated by flexure rather than shear effects) with given base moment capacity, M_{wu} the resulting maximum base shear demand can be several times larger than the base shear demand estimated using the first mode distribution of inertial forces. The bending moment diagrams corresponding to the lateral force patterns in Figs. 11.13a and 11.13b are shown in Fig. 11.13c.

In the linear-elastic range of response, the maximum base shear demand during a ground motion can be determined from modal analysis. The modal base shear force, which is equal to the sum of the inertial forces that develop in that mode, can be determined as the product of the effective modal mass and the modal acceleration. The effective modal mass is the part of the total mass responding to the ground motion in that mode, and depends on the mode shape and mass distribution over height. The modal acceleration depends on the modal period and linear-elastic response acceleration spectrum (for a given value of viscous damping). The effective modal mass decreases for higher modes, and thus, in the linear-elastic range, the largest modal contribution to the total base shear demand is from the first mode, and the higher mode contributions are usually negligible.

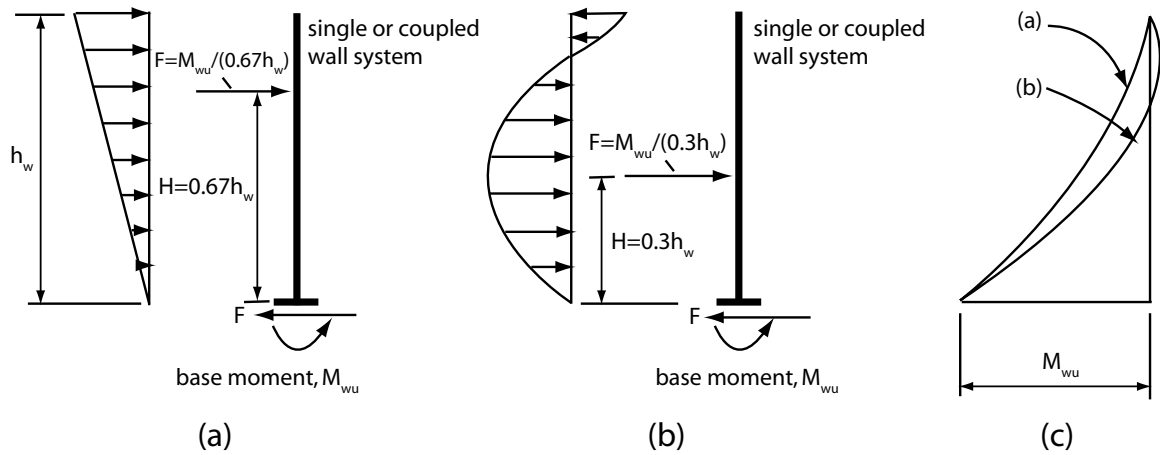


Fig. 11.13 Distribution of inertial forces: (a) $H=0.67h_w$; (b) $H=0.3h_w$; (c) bending moment diagrams (adapted from Paulay and Priestley 1992)

In the nonlinear range of response, the effect of higher modes on the maximum base shear demand increases. Nonlinear behavior results in a decrease in the lateral stiffness (i.e., softening) of the structure, which results in elongation of the modal periods. Period elongation typically results in a decrease in modal acceleration for the first mode and an increase in modal acceleration for the higher modes. Nonlinear behavior also changes the mode shapes, resulting in, for a typical wall, an increase in the effective modal mass for the first mode and a decrease in the effective modal mass for the higher modes. The effect of nonlinear behavior on the effective modal mass is small compared to the effect on the modal acceleration, and thus, the contribution of higher modes to the base shear demand increases and can be comparable to or even higher than the contribution of the first mode. In the nonlinear range of response under earthquake loading, the effect of higher modes on the maximum base shear demand of wall structures cannot be neglected.

Maximum base shear demands for unbonded post-tensioned hybrid coupled wall structures can be estimated using a method developed for uncoupled wall systems by Kabeyasawa (1993) and Aoyama (1993). In this method, the maximum base shear demand, $Q_{w,max}$ is estimated as the sum of a first mode component $Q_{1,max}$ and a higher mode component $Q_{h,max}$ as:

$$Q_{w,max} = Q_{1,max} + Q_{h,max} \quad (11.60)$$

The first mode component is estimated using the maximum base moment capacity (corresponding to the coupled wall ultimate state), M_{wu} and the resultant height of the first mode distribution of inertial forces, H_1 as:

$$Q_{1,max} = \frac{M_{wu}}{H_1} \quad (11.61)$$

The IBC 2000 (ICC 2000) distribution of equivalent lateral forces is similar to the first mode distribution of inertial forces and can also be used to determine H_1 .

The higher mode component of maximum base shear demand is estimated as:

$$Q_{h,max} = D_m m_w (PGA_s) \quad (11.62)$$

where, m_w is the total mass assigned to the coupled wall system (assumed to be equal to the total building mass, M divided by the number of coupled wall systems, n_w) and PGA_s is the peak acceleration for the survival-level ground motion.

The coefficient D_m depends on the mode shapes and mass distribution over the height of the structure. As described in Kurama (1997), the expression for D_m developed by Kabeyasawa (1993) and Aoyama (1993) can be written as:

$$D_m = \frac{m_w - m_{eff} + 0.7m_{eff,2}}{m_w} = 1 - \frac{m_{eff}}{m_w} + 0.7 \frac{m_{eff,2}}{m_w} \quad (11.63)$$

where, m_{eff} is the effective first mode mass and $m_{\text{eff},2}$ is the effective second mode mass assigned to the coupled wall system (assumed to be equal to the total building effective first and second mode masses, M_{eff} and $M_{\text{eff},2}$, respectively, divided by the number of coupled wall systems, n_w).

11.14 Chapter Summary

Performance-based seismic design requires estimates of structural capacities and seismic demands under different levels of seismic intensity. The main steps of the performance-based design procedure described in this chapter are summarized below. Application of this procedure to the design of two prototype structures is described in Chapter 12.

Step 1

Define the seismic demand levels, desired performance objectives, and allowable target roof drifts, Δ_{ts} and Δ_{td} , of the structure.

Step 2

Define the lateral system layout of the building, and then, select initial trial dimensions for the walls and the coupling beams.

Step 3

Perform a linear-elastic analysis of the structure to compute the linear elastic stiffnesses K_{wi} and K_{si} , first mode period, T_1 , first mode vibration shape, $\{\phi_1\}$, participation factor, Γ , and effective first mode mass, M_{eff} .

Step 4

Define the design acceleration response spectra and determine the survival-level and design-level response accelerations S_{as} and S_{ad} corresponding to the first mode period, T_1 .

Step 5

Select α and β_r parameters for an equivalent SDOF BP model to represent the structure.

Step 6

Assume survival-level and design-level displacement ductility demands, μ_{ts} and μ_{td} , corresponding to Δ_{ts} and Δ_{td} , respectively, and calculate strength ratios $R_{\mu s}$ and $R_{\mu d}$ from available R_{μ} - μ -T relationships for the equivalent SDOF BP model.

Step 7

Determine the total building design base shear force, Q_{sd} using the nonlinear static procedure described previously and revise $R_{\mu s}$ or $R_{\mu d}$ as necessary.

Step 8

Determine the coupled wall design base shear demand, Q_{wd} by distributing Q_{sd} vertically over the height and horizontally to the lateral load resisting members in the plan of the structure.

Step 9

Estimate the survival-level and design-level peak roof drift demands, Δ_s and Δ_d , of the structure and compare with the allowable target roof drifts, Δ_{ts} and Δ_{td} . If the design requirements cannot be achieved, the assumed μ_{ts} and μ_{td} values, trial wall and beam dimensions, and/or the number of coupled wall systems in the structure may need to be revised.

Step 10

Complete the detailed design of the concrete walls and the steel coupling beams to achieve a desired amount of coupling in each coupled wall system. This is described in Chapter 12. Consider all of the load combinations required by the governing model building code.

Step 11

Check all applicable seismic design criteria (i.e., acceptance criteria) to ensure that the target performance objectives are achieved (see Chapter 12).

CHAPTER 12

DESIGN OF PROTOTYPE STRUCTURES

This chapter describes the seismic design of two prototype unbonded post-tensioned hybrid coupled wall structures, referred to as Structures P1-CWUPT and P2-PWUPT, based on the performance-based design approach introduced in Chapter 11. The chapter is divided into the following sections: (1) design overview; (2) performance-based seismic design parameters; (3) linear-elastic structure properties; (4) design base shear demand; (5) preliminary design checks; (6) design of steel coupling beams; (7) design of wall piers in Structure P1-CWUPT; (8) design of wall piers in Structure P2-PWUPT; and (9) summary of design and final checks. The design of the prototype structures is critically evaluated in Chapters 13 and 15 based on nonlinear static analyses and nonlinear dynamic time-history analyses under a series of ground motion records representative of the seismic conditions used in the design.

12.1 Design Overview

Two eight-story office building structures are designed for a stiff soil site [corresponding to Site Class D in IBC 2000 (ICC 2000)] in Los Angeles, California. The plan view of the structures, which is identical for the two buildings, is shown in Fig. 12.1. The lateral load resistance of each structure in the E-W direction is provided by four identical unbonded post-tensioned hybrid coupled wall systems. This chapter focuses on

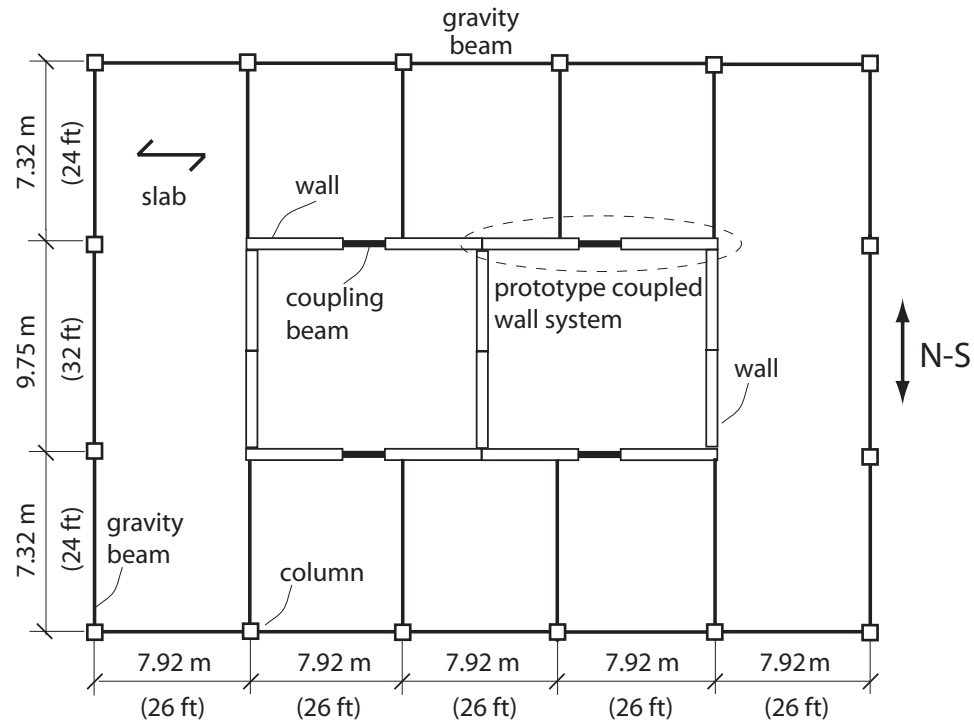


Fig. 12.1 Plan view of prototype buildings

the seismic design of these coupled wall systems. The seismic design of the lateral load resisting systems in the transverse N-S direction of the prototype structures is not addressed.

Two types of structures are considered: (1) with monolithic cast-in-place reinforced concrete wall piers (referred to as Structure P1-CWUPT); and (2) with precast concrete wall piers (referred to as Structure P2-PWUPT). These coupled wall systems are similar to the CIP-UPT and PRE-UPT systems described in Chapter 6, but the design properties are different.

The selection of the structure layout is based on the recommendations of the National Science Foundation *U.S.-Japan Cooperative Research Program on Composite*

and Hybrid Structures (Goel and Yamanouchi 1992). The center-to-center plan dimensions of the structure are $7.92 \text{ m} \times 5 \text{ bays} = 39.6 \text{ m}$ ($26 \text{ ft} \times 5 \text{ bays} = 130 \text{ ft}$) in the E-W direction and $9.75 \text{ m} \times 1 \text{ bay} + 7.32 \text{ m} \times 2 \text{ bays} = 24.4 \text{ m}$ ($32 \text{ ft} \times 1 \text{ bay} + 24 \text{ ft} \times 2 \text{ bays} = 80 \text{ ft}$) in the N-S direction.

The structure height is 32.6 m (107 ft) with 4.88 m (16 ft) for the first story and 3.96 m (13 ft) for the remaining seven stories. A summary of the general properties of the prototype structures is given in Table 12.1 and described below.

TABLE 12.1
GENERAL PROPERTIES OF THE PROTOTYPE STRUCTURES

Structure	n_w	h_w (m)	l_w (m)	t_w (mm)	l_b (m)	Beam section	d_b (mm)	b_{bf} (mm)	t_{bf} (mm)	t_{bw} (mm)	A_b (mm ²)	W (kN)	M (ton)	w_w (kN)	m_w (ton)
P1-CWUPT	4	32.6	4.88	356	2.13	W21× 147	560	318	29.2	18.3	27871	73712	7524	18428	1881
P2-PWUPT	4	32.6	4.88	356	2.13	W21× 147	560	318	29.2	18.3	27871	74568	7608	18642	1902

where, n_w is the number of coupled wall systems in the E-W direction, h_w , l_w , and t_w are the wall height, length, and thickness, respectively, l_b , d_b , b_{bf} , t_{bf} , t_{bw} , and A_b are the coupling beam length, depth, flange width, flange thickness, web thickness, and cross section area, respectively, W and M are the total building seismic weight and mass, and w_w and m_w are the seismic weight and mass assigned to one coupled wall system only, respectively.

12.1.1 Design Material Properties

The material properties used in the design of the prototype structures are as follows:

Cast-in-Place Concrete Wall Piers

Max. (i.e., peak) strength of unconfined conc. (normal wt.),	$f_c' = 41.4 \text{ MPa (6 ksi)}$
Young's modulus of wall concrete,	$E_c = 30441 \text{ MPa (4415 ksi)}$
Yield strength of mild steel reinforcement,	$f_{wsy} = 414 \text{ MPa (60 ksi)}$
Young's modulus of mild steel reinforcement,	$E_{ws} = 199955 \text{ MPa (29000 ksi)}$

Precast Concrete Wall Piers

Max. (i.e., peak) strength of unconfined conc. (normal wt.),	$f_c' = 41.4 \text{ MPa (6 ksi)}$
Young's modulus of wall concrete,	$E_c = 30441 \text{ MPa (4415 ksi)}$
Yield (i.e., linear-limit) strength of post-tensioning bars,	$f_{wpy} = 828 \text{ MPa (120 ksi)}$
Maximum (i.e., peak) strength of post-tensioning bars,	$f_{wpu} = 1035 \text{ MPa (150 ksi)}$
Young's modulus of post-tensioning bars,	$E_{wp} = 199955 \text{ MPa (29000 ksi)}$

Steel Coupling Beams

Yield strength of beam steel (A572 Grade 50 steel),	$f_{by} = 345 \text{ MPa (50 ksi)}$
Maximum strength of beam steel (A572 Grade 50 steel),	$f_{bm} = 448 \text{ MPa (65 ksi)}$
Young's modulus of beam steel,	$E_b = 199955 \text{ MPa (29000 ksi)}$
Yield strength of angle steel (A572 Grade 50 steel),	$f_{ay} = 345 \text{ MPa (50 ksi)}$
Young's modulus of angle steel,	$E_a = 199955 \text{ MPa (29000 ksi)}$
Yield (i.e., linear-limit) strength of post-tensioning strands,	$f_{bpy} = 1689 \text{ MPa (245 ksi)}$
Maximum (i.e., peak) strength of post-tensioning strands,	$f_{bpu} = 1862 \text{ MPa (270 ksi)}$
Young's modulus of post-tensioning strands,	$E_{bp} = 196508 \text{ MPa (28500 ksi)}$

12.1.2 Selection of Initial Dimensions for Structural Members

As described in Chapter 11, the proposed design approach requires the selection of initial dimensions for the structural members, provided below. Note that these initial dimensions may need to be modified during the detailed design of each structure.

Wall Piers

Each coupled wall system includes two identical concrete wall piers with rectangular cross sections. The wall pier length, $l_w=4.88$ m (16 ft) and wall thickness, $t_w=356$ mm (14 in.). The wall height, $h_w=32.6$ m (107 ft) with 4.88 m (16 ft) for the first story and 3.96 m (13 ft) for the upper stories. This results in a height, h_w to length, l_w aspect ratio of 6.69 for each wall pier.

Coupling Beams

To simplify the design process, the coupling beams at the floor and roof levels are assumed to be identical. A W21×147 section is selected, with length $l_b=2.13$ m (7 ft), depth $d_b=560$ mm (22 in.), and other geometric properties as provided in Table 12.1. This results in a coupling beam length, l_b to depth, d_b aspect ratio of 3.8.

Floor and Roof Slabs

For the structure with cast-in-place reinforced concrete wall piers (i.e., Structure P1-CWUPT), a 178 mm (7 in.) thick cast-in-place reinforced concrete slab is assumed for the floor and roof levels.

For the structure with precast concrete wall piers (i.e., Structure P2-PWUPT), 1.22 m \times 203 mm (4 ft \times 8 in.) hollow-core panels with 64 mm (2.5 in.) cast-in-place concrete topping is used for the floor and roof slabs. The hollow-core floor and roof panels span in the E-W direction.

Other Structural Members

Geometric properties of the other structural members in the prototype structures (i.e., walls in the N-S direction, gravity beams, and columns as shown in Fig. 12.1) are needed to estimate the total structure self weight. The gravity beams are assumed to have W24 \times 76 steel cross sections and the columns are assumed to have 610 mm \times 610 mm (24 in. \times 24 in.) concrete cross sections (for simplicity, the column size is assumed to be uniform over the structure height). The concrete walls in the transverse direction (N-S direction) are assumed to be 4.88 m (16 ft) long and 381 mm (15 in.) thick. Since the interaction between these structural members and the unbonded post-tensioned coupled wall systems in the prototype buildings is ignored, detailed design of the structural members other than the coupled wall systems is not addressed in this dissertation.

12.1.3 Design Gravity Loads and Seismic Weight

A summary of the gravity loads used in the design of Structures P1-CWUPT and P2-PWUPT is given below. The structures are assumed to have similar gravity loads.

Floor loads

Dead load: structure self weight + 1.44 kPa (30 psf) superimposed dead load

Live load: 2.39 kPa (50 psf)

Cladding: 8.03 kN/m (550 plf) on perimeter of building

Roof loads

Dead load: structure self weight + 1.44 kPa (30 psf) superimposed dead load

Live load: 0.57 kPa (12 psf)

Parapet: 8.03 kN/m (550 plf) on perimeter of building

Loads that are not considered include elevators, stairways, and any heavy equipment.

Based on the Precast/Prestressed Concrete Institute (PCI) Design Handbook (PCI 2004), the weight of the 1.22 m × 203 mm (4 ft × 8 in.) hollow core floor/roof slab panels in Structure P2-PWUPT is 2.68 kPa (56 psf) and the weight of the topping is 1.50 kPa (31 psf).

The 1.44 kPa (30 psf) superimposed dead load includes 0.96 kPa (20 psf) for partitions (ICBO 1997) and 0.48 kPa (10 psi) for ceiling, finish, electrical equipment, mechanical ducts, piping, etc.

The floor and roof live loads are taken from the American Society of Civil Engineers (ASCE) Standard for Minimum Design Loads for Buildings and Other Structures (ASCE 2003).

Based on Fig. 12.1 and the preliminary member dimensions, the seismic weights at the floor and roof levels of the prototype structures are calculated from the structure self weight plus the superimposed dead loads as shown in Table 12.2. The unfactored tributary floor/roof gravity dead and live loads for each coupled wall system are also provided in Table 12.2. Note that the dead and live loads are for the entire coupled wall system (two wall piers).

TABLE 12.2
SEISMIC WEIGHTS AND GRAVITY LOADS

Structure	Floor/Roof Level	Seismic Weights -entire building (kN)	Dead Loads -each coupled wall system (kN)	Live Loads -each coupled wall system (kN)
P1-CWUPT	roof	7953	659	33
	3 rd -8 th floor	9348	659	139
	2 nd floor	9672	731	139
P2-PWUPT	roof	8056	667	33
	3 rd -8 th floor	9456	667	139
	2 nd floor	9776	739	139

The floor and roof seismic weights in Table 12.2 are for the entire building. The resulting total building seismic weights (i.e., sum of the floor and roof seismic weights), W are shown in Table 12.1. The seismic weights, w_w for individual coupled wall systems are determined by dividing W with the number of coupled wall systems, n_w . The corresponding seismic masses, M and m_w are calculated by dividing the seismic weights, W and w_w by the gravitational acceleration, g .

12.1.4 Design Load Combination and Capacity Reduction Factors

No capacity reduction factors are applied in the design of the prototype structures. A single hypothetical load combination is used as follows:

$$\text{Design Load Combination: } 1.0D+0.25L+1.0Q_E \quad (12.1)$$

where,

D =effect of dead loads given in Table 12.2

L =effect of live loads given in Table 12.2 (including roof live load, with no live load reduction)

Q_E =effect of horizontal seismic forces

The 25% design live load is assumed to represent the amount of live load that may be acting on the structures during an earthquake. The analytical evaluation of the structures in Chapters 13 and 15 is also conducted under this hypothetical load condition. Note that code specified capacity reduction factors and load factors/combinations (e.g., ICC 2000, see Chapter 11) should be used in practice; however, this is not done in this dissertation to allow for more direct comparisons between the design estimations and the analysis results.

12.1.5 Design Scope and Limitations

Only the design of the coupled wall structures in the E-W direction of the prototype buildings is considered in this dissertation. The prototype buildings are assumed to have no plan or vertical irregularities and torsional loading effects (applied and accidental) are ignored. The floor and roof diaphragms are assumed to be rigid in their planes. The effect of the other structural members (e.g., floor/roof diaphragms, gravity system) on the behavior and design of the coupled wall structures is not considered.

12.2 Performance-Based Seismic Design Parameters

This section describes the parameters used in the performance-based seismic design of the prototype structures as follows: (1) allowable target roof drift demands; (2) allowable target inter-story drift demands; and (3) acceleration response spectra used in design.

12.2.1 Allowable Target Roof Drift Demands

The roof drift is defined as the lateral displacement of the structure at the roof level divided by the structure height. As described in Chapter 11, the proposed design approach requires the selection of allowable target roof drift demands for the “survival” and “design” seismic demand levels. The following allowable target roof drift demands are selected for the design of the prototype structures:

Survival-level demand, $\Delta_{ts}=1.75\%$

Design-level demand, $\Delta_{td}=1.17\%$

The design-level allowable roof drift demand, Δ_{td} is selected as 2/3 times the survival-level demand, Δ_{ts} in order to provide an adequate margin of safety between the life safety and collapse prevention performance levels used in design (see Chapter 11).

12.2.2 Allowable Inter-story Drift Demands

The inter-story drift is defined as the relative lateral displacement between two adjacent floor/roof levels in a structure divided by the story height. For wall structures, the inter-story drift demand is largest in the top story and is slightly larger than the roof drift demand. According to IBC 2000 (ICC 2000), the peak inter-story drift under the design-level earthquake should not exceed 2%. The 2% inter-story drift limit is often specified for controlling damage in basic access and life safety systems.

Because of the relatively small allowable target roof drift demands specified for design ($\Delta_{ts}=1.75\%$ and $\Delta_{td}=1.17\%$), it is expected that the peak inter-story drift demands of the prototype structures will satisfy the 2% limit in IBC 2000 (ICC 2000) not only for the design-level earthquake, but also for the survival-level earthquake. This is

investigated further in Chapter 15. For design purposes, allowable target inter-story drift demands of 2% and 1.33% are used for the survival and design seismic demand levels.

12.2.3 Acceleration Response Spectra Used in Design

The survival-level and design-level acceleration response spectra used in the design of the prototype structures are constructed based on the recommendations of IBC 2000 (ICC 2000) as described in Chapter 11. The mapped spectral response accelerations at short periods, S_s , and at 1 second period, S_1 , for the maximum considered earthquake (which is referred to as the survival-level earthquake in this dissertation) can be obtained from the contour maps in IBC 2000, from contour maps published by the Federal Emergency Management Agency (BSSC 1998), or from the United States Geological Survey (USGS 1996).

The S_s and S_1 values used in the design of the prototype structures (Table 12.3) were obtained from the online USGS National Seismic Hazard Mapping Project (USGS 1996) by specifying the latitude and longitude coordinates for the geographic center for Los Angeles. These acceleration coefficients were verified manually by inspecting hardcopy contour maps from IBC 2000.

TABLE 12.3

ACCELERATION RESPONSE SPECTRA

Site	S_s (g)	S_1 (g)	Site Soil	F_a	F_v	S_{MS} (g)	S_{M1} (g)	S_{DS} (g)	S_{D1} (g)	PGA_s (g)	PGA_d (g)
Los Angeles	2.05	0.81	Class D	1.0	1.5	2.05	1.22	1.37	0.81	0.82	0.55

Note: g, acceleration of gravity=9.81 m/sec.²(386 in./sec.²)

The site-adjusted survival-level spectral response accelerations for short periods, S_{MS} , and at 1 second period, S_{M1} (see Table 12.3) are determined by multiplying the S_s and S_1 values with the F_a and F_v site coefficients, respectively, for Site Class D.

Finally, the design-level spectral response accelerations at short periods, S_{DS} , and at 1 second period, S_{D1} (listed in Table 12.3) are determined by multiplying the S_{MS} and S_{M1} values by 2/3 (i.e., the “seismic margin”).

The resulting survival-level and design-level acceleration response spectra used in the design of the prototype structures are shown in Fig. 12.2. Note that these response spectra are the same as the DES spectra used to generate the a and b regression coefficients in Table 11.5 for Site Class D in Los Angeles.

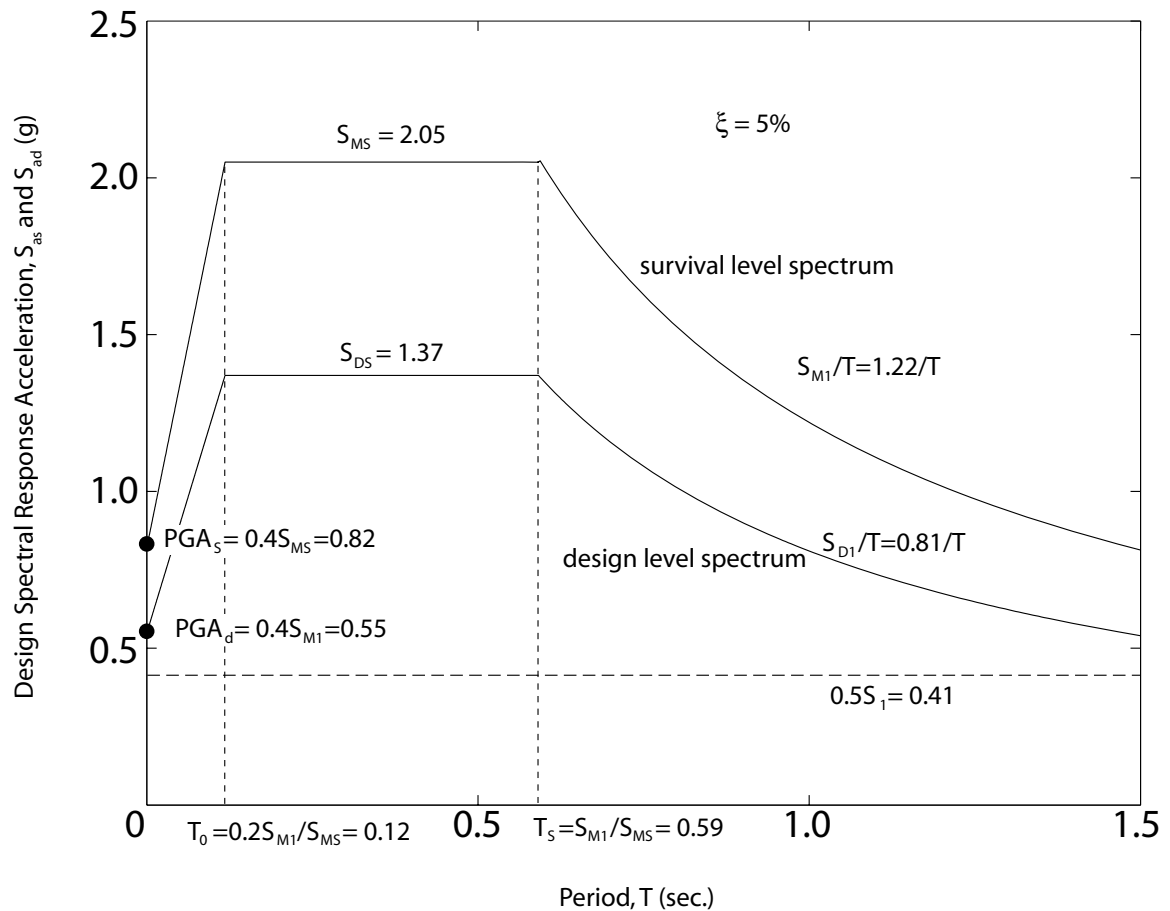


Fig. 12.2 Design-level and survival-level acceleration response spectra

Based on the provisions of IBC 2000 (ICC 2000), it is assumed that the prototype buildings are in Seismic Use Group I with an Occupancy Importance Factor of $I=1.0$. The buildings are assigned to Seismic Design Category E since $S_1>0.75g$. Note that for Seismic Design Category E, the spectral acceleration cannot be taken less than $0.5S_1=0.41g$. This limit is shown by the dashed horizontal line in Fig. 12.2.

12.3 Linear-Elastic Structure Properties

Linear-elastic analyses are conducted to determine the linear-elastic lateral stiffness, first (fundamental) vibration mode period and shape, and effective first and second mode masses of the prototype buildings. Out-of-plane and torsion effects are ignored, and it is assumed that the four coupled wall systems in the E-W direction of the buildings are connected through “rigid” floor and roof diaphragms.

12.3.1 Linear Elastic Stiffness

The linear-elastic lateral stiffness of the coupled wall systems, K_{wi} (i.e., slope of the base shear force versus roof displacement relationship in the initial linear-elastic range) in the prototype structures is estimated using the Matlab (2000) algorithm described in Chapter 8. Note that other appropriate structural analysis programs can also be used to conduct this linear-elastic analysis.

The input parameters to estimate K_{wi} include the gross wall and beam dimensions and the linear-elastic properties for wall concrete and beam steel. The deformations in the wall-contact regions adjacent to the coupling beams are ignored and the coupling beams

are assumed to be fixed to the walls with no top and seat angles. Shear deformations in the walls and the coupling beams are included.

The resulting linear-elastic stiffness of each coupled wall system, K_{wi} and of the building as a whole, K_{si} (determined by multiplying K_{wi} with the number of coupled wall systems, n_w) are given in Table 12.4. Note that the estimated lateral stiffnesses of Structures P1-CWUPT and P2-PWUPT are the same since the same dimensions and linear-elastic material properties are assumed for the lateral load resisting members in both structures.

TABLE 12.4
LINEAR-ELASTIC STIFFNESSES

Structure	K_{wi} (kN/mm)	K_{si} (kN/mm)
P1-CWUPT	105	420
P2-PWUPT	105	420

12.3.2 Period, Mode Shape, and Effective Mass

The Matlab algorithm described in Chapter 8 is also used to conduct linear-elastic modal analyses of the prototype structures. The structure seismic masses are lumped at the floor and roof levels, and are assumed to be distributed equally between the four coupled wall systems.

The resulting first mode period, T_1 , first mode shape, $\{\phi_1\}$, coupled wall effective masses for the first and second modes, m_{eff} and $m_{eff,2}$, and building effective masses for the first and second modes, M_{eff} and $M_{eff,2}$, are given in Table 12.5. The building effective

masses are determined by multiplying the coupled wall effective masses with the number of coupled wall systems, n_w in each building.

TABLE 12.5
LINEAR-ELASTIC MODAL ANALYSIS RESULTS

Structure	T_1 (sec.)	$\{\phi_1\}$ (base to roof)	m_{eff} (ton)	$m_{eff,2}$ (ton)	M_{eff} (ton)	$M_{eff,2}$ (ton)
P1-CWUPT	0.61	{0.0532 0.153 0.282 0.428 0.579 0.728 0.868 1.00}	1343	327	5372	1308
P2-PWUPT	0.62	{0.0532 0.153 0.282 0.428 0.579 0.728 0.868 1.00}	1360	331	5440	1324

12.4 Design Base Shear Demand

This section describes the determination of the coupled wall design base shear demand, Q_{wd} using the nonlinear static procedure outlined in Chapter 11.

12.4.1 Displacement Demand Relationships

As described in Chapter 11, an equivalent single-degree-of-freedom (SDOF) BP model is used to establish displacement ductility demand, μ relationships for the prototype structures. The form of the ductility demand relationship is:

$$R_\mu(\mu, T, \alpha) = [c(\mu - 1) + 1]^{1/c} \quad (12.2)$$

$$c(T, \alpha) = \frac{T^a}{T^a + 1} + \frac{b}{T} \quad (12.3)$$

BP model regression coefficients a and b for selected seismic design conditions are provided in Chapter 11. The coefficients used in the design of the prototype buildings, taken from Chapter 11, are listed in Table 12.6. Note that two sets of regression

coefficients, based on IND spectra and DES spectra, are provided in Chapter 11. The coefficients used in the design of the prototype structures are based on the DES spectra in Fig. 12.2, and thus, the resulting displacement demand estimates are expected to be compatible with the lateral strengths of the prototype structures. This is described in detail in Farrow and Kurama (2001, 2004).

It is assumed that the hysteretic characteristics of Structures P1-CWUPT and P2-PWUPT can be represented using SDOF BP models with $\beta_r=1/2$ and $\beta_r=1/3$, respectively. The larger β_r value used for Structure P1-CWUPT reflects the larger energy dissipation expected to occur near the bases of the cast-in-place wall piers in the structure, as compared with the smaller energy dissipation provided by the precast concrete wall piers in Structure P2-PWUPT. The post-yield stiffness for both structures is assumed to be equal to $\alpha=0.10$.

TABLE 12.6
DISPLACEMENT DEMAND RELATIONSHIPS

Structure	Period, T (sec.)	BP Model	Site Seismicity	Site Soil Class	Demand Level	Regression Coefficient (DES spectra)	
						<i>a</i>	<i>b</i>
P1-CWUPT	0.61	$\beta_r=1/2$, $\alpha=0.10$	Los Angeles	D	Survival	2.66	0.85
					Design	1.07	0.55
P2-PWUPT	0.62	$\beta_r=1/3$, $\alpha=0.10$	Los Angeles	D	Survival	2.84	0.88
					Design	1.17	0.59

Note that, as described in Chapter 11, the use of assumed values for α and β_r (based on the expected hysteretic characteristics of the prototype buildings) is often adequate for

seismic design, because of the relatively small effect of these parameters on the peak displacement demands. The most important factors affecting the displacement demands are the site seismicity, soil class, and demand level as discussed in Farrow and Kurama (2004).

12.4.2 Strength Ratios

The strength ratios, $R_{\mu s}$ and $R_{\mu d}$, for the survival and design seismic demand levels, respectively, are determined from Equations (12.2) and (12.3) using the a and b regression coefficients in Table 12.6, the estimated structure linear-elastic first mode period, T_1 (see Table 12.5), and the survival-level and design-level target displacement ductility demands, μ_{ts} and μ_{td} (corresponding to the allowable target roof drift demands, Δ_{ts} and Δ_{td} used in design).

For the prototype structures, the following target displacement ductility ratios are assumed for the survival and design seismic demand levels:

Survival-level demand, $\mu_{ts}=12$ corresponding to $\Delta_{ts}=1.75\%$

Design-level demand, $\mu_{td}=8$ corresponding to $\Delta_{td}=1.17\%$

The resulting strength ratios, $R_{\mu s}$ and $R_{\mu d}$, used in the design of the prototype structures are provided in Table 12.7.

TABLE 12.7
DISPLACEMENT DUCTILITY DEMANDS AND STRENGTH RATIOS

Structure	Demand Level	Δ_{ts} or Δ_{td} (%)	μ_{ts} or μ_{td}	$R_{\mu s}$ or $R_{\mu d}$
P1-CWUPT	Survival	1.75	12	6.2
	Design	1.17	8	6.1
P2-PWUPT	Survival	1.75	12	6.1
	Design	1.17	8	5.9

12.4.3 Building Design Base Shear Demands

As described in Chapter 11, the building design base shear demand, Q_{sd} is determined from:

$$Q_{sd} = \max(Q_{ds}, Q_{dd}) = \max\left(\frac{M_{eff} f_{\xi} S_{as}}{R_{\mu s}}, \frac{M_{eff} f_{\xi} S_{ad}}{R_{\mu d}}\right) \quad (12.4)$$

with the M_{eff} , $R_{\mu s}$, and $R_{\mu d}$ values for the prototype structures given in the previous sections. The survival-level and design-level site-adjusted linear-elastic spectral response accelerations, S_{as} and S_{ad} (corresponding to the period T_1 from Table 12.5) as determined from Figure 12.2, are listed in Table 12.8.

It is assumed that the prototype structures have a viscous damping ratio of $\xi_1=3\%$ in the first mode. Since the design spectra in Fig. 12.2 correspond to a viscous damping ratio of $\xi_0=5\%$, a damping adjustment coefficient, f_{ξ} equal to 1.13 (see Chapter 11), is used in Equation (12.4). The resulting building design base shear demands are provided in Table 12.8. It is observed that the lateral strength of both structures is governed by the survival-level demand.

TABLE 12.8
DESIGN BASE SHEAR DEMANDS

Structure	f_{ξ}	Demand Level	S_{as} or S_{ad} (g)	Q_{ds} or Q_{dd} (kN)	Q_{sd} (kN)	Q_{wd} (kN)
P1-CWUPT	1.13	Survival	1.99	19128	19128	4782
		Design	1.32	13113		
P2-PWUPT	1.13	Survival	1.98	19572	19572	4893
		Design	1.31	14441		

12.4.4 Coupled Wall Design Base Shear Demands

To allow for more direct comparisons between the design target seismic performance objectives and the estimated demands from the dynamic analyses in Chapter 15, the coupled wall design base shear demands, Q_{wd} are determined by distributing the total building design base shear demands, Q_{sd} equally between the coupled wall systems in each prototype structure as:

$$Q_{wd} = \frac{Q_{sd}}{n_w} \quad (12.5)$$

Thus, any torsional effects are ignored in the calculation of Q_{wd} . The resulting coupled wall design base shear demands for the prototype structures are provided in Table 12.8.

Note that in practice, the distribution of the building design base shear demand to the lateral load resisting members should be done based on the governing seismic design provisions, including any “applied” torsion (due to the differences between the center of mass and center of stiffness at the floor and roof levels) and “accidental” torsion (see Chapter 11).

12.5 Preliminary Design Checks

This section describes the preliminary design checks for the prototype structures prior to conducting a more detailed design of the wall and beam members as described later in the chapter. Three preliminary design checks are conducted: (1) peak roof drift demands; (2) peak inter-story drift demands; and (3) diagonal tension at wall pier bases.

12.5.1 Peak Roof Drift Demands

Once the coupled wall design base shear demands are determined, the trial structures are checked to verify that the displacement-based design objectives can be achieved. The peak lateral roof drift demands of the prototype structures are estimated based on the linear elastic stiffness, K_{wi} and the roof drift ductility demands, μ_{ts} and μ_{td} as:

$$\Delta_s = \mu_{ts} \frac{Q_{wd}}{h_w K_{wi}} \quad (12.6)$$

$$\Delta_d = \mu_{td} \frac{Q_{wd}}{h_w K_{wi}} \quad (12.7)$$

Note that since Q_{sd} and Q_{wd} for both structures are governed by Q_{ds} , the design-level strength ratios need to be revised as: $R_{\mu d} = (R_{\mu d} \text{ assumed in Table 12.7})(Q_{dd}/Q_{sd})$. The resulting revised $R_{\mu d}$ ratios and the corresponding revised design-level roof drift ductility demands from Equations (12.2) and (12.3) are given in Table 12.9.

The estimated survival-level and design-level roof drift demands, Δ_s and Δ_d for both prototype structures, also listed in Table 12.9, satisfy the allowable target roof drift demands, Δ_{ts} and Δ_{td} , respectively. Thus, the preliminary design checks for the peak roof drift demands of the structures are satisfied.

TABLE 12.9
PEAK ROOF DRIFT DEMANDS

Structure	Demand Level	Δ_{ts} or Δ_{td} (%)	$R_{\mu s}$ or $R_{\mu d}$	μ_{ts} or μ_{td}	Δ_s or Δ_d (%)
P1-CWUPT	Survival	1.75	6.2	12	1.67
	Design	1.17	4.2	5.1	0.71
P2-PWUPT	Survival	1.75	6.1	12	1.71
	Design	1.17	4.4	5.6	0.79

If the design requirements are not met (i.e., any of the allowable target roof drifts, Δ_{ts} or Δ_{td} , is exceeded or both Δ_s and Δ_d are significantly smaller than Δ_{ts} and Δ_{td} indicating an over-design), then, the assumed displacement ductility demands, μ_{ts} and μ_{td} , the trial wall and beam dimensions (e.g., wall length, l_w , beam length, l_b), and/or the number of coupled wall systems, n_w in the structures may need to be revised.

12.5.2 Peak Inter-story Drift Demands

The peak inter-story drift demands for the prototype structures are estimated based on the linear elastic deflected shape of each structure under the first mode lateral inertia force distribution. The inter-story drift demands are determined as the inter-story drifts in the top story (where the inter-story drift is largest over the structure height) when the roof drift reaches the estimated peak roof drift demand from Table 12.9, and are calculated as the average inter-story drifts of the left and right wall piers. The resulting peak inter-story drift demand estimates are shown in Table 12.10, together with the allowable target demands used in design. It is observed that both structures satisfy the inter-story drift demand requirements.

TABLE 12.10
PEAK INTER-STORY DRIFT DEMANDS

Structure	Demand Level	Allowable Demand (%)	Demand Estimate (%)
P1-CWUPT	Survival	2.00	1.92
	Design	1.33	0.81
P2-PWUPT	Survival	2.00	1.97
	Design	1.33	0.90

12.5.3 Diagonal Tension at Wall Pier Bases

To prevent shear (diagonal tension) failure of the concrete wall piers in the prototype structures, the diagonal tension capacity, $F_{w,dt}$ of the wall piers is required to be greater than the maximum wall pier base shear demand, $Q_{w,dt}$. Thus,

$$F_{w,dt} > Q_{w,dt} \quad (12.8)$$

For preliminary design, it assumed that 75% of the total maximum coupled wall base shear force demand, $Q_{w,max}$ is resisted by the compression-side wall, constituting the most critical condition for diagonal tension failure. Thus:

$$Q_{w,dt} = 0.75 Q_{w,max} \quad (12.9)$$

As described in Chapter 11, the maximum base shear demand, $Q_{w,max}$, of a coupled wall structure is calculated as the sum of a first mode component, $Q_{1,max}$, and a higher mode component $Q_{h,max}$ as:

$$Q_{w,max} = Q_{1,max} + Q_{h,max} \quad (12.10)$$

For the preliminary design of the prototype structures, the base shear demand for the first mode component is estimated as the design base shear demand, Q_{wd} , multiplied by an over-strength factor of 1.25 as:

$$Q_{1,max} = 1.25 Q_{wd} \quad (12.11)$$

The higher mode component of the maximum base shear demand, $Q_{h,max}$ is estimated as:

$$Q_{h,max} = D_m m_w (PGA_s) \quad (12.12)$$

with,

$$D_m = \frac{m_w - m_{eff} + 0.7m_{eff,2}}{m_w} = 1 - \frac{m_{eff}}{m_w} + 0.7 \frac{m_{eff,2}}{m_w} \quad (12.13)$$

where, m_w , PGA_s , m_{eff} , and $m_{eff,2}$ are given in Tables 12.1, 12.3, and 12.5. The resulting maximum coupled wall base shear demands for the prototype structures are listed in Table 12.11.

TABLE 12.11
DIAGONAL TENSION AT WALL PIER BASES

Structure	Demand Level	$Q_{l,max}$ (kN)	D_m	$Q_{h,max}$ (kN)	$Q_{w,max}$ (kN)	$Q_{w,dt}$ (kN)	$F_{w,dt}$ (kN)
P1-CWUPT	Survival	5976	0.41	6168	12144	9108	9261
P2-PWUPT	Survival	6116	0.41	6236	12352	9264	9261

Based on ACI 318-02 (ACI Committee 318 2002), the diagonal tension (shear) capacity of a concrete wall cannot be taken larger than

$$F_{w,dt} = 10A_w\sqrt{f'_c} \quad (12.14)$$

where, $A_w=l_wt_w$ is the gross cross-sectional area of a wall pier and f'_c is the compressive strength of unconfined concrete.

The largest attainable wall pier shear force capacities, $F_{w,dt}$ for both prototype structures, listed in Table 12.11, are greater than or sufficiently close to the corresponding maximum wall pier shear force demands, $Q_{w,dt}$. Thus, the preliminary design checks for the diagonal tension failure of the concrete wall piers are satisfied.

12.6 Design of Steel Coupling Beams

This section describes the detailed design of the coupling beams in the prototype structures. The design includes the following components: (1) design coupling beam shear force demand; (2) angle and post-tensioning contributions to coupling resistance; (3) coupling beam cross section; (4) beam post-tensioning; (5) top and seat angles and connections; (6) coupling beam shear force versus rotation behavior; (7) coupling beam rotation demands; (8) yielding of beam post-tensioning tendons; (9) fracture of top and seat angles; (10) shear slip at beam-to-wall interfaces; and (11) wall-contact regions.

The design approach aims to prevent the following failure modes in the structure: (1) yielding of the beam post-tensioning tendons or failure at the post-tensioning anchors; (2) local and/or global instability of the coupling beams; (3) fracture of the top and seat angles; (4) failure of the beam-to-wall, angle-to-wall, and angle-to-beam connections; and (5) failure of the concrete wall-contact regions.

Note that the discussion below is limited to coupled wall systems with two wall piers of the same length; however, it may be possible to extend the design recommendations to other wall configurations. As described previously, the coupling beams over the height of each structure are assumed to be identical.

12.6.1 Design Coupling Beam Shear Force Demand

The design coupling beam shear force demand, Q_{bd} is determined using the coupled wall design base shear demand, Q_{wd} (see Table 12.8). A target coupling degree, DOC, is selected for the structure, from which the design coupling beam shear force demand can be calculated as:

$$Q_{bd} = \frac{(DOC) Q_{wd} H}{1.05 n_b (l_w + l_b)} \quad (12.15)$$

where H is the resultant height of the equivalent lateral forces applied on the coupled wall system (based on the first mode distribution of inertial forces or the equivalent lateral force distribution from IBC 2000), n_b is the number of coupling beams over the height of the structure (usually equal to the number of stories), l_w is the length of a single wall pier, l_b is the coupling beam length, and the factor 1.05 is described in Chapter 8. The design parameters in Equation (12.15) are shown in Fig. 12.3.

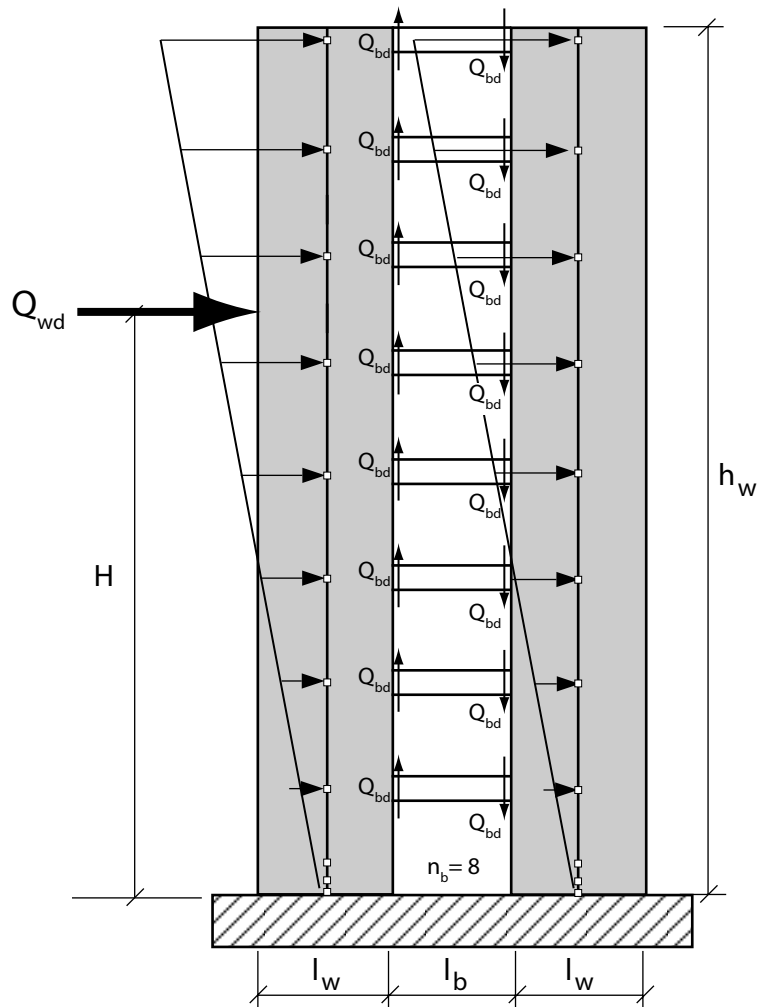


Fig. 12.3 Design coupling beam shear force demand

It is assumed that when the coupled wall design base shear demand, Q_{wd} is reached, the coupled wall system and the coupling beams are at their softening states as described in Chapters 8 and 10, respectively. Thus, the design approach requires that the coupling beam shear force capacity at the softening state, $V_{b,sof}$ be larger than the design coupling beam shear force demand, Q_{bd} as:

$$V_{b,sof} > Q_{bd} \quad (12.16)$$

A moderate level of coupling (e.g., $0.30 \leq \text{DOC} \leq 0.45$) is recommended for design, since over-coupling (e.g., $\text{DOC} \geq 0.60$) can cause excessive axial and shear forces in the wall piers as shown in Chapter 7.

A target coupling degree of $\text{DOC} = 0.35$ is selected for the design of the prototype structures. The resulting design coupling beam shear force demands, Q_{bd} are shown in Table 12.12.

TABLE 12.12
DESIGN COUPLING BEAM SHEAR FORCE DEMANDS

Structure	DOC	H (m)	Q_{bd} (kN)
P1-CWUPT	0.35	22.6	618
P2-PWUPT	0.35	22.6	654

12.6.2 Angle and Post-Tensioning Contributions to Coupling Resistance

Once the design coupling beam shear force demands for the prototype structures are determined, the next step is the design of the coupling beams to satisfy Equation

(12.16). For design purposes, the total coupling beam shear force demand, Q_{bd} is divided into two components as:

$$Q_{bd} = Q_{bd,a} + Q_{bd,p} \quad (12.17)$$

where, $Q_{bd,a}$ is resisted by the top and seat angles and $Q_{bd,p}$ is resisted by the beam post-tensioning steel.

Then, the coupling beam strength requirement in Equation (12.16) is re-written as:

$$V_{ba,sof} > Q_{bd,a} \quad (12.18a)$$

and

$$V_{bp,sof} > Q_{bd,p} \quad (12.18b)$$

where, $V_{ba,sof}$ represents the contribution of the top and seat angles to $V_{b,sof}$, and $V_{bp,sof}$ is the contribution of the beam post-tensioning force to $V_{b,sof}$.

Introducing the “angle strength ratio,” β_{ar} as:

$$\beta_{ar} = \frac{Q_{bd,a}}{Q_{bd,p}} \quad (12.19)$$

Then,

$$Q_{bd,a} = \frac{Q_{bd} \beta_{ar}}{\beta_{ar} + 1} \quad (12.20)$$

and

$$Q_{bd,p} = \frac{Q_{bd}}{\beta_{ar} + 1} \quad (12.21)$$

The proposed seismic design approach requires that a value for β_{ar} be selected for the structure. If the selected β_{ar} value is too large (i.e., the angle contribution is too large), then the coupling beams may not have enough restoring post-tensioning force to yield the

tension angles back in compression and close the gaps at the beam-to-wall interfaces. If the β_{ar} value is too small (i.e., the angle contribution is too small), then the energy dissipation of the system may be small.

For example, Figs. 12.4a-c show the beam shear force, V_b versus chord rotation, θ_b behaviors of three coupling beam subassemblages (similar to the subassemblages investigated in Chapters 3-5) under monotonic and cyclic loading. The angle behavior is assumed to be similar to the angle behavior described in Chapter 10. The solid lines on the right hand side of Fig. 12.4 show the monotonic beam shear force versus chord rotation behavior of each subassemblage and the dashed lines show the behavior of the same subassemblages with the angles removed.

The three subassemblages in Fig. 12.4 are designed to have similar coupling shear resistances; however, the beam post-tensioning steel areas, A_{bp} and the angle tension yield forces, T_{ayx} are varied (see Table 12.13), resulting in different angle and post-tensioning contributions (i.e., $V_{ba,sof}$ and $V_{bp,sof}$) to the total coupling shear resistance at the softening state ($V_{b,sof}$). The calculation of $V_{ba,sof}$ and $V_{bp,sof}$ is described later. The initial stress of the beam post-tensioning tendons in the three subassemblages is not varied in this investigation.

The angle strength ratios for the subassemblages, calculated as $\beta_{ar}=V_{ba,sof}/V_{bp,sof}$, vary between 0.66 and 1.27 (see Table 12.13). As the β_{ar} value is increased, the energy dissipation of the subassemblage increases (as indicated by the larger hysteresis loops in Fig. 12.4c as compared with Fig. 12.4a); however, the self-centering capability decreases (as indicated by the larger residual rotations of the subassemblage upon unloading). Thus,

β_{ar} is an important design parameter that influences the energy dissipation and self-centering capability of the coupling beams. Note, however, that the energy dissipation and self-centering capability of a multi-story coupled wall structure are affected by the properties of the concrete wall piers as well.

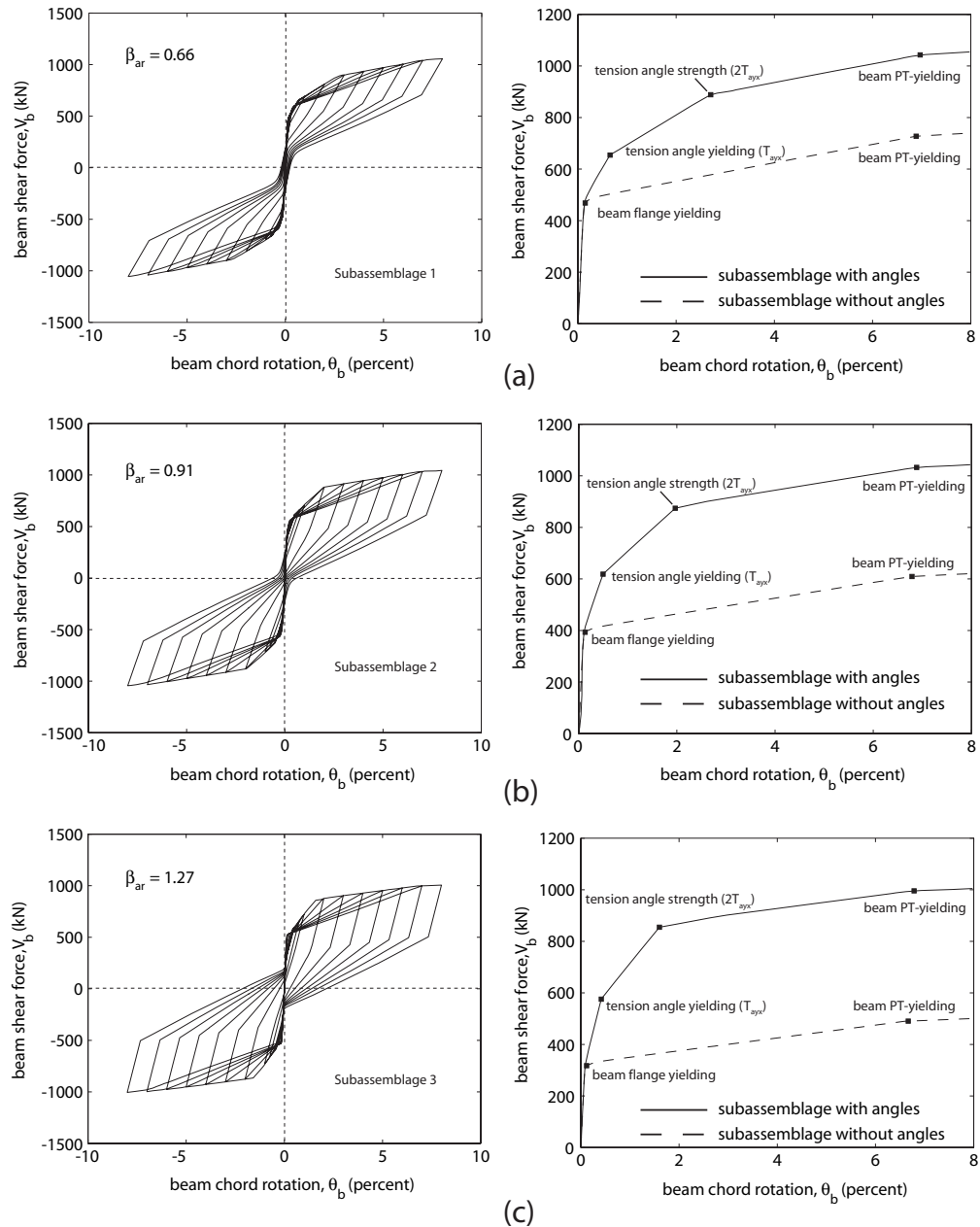


Fig. 12.4 Angle strength ratio, β_{ar} : (a) $\beta_{ar}=0.66$; (b) $\beta_{ar}=0.91$; (c) $\beta_{ar}=1.27$

TABLE 12.13

EFFECT OF β_{AR} ON COUPLING BEAM BEHAVIOR

Subassemblage	A_{bp} (mm ²)	T_{ayx} (kN)	$V_{b,sof}$ (kN)	$V_{ba,sof}$ (kN)	$V_{bp,sof}$ (kN)	β_{ar}
1	1680	273	774	307	467	0.66
2	1400	367	747	356	391	0.91
3	1120	440	716	400	316	1.27

The β_{ar} values used in the design of the prototype structures described in this chapter, as well as the resulting $Q_{bd,a}$ and $Q_{bd,p}$ values are provided in Table 12.14. A larger β_{ar} value is used for Structure P2-PWUPT in order to provide as much energy dissipation as possible through the top and seat angles, since the post-tensioned precast concrete wall piers are expected to provide little energy dissipation but a large amount of self-centering capability as shown in Chapter 7. Structure P1-CWUPT on the other hand uses a much smaller β_{ar} value to increase the self-centering capability of the entire coupled wall system through the beam post-tensioning tendons.

TABLE 12.14

COMPONENTS OF COUPLING BEAM DESIGN FORCES

Structure	β_{ar}	$Q_{bd,a}$ (kN)	$Q_{bd,p}$ (kN)
P1-CWUPT	0.051	30	588
P2-PWUPT	1.22	360	294

12.6.3 Coupling Beam Cross Section

The coupling beam cross section is determined based on Fig. 12.5a, which shows a preliminary free body diagram of the beam at the softening state, excluding the top and seat angle forces. It is assumed that: (1) flange cover plates are not used; (2) the neutral axis depth at the beam-to-wall interfaces is equal to the beam flange thickness, t_{bf} ; (3) the contact stresses at the beam ends have linear (i.e., triangular) distributions; and (4) the maximum beam contact stress is equal to the beam steel yield strength, f_{by} . Then, the coupling shear resistance due to the post-tensioning force, $V_{bp,sof}$ can be written as:

$$V_{bp,sof} = \frac{0.5 b_{bf} t_{bf} f_{by}}{l_b} \left(d_b - \frac{2t_{bf}}{3} \right) \quad (12.22)$$

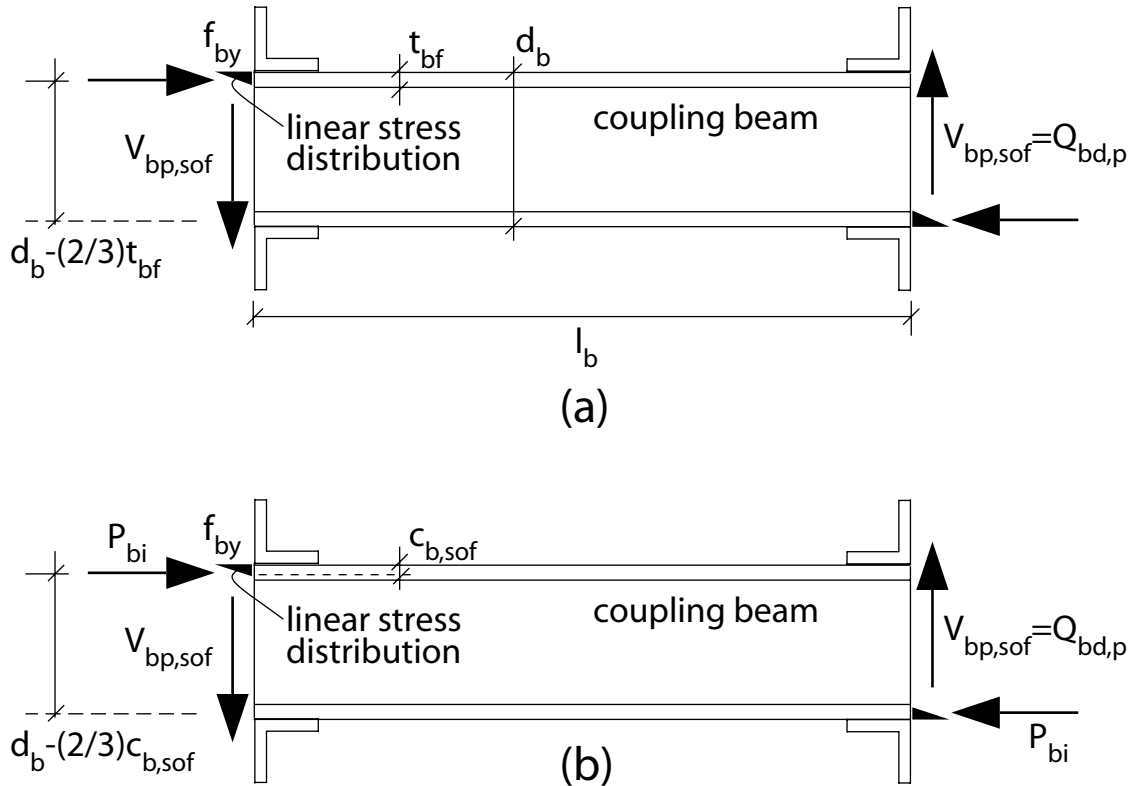


Fig. 12.5 Post-tensioning contribution to coupling resistance: (a) preliminary; (b) revised

For design, Equation (12.22) is used to select a beam cross-section with depth, d_b , flange width, b_{bf} , and flange thickness, t_{bf} , that satisfy the post-tensioning component of the design coupling beam shear force demand, $Q_{bd,p}$ as required in Equation (12.18b). The W21×147 cross section selected for the beams in the prototype structures satisfies this requirement.

In general, any cross section with compact web and flanges can be used for the coupling beams. Even though this dissertation focuses on beams with I-sections, other types of beams such as with hollow sections may also be used. The beam flange width, b_{bf} should not be larger than the wall thickness, t_w so that the entire flange is in contact with the wall.

12.6.4 Beam Post-Tensioning

The next step is the design of the beam post-tensioning tendons using the revised softening-state free body diagram in Fig. 12.5b. The total required initial beam post-tensioning force, P_{bi} is determined as:

$$P_{bi} = \frac{Q_{bd,p} l_b}{d_b - \frac{2}{3} c_{b,sof}} \quad (12.23)$$

where, $c_{b,sof}$ is the depth of the compression (i.e., contact) region at the beam end. The following assumptions are made in the expression for P_{bi} : (1) the beam post-tensioning force at the beam softening state is equal to the initial post-tensioning force, P_{bi} ; (2) the axial force in the beam is equal to the post-tensioning force; (3) the contact stresses at the beam ends have linear (i.e., triangular) distributions; and (4) the contact region is outside

the web. A non-rectangular compression region should be used if the contact region extends into the web.

The depth of the contact region at the beam softening state, $c_{b,sof}$, depends on the total compression force in the beam, which is assumed to be equal to P_{bi} . The effect of the top and seat angles is ignored and it is assumed that the largest compressive stress in the beam is equal to the yield strength of the steel, f_{by} . Then, the contact depth can be estimated as:

$$c_{b,sof} = \frac{2P_{bi}}{f_{by}b_{bf}} \quad (12.24)$$

Equations (12.23) and (12.24) are solved iteratively to determine P_{bi} and $c_{b,sof}$. An initial value of $c_{b,sof} = t_{bf}$ [similar to Equation (12.22)] can be used for this purpose, with convergence achieved in 5 to 10 iterations. Once P_{bi} is known, the total required beam post-tensioning steel area, A_{bp} , can be determined as:

$$A_{bp} = \sum a_{bp} = \frac{P_{bi}}{f_{bpi}} \quad (12.25)$$

where, f_{bpi} is the design initial stress in the post-tensioning steel. It is recommended that multi-strand tendons are used with f_{bpi} not more than $0.6f_{bpu}$, where f_{bpu} is the design maximum strength of the strands.

The total number of beam post-tensioning strands and tendons can be determined from:

$$n_{bp}n_{bt} = \frac{P_{bi}}{a_{bp}f_{bpi}} \quad (12.26)$$

where, n_{bt} is the number of post-tensioning tendons, n_{bp} is the number of strands per tendon, and a_{bp} is the area of a single strand. In the design of the prototype structures,

$\varnothing 15$ mm (0.6 in.) diameter post-tensioning strands with $a_{bp}=140$ mm² (0.217 in²) and $f_{bpi}=0.6f_{bpu}$ are used. The placement and distribution of the post-tensioning strands and tendons is depicted in Fig. 12.6 and the design is summarized in Table 12.15. Two eight-strand tendons are used in Structure P1-CWUPT, while only one eight-strand tendon is necessary in Structure P2-PWUPT as a result of the larger β_{ar} value used as described previously.

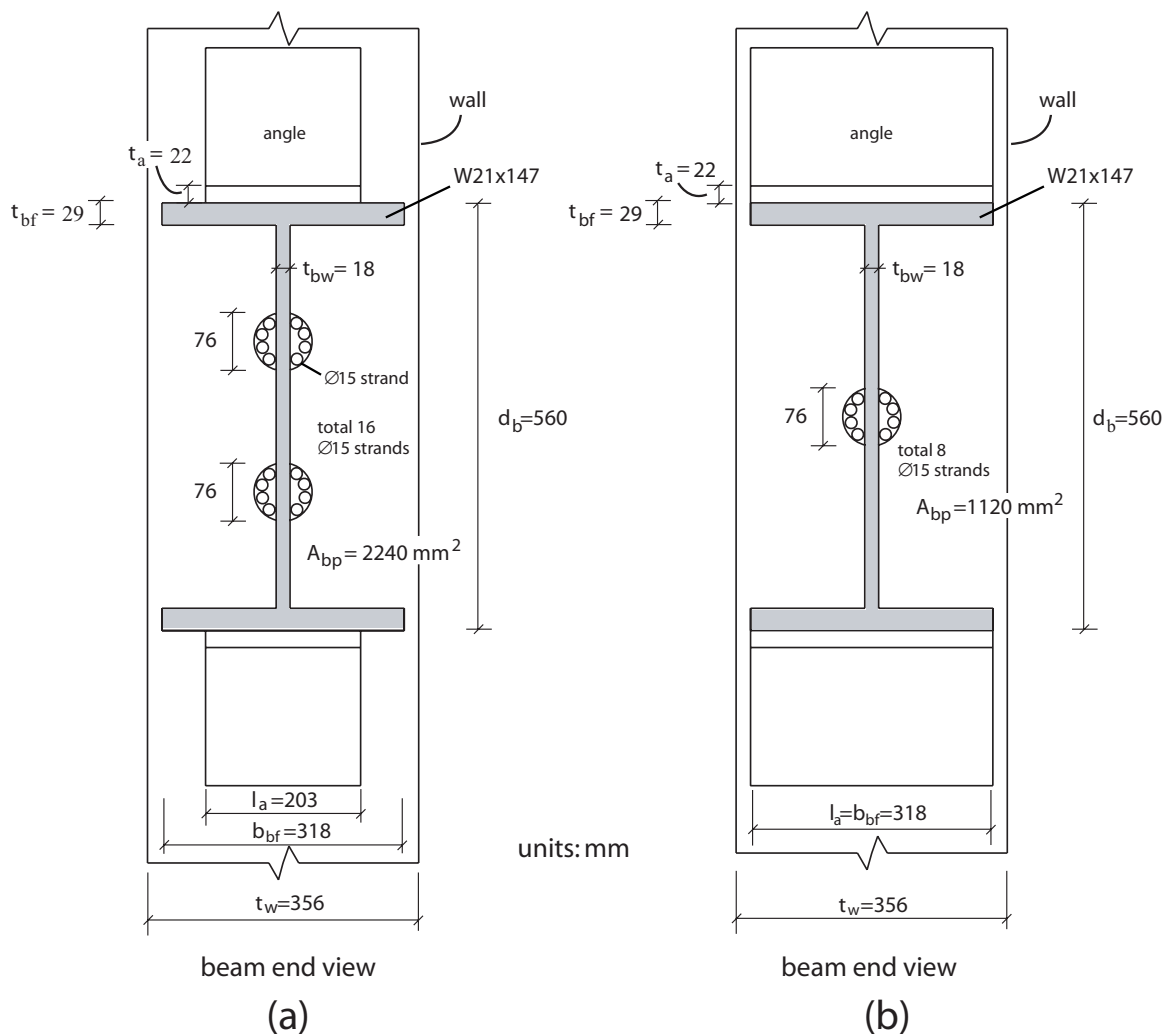


Fig. 12.6 Coupling beam and post-tensioning details:
(a) Structure P1-CWUPT; (b) Structure P2-PWUPT

TABLE 12.15

BEAM POST-TENSIONING

Structure	n_{bt}	n_{bp}	A_{bp} (mm ²)	P_{bi} (kN)	P_{by} (kN)	P_{bu} (kN)	$A_{bc}f_{by}$ (kN)	$A_{bc}f_{bm}$ (kN)	$c_{b,sof}$ (mm)	$V_{bp,sof}$ (kN)	$Q_{bd,p}$ (kN)
P1-CWUPT	2	8	2240	2500	3784	4170	9608	4159	*288	623	588
P2-PWUPT	1	8	1120	1251	1892	2085	9608	4159	29	316	294

Note: * $c_{b,sof}$ for Wall P1-CWUPT extends into beam web

Note that the elongations in the beam post-tensioning strands due to the lateral displacements of the structure are the same regardless of the distance of the tendons from the beam centerline (see Chapter 5). Thus, the strands can be placed symmetrically anywhere between the beam flanges on both sides of the web. The strands should be placed inside ungrouted post-tensioning ducts to achieve unbonded conditions, with a short length near the anchors grouted to prevent premature fracture of the strand wires at the anchors as observed in the subassembly experiments described in Chapter 9. The subassembly experiments did not show any advantage of using oversized post-tensioning ducts significantly larger than necessary for construction fit and tolerances, thus, this is not considered to be necessary.

Based on the experiments described in Chapter 9, two upper limits to the total beam post-tensioning steel area and force are recommended to prevent excessive local distortions and possible instability of the beam as follows. First, the total initial beam post-tensioning force, P_{bi} should be limited as:

$$P_{bi} < 0.25A_{bc}f_{by} \quad (12.27)$$

where, A_{bc} is the gross cross section area of the beam including the flange cover plates (if any). This requirement also ensures that gap opening (i.e., decompression) at the beam

ends occurs before the yielding of the beam in compression. It can be shown that gap opening and beam compression yielding would occur simultaneously if $P_{bi}=0.5A_{bc}f_{by}$ (ignoring the effect of the angles). It is assumed that the cover plate steel (if used) has the same design strength as the beam steel.

Second, it is recommended that

$$P_{by} < A_{bfc}f_{bm} \quad (12.28)$$

where,

$$P_{by} = \sum a_{bp}f_{bpy} \quad (12.29)$$

is the total yield strength of the beam post-tensioning steel, A_{bfc} is the cross section area of one beam flange plus cover plate (if any), and f_{bm} is the beam steel maximum (i.e., peak) strength. In the calculation of P_{by} , it is assumed that all of the beam post-tensioning strands yield simultaneously since they are prestressed by the same amount.

The coupling beams in both prototype structures satisfy Equations (12.27) and (12.28) as shown in Table 12.15. Note that for Structure P1-CWUPT, P_{bi} is a little larger than $0.25A_{bc}f_{by}$; however, the difference is smaller than 5 percent and is acceptable. If any of these two limits is not satisfied, a coupling beam with a larger cross section may be selected or the total post-tensioning steel area may be reduced. Alternatively, cover (i.e., reinforcing) plates may be used to strengthen the beam flanges (note that flange cover plates are not needed in the prototype structures). The cover plates (if needed) should be sufficiently long to prevent beam flange yielding where the plates are terminated and should extend over a length equal to, at least, the total beam depth, $d_{bc}=d_b+2t_c$ including the cover plates. The welds between the cover plates and the beam flanges should be designed for a force equal to

$$\begin{aligned} 1.25C_{b,pty} & \text{ for the 2}^{nd} \text{ and 3}^{rd} \text{ floor levels} \\ C_{b,pty} & \text{ for the upper floor/roof levels} \end{aligned} \quad (12.30)$$

where, the calculation of $C_{b,pty}$ is described later and the 1.25 factor accounts for the additional axial forces that develop in the lower floor coupling beams in a structure due to the lateral stiffness of the wall piers near the foundations as described in Chapter 7.

The post-tensioning anchors should be designed for the maximum tendon forces, P_{bu} based on the design maximum strength of the post-tensioning steel, f_{bpu} as:

$$P_{bu} = \sum a_{bp} f_{bpu} \quad (12.31)$$

Note that Equation (12.22) provides an approximation for the coupling shear resistance due to the post-tensioning force, $V_{bp,sof}$. Once the design of the beam post-tensioning tendons is finalized, a revised value for $V_{bp,sof}$ can be determined as:

$$V_{bp,sof} = \frac{P_{bi}}{l_b} \left(d_{bc} - \frac{2c_{b,sof}}{3} \right) \quad (12.32)$$

where $c_{b,sof}$ is from Equation (12.24). No cover plates are used in the coupling beams of the prototype structures, and thus, $d_{bc}=d_b$ (see Fig. 12.5b). As shown in Table 12.15, the design requirement given by Equation (12.18b) is satisfied for both prototype structures.

12.6.5 Top and Seat Angles and Connections

The top and seat angles are designed based on Fig. 12.7, which shows a free body diagram of the coupling beam at the softening state, excluding the post-tensioning forces. The angle forces are assumed to be acting parallel to the beam. The sum of the tension and compression angle forces (T_{ax} and C_{ax} , respectively) to satisfy the angle component of the design coupling beam shear force demand, $Q_{bd,a}$ can be determined as:

$$T_{ax} + C_{ax} = \frac{Q_{bd,a} l_b}{d_{bc} + t_a} \quad (12.33)$$

where, t_a is the angle leg thickness. Assuming $T_{ax}=1.5T_{ayx}$ (see assumed angle behavior for the coupling beam softening state in Chapter 10) and $C_{ax}=T_{ayx}$, and ignoring t_a , the required angle tension yield strength is

$$T_{ayx} = \frac{2 Q_{bd,a} l_b}{5 d_{bc}} \quad (12.34)$$

The angle thickness, t_a and gage length of the angle-to-wall connections, l_{gv} are determined to achieve the required angle tension yield strength T_{ayx} as described in Chapter 3 following Kishi and Chen (1990) and Lorenz et al. (1993). The final design details for the top and seat angles and connections used in the prototype structures are shown in Fig. 12.8. Angles with $L8 \times 8 \times 1/2$ and $L8 \times 8 \times 7/8$ cross sections are used in Structures P1-CWUPT and P2-PWUPT, respectively. The angle length is taken as 203 mm (8 in.) in Structure P1-CWUPT. Longer angles with length equal to the beam flange width, $b_{bf}=318$ mm (12.5 in.) are used in Structure P2-PWUPT. Note that it may also be possible to use thinner angles with 318 mm length in Structure P1-CWUPT; however, this was not investigated.

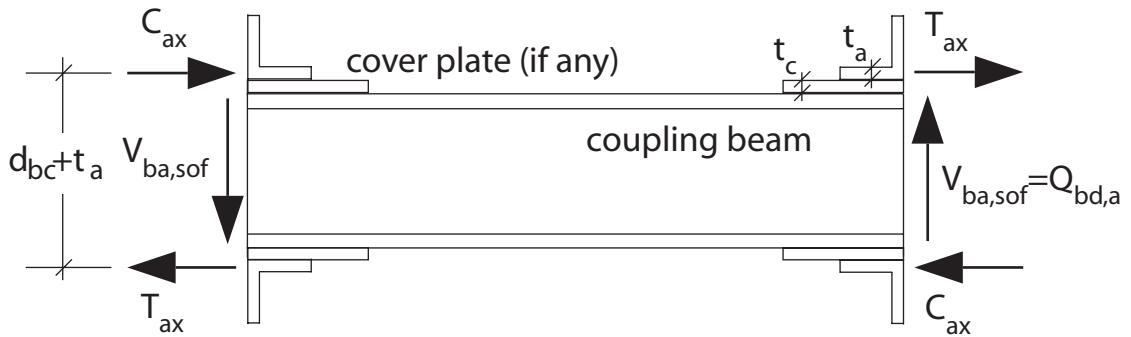


Fig. 12.7 Angle contribution to coupling resistance

The resulting T_{ayx} and C_{asx} values, as well as the coupling beam shear force resistance due to the top and seat angles, $V_{ba,sof}$ are given in Table 12.16. The $V_{ba,sof}$ values are determined from

$$V_{ba,sof} = \frac{(T_{ax} + C_{ax})(d_{bc} + t_a)}{l_b} \quad (12.35)$$

with $T_{ax} = 1.5T_{ayx}$ and $C_{ax} = (1/40)f_{ay}A_a \leq C_{asx}$, where C_{asx} is the slip capacity of the angle-to-beam connection bolts, f_{ay} is the angle steel yield strength, and A_a is the gross area of the angle leg cross section. It is observed that the prototype structures satisfy the design requirement given by Equation (12.18a).

TABLE 12.16
TOP AND SEAT ANGLES

Structure	T_{ayx} (kN)	C_{asx} (kN)	$V_{ba,sof}$ (kN)	$Q_{bd,a}$ (kN)
P1-CWUPT	53	425	44	30
P2-PWUPT	516	1063	432	360

In order to prevent slip of the angle-to-beam connection bolts as the angles are pulled away from the walls, it is recommended that the slip capacity of the angle-to-beam connection bolts, C_{asx} be greater than the maximum anticipated angle tension force, $2T_{ayx}$ as:

$$C_{asx} > 2T_{ayx} \quad (12.36)$$

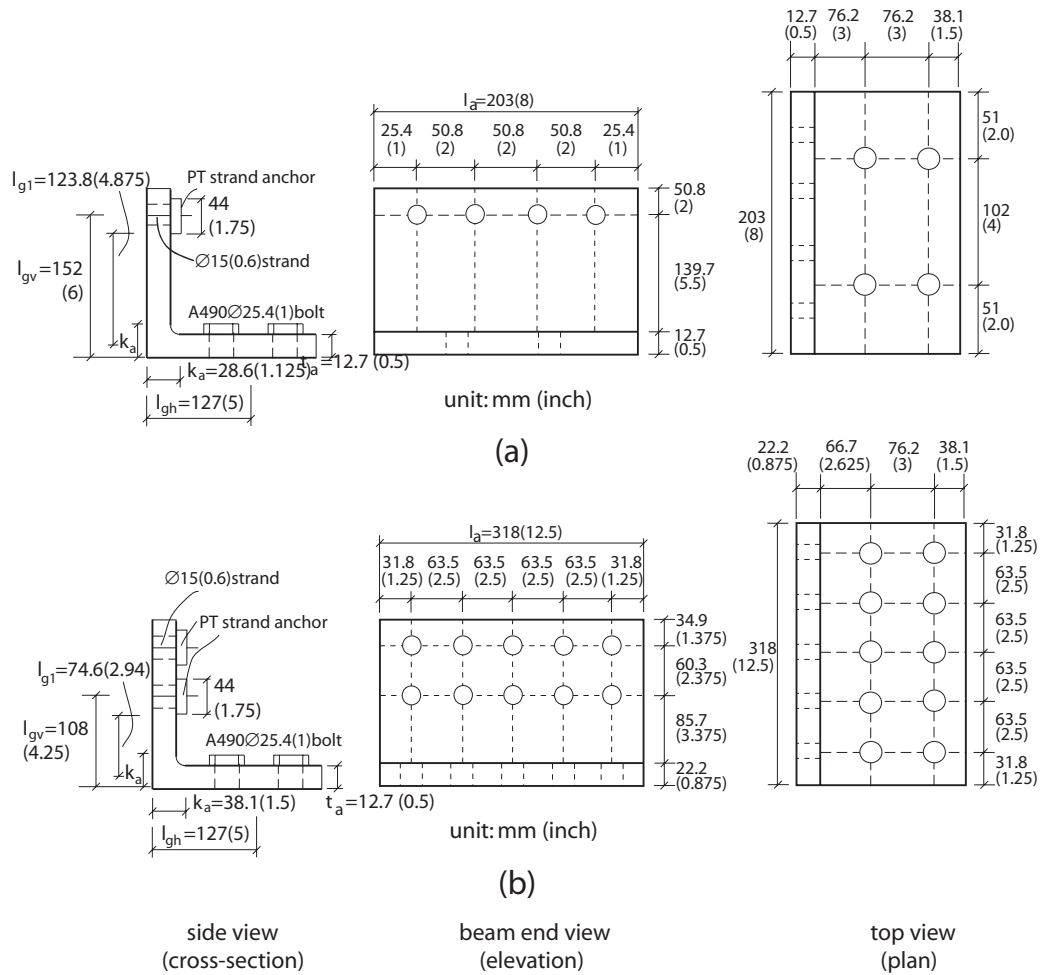


Fig. 12.8 Top and seat angle and connection details:
(a) Structure P1-CWUPT; (b) Structure P2-PWUPT

where, the factor 2 accounts for the over-strength observed in the angles from the subassembly experiments, as discussed in Chapter 9. Table 12.16 shows that the angles in the prototype structures satisfy this requirement. The angle-to-wall connections should also be designed for the maximum anticipated angle tension force, $2T_{ayx}$, including prying effects. As shown in Fig. 12.8, unbonded post-tensioning strands are used in the angle-to-wall connections of the prototype structures, similar to the subassembly test specimens in Chapter 9. More information on the design of the angle-to-beam and angle-to-wall connections is beyond the scope of this dissertation.

12.6.6 Coupling Beam Shear Force versus Rotation Behavior

The coupling beam shear force versus chord rotation (V_b - θ_b) behavior can be estimated from the structure design properties determined above. As shown by the solid lines in Fig. 12.9, the revised procedure in Chapter 10 is used to develop an idealized bi-linear V_b - θ_b relationship for each prototype structure based on the beam softening state (at $V_{b,sof}$, $\theta_{b,sof}$) and the PT-yielding state (at $V_{b,pty}$, $\theta_{b,pty}$). Key values calculated for the bi-linear coupling beam shear force versus chord rotation relationships are provided in Table 12.17. Note that the coefficient of 1.075 for $\theta_{b,pty}$ in Equation (10.13) is ignored conservatively. It is observed that the coupling beam shear force capacities at the softening state satisfy the design coupling beam shear force demands from Table 12.12, and thus the design requirement given in Equation (12.16) is met.

For comparison, the dashed lines in Fig. 12.9 show the smooth V_b - θ_b behaviors for Structures P1-CWUPT and P2-PWUPT using the fiber element subassemblage analytical model from Chapter 3. In general, the idealized bi-linear relationships capture the structure capacities from the fiber element models reasonably well.

TABLE 12.17

COUPLING BEAM SHEAR FORCE VERSUS ROTATION RELATIONSHIPS

Structure	Beam Softening State				Beam PT-yielding State					
	$C_{b,sof}$ (kN)	$c_{b,sof}$ (mm)	$V_{b,sof}$ (kN)	$\theta_{b,sof}$ (%)	$C_{b,pty}$ (kN)	$c_{b,pty}$ (mm)	$V_{b,pty}$ (kN)	$\theta_{bg,pty}$ (%)	$\theta_{bc,pty}$ (%)	$\theta_{b,pty}$ (%)
P1-CWUPT	2502	*261	689	0.17	3465	*30	770	6.99	0.25	7.24
P2-PWUPT	1251	26	738	0.19	1861	19	947	6.63	0.27	6.90

Note: * $c_{b,sof}$ for Walls P1-CWUPT and P2-PWUPT extend into beam web

12.6.7 Coupling Beam Rotation Demands

The survival-level and design-level coupling beam chord rotation demands, θ_s and θ_d , respectively, are estimated based on the idealized coupled wall displaced shape in Fig. 12.10 as:

$$\theta_s = \frac{\Delta_s (l_w + l_b)}{l_b} \quad (12.37)$$

$$\theta_d = \frac{\Delta_d (l_w + l_b)}{l_b} \quad (12.38)$$

where, Δ_s and Δ_d are the survival-level and design-level coupled wall roof drift demands, respectively. The above expressions for θ_s and θ_d assume, conservatively, that the rotations of the tension-side and compression-side wall piers occur about the compression corners of the wall piers at the base.

The estimated θ_s and θ_d demands corresponding to Δ_s and Δ_d demands in Table 12.9 are given in Table 12.18.

TABLE 12.18
COUPLING BEAM ROTATION DEMANDS

Structure	Demand Level	θ_s and θ_d (%)
P1-CWUPT	Survival	5.49
	Design	2.33
P2-PWUPT	Survival	5.62
	Design	2.59

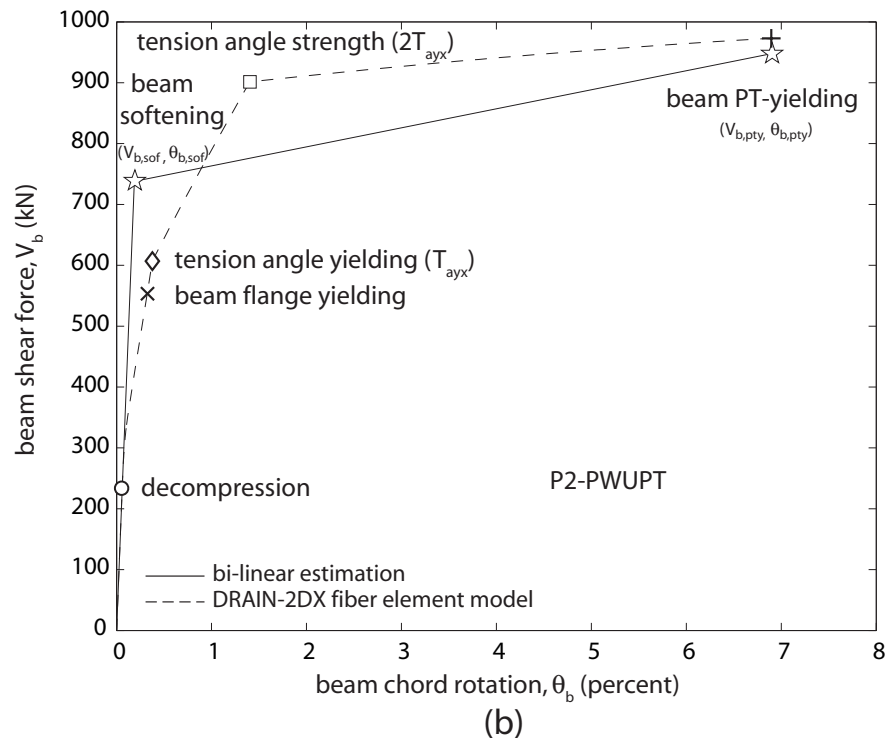
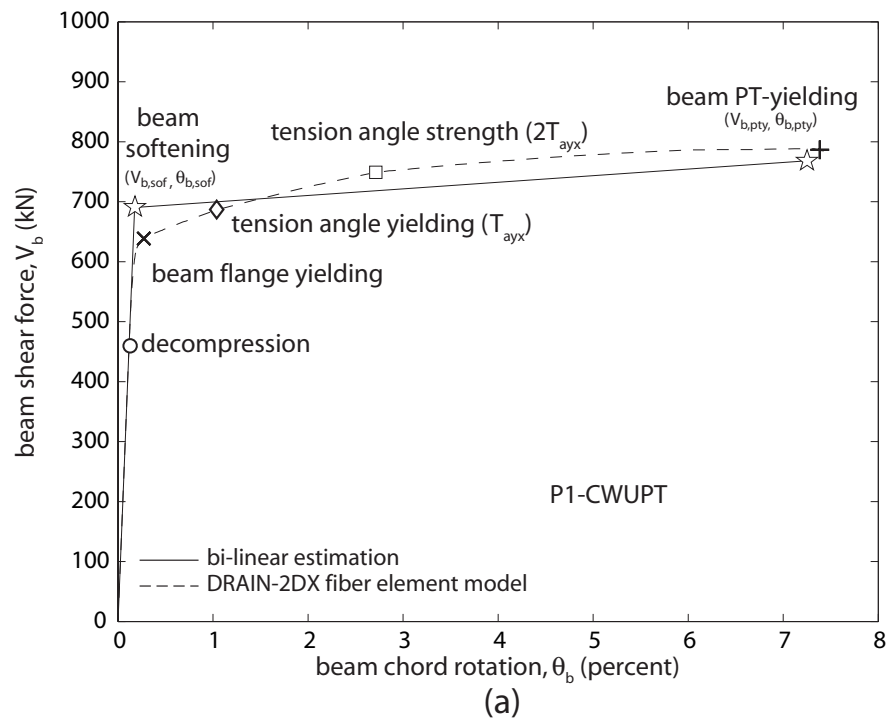


Fig. 12.9 Coupling beam shear force versus chord rotation (V_b - θ_b) relationships:
(a) Structure P1-CWUPT; (b) Structure P2-PWUPT

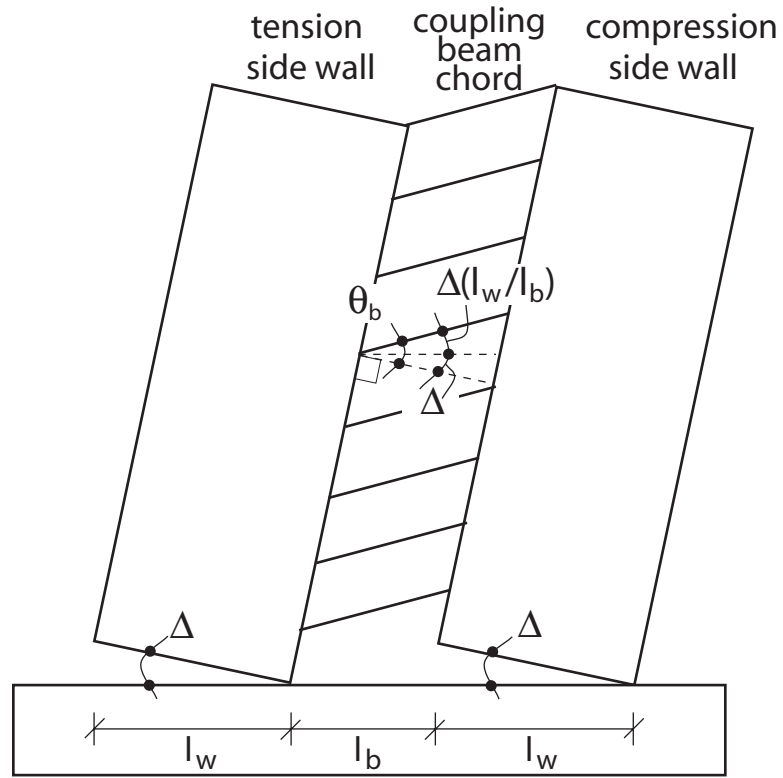


Fig. 12.10 Coupled wall idealized displaced shape

12.6.8 Yielding of Beam Post-Tensioning Tendons

As discussed in Chapter 11, the coupling beam chord rotation capacity at the beam PT-yielding state is required to be larger than the survival-level beam chord rotation demand (i.e., yielding of the beam post-tensioning tendons is not allowed to occur under the survival seismic demand level → Design Objective 1). Thus,

$$\theta_{b,pty} > \theta_s \quad (12.39)$$

where, $\theta_{b,pty}$ is the coupling beam chord rotation capacity at the PT-yielding state.

In addition, it is required that 2/3 times the coupling beam chord rotation capacity at the beam PT-yielding state be larger than the design-level beam chord rotation demand (Design Objective 2). Thus,

$$\frac{2}{3}\theta_{b,pty} > \theta_d \quad (12.40)$$

The $\theta_{b,pty}$ capacities for the coupling beams in the prototype structures, provided in Table 12.17, satisfy the rotation demands in Table 12.18. The initial stress in the beam post-tensioning strands, f_{bpi} , may be reduced if the design requirements in Equations (12.39) and (12.40) are not satisfied.

12.6.9 Fracture of Top and Seat Angles

Fracture of the top and seat angles prior to the survival demand level should be prevented. As shown in Fig. 12.11, the maximum deformation of the tension angles, u_{as} (i.e., the separation of the angle heel from the wall) under the survival-level beam rotation demand, θ_s can be estimated as:

$$u_{as} = \theta_s (d_{bc} + 0.5t_a - c_{b,pty}) \quad (12.41)$$

It is assumed that the depth of the compression (i.e., contact) region at the beam-to-wall interface is equal to $c_{b,pty}$ (see Table 12.17). The resulting survival-level tension angle deformation demands, u_{as} for the coupling beams in the prototype structures are shown in Table 12.19.

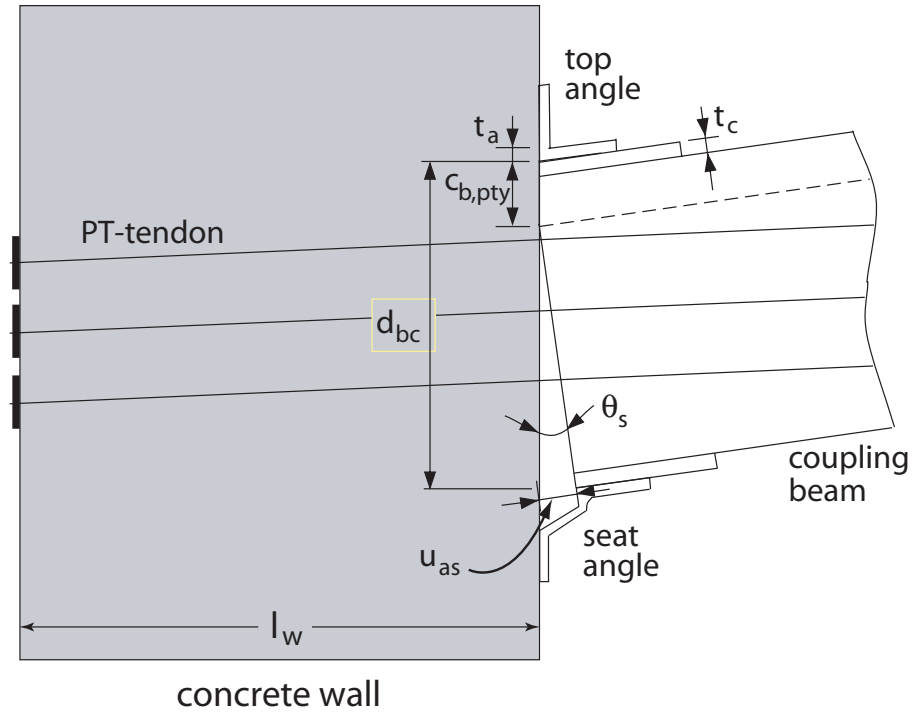


Fig. 12.11 Tension angle deformation

For comparison with the analysis results in Chapter 13, Table 12.19 also includes the estimated design-level tension angle deformation demands, u_{ad} for the prototype structures. These u_{ad} values were obtained by replacing θ_s with the design-level beam rotation demand θ_d in Equation (12.41) and using $c_{b,pty}$ as the contact depth at the beam ends under the design demand level.

TABLE 12.19

TENSION ANGLE DEFORMATION DEMANDS

Structure	u_{as} (mm)	u_{ad} (mm)
P1-CWUPT	30	13
P2-PWUPT	31	14

More research needs to be conducted on the deformation capacity of the top and seat angles to ensure that the survival level deformation demand, u_{as} can be reached without low cycle fracture of the angle legs. In the absence of a reliable method to estimate the deformation capacity of the angles, it is required that

$$u_{as} < 38 \text{ mm } (1.5 \text{ in.}) \quad (12.42)$$

This requirement is satisfied for both structures as shown in Table 12.19. If the deformation demands of the tension angles are larger than allowable, then a coupling beam with smaller depth may need to be selected.

12.6.10 Shear Slip at Beam-to-Wall Interfaces

The beam-to-wall connections should be designed to transfer the maximum coupling beam shear forces without slip at the beam ends. The design requirement is stated as:

$$V_{b,ss} > Q_{b,max} \quad (12.43)$$

where, $Q_{b,max}$ is the maximum shear slip demand as:

$$\begin{aligned} Q_{b,max} &= 1.25 V_{b,pty} \quad \text{for the 2nd and 3rd floor level} \\ Q_{b,max} &= V_{b,pty} \quad \text{for the upper floor / roof levels} \end{aligned} \quad (12.44)$$

with $V_{b,pty}$ from Table 12.17 and the 1.25 factor accounting for the increase in the lower floor coupling beam shear forces due to the lateral stiffness of the wall piers near the foundations as described in Chapter 7.

The shear slip capacity at the beam-to-wall interfaces, $V_{b,ss}$ is equal to

$$V_{b,ss} = V_{p,ss} + V_{a,ss} \quad (12.45)$$

where, $V_{p,ss}$ is the slip capacity due to the coupling beam end axial force and $V_{a,ss}$ is the slip capacity from the top and seat angle-to-wall connections.

The slip capacity due to the beam end axial force is assumed to be equal to

$$V_{p,ss} = \mu_{bw} P_{bi} \quad (12.46)$$

where, μ_{bw} is the coefficient of friction between the beam and the wall shim plates and P_{bi} is the total initial beam post-tensioning force (assuming that the beam end axial force when $Q_{b,max}$ is reached is equal to the initial post-tensioning force). A value of $\mu_{bw}=0.33$ for steel against steel friction surfaces can be used for design (AISC 2001).

The calculation of $V_{a,ss}$ depends on the type of the angle-to-wall connections. For unbonded post-tensioned angle-to-wall connections (as shown in Fig. 12.8), it is recommended that

$$V_{a,ss} = 2\mu_{aw} f_{awpi} A_{aw} \quad (12.47)$$

where, $\mu_{aw}=\mu_{bw}=0.33$ is the coefficient of friction between the angle vertical leg and the wall shim plates; f_{awpi} is the initial stress of the post-tensioning strands used in the angle-to-wall connections; and A_{aw} is the total area of the post-tensioning steel used in an angle-to-wall connection (for one angle). A value of $f_{awpi}=0.5f_{awpu}$ is used in the design of the prototype structures, where $f_{awpu}=1862$ MPa (270 ksi) is the maximum strength of the angle-to-wall connection strands.

The estimated shear slip capacities and demands at the beam-to-wall interfaces of the prototype structures are given in Table 12.20. Both structures satisfy the design requirement in Equation (12.43).

TABLE 12.20
SHEAR SLIP AT BEAM-TO-WALL INTERFACES

Structure	μ_{aw} and μ_{bw}	A_{aw} (mm ²)	f_{awpi} (MPa)	$V_{a,ss}$ (kN)	P_{bi} (kN)	$V_{p,ss}$ (kN)	$V_{b,ss}$ (kN)	$Q_{b,max}$ (kN)	
								2 nd and 3 rd	upper
P1-CWUPT	0.33	560	931	344	2500	825	1169	963	770
P2-PWUPT	0.33	1400	931	860	1251	413	1273	1184	947

12.6.11 Wall-Contact Regions

The wall-contact regions adjacent to the coupling beams should be designed for a compressive force equal to

$$\begin{aligned}
 C_{wc} &= 1.25C_{b,pty} && \text{for the 2nd and 3rd floor levels} \\
 C_{wc} &= C_{b,pty} && \text{for the upper floor/roof levels}
 \end{aligned}
 \tag{12.48}$$

where, $C_{b,pty}$ from Table 12.17 is the compression force in the beam at the beam PT-yielding state and the 1.25 factor accounts for the additional axial forces that develop in the lower floor coupling beams in a structure due to the lateral stiffness of the wall piers near the foundations as described in Chapter 7.

Shim plates should be used at the beam-to-wall interfaces, with the total thickness of the shim plate, t_{sh} and wall embedded plate, t_e equal to at least the thickness of the beam flange, t_{bf} . The shim plates should be terminated at the coupling beam web, thus preventing contact between the web and the walls as described in Chapter 9.

Concrete confinement should be provided in the wall-contact regions near the coupling beam flanges. Assuming a 3:4 spread for the contact stresses as shown in Fig. 12.12 and assuming that the contact depth at the beam-to-shim-plate interface is equal to

$c_{b,pty}$, the nominal concrete compressive stress behind the embedded plate can be estimated as:

$$\sigma_{wc} = \frac{C_{wc}}{(c_{b,pty} + 1.5t_e + 1.5t_{sh})(b_{bf} + 1.5t_e + 1.5t_{sh})} \quad (12.49)$$

Since the $c_{b,pty}$ values in Table 12.17 are calculated based on an isolated coupled wall subassembly, they should be multiplied by 1.25 for the design of the 2nd and 3rd floor level wall-contact regions using Equation (12.49). Further, Equation (12.49) should be modified if $c_{b,pty} > t_{bf} + t_c$ and the beam compression region is not rectangular. In order to simplify the calculation in that case, it would be a reasonable approximation to replace $c_{b,pty}$ with $t_{bf} + t_c$, provided that the beam web thickness t_{bw} is much smaller than the flange width b_{bf} . Note also that the term $(b_{bf} + 1.5t_e + 1.5t_{sh})$ in Equation (12.49) cannot be taken greater than the wall thickness, t_w .

The maximum compressive strength of the confined concrete in the wall-contact regions, f_{ccw} should be larger than σ_{wc} to limit the deformations in the wall-contact regions. Thus,

$$f_{ccw} > \sigma_{wc} \quad (12.50)$$

The final design details for the wall-contact regions in the prototype structures, including the shim plate, embedded plate, and concrete confinement reinforcement are given in Table 12.21 and Fig. 12.13. Two steel spirals are used to confine the concrete in the wall-contact regions at each beam end, one spiral near each beam flange. The stress-strain behaviors of the confined concrete in the prototype structures, as estimated using Mander et al. (1988), are shown in Fig. 12.13. The spiral reinforcement properties are kept constant at all of the floor and roof levels in each structure.

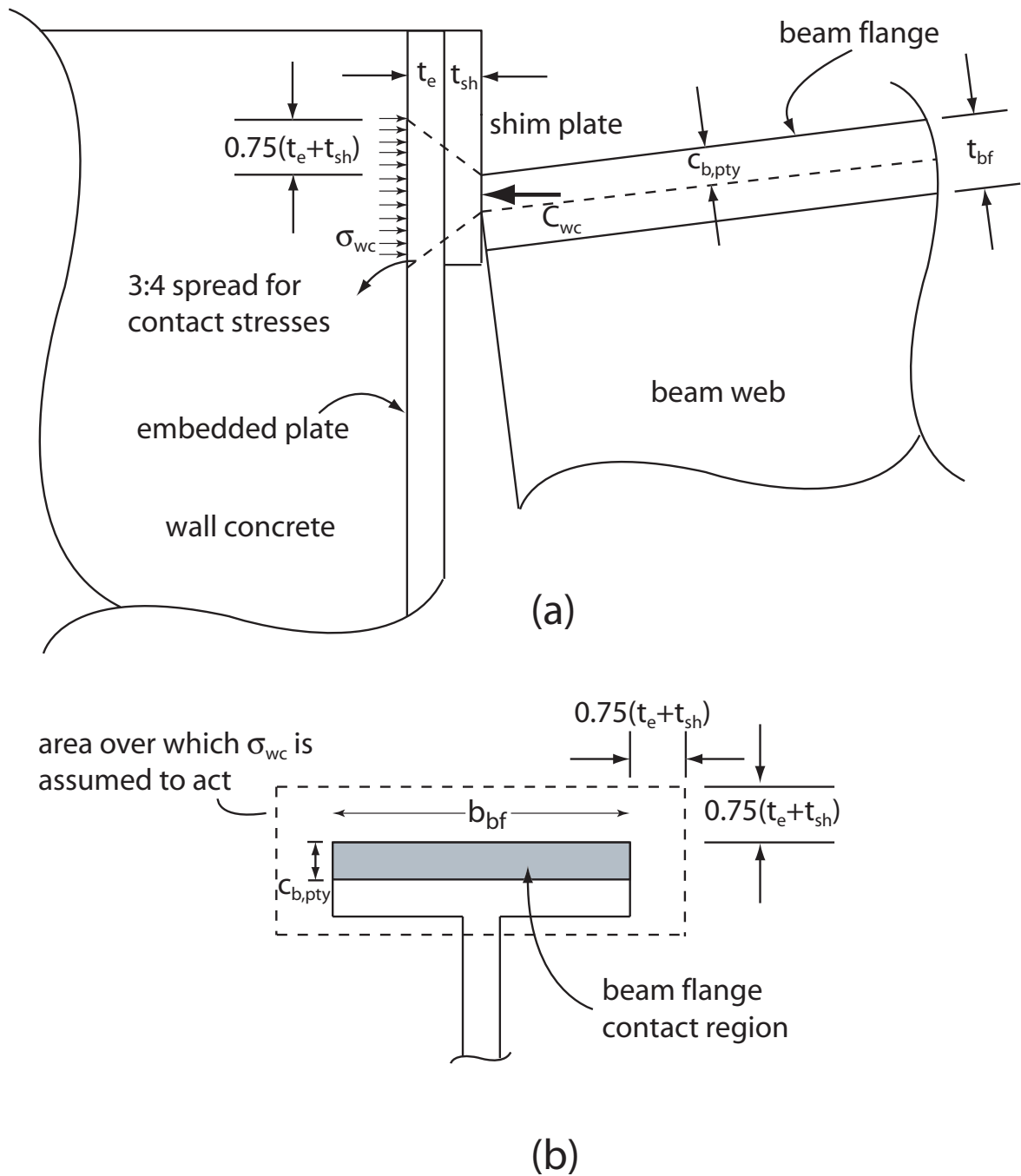


Fig. 12.12 Wall-contact region stresses: (a) side view; (b) beam end view

As shown in Table 12.21, the resulting confined concrete strengths are adequate to satisfy the design requirement in Equation (12.50) for both prototype structures.

TABLE 12.21
WALL-CONTACT REGIONS

Structure	C_{wc} (kN)		t_{sh} (mm)	t_e (mm)	$c_{b,pty}$ (mm)		σ_{wc} (MPa)		f_{ccw} (MPa)	
	2 nd and 3 rd	upper			2 nd and 3 rd	upper	2 nd and 3 rd	upper	2 nd and 3 rd	upper
P1-CWUPT	4730	3784	38	38	92.8	30.1	92.4	74.4	98.7	98.7
P2-PWUPT	2365	1892	16	16	23.7	19.0	82.1	63.7	90.4	90.4

12.7 Design of Wall Piers In Structure P1-CWUPT

This section describes the design of the cast-in-place reinforced concrete wall piers in Structure P1-CWUPT. The design includes the following components: (1) wall pier flexural reinforcement; (2) concrete confinement at wall pier bases; (3) diagonal tension at wall pier bases; and (4) shear slip at coupled wall base. Only the cross-sections of the wall piers at the base are designed. The design and curtailment of the reinforcement over the height of the structures are not addressed in this dissertation.

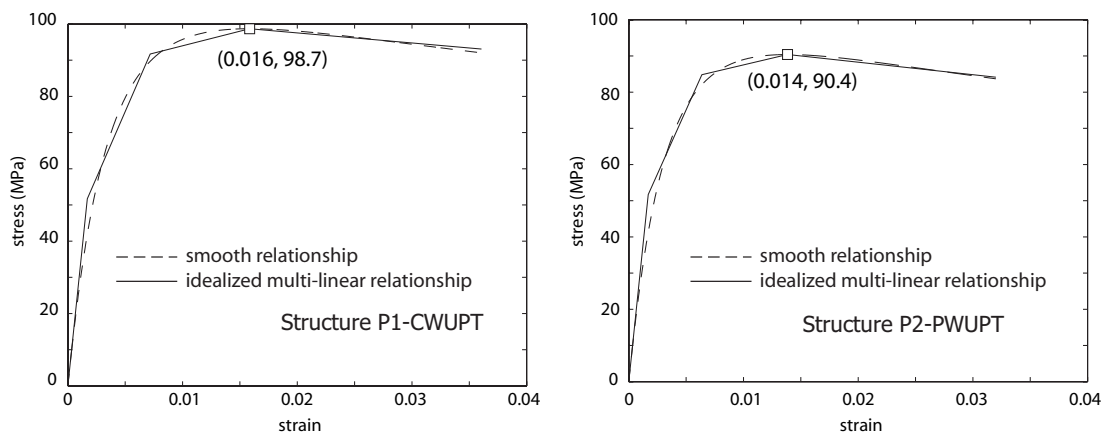
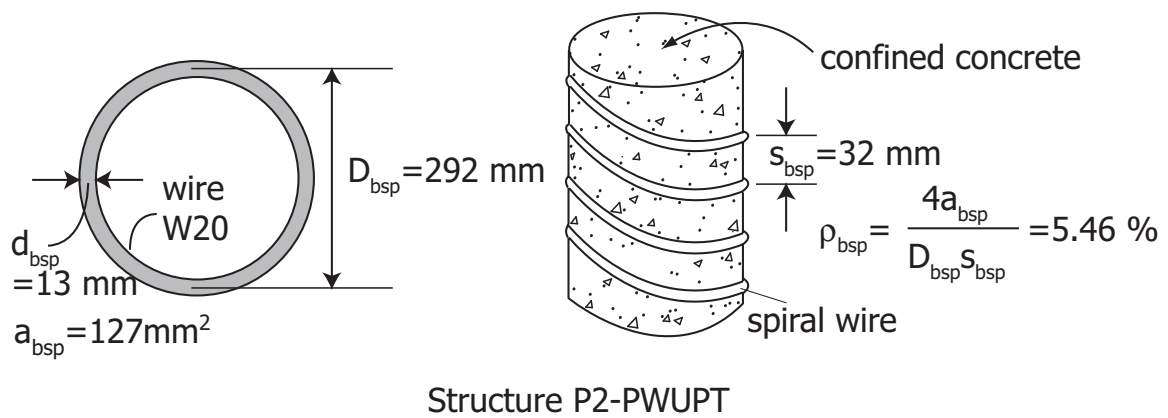
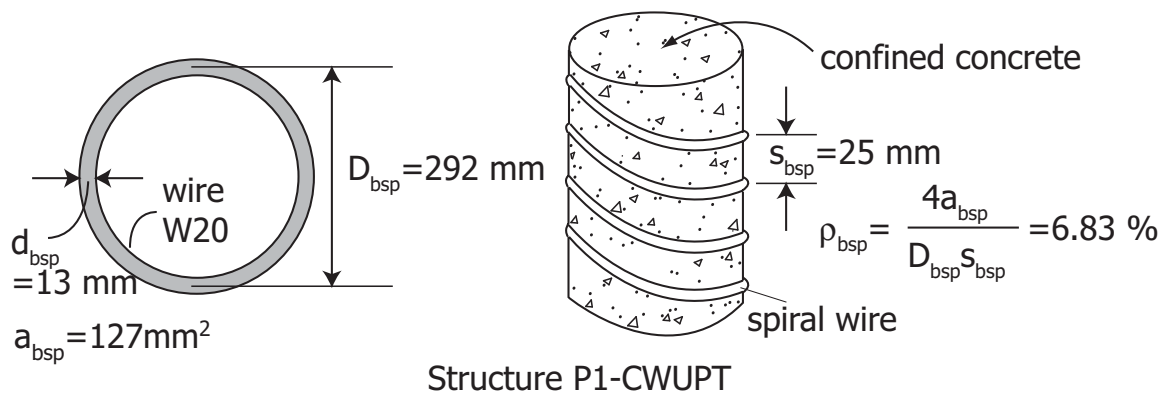


Fig. 12.13 Wall-contact region concrete confinement

12.7.1 Wall Pier Flexural Reinforcement

The design of the wall pier flexural reinforcement to satisfy the design coupled wall base shear force demand, Q_{wd} is based on the coupled wall softening state described in Chapters 7 and 8. The design criterion is given as:

$$F_{ws} > Q_{wd} \quad (12.51)$$

where, F_{ws} is the coupled wall base shear force capacity at the wall softening state.

The following assumptions are made for the design of the wall flexural reinforcement, similar to the assumptions made in Chapter 8 for the estimation of the coupled wall softening state: (1) the coupling beam shear forces are equal to $V_{b,sof}$; (2) the strain distributions at the bases of the wall piers are linear; (3) the concrete compressive stresses at the bases of the wall piers have linear distributions; (4) the neutral axis depth at the base of the compression-side wall (i.e., right-side wall for lateral loads applied from left to right) is located at the centerline of the wall (i.e., $c_{cws}=0.5l_w$); and (5) the strain and stress in the extreme flexural reinforcement of the tension-side wall are equal to the yield strain ϵ_{wsy} and yield stress f_{wsy} , respectively.

An iterative design procedure is followed as described below.

Step 1

Select trial details for the amount and layout of the flexural reinforcement in the wall pier cross sections. A sample trial section (Trial 1) for Structure P1-CWUPT is given in Fig. 12.14a. Note that the cross section of only one of the wall piers is shown and the details of the other wall pier are identical. It is assumed that 14 \varnothing 15.9mm reinforcing bars at 457 mm spacing are used within the central region of each wall pier

and eleven layers of reinforcing bars (each layer with a total steel area of 1290 mm²) at 76 mm spacing are used within the end regions.

Step 2

Estimate the axial forces at the bases of the tension-side and compression-side walls, N_{tws} and N_{cws} , respectively, as:

$$N_{tws} = \sum G - 1.05 \sum V_{b,sof} \quad (12.52)$$

$$N_{cws} = \sum G + 1.05 \sum V_{b,sof} \quad (12.53)$$

where, G represents the factored gravity loads applied at the floor and roof levels of a wall pier, $V_{b,sof}$ is from Table 12.17, and the 1.05 factor is described in Chapter 8. It is assumed that the coupled wall gravity loads (see Table 12.2 for the unfactored gravity loads) are distributed equally between the tension-side and compression-side wall piers.

Step 3

Determine the bending moment resistances of the tension-side and compression-side walls, M_{tws} and M_{cws} respectively, and the total base moment and base shear force resistances of the coupled wall system, M_{ws} and F_{ws} respectively, using the procedure described in Chapter 8.

Step 4

Compare F_{ws} with Q_{wd} to check the adequacy of the trial cross section.

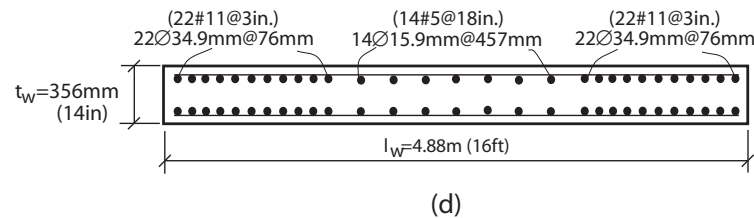
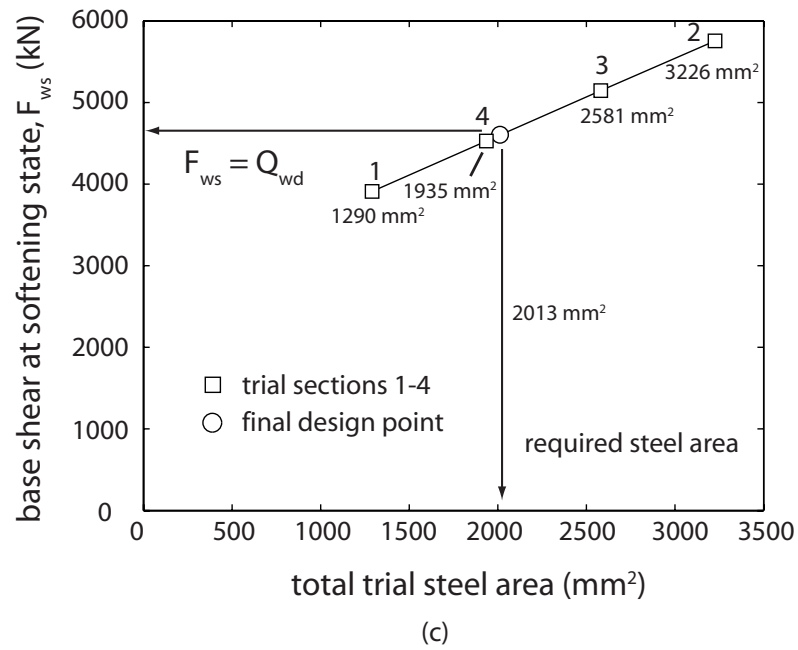
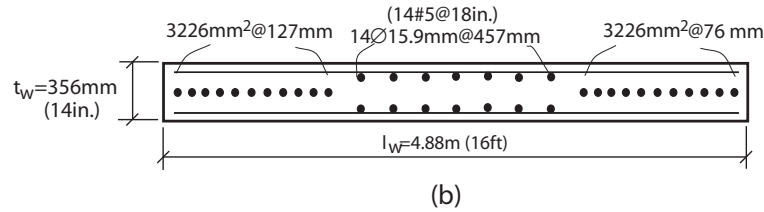
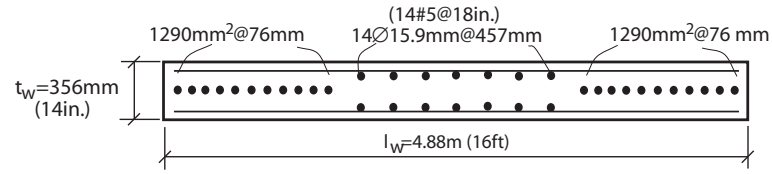


Fig. 12.14 Wall pier flexural reinforcement: (a) trial section 1; (b) trial section 2; (c) flexural steel area versus base shear resistance; (d) final wall cross section

Step 5

If necessary (as determined from the comparison in Step 4), repeat Steps 2-4 for other trial sections (e.g., see Fig. 12.14b for Trial 2).

Step 6

Plot the coupled wall base shear force capacity at the wall softening state, F_{ws} determined for the trial cross sections against the corresponding reinforcing steel areas used in the end regions of each section as shown in Fig. 12.14c. Use interpolation to determine the required area of wall flexural reinforcement to satisfy the coupled wall design base shear force demand Q_{wd} and select the reinforcement.

The resulting wall pier cross section for Structure P1-CWUPT is shown in Fig. 12.14d with the design details summarized in Table 12.22. A positive wall axial force represents a compressive force. A total of 44Ø34.9 mm reinforcing bars and 14Ø15.9 mm bars are used in each wall pier, with the total pier flexural reinforcement area, A_{ws} given in Table 12.22. It is observed that the coupled wall base shear capacity at the wall softening state F_{ws} is smaller than but sufficiently close to the design base shear demand, Q_{wd} , and thus, the design is considered acceptable for Equation (12.51).

TABLE 12.22

WALL PIER FLEXURAL REINFORCEMENT

Structure	A_{ws} (mm ²)	ΣG (kN)	$\Sigma V_{b,sof}$ (kN)	N_{tws} (kN)	N_{cws} (kN)	c_{tws} (mm)	M_{tws} (kN.m)	M_{cws} (kN.m)	M_{wbs} (kN.m)	M_{ws} (kN.m)	F_{ws} (kN)	Q_{wd} (kN)
P1-CWUPT	47084	2798	5515	-2993	8589	1270	29241	32099	40607	101946	4603	4782

12.7.2 Concrete Confinement at Wall Pier Bases

As discussed in Chapter 11, the coupled wall roof drift capacity at the wall ultimate state is required to be larger than the survival-level coupled wall roof drift demand (i.e., crushing of the confined concrete at the bases of the wall piers is not allowed to occur under the survival seismic demand level \rightarrow Design Objective 1). Thus,

$$\Delta_{wu} > \Delta_s \quad (12.54)$$

In addition, it is required that 2/3 times the coupled wall roof drift capacity at the wall ultimate state be larger than the design-level coupled wall roof drift demand (Design Objective 2). Thus,

$$\frac{2}{3} \Delta_{wu} > \Delta_d \quad (12.55)$$

where, Δ_{wu} is the coupled wall roof drift capacity at the wall ultimate state and Δ_s and Δ_d are the survival-level and design-level roof drift demands, respectively.

Note that since Δ_d is smaller than $(2/3)\Delta_s$ for the prototype structures, the design requirement in Equation (12.55) is automatically satisfied when Equation (12.54) is satisfied.

The following assumptions are made in the design of the confinement reinforcement at the bases of the wall piers, similar to the assumptions made in Chapter 8 for the estimation of the coupled wall ultimate state: (1) the maximum compression strain in the confined concrete at the base of the compression-side wall is equal to the ultimate (i.e., crushing) strain of the confined concrete, ϵ_{ccu} ; (2) the strain distributions at the bases of the wall piers are linear; (3) the height of the “plastic hinge,” h_{wp} at the base of the compression-side wall is equal to the confined thickness of the wall, t_{wc} (estimated as the wall thickness minus the unconfined cover concrete thicknesses); (4) the coupling degree

at the wall ultimate state, DOC_{wu} is equal to the design coupling degree, DOC ; and (5) the neutral axis depth at the base of the compression-side wall at the wall ultimate state is equal to $c_{cwu}=0.2l_w$.

The design procedure is described below.

Step 1

Estimate the curvature at the base of the compression-side wall when the survival-level roof drift demand, Δ_s is reached as:

$$\phi_{cwu} = \frac{(DOC)_{wu} \Delta_s}{1.85h_{wp}} = \frac{(DOC)\Delta_s}{1.85t_{wc}} \quad (12.56)$$

where $h_{wp}=t_{wc}$ and $DOC_{wu}=DOC$ based on Assumptions (3) and (4), respectively. This equation follows from the estimation of the coupled wall ultimate state in Chapter 8.

Step 2

Estimate the required ultimate strain for the confined concrete at the base of the compression-side wall as:

$$\varepsilon_{ccu} = c_{cwu}\phi_{cwu} \quad (12.57)$$

where $c_{cwu}=0.2l_w$ based on Assumption (5).

Step 3

Design the concrete confinement to achieve ε_{ccu} . A concrete confinement model, such as the model developed by Mander et al. (1988), can be used for this purpose.

As shown in Fig. 12.15, spiral reinforcement is used to confine the concrete at the bases of the wall piers in Structure P1-CWUPT. The stress-strain behavior of the

confined concrete, as estimated using Mander et al. (1988), is also shown in Fig. 12.15. It is recommended that the confinement reinforcement be provided over a height equal to at least the first story height. The concrete confinement should be used over a wall length, l_{wc} where the concrete compression strains exceed the assumed unconfined concrete crushing strain, ϵ_{cu} as:

$$l_{wc} = c_{cwu} \left(1 - \frac{\epsilon_{cu}}{\epsilon_{ccu}} \right) \quad (12.58)$$

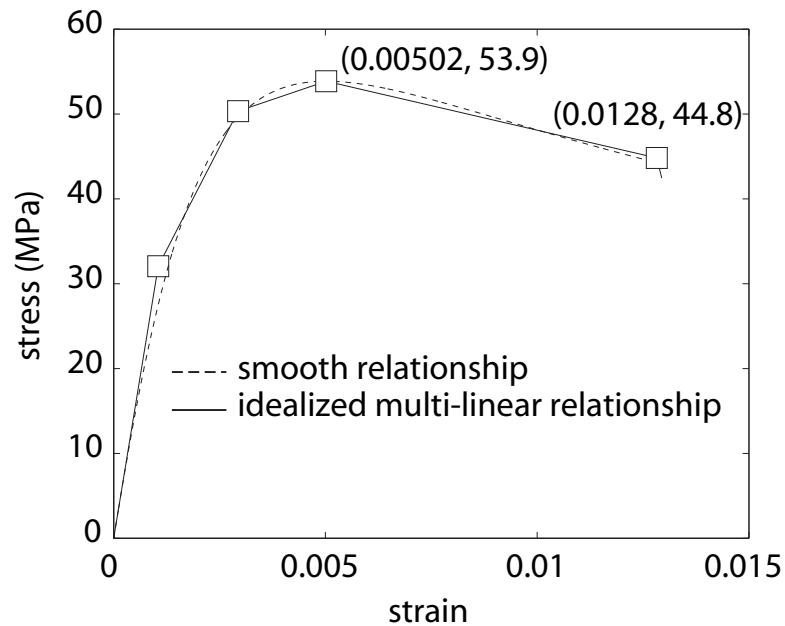
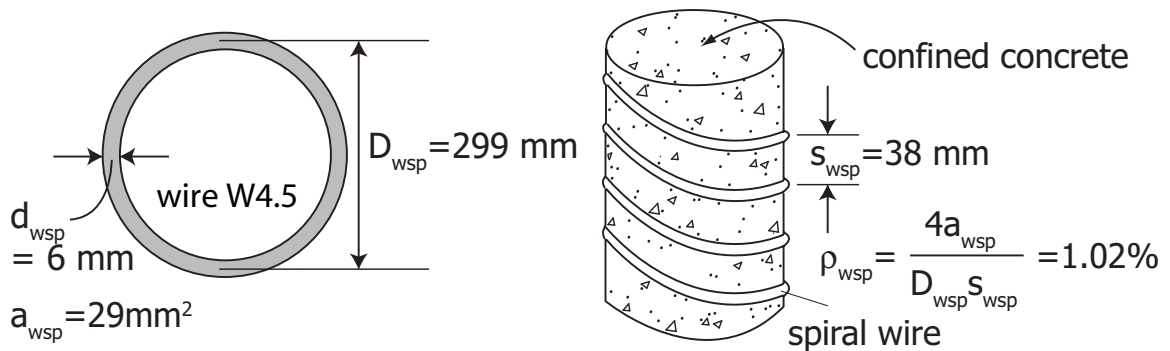


Fig. 12.15 Concrete confinement at wall pier bases

Table 12.23 shows the wall pier confined concrete ultimate strain required by Equation (12.57) as well as the strain capacity for the confined concrete. Since the strain capacity is larger than the required strain, crushing of the confined concrete under the survival demand level is prevented.

TABLE 12.23
CONCRETE CONFINEMENT AT WALL PIER BASES

Structure	ϵ_{ccu} required	ϵ_{ccu} provided	l_{wc} (mm)
P1-CWUPT	0.0090	0.012	732

12.7.3 Diagonal Tension at Wall Pier Bases

To prevent shear (diagonal tension) failure of the concrete wall piers in the prototype structures, the diagonal tension capacity, $F_{w,dt}$ of the wall piers is required to be greater than the maximum wall pier base shear demand, $Q_{w,dt}$. Thus,

$$F_{w,dt} > Q_{w,dt} \quad (12.59)$$

Because of the compression forces that develop in the compression-side wall pier due to coupling, a larger portion of the total coupled wall base shear force is carried by the compression-side wall. It is assumed that the portion of the total maximum coupled wall base shear demand, $Q_{w,max}$ carried by the compression-side wall can be estimated as:

$$Q_{w,dt} = \frac{M_{cws} + M_{wbs}}{M_{tws} + M_{cws} + M_{wbs}} Q_{w,max} \quad (12.60)$$

where, $Q_{w,dt}$ is the maximum wall pier base shear demand, M_{tws} and M_{cws} are the base moment resistances of the tension-side and compression-side wall piers at the softening

state (see Table 12.22), and M_{wbs} is the contribution of the coupling beam shear forces to the coupled wall base shear resistance at the softening state.

As described in Chapter 11, the maximum base shear demand, $Q_{w,max}$, of a coupled wall structure is calculated as the sum of a first mode component, $Q_{1,max}$, and a higher mode component $Q_{h,max}$ as:

$$Q_{w,max} = Q_{1,max} + Q_{h,max} \quad (12.61)$$

The base shear demand for the first mode component is estimated as the coupled wall base shear capacity at the wall ultimate state, F_{wu} as:

$$Q_{1,max} = F_{wu} \quad (12.62)$$

The estimation of F_{wu} is described in Chapter 8. The higher mode component of the maximum base shear demand, $Q_{h,max}$ is estimated as:

$$Q_{h,max} = D_m m_w (PGA_s) \quad (12.63)$$

with,

$$D_m = \frac{m_w - m_{eff} + 0.7m_{eff,2}}{m_w} = 1 - \frac{m_{eff}}{m_w} + 0.7 \frac{m_{eff,2}}{m_w} \quad (12.64)$$

where, m_w , PGA_s , m_{eff} , and $m_{eff,2}$ are given in Tables 12.1, 12.3, and 12.5.

The resulting maximum base shear demands for Structure P1-CWUPT are listed in Table 12.24. Note that in the preliminary design check described in Section 12.5.3, $Q_{w,dt}$ was assumed to be equal to 75% of the maximum coupled wall base shear force demand, $Q_{w,max}$. Based on the design values in Table 12.24, Equation (12.60) gives a distribution ratio of 71%.

TABLE 12.24
DIAGONAL TENSION AT WALL PIER BASES

Structure	Demand Level	$Q_{l,max}$ (kN)	D_m	$Q_{h,max}$ (kN)	$Q_{w,max}$ (kN)	$Q_{w,dt}$ (kN)	$F_{w,dt}$ (kN)
P1-CWUPT	Survival	6988	0.41	6168	13156	9341	9261

Based on ACI 318-02 (ACI Committee 318 2002), the maximum attainable shear capacity of a concrete wall can be estimated as:

$$F_{w,dt} = 10A_w\sqrt{f'_c} \quad (12.65)$$

where, $A_w=l_wt_w$ is the gross cross-sectional area of a wall pier and f'_c is the compressive strength of unconfined concrete.

The maximum attainable wall pier shear force capacity, $F_{w,dt}$ for Structure P1-CWUPT, listed in Table 12.24, is smaller than but sufficiently close to the maximum wall pier base shear force demand, $Q_{w,dt}$. Thus, the design is considered acceptable for Equation (12.59). The selection and placement of the wall pier transverse reinforcement to satisfy $Q_{w,dt}$ is not discussed in this dissertation.

12.7.4 Shear Slip at Coupled Wall Base

To prevent shear slip failure between the coupled wall structure and the foundation, the shear slip capacity of the structure at the base, $F_{w,ss}$ is required to be larger than the survival-level maximum base shear force demand, $Q_{w,max}$. Thus,

$$F_{w,ss} > Q_{w,max} \quad (12.66)$$

The total shear slip capacity $F_{w,ss}$ is equal to the slip capacity provided by the two wall piers, which can be calculated as the sum of two components. The first component $F_{g,ss}$ is the slip capacity due to the wall gravity load and the second component $F_{s,ss}$ is the slip capacity due to the wall longitudinal mild steel reinforcement at the base as:

$$F_{w,ss} = F_{g,ss} + F_{s,ss} \quad (12.67)$$

with

$$F_{g,ss} = 2\mu_{wf} \Sigma G \quad (12.68)$$

$$F_{s,ss} = 2\mu_{wf} A_{ws} f_{wsy} \quad (12.69)$$

where, μ_{wf} is the coefficient of friction between the wall and the foundation, G represents the factored gravity loads acting at the floor and roof levels of a wall pier, and A_{ws} is the total area of developed vertical reinforcement crossing the wall-to-foundation joint at the base of a single wall pier. A value of $\mu_{wf}=1.0$ is recommended for design. It is assumed that the coupled wall gravity loads (see Table 12.2 for the unfactored gravity loads) are distributed equally between the tension-side and compression-side wall piers.

The estimated shear slip capacity for Structure P1-CWUPT, shown in Table 12.25, satisfies the design requirement given by Equation (12.65).

TABLE 12.25
SHEAR SLIP AT COUPLED WALL BASE

Structure	Demand Level	μ_{wf}	ΣG (kN)	$F_{g,ss}$ (kN)	A_{ws} (mm ²)	$F_{s,ss}$ (kN)	$F_{w,ss}$ (kN)	$Q_{w,max}$ (kN)
P1-CWUPT	Survival	1.0	2798	5596	47084	38956	44552	13156

12.8 Design of Wall Piers In Structure P2-PWUPT

This section describes the design of the post-tensioned precast concrete wall piers in Structure P2-PWUPT. The design includes the following components: (1) wall pier post-tensioning steel reinforcement; (2) yielding of wall pier post-tensioning steel; (3) concrete confinement at wall pier bases; (4) diagonal tension at wall pier bases; and (5) shear slip at coupled wall base.

12.8.1 Wall Pier Post-Tensioning Steel Reinforcement

The design of the wall pier post-tensioning steel reinforcement to satisfy the design coupled wall base shear force demand, Q_{wd} is based on the coupled wall softening state described in Chapters 7 and 8. The design criterion is given as:

$$F_{ws} > Q_{wd} \quad (12.70)$$

where, F_{ws} is the coupled wall base shear force capacity at the wall softening state.

The following assumptions are made in the design of the wall pier post-tensioning steel reinforcement, similar to the assumptions made in Chapter 8 for the estimation of the coupled wall softening state: (1) the coupling beam shear forces are equal to $V_{b,sof}$; (2) the strain distributions at the bases of the wall piers are linear; (3) the concrete compressive stresses at the bases of the wall piers have linear distributions; (4) the neutral axis depth at the base of the compression-side wall (i.e., right-side wall for lateral loads applied from left to right) is located at the centerline of the wall (i.e., $c_{cws}=0.5l_w$); (5) the stresses in the wall pier post-tensioning bars are equal to the initial stress f_{wpi} ; and (6) the

maximum concrete compression stress at the base of the tension-side wall is equal to the design unconfined concrete strength, f'_c .

An iterative design procedure is followed as described below.

Step 1

Assume a trial value for the total area of the post-tensioning steel reinforcement in each wall pier, A_{wp} . Then, the total initial wall pier post-tensioning force can be determined as:

$$P_{wi} = A_{wp} f_{wpi} \quad (12.71)$$

Step 2

Estimate the axial forces at the bases of the tension-side and compression-side walls, N_{tws} and N_{cws} , respectively, as:

$$N_{tws} = \sum G - 1.05 \sum V_{b,sof} + P_{wi} \quad (12.72)$$

$$N_{cws} = \sum G + 1.05 \sum V_{b,sof} + P_{wi} \quad (12.73)$$

where, G represents the factored gravity loads applied at the floor and roof levels of a wall pier, $V_{b,sof}$ is from Table 12.17, and the 1.05 factor is described in Chapter 8. It is assumed that the coupled wall gravity loads (see Table 12.2 for the unfactored gravity loads) are distributed equally between the tension-side and compression-side wall piers.

Step 3

Determine the neutral axis (i.e., contact) depth at the base of the tension-side wall (i.e., the depth over which the wall is in contact with the foundation) as:

$$c_{tws} = \frac{2N_{tws}}{f'_c t_w} \quad (12.74)$$

Step 4

Determine the moment resistances of the tension-side and compression-side walls, M_{tws} and M_{cws} respectively, and the total base moment and base shear force resistances of the coupled wall system, M_{ws} and F_{ws} respectively, using the procedure described in Chapter 8.

Step 5

Repeat Steps 1-4 until the coupled wall base shear resistance F_{ws} satisfies the design demand Q_{wd} .

Step 6

Once the required area of the wall pier post-tensioning steel A_{wp} is known, the number and placement of the wall post-tensioning tendons can be determined. High strength post-tensioning bars are used for the precast concrete wall piers in this dissertation. The total number of post-tensioning bars in each wall pier can be determined from:

$$n_{wp} = \frac{A_{wi}}{a_{wp}} \quad (12.75)$$

where, a_{wp} is the area of one bar.

The resulting wall pier cross-section for Structure P2-PWUPT is shown in Fig. 12.16 with the design details summarized in Table 12.26. A total of sixteen Ø44 mm (1.75 in.) diameter deformed post-tensioning bars spaced at 203 mm (8 in.) are used in each wall pier, with $a_{wp}=1690 \text{ mm}^2$ (2.62 in²) and $f_{wpi}=0.675f_{wpu}$, where $f_{wpu}=1035 \text{ MPa}$ (150 ksi) is the design ultimate strength of the bars. Since the coupled wall base shear force capacity at the wall softening state F_{ws} in Table 12.26 is larger than the design base shear demand, Q_{wd} , Equation (12.70) is satisfied.

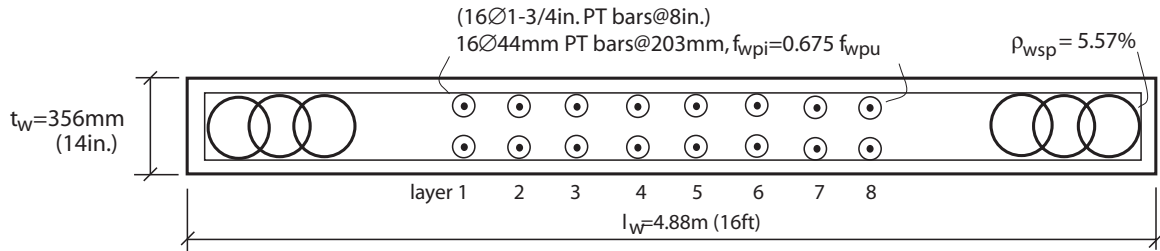


Fig. 12.16 Wall pier post-tensioning steel reinforcement

TABLE 12.26

WALL PIER POST-TENSIONING STEEL REINFORCEMENT

Structure	A_{wp} (mm ²)	P_{wi} (kN)	ΣG (kN)	$\Sigma V_{b,sof}$ (kN)	N_{tws} (kN)	N_{cws} (kN)	c_{tws} (mm)	M_{tws} (kN.m)	M_{cws} (kN.m)	M_{wbs} (kN.m)	M_{ws} (kN.m)	F_{ws} (kN)	Q_{wd} (kN)
P2-PWUPT	27045	18879	2829	5904	15509	27907	1844	27217	45327	45422	117970	5226	4893

12.8.2 Yielding of Wall Pier Post-Tensioning Steel

As discussed in Chapter 11, the coupled wall roof drift capacity at the wall PT-yielding state is required to be larger than the design-level coupled wall roof drift demand (i.e., yielding of the wall pier post-tensioning tendons is not allowed to occur under the design seismic demand level → Design Objective 2). Thus,

$$\Delta_{wy} > \Delta_d \quad (12.76)$$

where, Δ_{wy} is the coupled wall roof drift capacity at the wall PT-yielding state (described in Chapters 7 and 8) and Δ_d is the design-level roof drift demand.

For the wall and beam properties determined previously, Δ_{wy} can be estimated based on the following assumptions: (1) the maximum stress in the wall pier post-tensioning tendons is equal to the yield stress, f_{wpy} (corresponding to the linear limit strain of the post-tensioning steel); and (2) the neutral axis depth at the base of the tension-side wall is one half the neutral axis depth from the wall softening state, thus, $c_{twy}=0.5c_{tws}$.

The design procedure is described below.

Step 1

Estimate the elongation (due to the lateral displacements of the walls) of the wall pier post-tensioning tendon that yields (usually the extreme tendon on the tension side of the structure) as:

$$u_{wpy} = \frac{(f_{wpy} - f_{wpi})l_{wpu}}{E_{wp}} \quad (12.77)$$

where, $l_{wpu}=h_w$ is the unbonded length and E_{wp} is the Young's modulus of the wall post-tensioning steel.

Step 2

Estimate the roof drift capacity at the wall PT-yielding state as:

$$\Delta_{wy} = \frac{u_{wpy}}{d_{wpl} - c_{twy}} \quad (12.78)$$

where, d_{wpl} is the distance of the post-tensioning tendon that yields from the compression corner of the tension-side wall and $c_{twy}=0.5c_{tw}$ from Assumption (2).

The estimated maximum elongation in the post-tensioning bars of Structure P2-PWUPT at the wall PT-yielding state, u_{wpy} is given in Table 12.27. The resulting Δ_{wy} capacity for the structure is larger than the design-level roof drift demand, Δ_d . Thus Equation (12.76) is satisfied. If this design requirement is not satisfied, then the initial stress in the wall pier post-tensioning tendons, f_{wpi} , may need to be reduced.

TABLE 12.27
YIELDING OF WALL PIER POST-TENSIONING STEEL

Structure	u_{wpy} (mm)	Δ_{wy} (%)	Δ_d (%)
P2-PWUPT	23	1.06	0.79

Note that the wall pier post-tensioning anchors should be designed for the maximum tendon forces, P_{wu} based on the design maximum strength of the post-tensioning steel, f_{wpu} as $P_{wu} = \sum a_{wp} f_{wpu}$.

12.8.3 Concrete Confinement at Wall Pier Bases

As discussed in Chapter 11, the coupled wall roof drift capacity at the wall ultimate state is required to be larger than the survival-level coupled wall roof drift demand (i.e., crushing of the confined concrete at the bases of the wall piers is not allowed to occur under the survival seismic demand level → Design Objective 1). Thus,

$$\Delta_{wu} > \Delta_s \quad (12.79)$$

where, Δ_{wu} is the coupled wall roof drift capacity at the wall ultimate state and Δ_s is the survival-level roof drift demand.

The following assumptions are made in the design of the confinement reinforcement at the bases of the wall piers, similar to the assumptions made in Chapter 8 for the estimation of the coupled wall ultimate state: (1) the maximum compression strain in the confined concrete at the base of the compression-side wall is equal to the ultimate (i.e., crushing) strain of the confined concrete, ϵ_{ccu} ; (2) the strain distributions at the bases of the wall piers are linear; (3) the height of the “plastic hinge,” h_{wp} at the base of the compression-side wall is equal to the confined thickness of the wall, t_{wc} (estimated as the wall thickness minus the unconfined cover concrete thicknesses); and (4) the neutral axis depth at the base of the compression-side wall at the wall ultimate state is equal to $c_{cwu}=0.2l_w$.

The design procedure is described below.

Step 1

Estimate the curvature at the base of the compression-side wall when the survival-level roof drift demand, Δ_s is reached as:

$$\phi_{cwu} = \frac{A_s}{1.5h_{wp}} \quad (12.80)$$

where, $h_{wp}=t_{wc}$ from Assumption (3). This equation follows from the estimation of the coupled wall ultimate state in Chapter 8.

Step 2

Estimate the required ultimate strain for the confined concrete at the base of the compression-side wall as:

$$\varepsilon_{ccu} = c_{cwu}\phi_{cwu} \quad (12.81)$$

where, $c_{cwu}=0.2l_w$ from Assumption (4).

Step 3

Design the concrete confinement to achieve ε_{ccu} . A concrete confinement model, such as the model developed by Mander et al. (1988), can be used for this purpose.

As shown in Fig. 12.17, spiral reinforcement is used to confine the concrete at the bases of the wall piers in Structure P2-PWUPT. The stress-strain behavior of the confined concrete, as estimated using Mander et al. (1988), is also shown in Fig. 12.17. It is recommended that the confinement reinforcement be provided over a height equal to at least the first story height. The concrete confinement should be used over a wall length, l_{wc} where the concrete compression strains exceed the assumed unconfined concrete crushing strain, ε_{cu} as:

$$l_{wc} = c_{cwu} \left(1 - \frac{\varepsilon_{cu}}{\varepsilon_{ccu}}\right) \quad (12.82)$$

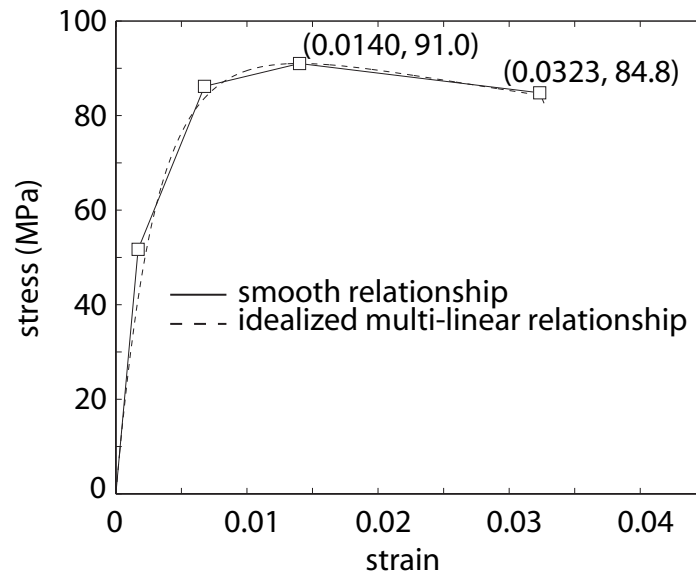
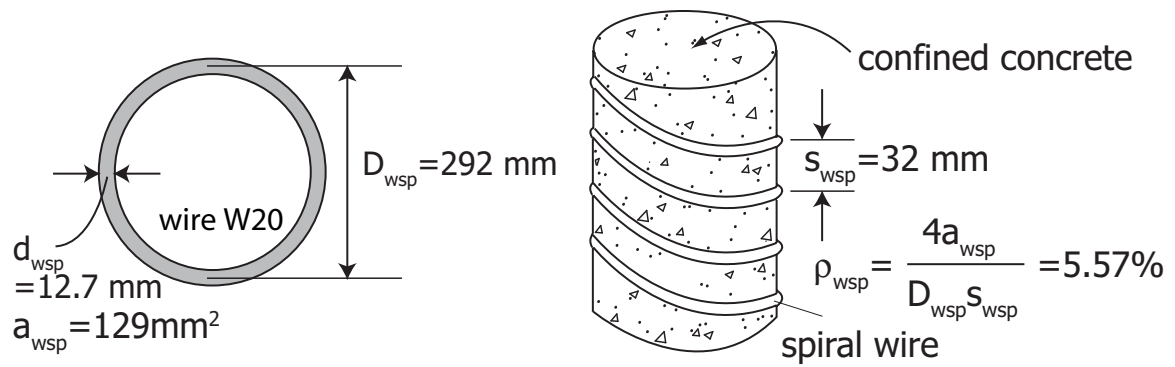


Fig. 12.17 Concrete confinement at wall pier bases

Table 12.28 shows the wall pier confined concrete ultimate strain required by Equation (12.81) as well as the strain capacity for the confined concrete. Since the strain capacity is equal to the required strain, crushing of the confined concrete under the survival demand level is prevented.

TABLE 12.28

CONCRETE CONFINEMENT AT WALL PIER BASES

Structure	ϵ_{ccu} required	ϵ_{ccu} provided	l_{wc} (mm)
P2-PWUPT	0.032	0.032	878

12.8.4 Diagonal Tension at Wall Pier Bases

To prevent shear (diagonal tension) failure of the concrete wall piers in the prototype structures, the diagonal tension capacity, $F_{w,dt}$ of the wall piers is required to be greater than the maximum wall pier base shear demand, $Q_{w,dt}$. Thus,

$$F_{w,dt} > Q_{w,dt} \quad (12.83)$$

Because of the compression forces that develop in the compression-side wall pier due to coupling, a larger portion of the total coupled wall base shear force is carried by the compression-side wall. It is assumed that the portion of the total maximum coupled wall base shear force demand, $Q_{w,max}$ carried by the compression-side wall can be estimated as:

$$Q_{w,dt} = \frac{M_{cws} + M_{wbs}}{M_{tws} + M_{cws} + M_{wbs}} Q_{w,max} \quad (12.84)$$

where, $Q_{w,dt}$ is the maximum wall pier base shear demand, M_{tws} and M_{cws} are the base moment resistances of the tension-side and compression-side wall piers at the softening state (see Table 12.22), and M_{wbs} is the contribution of the coupling beam shear forces to the coupled wall base shear resistance at the softening state.

As described in Chapter 11, the maximum base shear demand, $Q_{w,max}$, of a coupled wall structure is calculated as the sum of a first mode component, $Q_{1,max}$, and a higher mode component $Q_{h,max}$ as:

$$Q_{w,max} = Q_{1,max} + Q_{h,max} \quad (12.85)$$

The base shear demand for the first mode component is estimated as the coupled wall base shear capacity at the wall ultimate state, F_{wu} as:

$$Q_{1,max} = F_{wu} \quad (12.86)$$

The estimation of F_{wu} is described in Chapter 8. The higher mode component of the maximum base shear demand, $Q_{h,max}$ is estimated as:

$$Q_{h,max} = D_m m_w (PGA_s) \quad (12.87)$$

with,

$$D_m = \frac{m_w - m_{eff} + 0.7m_{eff,2}}{m_w} = 1 - \frac{m_{eff}}{m_w} + 0.7 \frac{m_{eff,2}}{m_w} \quad (12.88)$$

where, m_w , PGA_s , m_{eff} , and $m_{eff,2}$ are given in Tables 12.1, 12.3, and 12.5.

The resulting maximum base shear demands for Structure P2-PWUPT are listed in Table 12.29. Note that in the preliminary design check described in Section 12.5.3, $Q_{w,dt}$ was assumed to be equal to 75% of the maximum coupled wall base shear force demand, $Q_{w,max}$. Based on the design values in Table 12.29, Equation (12.84) gives a distribution ratio of 76%.

TABLE 12.29
DIAGONAL TENSION AT WALL PIER BASES

Structure	Demand Level	$Q_{1,max}$ (kN)	D_m	$Q_{h,max}$ (kN)	$Q_{w,max}$ (kN)	$Q_{w,dt}$ (kN)	$F_{w,dt}$ (kN)
P2-PWUPT	Survival	6863	0.41	6236	13099	9955	9261

Based on ACI 318-02 (ACI Committee 318 2002), the maximum attainable shear capacity of a concrete wall can be estimated as:

$$F_{w,dt} = 10 A_w \sqrt{f'_c} \quad (12.89)$$

where, $A_w = l_{wt_w}$ is the gross cross-sectional area of a wall pier and f'_c is the compressive strength of unconfined concrete.

The maximum attainable wall pier shear force capacity, $F_{w,dt}$ for Structure P2-PWUPT, listed in Table 12.29, is smaller than but sufficiently close to the maximum wall pier base shear force demand, $Q_{w,dt}$. Thus, the design is considered acceptable for Equation (12.83). The selection and placement of the wall pier transverse reinforcement to satisfy $Q_{w,dt}$ is not discussed in this dissertation.

12.8.5 Shear Slip at Coupled Wall Base

To prevent shear slip failure between the coupled wall structure and the foundation, the shear slip capacity of the structure at the base, $F_{w,ss}$ is required to be larger than the survival-level maximum base shear force demand, $Q_{w,max}$. Thus,

$$F_{w,ss} > Q_{w,max} \quad (12.90)$$

The total shear slip capacity $F_{w,ss}$ is equal to the slip capacity provided by the two wall piers, which can be calculated as the sum of two components. The first component $F_{g,ss}$ is the slip capacity due to the wall gravity load and the second component $F_{p,ss}$ is the slip capacity due to the wall post-tensioning force as:

$$F_{w,ss} = F_{g,ss} + F_{p,ss} \quad (12.91)$$

with

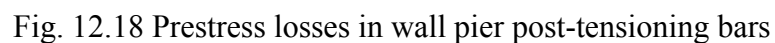
$$F_{g,ss} = 2\mu_{wf} \sum G \quad (12.92)$$

$$F_{p,ss} = 2\mu_{wf} \sum a_{wp} f_{wpr} \quad (12.93)$$

where, μ_{wf} is the coefficient of friction between the wall and the foundation, G represents the factored gravity loads acting at the floor and roof levels of a wall pier, a_{wp} is the area of one wall post-tensioning bar, and f_{wpr} represents the residual stresses in the wall post-

Under reversed cyclic loading up to the survival-level roof drift demand Δ_s , prestress losses occur in the wall pier post-tensioning bars if the maximum bar strain exceeds the yield (i.e., linear limit) strain. This loss of prestress must be considered in calculating $F_{p,ss}$ based on Equation (12.93). Referring to Fig. 12.18, the residual stress after losses in a post-tensioning bar can be estimated as:

where, f_{wpy} is the yield strength, f_{wpi} is the initial stress (i.e., stress before the application of lateral loads), α_{wp} is the post-yield stiffness ratio, E_{wp} is the linear-elastic stiffness, and



ε_{wps} is the maximum strain reached in the wall post-tensioning bar under the survival-level ground motion. Equation (12.94) can be simplified by assuming, conservatively, that $\alpha_{pi}=0$, which gives

$$f_{wpr} = f_{wpy} + f_{wpi} - E_{wp}\varepsilon_{wps} \quad (12.95)$$

It should be conservatively assumed that the survival-level roof drift demand, Δ_s is reached in the positive and negative directions of loading, and then, the structure is brought back to zero displacement. Thus, under symmetric reversed cyclic loading, the post-tensioning bars of the right-side wall pier will have the same amount of prestress losses as the bars in the left-side wall pier. When the lateral loads are applied from left to right, the maximum strains reached in the post-tensioning bars of the left-side wall pier (i.e., tension-side wall pier) can be estimated as:

$$\varepsilon_{wps} = \frac{\Delta_s (d_{wp} - c_{twu})}{l_{wpu}} + \varepsilon_{wpi} \quad (12.96)$$

where, d_{wp} is the distance of each bar from the compression corner of the tension-side wall pier, c_{twu} is the neutral axis (i.e., contact) depth at the base of the tension-side wall pier at the coupled wall ultimate state, l_{wpu} is the unbonded length of the wall post-tensioning bar (usually equal to the wall height, h_w), and ε_{wpi} is the initial strain of the bar. The neutral axis depth at the base of the tension-side wall is taken as $c_{twu}=c_{twy}=0.5c_{tws}$.

Using the above procedure, Table 12.30 shows the residual post-tensioning bar stresses, f_{wpr} in the tension-side wall of Structure P2-PWUPT after displacing the structure in one direction to the estimated survival-level roof drift demand, Δ_s , and then,

unloading it to zero lateral displacement. Note that $f_{wpr}=f_{wpi}$ if ϵ_{wps} is less than or equal to the yield strain, ϵ_{wpy} .

When the structure is displaced in the opposite direction, the post-tensioning bar layers 5 through 8 may experience larger tension strains. In other words, considering loading in both the positive and negative directions of displacement, the residual bar stresses in post-tensioning bar layers 5 through 8 may be smaller than the values shown in Table 12.30. In the design of Structure P2-PWUPT, the total residual post-tensioning bar force was conservatively calculated as four times the sum of the residual forces in post-tensioning bars layers 1 through 4, as shown in Table 12.30. It can be seen that the estimated shear slip capacity of the structure satisfies the design requirement given by Equation (12.90).

TABLE 12.30
SHEAR SLIP AT COUPLED WALL BASE

μ_{wf}	ΣG (kN)	$F_{g,ss}$ (kN)	c_{twu} (mm)	l_{wpu} (m)	bar layer no.	d_{wp} (m)	f_{wpr} (MPa)	$4 \sum_{i=1}^4 f_{wpr}(2a_{wp})$	$F_{p,ss}$ (kN)	$F_{w,ss}$ (kN)	$Q_{w,max}$ (kN)
0.7	2829	3961	922	32.6	1	3.15	620	33594	23516	27477	13099
					2	2.95	642				
					3	2.74	664				
					4	2.54	686				
					5	2.34	698				
					6	2.13	698				
					7	1.93	698				
					8	1.73	698				

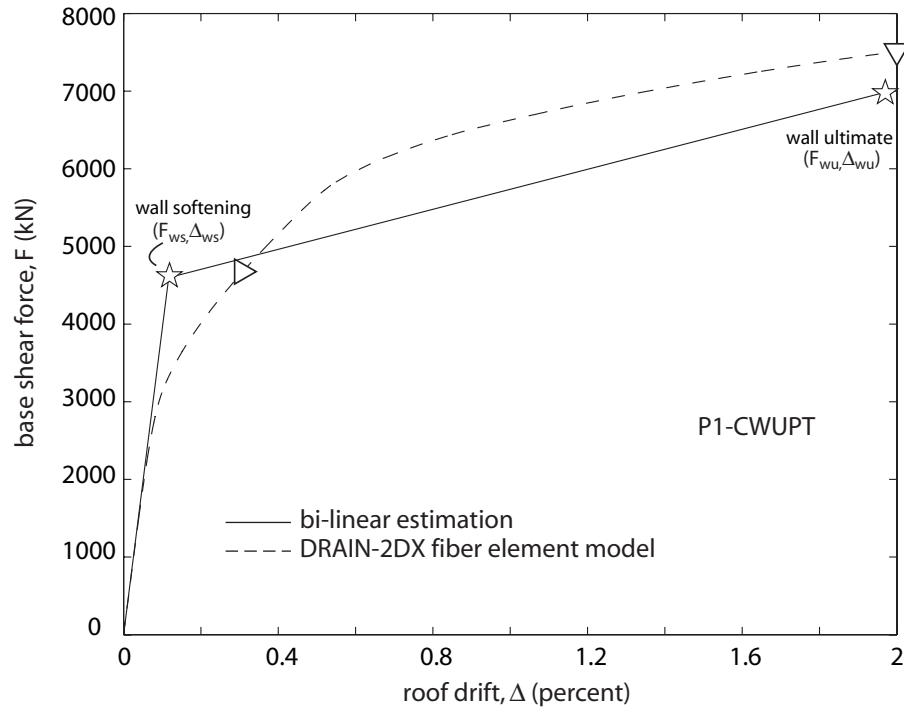
12.9 Summary Of Design and Final Checks

This section provides a summary of the designs for Structures P1-CWUPT and P2-PWUPT and conducts final design checks as follows: (1) lateral load versus deformation relationships; and (2) design criteria.

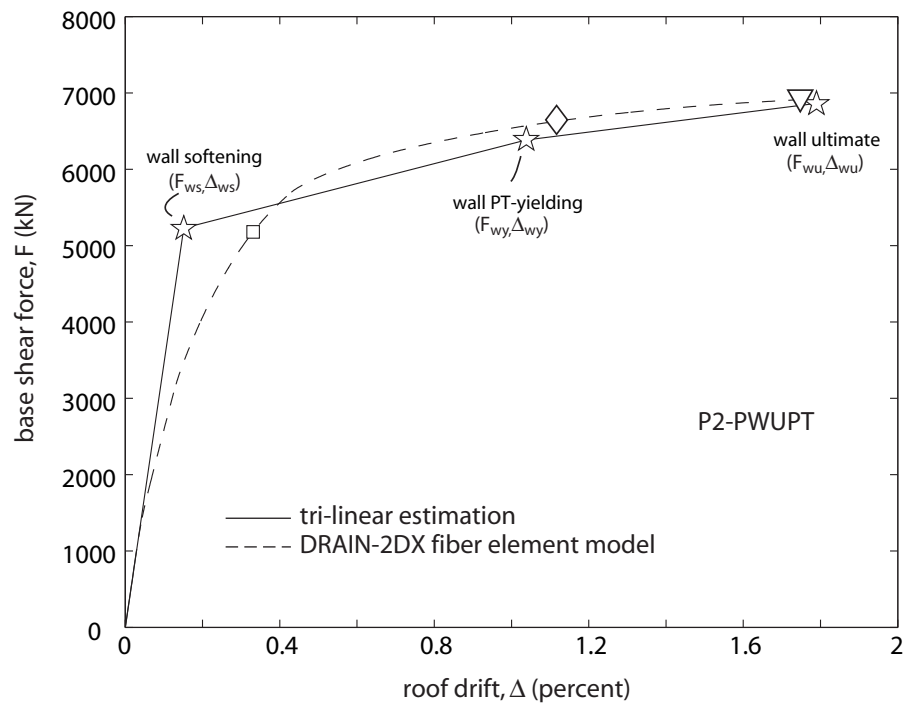
12.9.1 Lateral Load versus Deformation Relationships

Based on the structure design properties from the previous sections, the solid lines in Figs. 12.19a and 12.19b show the idealized coupled wall base shear force versus roof drift (F - Δ) relationships for Structures P1-CWUPT and P2-PWUPT, respectively. The procedures described in Chapter 8 and the idealized V_b - θ_b relationships in Fig. 12.9 are used to develop a bi-linear F - Δ relationship for Structure P1-CWUPT and a tri-linear F - Δ relationship for Structure P2-PWUPT. The bi-linear relationship for Structure P1-CWUPT is based on the coupled wall softening state (at F_{ws} , Δ_{ws}) and the coupled wall ultimate state (at F_{wu} , Δ_{wu}). In addition to these two states, the tri-linear relationship for Structure P2-PWUPT also uses the wall PT-yielding state (at F_{wy} , Δ_{wy}). A first-mode-shape distribution of lateral loads over the height of the walls is assumed with the lateral loads equally divided between the left and right wall piers.

The results from the idealized F - Δ relationships (star markers in Fig. 12.19) are summarized in Table 12.31. Comparisons of the estimated capacities with the design demands from the previous sections indicate that the design of both prototype structures is satisfactory.



(a)



(b)

Fig. 12.19 Coupled wall base shear force versus roof drift (F - Δ) relationships:
(a) Structure P1-CWUPT; (b) Structure P2-PWUPT

TABLE 12.31

IDEALIZED F- Δ BEHAVIORS FOR STRUCTURES P1-CWUPT AND P2-PWUPT

Structure	Wall Softening State		Wall PT-yielding State		Wall Ultimate State	
	F_{ws} (kN)	Δ_{ws} (%)	F_{wy} (kN)	Δ_{wy} (%)	F_{wu} (kN)	Δ_{wu} (%)
P1-CWUPT	4603	0.13	-	-	6988	1.97
P2-PWUPT	5226	0.15	6383	1.06	6863	1.79

For comparison, the dashed lines in Fig. 12.19 show the smooth F- Δ behaviors of Structures P1-CWUPT and P2-PWUPT using the fiber element analytical model from Chapter 6. In general, the idealized relationships capture the structure capacities from the fiber element models reasonably well. More detailed information on the expected behavior of the prototype structures using the fiber element models is given in Chapter 13.

12.9.2 Design Criteria

As demonstrated throughout the previous sections of this chapter, the seismic design of a coupled wall structure involves establishing structure demands and providing structure capacities until required design criteria are satisfied. A summary of the final design comparisons between the estimated demands and capacities of Structures P1-CWUPT and P2-PWUPT are given in Table 12.32, with the required design criteria listed below. Note that the structure design capacities and demands in Table 12.32 are estimated using the idealized design relationships and procedures from Chapters 5, 8, 10, and 11, without the simplifying assumptions made during the design of the structures. As

expected, the comparisons between the capacities and the demands indicate that the prototype structures satisfy all of the required design criteria reasonably well.

(1) To satisfy the displacement-based design requirement, the roof drift capacity of the coupled wall structure at the wall ultimate state, Δ_{wu} should be larger than the allowable survival-level roof drift demand, Δ_s . Thus,

$$\Delta_{wu} > \Delta_s \quad (12.97)$$

(2-1) For systems with cast-in-place concrete walls, 2/3 times the roof drift capacity of the coupled wall structure at the wall ultimate state, Δ_{wu} should be larger than the allowable design-level roof drift demand, Δ_d . This requirement ensures that an adequate margin of reserve displacement capacity exists between the survival-level and design-level demands, and between the collapse prevention and life safety performance levels. Thus,

$$(2/3)\Delta_{wu} > \Delta_d \quad (12.98)$$

(2-2) For systems with precast concrete walls, the roof drift capacity of the coupled wall structure at the wall PT-yielding state, Δ_{wy} should be larger than the allowable design-level roof drift demand, Δ_d . This requirement ensures that yielding of the wall post-tensioning steel does not occur under the design-level earthquake and that an adequate margin of reserve displacement capacity exists between the survival-level and design-level demands. Thus,

$$\Delta_{wy} > \Delta_d \quad (12.99)$$

TABLE 12.32

SEISMIC DESIGN CRITERIA FOR STRUCTURES P1-CWUPT AND P2-PWUPT

Design Criterion		P1-CWUPT		P2-PWUPT	
		Capacity	Demand	Capacity	Demand
(1)	$\Delta_{wu} > \Delta_s$	1.97%	1.67%	1.79%	1.71%
(2)	$(2/3)\Delta_{wu} > \Delta_d$ (P1-CWUPT) $\Delta_{wy} > \Delta_d$ (P2-PWUPT)	1.31%	0.71%	1.06%	0.79%
(3)	$F_{ws} > Q_{wd}$	4603 kN	4782 kN	5226 kN	4893 kN
(4)	$F_{w,ss} > Q_{w,max}$	44614 kN	13156 kN	27477 kN	13099 kN
(5)	$F_{w,dt} > Q_{w,dt}$	9261 kN	9341 kN	9261 kN	9955 kN
(6)	$V_{ba,sof} > Q_{bd,a}$	44 kN	30 kN	432 kN	360 kN
	$V_{bp,sof} > Q_{bd,p}$	623 kN	588 kN	316 kN	294 kN
(7)	$\theta_{b,pty} > \theta_s$	7.24%	5.49%	6.90%	5.62%
(8)	$(2/3)\theta_{b,pty} > \theta_d$	4.83%	2.33%	4.60%	2.59%
(9)	$V_{b,ss} > Q_{b,max}$	1169 kN	963 kN	1273 kN	1184 kN
(10)	$f_{ccw} > \sigma_{wc}$	98.7 MPa	92.4 MPa	90.4 MPa	82.1 MPa
(11)	$P_{bi} < 0.25A_{bc}f_{by}$	2402 kN	2500 kN	2402 kN	1251 kN
(12)	$P_{by} < A_{bfc}f_{bm}$	4159 kN	3784 kN	4159 kN	1892 kN
(13)	$u_{as} < 38 \text{ mm (1.5 in.)}$	38 mm	30 mm	38 mm	31 mm
(14)	$C_{asx} > 2T_{ayx}$	425 kN	106 kN	1063 kN	1032 kN

(3) To prevent premature “softening” of the structure, an adequate lateral strength needs to be ensured. The base shear capacity of the coupled wall system at the wall softening state, F_{ws} should be larger than the design base shear force demand, Q_{wd} . Thus,

$$F_{ws} > Q_{wd} \quad (12.100)$$

(4) To prevent shear slip failure between the coupled wall structure and the foundation, the shear slip capacity of the structure at the base, $F_{w,ss}$ should be larger than the survival-level maximum base shear force demand, $Q_{w,max}$. Thus,

$$F_{w,ss} > Q_{w,max} \quad (12.101)$$

(5) To prevent diagonal tension failure of the wall piers, the diagonal tension capacity of each wall pier, $F_{w,dt}$ should be larger than the survival-level maximum wall pier shear force demand, $Q_{w,dt}$. Thus,

$$F_{w,dt} > Q_{w,dt} \quad (12.102)$$

(6) To ensure that the target coupling degree, DOC and angle strength ratio, β_{ar} selected during design are satisfied, the contribution of the top and seat angles, $V_{ba,sof}$ and the contribution of the beam post-tensioning force, $V_{bp,sof}$ to the coupling beam shear force capacity at the beam softening state, $V_{b,sof}$ should be larger than the corresponding demands, $Q_{bd,a}$ and $Q_{bd,p}$, respectively. Thus,

$$V_{ba,sof} > Q_{bd,a} \quad (12.103)$$

$$V_{bp,sof} > Q_{bd,p} \quad (12.104)$$

(7) To prevent yielding of the beam post-tensioning steel under the survival seismic demand level, the chord rotation capacity of the coupling beams at the beam PT-yielding state, $\theta_{b,pty}$ should be larger than the survival-level beam chord rotation demand, θ_s . Thus,

$$\theta_{b,pty} > \theta_s \quad (12.105)$$

(8) 2/3 times the chord rotation capacity of the coupling beams at the beam PT-yielding state, $\theta_{b,pty}$ should be larger than the design-level beam chord rotation demand, θ_d . This requirement ensures that an adequate margin of reserve displacement capacity exists between the survival-level and design-level demands, and between the collapse prevention and life safety performance levels. Thus,

$$(2/3)\theta_{b,pty} > \theta_d \quad (12.106)$$

(9) To prevent shear slip at the ends of the coupling beams, the shear slip capacity at the beam-to-wall interfaces, $V_{b,ss}$ should be larger than the survival-level maximum beam shear force demand, $Q_{b,max}$. Thus,

$$V_{b,ss} > Q_{b,max} \quad (12.107)$$

(10) To transfer the coupling beam contact stresses with little deformation in the wall concrete, the compressive strength of the confined concrete in the beam-to-wall-contact regions, f_{ccw} should be larger than the maximum anticipated concrete contact stresses under the survival seismic demand level, σ_{wc} . Thus,

$$f_{ccw} > \sigma_{wc} \quad (12.108)$$

(11) To prevent excessive local distortions and possible instability of the coupling beams, the total initial beam post-tensioning force, P_{bi} should be smaller than 0.25 times the axial yield strength of the coupling beam cross section (plus cover plates, if used). Thus,

$$P_{bi} < 0.25A_{bc}f_{by} \quad (12.109)$$

(12) To prevent excessive local distortions and possible instability of the coupling beams, the total yield strength of the beam post-tensioning tendons, P_{by} should be smaller than the maximum axial strength of one coupling beam flange (plus cover plate, if used). Thus,

$$P_{by} < A_{bfc}f_{bm} \quad (12.110)$$

(13) To prevent low cycle fatigue fracture of the top and seat angles, the maximum anticipated deformation of the angles in tension under the survival demand level should be smaller than the deformation capacity of the angles in tension. More research needs to

be conducted on the behavior and capacity of the top and seat angles to ensure that the design deformation can be reached without fracture. Based on the subassemblage experiment results in Chapter 9, it is suggested that the deformation of the tension angles under the survival demand level u_{as} be smaller than 38 mm (1.5 in.). Thus,

$$u_{as} < 38 \text{ mm (1.5 in.)} \quad (12.111)$$

(14) To prevent slip of the angle-to-beam connection bolts as the angles are pulled away from the walls, the slip capacity of the angle-to-beam bolts, C_{asx} should be larger than the maximum anticipated strength of the angles in tension, $2T_{ayx}$. Thus,

$$C_{asx} > 2T_{ayx} \quad (12.112)$$

(15) The angle-to-wall connections should also be designed for the maximum anticipated strength of the angles in tension. No detailed design information is provided in the dissertation on this topic.

(16) The coupling beam and wall pier (in the case of precast concrete walls) post-tensioning anchors should be designed for the maximum tendon forces based on the design maximum strength of the post-tensioning steel. No detailed design information is provided in the dissertation on this topic.

(17) If cover plates are used to strengthen the coupling beam flanges, the welds between the cover plates and the flanges should be designed for the maximum anticipated forces. No detailed design information is provided in the dissertation on this topic.

CHAPTER 13

BEHAVIOR OF PROTOTYPE STRUCTURES UNDER STATIC LATERAL LOADING

This chapter discusses the expected behavior of prototype Structures P1-CWUPT and P2-PWUPT from Chapter 12 under static lateral loading. Evaluations of the global behavior of the structures as well as the local behavior of the wall piers and the coupling beams are provided. The behavior of Structure P1-CWUPT is compared with the behavior of a similar structure with embedded steel coupling beams. The chapter is organized into the following sections: (1) introduction; (2) behavior under monotonic loading; (3) behavior under reversed cyclic loading; and (4) structure with embedded steel coupling beams.

13.1 Introduction

The nonlinear behavior of each prototype coupled wall structure is investigated under static lateral loads combined with gravity loads using the DRAIN-2DX (Prakash et al. 1993) fiber element model described in Chapter 6 including the modifications recommended in Chapter 10. The wall-contact elements from Chapter 6 and the vertical angle elements from Chapter 10 are not used in the modeling of the structures in order to simplify the models and reduce computation time. Previous analytical investigations have

shown that these elements do not have a significant effect on the behavior of multi-story coupled wall structures, and thus, they can be ignored.

The analyses are conducted by applying loads on the structures in the following order: (1) beam and wall pier (for Structure P2-PWUPT) post-tensioning forces; (2) gravity loads applied at the floor and roof levels; and (3) equivalent lateral forces applied at the floor and roof levels in displacement control.

The beam and wall pier post-tensioning element forces are applied all at once. Then, the gravity loads, G are applied under the same load combination used in design with 100% of the unfactored design dead load (D) plus 25% of the unreduced unfactored design live load (L) to represent the amount of gravity loading that may be acting on the structure during an earthquake. The use of the same load combination in the design and analysis of the structures allows for more direct comparisons between the target seismic performance objectives and the estimated structure demands and capacities.

As described in Chapter 7, the gravity loads are applied at the wall-height element nodes at the floor and roof levels, with no loads applied along the length of the coupling beams. Table 13.1 provides a summary of the gravity loads applied on the left and right wall piers in Structures P1-CWUPT and P2-PWUPT.

The displacement controlled nonlinear lateral load analyses are conducted based on the lateral displacement of Node 54 (as shown in Fig. 7.1) with respect to the wall base. A first mode distribution of lateral loads applied from left to right over the height of the walls is used. For each coupled wall system, the lateral loads are equally divided between the left and right wall piers and are applied at the wall-height element nodes at the floor

TABLE 13.1

WALL PIER GRAVITY LOADS IN STRUCTURES P1-CWUPT AND P2-PWUPT

Level	Structure P1-CWUPT		Structure P2-PWUPT	
	1.0D (kN)	0.25L (kN)	1.0D (kN)	0.25L (kN)
Roof	330	4	334	4
8 th floor	330	17	334	17
7 th floor	330	17	334	17
6 th floor	330	17	334	17
5 th floor	330	17	334	17
4 th floor	330	17	334	17
3 rd floor	330	17	334	17
2 nd floor	366	17	370	17

and roof levels (at the same nodes where the gravity loads are applied). Note that inertial force distributions significantly different than the assumed first mode lateral load distribution may occur during an earthquake (e.g., Ghosh and Markevicius 1990; Paulay and Priestley 1992; Eberhard and Sozen 1993; Kabeyasawa 1993; Aoyama 1993; Otani et al. 1994; Kurama et al. 1997, 1999b); however, this is not investigated in this chapter.

13.2 Behavior Under Monotonic Loading

This section evaluates the behavior of Structures P1-CWUPT and P2-PWUPT under monotonic lateral loads combined with gravity loads as follows: (1) coupled wall base shear force versus roof drift behaviors; (2) wall pier base flexural steel strains and stresses; (3) wall pier base axial forces; (4) wall pier base shear forces; (5) wall pier base moments; (6) degree of coupling; (7) wall pier base concrete strains; (8) coupling beam shear force versus chord rotation behaviors; (9) coupling beam axial forces and post-tensioning forces; (10) coupling beam end strains; and (11) tension angle force versus deformation behaviors.

Note that the lateral load behaviors of Structures P1-CWUPT and P2-PWUPT are similar to the behaviors of the CIP-UPT and PRE-UPT systems discussed in Chapter 7. Thus, the sections below make frequent references to Chapter 7 in evaluating the results.

13.2.1 Coupled Wall Base Shear Force versus Roof Drift Behaviors

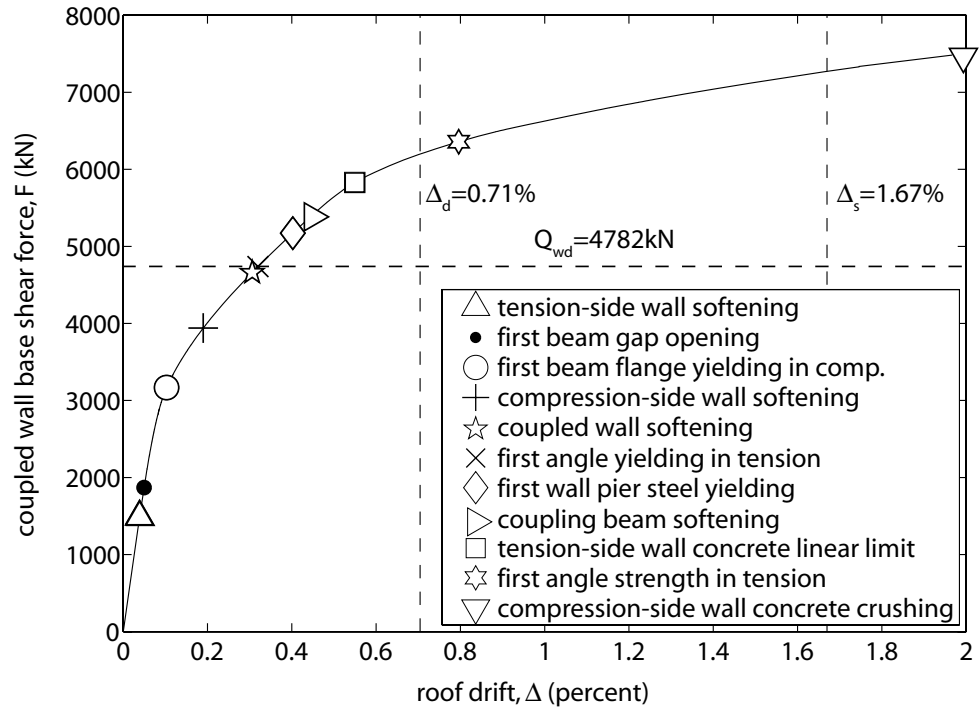
Figs. 13.1a and 13.1b show the coupled wall base shear force versus roof drift ($F-\Delta$) behaviors of Structures P1-CWUPT and P2-PWUPT, respectively (same as the dashed lines in Fig. 12.19a and 12.19b, respectively). The base shear force is calculated as the sum of the lateral forces applied over the height of the structures, and the roof drift is calculated as the average lateral displacement of the tension-side wall (i.e., left-side wall for lateral loads applied from left to right) and the compression-side wall (i.e., right side wall) at the roof (i.e., at Nodes 27 and 54 in Fig. 7.1) divided by the wall height to the base, h_w .

The following states are identified on the $F-\Delta$ relationships in Fig. 13.1, similar to the states described in Chapters 7 and 8:

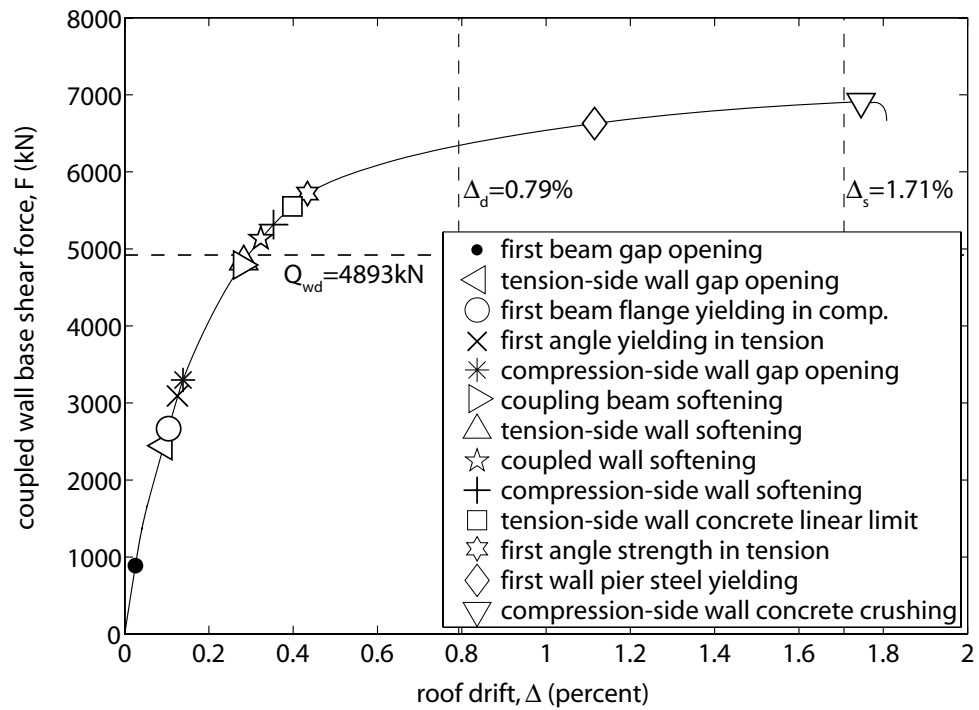
(1) Tension-side wall softening (Δ markers) – This state is defined as the state when the neutral axis at the base of the tension-side wall pier reaches the centerline of the wall pier.

(2) First beam gap opening (\bullet markers) – This state is defined as the state when gap opening initiates at the beam-to-wall interfaces of the structure.

(3) Tension-side wall gap opening (\triangleleft marker) – This state is defined as the state when gap opening initiates at the base of the tension-side wall pier in Structure P2-PWUPT.



(a)



(b)

Fig. 13.1 Coupled wall base shear force versus roof drift behaviors:
(a) Structure P1-CWUPT; (b) Structure P2-PWUPT

(4) First beam flange yielding in compression (\circ markers) – This state is defined as the state when compression yielding of the coupling beam flanges occurs for the first time in the structure.

(5) Compression-side wall softening (+ markers) – This state is defined as the state when the neutral axis at the base of the compression-side wall pier reaches the centerline of the wall pier.

(6) First angle yielding in tension (\times markers) – This state is defined as the state when the force in the tension angles reaches the angle yield strength, T_{ayx} for the first time in the structure.

(7) Compression-side wall gap opening (\ast marker) – This state is defined as the state when gap opening initiates at the base of the compression-side wall pier in Structure P2-PWUPT.

(8) Coupled wall softening (\star markers) – As discussed in Chapter 8, the base shear force at this state, F_{ws} is taken as the average of the maximum and minimum base shear forces from the compression-side wall softening, first wall pier steel yielding, and coupling beam softening states for Structure P1-CWUPT and from the compression-side wall softening, tension-side wall concrete linear limit, and coupling beam softening states for Structure P2-PWUPT. The roof drift at the coupled wall softening state, Δ_{ws} is taken as the roof drift corresponding to F_{ws} .

(9) First wall pier steel yielding (\diamond markers) – This state is defined as the first yielding of the wall pier mild flexural reinforcing bars in Structure P1-CWUPT and as the first yielding of the wall pier post-tensioning bars in Structure P2-PWUPT (also referred to as the coupled wall PT-yielding state, reached at F_{wy} and Δ_{wy} , as described in Chapter

8). Note that the linear limit point on the steel stress-strain relationship is used to identify the yielding of the post-tensioning bars.

(10) Tension-side wall concrete linear limit (\square markers) – This state is defined as the state when the maximum confined concrete compression stress at the base of the tension-side wall pier reaches the linear limit (i.e., limit of proportionality) stress of the confined concrete.

(11) Coupling beam softening (\triangleright markers) – This state is defined as the state when the average coupling beam shear force in the structure (i.e., the sum of the shear forces in the coupling beams divided by the number of beams) is equal to $1.05V_{b,sof}$, where $V_{b,sof}$ is the softening state coupling shear force for an isolated subassembly (see Chapters 10 and 12) and the factor 1.05 is described in Chapter 8.

(12) First angle strength in tension (\star markers) – This state is defined as the state when the force in the tension angles reaches the full angle tension strength, $2T_{ayx}$ for the first time (based on the revised tension angle model in Chapter 10) in the structure.

(13) Compression-side wall concrete crushing (∇ markers) – This state, also referred to as the coupled wall ultimate state (reached at F_{wu} and Δ_{wu}) in Chapter 8, is defined as the state when the extreme strain in the confined concrete at the base of the compression-side wall pier reaches the crushing strain, ϵ_{ccu} .

Fig. 13.1 shows that, due to the larger compressive axial forces in the wall piers as a result of post-tensioning, Structure P2-PWUPT reaches the tension-side wall softening state (Δ markers) and the compression-side wall softening state (+ markers) at larger base shear forces than Structure P1-CWUPT. Furthermore, as a result of the smaller coupling beam post-tensioning forces while the beam cross section is kept the same, Structure P2-

PWUPT reaches the first beam gap opening state (● markers) at a smaller base shear force than Structure P1-CWUPT. Due to the earlier gap opening at the coupling beam ends, Structure P2-PWUPT also reaches the first beam flange yielding in compression state (○ markers) at a smaller base shear force than Structure P1-CWUPT.

The horizontal dashed lines in Figs. 13.1a and 13.1b show the coupled wall base shear demands, Q_{wd} from Chapter 12 ($Q_{wd}=4782$ kN for Structure P1-CWUPT and $Q_{wd}=4893$ kN for Structure P2-PWUPT). It is observed that the base shear capacities of the prototype structures at the coupled wall softening state, F_{ws} (▷ markers) satisfy the Q_{wd} demands.

Similarly, the vertical dashed lines in Figs. 13.1a and 13.1b show the design-level and survival-level roof drift demands, Δ_d and Δ_s , respectively, from Chapter 12 ($\Delta_d=0.71\%$, $\Delta_s=1.67\%$ for Structure P1-CWUPT, and $\Delta_d=0.79\%$, $\Delta_s=1.71\%$ for Structure P2-PWUPT). As required by design, for both structures, the roof drift capacities at the coupled wall ultimate state (▽ markers), Δ_{wu} satisfy the Δ_s demands. In addition, the roof drift capacity at the coupled wall PT-yielding state (◇ marker), Δ_{wy} for Structure P2-PWUPT satisfies the Δ_d demand.

Note that, for both structures, yielding of the coupling beam post-tensioning tendons (i.e., beam PT-yielding state) occurs after the coupled wall ultimate state, and, thus is not shown in Fig. 13.1. As required by design, yielding of the beam post-tensioning tendons does not occur under the survival level demand.

A more detailed evaluation of the behavior of the prototype structures is provided in the following sections. A summary of the results from the analyses is given in Table 13.2, together with estimated values from the idealized relationships and procedures in

Chapters 5, 8, 10, and 11. It is observed that the coupled wall base shear force, F and roof drift, Δ can be obtained with good accuracy using the idealized relationships. Note that the estimated values in Table 13.2 do not use the simplifying assumptions made during the design of the structures in Chapter 12.

TABLE 13.2

COMPARISONS BETWEEN ESTIMATION AND ANALYTICAL RESULTS

	P1-CWUPT				P2-PWUPT					
	Wall Softening State		Wall Ultimate State		Wall Softening State		Wall PT-yielding State		Wall Ultimate State	
	DRAIN	estimate	DRAIN	estimate	DRAIN	estimate	DRAIN	estimate	DRAIN	estimate
coupled wall base shear force F (kN)	4670	4603	7335	6988	5182	5226	6628	6383	6912	6863
coupled wall base moment M_w (kN-m)	105644	101946	165800	161323	117150	117970	149895	144019	156302	154844
coupled wall roof drift Δ (%)	0.31	0.13	2.01	1.97	0.33	0.15	1.12	1.06	1.75	1.79
tension wall base shear force F_{tw} (kN)	1735	-	1797	-	1352	-	992	-	952	-
compression wall base shear force F_{cw} (kN)	2940	-	5591	-	3741	-	5431	-	5711	-
tension wall base moment M_{tw} (kN-m)	24250	29241	41787	41604	26702	27217	32680	32866	34894	-
compression wall base moment M_{cw} (kN-m)	41810	32099	74083	76242	43855	45327	59427	58235	61800	-
degree of coupling DOC (percent)	36	40	28	40	37	39	34	37	34	34
tension wall base axial force N_{tw} (kN)	-2727	-2993	-3759	-3372	15435	15509	15741	16039	17699	16489
compression wall base axial force N_{cw} (kN)	8384	8589	9416	9047	27769	27907	30460	31132	31821	32742
tension wall PT force P_{tw} (kN)	-	-	-	-	19158	18879	20928	21128	21862	23018
compression wall PT force P_{cw} (kN)	-	-	-	-	18384	18879	19620	20403	20786	21764
tension wall neutral axis depth c_{tw} (mm)	1285	1270	615	635	2159	1844	963	922	838	922
Comp. wall neutral axis depth c_{cw} (mm)	2019	2438	955	932	2591	2438	1219	1219	1118	1219
average coupling beam shear force V_b (kN)	694	689	823	743	820	738	1001	860	1026	926
average coupling beam chord rotation θ_b (%)	0.87	0.17	5.53	6.24	0.95	0.19	3.46	2.82	5.48	4.86

13.2.2 Wall Pier Base Flexural Steel Strains and Stresses

Figs. 13.2a and 13.2b show the stresses in selected layers of flexural mild steel reinforcement at the bases of the tension-side and compression-side wall piers from Structure P1-CWUPT, respectively, versus the coupled wall roof drift, Δ .

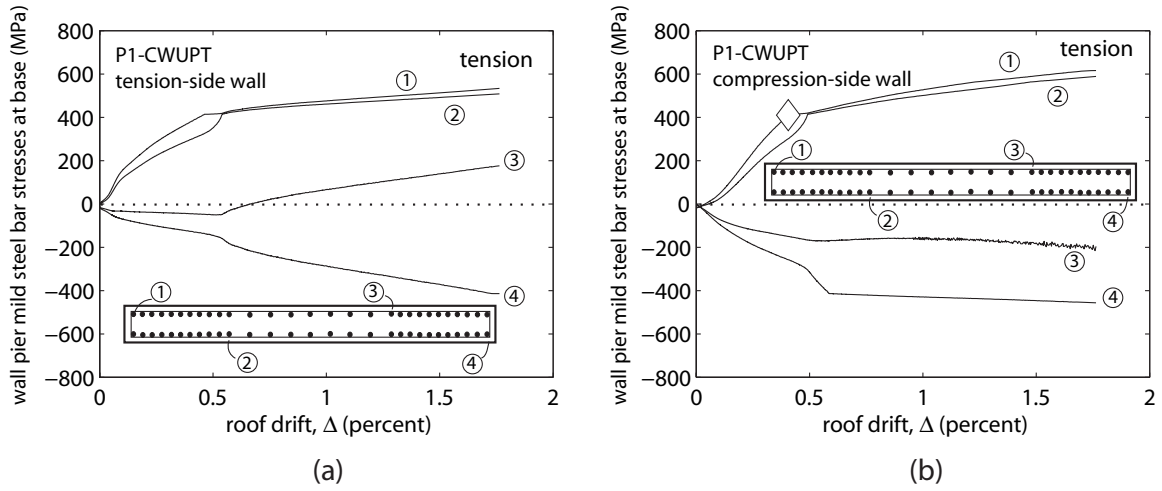


Fig. 13.2 Wall pier flexural mild steel stresses at base of Structure P1-CWUPT:
(a) tension-side wall; (b) compression-side wall

Similarly, Figs. 13.3a and 13.3b show the stresses, f_{wp1} through f_{wp8} , in the eight pairs of post-tensioning bars of the tension-side and compression-side wall piers from Structure P2-PWUPT, respectively. The corresponding stress-strain (f_{wp} - ϵ_{wp}) behaviors of the post-tensioning bars are shown in Figs. 13.4a and 13.4b, respectively. Similar to the PRE-UPT system in Chapter 7, the post-tensioning bar strains in the tension-side wall pier are larger than the strains in the compression-side wall pier since the tension-side wall is subjected to tension forces from the coupling beams. As expected, the post-tensioning bars that are further away from the compression (i.e., right) corner at the base of each wall pier reach larger tensile strains.

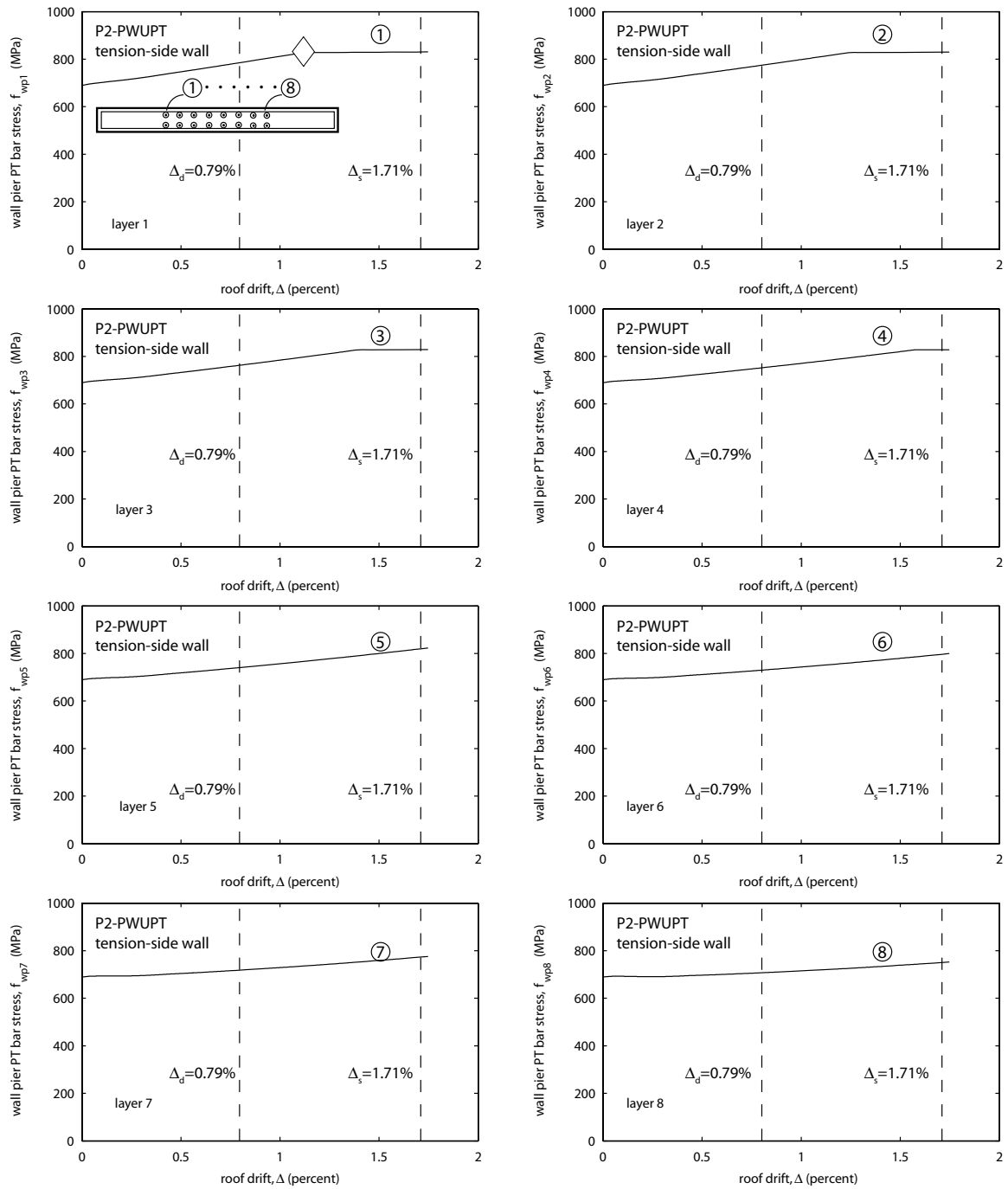


Fig. 13.3a Wall pier post-tensioning bar stresses
in Structure P2-PWUPT: tension-side wall

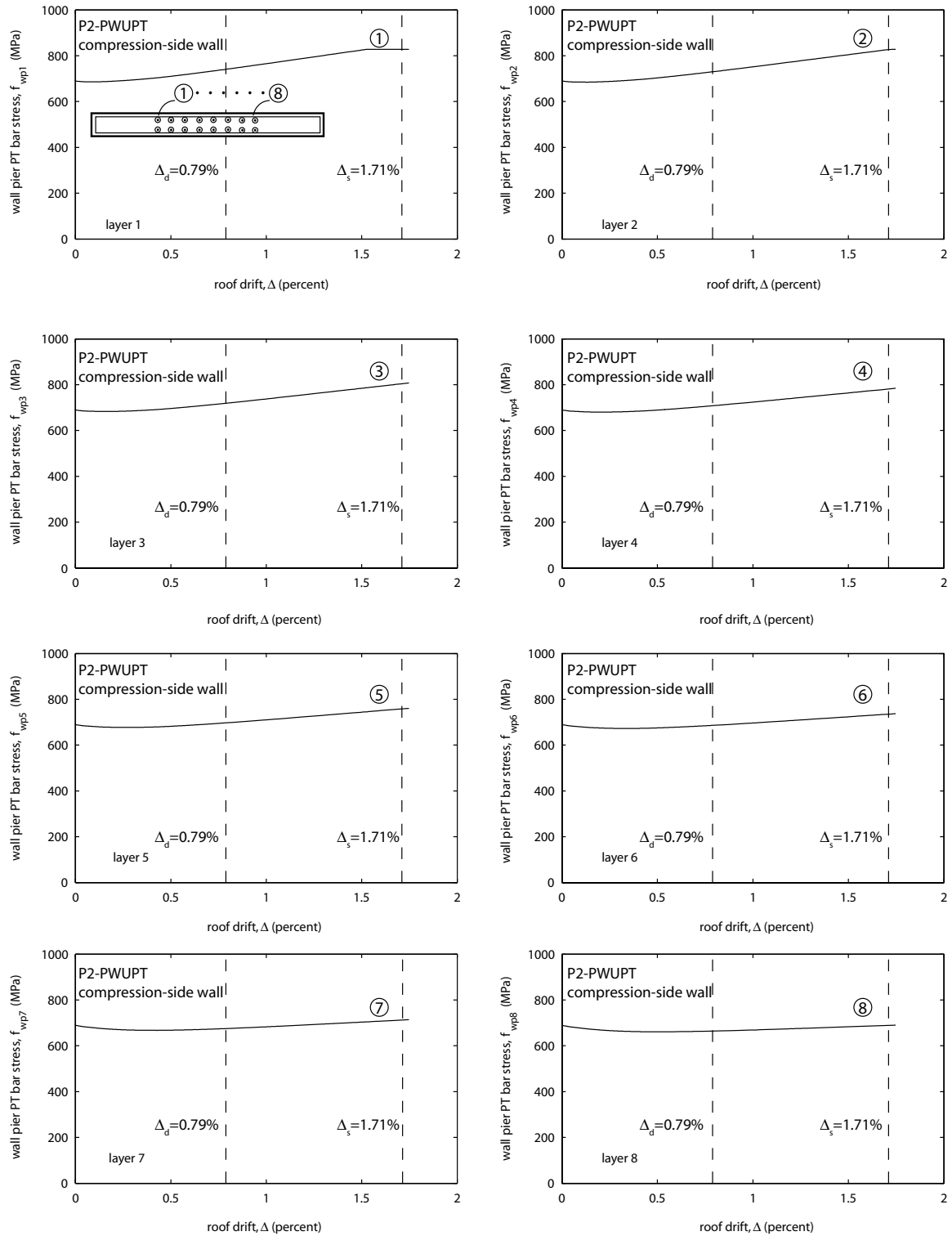


Fig. 13.3b Wall pier post-tensioning bar stresses
in Structure P2-PWUPT: compression-side wall

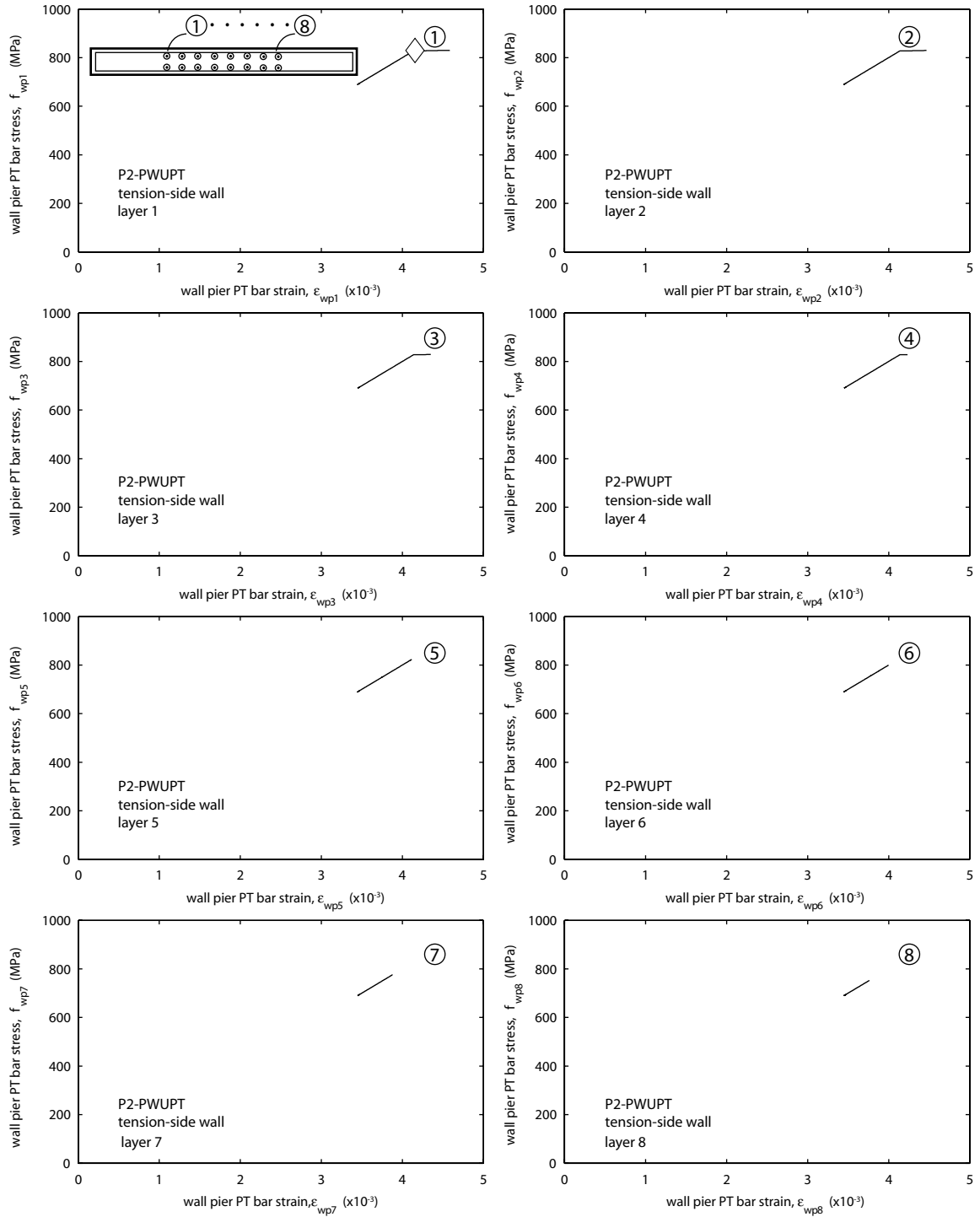


Fig. 13.4a Wall pier post-tensioning bar stress-strain behaviors
for Structure P2-PWUPT: tension-side wall

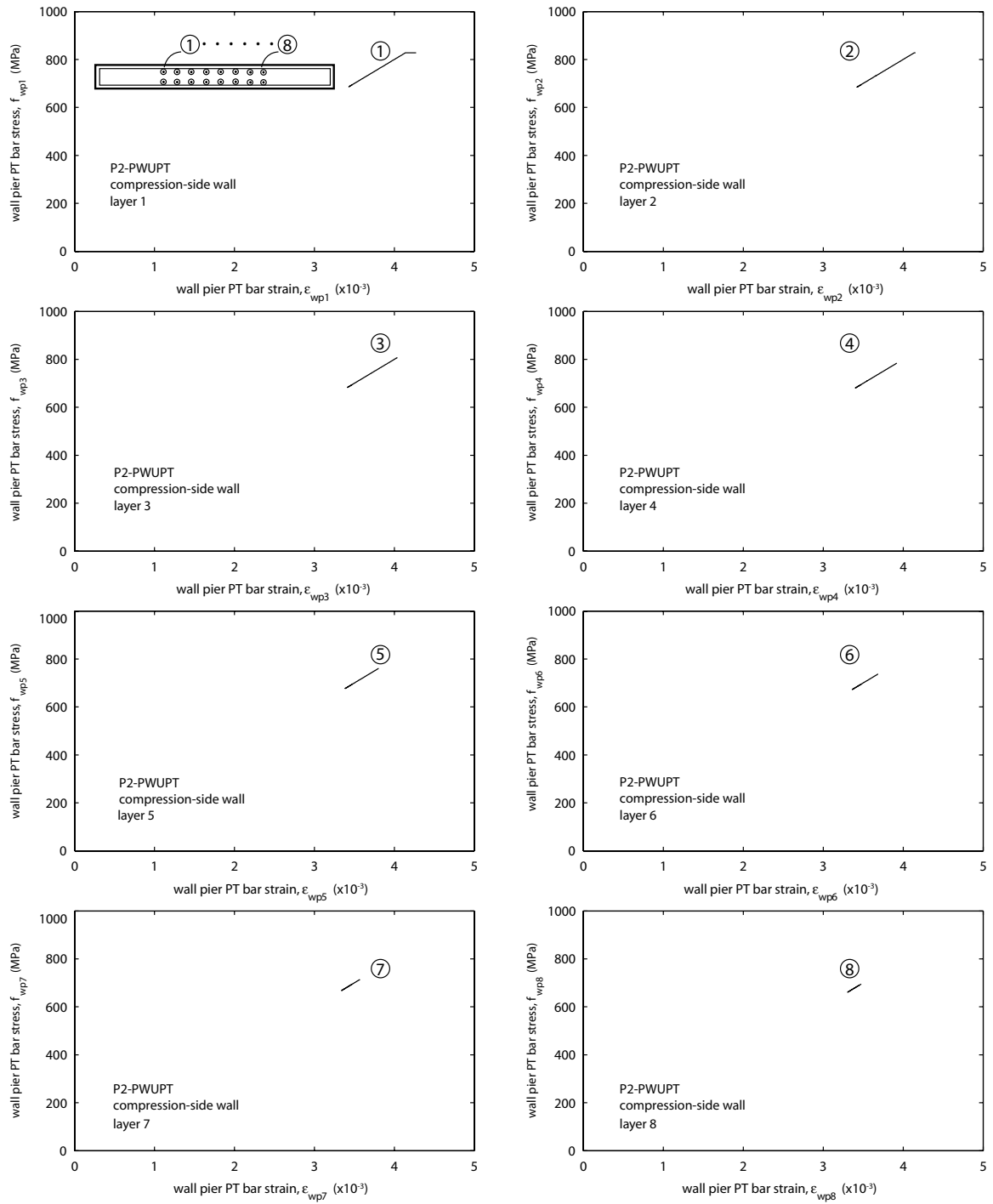


Fig. 13.4b Wall pier post-tensioning bar stress-strain behaviors for Structure P2-PWUPT: compression-side wall

The vertical dashed lines in Fig. 13.3 show the design-level and survival-level roof drift demands (Δ_d and Δ_s , respectively) from Chapter 12. As required by design, none of the wall pier post-tensioning bars yields under the design-level roof drift demand, Δ_d . As the structure is displaced further to the survival demand level, the four pairs of post-tensioning bars furthest away from the compression corner of the tension-side wall (i.e., f_{wp1} through f_{wp4}) yield beginning at a roof drift of, approximately, $\Delta_{wy}=1.12\%$, corresponding to the coupled wall PT-yielding state (see Fig. 13.1b and Table 13.2). In the compression-side wall, only the first pair of bars (f_{wp1}) furthest away from the compression corner yields at a roof drift of, approximately, $\Delta=1.5\%$. As a result of the use of unbonded tendons, the strains in the wall pier post-tensioning bars remain small, even for the bars that yield (see Fig. 13.4).

As shown in Table 13.2, the total post-tensioning forces in the tension-side and compression-side wall piers, P_{tw} and P_{cw} , and the roof drift at the wall PT-yielding state, Δ_{wy} can be estimated with good accuracy using the idealized relationships and procedures from Chapters 5, 8, 10, and 11.

13.2.3 Wall Pier Base Axial Forces

The solid and dashed lines in Figs. 13.5a and 13.5b show the axial forces, N_{tw} and N_{cw} , at the bases of the tension-side and compression-side wall piers in Structures P1-CWUPT and P2-PWUPT, respectively. A positive wall pier axial force indicates a compressive force. The markers shown in Figs. 13.5a and 13.5b are the same as the markers in Figs. 13.1a and 13.1b, respectively.

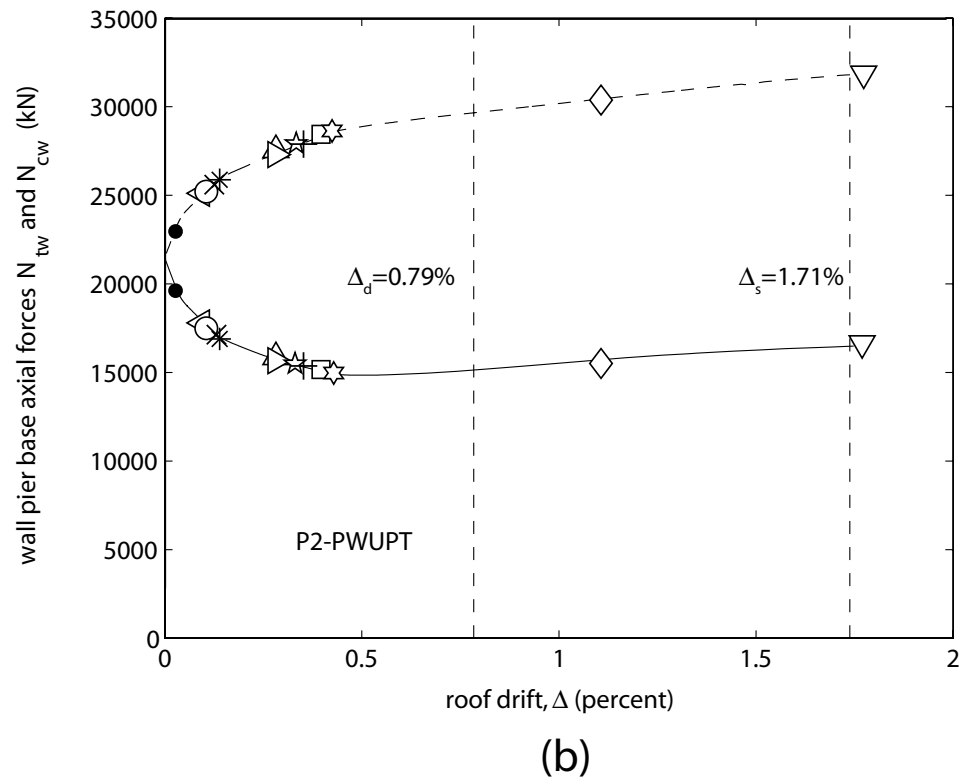
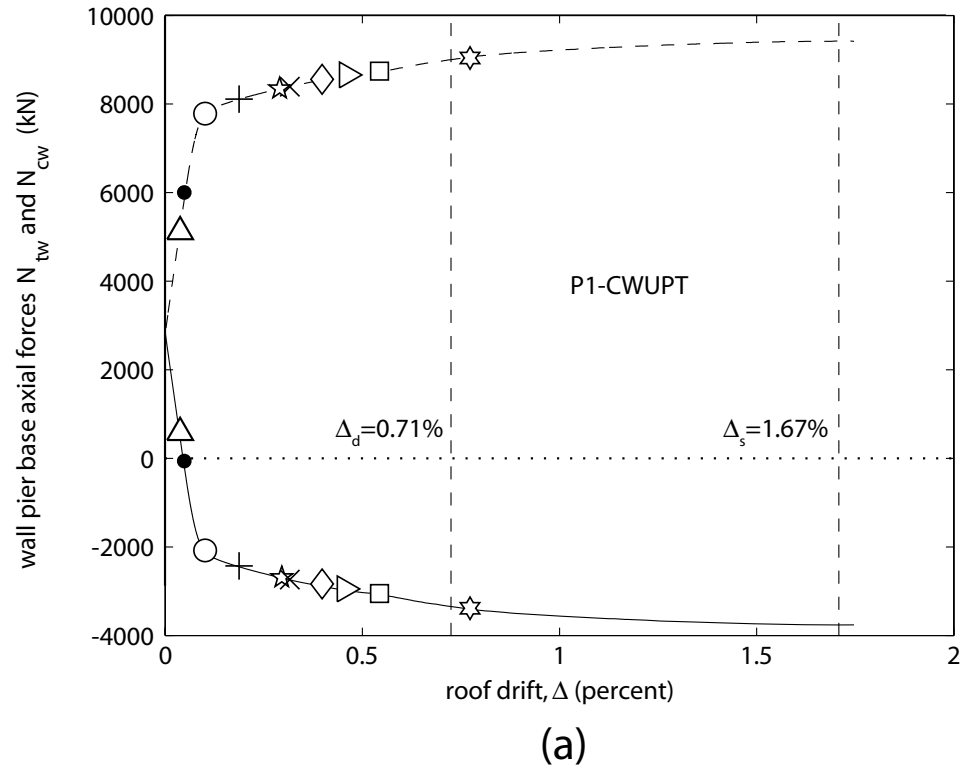


Fig. 13.5 Wall pier base axial forces: (a) Structure P1-CWUPT; (b) Structure P2-PWUPT

Figs. 13.6a and 13.6b show the contributions of the wall pier gravity loads, N_{twg} and N_{cwg} , wall pier post-tensioning forces (for Structure P2-PWUPT only), N_{twp} and N_{cwp} , and coupling beam shear forces, N_{twb} and N_{cwb} , on the wall pier axial forces, N_{tw} and N_{cw} in Structures P1-CWUPT and P2-PWUPT, respectively. The vertical lines in Figs. 13.5 and 13.6 show the design-level and survival-level roof drift demands, Δ_d and Δ_s , respectively, from Chapter 12.

Similar to the results in Chapter 7, Figs. 13.5 and 13.6 show that the post-tensioning of the precast concrete walls in Structure P2-PWUPT results in significantly

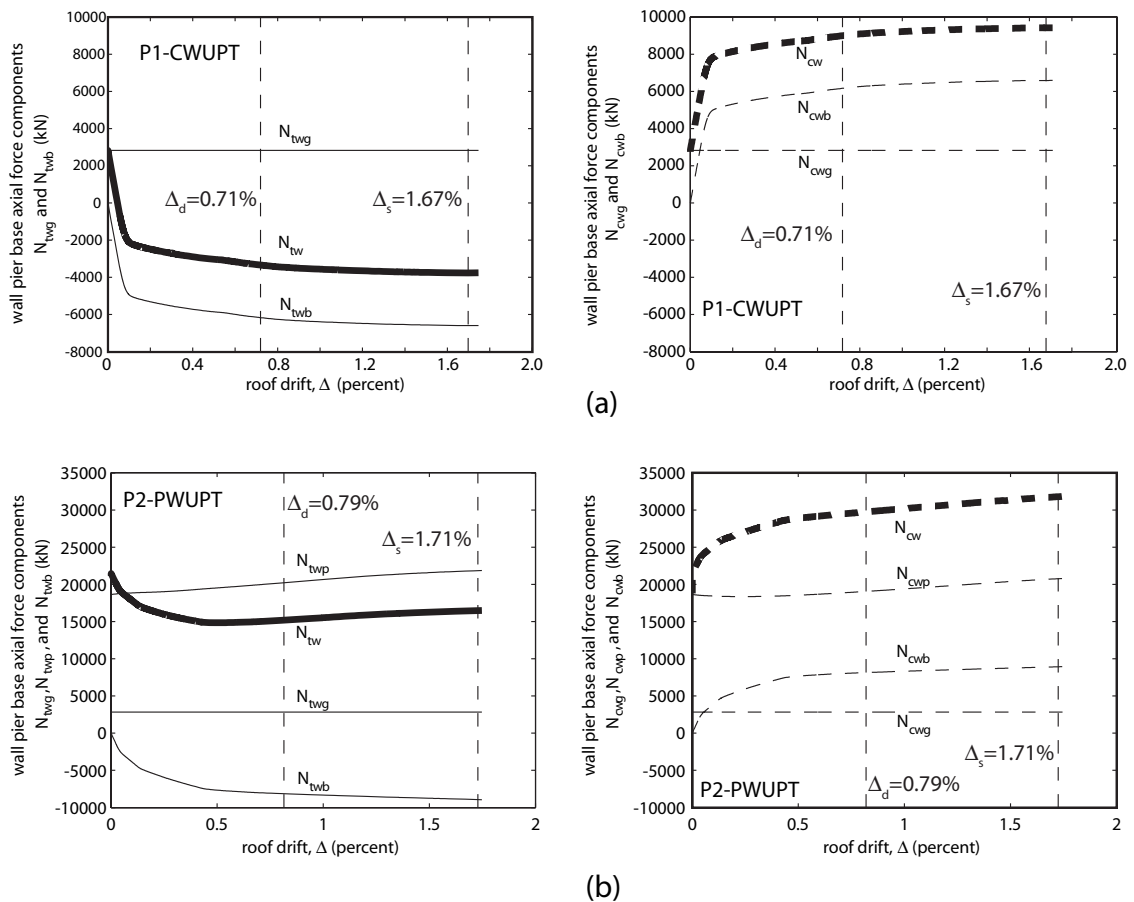


Fig. 13.6 Components of wall pier base axial forces:
(a) Structure P1-CWUPT; (b) Structure P2-PWUPT

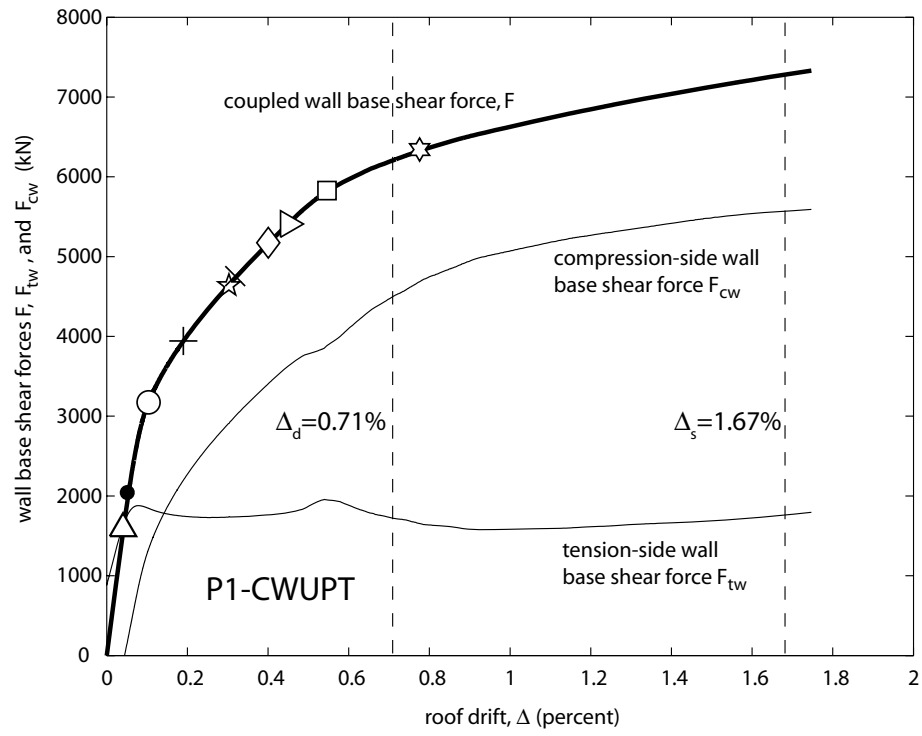
larger compressive axial forces than the forces in the cast-in-place concrete walls of Structure P1-CWUPT. The coupling shear forces result in tensile axial forces in the tension-side walls and compressive axial forces in the compression-side walls (N_{twb} and N_{cwb} , respectively). Thus, as the structures are displaced laterally, the compressive axial forces in the compression-side walls increase and the axial forces in the tension-side walls decrease.

For Structure P1-CWUPT, the axial force at the base of the tension-side wall reverses direction and goes into tension at a roof drift of approximately $\Delta=0.04\%$, while the wall pier axial forces in Structure P2-PWUPT remain compressive throughout the analysis as a result of the wall post-tensioning forces. A small increase in the axial force of the tension-side wall of Structure P2-PWUPT is observed after a roof drift of, approximately, $\Delta=0.5\%$ because of the increase in the wall post-tensioning bar forces due to increased gap opening at the wall-to-foundation horizontal joint.

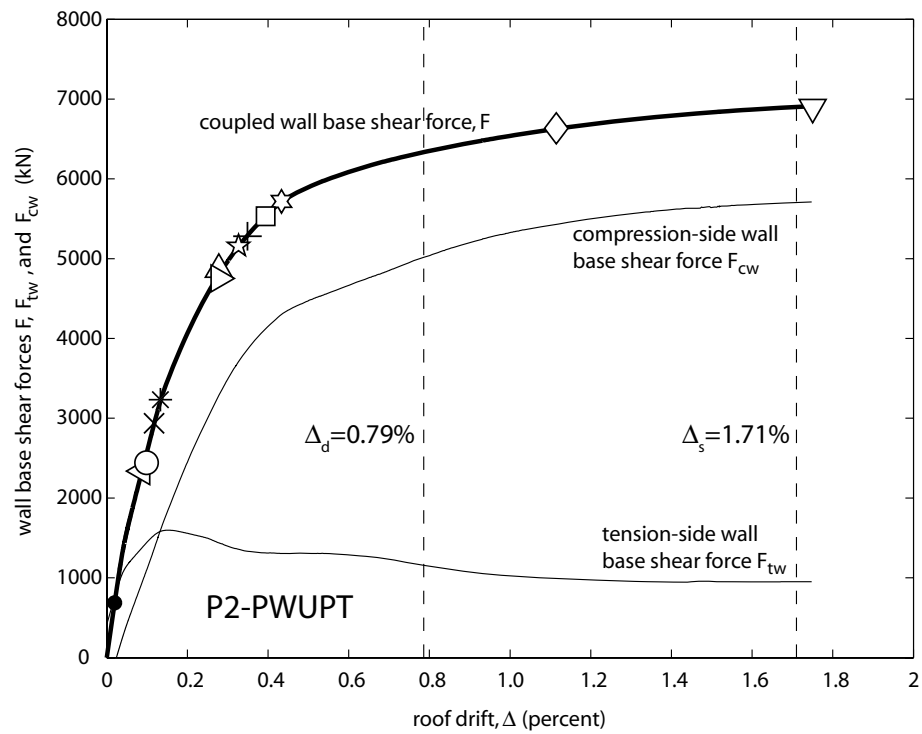
As shown in Table 13.2, the wall pier base axial forces, N_{tw} and N_{cw} , can be estimated with good accuracy using the idealized relationships and procedures from Chapters 5, 8, 10, and 11.

13.2.4 Wall Pier Base Shear Forces

The thin solid lines in Figs. 13.7a and 13.7b show the shear forces, F_{tw} and F_{cw} , at the bases of the tension-side and compression-side wall piers in Structures P1-CWUPT and P2-PWUPT, respectively. The vertical lines show the design-level and survival-level roof drift demands, Δ_d and Δ_s , from Chapter 12. The markers shown in Figs. 13.7a and 13.7b are the same as the markers in Figs. 13.1a and 13.1b, respectively.



(a)



(b)

Fig. 13.7 Wall base shear forces: (a) Structure P1-CWUPT; (b) Structure P2-PWUPT

Similar to the results in Chapter 7, the base shear force versus roof drift relationships for the tension-side and compression-side walls do not pass through the origin since shear forces develop in the wall piers upon the application of the coupling beam post-tensioning forces, with no external lateral loads.

The sum of the tension-side and compression-side wall base shear forces, $F_{tw}+F_{cw}$, shown using the thick solid lines in Fig. 13.7, is approximately equal to the total coupled wall base shear force, F from the applied lateral forces. The corresponding F_{cw}/F ratios for the prototype structures are depicted using the solid lines in Fig. 13.8 and show that, in both structures, most of the coupled wall base shear force is resisted by the compression-side wall (roughly 75% at large roof drift values), as a result of the larger compressive axial forces that develop as compared with the smaller axial forces in the tension-side wall. This will be discussed further in Chapter 15 based on the dynamic analysis results of the prototype structures.

Note that since F_{cw} and F_{tw} can not be directly obtained in design, the proposed design approach in Chapter 12 uses the ratio $(M_{cw}+M_{wb})/(M_{tw}+M_{cw}+M_{wb})$ to estimate the distribution of the total coupled wall base shear force demand to the compression-side wall pier, where, M_{cw} and M_{tw} are the compression-side and tension-side wall base moments and M_{wb} is the contribution of the coupling beam shear forces to the total coupled wall base moment. Fig. 13.8 shows that the ratio used in design (dashed lines) is reasonably close to the F_{cw}/F ratio from the fiber element model at large roof drift levels.

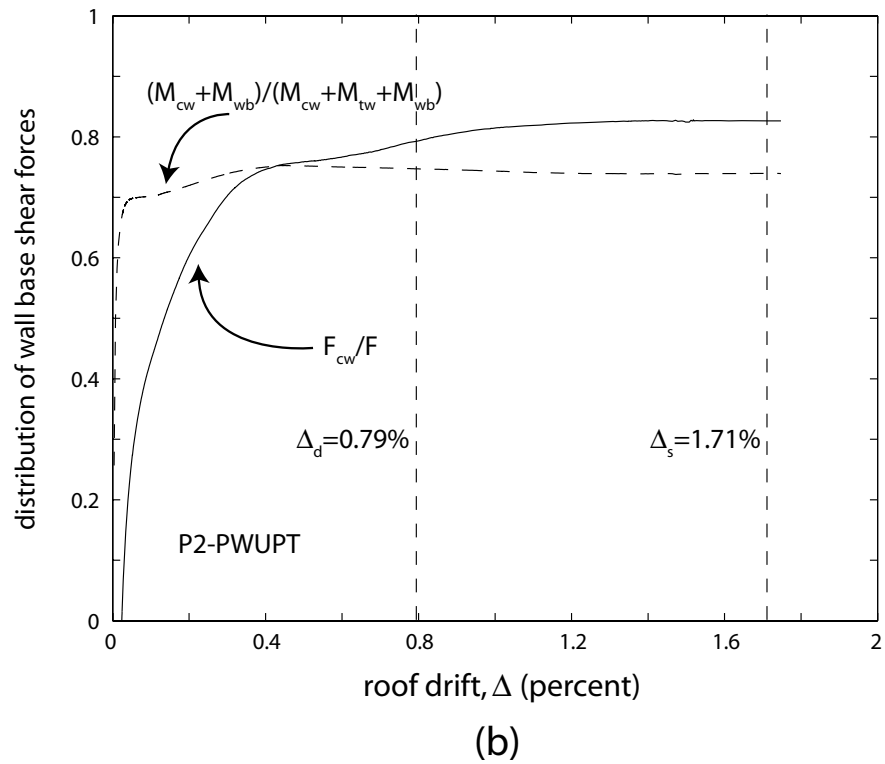
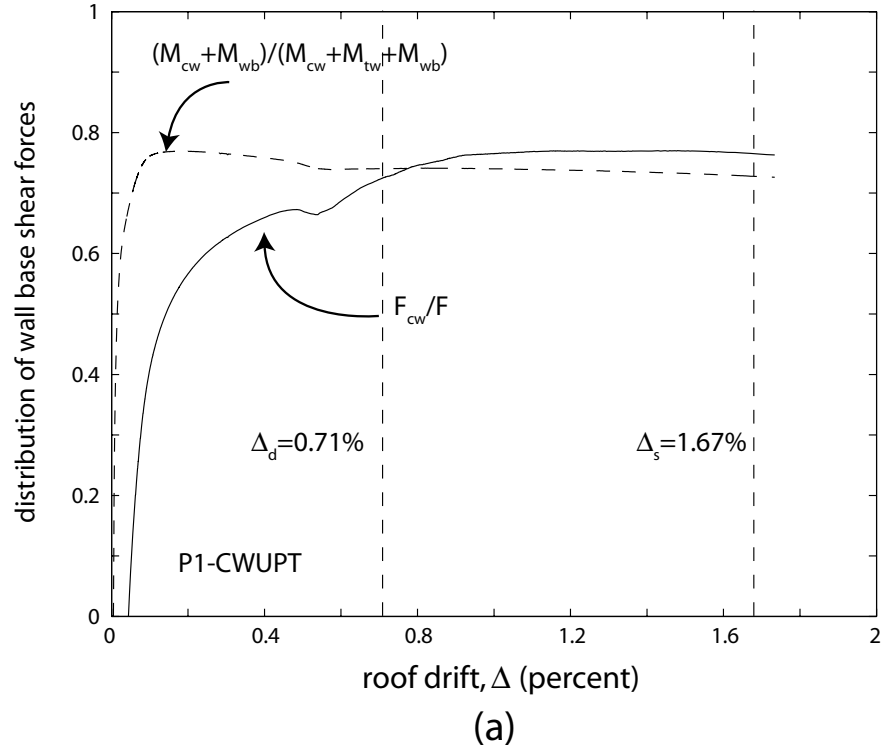


Fig. 13.8 Ratio of compression-side wall base shear force to total coupled wall base shear force: (a) Structure P1-CWUPT; (b) Structure P2-PWUPT

13.2.5 Wall Pier Base Moments

Figs. 13.9a and 13.9b show the contributions of the tension-side wall base moment, M_{tw} , the compression-side wall base moment, M_{cw} , and the base moment due to the coupling force couple, M_{wb} , to the total coupled wall base moment resistance, M_w of Structures P1-CWUPT and P2-PWUPT, respectively. The vertical lines represent the design-level and survival-level roof drift demands, Δ_d and Δ_s , respectively, from Chapter 12. The markers shown in Figs. 13.9a and 13.9b are the same as the markers in Figs. 13.1a and 13.1b, respectively.

Similar to the base shear forces in Fig. 13.7, the base moment versus roof drift relationships for the tension-side and compression-side walls do not pass through the origin since bending moments develop in the wall piers upon the application of the coupling beam post-tensioning forces, with no external lateral loads. It is observed that the compression-side wall has a larger contribution to the coupled wall base moment than the contribution of the tension-side wall, as a result of the larger compressive axial forces that develop in the compression-side wall. The base moment resistances of the tension-side and compression-side walls, M_{tw} and M_{cw} , in both structures increase with increasing roof drift regardless of the wall pier axial forces.

As shown in Table 13.2, the wall base moments, M_w , M_{tw} , and M_{cw} can be estimated with good accuracy using the idealized relationships and procedures from Chapters 5, 8, 10, and 11.

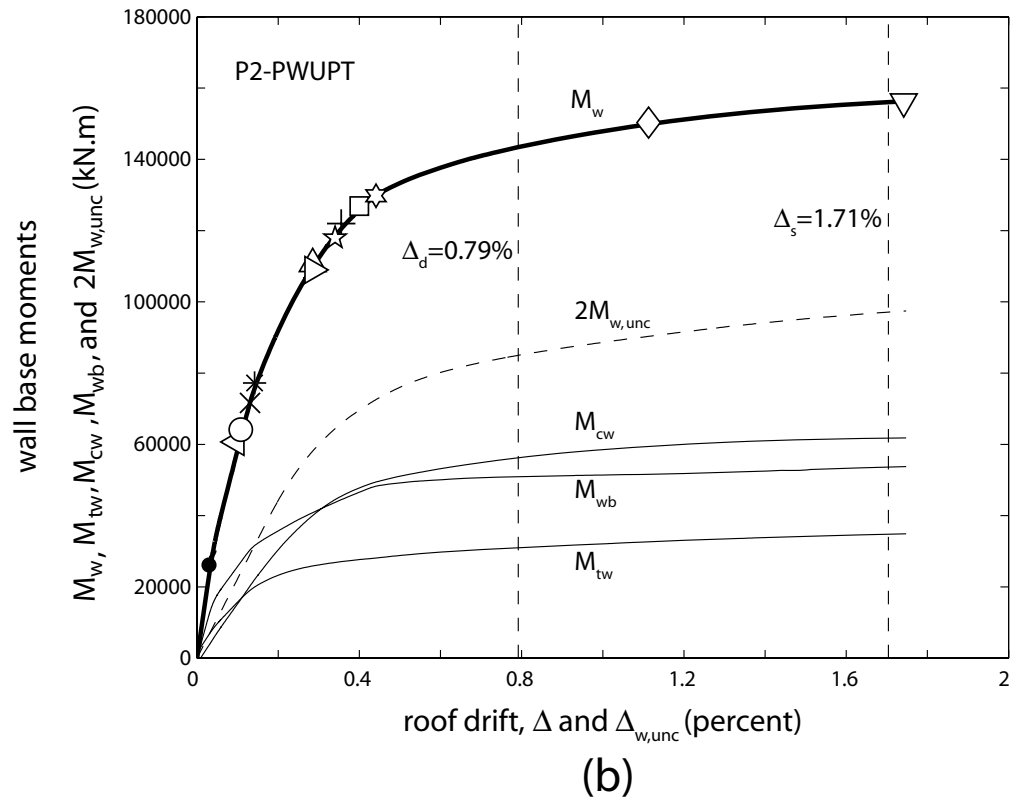
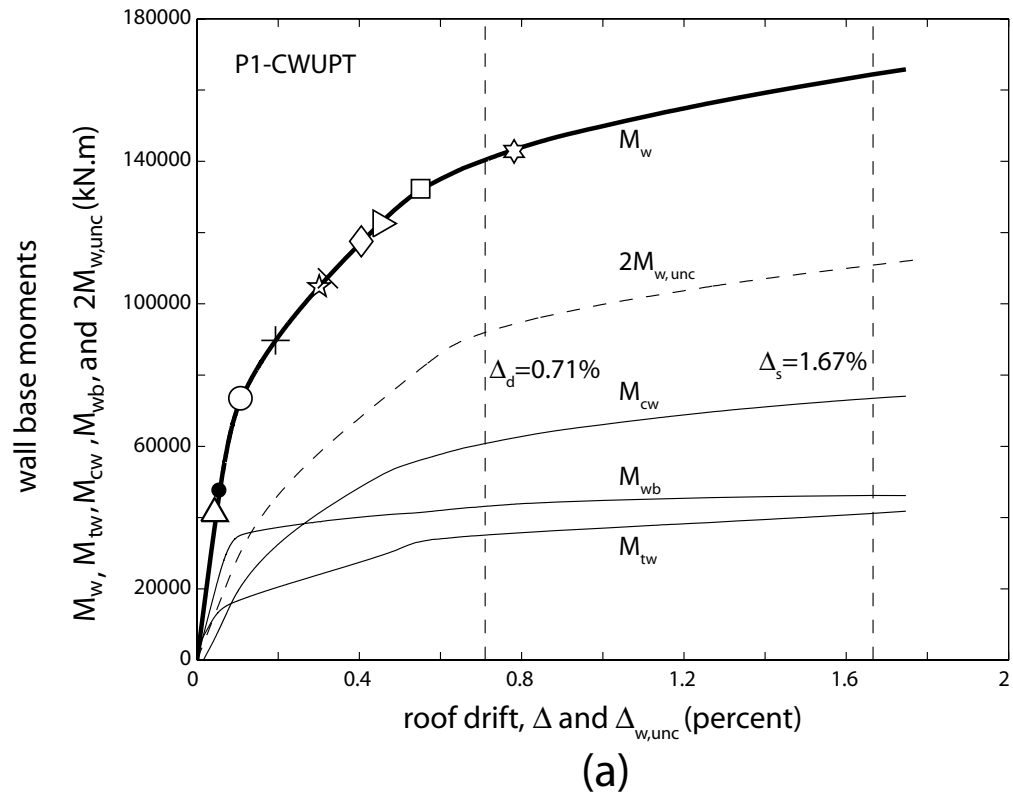
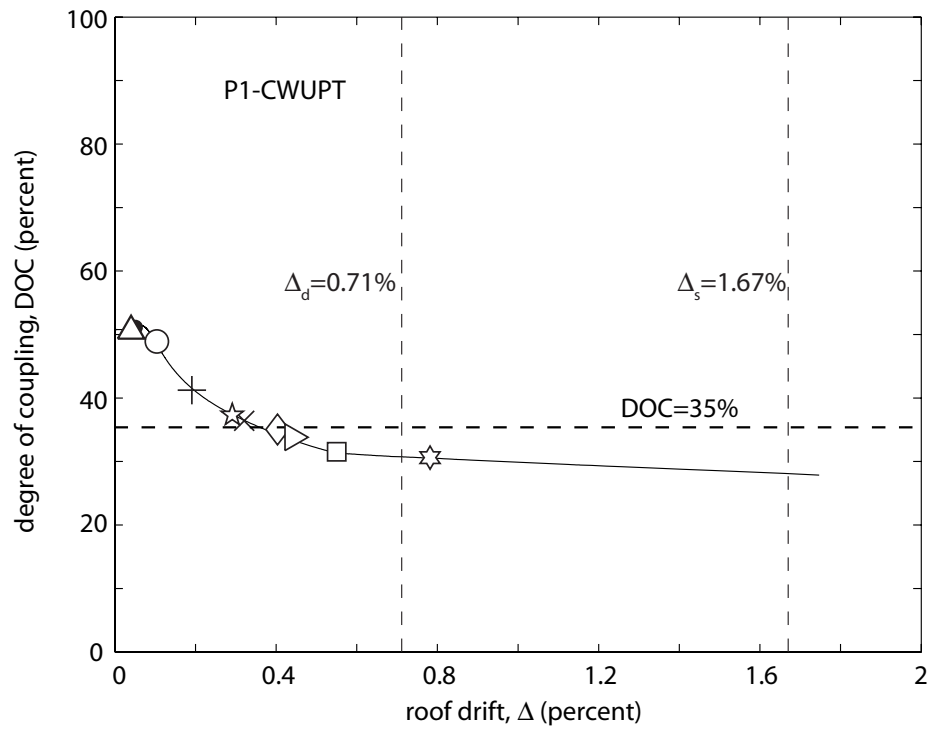


Fig. 13.9 Wall base moments: (a) Structure P1-CWUPT; (b) Structure P2-PWUPT

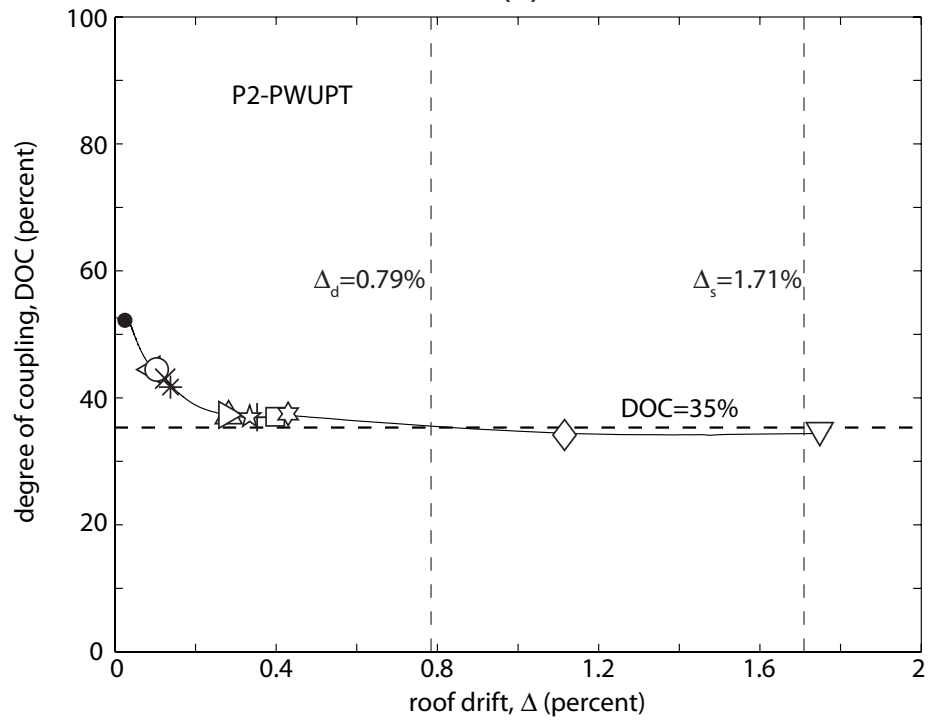
13.2.6 Degree of Coupling

The dashed lines in Fig. 13.9a and 13.9b show the sum of the base moment resistances, $2M_{w,unc}$, of the left-side and right-side wall piers without coupling (i.e., two wall piers with no coupling beams) for Structures P1-CWUPT and P2-PWUPT, respectively. Comparing $2M_{w,unc}$ with the total coupled wall base moment, M_w , there is a significant increase in the lateral stiffness and strength of the walls as a result of coupling. The degree of coupling, DOC for the structures, calculated using Equation (2.2), is shown in Fig. 13.10. The vertical lines show the design-level and survival-level roof drift demands, Δ_d and Δ_s , respectively, from Chapter 12, and the horizontal lines show the target degree of coupling DOC=35% used in the design of the structures. The markers shown in Figs. 13.10a and 13.10b are the same as the markers in Figs. 13.1a and 13.1b, respectively.

It is observed that, in the initial range of response ($\Delta < \sim 0.3\%$), the coupling degree values for the prototype structures are larger than the target value used in design; however, as the structures are displaced laterally into the nonlinear range, the coupling degree decreases. For Structure P1-CWUPT, the coupling degree, DOC reaches the target value at approximately $\Delta = 0.37\%$ and drops to a value of DOC=28% when Δ_s is reached. For Structure P2-PWUPT, the coupling degree is very close to the target value for $\Delta > 0.3\%$. The larger decrease in the DOC value of Structure P1-CWUPT as compared with the DOC value of Structure P2-PWUPT as the structures are displaced into the nonlinear range may be because of the larger strain hardening that occurs in the flexural reinforcement of the monolithic cast-in-place reinforced concrete wall piers in Structure P1-CWUPT.



(a)



(b)

Fig. 13.10 Degree of coupling: (a) Structure P1-CWUPT; (b) Structure P2-PWUPT

As shown in Table 13.2, the coupling degree of the walls, DOC can be estimated with good accuracy using the idealized relationships and procedures from Chapters 5, 8, 10, and 11.

13.2.7 Wall Pier Base Concrete Strains

Figs. 13.11a and 13.11b show the neutral axis (i.e., contact) depths, c_{tw} and c_{cw} (measured from the compression corners of the wall piers) at the bases of the tension-side and compression-side wall piers in Structures P1-CWUPT and P2-PWUPT, respectively. The c_{tw} and c_{cw} values are normalized with respect to the wall pier length, $l_w=4.88$ m. The corresponding extreme confined concrete compression strains, ϵ_{tce} and ϵ_{cce} of the tension-side and compression-side wall piers at the base are shown in Figs. 13.12a and 13.12b, respectively, with the confined concrete crushing strains, ϵ_{ccu} shown by the dashed horizontal lines. For each structure, the markers in Figs. 13.11 and 13.12 are the same as the markers in Fig. 13.1.

The vertical lines in Figs. 13.11 and 13.12 show the design-level and survival-level roof drift demands, Δ_d and Δ_s , respectively, from Chapter 12. For both prototype structures, the c_{tw} and c_{cw} values change little between the design and survival demand levels and the c_{cw} values for the compression-side wall piers are very close to $0.2l_w$ as assumed in design for Structure P2-PWUPT (see Chapter 12).

As required by design, crushing of the confined concrete at the bases of the wall piers in the prototype structures does not occur under the survival-level demand. Similar to the results in Chapter 7, the compression-side wall piers have larger concrete compression strains than the tension-side wall piers as a result of the larger compression

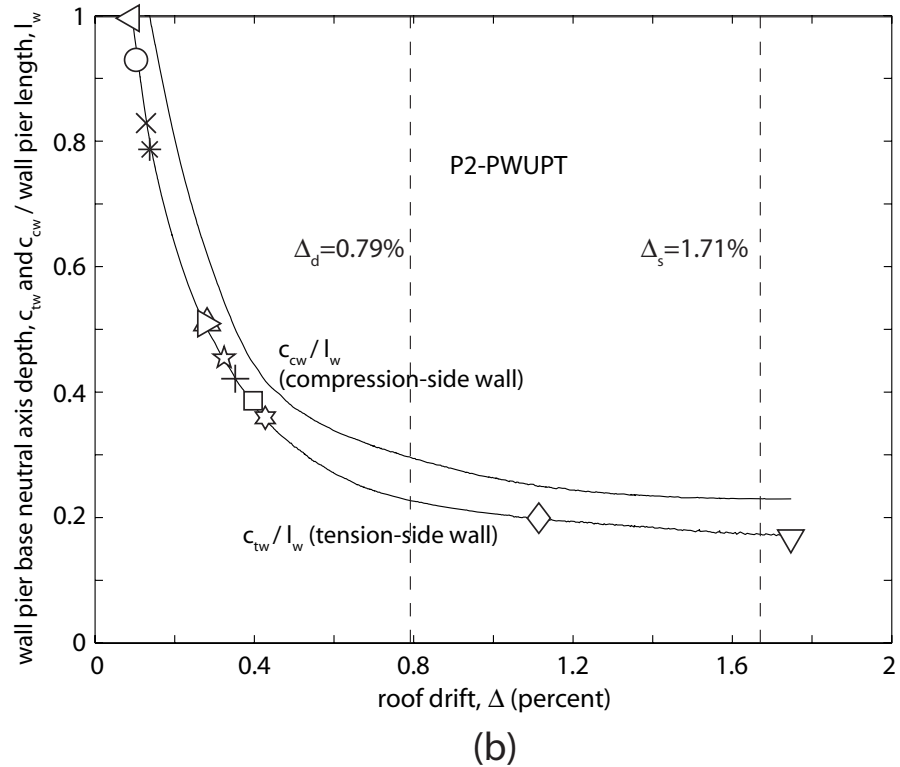
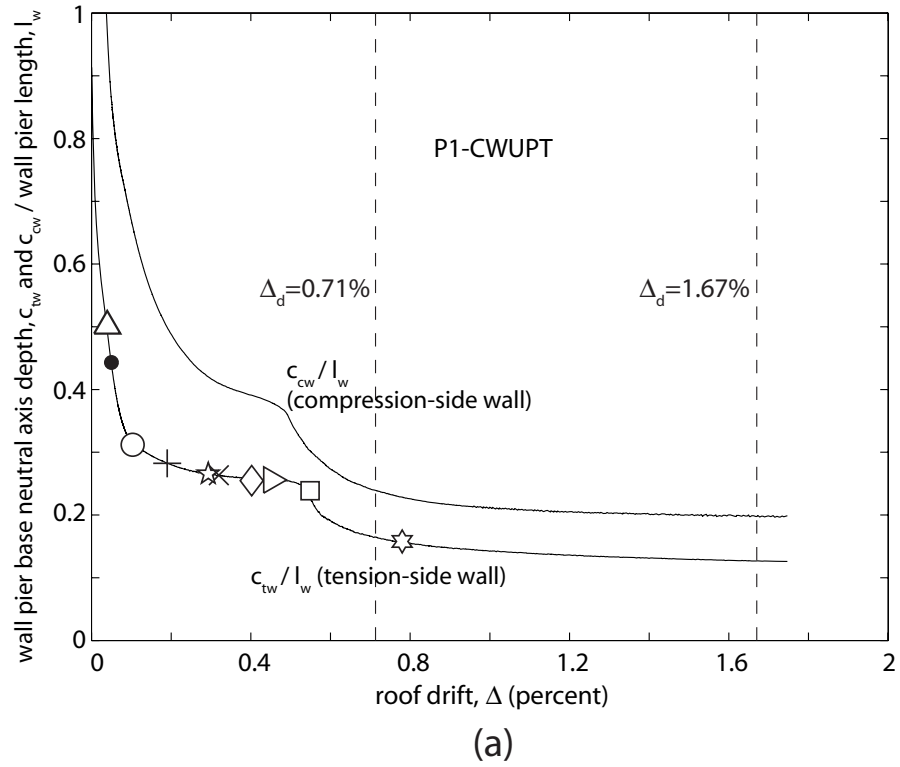


Fig. 13.11 Wall pier base neutral axis (i.e., contact) depths:
(a) Structure P1-CWUPT; (b) Structure P2-PWUPT

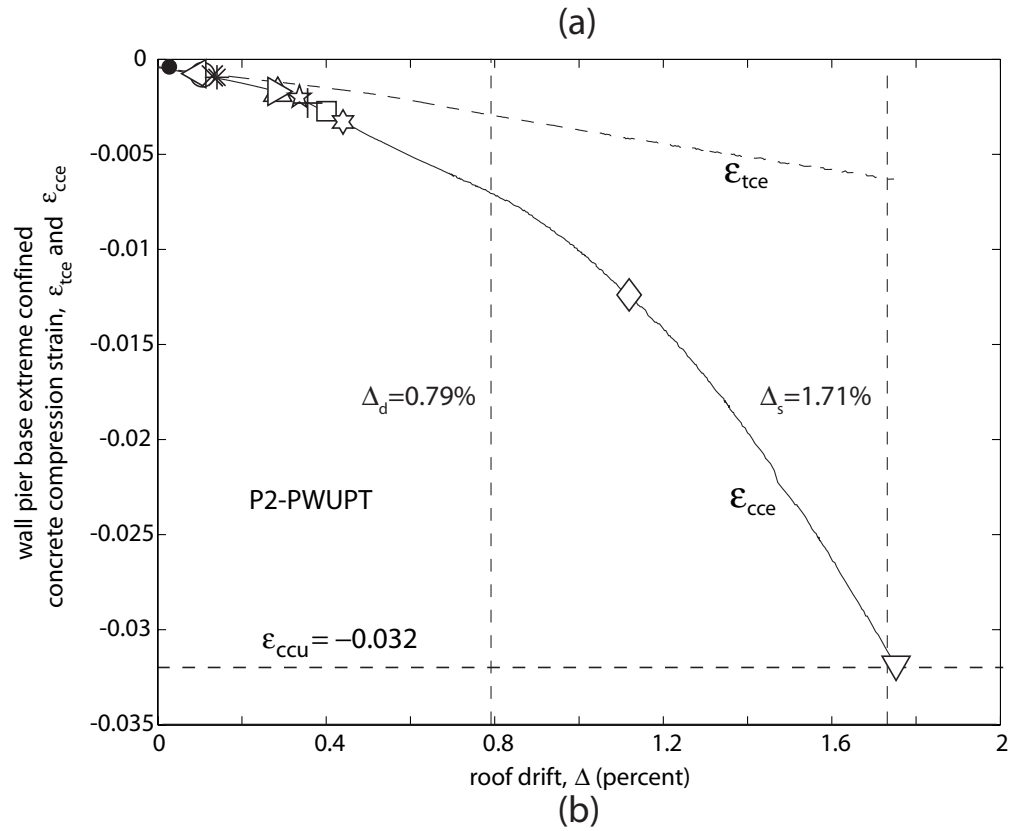
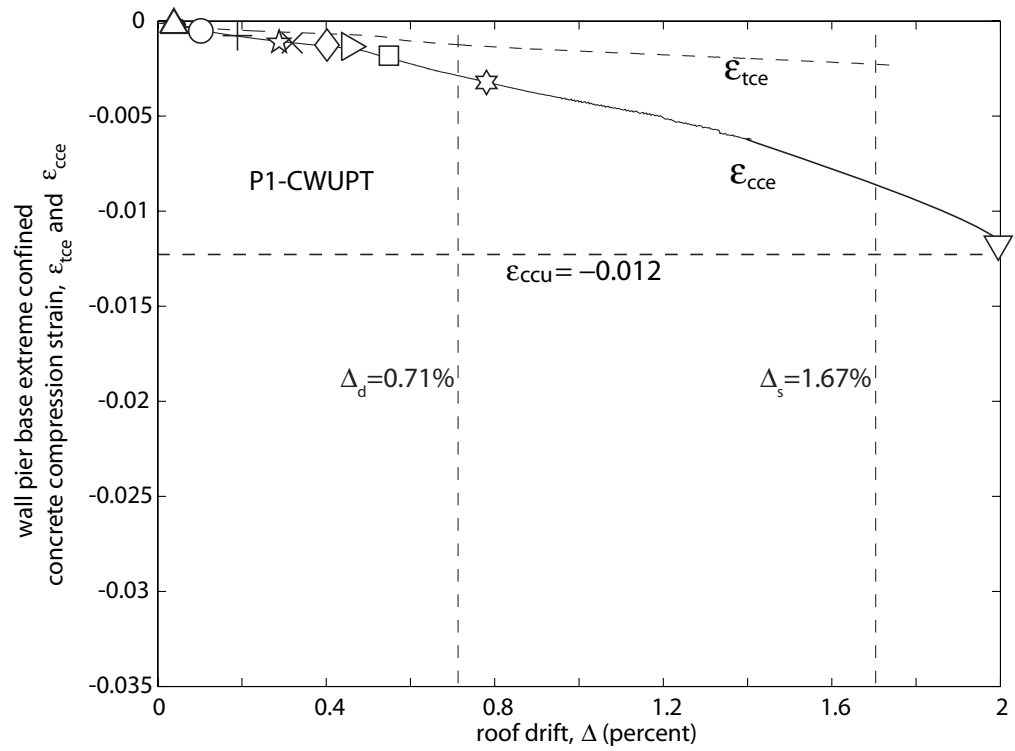


Fig. 13.12 Wall pier base extreme confined concrete compression strains:
(a) Structure P1-CWUPT; (b) Structure P2-PWUPT

forces due to the coupling effect. Furthermore, the wall pier compression strains in Structure P2-PWUPT are significantly larger than the strains in Structure P1-CWUPT due to the additional compressive axial forces from the wall post-tensioning bars. This results in a significantly larger amount of wall pier concrete confinement reinforcement at the base of Structure P2-PWUPT as shown in Chapter 12.

As required by design, crushing of the confined concrete under the survival demand level is prevented in both prototype structures, since the maximum concrete compression strains at Δ_s are smaller than the corresponding confined concrete crushing strains, ϵ_{ccu} .

Table 13.2 shows that the wall pier contact depths, c_{tw} and c_{cw} , and the coupled wall roof drift at the wall ultimate state, Δ_{wu} can be estimated with good accuracy using the idealized relationships and procedures from Chapters 5, 8, 10, and 11.

13.2.8 Coupling Beam Shear Force versus Chord Rotation Behaviors

The solid lines in Figs. 13.13a-13.13(h) show the shear force versus chord rotation ($V_b-\theta_b$) behaviors of the eight coupling beams in Structure P1-CWUPT, respectively. Similar results for the coupling beams in Structure P2-PWUPT are shown in Fig. 13.14. The chord rotation values for the coupling beams are measured from a tangent drawn at the left end of each beam as described in Chapter 7.

For comparison, the dashed lines in Figs. 13.13 and 13.14 show the coupling beam shear force versus chord rotation behaviors of isolated subassemblages from Structures P1-CWUPT and P2-PWUPT, respectively, and the horizontal lines show the design coupling shear force demand, Q_{bd} from Chapter 12. For both structures, the coupling beams from the multi-story and subassemblage models have similar $V_b-\theta_b$ behaviors

except for the second floor beam due to the effect of the fixed boundary conditions assumed at the wall pier bases. The design coupling shear force demands are satisfied for all of the coupling beams in the structures.

The dashed vertical lines in Figs. 13.13 and 13.14 show the design-level and survival-level coupling beam chord rotation demands, θ_d and θ_s , respectively, from Chapter 12 and the solid vertical lines show the beam chord rotation demands from the nonlinear lateral load analysis of each structure (using the DRAIN-2DX fiber element model) corresponding to the design-level and survival-level roof drift demands, Δ_d and Δ_s , from Chapter 12. The results indicate that the beam chord rotation demands from design (Chapter 12) are close to or larger than (resulting in conservative estimates) the rotation demands from the nonlinear analyses of the structures, verifying the idealized structure deflected shape in Fig. 12.10. As described previously, yielding of the beam post-tensioning tendons is prevented under the survival level demand.

Table 13.2 shows that the average coupling beam shear forces, V_b and the average beam chord rotation values, θ_b over the height of each structure can be estimated with good accuracy using the idealized relationships and procedures from Chapters 5, 8, 10, and 11. Note that the θ_b values at the wall softening state are not estimated well since the initial linear elastic stiffness of the structure is used in the estimation.

13.2.9 Coupling Beam Axial Forces and Post-Tensioning Forces

The solid lines in Figs. 13.15 and 13.16 show the midspan axial force versus chord rotation (N_b - θ_b) behaviors of the coupling beams in Structures P1-CWUPT and P2-PWUPT, respectively. A positive beam axial force indicates a compressive force. For

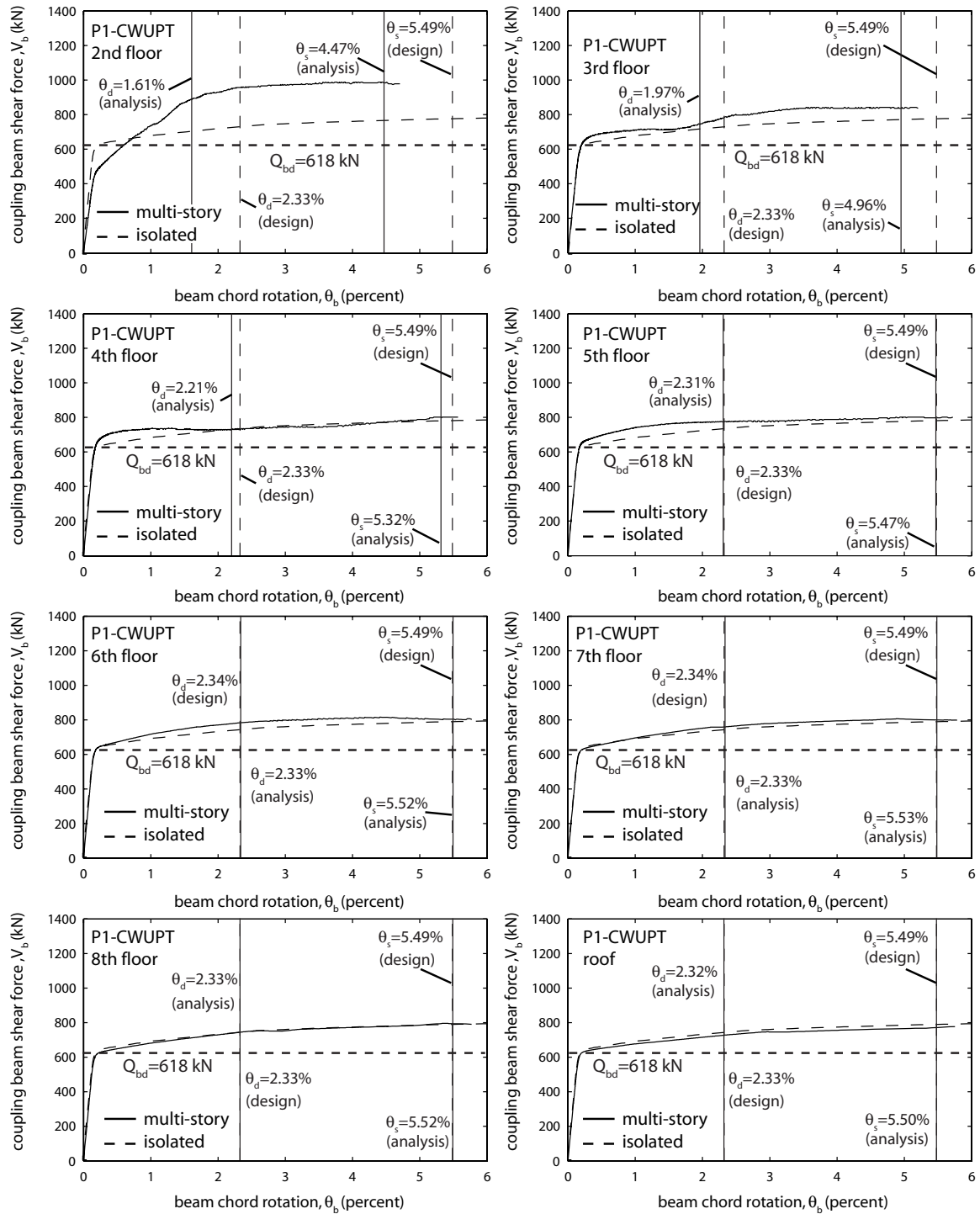


Fig. 13.13 Coupling beam shear force versus chord rotation behaviors for Structure P1-CWUPT

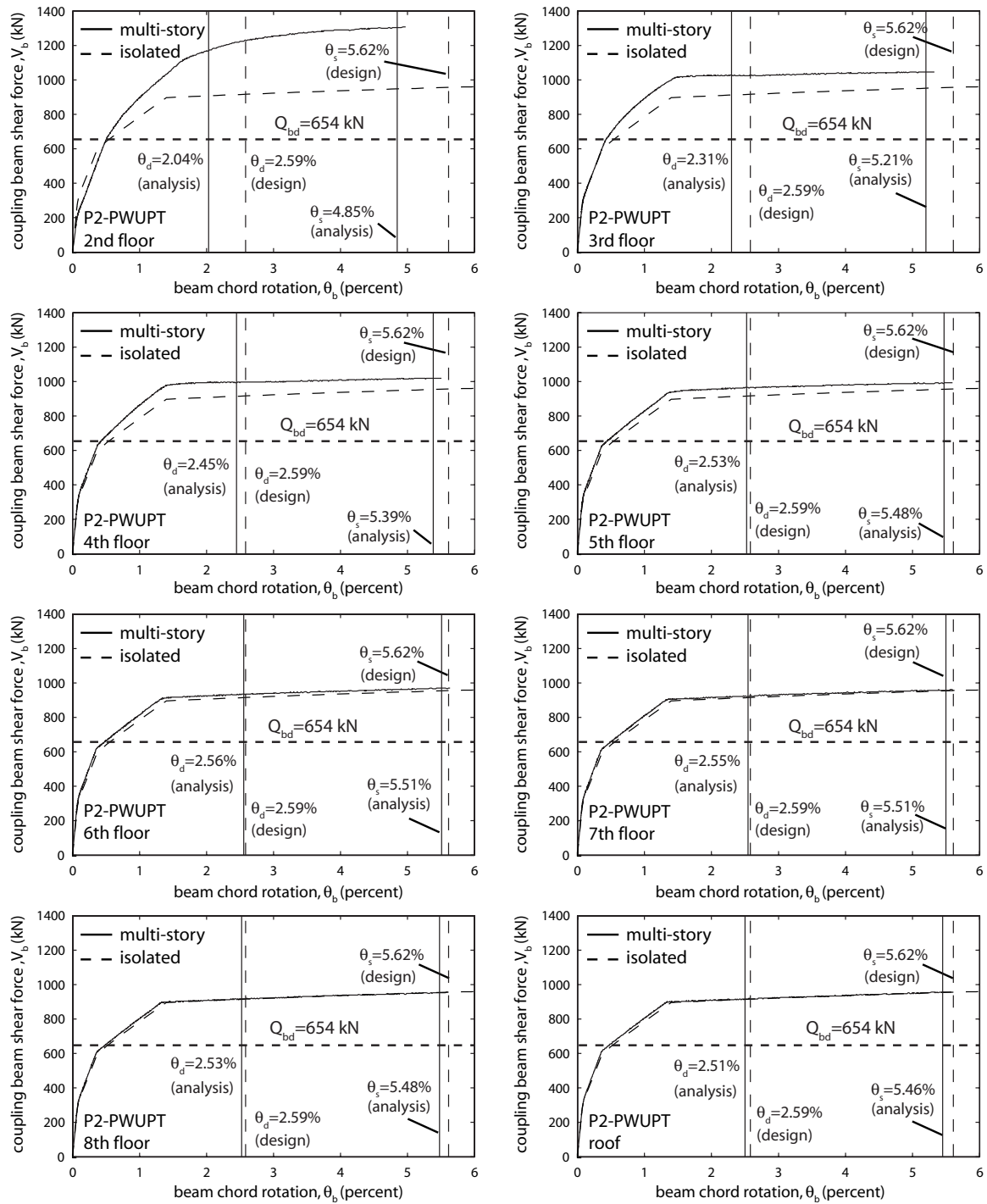


Fig. 13.14 Coupling beam shear force versus chord rotation behaviors for Structure P2-PWUPT

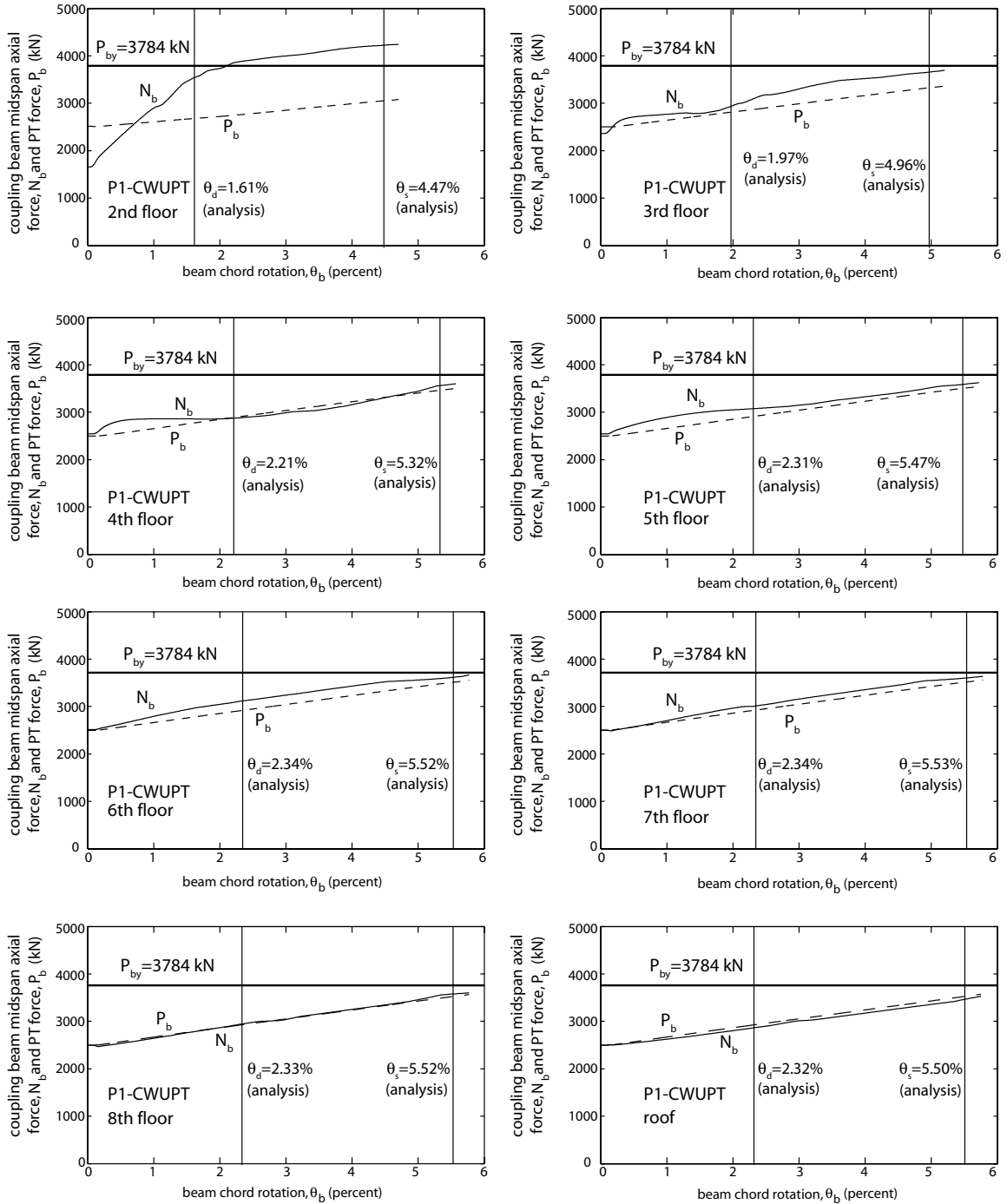


Fig. 13.15 Coupling beam axial forces and post-tensioning forces in Structure P1-CWUPT

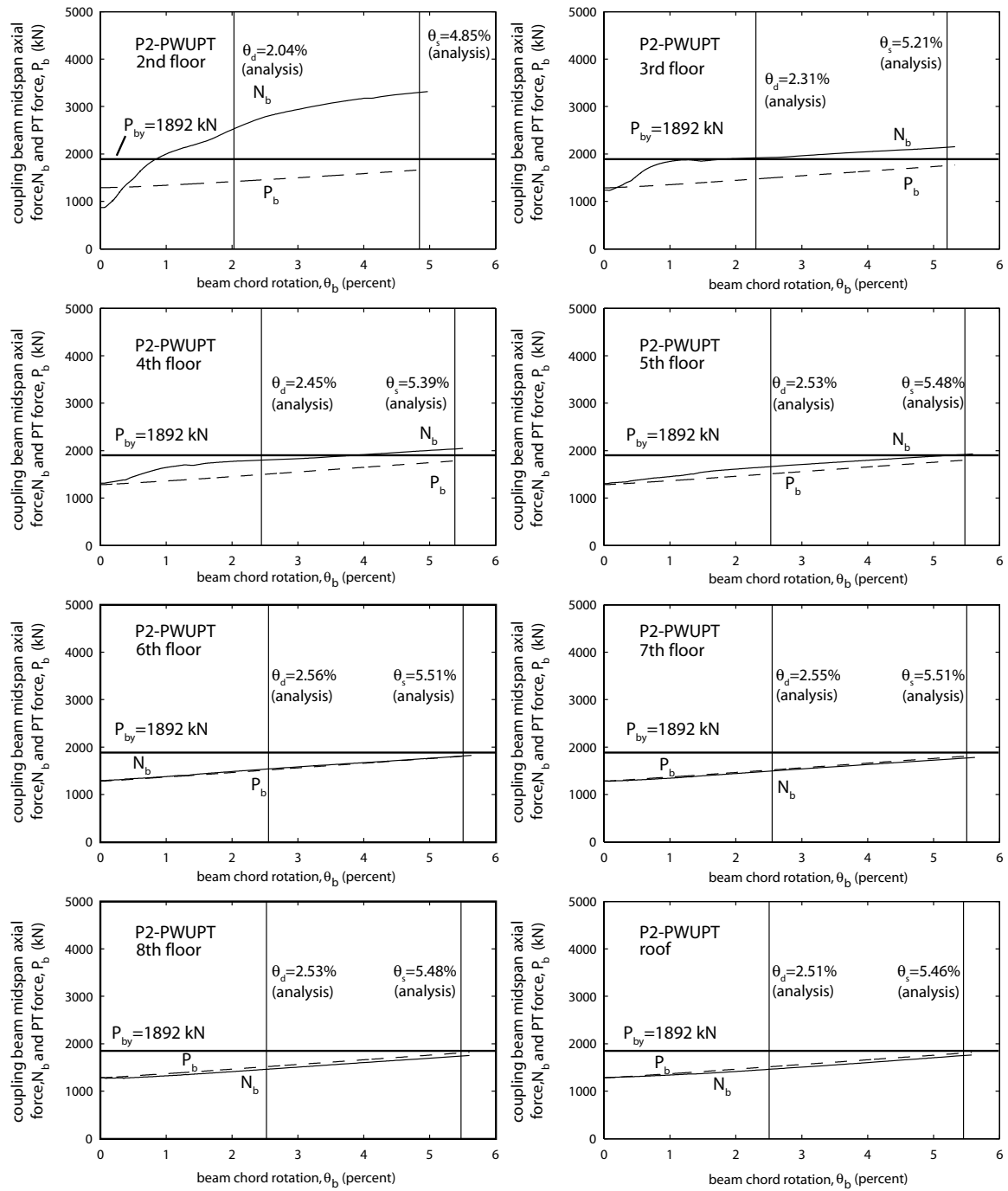


Fig. 13.16 Coupling beam axial forces and post-tensioning forces in Structure P2-PWUPT

comparison, the dashed lines show the total forces in the post-tensioning tendons, P_b of each coupling beam, the horizontal lines show the total yield strength of the post-tensioning tendons, P_{by} , and the vertical lines show the design-level and survival-level beam chord rotation demands, θ_d and θ_s , respectively, from the nonlinear analysis of each structure (using the DRAIN-2DX model) corresponding to the design-level and survival-level roof drift demands, Δ_d and Δ_s , from Chapter 12.

As discussed in detail in Chapter 7, the axial force in the second floor coupling beam is significantly different than the total post-tensioning tendon force because of the fixed conditions assumed at the bases of the wall piers. The axial forces in the upper level beams are close to the post-tensioning tendon forces, indicating that the effect of the foundation conditions quickly diminishes above the base.

13.2.10 Coupling Beam End Strains

Figs. 13.17 and 13.18 show the neutral axis (i.e., contact) depths, c_b (normalized with respect to the beam depth, $d_b=559$ mm) at the left ends of the coupling beams in Structures P1-CWUPT and P2-PWUPT, respectively. The behaviors at the right ends of the coupling beams are similar. The vertical lines show the design-level and survival-level beam chord rotation demands, θ_d and θ_s , respectively, from the nonlinear analysis of each structure (using the DRAIN-2DX model) corresponding to the design-level and survival-level roof drift demands, Δ_d and Δ_s , from Chapter 12 and the horizontal lines represent the thickness of the beam flange, t_{bf} . It is observed that the beam-to-wall contact depths of the prototype structures remain within the flange (except for the second floor beam of Structure P1-CWUPT) during most of the nonlinear response.

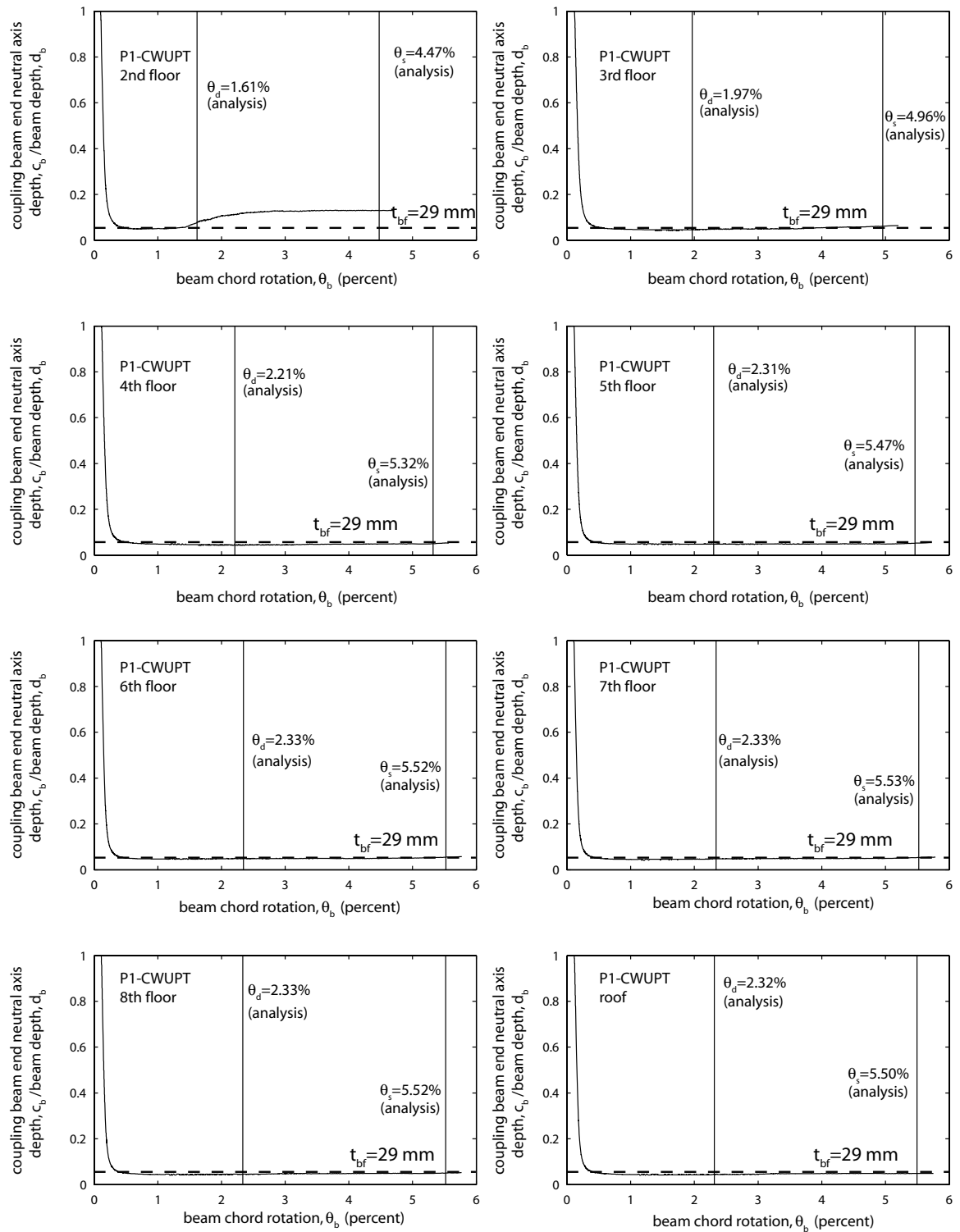


Fig. 13.17 Coupling beam end neutral axis (i.e., contact) depths for Structure P1-CWUPT

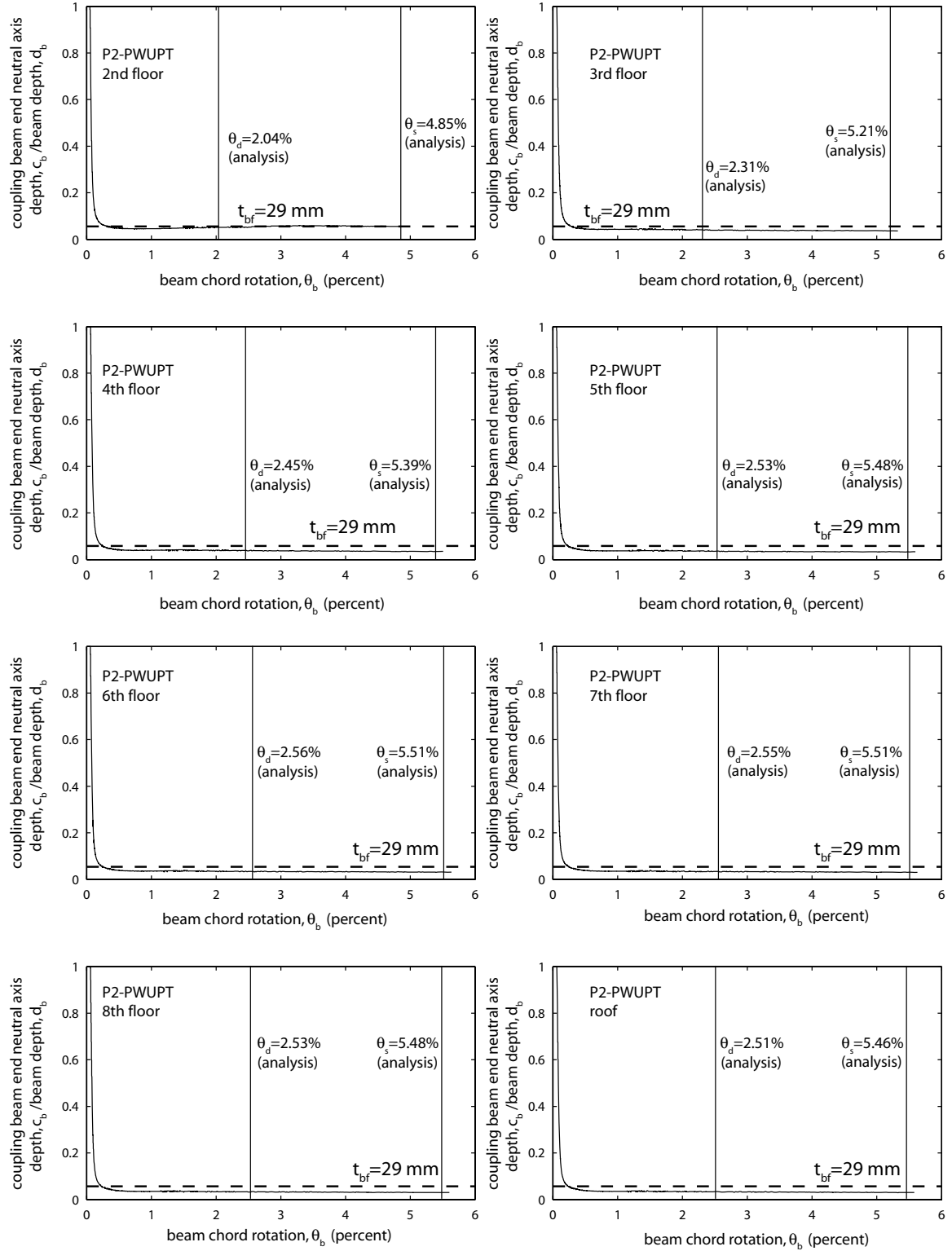


Fig. 13.18 Coupling beam end neutral axis (i.e., contact) depths for Structure P2-PWUPT

The corresponding extreme steel compression strains, ϵ_{be} at the left ends of the coupling beams are shown in Figs. 13.19 and 13.20, respectively. In general, the coupling beams over the height of each structure have similar behaviors, with the largest strains occurring in the second floor beam. The extreme compression strains in the beams of Structure P2-PWUPT are significantly smaller than the strains in the beams of Structure P1-PWUPT due to the smaller beam post-tensioning forces.

13.2.11 Tension Angle Force versus Deformation Behaviors

Figs. 13.21 and 13.22 show the force versus deformation behaviors of the tension angles at the left ends of the coupling beams in Structures P1-CWUPT and P2-PWUPT, respectively. The behaviors of the tension angles at the right ends of the coupling beams are similar. The dashed vertical lines show the design-level and survival-level tension angle deformation demands, u_{ad} and u_{as} , from Chapter 12 and the solid vertical lines show the tension angle deformation demands from the nonlinear lateral load analysis of each structure (using the DRAIN-2DX fiber element model) corresponding to the design-level and survival-level roof drift demands, Δ_d and Δ_s , from Chapter 12. The results indicate that the tension angle deformation demands from design (Chapter 12) are reasonably close to or larger than (resulting in conservative estimates) the angle deformation demands from the nonlinear analyses of the structures, verifying the idealized beam end displaced shape in Fig. 12.11.

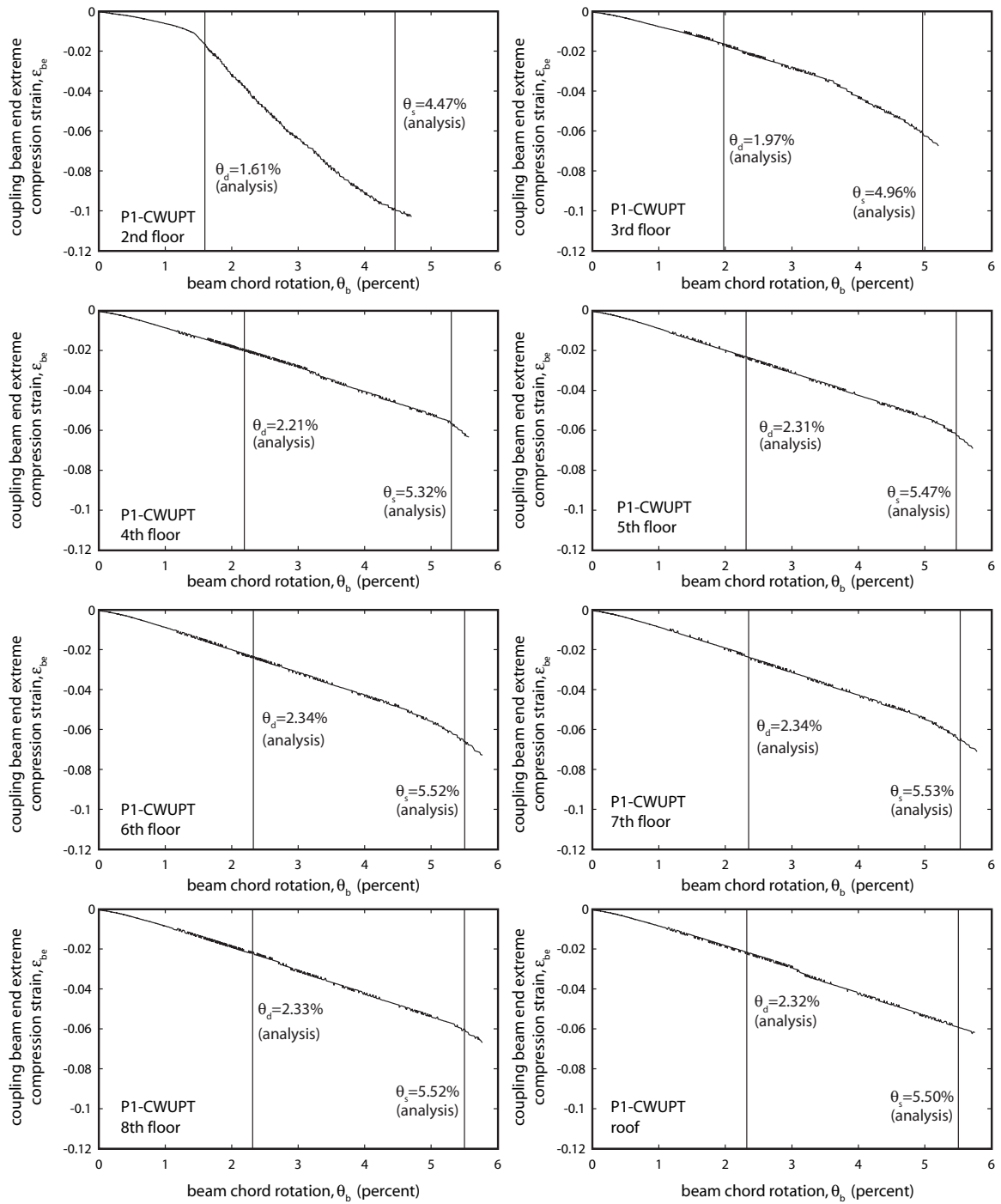


Fig. 13.19 Coupling beam end extreme steel compression strains for Structure P1-CWUPT

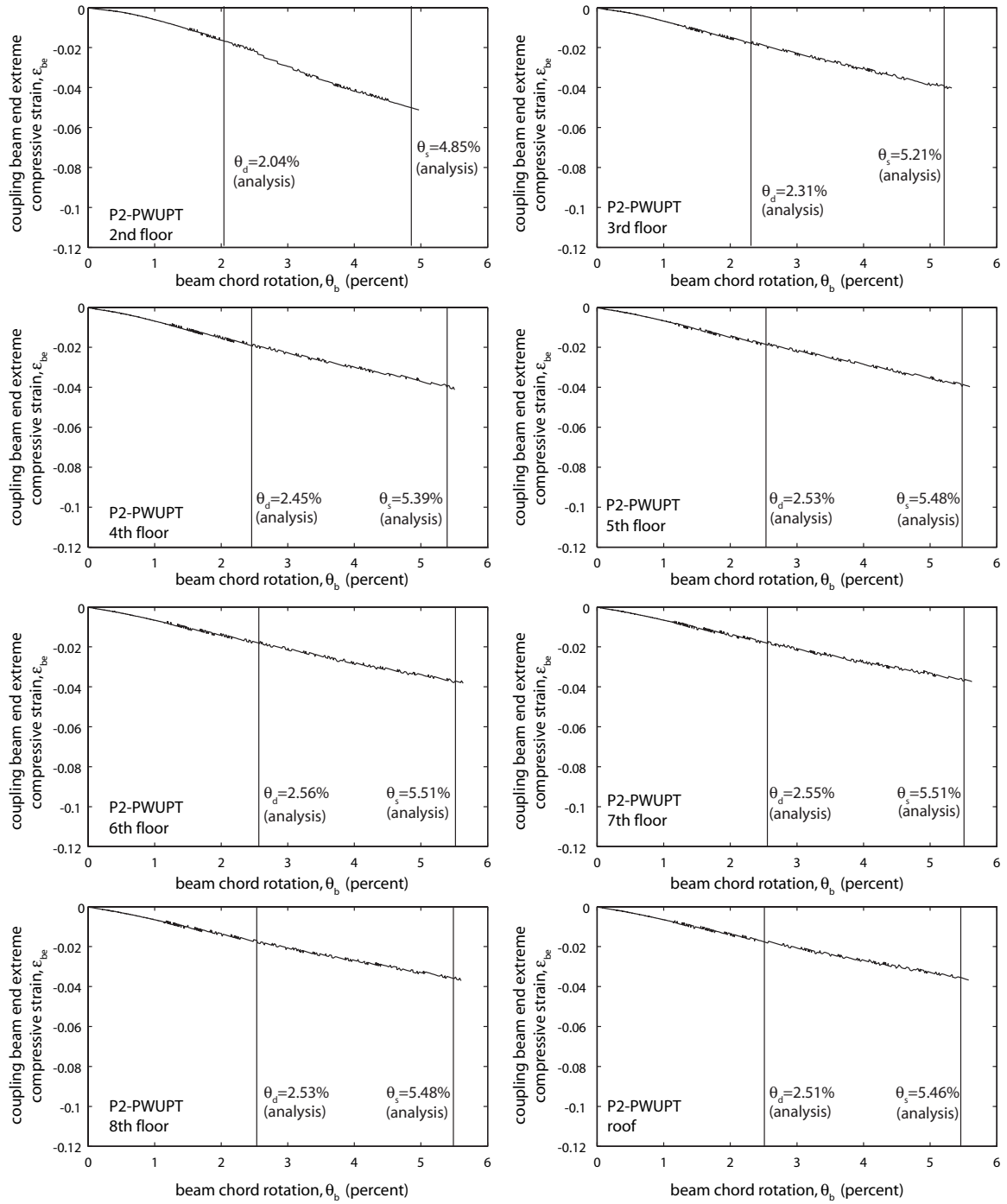


Fig. 13.20 Coupling beam end extreme steel compression strains for Structure P2-PWUPT

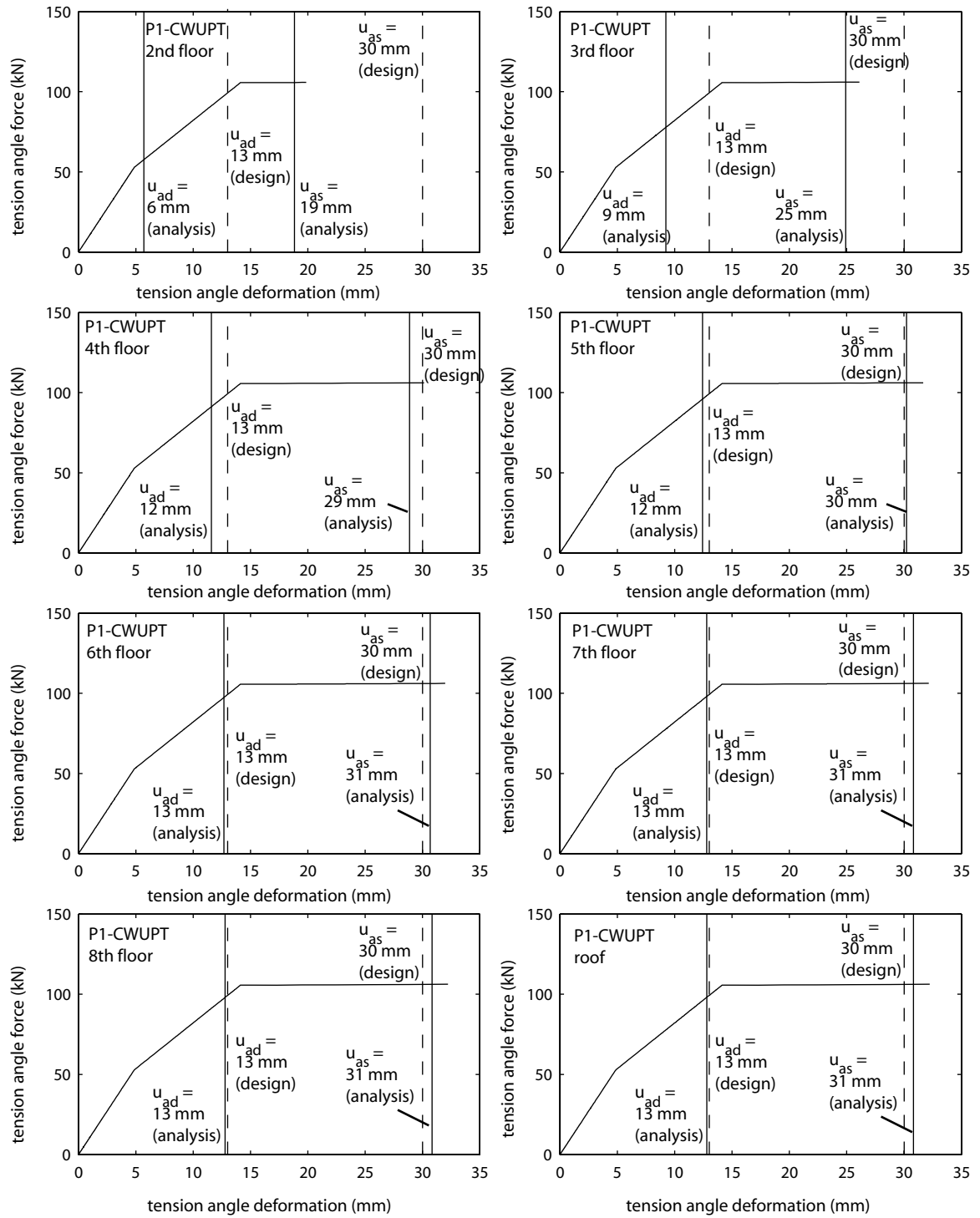


Fig. 13.21 Coupling beam tension angle force-deformation behaviors for Structure P1-CWUPT

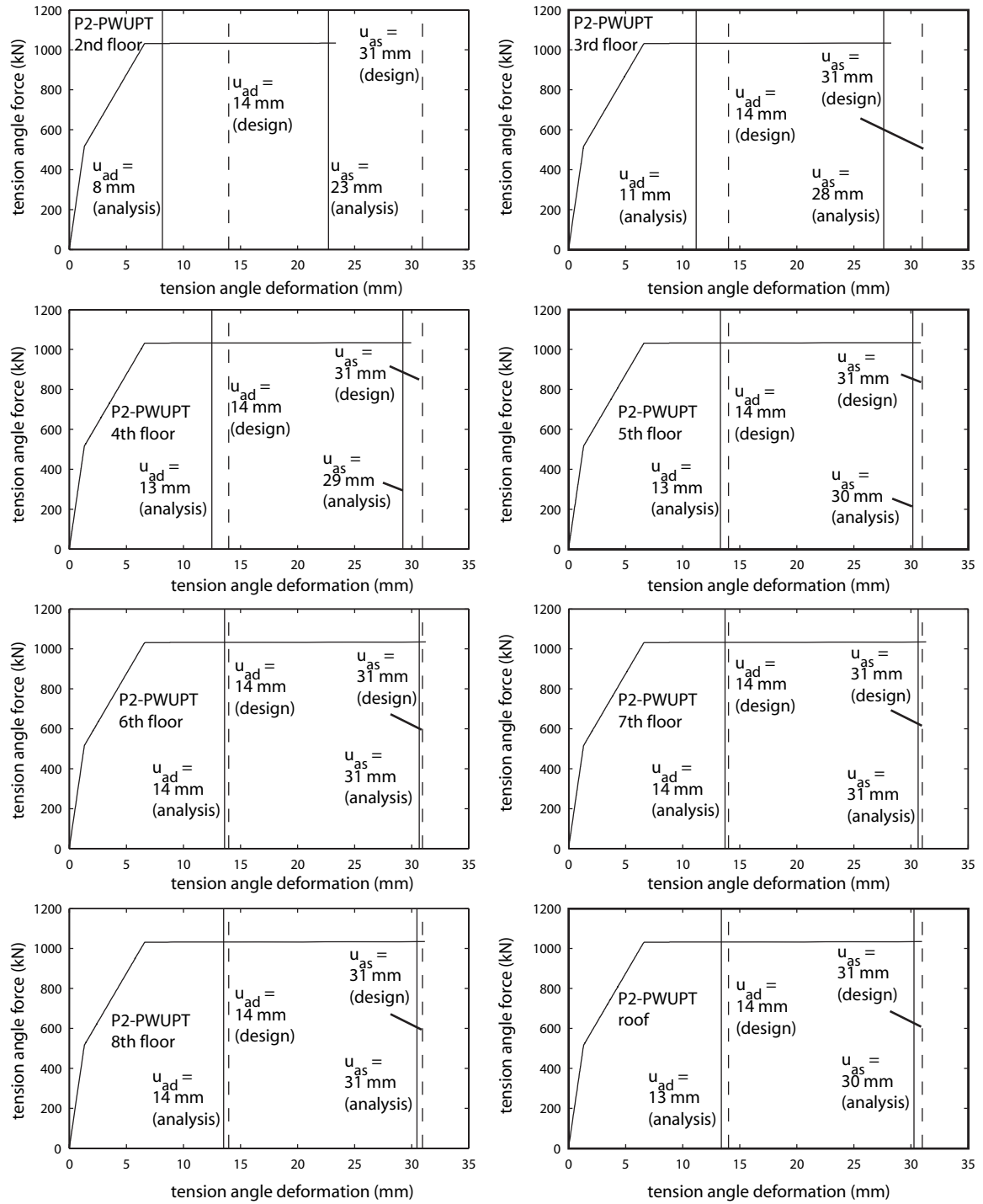


Fig. 13.22 Coupling beam tension angle force-deformation behaviors for Structure P2-PWUPT

For both structures, the tension angles at the second floor level have the smallest deformations, because, the fixed boundary conditions assumed at the bases of the wall piers restrain the opening of gaps at the beam-to-wall interfaces. The largest survival-level tension angle deformations from the nonlinear analyses of Structures P1-CWUPT and P2-PWUPT are 32 mm and 31 mm, respectively, which are both smaller than the design limit of 38 mm from Chapter 12. The smaller angle forces in Structure P1-CWUPT, as designed in Chapter 12 with the use of a small top and seat angle ratio ($\beta_{ar}=0.051$), are noticeable in the plots.

13.3 Behavior Under Reversed Cyclic Loading

This section describes the behavior of Structures P1-CWUPT and P2-PWUPT under reversed cyclic lateral loads combined with gravity loads. The structures are displaced to roof drift values of $\Delta=\pm 0.5, 0.75, 1, 1.25, 1.5$, and 1.75% , with one cycle of loading at each displacement amplitude. Note that the largest roof drift of 1.75% is slightly larger than the survival-level roof drift demand, Δ_s for both structures. The section is organized as follows: (1) coupled wall base shear force versus roof drift behaviors; (2) wall pier post-tensioning forces in Structure P2-PWUPT; (3) wall pier base axial forces; (4) wall pier base shear forces; (5) wall pier base moments; (6) degree of coupling; (7) wall pier base concrete strains; (8) coupling beam shear force versus chord rotation behaviors; (9) coupling beam axial forces and post-tensioning forces; (10) coupling beam end strains; and (11) angle force versus deformation behaviors.

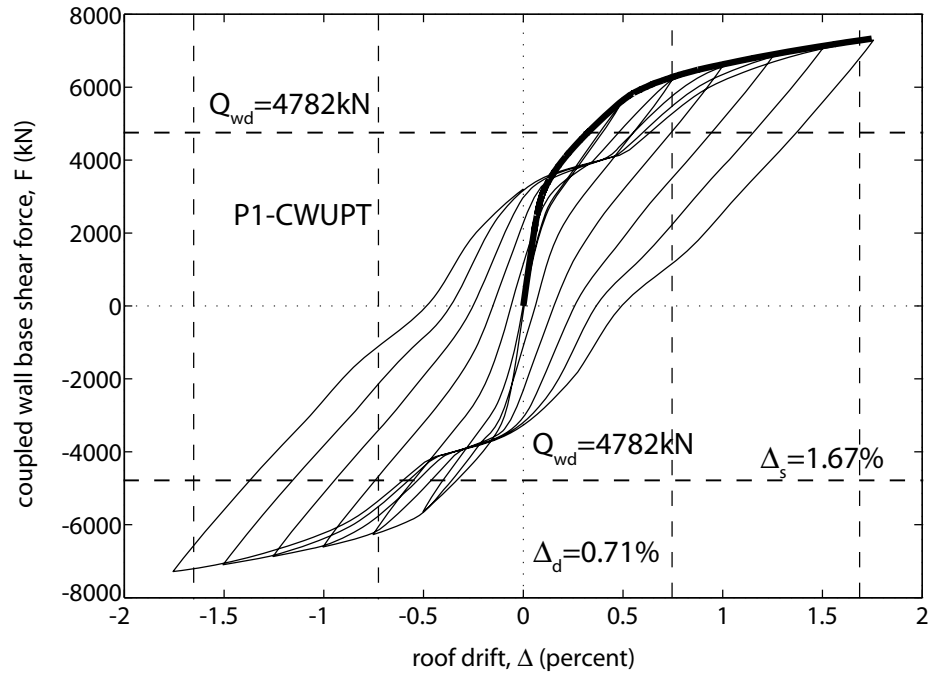
13.3.1 Coupled Wall Base Shear Force versus Roof Drift Behaviors

Figs. 13.23a and 13.23b show the coupled wall base shear force versus roof drift (F- Δ) behaviors from the reversed cyclic lateral load analyses of Structures P1-CWUPT and P2-PWUPT, respectively. For comparison, the behaviors from the monotonic lateral load analyses in Fig. 13.1 are shown using the thick solid lines.

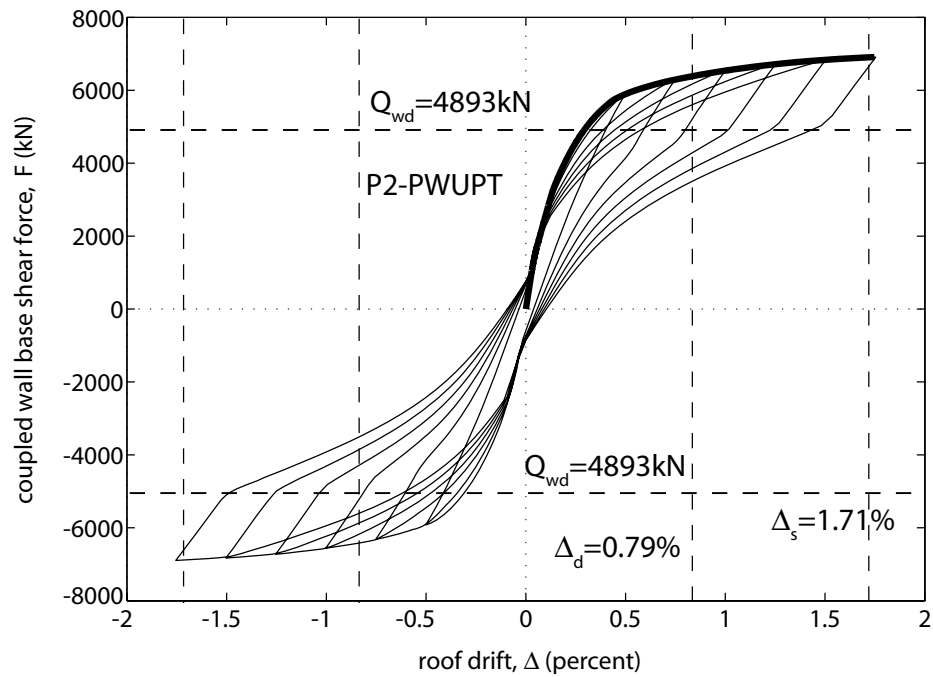
The results in Fig. 13.23 indicate that Structure P1-CWUPT has a larger amount of inelastic energy dissipation than Structure P2-PWUPT, which occurs as a result of the yielding of the mild steel reinforcement at the base of the wall piers. In contrast, the unbonded post-tensioning bars used as flexural reinforcement in the precast concrete wall piers of Structure P2-PWUPT provide little inelastic energy dissipation; since the yielding of the bars is significantly reduced as a result of the use of unbonded bars (see Figs. 13.3 and 13.4).

It is also observed that Structure P1-CWUPT has a smaller amount of self-centering capability than Structure P2-PWUPT. As an example, the residual roof drifts of Structures P1-CWUPT and P2-PWUPT upon unloading from a roof drift of 1.75% are equal to 0.49% and 0.10%, respectively. The increased self-centering capability of Structure P2-PWUPT occurs as a result of the additional restoring forces provided by the post-tensioning bars used as flexural reinforcement in the precast concrete wall piers.

Note that the residual roof drifts of Structure P1-CWUPT in Fig. 13.23a are larger than the residual roof drifts of the CIP-UPT system in Fig. 7.23a. This is because, Structure P1-CWUPT has a much smaller coupling degree ($\text{DOC} \approx 35\%$) than the CIP-UPT system ($\text{DOC} \approx 60\%$), and thus, the beam post-tensioning tendons provide a smaller amount of restoring force to pull the wall piers back towards their original undisplaced



(a)



(b)

Fig. 13.23 Cyclic coupled wall base shear force versus roof drift behaviors:
(a) Structure P1-CWUPT; (b) Structure P2-PWUPT

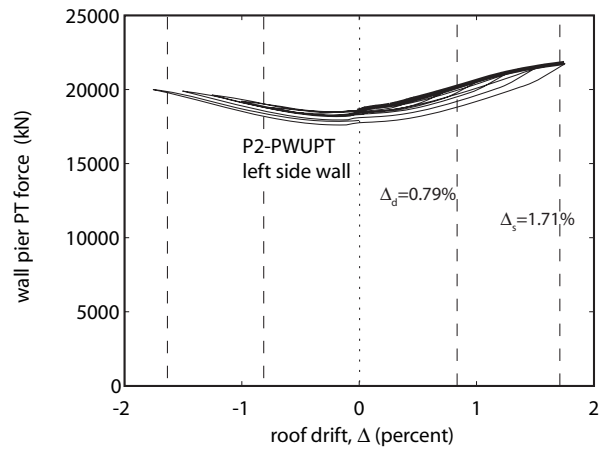
position. Note that the hysteresis loop of Structure P1-CWUPT in Fig. 13.23a appears more like the one in Fig. 7.23d (without top and seat angles) than Fig. 7.23a (with top and seat angles). This is possibly because the top-and-seat angles in Structure P1-CWUPT are designed to have relatively small angle tension yield strength (53 kN).

The vertical dashed lines in Fig. 13.23 show the design-level and survival-level roof drift demands, Δ_d and Δ_s , respectively, and the horizontal dashed lines show the coupled wall base shear demands, Q_{wd} from Chapter 12. As expected, the base shear capacities of the prototype structures satisfy the Q_{wd} demands.

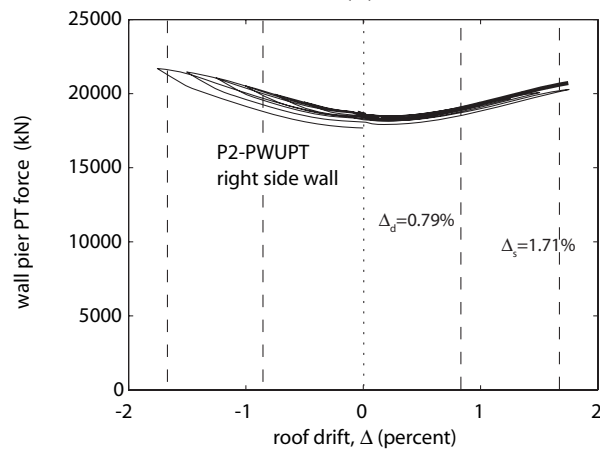
13.3.2 Wall Pier Post-Tensioning Forces in Structure P2-PWUPT

Figs. 13.24a and 13.24b show the total force in the post-tensioning bars of the left-side and right-side wall piers, respectively, from the reversed cyclic lateral load analysis of Structure P2-PWUPT and Fig. 13.24c shows the total coupled wall post-tensioning force as the sum of the left-side and right-side wall pier post-tensioning bar forces. For comparison, the thick solid lines represent the behavior from the monotonic lateral load analysis of the structure and the vertical dashed lines show the design-level and survival-level roof drift demands, Δ_d and Δ_s , respectively, from Chapter 12.

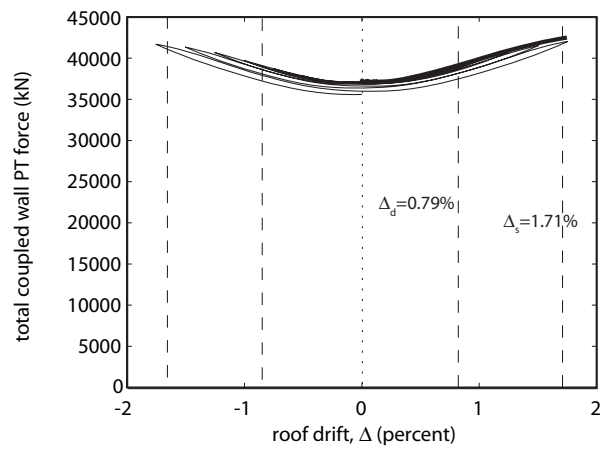
The results in Fig. 13.24 show that the variations in the wall pier post-tensioning bar forces during the cyclic lateral displacements of the structure are small as a result of the use of unbonded bars. As described previously, a small amount of yielding in the wall pier post-tensioning bars occurs when the structure is displaced beyond the PT-yielding state. The yielding of the wall pier post-tensioning bars results in a small amount of loss in the post-tensioning bar forces under cyclic loading; however, this loss is mostly



(a)



(b)



(c)

Fig. 13.24 Cyclic wall post-tensioning forces for Structure P2-PWUPT:
(a) left-side wall pier; (b) right-side wall pier; (c) total coupled wall

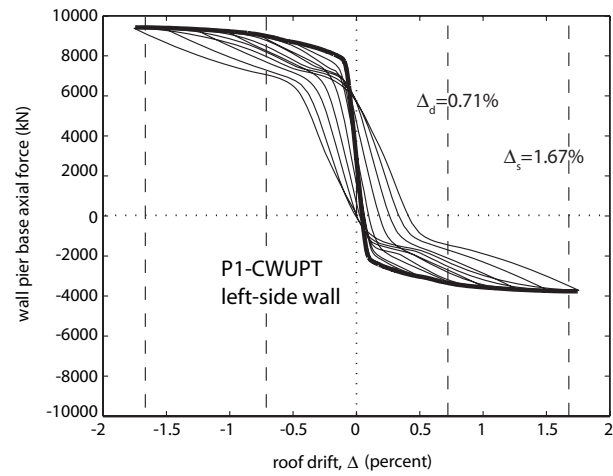
negligible. Thus, it is concluded that the initial post-tensioning forces in the wall piers of Structure P2-PWUPT are mostly maintained throughout the lateral displacement history.

13.3.3 Wall Pier Base Axial Forces

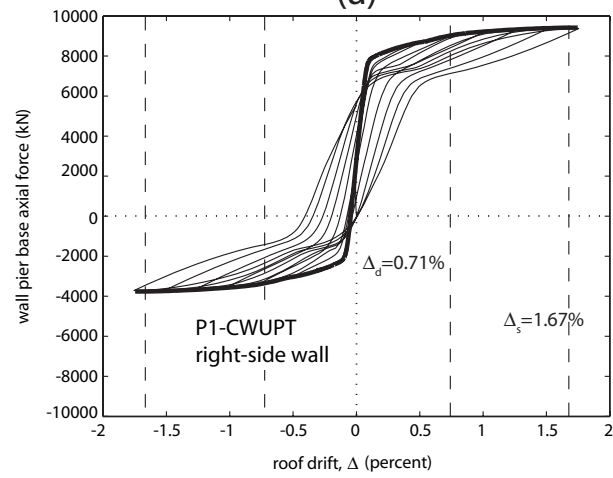
Figs. 13.25a and 13.25b show the axial forces at the bases of the left-side and right-side wall piers, respectively, from the reversed cyclic lateral load analysis of Structure P1-CWUPT. A positive wall pier axial force indicates a compressive force. For comparison, the behaviors from the monotonic analysis results in Fig. 13.5 are shown using the thick solid lines, and the vertical dashed lines show the design-level and survival-level roof drift demands, Δ_d and Δ_s , respectively, from Chapter 12.

The thick solid line in Fig. 13.25c shows the total coupled wall base axial force (i.e., sum of the left-side and right-side wall pier base axial forces) plotted against the cyclic loading duration. The left-side and right-side wall pier base axial forces (thin solid and dashed lines, respectively) are also plotted in Fig. 13.25c, with square markers showing the peak roof drifts during each displacement cycle. Since the coupling-induced axial forces in the left-side and right-side wall piers cancel each other, the total coupled wall axial force in Structure P1-CWUPT is equal to the gravity loading, and thus, remains constant during the cyclic analysis.

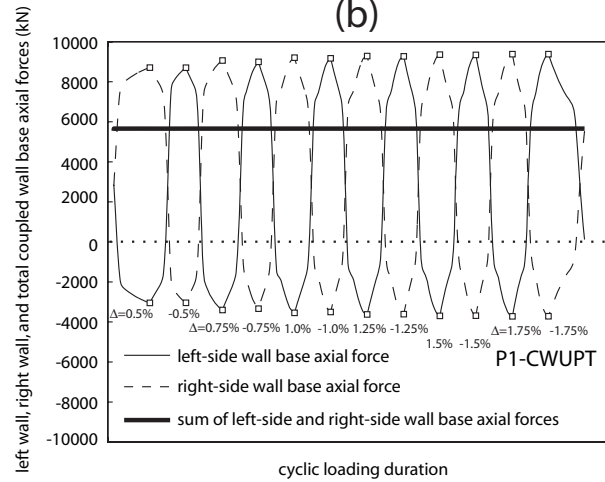
Similar plots for the wall pier base axial forces in Structure P2-PWUPT are given in Figs. 13.26a, 13.26b, and 13.26c. Different from Structure P1-CWUPT, the left-side and right-side wall pier axial forces in Structure P2-PWUPT remain compressive throughout the analysis, as a result of the wall pier post-tensioning forces. Note also that



(a)



(b)



(c)

Fig. 13.25 Cyclic wall base axial forces for Structure P1-CWUPT: (a) left-side wall pier; (b) right-side wall pier; (c) total coupled wall

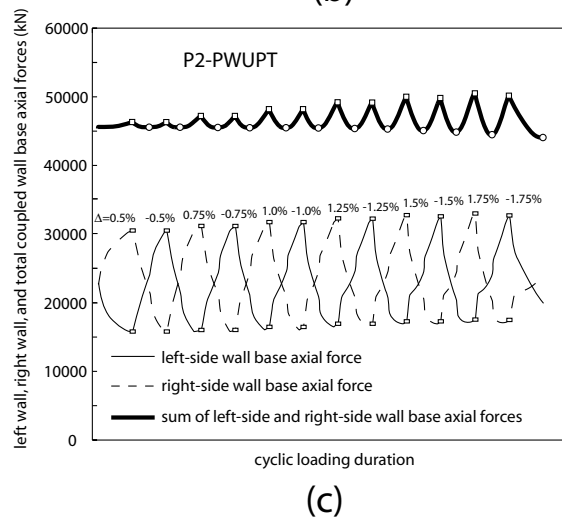
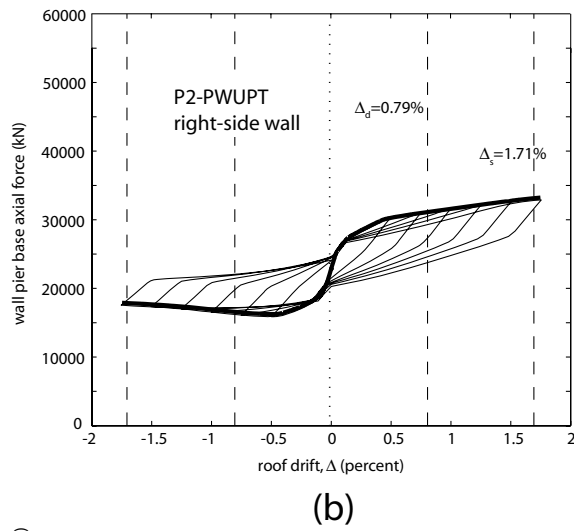
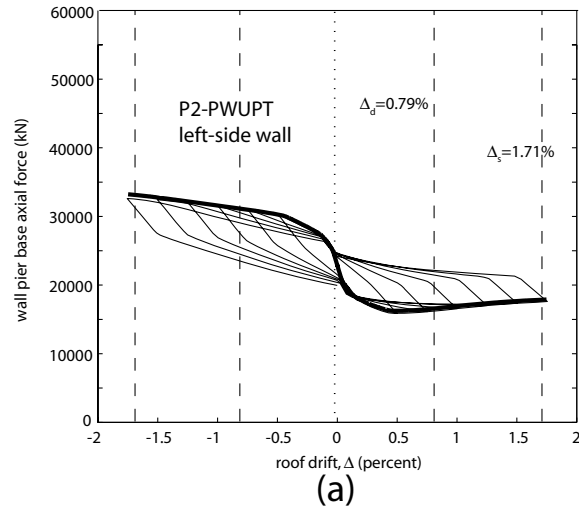


Fig. 13.26 Cyclic wall base axial forces for Structure P2-PWUPT:
(a) left-side wall pier; (b) right-side wall pier; (c) total coupled wall

the total coupled wall base axial force in Structure P2-PWUPT (thick solid line in Fig. 13.26c) varies during the cyclic loading history, since the wall pier post-tensioning forces vary as shown in Fig. 13.24.

13.3.4 Wall Pier Base Shear Forces

Figs. 13.27a and 13.27b show the shear forces at the bases of the left-side and right-side wall piers, respectively, from the reversed cyclic lateral load analysis of Structure P1-CWUPT. For comparison, the behaviors from the monotonic analysis results in Fig. 13.7 are shown using the thick solid lines, and the vertical dashed lines show the design-level and survival-level roof drift demands, Δ_d and Δ_s , respectively, from Chapter 12. Similar plots for the wall pier base shear forces in Structure P2-PWUPT are given in Figs. 13.28a and 13.28b.

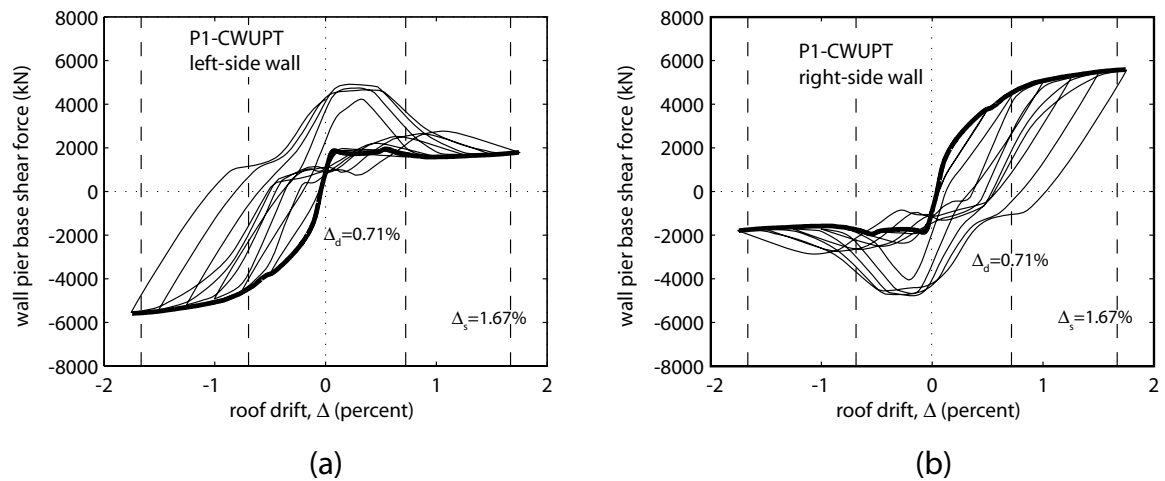


Fig. 13.27 Cyclic wall pier base shear forces for Structure P1-CWUPT:
(a) left-side wall pier; (b) right-side wall pier

It is observed that in each structure, the base shear versus roof drift behavior of the left-side wall pier under positive roof drift is similar to the behavior of the right-side wall pier under negative roof drift and vice versa. The sum of the left-side and right-side wall pier base shear forces is approximately equal to the total coupled wall base shear force F in Fig. 13.23, which is symmetric in the positive and negative roof drift directions.

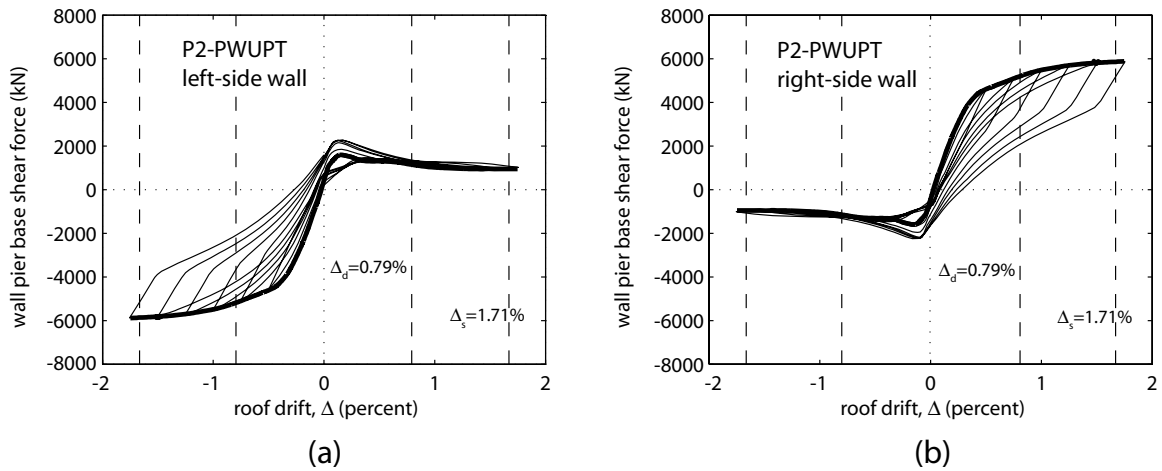


Fig. 13.28 Cyclic wall pier base shear forces for Structure P2-PWUPT:
(a) left-side wall pier; (b) right-side wall pier

13.3.5 Wall Pier Base Moments

Figs. 13.29a and 13.29b show the bending moments at the bases of the left-side and right-side wall piers, respectively, from the reversed cyclic lateral load analysis of Structure P1-CWUPT. Similarly, Fig. 13.29c shows the contribution of the coupling beam forces to the total coupled wall base moment, and Fig. 13.29d shows the total coupled wall base moment, M_w (i.e., sum of the left-side wall pier base moment, right-side wall pier base moment, and base moment due to the coupling forces). For comparison, the behaviors from the monotonic lateral load analysis results in Fig. 13.9

are shown using the thick solid lines, and the vertical dashed lines show the design-level and survival-level roof drift demands, Δ_d and Δ_s , respectively, from Chapter 12. Similar plots for the wall base moments in Structure P2-PWUPT are given in Fig. 13.30.

By inspecting the different contributions to the total coupled wall base moment in Fig. 13.29, it is concluded that almost all of the inelastic energy dissipation in Structure P1-CWUPT is provided by the monolithic cast-in-place reinforced concrete wall piers. This is expected since a small value for the coupling beam top and seat angle ratio

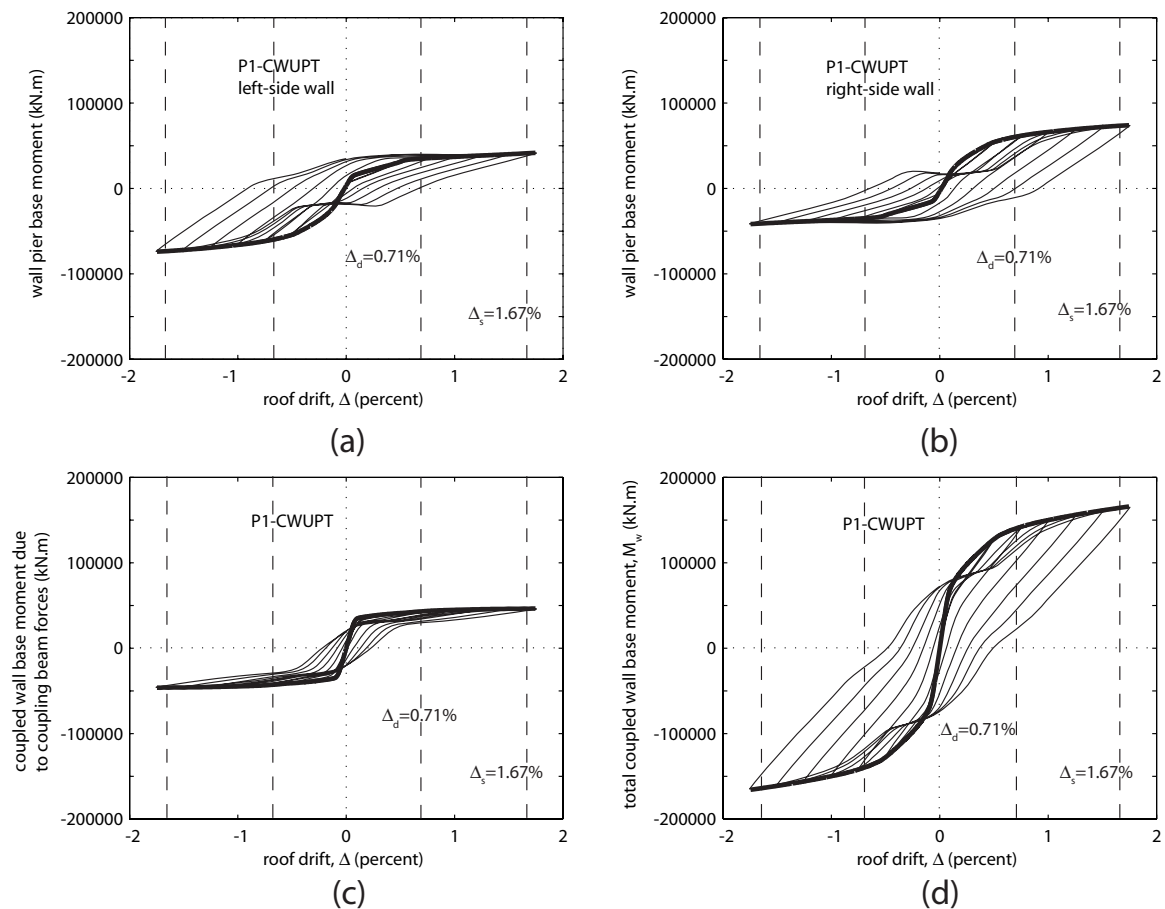


Fig. 13.29 Cyclic wall base moments for Structure P1-CWUPT: (a) left-side wall pier base moment; (b) right-side wall pier base moment; (c) coupling base moment; (d) total coupled wall base moment

($\beta_{ar}=0.051$) is used in the design of Structure P1-CWUPT in Chapter 12, and thus, the angle contribution to the coupling beam forces is small. In contrast, the results in Fig. 13.30 show that the coupling beams provide almost all of the inelastic energy dissipation in Structure P2-PWUPT, since the energy dissipation from the left-side and right-side wall piers is small and a large value for the coupling beam angle ratio ($\beta_{ar}=1.22$) is used in the design of the structure in Chapter 12.

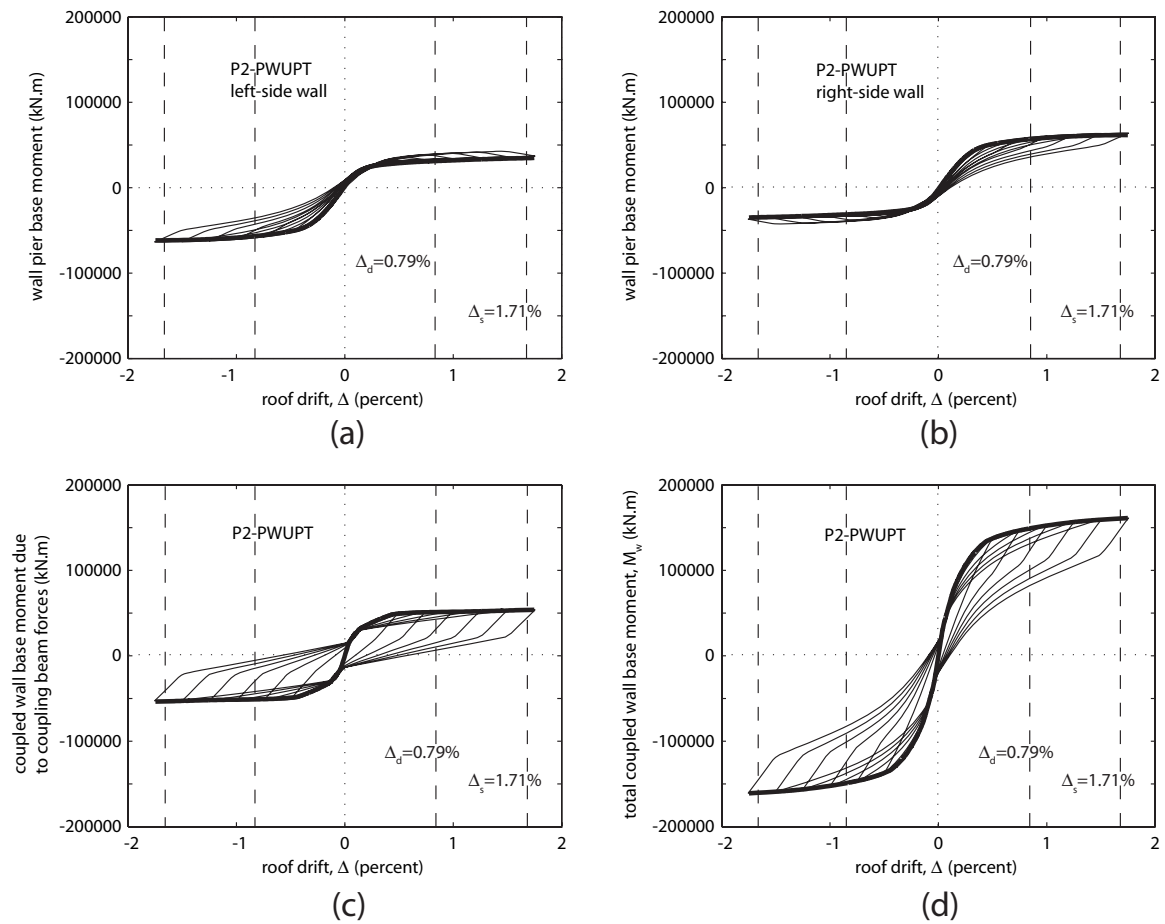


Fig. 13.30 Cyclic wall base moments for Structure P2-PWUPT: (a) left-side wall pier base moment; (b) right-side wall pier base moment; (c) coupling base moment; (d) total coupled wall base moment

13.3.6 Degree of Coupling

Figs. 13.31a and 13.31b show the degree of coupling, DOC [using Equation (2.2)], from the reversed cyclic lateral load analyses of Structures P1-CWUPT and P2-PWUPT, respectively. For comparison, the behaviors from the monotonic analysis results in Fig. 13.10 are shown using the thick solid lines, and the vertical dashed lines show the design-level and survival-level roof drift demands, Δ_d and Δ_s , respectively, from Chapter 12.

The results in Fig. 13.31 show that the degree of coupling shows great variation during the cyclic lateral displacements of the structures. The monotonic DOC curve provides a good representation of the envelope behavior from the cyclic analysis results. It is observed that in between the peak displacements in the positive and negative directions, the DOC values from the cyclic analyses can drop down to a value close to zero and can also take a value greater than 100%. Values of DOC close to zero indicate that the contribution of the coupling beam forces to the total coupled wall base moment resistance is negligible at those instances in the cyclic analysis. Conversely, values of DOC greater than 100% (not plotted in Fig. 13.31) indicate that the coupled wall base moment due to the coupling beam forces is greater than the total coupled wall base moment resistance, which means that the sum of the left-side and right-side wall pier base moments has a negative contribution to the total coupled wall base moment at those instances.

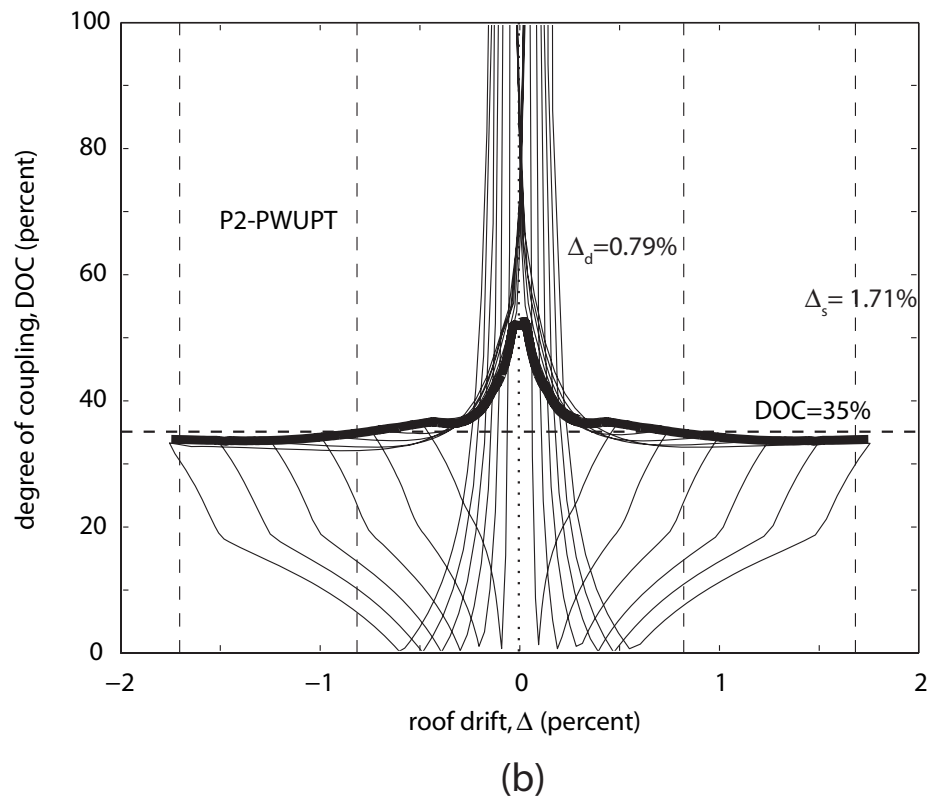
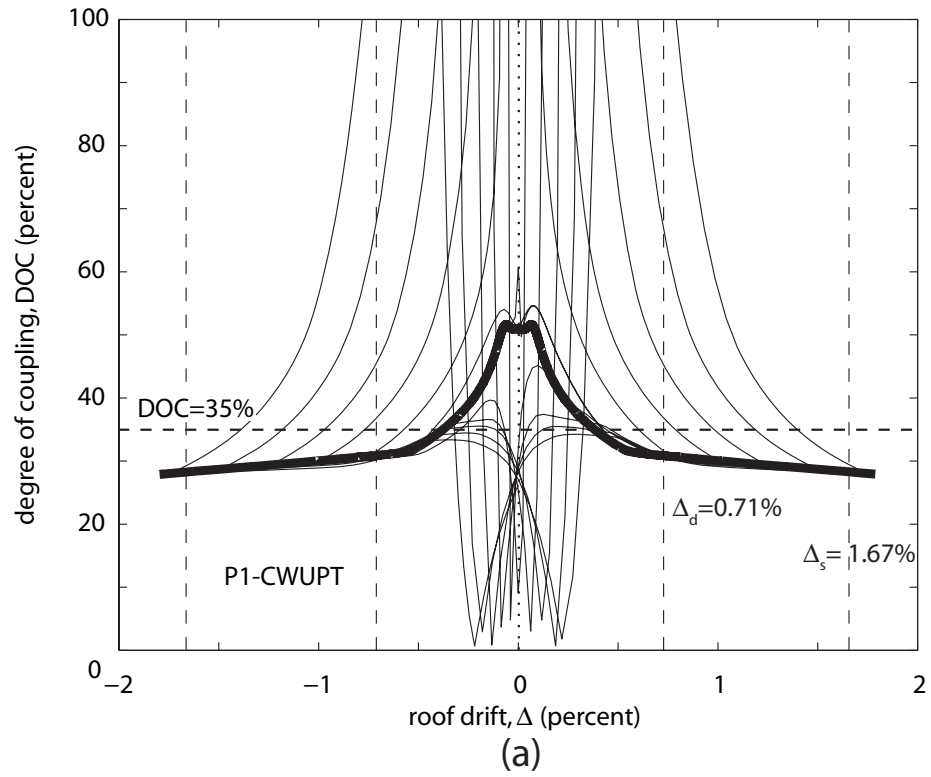


Fig. 13.31 Degree of coupling: (a) Structure P1-CWUPT; (b) Structure P2-PWUPT

The horizontal lines in Fig. 13.31 show the target degree of coupling $DOC=35\%$ used in the design of the structures in Chapter 12. In general, the envelope DOC values from the cyclic analyses are reasonably close to the target value, especially for Structure P2-PWUPT, as described in more detail based on the monotonic analysis results in Section 13.2.6.

13.3.7 Wall Pier Base Concrete Strains

Figs. 13.32a and 13.32b show the neutral axis (i.e., contact) depths (measured from the compression corners of the wall piers) at the bases of the left-side and right-side wall piers, respectively, from the reversed cyclic lateral load analysis of Structure P1-CWUPT. Note that the compression corners of the wall piers alternate between the right and left corners as the structure is displaced cyclically. The contact (i.e., compression) depths are normalized with respect to the wall length, $l_w=4.88$ m and are plotted against the cyclic loading duration. The corresponding extreme confined concrete compression strains at the left and right ends of the wall piers are shown in Figs. 13.32c and 13.32d, respectively, with the confined concrete crushing strains, ϵ_{ccu} shown by the horizontal lines. Similar plots for the wall pier base contact depths and extreme confined concrete strains in Structure P2-PWUPT are given in Fig. 13.33.

Examining the results in Fig. 13.33, it is observed that the contact depths at the bases of the wall piers in Structure P2-PWUPT remain larger than zero throughout the entire loading duration, indicating that both wall piers maintain contact with the foundation. This is because of the additional compressive wall pier axial forces in Structure P2-PWUPT provided by the wall post-tensioning bars. Full contact at the bases

of the wall piers in Structure P2-PWUPT is indicated by the normalized contact depths in Figs. 13.33a and 13.33b reaching a value of 1. In contrast, full contact of the wall piers in Structure P1-CWUPT rarely occurs and full uplift of the tension-side wall pier (as indicated by the normalized contact depths in Figs. 13.32a and 13.32b reaching a value of 0) is quite common, during which the entire lateral resistance of the wall pier is provided by the flexural mild steel reinforcement at the base.

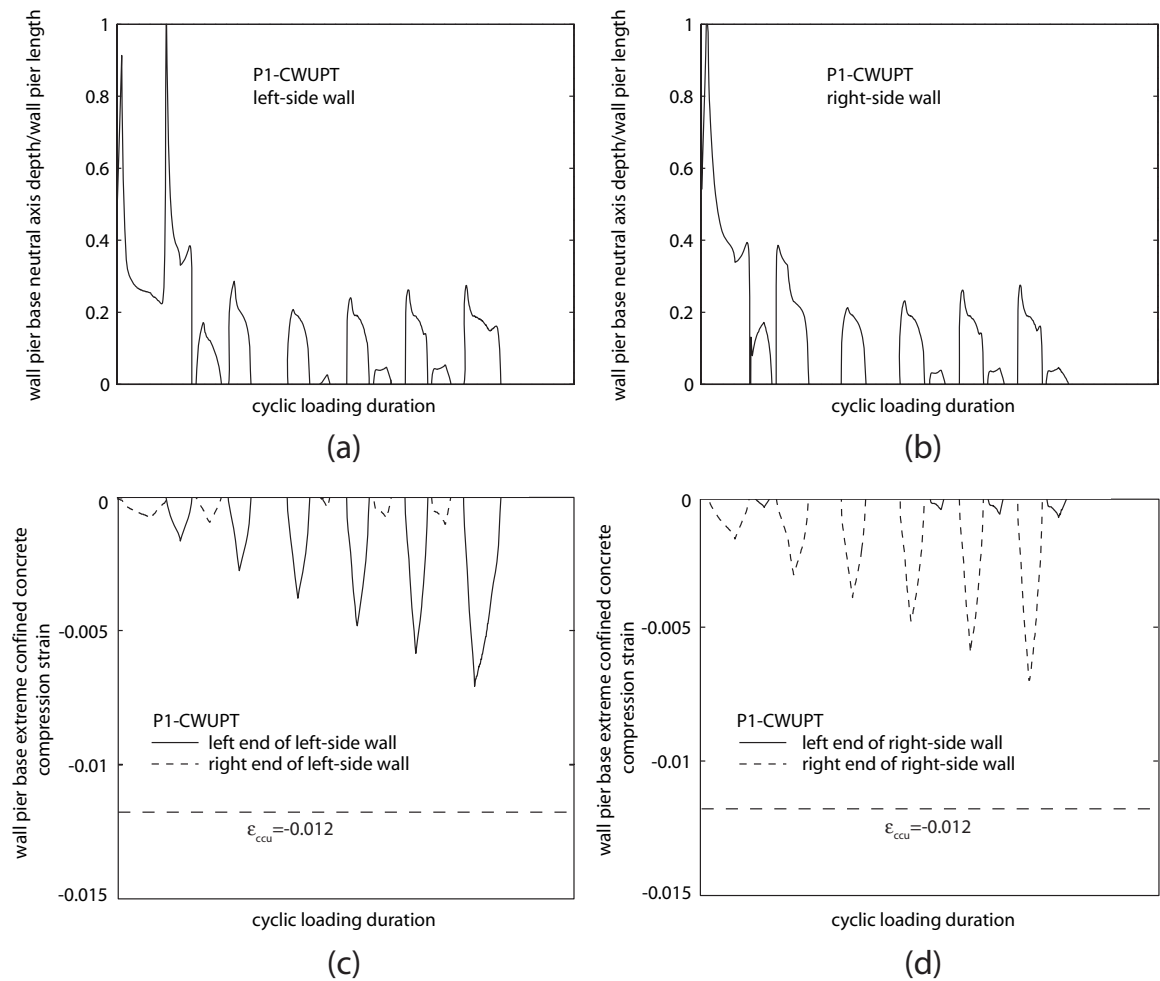


Fig. 13.32 Cyclic wall pier base neutral axis (i.e., contact) depths and extreme confined concrete compression strains for Structure P1-CWUPT: (a) left-side wall pier contact depth; (b) right-side wall pier contact depth; (c) left-side wall pier concrete strains; (d) right-side wall pier concrete strains

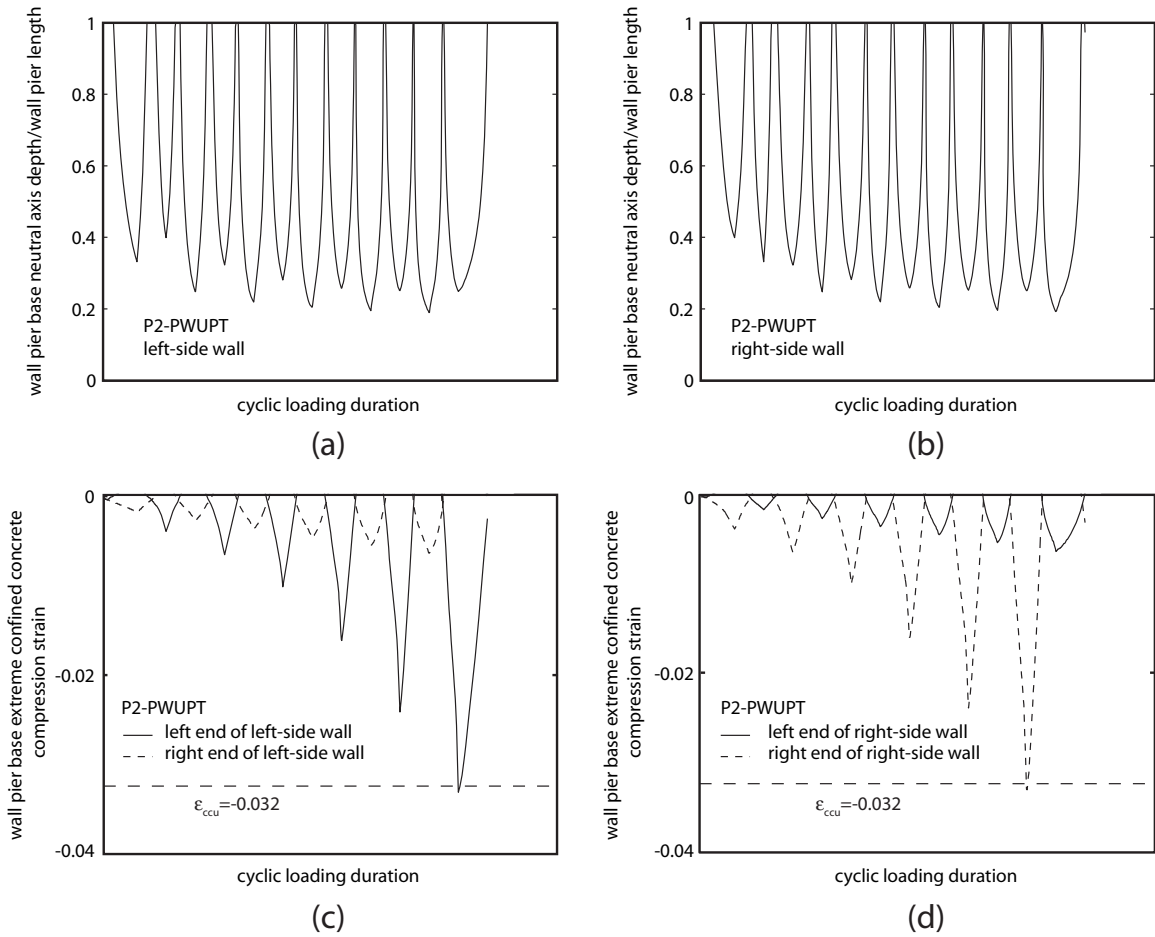


Fig. 13.33 Cyclic wall pier base neutral axis (i.e., contact) depths and extreme confined concrete strains for Structure P2-PWUPT: (a) left-side wall pier contact depth; (b) right-side wall pier contact depth; (c) left-side wall pier concrete strains; (d) right-side wall pier concrete strains

Similar to the monotonic analysis results in Section 13.2.7, significantly larger extreme confined concrete compression strains occur in the wall piers of Structure P2-PWUPT as compared with Structure P1-CWUPT, due to the additional compressive wall pier axial forces from the wall post-tensioning bars. Furthermore, in each wall pier, larger compression strains occur at the outer end than the strains at the inner end (coupling beam end) of the pier. As required by design, crushing of the confined concrete under the survival demand level is prevented in both prototype structures, since the maximum

confined concrete compression strains are smaller than the corresponding confined concrete crushing strains, ϵ_{ccu} .

13.3.8 Coupling Beam Shear Force versus Chord Rotation Behaviors

Figs. 13.34 and 13.35 show the cyclic shear force versus chord rotation (V_b - θ_b) behaviors of the coupling beams in Structures P1-CWUPT and P2-PWUPT, respectively. For comparison, the behaviors from the monotonic analysis results in Figs. 13.13 and 13.14 are shown using the thick solid lines, and the vertical solid lines show the design-level and survival-level beam chord rotation demands, θ_d and θ_s , respectively, from the monotonic nonlinear analysis of each structure (using the DRAIN-2DX model) corresponding to the design-level and survival-level roof drift demands, Δ_d and Δ_s , from Chapter 12.

As expected, a larger amount of inelastic energy dissipation is provided by the coupling beams in Structure P2-PWUPT, since a larger value of the top and seat angle ratio ($\beta_{ar}=1.22$) is used in design. The differences between the behaviors of the second floor beam and the upper floor beams (as a result of the fixed foundation conditions at the base of the structure) are more pronounced in Structure P1-CWUPT.

13.3.9 Coupling Beam Axial Forces and Post-Tensioning Forces

The solid lines in Figs. 13.36 and 13.37 show the midspan axial force, N_b , versus the cyclic loading duration behaviors of the coupling beams in Structures P1-CWUPT and P2-PWUPT, respectively. A positive beam axial force indicates a compressive force. For comparison, the dashed lines show the total forces in the post-tensioning tendons, P_b

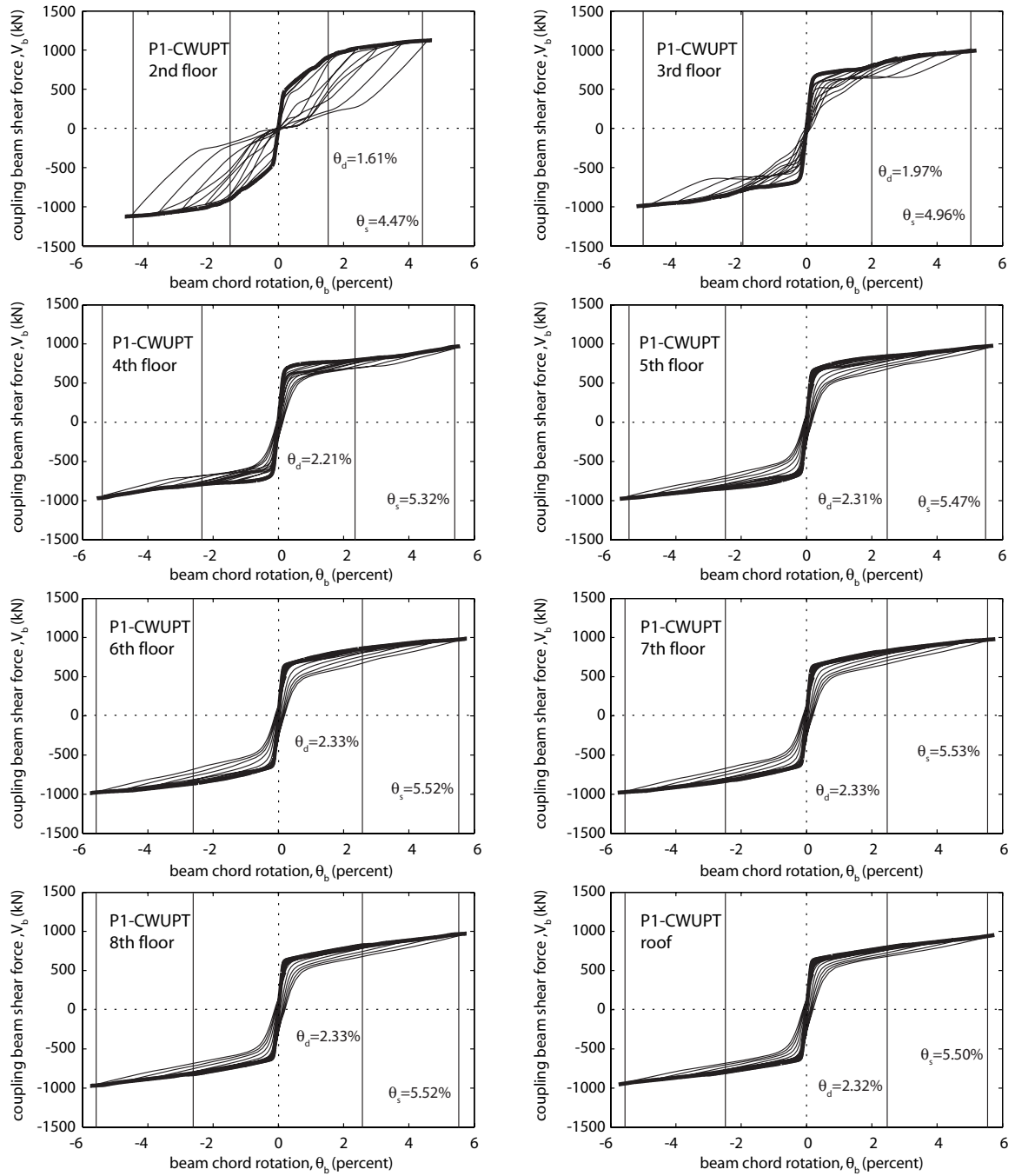


Fig. 13.34 Cyclic coupling beam shear force versus chord rotation behaviors for Structure P1-CWUPT

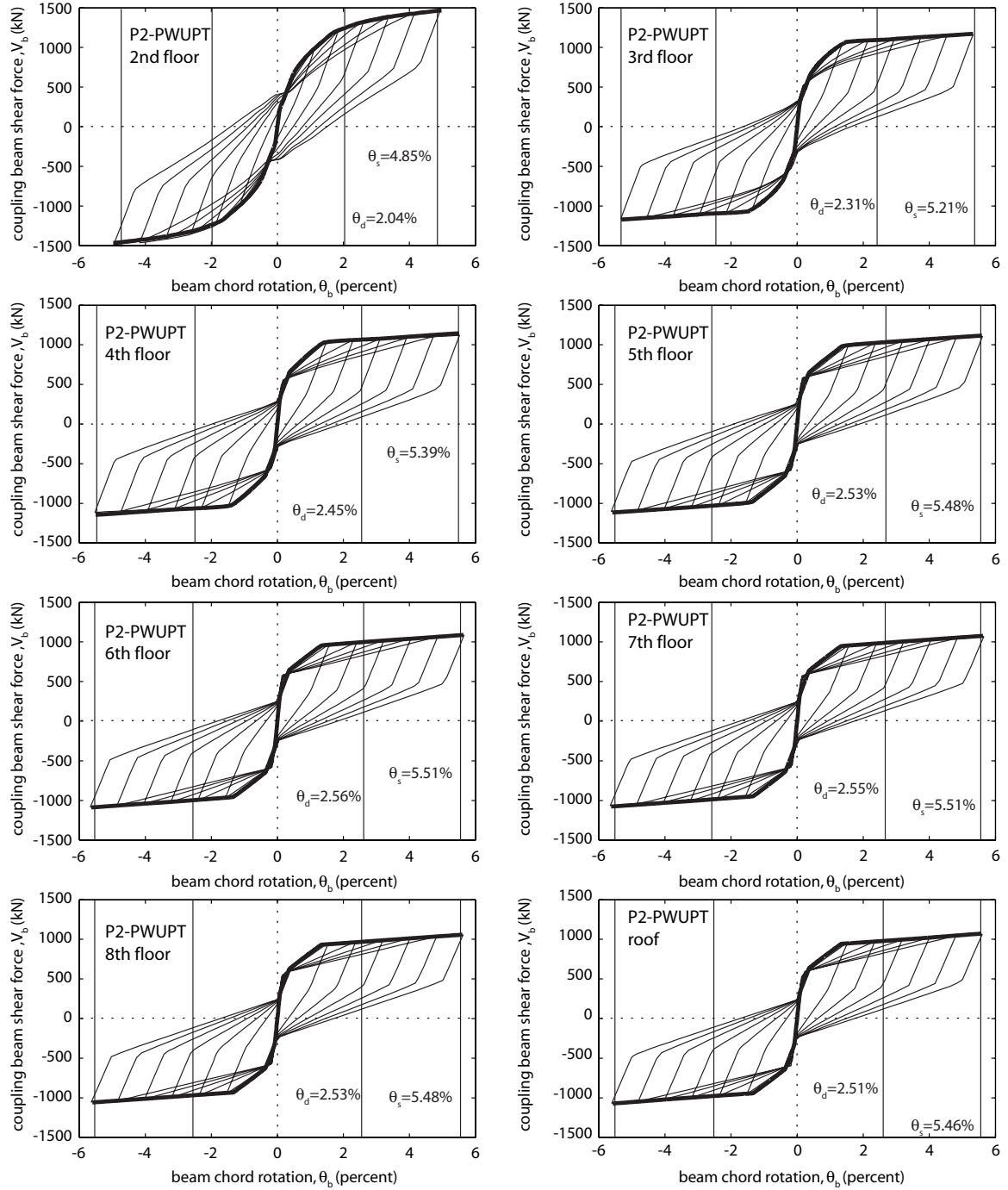


Fig. 13.35 Cyclic coupling beam shear force versus chord rotation behaviors for Structure P2-PWUPT

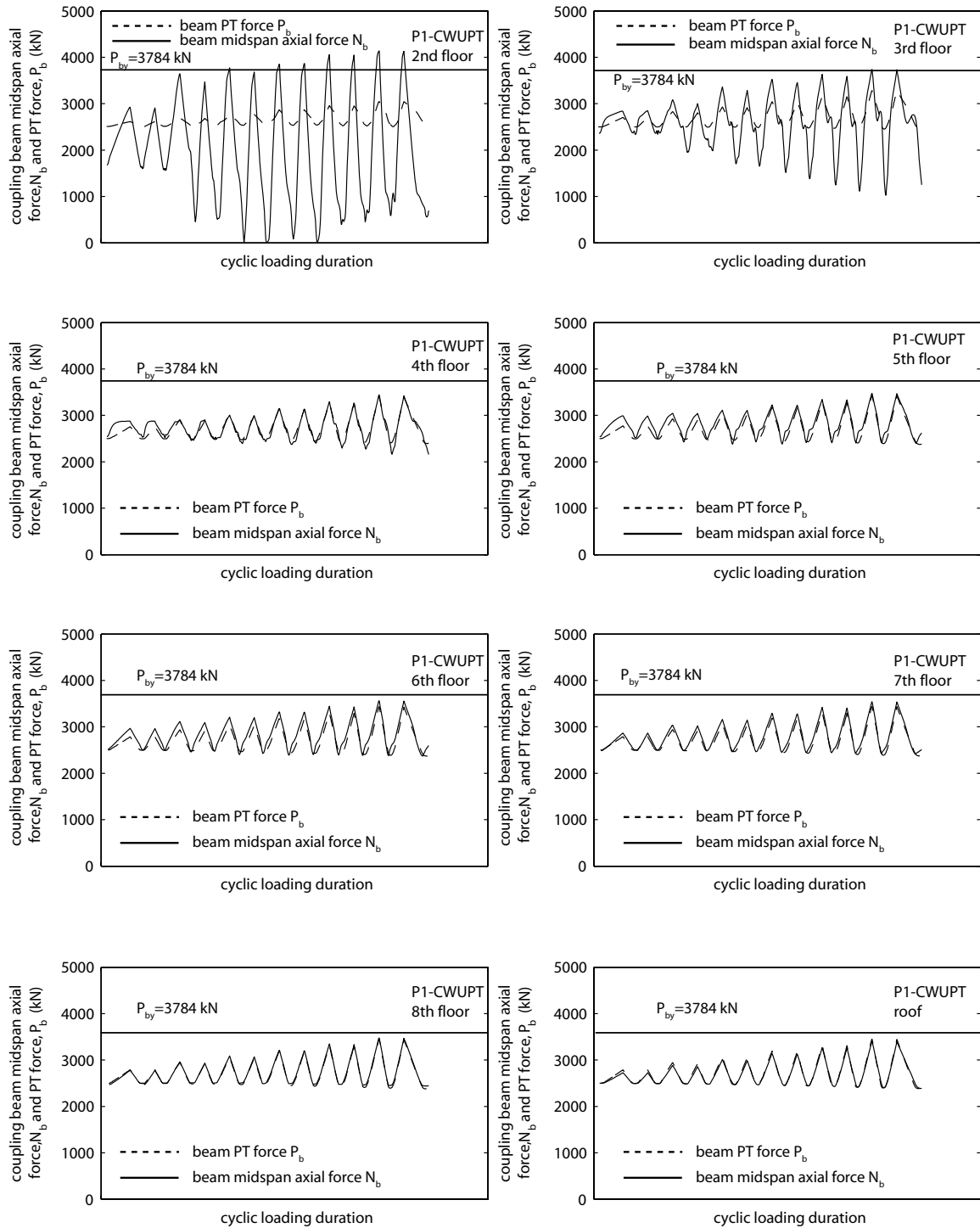


Fig. 13.36 Cyclic coupling beam axial forces and post-tensioning forces in Structure P1-CWUPT

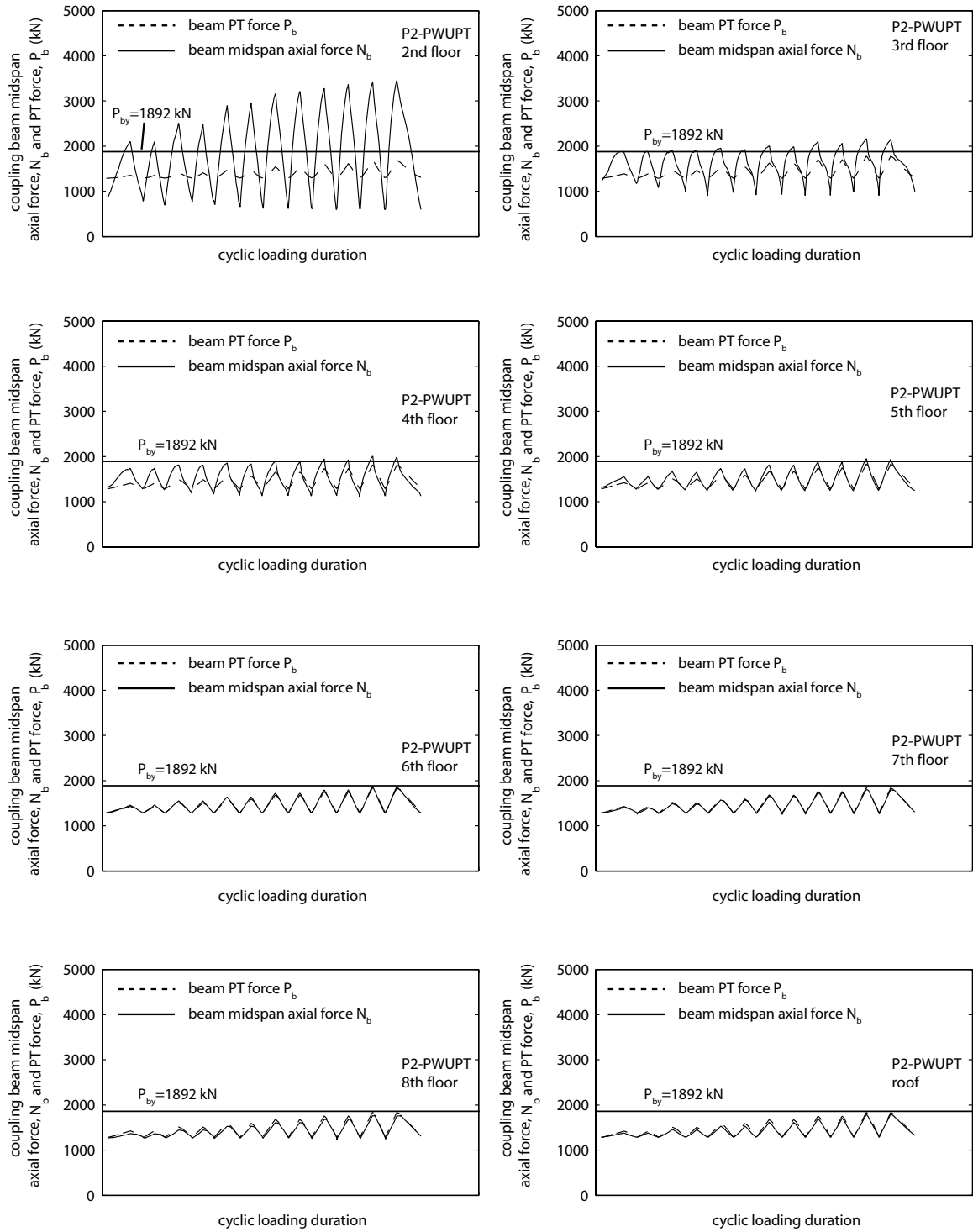


Fig. 13.37 Cyclic coupling beam axial forces and post-tensioning forces in Structure P2-PWUPT

of each coupling beam and the horizontal lines show the total yield strength of the coupling beam post-tensioning tendons, P_{by} .

The larger coupling beam post-tensioning forces in Structure P1-CWUPT, as designed in Chapter 12 with the use of a small top and seat angle ratio ($\beta_{ar}=0.051$), are noticeable in the plots. Since the yielding of the beam post-tensioning tendons is prevented by design, there is no prestress loss in the beam post-tensioning tendons other than a small, negligible amount that occurs due to the compression yielding and shortening of the coupling beams under the effect of the beam axial forces.

Similar to the monotonic analysis results in Section 13.2.9, significant differences are observed between the behaviors of the second floor coupling beam and the upper floor beams in both structures. The axial forces in the lower floor beams of Structure P1-CWUPT go through larger variations and differences from the total beam post-tensioning force under cyclic loading as compared with the lower floor beams of Structure P2-PWUPT. Furthermore, despite the larger coupling beam post-tensioning forces in Structure P1-CWUPT, complete loss of axial force is observed in the second floor beam during cyclic response, while the beam axial forces in Structure P2-PWUPT remain compressive throughout the analysis. This is because of the nonlinear inelastic behavior that occurs at the bases of the monolithic cast-in-place reinforced concrete wall piers in Structure P1-CWUPT as compared with the nonlinear but mostly elastic behavior at the bases of the precast concrete wall piers in Structure P2-PWUPT.

13.3.10 Coupling Beam End Strains

Figs. 13.38 and 13.39 show the neutral axis (i.e., contact) depths, c_b at the left ends of the coupling beams from the reversed cyclic lateral load analyses of Structures P1-CWUPT and P2-PWUPT, respectively. The behaviors at the right ends of the coupling beams are similar. The c_b values are measured from the compression corners of the beams and are normalized with respect to the beam depth, $d_b=559$ mm, where the horizontal lines represent the thickness of the beam flange, t_{bf} . Note that the compression corners of the beams alternate between the top and bottom corners as the structure is displaced cyclically. The corresponding extreme steel compression strains, ϵ_{be} at the left end top corners of the coupling beams are shown in Figs. 13.40 and 13.41.

It is observed that the coupling beams in both structures maintain contact with the wall piers at both ends during the entire nonlinear displacement history, indicating that the beam post-tensioning tendons provide a sufficient restoring force to yield the tension angles back in compression and close the gaps at the beam ends.

Similar to the monotonic analysis results in Figs. 13.19 and 13.20, the extreme compression strains in the coupling beams of Structure P2-PWUPT are smaller than the strains in the beams of Structure P1-PWUPT due to the smaller beam post-tensioning force.

13.3.11 Angle Force versus Deformation Behaviors

Figs. 13.42 and 13.43 show the cyclic force versus deformation behaviors of the top angles at the left ends of the coupling beams in Structures P1-CWUPT and P2-PWUPT, respectively. The behaviors of the other angles at each floor/roof level are

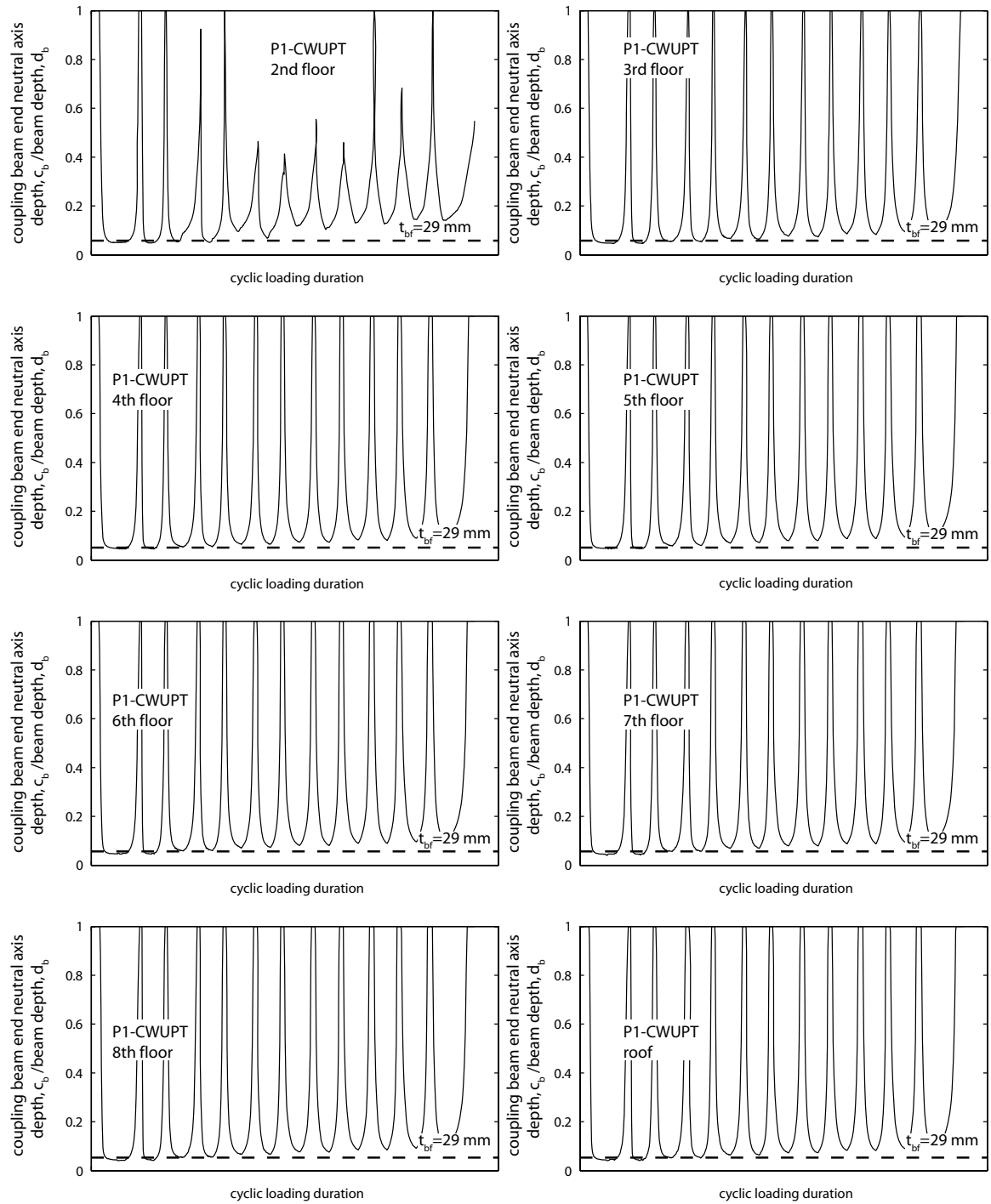


Fig. 13.38 Cyclic coupling beam end neutral axis (i.e., contact) depths for Structure P1-CWUPT

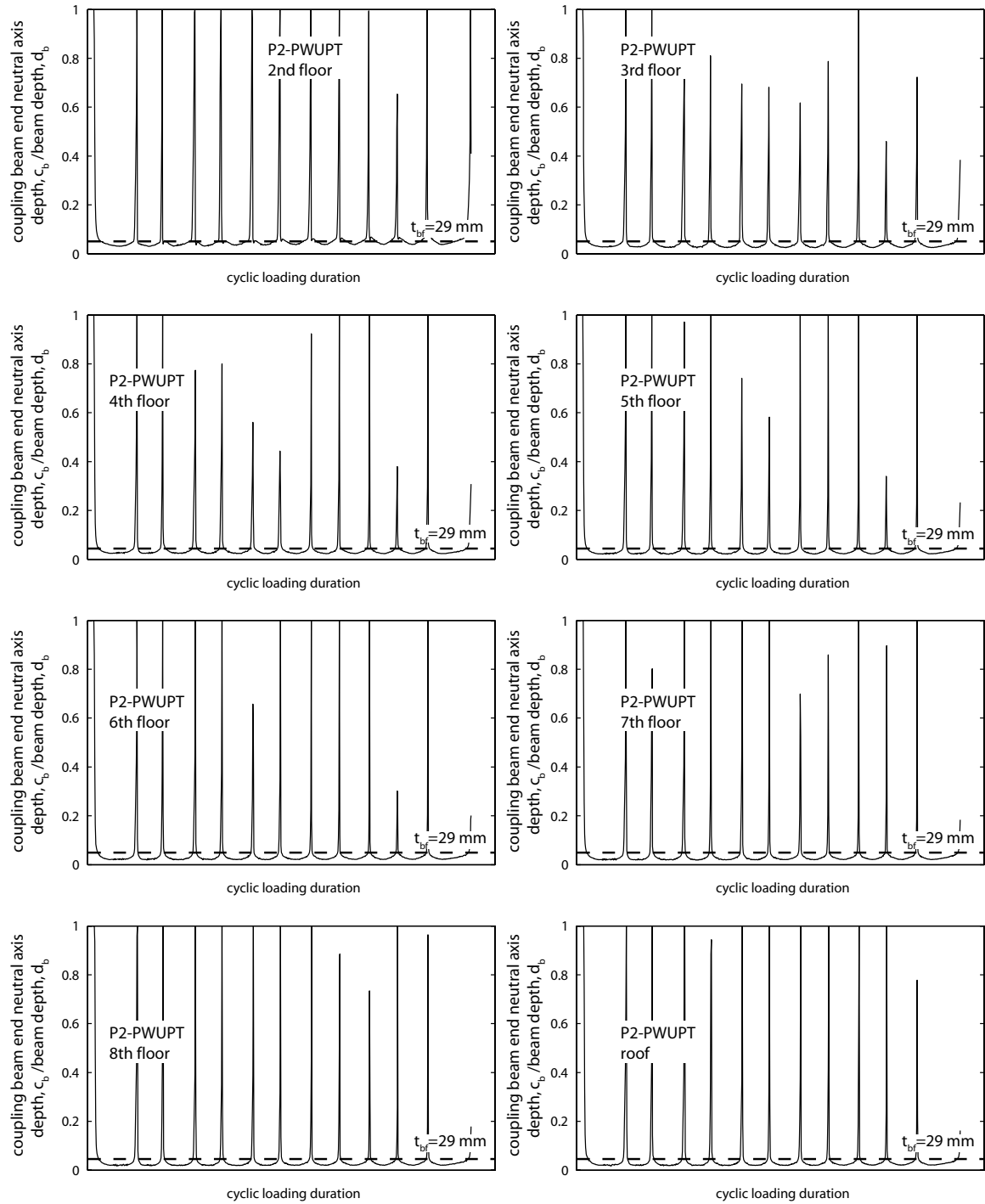


Fig. 13.39 Cyclic coupling beam end neutral axis (i.e., contact) depths for Structure P2-PWUPT

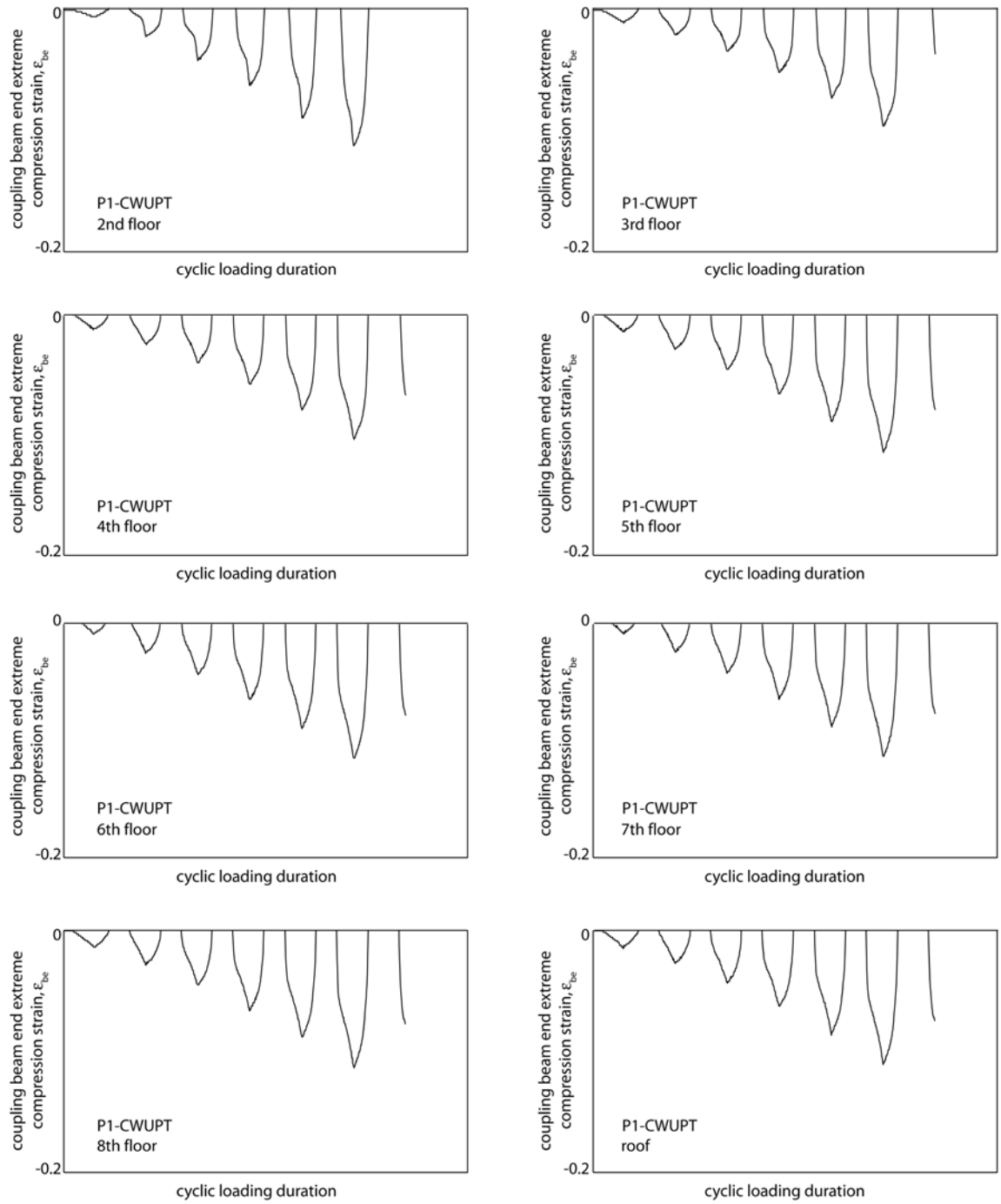


Fig. 13.40 Cyclic coupling beam end extreme steel compression strains for Structure P1-CWUPT

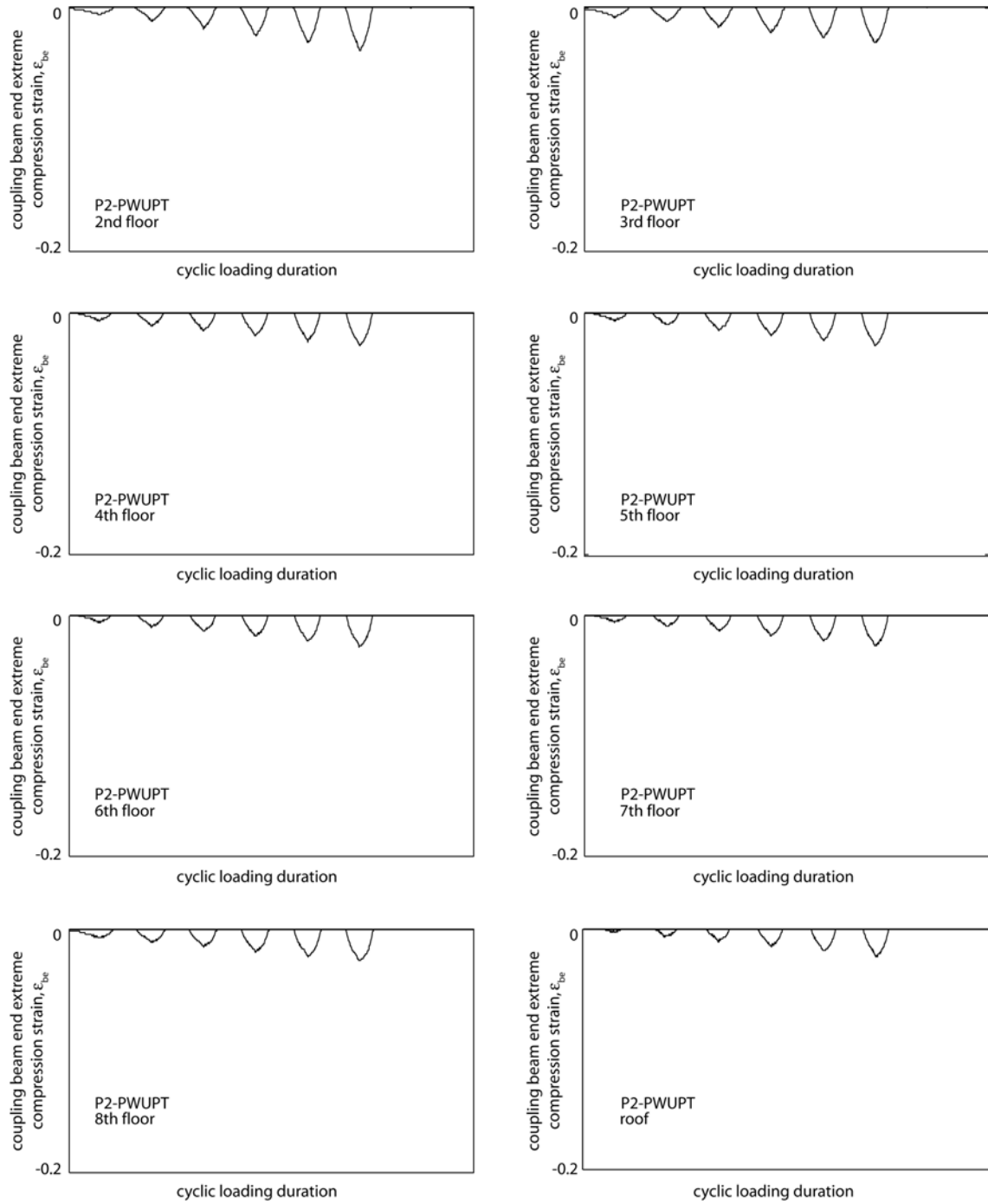


Fig. 13.41 Cyclic coupling beam end extreme steel compression strains for Structure P2-PWUPT

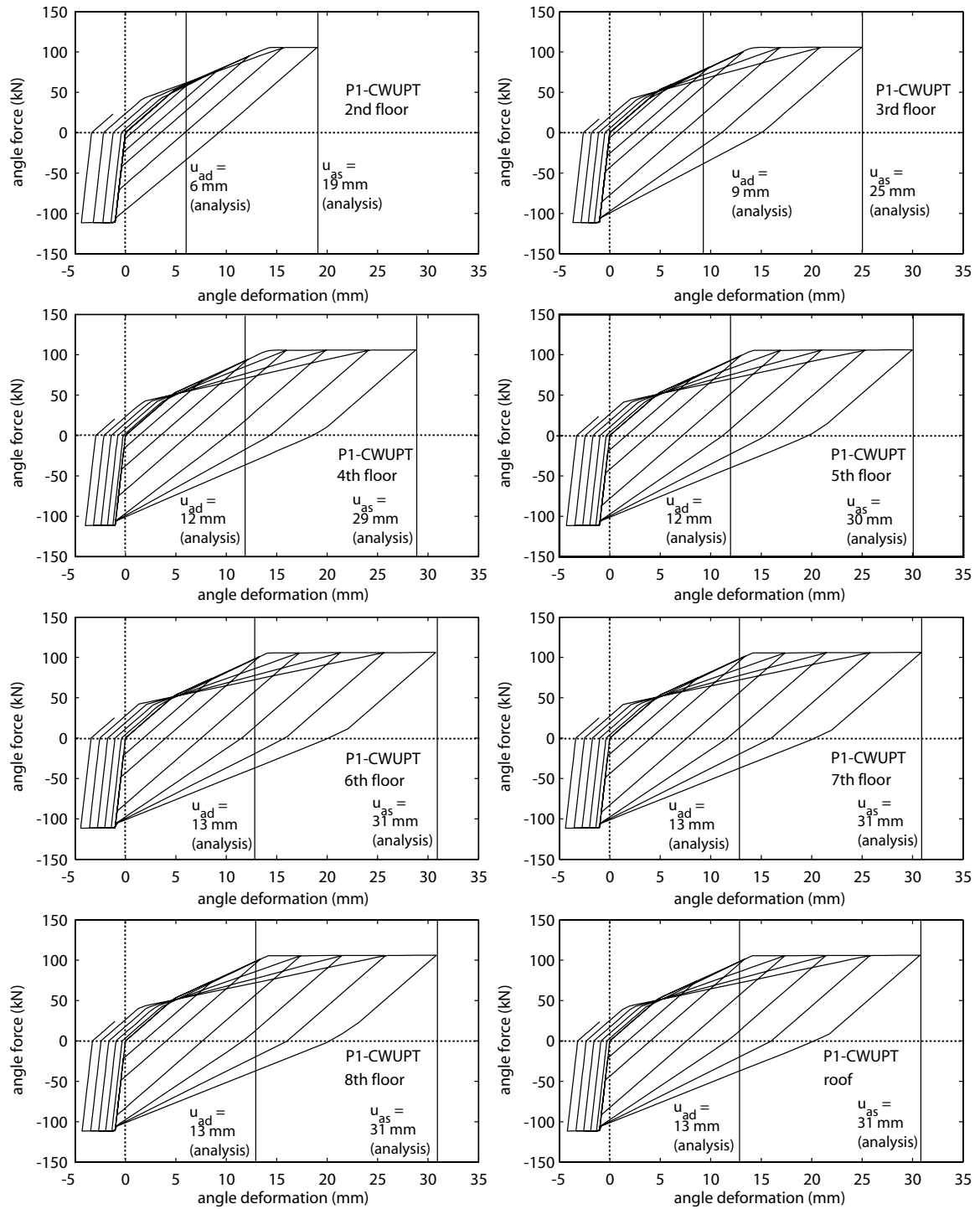


Fig. 13.42 Cyclic coupling beam angle force versus deformation behaviors for Structure P1-CWUPT

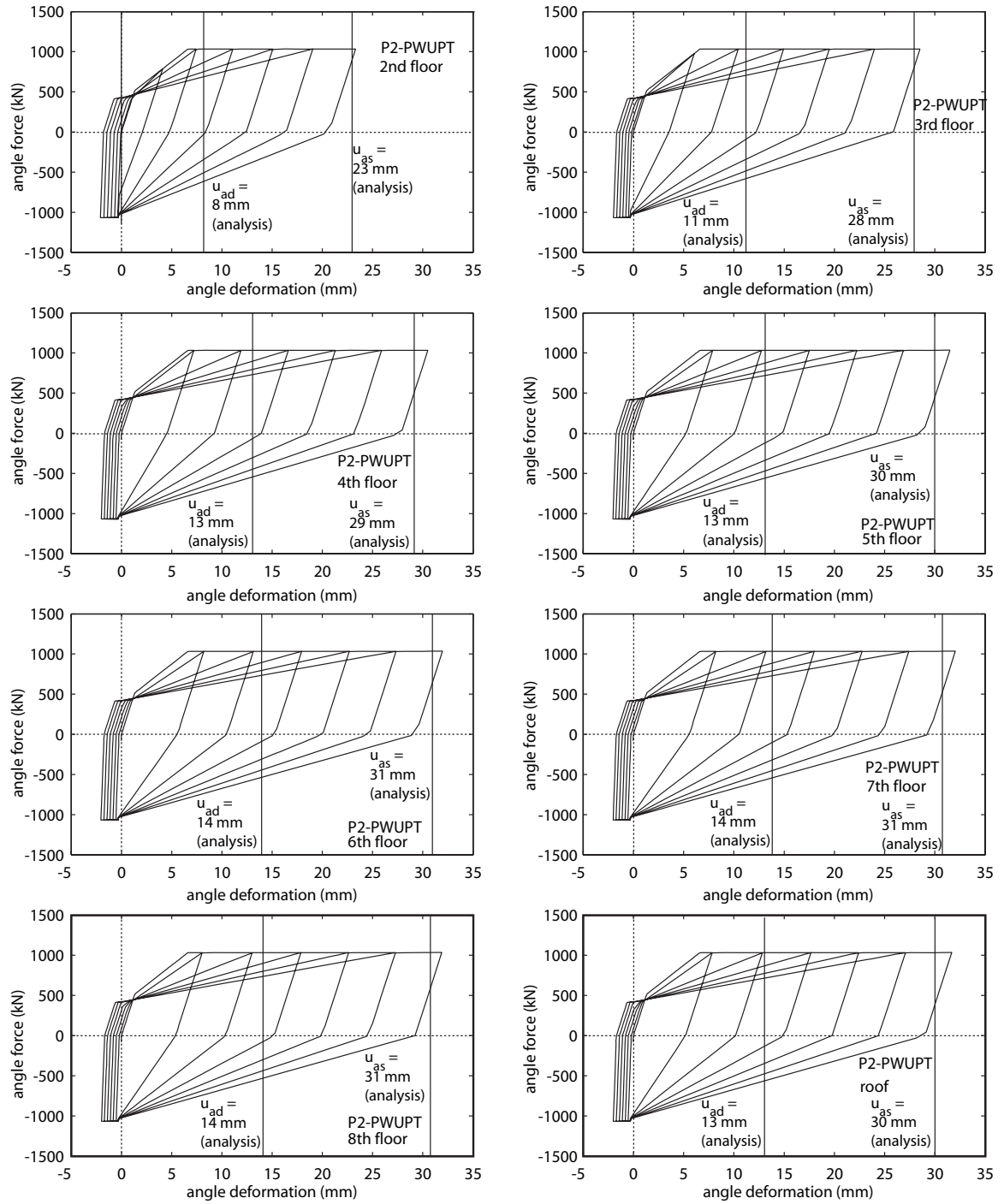


Fig. 13.43 Cyclic coupling beam angle force versus deformation behaviors for Structure P2-PWUPT

similar. The vertical lines show the design-level and survival-level tension angle deformation demands, u_{ad} and u_{as} , from the monotonic nonlinear lateral load analysis of each structure (using the DRAIN-2DX fiber element model) corresponding to the design-level and survival-level roof drift demands, Δ_d and Δ_s , from Chapter 12.

Similar to the monotonic analysis results, for both structures, the angles at the second floor level have the smallest tension deformations, because, the fixed boundary conditions assumed at the bases of the wall piers restrain the opening of gaps at the beam-to-wall interfaces. The smaller angle forces in Structure P1-CWUPT, as designed in Chapter 12 with the use of a small top and seat angle ratio ($\beta_{ar}=0.051$), are noticeable in the plots.

13.4 Structure With Embedded Steel Coupling Beams

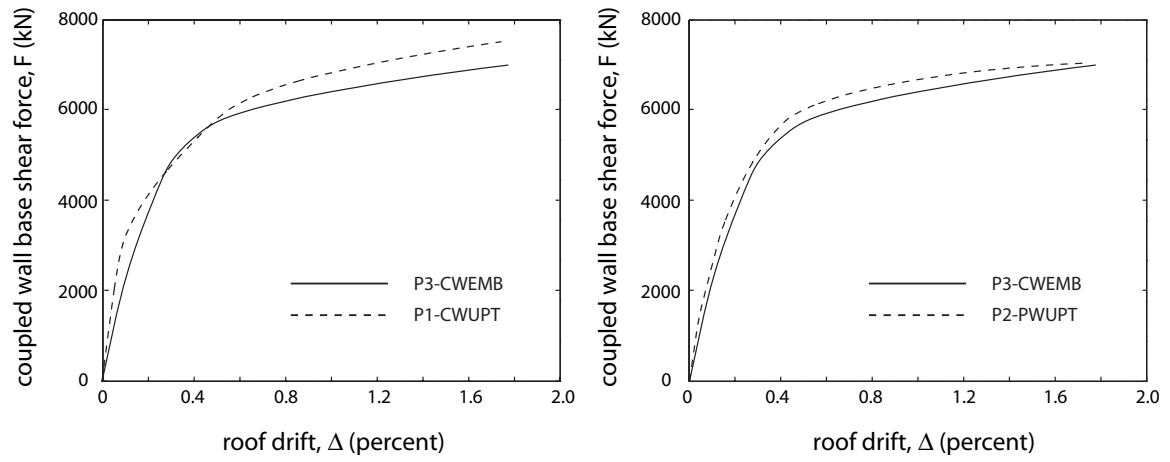
Similar to the CIP-EMB system in Chapter 7, the coupling beams in Structure P1-CWUPT are modified to represent a conventional hybrid system with embedded steel coupling beams, referred to as Structure P3-CWEMB. As described in Chapter 4, the lateral strength of a post-tensioned steel coupling beam is smaller than the lateral strength of an embedded beam of the same size, since the post-tensioned beam cannot develop the full yield and plastic moment capacity of the cross section. Thus, to facilitate a comparative investigation, smaller coupling beams are used in Structure P3-CWEMB (with a W12×136 section) than the beams in Structure P1-CWUPT (with a W21×147 section) such that the monotonic $F-\Delta$ relationships of the two coupled wall structures are similar. All of other design parameters for Structures P1-CWUPT and P3-CWEMB are the same.

It is assumed that the embedment lengths of the coupling beams in Structure P3-CWEMB are equal to $l_{be}=1.22$ m (48 in.) at each end, with a clear span length of $l_b=2.13$ m (7 ft). In the analytical modeling of the structure, the lengths of the embedded steel coupling beams are taken as $l_{b,eff}=(2/3)l_{be}+l_b$ as described in Chapter 3.

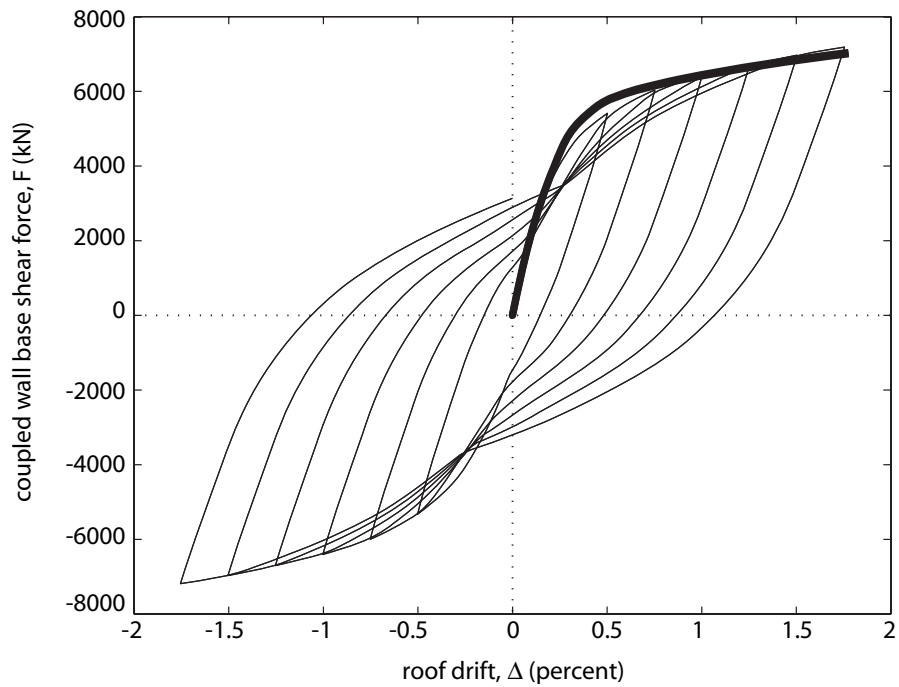
13.4.1 Behaviors Under Monotonic and Cyclic Loading

The solid curves in Figs. 13.44a and 13.44b show the coupled wall base shear force versus roof drift ($F-\Delta$) behaviors of Structure P3-CWEMB under monotonic and reversed cyclic lateral loads, respectively. For comparison, the monotonic $F-\Delta$ behaviors of Structures P1-CWUPT and P2-PWUPT are shown with the dashed curves in Fig. 13.44a.

As expected, Structure P3-CWEMB has a larger inelastic energy dissipation and smaller self-centering capability than Structures P1-CWUPT and P2-PWUPT. As an example, the residual roof drift of Structure P3-CWEMB upon unloading from a roof drift of 1.75% is equal to 1.07%, whereas the residual roof drifts of Structures P1-CWUPT and P2-PWUPT upon unloading from the same roof drift are equal to 0.49% and 0.10%, respectively (see Section 13.3.1). The increased energy dissipation capability of Structure P3-CWEMB occurs as a result of the yielding of the embedded steel coupling beams.



(a)



(b)

Fig. 13.44 Coupled wall base shear force versus roof drift behavior of Structure P3-CWEMB: (a) monotonic loading; (b) cyclic loading

13.5 Chapter Summary

This chapter investigates the behavior of prototype Structures P1-CWUPT and P2-PWUPT from Chapter 12 under both monotonic and cyclic lateral loading, using the DRAIN-2DX (Prakash et al. 1993) fiber element model described in Chapter 6 including the modifications recommended in Chapter 10. Evaluations of the global behavior of the structures as well as the local behavior of the wall piers and the coupling beams are provided. The analysis results indicate that the design procedures developed in Chapter 12 are valid. The estimations of the various design parameters and structure capacities in Chapter 12 match reasonably well with the analytical results in this chapter.

CHAPTER 14

GROUND MOTION RECORDS FOR DYNAMIC ANALYSES

This chapter describes the ground motion records used in the nonlinear dynamic time-history analyses of Structures P1-CWUPT and P2-PWUPT from Chapter 12 as follows: (1) overview; (2) design-level ground motion records; and (3) survival level ground motion records. The dynamic analyses of the prototype structures are described in Chapter 15.

14.1 Overview

A considerable number of dynamic analyses using different ground motion records are often needed to derive clear conclusions about the seismic behavior of nonlinear structures. The results from these dynamic analyses depend on the characteristics of the ground motions as well as the vibration characteristics of the structures. Ground motion characteristics depend on many factors, including the seismicity of the region, magnitude, epicentral distance, fault rupture mechanism, fault rupture direction, and site soil profile.

A total of forty “far-fault” ground motion records compiled by the SAC steel project (Somerville et al. 1997) are used in the dynamic analyses of the prototype structures in this dissertation. SAC is a joint venture with the following partners: the Structural Engineers Association of California (SEAOC), the Applied Technology Council (ATC), and California Universities for Research in Earthquake Engineering

(CUREE). The ground motions are for stiff soil sites [site class D in IBC 2000 (ICC 2000)] in Los Angeles, similar to the site conditions used in the design of the structures in Chapter 12, and are grouped into two ensembles based on the seismic demand level: (1) twenty design-level records (with a 10% probability of being exceeded in 50 years); and (2) twenty survival-level records (with a 2% probability of being exceeded in 50 years).

For each ground motion, two horizontal components, rotated 45 degrees away from the fault-normal and fault-parallel orientations, are provided by the SAC steel project. These ground motions were scaled by the SAC steel project based on target linear-elastic smooth acceleration response spectra as described in Somerville et al. (1997). The probabilistic ground motion spectra published by the United States Geological Survey (Frankel et al. 1996, BSSC 1998, ICC 2000), modified to represent site class D, were used as the target spectra. In order to preserve the variability in the characteristics of the individual ground motions, the shapes of the acceleration response spectra of the records were not modified in the scaling procedure. Instead, for each ground motion, a single scaling factor was found that minimized the weighted sum of the squared error between the average 5%-damped linear-elastic acceleration response spectra of the two horizontal components and the corresponding target response spectrum in the period range of 0.3 to 4 sec. This scale factor was then applied to both components of the ground motion, thus retaining the ratios between the components at all periods. The weights used in the determination of the ground motion scaling factors were 0.1, 0.3, 0.3, and 0.3 for periods of 0.3, 1, 2, and 4 sec., respectively.

SAC ground motion records LA01-LA20 (20 recorded motions) are used in this dissertation to represent the design-level seismic demand and SAC records LA21-LA40

(10 simulated and 10 recorded motions) are used to represent the survival-level seismic demand, as described in more detail below. The names of these records are kept the same as the names used by SAC (Somerville et al. 1997).

Note that reliable nonlinear dynamic time-history analysis results depend on the use of realistic ground motion records with phasing and response spectral characteristics that are appropriate for the magnitude, distance, site conditions, and wave propagation properties of the region. According to Somerville et al. (1997), the SAC ground motion records provide a sample of this variability in phasing and spectra through a set of time histories that are realistic not only in their average properties but also in their individual characteristics. Thus, it is expected that the dynamic analysis results presented in Chapter 15 are characteristic of the conditions considered in the design of the prototype structures. Nevertheless, it should be stated that the findings and conclusions are conditioned on the ability of the SAC ground motions to suitably represent site soil conditions, site seismicity, and seismic demand level. More information on the ground motion records used in this dissertation can be found in Farrow and Kurama (2001).

14.2 Design-Level Ground Motion Records

The acceleration time-histories and the 5%-damped linear-elastic pseudo-acceleration response spectra of the SAC design-level LA01-LA20 ground motions are shown in Figs. 14.1 and 14.2, respectively. The dashed lines in Fig. 14.2 show the mean acceleration spectra of the 20 ground motions in the ensemble and the thick solid lines show the design-level spectrum used in the design of the prototype structures (see Fig. 12.2), respectively.

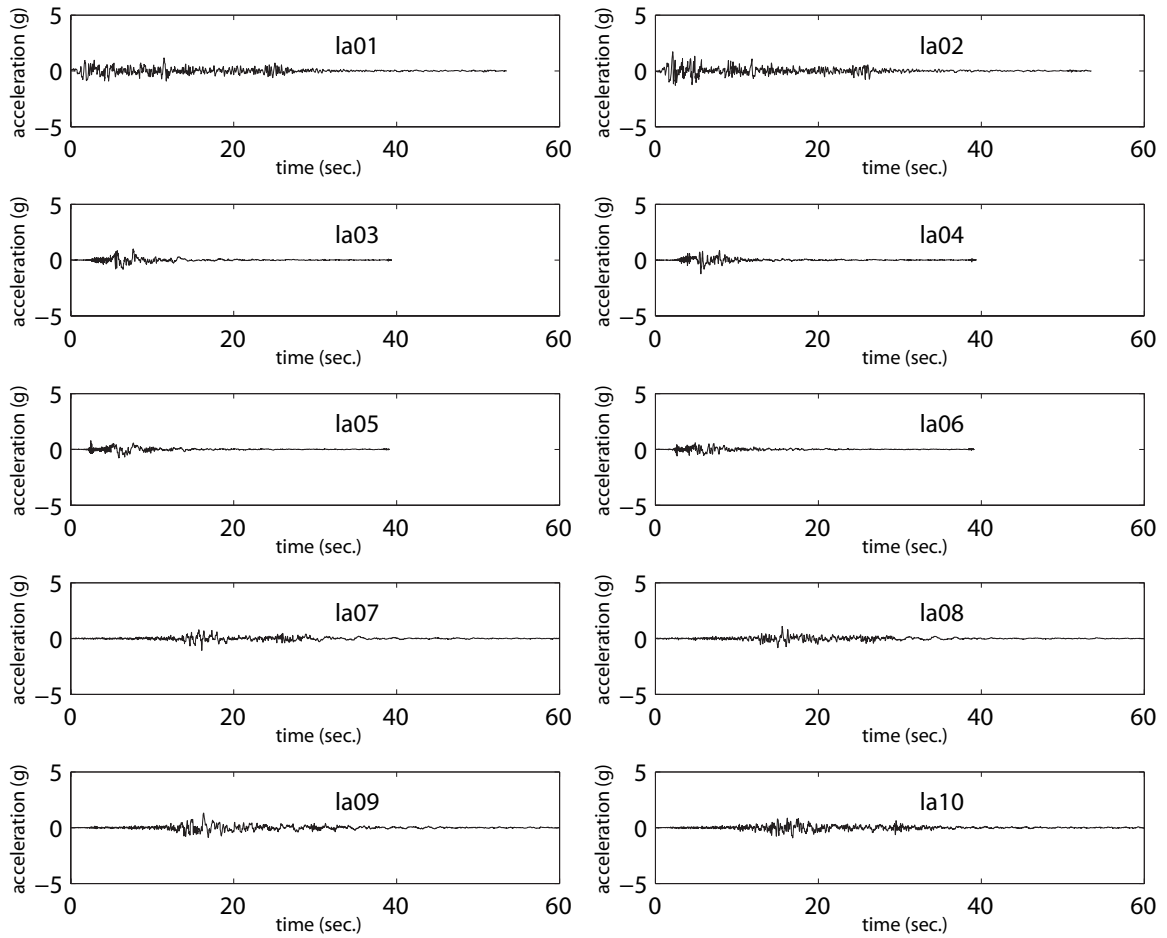


Fig. 14.1a Acceleration time-histories of the SAC design-level ground motions (LA01-LA10)

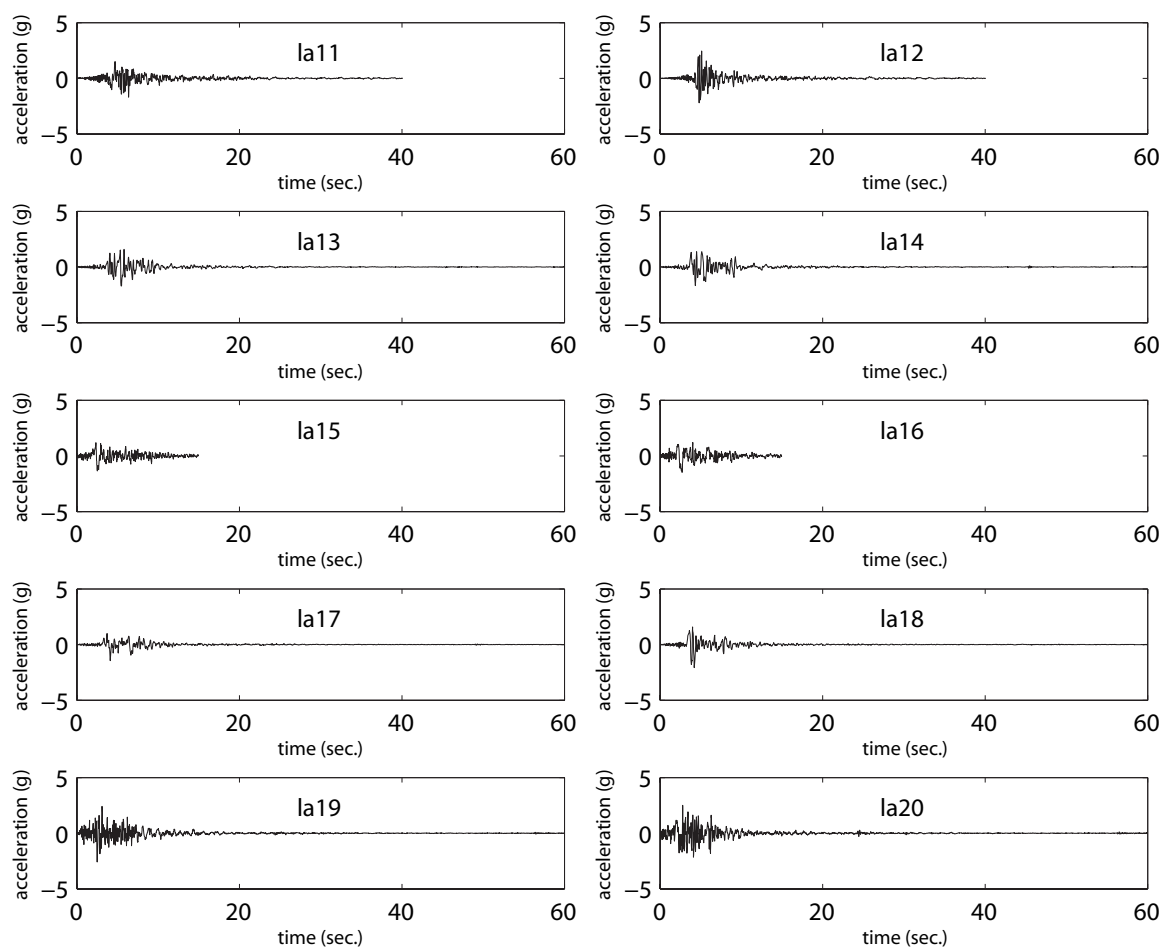


Fig. 14.1b Acceleration time-histories of the SAC design-level ground motions (LA11-LA20)

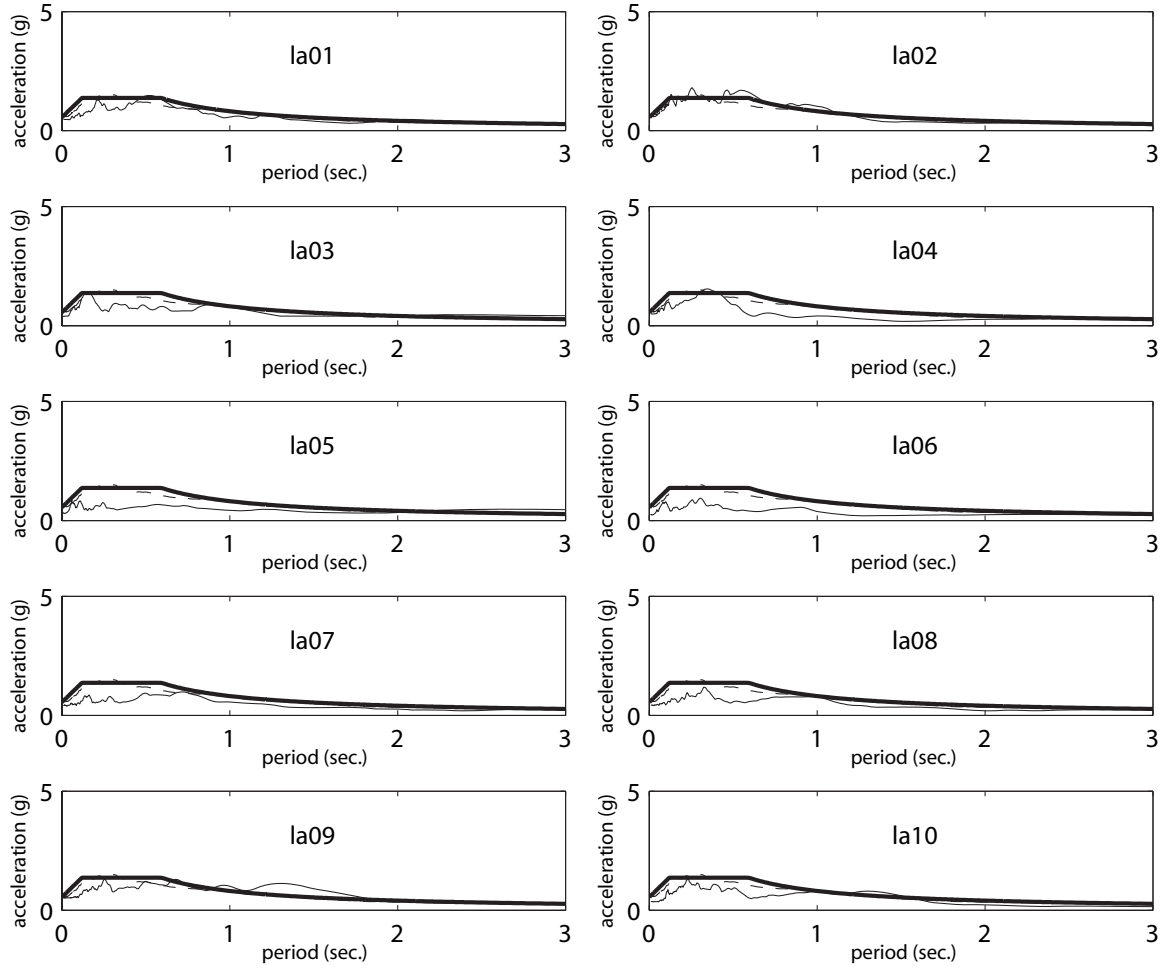


Fig. 14.2a 5%-damped linear-elastic pseudo-acceleration response spectra of the SAC design-level ground motions (LA01-LA10)

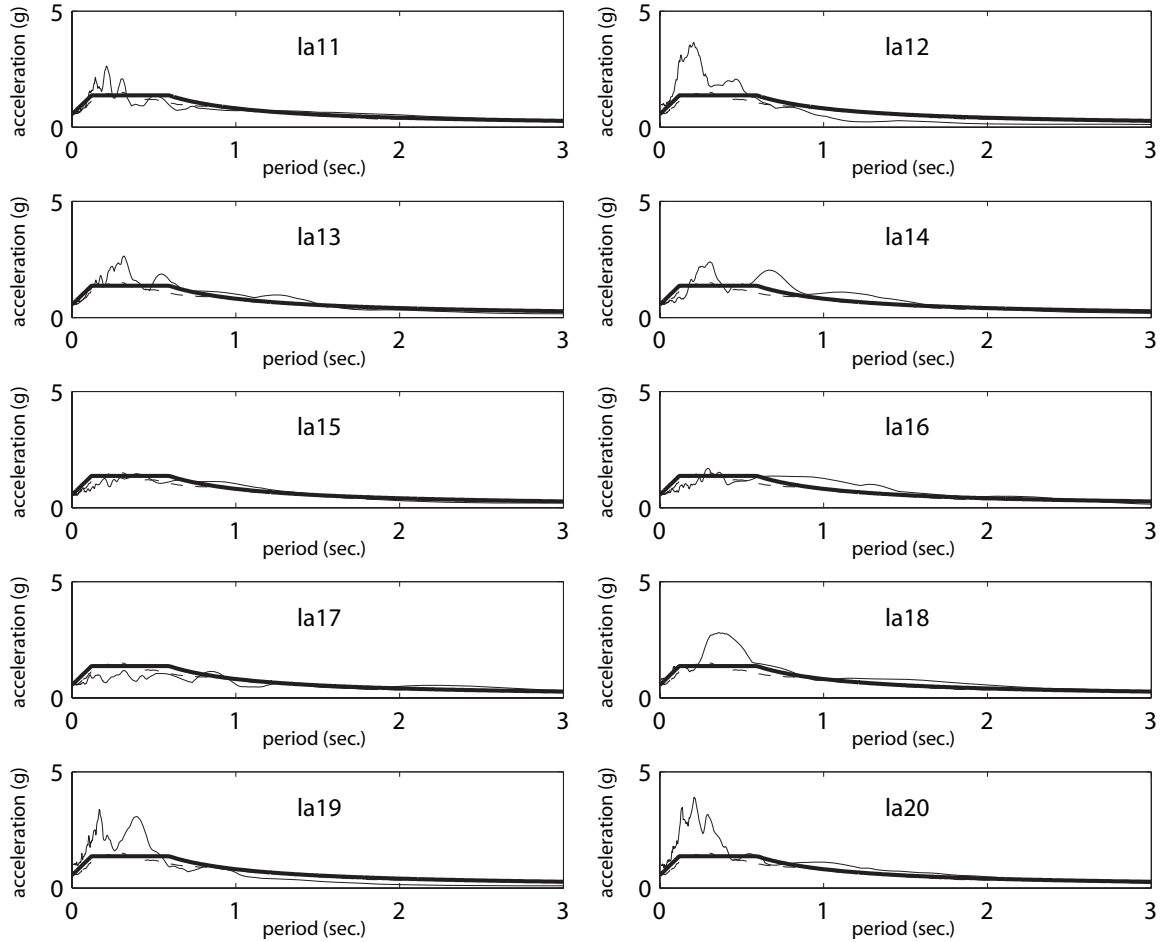


Fig. 14.2b 5%-damped linear-elastic pseudo-acceleration response spectra of the SAC design-level ground motions (LA11-LA20)

Table 14.1 provides the following information on the SAC LA01-LA20 ground motion records: (1) record site location; (2) earthquake magnitude; (3) epicentral distance; (4) SAC scale factor; (5) peak ground acceleration, PGA; and (6) maximum incremental velocity, MIV. The MIV of a ground motion is equal to the maximum area under the acceleration time-history of the record between two successive zero-acceleration crossings. Previous research has shown that a strong correlation exists between the MIV and the severity of a ground motion (Farrow and Kurama 2001; Kurama and Farrow 2003).

TABLE 14.1

SAC DESIGN-LEVEL GROUND MOTION RECORDS LA01-LA20

Record Name	Site Location	EQ Magnitude	Distance (km)	Scale Factor	PGA (cm/sec²)	MIV (cm/sec.)
LA01	Imperial Valley, 1940, El Centro	6.9	10	2.01	452	88.9
LA02	Imperial Valley, 1940, El Centro	6.9	10	2.01	663	81.0
LA03	Imperial Valley, 1979, Array #05	6.5	4.1	1.01	386	103
LA04	Imperial Valley, 1979, Array #05	6.5	4.1	1.01	479	74.6
LA05	Imperial Valley, 1979, Array #06	6.5	1.2	0.84	296	106
LA06	Imperial Valley, 1979, Array #06	6.5	1.2	0.84	230	81.6
LA07	Landers, 1992, Barstow	7.3	36	3.20	413	59.1
LA08	Landers, 1992, Barstow	7.3	36	3.20	417	71.5
LA09	Landers, 1992, Yermo	7.3	25	2.17	510	135
LA10	Landers, 1992, Yermo	7.3	25	2.17	353	76.4
LA11	Loma Prieta, 1989, Gilroy	7.0	12	1.79	652	79.4
LA12	Loma Prieta, 1989, Gilroy	7.0	12	1.79	951	86.8
LA13	Northridge, 1994, Newhall	6.7	6.7	1.03	665	84.6
LA14	Northridge, 1994, Newhall	6.7	6.7	1.03	645	132
LA15	Northridge, 1994, Rinaldi RS	6.7	7.5	0.79	523	124
LA16	Northridge, 1994, Rinaldi RS	6.7	7.5	0.79	569	165
LA17	Northridge, 1994, Sylmar	6.7	6.4	0.99	558	102
LA18	Northridge, 1994, Sylmar	6.7	6.4	0.99	801	139
LA19	North Palm Springs, 1986	6.0	6.7	2.97	999	48.6
LA20	North Palm Springs, 1986	6.0	6.7	2.97	968	122

14.3 Survival-Level Ground Motion Records

The acceleration time-histories and the 5%-damped linear-elastic pseudo-acceleration response spectra of the SAC survival-level LA21-LA40 ground motions are shown in Figs. 14.3 and 14.4, respectively. The dashed lines in Fig. 14.4 show the mean acceleration spectra of the 20 ground motions in the ensemble and the thick solid lines show the survival-level spectrum used in the design of the prototype structures (see Fig. 12.2), respectively.

Table 14.2 provides further information on the SAC LA21-LA40 ground motion records similar to Table 14.1 above for the design-level records.

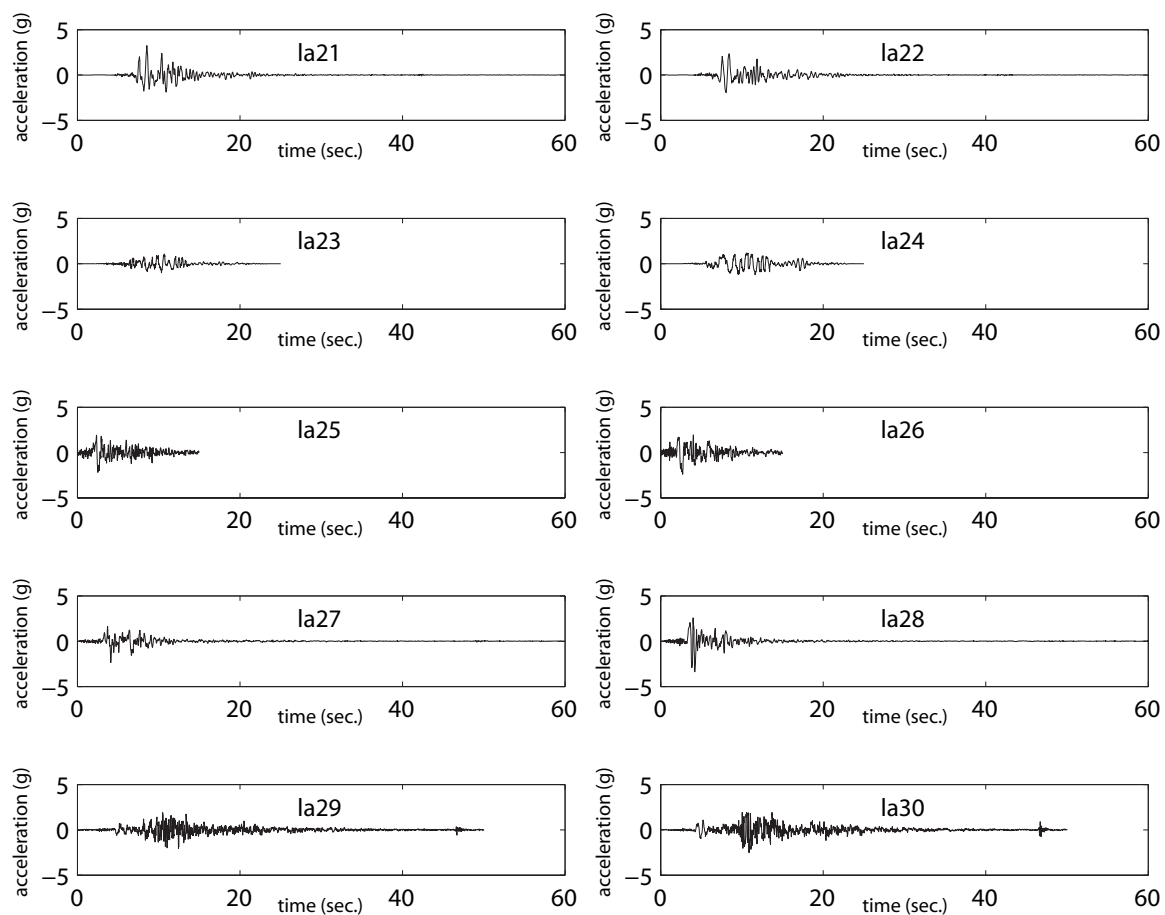


Fig. 14.3a Acceleration time-histories of the SAC survival-level ground motions (LA21-LA30)

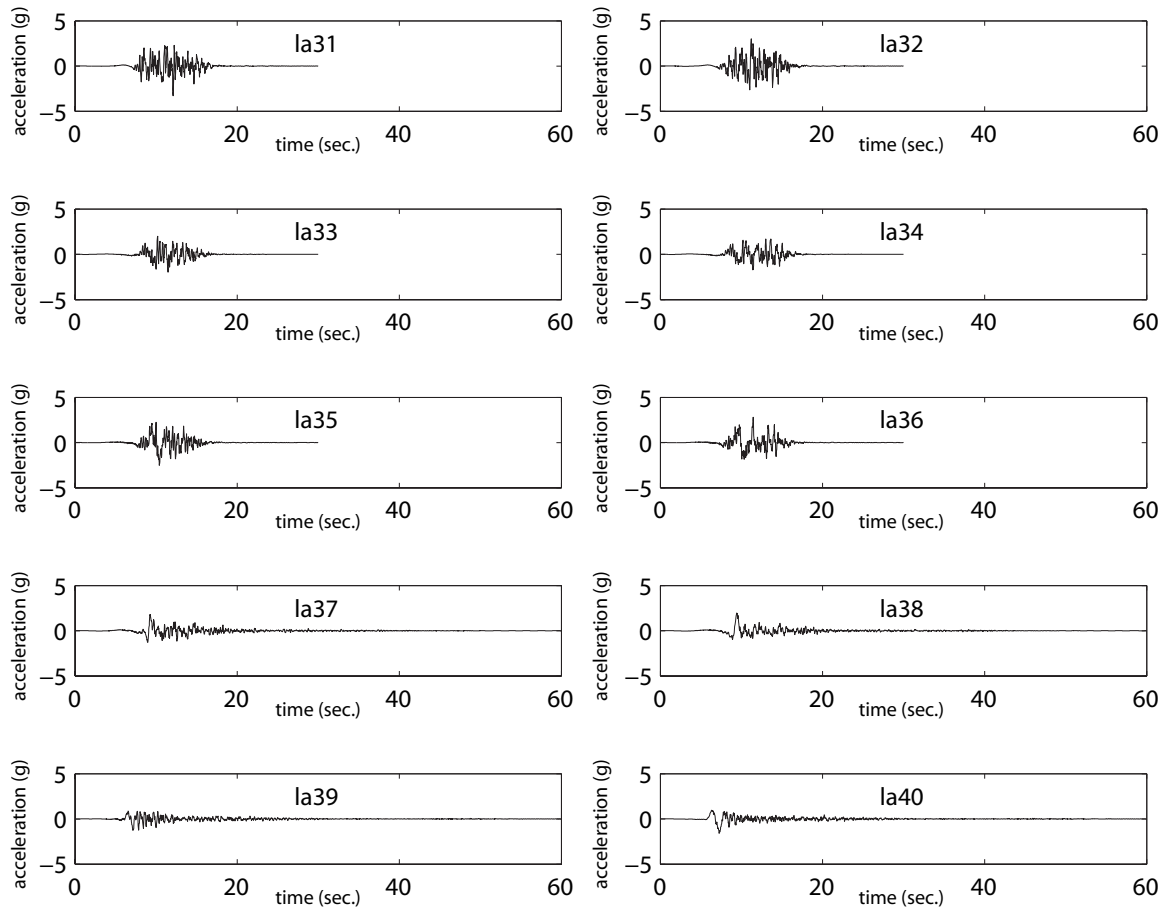


Fig. 14.3b Acceleration time-histories of the SAC survival-level ground motions (LA31-LA40)

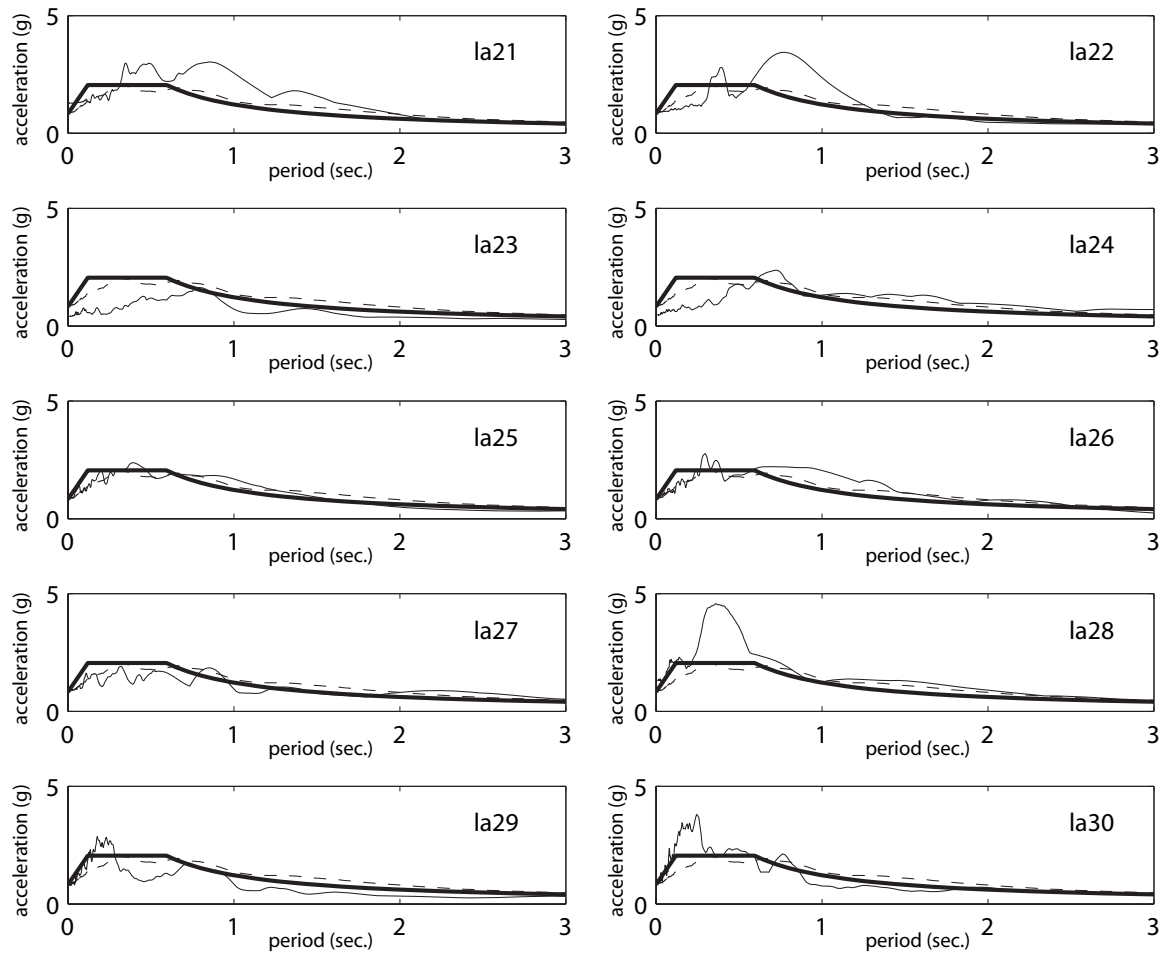


Fig. 14.4a 5%-damped linear-elastic pseudo-acceleration response spectra of the SAC survival-level ground motions (LA21-LA30)

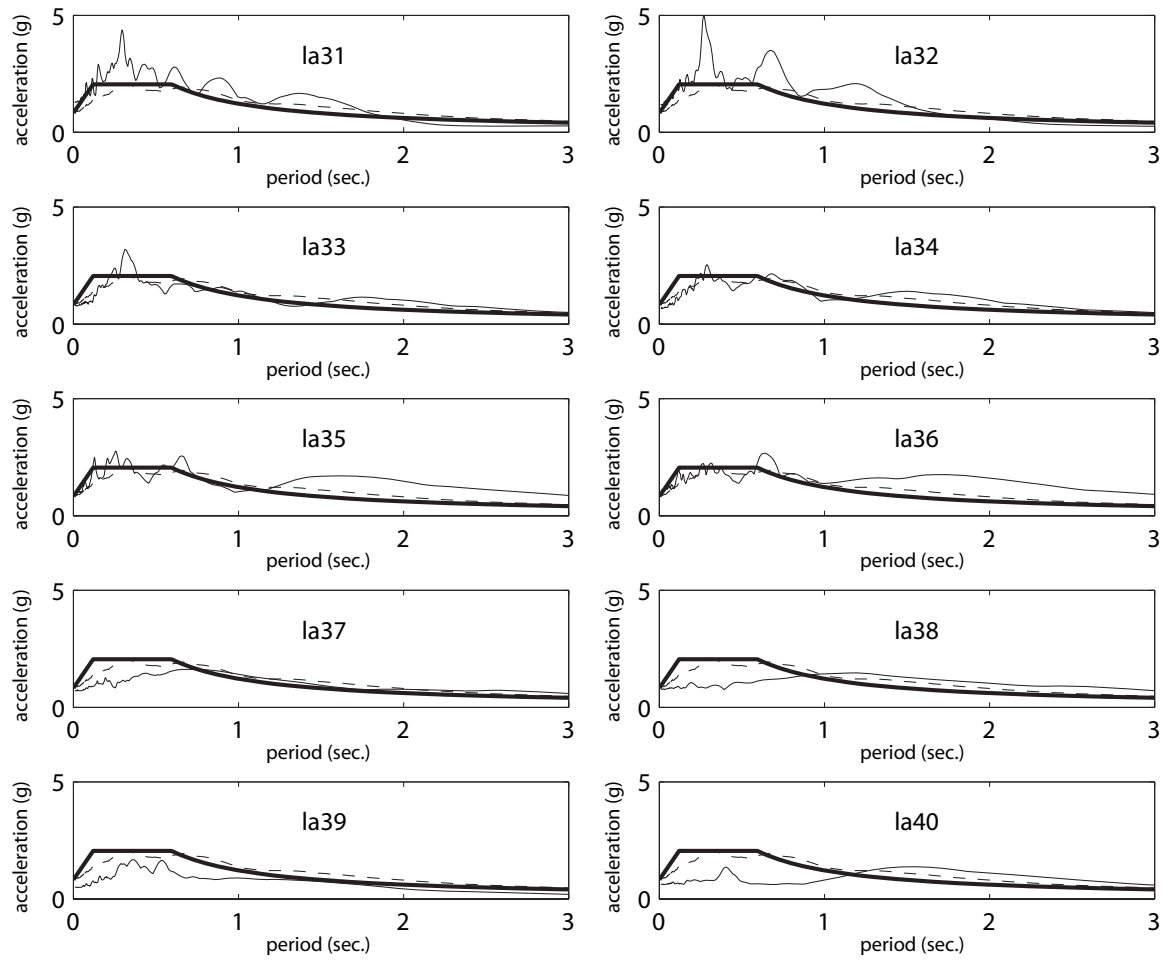


Fig. 14.4b 5%-damped linear-elastic pseudo-acceleration response spectra of the SAC survival-level ground motions (LA31-LA40)

TABLE 14.2

SAC SURVIVAL-LEVEL GROUND MOTION RECORDS LA21-LA40

Record Name	Site Location	EQ Magnitude	Distance (km)	Scale Factor	PGA (cm/sec²)	MIV (cm/sec.)
LA21	Kobe, 1995	6.9	3.4	1.15	1258	274
LA22	Kobe, 1995	6.9	3.4	1.15	903	242
LA23	Loma Prieta, 1989	7.0	3.5	0.82	410	86.9
LA24	Loma Prieta, 1989	7.0	3.5	0.82	464	211
LA25	Northridge, 1994	6.7	7.5	1.29	852	202
LA26	Northridge, 1994	6.7	7.5	1.29	925	269
LA27	Northridge, 1994	6.7	6.4	1.61	909	166
LA28	Northridge, 1994	6.7	6.4	1.61	1304	226
LA29	Tabas, 1974	7.4	1.2	1.08	793	92.2
LA30	Tabas, 1974	7.4	1.2	1.08	973	128
LA31	Elysian Park (simulated)	7.1	17	1.43	1271	208
LA32	Elysian Park (simulated)	7.1	17	1.43	1164	260
LA33	Elysian Park (simulated)	7.1	11	0.97	767	188
LA34	Elysian Park (simulated)	7.1	11	0.97	668	161
LA35	Elysian Park (simulated)	7.1	11	1.10	973	343
LA36	Elysian Park (simulated)	7.1	11	1.10	1079	329
LA37	Palos Verdes (simulated)	7.1	1.5	0.90	698	263
LA38	Palos Verdes (simulated)	7.1	1.5	0.90	761	302
LA39	Palos Verdes (simulated)	7.1	1.5	0.88	491	117
LA40	Palos Verdes (simulated)	7.1	1.5	0.88	613	279

CHAPTER 15

BEHAVIOR OF PROTOTYPE STRUCTURES UNDER EARTHQUAKE LOADING

This chapter investigates the response of prototype Structures P1-CWUPT and P2-PWUPT from Chapter 12 under earthquake loading. A series of nonlinear dynamic time-history analyses of the structures are conducted using the twenty survival-level and twenty design-level ground motion records from Chapter 14. Evaluations of the global behavior of the structures as well as the local behavior of the wall piers and the coupling beams are provided. The effect of coupling is investigated by comparing the dynamic analysis results for the prototype coupled wall systems with results obtained from dynamic analyses of uncoupled concrete wall piers.

The chapter is divided into the following sections: (1) analytical model for dynamic analyses; (2) Structure P1-CWUPT; (3) Structure P2-PWUPT; and (4) uncoupled concrete wall systems.

15.1 Analytical Model for Dynamic analyses

The dynamic analyses of the prototype structures are conducted using the fiber element model from Chapter 13 with the DRAIN-2DX Program (Prakash et al. 1993) as the analytical platform. The modeling of the building mass and viscous damping, as well as the time step used in the dynamic analyses are described below.

15.1.1 Building Mass

The total building mass is calculated as the seismic weight, W from Chapter 12 divided by the acceleration due to gravity, g . Similar to the assumptions used in the design of the prototype structures, the total building mass is assumed to be distributed equally between the four coupled wall systems in the E-W direction and the mass assigned to each coupled wall system is assumed to be distributed equally between the two concrete wall piers.

In the analytical model of a coupled wall system, the mass assigned to each wall pier is distributed to the floor and roof levels based on the distribution of the seismic weight over the height of the structure in Chapter 12. The wall pier floor and roof masses are lumped at the horizontal degrees-of-freedom of the fiber element nodes at these levels.

15.1.2 Viscous Damping

The “inherent” structural damping is modeled using a viscous damping matrix, $[C]$ that is proportional to the lumped mass matrix, $[M]$ and the structure stiffness matrix, $[K]$ as (Prakash et al. 1993):

$$[C] = \alpha_d[M] + \beta_d[K] \quad (15.1)$$

This form of damping is called “Rayleigh damping” as described in detail in standard textbooks on structural dynamics (e.g., Clough and Penzien 1993, Chopra 1995). The component of $[C]$ proportional to $[M]$ (i.e., mass proportional damping) introduces dashpots at each degree-of-freedom with mass. These dashpots have damping coefficients given by $\alpha_d[M]$. The component of $[C]$ proportional to $[K]$ (i.e., stiffness proportional damping) introduces dashpots parallel to the structural elements, with

damping coefficients given by β_d [K]. In the DRAIN-2DX Program, the stiffness proportional damping is based on the initial linear-elastic stiffness of the structural elements and remains constant during a nonlinear analysis. Since the mass proportional damping also remains constant, the damping matrix [C] remains constant during an analysis.

The Rayleigh damping factors, α_d and β_d , are determined using assumed damping ratios ξ_m and ξ_n (as a percentage of critical damping) for two selected modes of vibration (with periods T_m and T_n). Because detailed information about the variation of the damping ratio with period is not available, it is assumed that the damping ratios for the two modes are the same (i.e., $\xi_m = \xi_n = \xi$). In this case, the Rayleigh damping factors are given by:

$$\begin{Bmatrix} \alpha_d \\ \beta_d \end{Bmatrix} = \frac{\xi}{\pi(T_m + T_n)} \begin{Bmatrix} 4\pi^2 \\ T_m T_n \end{Bmatrix} \quad (15.2)$$

Usually, T_m is taken as the first mode period and T_n is the period of one of the higher modes of vibration that is assumed to contribute significantly to the dynamic response of the structure. The dynamic analyses of the prototype structures were conducted using a damping ratio of $\xi=3\%$ for the first and third linear-elastic modes of vibration. The assumed damping ratio of 3% is considered to be a conservative lower-bound value (to result in higher seismic demands from the dynamic analyses) for the type of structures investigated in this dissertation.

Periods and the resulting damping ratios for the first eight linear-elastic vibration modes of Structures P1-CWUPT and P2-PWUPT are given in Table 15.1. Equation (15.2) ensures that the assumed damping ratio of $\xi=3\%$ is achieved for the first and third modes.

The second mode has a damping ratio smaller than 3%, while modes higher than the third mode have damping ratios larger than 3% increasing monotonically with decreasing period. Table 15.1 shows that even though a damping ratio of 3% is specified only for the first and third modes, the resulting damping ratios for the second and fourth modes are reasonable.

TABLE 15.1
PERIOD AND DAMPING RATIOS FOR THE FIRST EIGHT MODES OF THE
PROTOTYPE STRUCTURES

		1 st mode	2 nd mode	3 rd mode	4 th mode	5 th mode	6 th mode	7 th mode	8 th mode
Structure P1-CWUPT	Period, T (sec.)	0.59	0.14	0.060	0.036	0.030	0.029	0.027	0.026
	Damping ratio, ξ (%)	3.0	1.8	3.0	4.5	5.4	5.6	6.0	6.2
Structure P2-PWUPT	Period, T (sec.)	0.61	0.15	0.066	0.040	0.030	0.029	0.028	0.027
	Damping ratio, ξ (%)	3.0	1.9	3.0	4.9	6.3	6.6	6.8	6.9

15.1.3 Time Step

The accuracy of nonlinear dynamic time-history analysis depends on the time step used in the numerical time-marching algorithm. For a single-degree-of-freedom system, Clough and Penzien (1993) recommend a time step shorter than or equal to one-tenth the linear elastic period of vibration. For the dynamic analyses of the prototype structures, a constant time step of 0.01 sec. was used. This time step is shorter than one-tenth the period of the first two modes of the structures (see Table 15.1). Previous analyses (Kurama et al. 1997) of uncoupled concrete structural walls with similar period ranges show that the differences between results from dynamic analyses conducted using a time

step of 0.001 sec. and 0.01 sec. are not significant. Thus, the time step of 0.01 sec. is considered to be adequate to capture the dynamic characteristics of the structures in this dissertation.

15.2 Structure P1-CWUPT

This section discusses the results from the nonlinear dynamic time-history analyses of Structure P1-CWUPT as follows: (1) floor/roof drifts; (2) inter-story drifts; (3) floor/roof accelerations; (4) wall base axial forces; (5) wall base shear forces; (6) wall base diagonal tension and shear slip failure; (7) wall base moments; (8) wall base strains; (9) coupling beam chord rotations; (10) coupling beam axial forces; (11) coupling beam post-tensioning forces; (12) coupling beam shear forces; (13) coupling beam shear slip failure; and (14) angle deformations.

15.2.1 Floor/Roof Drifts

The peak coupled wall roof drift demands from the dynamic analyses of Structure P1-CWUPT under the twenty survival-level SAC ground motion records (LA21-LA40) and twenty design-level records (LA01-LA20) are listed in Tables 15.2 and 15.3, respectively. As described in Chapter 13, the roof drift, Δ is calculated as the average lateral displacement of the left and right wall piers at the roof divided by the wall height to the base, h_w .

TABLE 15.2
PEAK ROOF DRIFT DEMANDS FOR STRUCTURE P1-CWUPT
UNDER SURVIVAL LEVEL GROUND MOTIONS

ground motion	LA21	LA22	LA23 ^c	LA24	LA25 ^a	LA26	LA27	LA28	LA29	LA30	estimate (design)	standard deviation
peak roof drift (%)	1.91	1.39	0.69	1.45	1.79	2.49	1.43	1.79	0.76	0.98	1.67	0.82
ground motion	LA31	LA32	LA33	LA34	LA35 ^b	LA36	LA37	LA38	LA39	LA40	mean	standard deviation/mean
peak roof drift (%)	1.74	1.92	1.15	1.26	3.62	3.51	2.30	2.63	0.77	1.82	1.77	0.46

^a The peak demand under this ground motion is closest to the mean demand

^b The peak demand under this ground motion is the largest demand

^c The peak demand under this ground motion is the smallest demand

TABLE 15.3
PEAK ROOF DRIFT DEMANDS FOR STRUCTURE P1-CWUPT
UNDER DESIGN LEVEL GROUND MOTIONS

ground motion	LA01 ^a	LA02	LA03	LA04	LA05	LA06 ^c	LA07	LA08	LA09	LA10	estimate (design)	standard deviation
peak roof drift (%)	0.75	0.81	0.90	0.29	0.39	0.26	0.55	0.68	0.89	0.67	0.71	0.32
ground motion	LA11	LA12	LA13	LA14	LA15	LA16 ^b	LA17	LA18	LA19	LA20	mean	standard deviation/mean
peak roof drift (%)	0.58	0.53	1.09	1.18	0.89	1.50	0.70	0.88	0.63	1.21	0.77	0.41

^a The peak demand under this ground motion is closest to the mean demand

^b The peak demand under this ground motion is the largest demand

^c The peak demand under this ground motion is the smallest demand

The mean peak roof drift demands from the survival-level dynamic analyses in Table 15.2 is 1.77%, which is close to the estimated survival-level roof drift demand of $\Delta_s=1.67\%$ and the allowable target roof drift demand of $\Delta_{ts}=1.75\%$ from Chapter 12. As an example, Fig. 15.1 shows the roof drift time history of Structure P1-CWUPT under the

LA25 ground motion, for which the peak roof drift demand is closest to the mean demand from the twenty records (see Table 15.2). The dashed horizontal lines indicate the design estimate for the peak roof drift demand, Δ_s from Chapter 12. It is observed that the oscillations of the structure are generally centered around the original zero-drift position demonstrating a large self-centering capability.

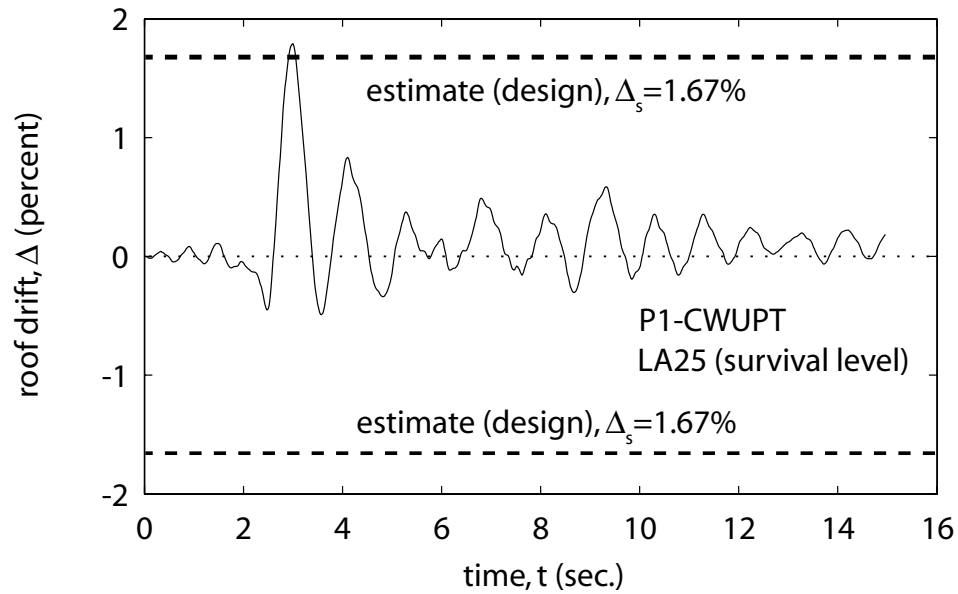


Fig. 15.1 Roof drift time history for Structure P1-CWUPT

The mean peak roof drift demand from the design-level analyses in Table 15.3 is 0.77%, which is close to the estimated design-level roof drift demand of $\Delta_d=0.71\%$ and smaller than the allowable target roof drift demand of $\Delta_{td}=1.17\%$ from Chapter 12. It is concluded that the displacement-based design objectives under the survival-level and design-level ground motions are, on average, satisfied.

Fig. 15.2 plots the peak coupled wall roof drift demands from Tables 15.2 and 15.3 (□ markers) against the maximum incremental velocity (MIV) of the ground motion

records (see Tables 14.2 and 14.1 for the MIV values of the LA21-LA40 and the LA01-LA20 records, respectively), where the dashed and solid horizontal lines represent the design estimate (from Chapter 12) and the mean peak roof drift demand, respectively, for each data set. It is observed that the peak roof drift demands tend to be larger under ground motions with larger MIV (i.e., there seems to be a correlation between MIV and the peak roof drift demand, especially for the survival-level records). Furthermore, there is a significant amount of scatter in the data indicating that, while the design objectives are satisfied on average, the peak roof drift demand may be significantly larger or significantly smaller than the design estimate, depending on the earthquake. This is investigated in more detail in Kurama and Farrow (2003).

15.2.2 Inter-Story Drifts

The peak coupled wall inter-story drift demands from the dynamic analyses of Structure P1-CWUPT under the twenty survival-level SAC ground motion records (LA21-LA40) and twenty design-level records (LA01-LA20) are listed in Tables 15.4 and 15.5, respectively. The inter-story drift is defined as the relative lateral displacement between two adjacent floor/roof levels in a structure divided by the story height and is calculated as the average inter-story drift of the left and right wall piers.

The mean peak inter-story drift demand from the twenty survival-level analyses in Table 15.4 is 2.05%, which is close to the estimated survival-level inter-story drift demand of 1.92% (occurring in the eighth story) from Chapter 12. As an example, Fig. 15.3 shows the inter-story drift time histories of Structure P1-CWUPT under the LA40

TABLE 15.4

PEAK INTER-STORY DRIFT DEMANDS FOR STRUCTURE P1-CWUPT
UNDER SURVIVAL LEVEL GROUND MOTIONS

ground motion	LA21	LA22	LA23 ^c	LA24	LA25	LA26	LA27	LA28	LA29	LA30	estimate (design)	standard deviation
peak inter-story drift (%)	2.25	1.64	0.85	1.67	2.08	2.85	1.64	2.06	0.93	1.24	1.92	0.90
ground motion	LA31	LA32	LA33	LA34	LA35 ^b	LA36	LA37	LA38	LA39	LA40 ^a	mean	standard deviation/mean
peak inter-story drift (%)	2.19	2.28	1.38	1.50	4.00	3.92	2.60	2.93	0.93	2.05	2.05	0.44

^a The peak demand under this ground motion is closest to the mean demand

^b The peak demand under this ground motion is the largest demand

^c The peak demand under this ground motion is the smallest demand

TABLE 15.5

PEAK INTER-STORY DRIFT DEMANDS FOR STRUCTURE P1-CWUPT
UNDER DESIGN LEVEL GROUND MOTIONS

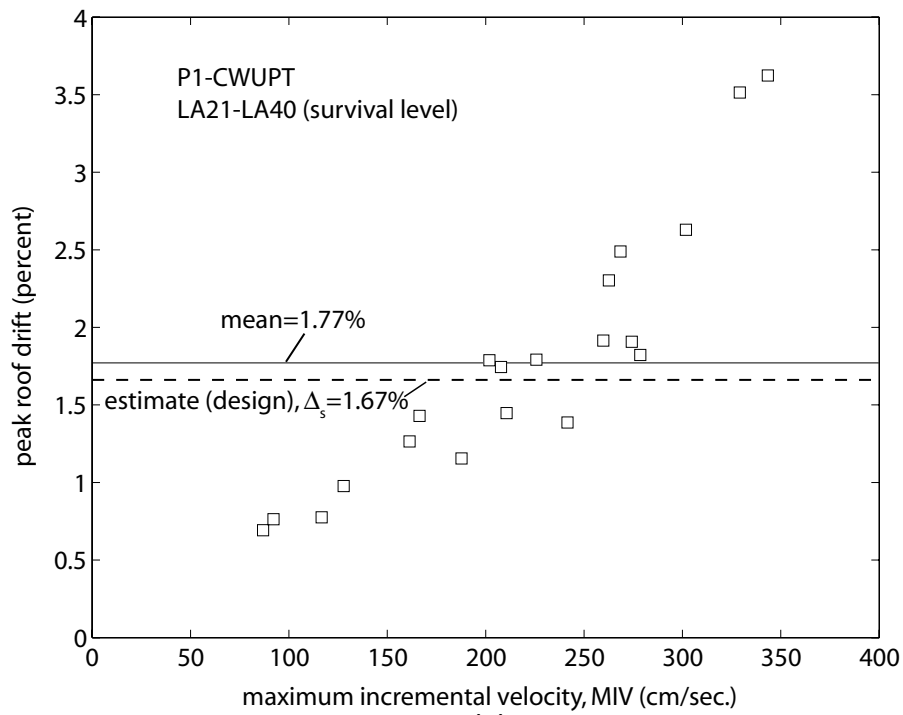
ground motion	LA01	LA02 ^a	LA03	LA04	LA05	LA06 ^c	LA07	LA08	LA09	LA10	estimate (design)	standard deviation
peak inter-story drift (%)	0.87	0.96	1.07	0.35	0.46	0.33	0.73	0.86	1.06	0.80	0.81	0.36
ground motion	LA11	LA12	LA13	LA14	LA15	LA16 ^b	LA17	LA18	LA19	LA20	mean	standard deviation/mean
peak inter-story drift (%)	0.73	0.82	1.35	1.40	1.02	1.73	0.84	1.04	0.81	1.50	0.94	0.39

^a The peak demand under this ground motion is closest to the mean demand

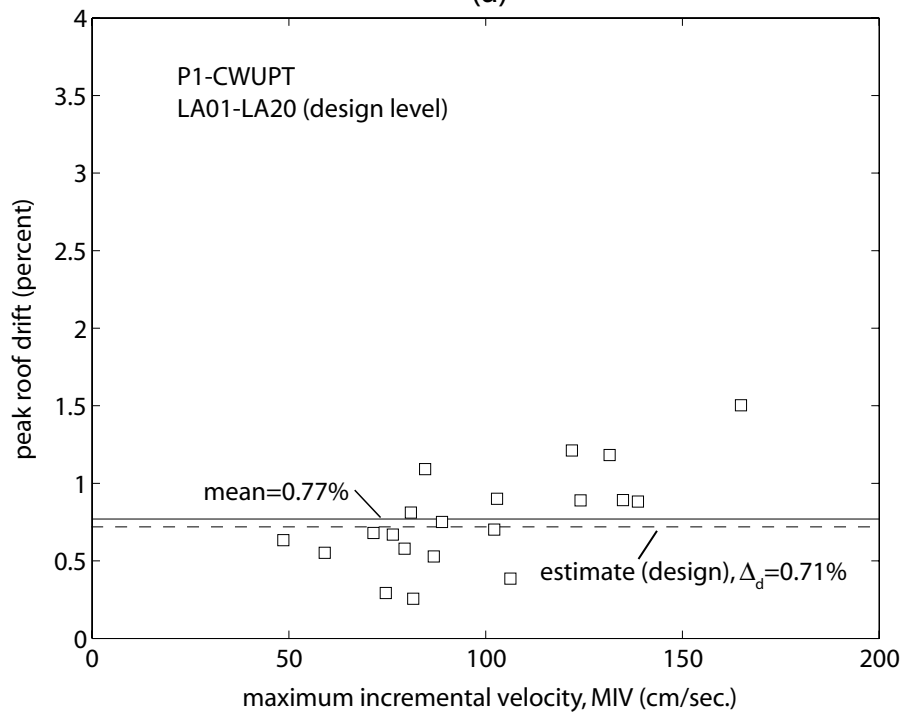
^b The peak demand under this ground motion is the largest demand

^c The peak demand under this ground motion is the smallest demand

ground motion, for which the peak inter-story drift demand is closest to the mean demand from the twenty records (see Table 15.4). It is observed that the drifts of all eight stories are in phase, and thus, the deflected shape of the structure is governed by the first vibration mode. As expected, the peak inter-story drift demand (2.05%) occurs in the



(a)



(b)

Fig. 15.2 Peak roof drift demands for Structure P1-CWUPT:
(a) survival level; (b) design level

eighth (top) story (indicating a flexure dominated deflected shape) and is larger than the corresponding peak roof drift demand of 1.82% from Table 15.2. The dashed horizontal lines show the design estimate for the peak inter-story drift demand in the eighth story from Chapter 12.

The mean peak inter-story drift demand from the twenty design-level analyses in Table 15.5 is 0.94%, which is close to the estimated design-level inter-story drift demand of 0.81% from Chapter 12. As discussed in Chapter 12, according to IBC 2000 (ICC 2000), the peak inter-story drift demand under the design-level ground motion should not exceed 2%. Because of the relatively small allowable target roof drift demands used in design ($\Delta_{ts}=1.75\%$ and $\Delta_{td}=1.17\%$), the peak inter-story drift demands in Tables 15.4 and 15.5 satisfy the 2% limit not only for the design-level ground motions, but also for many of the survival-level motions.

Note that, for both ground motion sets, the ratio between the mean and estimated peak inter-story drift demands is similar to the ratio between the mean and estimated peak roof drift demands. In general, the trends observed for the peak roof drift demands in the previous section are also valid for the peak inter-story drift demands.

Fig. 15.4 plots the peak coupled wall inter-story drift demands from Tables 15.4 and 15.5 (\square markers) against the maximum incremental velocity (MIV) of the ground motion records (see Tables 14.2 and 14.1), where the dashed and solid horizontal lines represent the design estimate (for the eighth story, from Chapter 12) and the mean peak inter-story drift demand, respectively, for each data set. Similar to the peak roof drift demands discussed in the previous section, there is a significant amount of scatter in the

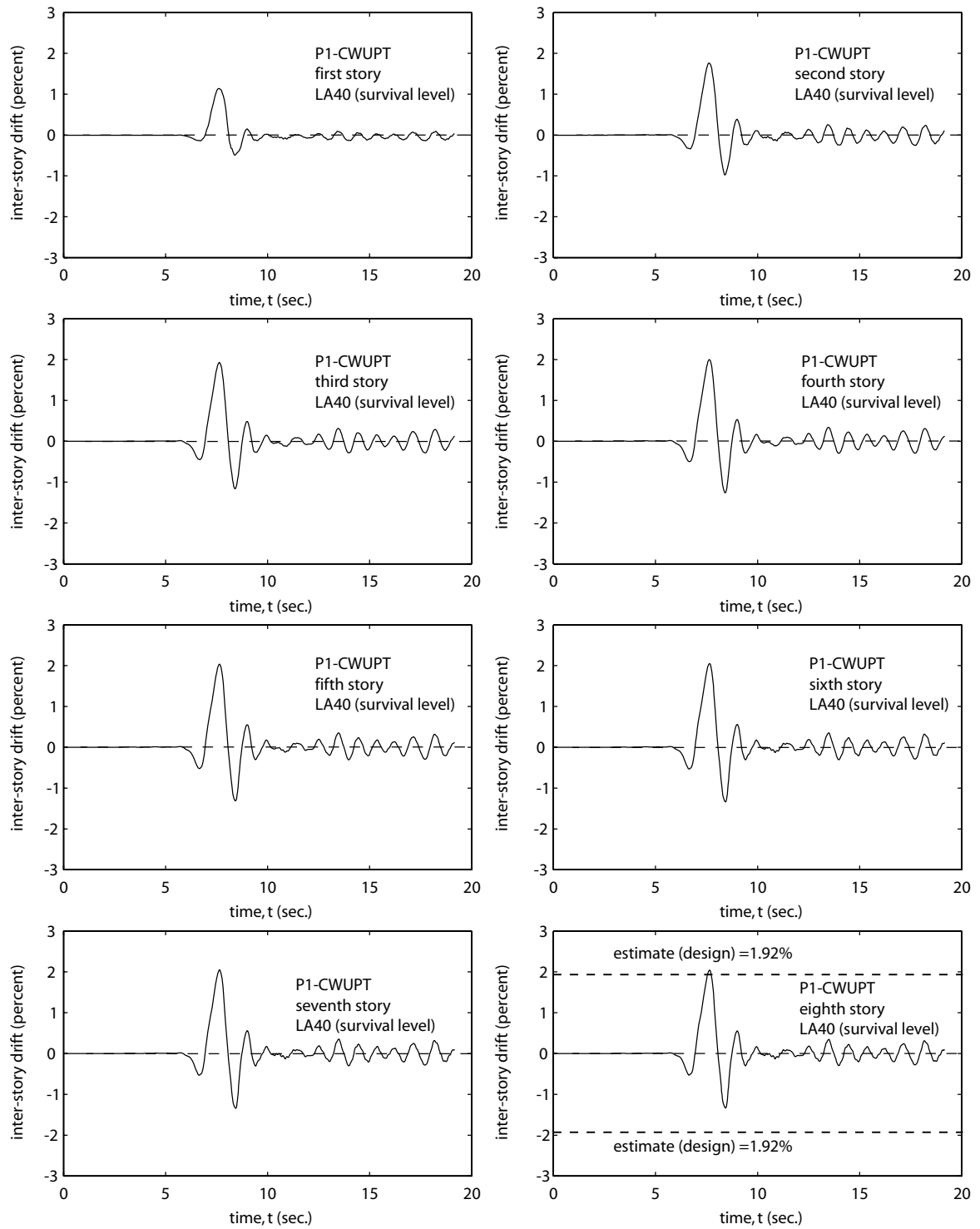


Fig. 15.3 Inter-story drift time histories for Structure P1-CWUPT

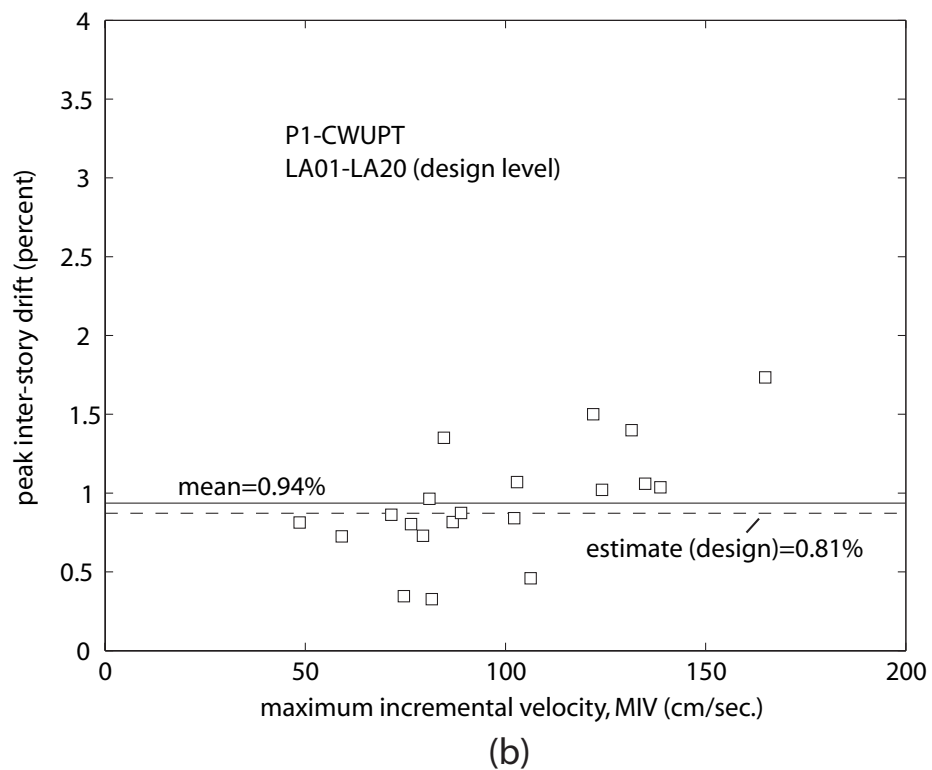
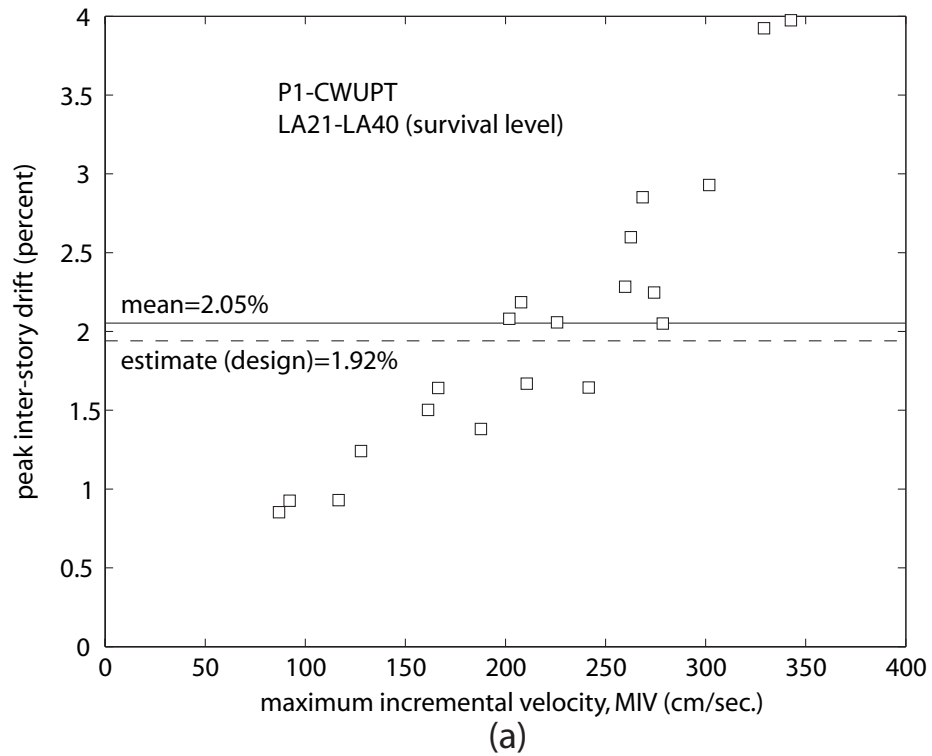


Fig. 15.4 Peak inter-story drift demands for Structure P1-CWUPT:
(a) survival level; (b) design level

peak inter-story drift demands, and the demands tend to be larger under the ground motions with larger MIV (i.e., there seems to be a correlation between MIV and the peak inter-story drift demand, especially for the survival level records).

15.2.3 Floor/Roof Accelerations

The peak absolute floor/roof acceleration demands from the dynamic analyses of Structure P1-CWUPT under the twenty survival-level SAC ground motion records (LA21-LA40) and twenty design-level records (LA01-LA20) are listed in Tables 15.6 and 15.7, respectively. The accelerations are calculated as the average total absolute lumped mass accelerations (i.e., relative accelerations with respect to the ground plus the ground acceleration) at the floor/roof levels of the left and right wall piers.

TABLE 15.6

PEAK FLOOR/ROOF ACCELERATION DEMANDS FOR STRUCTURE P1-CWUPT
UNDER SURVIVAL LEVEL GROUND MOTIONS

ground motion	LA21	LA22	LA23	LA24	LA25	LA26	LA27	LA28	LA29 ^b	LA30	standard deviation	
peak floor/roof acceleration (g)	1.76	1.53	1.03	1.26	1.59	1.44	1.17	1.70	2.65	2.52	0.51	
ground motion	LA31	LA32	LA33	LA34	LA35	LA36 ^a	LA37	LA38 ^c	LA39	LA40	mean	standard deviation/mean
peak floor/roof acceleration (g)	2.48	2.01	1.43	1.25	1.98	1.59	1.16	0.92	1.34	1.00	1.59	0.32

^a The peak demand under this ground motion is closest to the mean demand

^b The peak demand under this ground motion is the largest demand

^c The peak demand under this ground motion is the smallest demand

TABLE 15.7

PEAK FLOOR/ROOF ACCELERATION DEMANDS FOR STRUCTURE P1-CWUPT
UNDER DESIGN LEVEL GROUND MOTIONS

ground motion	LA01	LA02	LA03	LA04	LA05	LA06 ^c	LA07	LA08	LA09	LA10	standard deviation	
peak floor/roof acceleration (g)	1.13	1.76	1.27	0.87	0.74	0.71	1.07	1.04	1.17	0.98	0.57	
Ground motion	LA11	LA12	LA13	LA14 ^a	LA15	LA16	LA17	LA18	LA19	LA20 ^b	mean	standard deviation/mean
peak floor/roof acceleration (g)	1.45	2.26	1.52	1.33	1.22	1.08	1.14	1.16	2.41	2.94	1.36	0.42

^a The peak demand under this ground motion is closest to the mean demand

^b The peak demand under this ground motion is the largest demand

^c The peak demand under this ground motion is the smallest demand

As an example, Fig. 15.5 shows the floor/roof acceleration time histories of Structure P1-CWUPT under the survival-level LA36 ground motion, for which the peak acceleration demand (occurring at the third floor in this case) is closest to the mean demand from the twenty records (see Table 15.6). It is observed that the peak acceleration demand does not necessarily occur at the roof level.

Fig. 15.6 plots the peak floor/roof acceleration demands (\square markers) from Tables 15.6 and 15.7 against the maximum incremental velocity (MIV) of the ground motion records, as well as the peak ground accelerations (PGA, \bullet markers) of the records (see Tables 14.2 and 14.1). The solid horizontal lines represent the mean peak floor/roof acceleration demand and the mean peak ground acceleration for each data set. As expected, the peak floor/roof acceleration demands are larger than the peak ground accelerations. There is a significant amount of scatter in the peak floor/roof acceleration demands; however, unlike the peak roof drift and peak inter-story drift demands

discussed in the previous sections, no significant correlation exists between the peak floor/roof acceleration demand and the MIV. It is also interesting to note that the design-level LA20 ground motion record results in a larger peak floor/roof acceleration demand than all of the other records, including the survival-level records.

15.2.4 Wall Base Axial Forces

The peak tensile and compression wall pier base axial force demands from the dynamic analyses of Structure P1-CWUPT under the twenty survival-level SAC ground motion records (LA21-LA40) and twenty design-level records (LA01-LA20) are listed in Tables 15.8 through 15.11. The wall pier base axial forces are obtained directly from the fiber beam-column elements used for the wall piers in the analysis model, where a positive force indicates compression.

TABLE 15.8
PEAK WALL PIER BASE TENSILE AXIAL FORCE DEMANDS FOR
STRUCTURE P1-CWUPT UNDER SURVIVAL LEVEL GROUND MOTIONS

ground motion	LA21	LA22	LA23 ^c	LA24	LA25	LA26	LA27	LA28	LA29	LA30 ^b	estimate (idealized)	standard deviation
peak wall pier base tension force (kN)	-3811	-3840	-3427	-3681	-3893	-3723	-3829	-3844	-3550	-3924	-3372	-142
ground motion	LA31	LA32	LA33 ^a	LA34	LA35	LA36	LA37	LA38	LA39	LA40	mean	standard deviation/mean
peak wall pier base tension force (kN)	-3862	-3858	-3728	-3847	-3811	-3863	-3877	-3650	-3488	-3880	-3769	0.038

^a The peak demand under this ground motion is closest to the mean demand

^b The peak demand under this ground motion is the largest demand

^c The peak demand under this ground motion is the smallest demand

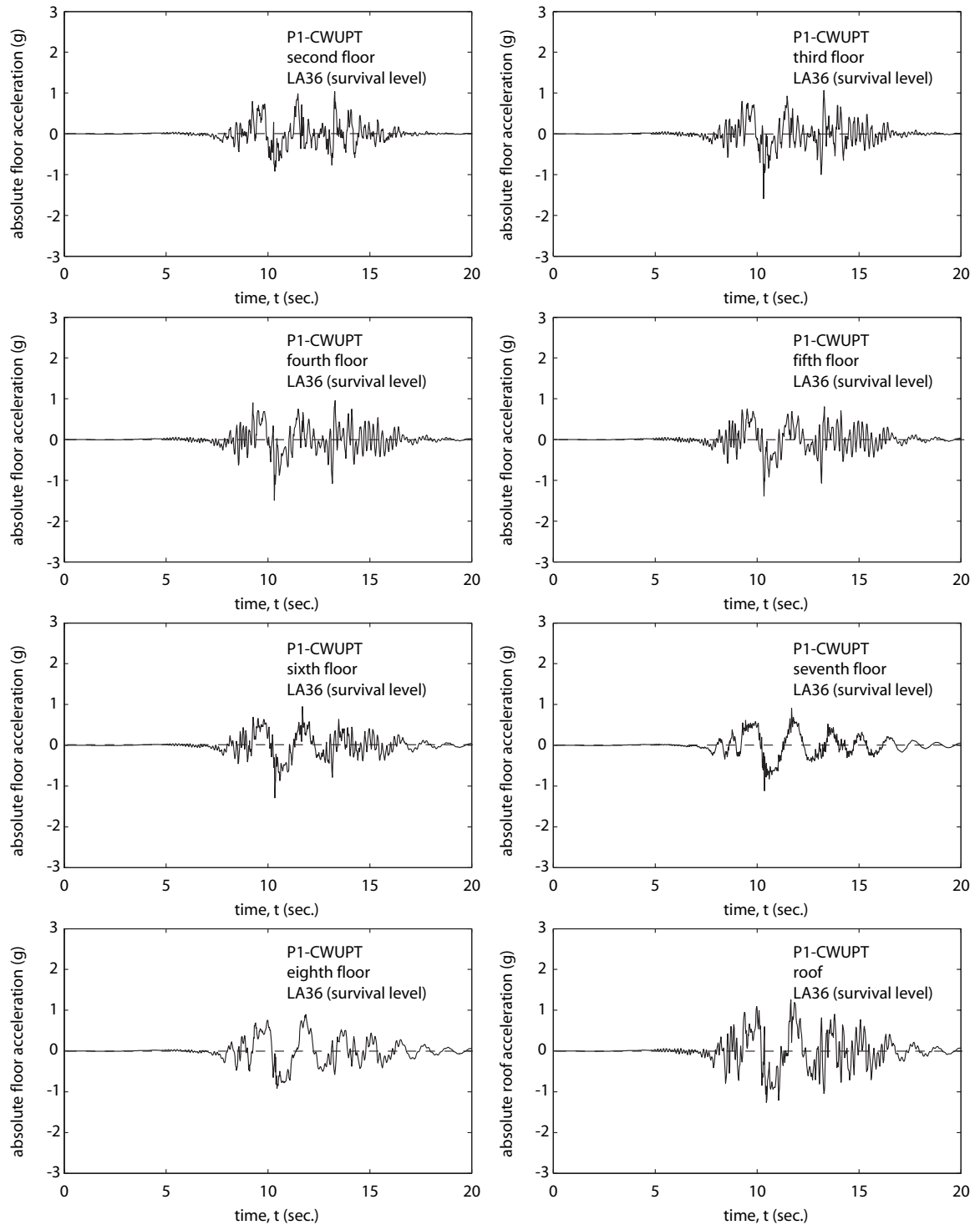
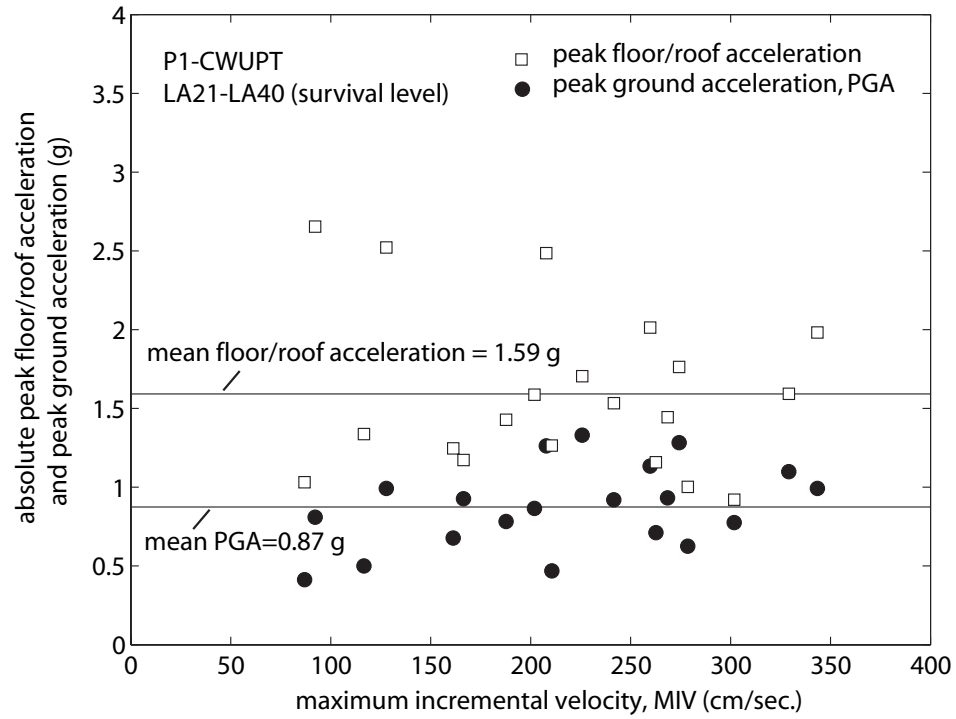
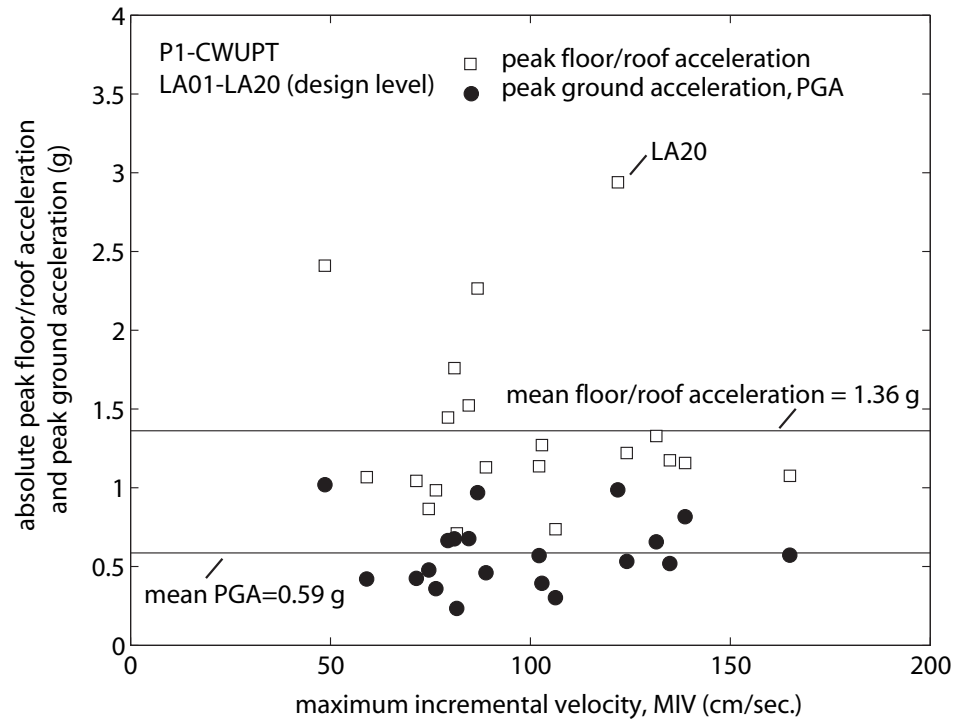


Fig. 15.5 Floor/roof acceleration time histories for Structure P1-CWUPT



(a)



(b)

Fig. 15.6 Peak floor/roof acceleration demands for Structure P1-CWUPT:
(a) survival level; (b) design level

TABLE 15.9

PEAK WALL PIER BASE TENSILE AXIAL FORCE DEMANDS FOR
STRUCTURE P1-CWUPT UNDER DESIGN LEVEL GROUND MOTIONS

ground motion	LA01	LA02	LA03	LA04	LA05	LA06 ^c	LA07	LA08	LA09	LA10	standard deviation	
peak wall pier base tension force (kN)	-3462	-3670	-3702	-2997	-2987	-2626	-3452	-3284	-3607	-3429	-349	
ground motion	LA11	LA12 ^a	LA13	LA14	LA15	LA16	LA17	LA18	LA19	LA20 ^b	mean	standard deviation/mean
peak wall pier base tension force (kN)	-3272	-3464	-3724	-3616	-3713	-3828	-3420	-3588	-4012	-4093	-3497	0.10

^a The peak demand under this ground motion is closest to the mean demand

^b The peak demand under this ground motion is the largest demand

^c The peak demand under this ground motion is the smallest demand

TABLE 15.10

PEAK WALL PIER BASE COMPRESSION AXIAL FORCE DEMANDS FOR
STRUCTURE P1-CWUPT UNDER SURVIVAL LEVEL GROUND MOTIONS

ground motion	LA21	LA22	LA23 ^c	LA24	LA25	LA26	LA27	LA28	LA29	LA30	estimate (idealized)	standard deviation
peak wall pier base compression force (kN)	10635	10235	9279	9977	10853	11160	10097	10586	9501	10319	9047	596
ground motion	LA31	LA32	LA33	LA34 ^a	LA35	LA36 ^b	LA37	LA38	LA39	LA40	mean	standard deviation/mean
peak wall pier base compression force (kN)	11120	10831	9977	10368	11129	11209	10853	10697	9381	10066	10414	0.057

^a The peak demand under this ground motion is closest to the mean demand

^b The peak demand under this ground motion is the largest demand

^c The peak demand under this ground motion is the smallest demand

TABLE 15.11

PEAK WALL PIER BASE COMPRESSION AXIAL FORCE DEMANDS FOR
STRUCTURE P1-CWUPT UNDER DESIGN LEVEL GROUND MOTIONS

ground motion	LA01	LA02	LA03	LA04	LA05	LA06 ^c	LA07	LA08	LA09	LA10 ^a	standard deviation	
peak wall pier base compression force (kN)	9465	9728	9901	8749	8669	8389	9252	9118	9585	9496	556	
ground motion	LA11	LA12	LA13	LA14	LA15	LA16	LA17	LA18	LA19	LA20 ^b	mean	standard deviation/mean
peak wall pier base compression force (kN)	9118	9150	10275	9781	9710	10422	9421	9496	9817	10502	9502	0.059

^a The peak demand under this ground motion is closest to the mean demand

^b The peak demand under this ground motion is the largest demand

^c The peak demand under this ground motion is the smallest demand

Since the proposed design approach does not require the estimation of the survival-level and design-level wall pier axial forces, the results from the dynamic analyses are compared with the results from the static idealized bi-linear pushover analysis of the structure in Chapter 13. The tension-side and compression-side wall pier base axial forces, N_{twu} and N_{cwu} , corresponding to the estimated coupled wall ultimate state are given in Tables 15.8 and 15.10, respectively (see also Table 13.2). The results show that the peak tensile and compressive axial force demands from the dynamic analyses are underestimated by the axial forces, N_{twu} and N_{cwu} , from the idealized pushover analysis by 10-15%. This is possibly because of the underestimated coupling beam shear forces as described later in more detail.

As an example, Fig. 15.7 shows the axial force time histories at the bases of the left-side and right-side wall piers in Structure P1-CWUPT under the survival-level LA33 ground motion, for which the peak wall pier base tensile axial force demands (occurring

in the right-side wall pier) is closest to the mean demand from the twenty records (see Table 15.8). Similarly, Fig. 15.8 shows the axial force time histories at the bases of the left-side and right-side wall piers in Structure P1-CWUPT under the survival-level LA34 ground motion, for which the peak compressive axial force (occurring in the right-side wall pier) is closest to the mean demand from the twenty records (see Table 15.10). The dashed horizontal lines indicate the estimated idealized wall pier base axial forces, N_{twu} and N_{cwu} , from the bi-linear static pushover analysis in Chapter 13 at the coupled wall ultimate state.

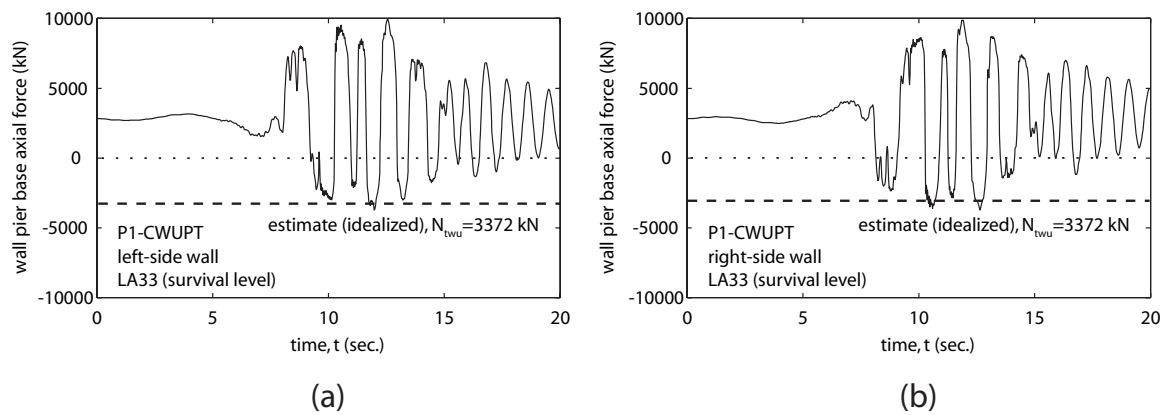


Fig. 15.7 Wall pier base axial force time histories for Structure P1-CWUPT:
(a) left-side wall; (b) right-side wall

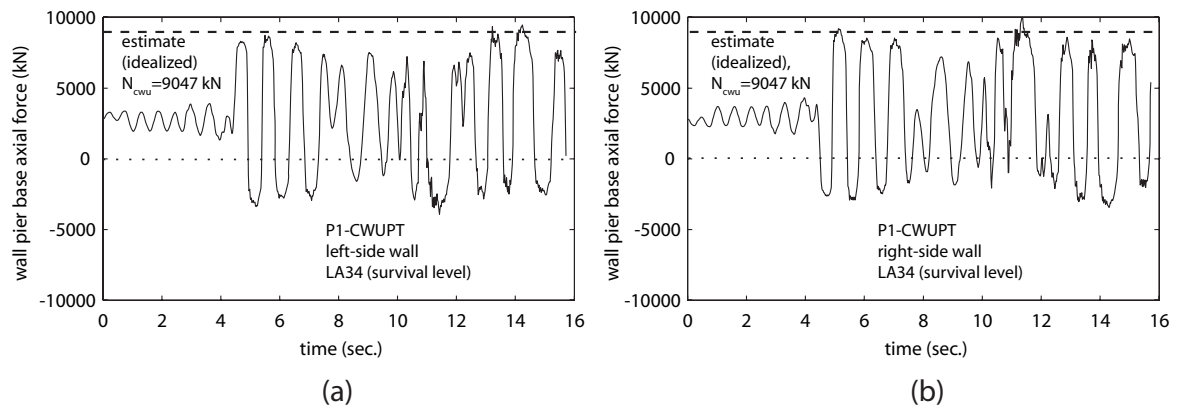


Fig. 15.8 Wall pier base axial force time histories for Structure P1-CWUPT:
(a) left-side wall; (b) right-side wall

Fig. 15.9 plots the peak tensile (\circ markers) and peak compressive (\square markers) wall pier base axial force demands from Tables 15.8-15.11 against the maximum incremental velocity (MIV) of the ground motion records (see Tables 14.2 and 14.1), where the dashed and solid horizontal lines represent the estimated idealized wall pier base axial force (from Chapter 13) and the mean peak wall pier base axial force demand, respectively, for each data set. It is observed that there is very little scatter or variation in the peak wall pier base axial force demands in each data set, and that the peak wall pier base axial force demands under the survival-level and design-level ground motions are similar.

15.2.5 Wall Base Shear Forces

The peak total coupled wall base shear force demands from the dynamic analyses of Structure P1-CWUPT under the twenty survival-level SAC ground motion records (LA21-LA40) and twenty design-level records (LA01-LA20) are listed in Tables 15.12 and 15.13, respectively. The coupled wall base shear force, F is equal to the sum of the floor and roof level wall pier inertia forces, which are calculated as the lumped mass times the total absolute acceleration (i.e., relative acceleration with respect to the ground plus the ground acceleration) at each floor/roof level.

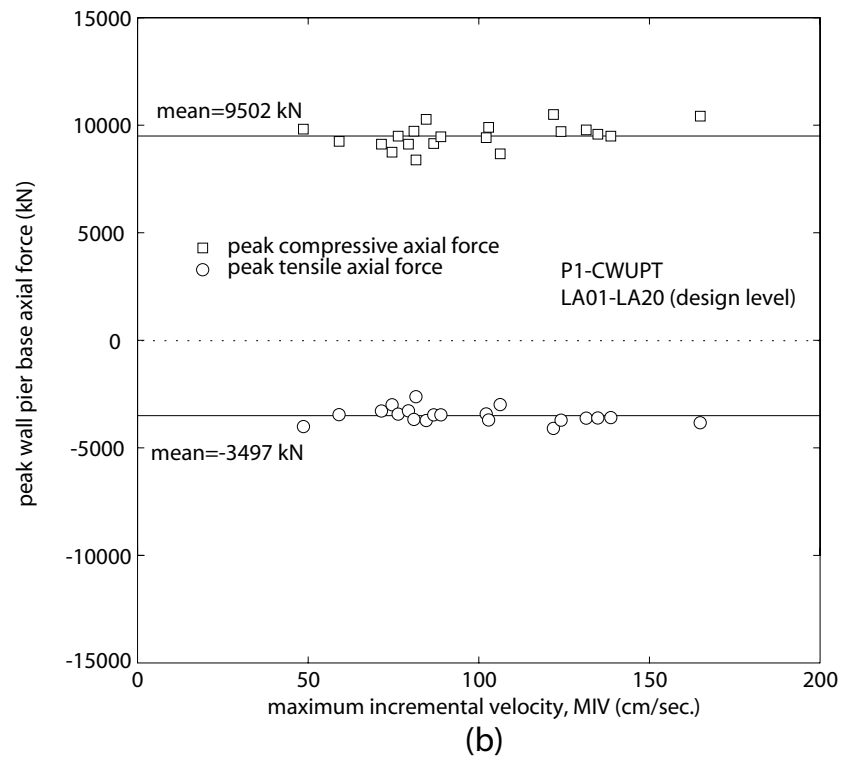
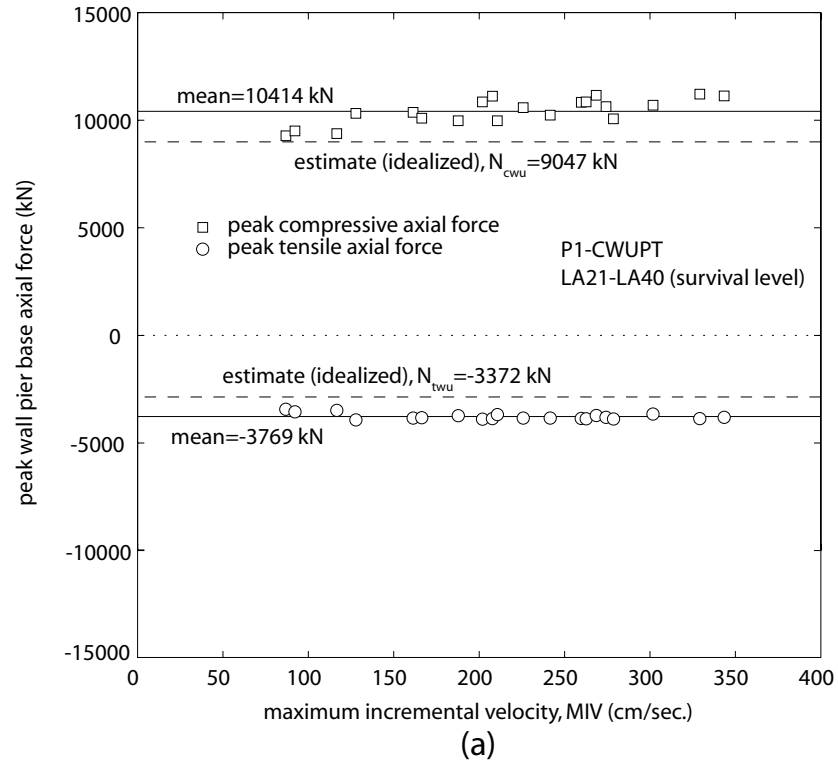


Fig. 15.9 Peak wall pier base axial force demands for Structure P1-CWUPT:
(a) survival level; (b) design level

TABLE 15.12

PEAK COUPLED WALL BASE SHEAR FORCE DEMANDS FOR STRUCTURE

P1-CWUPT UNDER SURVIVAL LEVEL GROUND MOTIONS

ground motion	LA21	LA22	LA23 ^c	LA24	LA25	LA26	LA27	LA28	LA29	LA30 ^b	estimate (design)	standard deviation
peak coupled wall base shear force (kN)	13001	11007	7392	9873	12253	12822	9383	12768	14891	15683	13156	2351
ground motion	LA31	LA32	LA33	LA34	LA35	LA36	LA37	LA38 ^a	LA39	LA40	mean	standard deviation/mean
peak coupled wall base shear force (kN)	14217	14771	11699	10397	15585	13601	10855	11887	8392 ^c	10514	12050	0.20

^a The peak demand under this ground motion is closest to the mean demand

^b The peak demand under this ground motion is the largest demand

^c The peak demand under this ground motion is the smallest demand

TABLE 15.13

PEAK COUPLED WALL BASE SHEAR FORCE DEMANDS FOR STRUCTURE

P1-CWUPT UNDER DESIGN LEVEL GROUND MOTIONS

ground motion	LA01	LA02	LA03	LA04	LA05	LA06 ^c	LA07	LA08	LA09	LA10	standard deviation	
peak coupled wall base shear force (kN)	8876	10763	9630	6125	5860	5602	6971	8032	9099	8522	3002	
ground motion	LA11 ^a	LA12	LA13	LA14	LA15	LA16	LA17	LA18	LA19	LA20 ^b	mean	standard deviation/mean
peak coupled wall base shear force (kN)	9843	15359	10641	10191	9109	10599	8199	11263	14593	16797	9804	0.31

^a The peak demand under this ground motion is closest to the mean demand

^b The peak demand under this ground motion is the largest demand

^c The peak demand under this ground motion is the smallest demand

Comparisons of the peak coupled wall base shear force demands in Tables 15.12 and 15.13 with the coupled wall base shear forces reached during the static push-over analysis of the structure in Chapter 13 show that the forces from the dynamic analyses are significantly larger than the forces from the static analysis. As discussed in Chapter 11, the differences between the static and dynamic analysis forces are because of the contribution of higher modes of vibration to the dynamic response of the structure.

The mean peak coupled wall base shear force demand from the twenty survival-level ground motions is 12050 kN, which is close to and smaller than the estimated maximum coupled wall base shear force demand of $Q_{w,max}=13156$ kN from Chapter 12. Thus, the method used in Chapter 12 to estimate the coupled wall base shear force demand of the prototype structures including the effect of higher modes appears to be valid. Note that the design approach does not require the estimation of the maximum coupled wall base shear force demand under the design-level earthquake; and thus, no design-level estimate is provided in Table 15.13.

As an example, Fig. 15.10 shows the coupled wall base shear force time history of Structure P1-CWUPT under the survival-level LA38 ground motion, for which the peak coupled wall base shear force demand is closest to the mean demand from the twenty records (see Table 15.12). The dashed horizontal lines indicate the design estimate for the maximum coupled wall base shear force demand, $Q_{w,max}$ from Chapter 12.

Fig. 15.11 plots the peak coupled wall base shear force demands from Tables 15.12 and 15.13 (\square markers) against the maximum incremental velocity (MIV) of the ground motion records (see Tables 14.2 and 14.1), where the dashed and solid horizontal lines represent the design estimate (from Chapter 12) and the mean peak coupled wall

base shear force demand, respectively, for each data set. Significant scatter is observed in the data indicating that, while the survival-level design estimate matches the mean demand from the dynamic analyses quite well, the coupled wall base shear force demand may be considerably larger or smaller than the estimated demand, depending on the earthquake. It is also interesting to note that the design-level LA20 ground motion record results in a larger peak coupled wall base shear force demand than all of the other records, including the survival-level records. Some correlation can be observed between the peak coupled wall base shear force demands in Fig. 15.11 and the peak acceleration demands in Fig. 15.6.

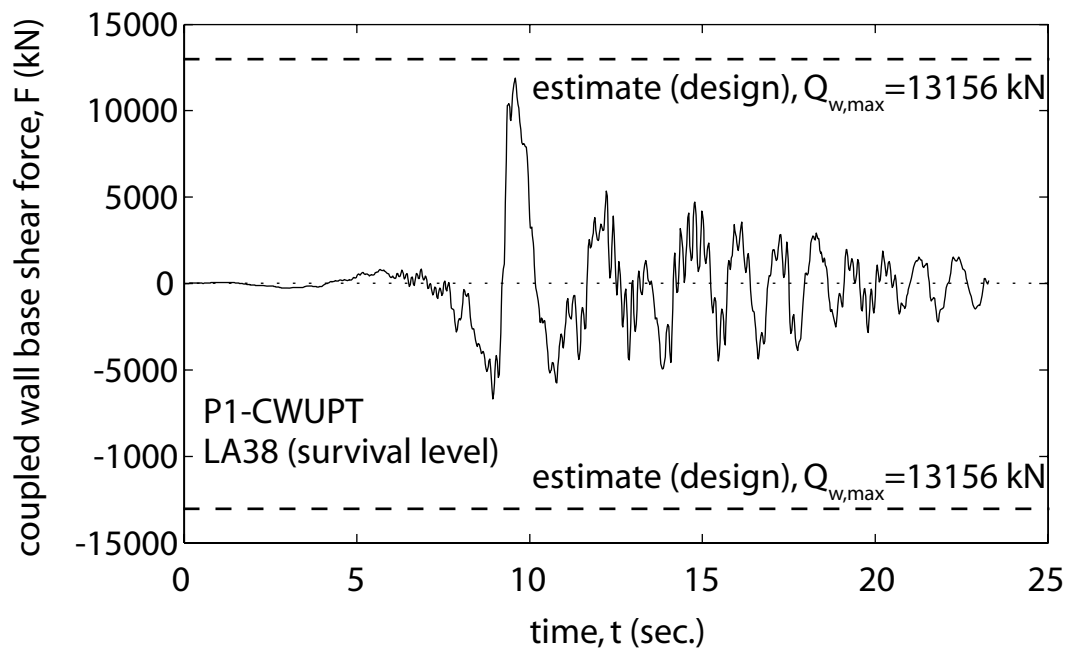
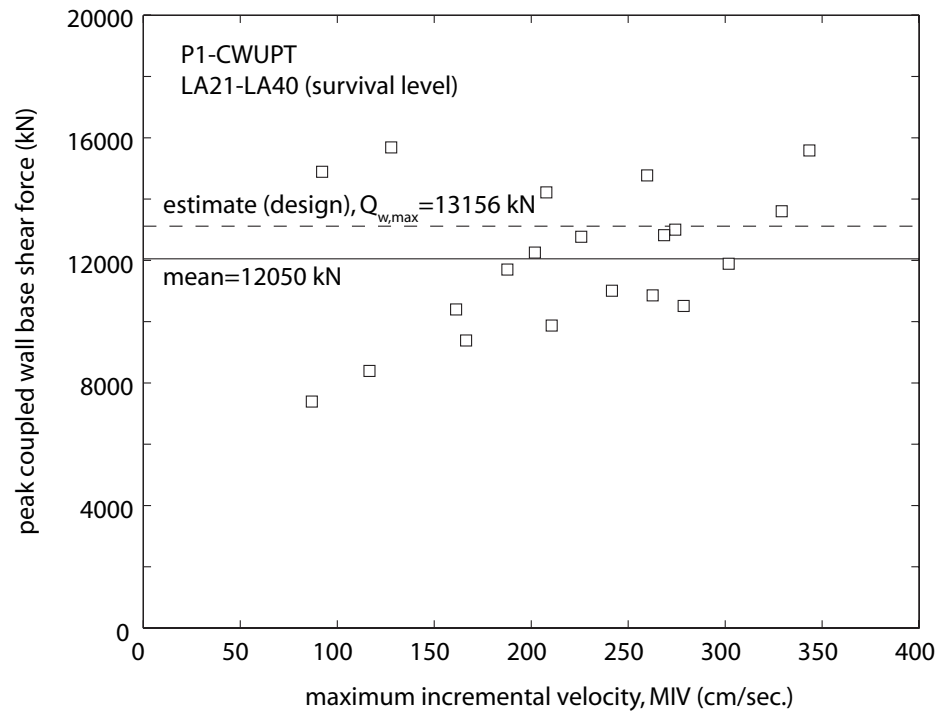
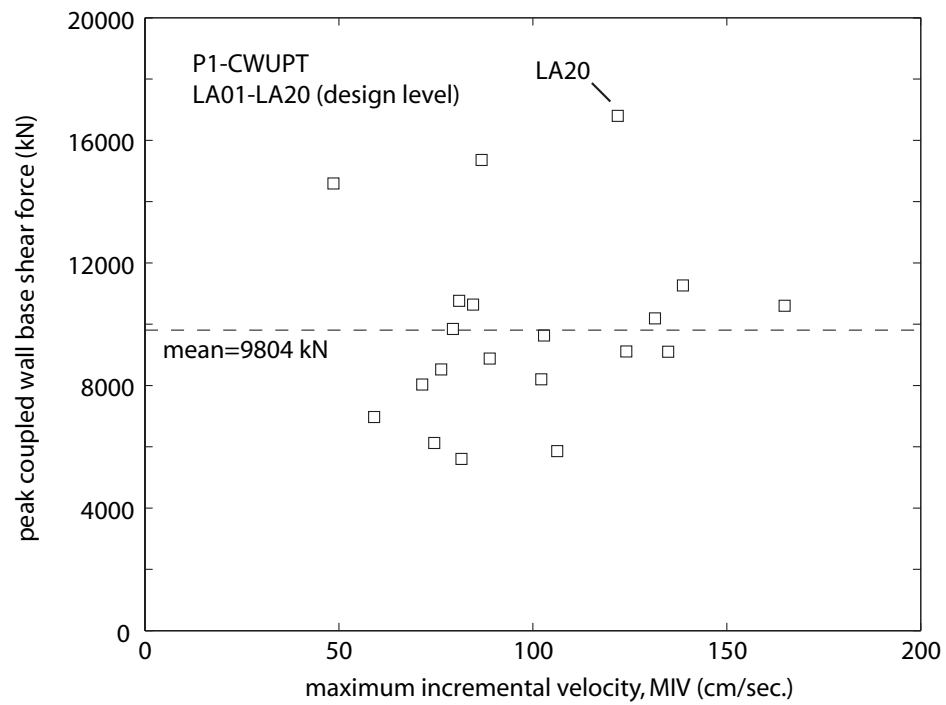


Fig. 15.10 Coupled wall base shear force time history for Structure P1-CWUPT



(a)



(b)

Fig. 15.11 Peak coupled wall base shear force demands for Structure P1-CWUPT:
(a) survival level; (b) design level

The peak wall pier base shear force demands from the dynamic analyses of Structure P1-CWUPT under the twenty survival-level SAC ground motion records (LA21-LA40) and twenty design-level records (LA01-LA20) are listed in Tables 15.14 and 15.15, respectively. The wall pier base shear forces are calculated from the equilibrium of the floor/roof level wall pier inertia forces, with the coupling beam midspan axial forces and beam post-tensioning tendon forces from the analysis model (obtained from the fiber beam-column elements and the truss elements representing the coupling beams and the beam post-tensioning tendons, respectively).

TABLE 15.14
PEAK WALL PIER BASE SHEAR FORCE DEMANDS FOR
STRUCTURE P1-CWUPT UNDER SURVIVAL LEVEL GROUND MOTIONS

ground motion	LA21	LA22	LA23 ^c	LA24	LA25	LA26	LA27	LA28 ^a	LA29	LA30	estimate (design)	standard deviation
peak wall pier base shear force (kN)	8770	6720	5098	7055	8330	8794	6519	8152	9324	9935	9341	1326
ground motion	LA31	LA32 ^b	LA33	LA34	LA35	LA36	LA37	LA38	LA39	LA40	mean	standard deviation/mean
peak wall pier base shear force (kN)	9551	10015	7644	7666	8337	9057	7451	8497	5798	7679	8020	0.17

^a The peak demand under this ground motion is closest to the mean demand

^b The peak demand under this ground motion is the largest demand

^c The peak demand under this ground motion is the smallest demand

TABLE 15.15

PEAK WALL PIER BASE SHEAR FORCE DEMANDS FOR STRUCTURE

P1-CWUPT UNDER DESIGN LEVEL GROUND MOTIONS

ground motion	LA01	LA02	LA03	LA04	LA05	LA06 ^c	LA07	LA08	LA09 ^a	LA10	standard deviation	
peak wall pier base shear force (kN)	5993	6025	6950	3936	3981	3193	4599	4886	6313	6052	1671	
ground motion	LA11	LA12	LA13	LA14	LA15	LA16	LA17	LA18	LA19	LA20 ^b	mean	standard deviation/mean
peak wall pier base shear force (kN)	5833	9415	7304	6489	6035	6815	5777	7584	8736	9085	6250	0.27

^a The peak demand under this ground motion is closest to the mean demand

^b The peak demand under this ground motion is the largest demand

^c The peak demand under this ground motion is the smallest demand

The mean peak wall pier base shear force demand from the twenty survival-level analyses is 8020 kN, which is reasonably close to and smaller than the estimated maximum wall pier base shear force demand of $Q_{w,dt}=9341$ kN from Chapter 12. Thus, the method used in Chapter 12 to estimate the maximum wall pier base shear force demand appears to be valid. Note that the design approach does not require the estimation of the maximum wall pier base shear force demand under the design-level earthquake; and thus, no design-level estimate is provided in Table 15.15.

As an example, Fig. 15.12 shows the shear force time histories at the bases of the left-side and right-side wall piers in Structure P1-CWUPT under the survival-level LA28 ground motion, for which the peak wall pier base shear force demand (occurring in the left-side wall pier) is closest to the mean demand from the twenty records (see Table 15.14). The dashed horizontal lines indicate the design estimate for the maximum wall pier base shear force demand, $Q_{w,dt}$ from Chapter 12. It is observed that there are residual

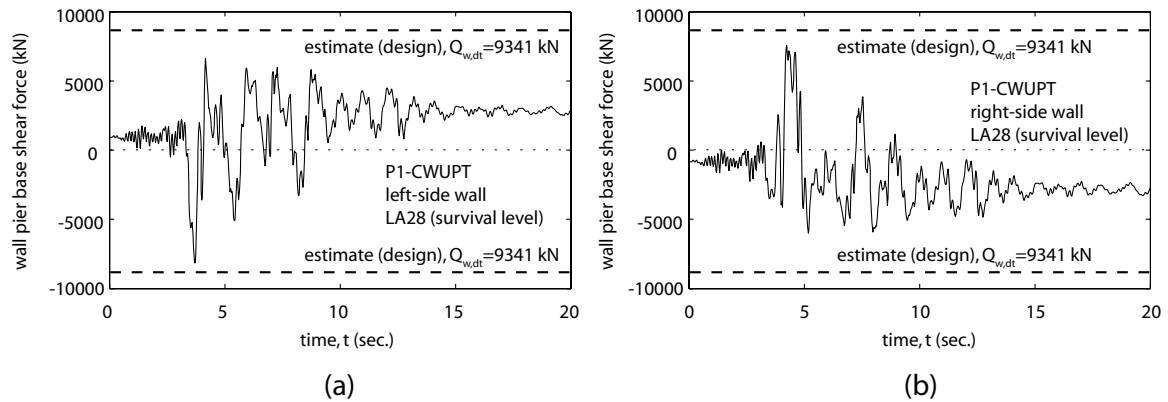
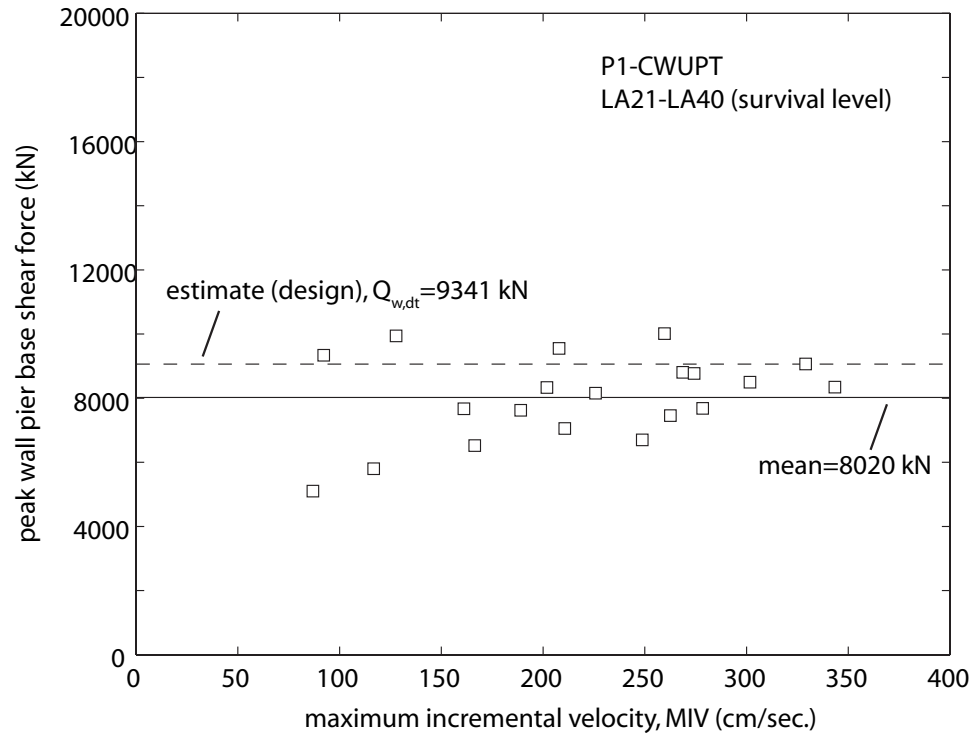


Fig. 15.12 Wall pier base shear force time histories for Structure P1-CWUPT: (a) left-side wall; (b) right-side wall

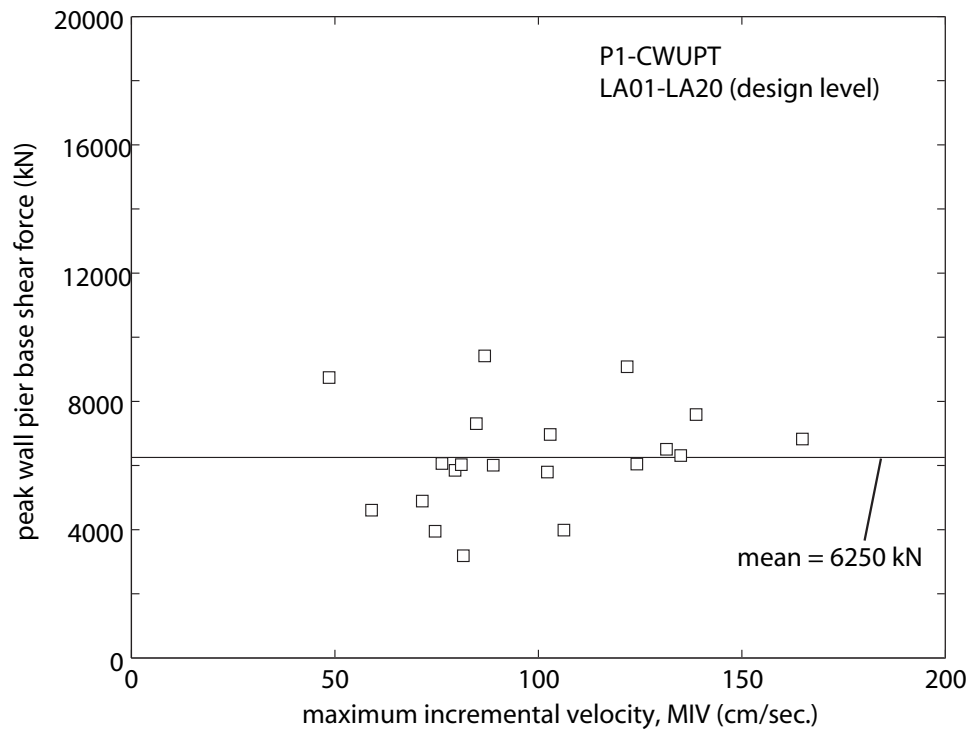
base shear forces in the left-side and right-side wall piers at the end of the ground motion, even though the coupled wall base shear force is close to zero.

Fig. 15.13 plots the peak wall pier base shear force demands from Tables 15.14 and 15.15 (\square markers) against the maximum incremental velocity (MIV) of the ground motion records (see Tables 14.2 and 14.1), where the dashed and solid horizontal lines represent the design estimate (from Chapter 12) and the mean peak wall pier base shear force demand, respectively, for each data set. Similar to the peak coupled wall base shear force demands in Fig. 15.11, significant scatter is observed in the peak wall pier base shear force demands and the demands for some of the design-level ground motion records are similar to the largest demand from the survival-level records.

If the peak wall pier base shear force demands in Tables 15.14 and 15.15 are divided by the corresponding peak coupled wall base shear force demands in Tables 15.12 and 15.13, the wall pier base shear force distribution ratios are obtained. The mean wall pier base shear force distribution ratio from the twenty survival-level analyses is 0.67, which is close to the design ratio of $Q_{w,dt}/Q_{w,max}=0.71$ from Chapter 12.



(a)



(b)

Fig. 15.13 Peak wall pier base shear force demands for Structure P1-CWUPT:
(a) survival level; (b) design level

Note that the peak wall pier base shear force demands in Tables 15.14 and 15.15 and the corresponding peak coupled wall base shear force demands in Tables 15.12 and 15.13 do not necessarily occur at the same time during each dynamic analysis. Thus, Tables 15.16 and 15.17 show the peak ratio of the wall pier base shear force to the corresponding coupled wall base shear force occurring at the same time during each analysis. The mean value of the peak wall pier base shear force distribution ratio from the twenty survival-level analyses in Table 15.16 is 0.69, which is close to the value used in design and the value calculated from the peak wall pier and peak coupled wall base shear force demands above.

TABLE 15.16
PEAK WALL PIER BASE SHEAR FORCE DISTRIBUTION RATIOS FOR
STRUCTURE P1-CWUPT UNDER SURVIVAL LEVEL GROUND MOTIONS

ground motion	LA21	LA22	LA23	LA24	LA25	LA26	LA27	LA28	LA29	LA30	estimate (design)	standard deviation
peak base shear force distribution ratio	0.67	0.66	0.75	0.71	0.68	0.69	0.74	0.71	0.65	0.63	0.71	0.047
ground motion	LA31	LA32	LA33	LA34	LA35	LA36	LA37	LA38	LA39	LA40	mean	standard deviation/mean
peak base shear force distribution ratio	0.67	0.68	0.72	0.74	0.53	0.67	0.69	0.71	0.69	0.73	0.69	0.069

15.2.6 Wall Base Diagonal Tension and Shear Slip Failure

It is shown in the previous section that the mean peak wall pier base shear force demand under the twenty survival-level ground motion records in Table 15.14 is smaller than the estimated design maximum wall pier base shear force demand from Chapter 12.

TABLE 15.17

PEAK WALL PIER SHEAR FORCE DISTRIBUTION RATIOS FOR
STRUCTURE P1-CWUPT UNDER DESIGN LEVEL GROUND MOTIONS

ground motion	LA01	LA02	LA03	LA04	LA05	LA06	LA07	LA08	LA09	LA10	standard deviation	
peak base shear force distribution ratio	0.69	0.64	0.74	0.64	0.68	0.57	0.72	0.65	0.75	0.73	0.064	
ground motion	LA11	LA12	LA13	LA14	LA15	LA16	LA17	LA18	LA19	LA20	mean	standard deviation/mean
peak base shear force distribution ratio	0.69	0.63	0.77	0.76	0.76	0.76	0.74	0.69	0.63	0.56	0.69	0.093

Thus, it is concluded that diagonal tension failure of the wall piers in Structure P1-CWUPT can be, on average, prevented as long as the design diagonal tension capacity $F_{w,dt}=9261$ kN from Chapter 12 is achieved and maintained.

Similarly, the mean peak coupled wall base shear force demand under the twenty survival-level ground motion records in Table 15.12 is smaller than the estimated design maximum coupled wall base shear force demand from Chapter 12. Furthermore, the design shear slip capacity estimated for Structure P1-CWUPT in Chapter 12 is equal to $F_{w,ss}=44614$ kN, which is larger than the peak coupled wall base shear force demands under all of the survival-level and design-level ground motion records in Tables 15.12 and 15.13. Thus, it is concluded that shear slip failure of the structure does not occur.

15.2.7 Wall Base Moments

The peak wall pier base moment demands from the dynamic analyses of Structure P1-CWUPT under the twenty survival-level SAC ground motion records (LA21-LA40) and twenty design-level records (LA01-LA20) are listed in Tables 15.18 and 15.19,

TABLE 15.18

PEAK WALL PIER BASE MOMENT DEMANDS FOR STRUCTURE P1-CWUPT
UNDER SURVIVAL LEVEL GROUND MOTIONS

ground motion	LA21	LA22	LA23 ^c	LA24	LA25	LA26	LA27 ^a	LA28	LA29	LA30	estimate (idealized)	standard deviation
peak wall pier base moment (kN.m)	77583	71584	61415	70781	76046	79854	73640	77549	65381	71177	76242	6169
ground motion	LA31	LA32	LA33	LA34	LA35	LA36 ^b	LA37	LA38	LA39	LA40	mean	standard deviation/mean
peak wall pier base moment (kN.m)	79255	78351	72386	73109	82509	83051	80532	79594	62828	76815	74672	0.083

^a The peak demand under this ground motion is closest to the mean demand

^b The peak demand under this ground motion is the largest demand

^c The peak demand under this ground motion is the smallest demand

TABLE 15.19

PEAK WALL PIER BASE MOMENT DEMANDS FOR STRUCTURE P1-CWUPT
UNDER DESIGN LEVEL GROUND MOTIONS

ground motion	LA01	LA02	LA03	LA04	LA05	LA06 ^c	LA07	LA08	LA09	LA10	standard deviation	
peak wall pier base moment (kN.m)	63573	65121	68285	45508	50976	38153	57891	58602	65641	62997	8716	
ground motion	LA11	LA12	LA13	LA14	LA15	LA16	LA17	LA18	LA19 ^a	LA20 ^b	mean	standard deviation/mean
peak wall pier base moment (kN.m)	59789	60625	67821	69595	67211	72521	63347	65257	62082	73753	61937	0.14

^a The peak demand under this ground motion is closest to the mean demand

^b The peak demand under this ground motion is the largest demand

^c The peak demand under this ground motion is the smallest demand

respectively. The wall pier base moments are calculated from the equilibrium of the floor/roof level wall pier inertia forces with the coupling beam midspan axial forces and beam post-tensioning tendon forces from the analysis model (obtained from the fiber beam-column elements and the truss elements representing the coupling beams and the beam post-tensioning tendons, respectively).

Since the proposed design approach does not require the estimation of the survival-level and design-level wall pier base moments, the results from the dynamic analyses are compared with the results from the static idealized bi-linear pushover analysis of the structure in Chapter 13. The bending moment at the base of the compression-side wall pier (which has a larger base moment than the tension side wall pier), M_{cwu} , corresponding to the estimated coupled wall ultimate state is given in Table 15.18 (see also Table 13.2). The results show that the wall pier base moment, M_{cwu} from the idealized pushover analysis provides a good estimate of the peak wall pier base moment demands from the dynamic analyses.

As an example, Fig. 15.14 shows the bending moment time histories at the bases of the left-side and right-side wall piers in Structure P1-CWUPT under the survival-level LA27 ground motion, for which the peak wall pier base moment demand (occurring in the right-side wall pier) is closest to the mean demand from the twenty records (see Table 15.18). The dashed horizontal lines indicate the estimated idealized compression-side wall pier base moment, M_{cwu} from the bi-linear static pushover analysis in Chapter 13 at the coupled wall ultimate state.

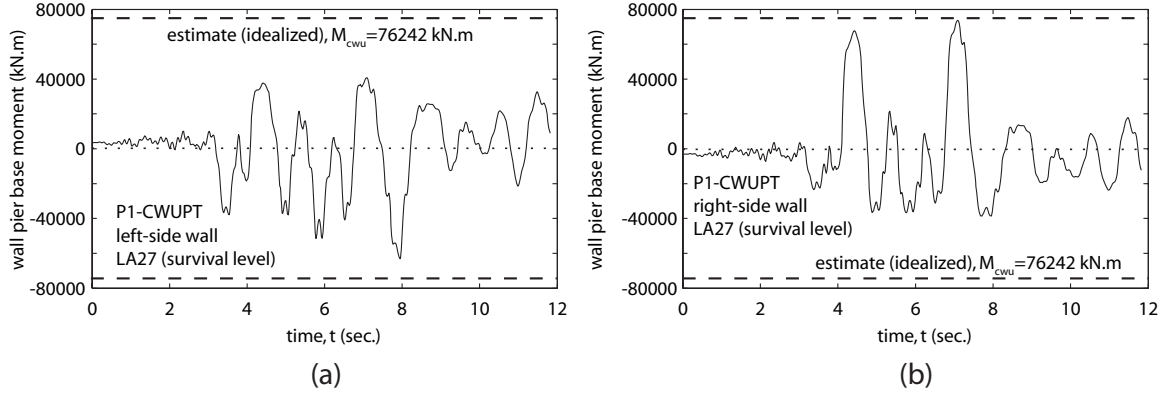
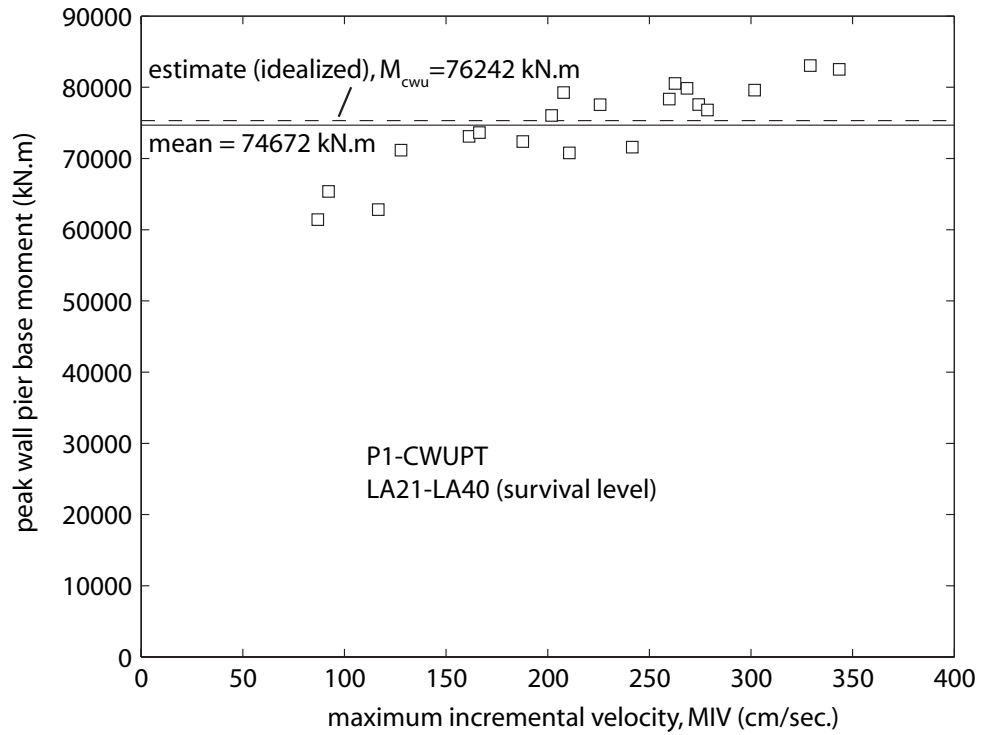


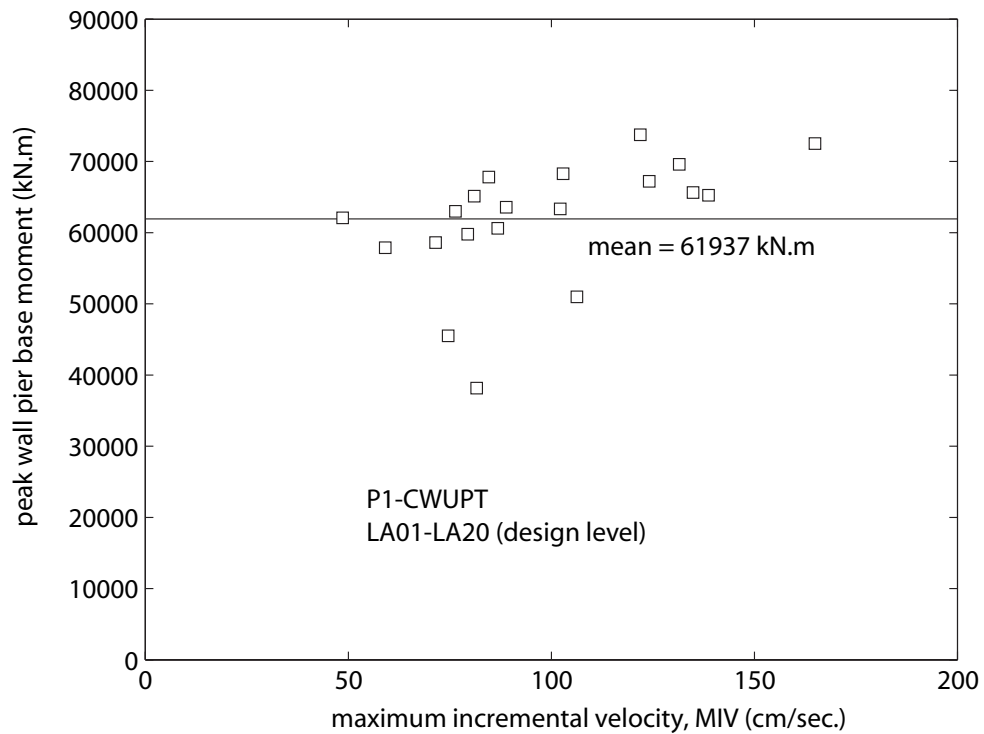
Fig. 15.14 Wall pier base moment time histories for Structure P1-CWUPT:
(a) left-side wall; (b) right-side wall

Fig. 15.15 plots the peak wall pier base moment demands from Tables 15.18 and 15.19 (\square markers) against the maximum incremental velocity (MIV) of the ground motion records (see Tables 14.2 and 14.1), where the dashed and solid horizontal lines represent the estimated idealized wall pier base moment (from Chapter 13) and the mean peak wall pier base moment demand, respectively, for each data set. A considerable amount of scatter is observed in the peak wall pier base moment demands in each data set.

The peak total coupled wall base moment demands from the dynamic analyses of Structure P1-CWUPT under the twenty survival-level SAC ground motion records (LA21-LA40) and twenty design-level records (LA01-LA20) are listed in Tables 15.20 and 15.21, respectively. The coupled wall base moment, M_w is calculated from the equilibrium of the floor and roof level wall pier inertia forces.



(a)



(b)

Fig. 15.15 Peak wall pier base moment demands for Structure P1-CWUPT:
(a) survival level; (b) design level

TABLE 15.20

PEAK COUPLED WALL BASE MOMENT DEMANDS FOR
STRUCTURE P1-CWUPT UNDER SURVIVAL LEVEL GROUND MOTIONS

ground motion	LA21	LA22 ^a	LA23 ^c	LA24	LA25	LA26	LA27	LA28	LA29	LA30	estimate (idealized)	standard deviation
peak coupled wall base moment (kN.m)	192510	183300	146210	174890	189995	212398	171370	192660	153340	169320	161323	20742
ground motion	LA31	LA32	LA33	LA34	LA35	LA36 ^b	LA37	LA38	LA39	LA40	mean	standard deviation/mean
peak coupled wall base moment (kN.m)	191080	197140	169270	175180	217570	220260	193770	202460	152960	182400	184404	0.11

^a The peak demand under this ground motion is closest to the mean demand

^b The peak demand under this ground motion is the largest demand

^c The peak demand under this ground motion is the smallest demand

TABLE 15.21

PEAK COUPLED WALL BASE MOMENT DEMANDS FOR
STRUCTURE P1-CWUPT UNDER DESIGN LEVEL GROUND MOTIONS

ground motion	LA01 ^a	LA02	LA03	LA04	LA05	LA06 ^c	LA07	LA08	LA09	LA10	standard deviation	
peak coupled wall base moment (kN.m)	149230	154190	159220	113430	121560	101580	136710	145150	159340	147730	19993	
ground motion	LA11	LA12	LA13	LA14	LA15	LA16 ^b	LA17	LA18	LA19	LA20	mean	standard deviation/mean
peak coupled wall base moment (kN.m)	144120	144360	172870	168900	155660	180920	146650	156230	145510	176880	149010	0.13

^a The peak demand under this ground motion is closest to the mean demand

^b The peak demand under this ground motion is the largest demand

^c The peak demand under this ground motion is the smallest demand

Similar to the wall pier base moments, the peak coupled wall base moment demands from the dynamic analyses are compared with the results from the static idealized bi-linear pushover analysis of the structure in Chapter 13. The coupled wall base moment, M_{wu} corresponding to the estimated coupled wall ultimate state is given in Table 15.20 (see also Table 13.2). The results show that the coupled wall base moment, M_{wu} from the idealized pushover analysis underestimates the peak coupled wall base moment demands from the dynamic analyses, even though the wall pier base moment demands are estimated reasonably well. This is possibly because of the underestimated coupling beam shear forces as described later in more detail.

As an example, Fig. 15.16 shows the coupled wall base moment time history of Structure P1-CWUPT under the survival-level LA22 ground motion, for which the peak coupled wall base moment demand is closest to the mean demand from the twenty records (see Table 15.20). The dashed horizontal lines indicate the estimated idealized coupled wall base moment, M_{wu} from the bi-linear static pushover analysis in Chapter 13 at the coupled wall ultimate state.

Fig. 15.17 plots the peak coupled wall base moment demands from Tables 15.20 and 15.21 (\square markers) against the maximum incremental velocity (MIV) of the ground motion records (see Tables 14.2 and 14.1), where the dashed and solid horizontal lines represent the estimated idealized coupled wall base moment (from Chapter 13) and the mean peak coupled wall base moment demand, respectively, for each data set. Similar to the peak wall pier base moment demands, a considerable amount of scatter is observed in the peak coupled wall base moment demands in each data set.

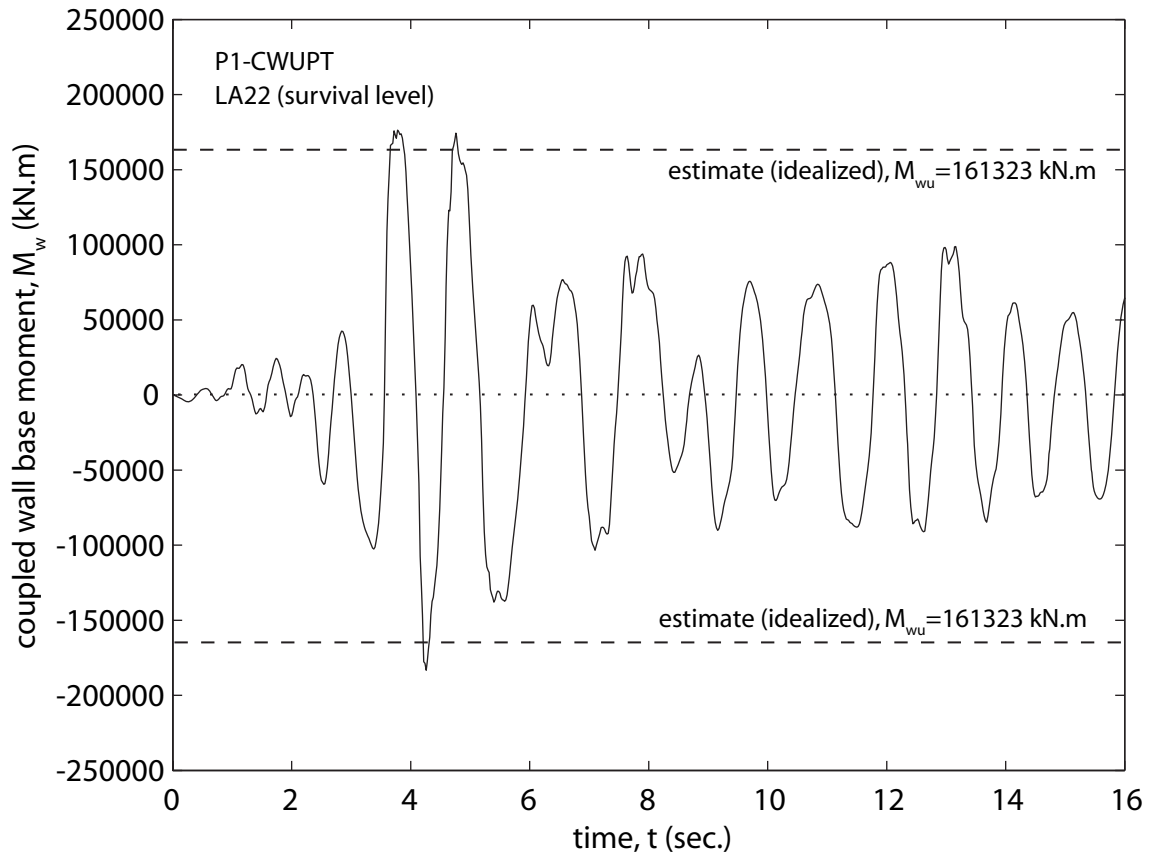
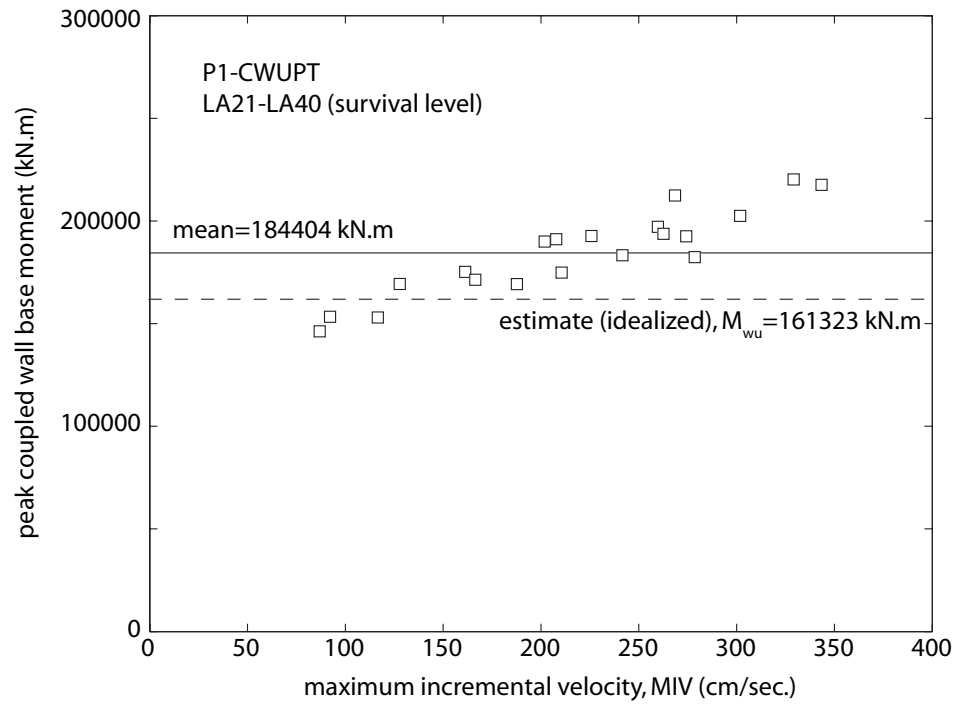


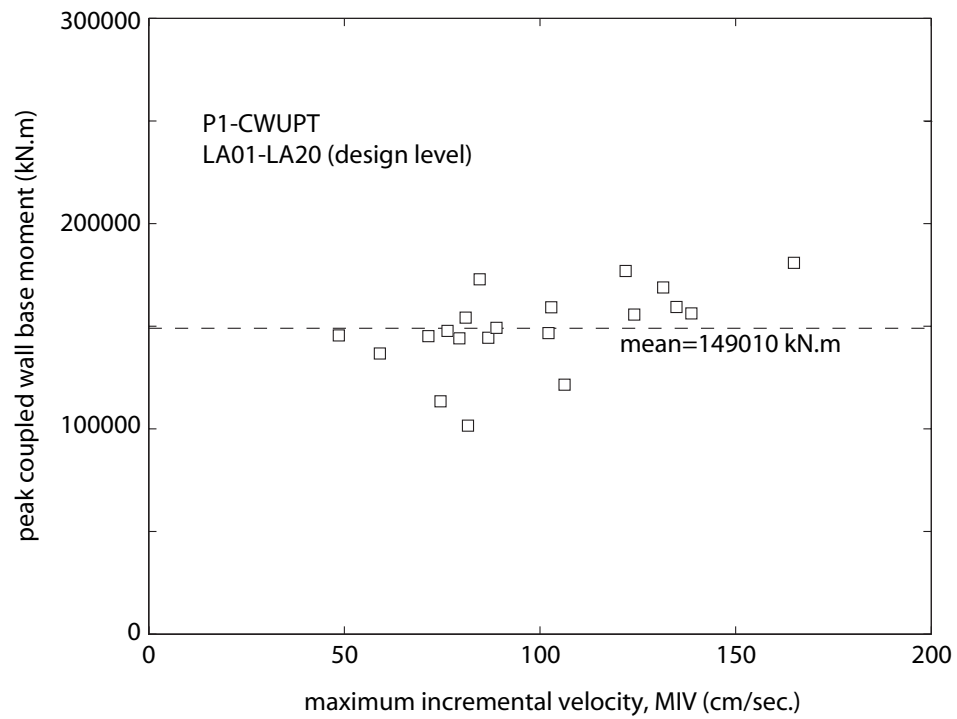
Fig. 15.16 Coupled wall base moment time history for Structure P1-CWUPT

15.2.8 Wall Base Strains

The peak confined concrete compression strain demands at the bases of the wall piers from the dynamic analyses of Structure P1-CWUPT under the twenty survival-level SAC ground motion records (LA21-LA40) and twenty design-level records (LA01-LA20) are listed in Tables 15.22 and 15.23, respectively. The concrete compression strains are determined directly from the fiber beam-column elements used for the wall piers in the analysis model.



(a)



(b)

Fig. 15.17 Peak coupled wall base moment demands for Structure P1-CWUPT:
(a) survival level; (b) design level

TABLE 15.22

PEAK WALL PIER BASE CONFINED CONCRETE COMPRESSION STRAIN
DEMANDS FOR STRUCTURE P1-CWUPT UNDER SURVIVAL LEVEL GROUND
MOTIONS

ground motion	LA21	LA22	LA23	LA24	LA25	LA26	LA27	LA28	LA29	LA30	estimate (design)	standard deviation
peak confined concrete strain (10^{-3})	-8.2	-5.4	-3.0	-5.1	-7.2	-11.0	-6.0	-8.3	-3.5	-4.9	-9.0	-4.4
ground motion	LA31	LA32 ^a	LA33	LA34	LA35	LA36 ^b	LA37	LA38	LA39 ^c	LA40	mean	standard deviation/mean
peak confined concrete strain (10^{-3})	-9.1	-8.4	-5.4	-5.6	-17.6	-19.0	-11.6	-11.7	-3.3	-8.0	-8.1	0.54

^a The peak demand under this ground motion is closest to the mean demand

^b The peak demand under this ground motion is the largest demand

^c The peak demand under this ground motion is the smallest demand

TABLE 15.23

PEAK WALL PIER BASE CONFINED CONCRETE COMPRESSION STRAIN
DEMANDS FOR STRUCTURE P1-CWUPT UNDER DESIGN LEVEL GROUND
MOTIONS

ground motion	LA01	LA02	LA03	LA04	LA05	LA06 ^c	LA07	LA08	LA09	LA10	standard deviation	
peak confined concrete strain (10^{-3})	-3.1	-3.5	-4.2	-1.2	-1.4	-1.0	-2.2	-2.3	-3.7	-3.0	-1.4	
ground motion	LA11	LA12	LA13	LA14	LA15	LA16	LA17 ^a	LA18	LA19	LA20 ^b	mean	standard deviation/mean
peak confined concrete strain (10^{-3})	-2.6	-2.6	-4.2	-4.6	-4.2	-5.8	-3.1	-3.5	-3.0	-6.1	-3.3	0.42

^a The peak demand under this ground motion is closest to the mean demand

^b The peak demand under this ground motion is the largest demand

^c The peak demand under this ground motion is the smallest demand

The mean peak wall pier base confined concrete compression strain demand from the survival-level dynamic analyses in Table 15.22 is -0.0081, which is smaller than and close to the estimated wall pier base confined concrete strain demand of -0.0090 from Chapter 12. Thus, the method used in Chapter 12 to estimate the wall pier base confined concrete compression strain demand seems to be valid. Note that the design approach does not require the estimation of the confined concrete compression strain demand under the design-level earthquake; and thus, no design-level estimate is provided in Table 15.23.

As an example, Fig. 15.18 shows the extreme confined concrete compression strain time histories at the base of Structure P1-CWUPT under the survival-level LA32 ground motion, for which the peak wall pier base confined concrete compression strain demand (occurring at the left end of the left-side wall pier) is closest to the mean demand from the twenty records (see Table 15.22). A total of four strain time histories are shown for the left and right ends of the left-side and right-side wall piers, where the dashed horizontal lines indicate the design estimate for the wall pier base confined concrete compression strain demand from Chapter 12.

Fig. 15.19 plots the peak wall pier base confined concrete compression strain demands from Tables 15.22 and 15.23 (\square markers) against the maximum incremental velocity (MIV) of the ground motion records (see Tables 14.2 and 14.1), where the dashed and solid horizontal lines represent the design estimate and the mean peak wall pier base confined concrete compression strain demand, respectively, for each data set.

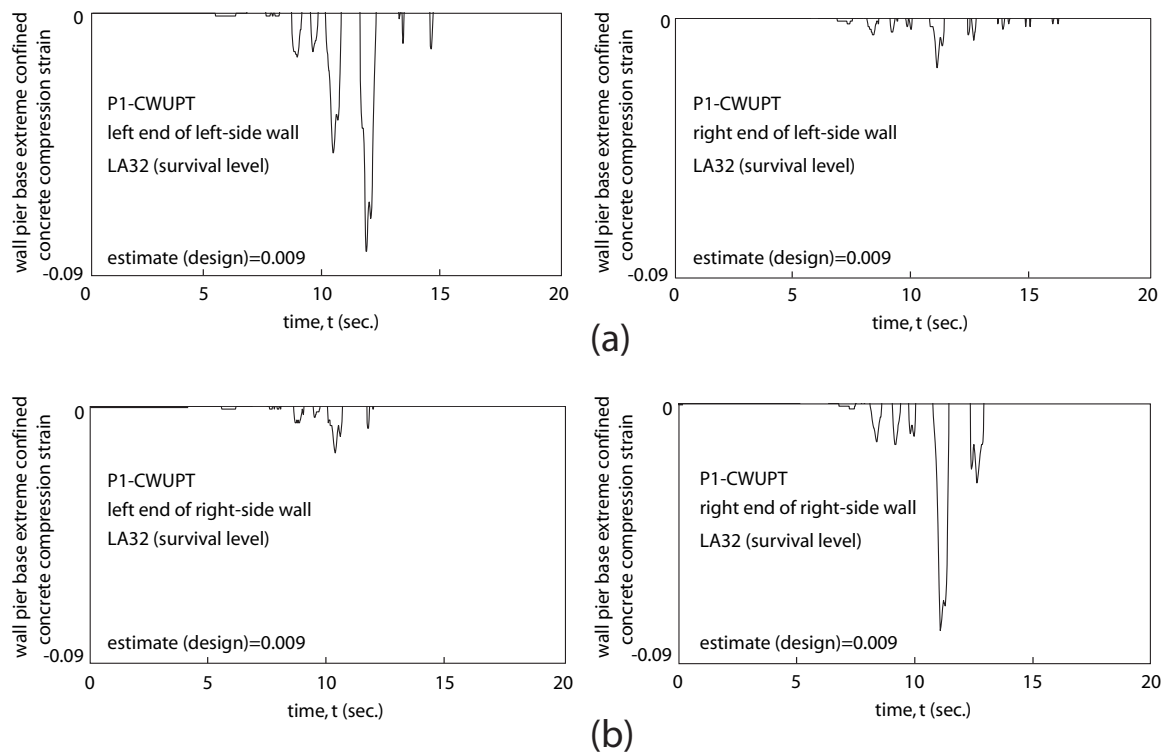
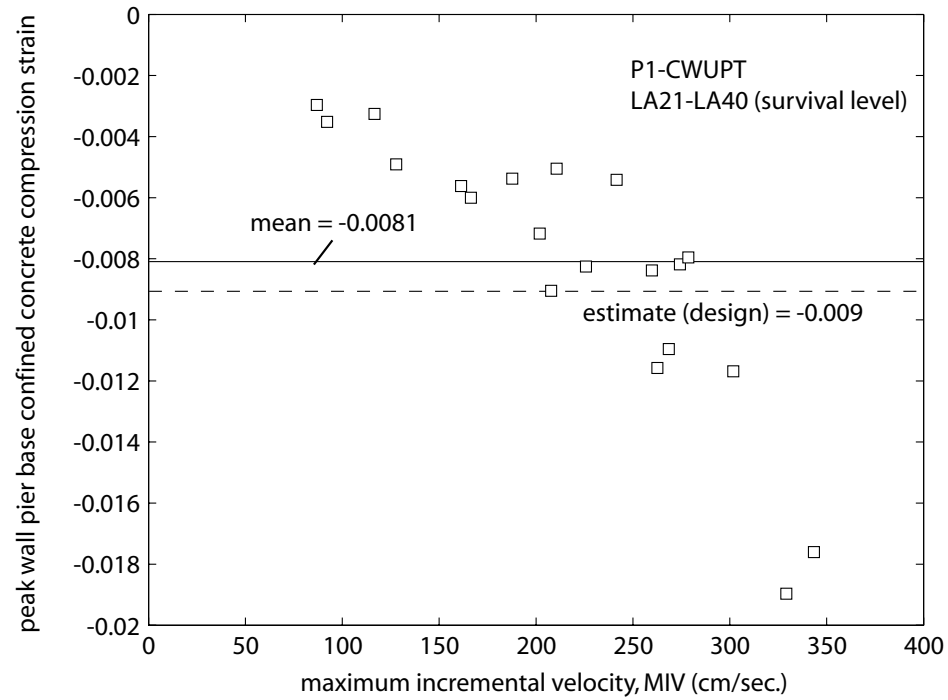


Fig. 15.18 Wall pier base extreme confined concrete compression strain time histories for Structure P1-CWUPT: (a) left-side wall; (b) right-side wall

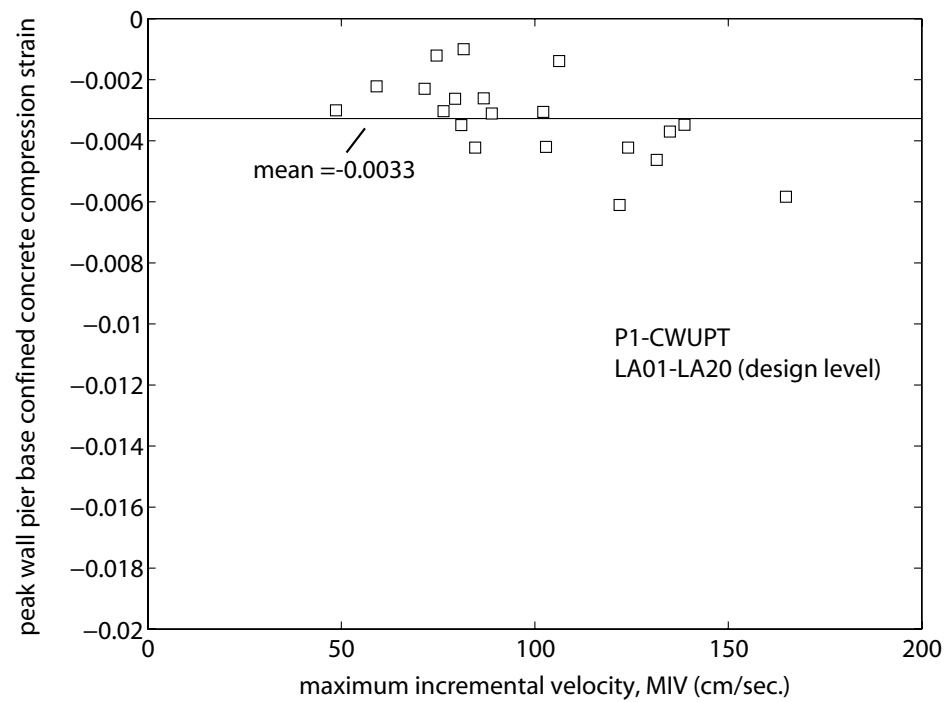
The trends for the peak wall pier base confined concrete compression strain demands in Fig. 15.19 are similar to the trends for the peak coupled wall roof drift demands in Fig. 15.2.

15.2.9 Coupling Beam Chord Rotations

The peak coupling beam chord rotation demands from the dynamic analyses of Structure P1-CWUPT under the twenty survival-level SAC ground motion records (LA21-LA40) and twenty design-level records (LA01-LA20) are listed in Tables 15.24 and 15.25, respectively. As described in Chapter 7, the coupling beam chord rotation, θ_b , is measured from a tangent drawn at the left end of each beam.



(a)



(b)

Fig. 15.19 Peak wall pier base confined concrete compression strain demands for Structure P1-CWUPT: (a) survival level; (b) design level

TABLE 15.24

PEAK COUPLING BEAM CHORD ROTATION DEMANDS FOR STRUCTURE P1-
CWUPT UNDER SURVIVAL LEVEL GROUND MOTIONS

ground motion	LA21	LA22	LA23 ^c	LA24	LA25	LA26	LA27	LA28	LA29	LA30	estimate (design)	standard deviation
peak coupling beam chord rotation (%)	3.27	2.21	1.17	2.44	3.17	4.35	2.46	3.10	1.28	1.71	5.49	1.45
ground motion	LA31 ^a	LA32	LA33	LA34	LA35 ^b	LA36	LA37	LA38	LA39	LA40	mean	standard deviation/mean
peak coupling beam chord rotation (%)	3.06	3.34	1.97	2.21	6.37	6.13	4.04	4.62	1.33	3.18	3.08	0.47

^a The peak demand under this ground motion is closest to the mean demand

^b The peak demand under this ground motion is the largest demand

^c The peak demand under this ground motion is the smallest demand

TABLE 15.25

PEAK COUPLING BEAM CHORD ROTATION DEMANDS FOR STRUCTURE
P1-CWUPT UNDER DESIGN LEVEL GROUND MOTIONS

ground motion	LA01	LA02	LA03	LA04	LA05	LA06 ^c	LA07	LA08 ^a	LA09	LA10	estimate (design)	standard deviation
peak coupling beam chord rotation (%)	1.79	1.35	0.93	0.35	0.58	0.16	0.97	1.20	1.30	1.12	2.33	0.65
ground motion	LA11	LA12	LA13	LA14	LA15	LA16 ^b	LA17	LA18	LA19	LA20	mean	standard deviation/mean
peak coupling beam chord rotation (%)	0.71	0.62	1.98	2.05	1.48	2.63	1.17	1.50	0.90	2.25	1.25	0.52

^a The peak demand under this ground motion is closest to the mean demand

^b The peak demand under this ground motion is the largest demand

^c The peak demand under this ground motion is the smallest demand

The mean peak coupling beam chord rotation demand from the survival-level dynamic analyses in Table 15.24 is 3.08%, which is significantly smaller than the estimated survival-level coupling beam chord rotation demand of $\theta_s=5.49\%$ from Chapter 12. As an example, Fig. 15.20 shows the chord rotation time histories for the eight coupling beams in Structure P1-CWUPT under the survival-level LA31 ground motion, for which the peak coupling beam chord rotation demand (occurring in the roof beam) is closest to the mean demand from the twenty records (see Table 15.24).

Similarly, the mean peak coupling beam chord rotation demand from the design-level analyses in Table 15.25 is 1.25%, which is significantly smaller than the estimated design-level coupling beam chord rotation demand of $\theta_d=2.33\%$ from Chapter 12. It is concluded that the displacement-based design objectives under the survival-level and design-level ground motions are satisfied; however, the procedure to estimate the coupling beam chord rotation demands may need to be improved to prevent an overly-conservative design.

Fig. 15.21 plots the peak coupling beam chord rotation demands from Tables 15.24 and 15.25 (\square markers) against the maximum incremental velocity (MIV) of the ground motion records (see Tables 14.2 and 14.1), where the dashed and solid horizontal lines represent the design estimate (from Chapter 12) and the mean peak coupling beam chord rotation demand, respectively, for each data set. It is observed that the coupling beam chord rotation demands tend to follow similar trends to the coupled wall roof drift demands in Fig. 15.2.

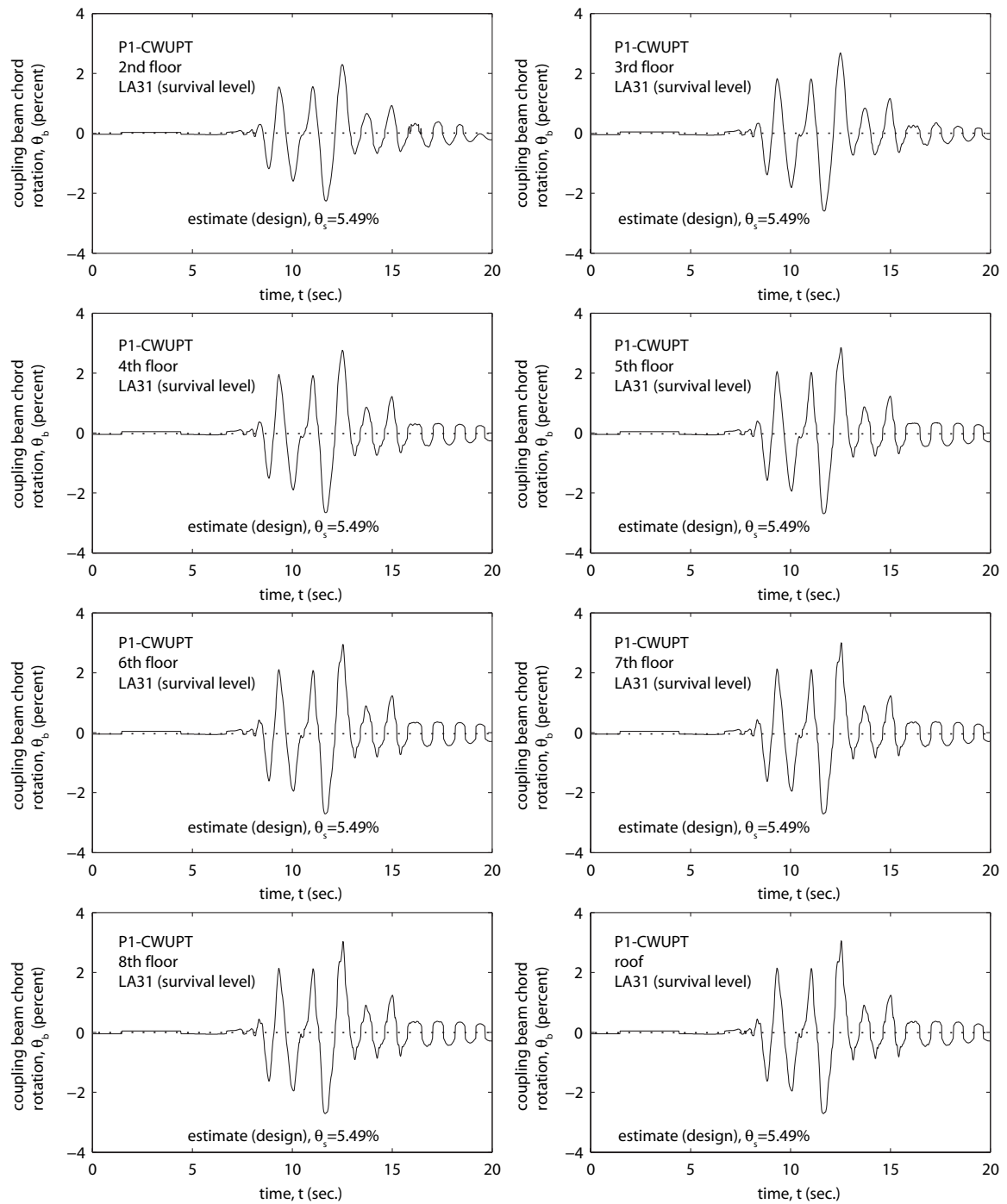


Fig. 15.20 Coupling beam chord rotation time histories for Structure P1-CWUPT

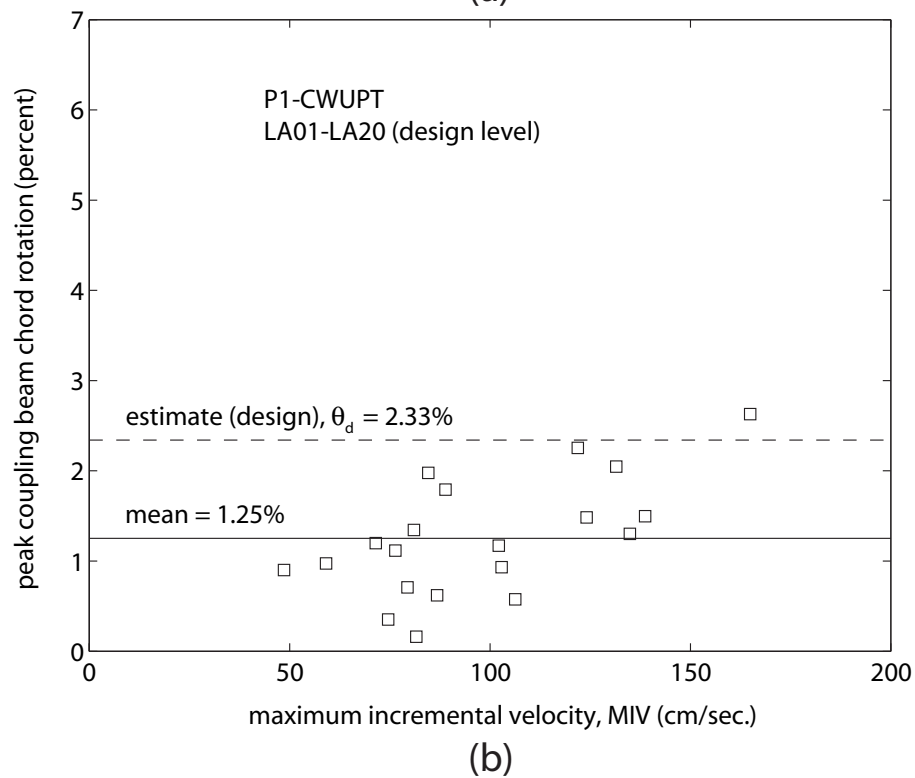
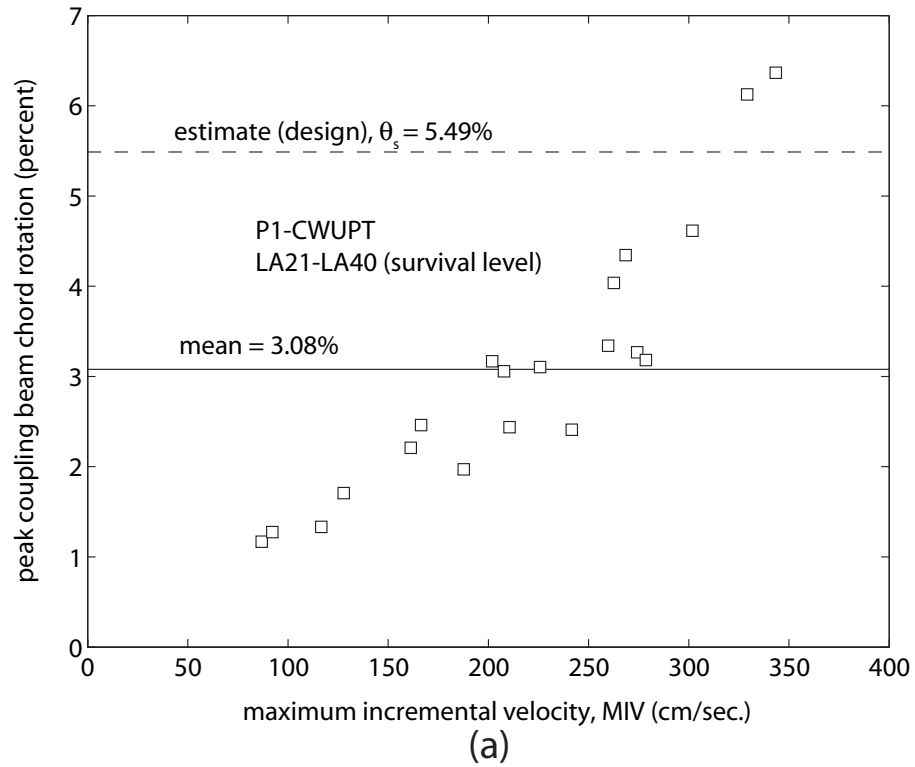


Fig. 15.21 Peak coupling beam chord rotation demands for Structure P1-CWUPT:
(a) survival level; (b) design level

15.2.10 Coupling Beam Axial Forces

The peak axial force demands at the midspan of the coupling beams from the dynamic analyses of Structure P1-CWUPT under the twenty survival-level SAC ground motion records (LA21-LA40) and twenty design-level records (LA01-LA20) are listed in Tables 15.26 and 15.27, respectively. The coupling beam midspan axial forces, N_b are determined directly from the fiber beam-column elements at the beam midspan locations in the analysis model.

TABLE 15.26
PEAK COUPLING BEAM MIDSPAN AXIAL FORCE DEMANDS FOR
STRUCTURE P1-CWUPT UNDER SURVIVAL LEVEL GROUND MOTIONS

ground motion	LA21	LA22	LA23 ^c	LA24	LA25 ^a	LA26	LA27	LA28	LA29	LA30	estimate (design)	standard deviation
peak coupling beam midspan axial force (kN)	4231	4037	3588	3933	4110	4303	4053	4211	3785	4086	4730	257
ground motion	LA31	LA32	LA33	LA34	LA35	LA36 ^b	LA37	LA38	LA39	LA40	mean	standard deviation/mean
peak coupling beam midspan axial force (kN)	4204	4309	4033	4178	4506	4586	4318	4326	3616	4200	4131	0.062

^a The peak demand under this ground motion is closest to the mean demand

^b The peak demand under this ground motion is the largest demand

^c The peak demand under this ground motion is the smallest demand

TABLE 15.27

PEAK COUPLING BEAM MIDSPAN AXIAL FORCE DEMANDS FOR
STRUCTURE P1-CWUPT UNDER DESIGN LEVEL GROUND MOTIONS

ground motion	LA01	LA02	LA03	LA04	LA05	LA06 ^c	LA07	LA08	LA09	LA10 ^b	standard deviation	
peak coupling beam midspan axial force (kN)	4670	3833	3947	3051	3048	2955	3363	3419	3845	5800	744	
ground motion	LA11	LA12	LA13	LA14	LA15	LA16 ^a	LA17	LA18	LA19	LA20	mean	standard deviation/mean
peak coupling beam midspan axial force (kN)	3431	4897	3851	5106	3879	4079	4590	3830	3846	4577	4001	0.19

^a The peak demand under this ground motion is closest to the mean demand

^b The peak demand under this ground motion is the largest demand

^c The peak demand under this ground motion is the smallest demand

As discussed in Chapter 13, the largest coupling beam axial forces develop in the lowest beam at the second floor level as a result of the fixed boundary conditions assumed at the wall pier bases. The mean peak coupling beam midspan axial force demand from the survival-level dynamic analyses in Table 15.26 is 4131 kN, which is reasonably close to and smaller than the design force of, approximately, $1.25P_{by}=4730$ kN from Chapter 12. Thus, the axial force used in Chapter 12 for the design of the coupling beams appears to be valid. Note that the design approach does not require the estimation of the coupling beam axial force under the design-level earthquake; and thus, no design-level estimate is provided in Table 15.27.

As an example, Fig. 15.22 shows the midspan axial force time histories for the eight coupling beams in Structure P1-CWUPT under the survival-level LA25 ground motion, for which the peak coupling beam midspan axial force demand (always occurring in the second floor beam) is closest to the mean demand from the twenty records (see Table 15.26). The dashed horizontal lines indicate the design estimate for the peak

coupling beam midspan axial force, which is equal to $1.25P_{by}$ for the second and third floor beams and P_{by} for the upper level beams. It is observed that the peak midspan axial force demands in the upper level beams are very close to the design estimate. Note also that there is a considerable loss in the second floor beam axial force as discussed in Chapter 13, resulting in a smaller axial force in this beam at the end of the earthquake as compared with the upper level beams.

Fig. 15.23 plots the peak coupling beam midspan axial force demands from Tables 15.26 and 15.27 (\square markers) against the maximum incremental velocity (MIV) of the ground motion records (see Tables 14.2 and 14.1), where the dashed and solid horizontal lines represent the design estimate (from Chapter 12) and the mean peak coupling beam midspan axial force demand, respectively, for each data set. The mean peak coupling beam midspan axial force demands under the survival-level and design-level ground motions are similar; however, the design-level demands show a larger amount of scatter. It is interesting to note that the peak coupling beam midspan axial force demands under some of the design-level ground motion records are larger than the largest axial force demand under the survival-level records.

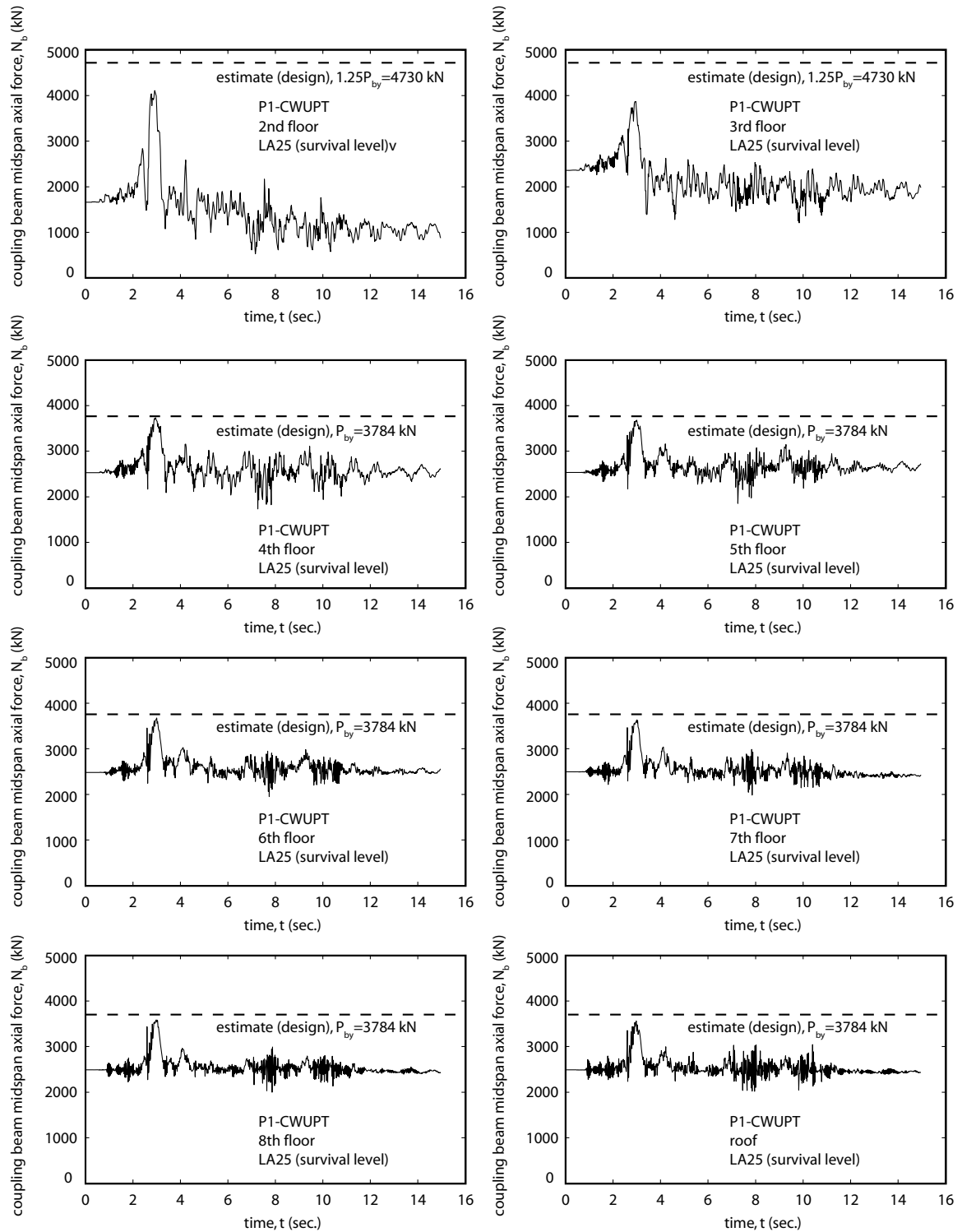
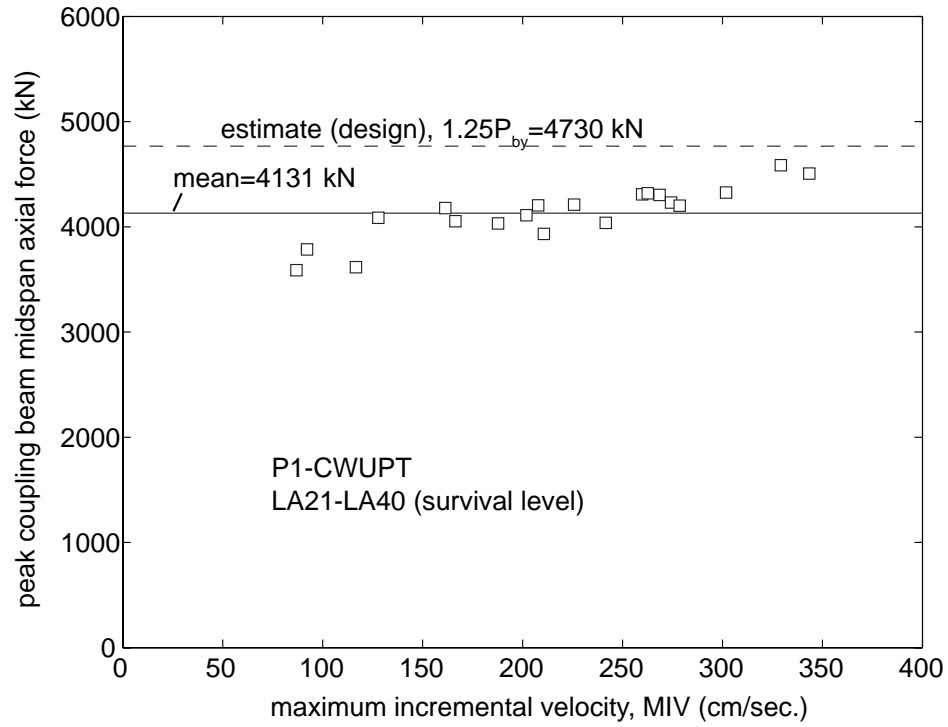
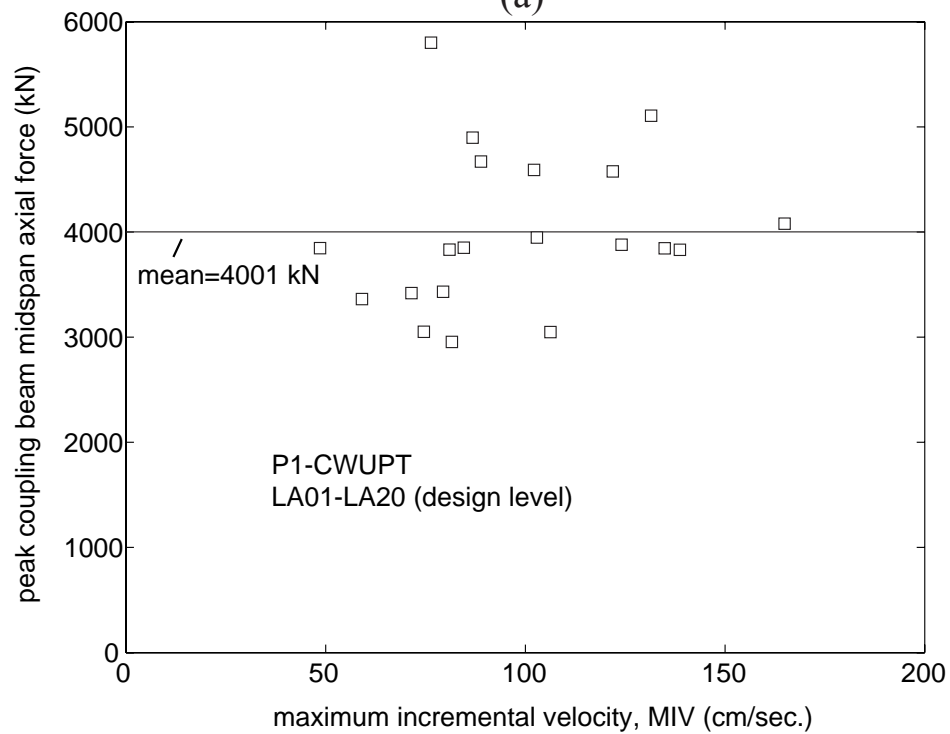


Fig. 15.22 Coupling beam midspan axial force time histories for Structure P1-CWUPT



(a)



(b)

Fig. 15.23 Peak coupling beam midspan axial force demands for Structure P1-CWUPT:
(a) survival level; (b) design level

15.2.11 Coupling Beam Post-Tensioning Forces

The peak coupling beam post-tensioning force demands from the dynamic analyses of Structure P1-CWUPT under the twenty survival-level SAC ground motion records (LA21-LA40) and twenty design-level records (LA01-LA20) are listed in Tables 15.28 and 15.29, respectively. The beam post-tensioning forces, P_b are calculated as the sum of the forces in the truss elements representing the beam post-tensioning tendons at each floor/roof level in the analytical model.

TABLE 15.28
PEAK COUPLING BEAM POST-TENSIONING FORCE DEMANDS FOR
STRUCTURE P1-CWUPT UNDER SURVIVAL LEVEL GROUND MOTIONS

ground motion	LA21	LA22	LA23 ^c	LA24	LA25	LA26	LA27	LA28	LA29	LA30	estimate (design)	standard deviation
peak coupling beam post-tensioning force (kN)	3658	3357	2913	3317	3627	3851	3354	3601	2940	3112	3784	351
ground motion	LA31 ^a	LA32	LA33	LA34	LA35 ^b	LA36	LA37	LA38	LA39	LA40	mean	standard deviation/mean
peak coupling beam post-tensioning force (kN)	3574	3671	3181	3285	4052	4022	3820	3877	2976	3611	3490	0.10

^a The peak demand under this ground motion is closest to the mean demand

^b The peak demand under this ground motion is the largest demand

^c The peak demand under this ground motion is the smallest demand

TABLE 15.29

PEAK COUPLING BEAM POST-TENSIONING FORCE DEMANDS FOR
STRUCTURE P1-CWUPT UNDER DESIGN LEVEL GROUND MOTIONS

ground motion	LA01	LA02 ^a	LA03	LA04	LA05	LA06 ^c	LA07	LA08	LA09	LA10	standard deviation	
peak coupling beam post-tensioning force (kN)	2914	2968	3038	2642	2704	2634	2851	2926	3009	2897	204	
ground motion	LA11	LA12	LA13	LA14	LA15	LA16 ^b	LA17	LA18	LA19	LA20	mean	standard deviation/mean
peak coupling beam post-tensioning force (kN)	2865	2901	3201	3212	3027	3431	2908	3030	2867	3302	2966	0.069

^a The peak demand under this ground motion is closest to the mean demand

^b The peak demand under this ground motion is the largest demand

^c The peak demand under this ground motion is the smallest demand

The mean peak coupling beam post-tensioning force demand from the survival-level dynamic analyses in Table 15.28 is close to and smaller than the total yield force of the coupling beam post-tensioning tendons, $P_{by}=3784$ kN from Chapter 12; and thus, the yielding of the beam post-tensioning tendons is prevented as required by design. As an example, Fig. 15.24 shows the post-tensioning force time histories for the eight coupling beams in Structure P1-CWUPT under the survival-level LA31 ground motion, for which the peak coupling beam post-tensioning force demand (occurring in the roof beam) is closest to the mean demand from the twenty records (see Table 15.28). The dashed horizontal lines indicate the total yield force of the coupling beam post-tensioning tendons, P_{by} . It is observed that there is almost no loss in the coupling beam post-tensioning forces during the ground motion since the tendons do not to yield. The smallest post-tensioning force develops in the second floor coupling beam, since the fixed foundation conditions at the bases of the wall piers restrain the opening of gaps at

the beam ends, and thus, limit the elongation of the post-tensioning tendons during the ground motion.

Fig. 15.25 plots the peak coupling beam post-tensioning force demands from Tables 15.28 and 15.29 (\square markers) against the maximum incremental velocity (MIV) of the ground motion records (see Tables 14.2 and 14.1), where the dashed and solid horizontal lines represent the design estimate (from Chapter 12) and the mean peak coupling beam post-tensioning force demand, respectively, for each data set. It is observed that yielding of the coupling beam post-tensioning tendons occurs under some of the survival-level ground motion records, since the design roof drift from Chapter 12 is exceeded (see Fig. 15.2).

15.2.12 Coupling Beam Shear Forces

The peak coupling beam shear force demands from the dynamic analyses of Structure P1-CWUPT under the twenty survival-level SAC ground motion records (LA21-LA40) and twenty design-level records (LA01-LA20) are listed in Tables 15.30 and 15.31, respectively. The coupling beam shear forces, V_b are calculated based on the equilibrium of the wall pier floor/roof level applied gravity loads and the wall pier axial forces above and below each floor/roof level as determined from the fiber beam-column elements used for the wall piers in the analytical model.

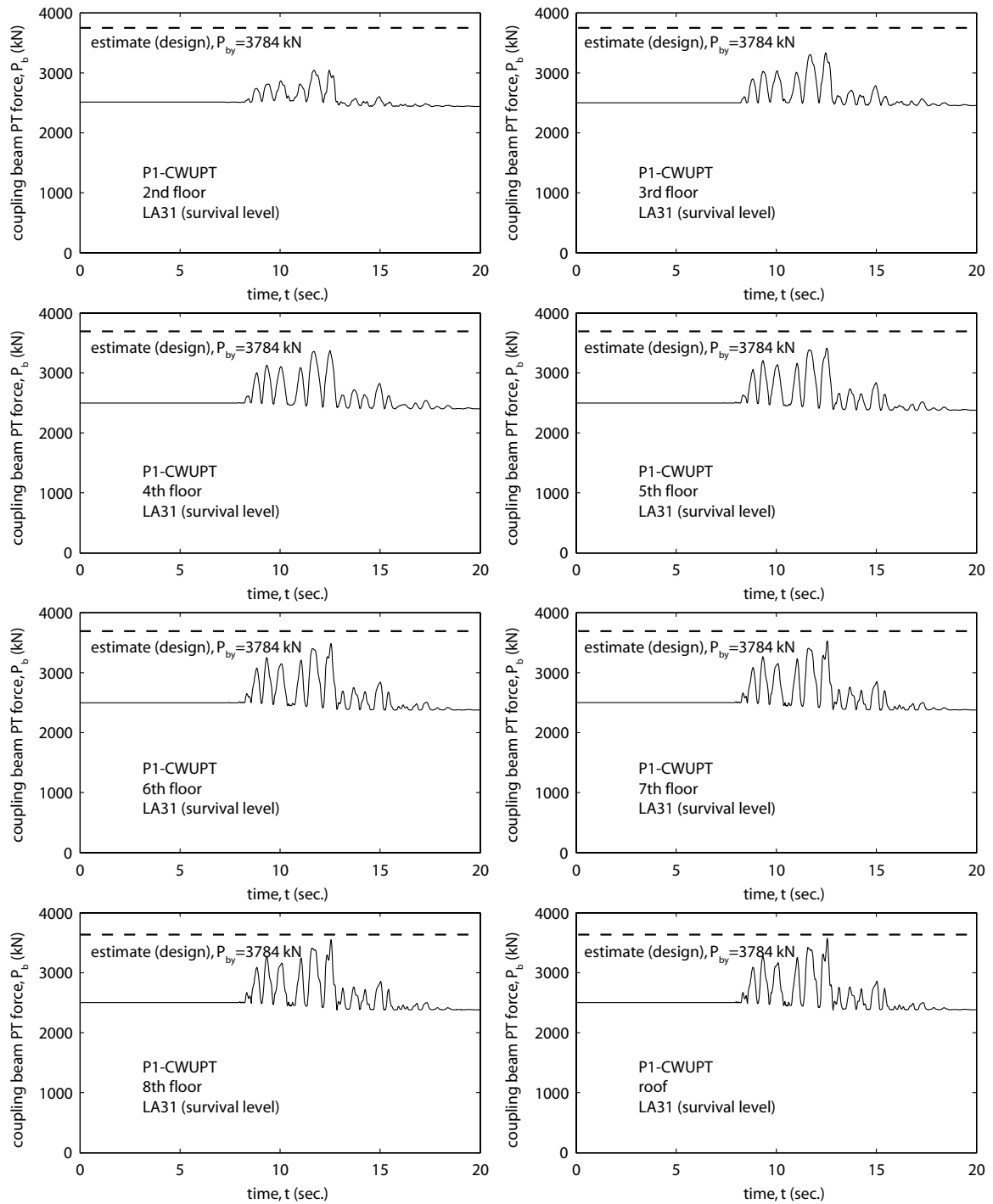
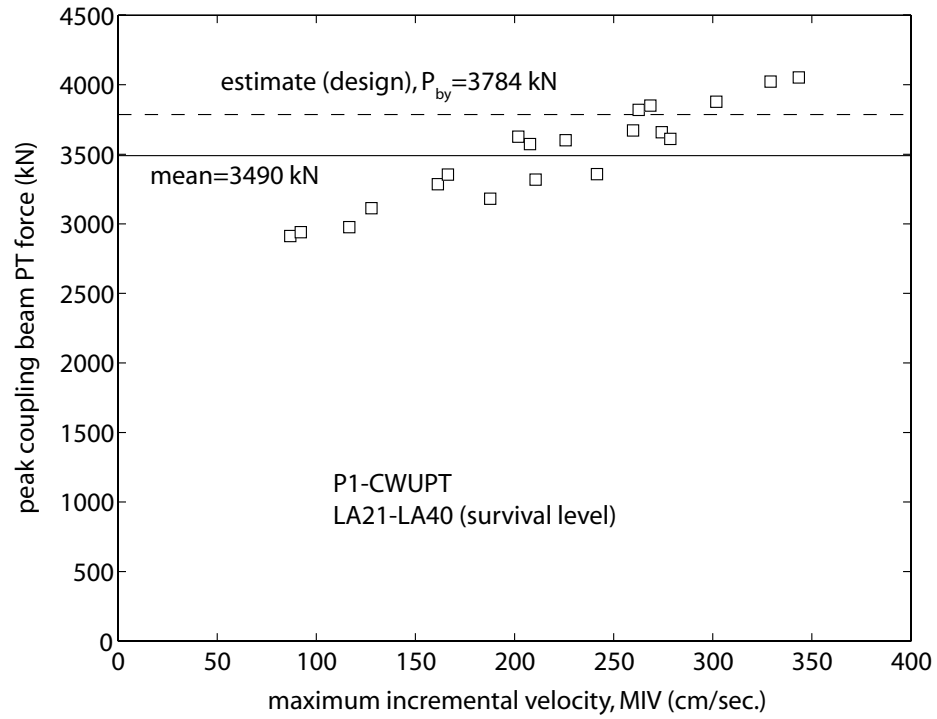
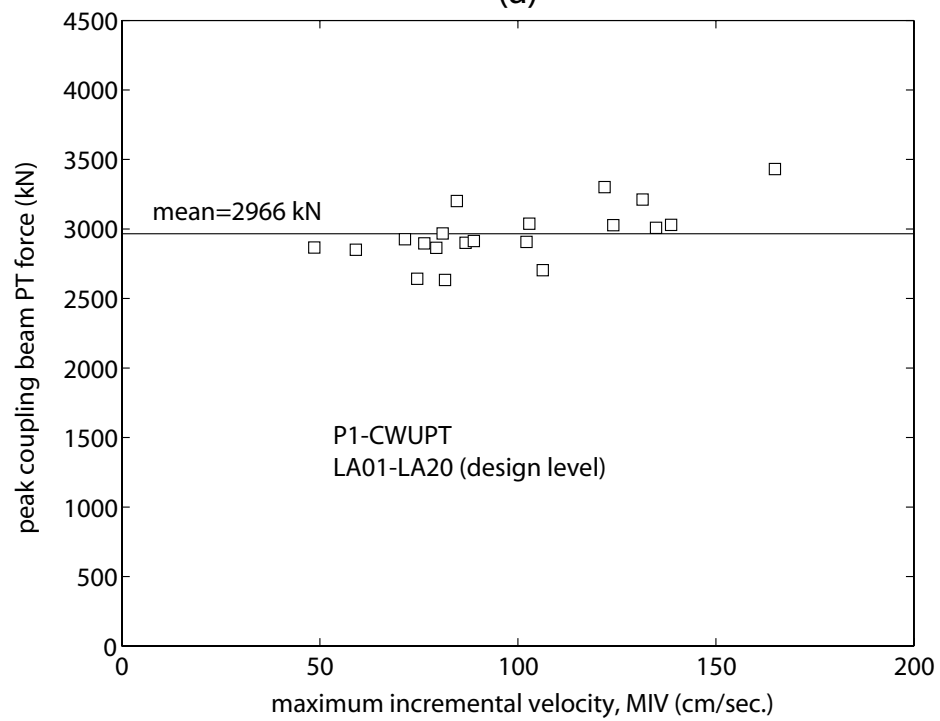


Fig. 15.24 Coupling beam post-tensioning force time histories for Structure P1-CWUPT



(a)



(b)

Fig. 15.25 Peak coupling beam post-tensioning force demands for Structure P1-CWUPT:
(a) survival level; (b) design level

TABLE 15.30

PEAK COUPLING BEAM SHEAR FORCE DEMANDS FOR STRUCTURE

P1-CWUPT UNDER SURVIVAL LEVEL GROUND MOTIONS

ground motion	LA21	LA22 ^b	LA23	LA24	LA25	LA26	LA27	LA28 ^a	LA29	LA30	estimate (design)	standard deviation
peak coupling beam shear force (kN)	1432	1659	1101	1115	1210	1335	1103	1232	1140	1145	963	151
ground motion	LA31	LA32	LA33	LA34	LA35	LA36	LA37	LA38	LA39 ^c	LA40	mean	standard deviation/mean
peak coupling beam shear force (kN)	1286	1152	1115	1141	1375	1423	1156	1136	1087	1114	1223	0.12

^a The peak demand under this ground motion is closest to the mean demand

^b The peak demand under this ground motion is the largest demand

^c The peak demand under this ground motion is the smallest demand

TABLE 15.31

PEAK COUPLING BEAM SHEAR FORCE DEMANDS FOR STRUCTURE

P1-CWUPT UNDER DESIGN LEVEL GROUND MOTIONS

ground motion	LA01	LA02	LA03	LA04	LA05	LA06 ^c	LA07	LA08	LA09 ^a	LA10	standard deviation	
peak coupling beam shear force (kN)	1089	1133	1127	1050	1057	1019	1093	1086	1098	1059	63	
ground motion	LA11	LA12	LA13	LA14	LA15	LA16	LA17	LA18	LA19 ^b	LA20	mean	standard deviation/mean
peak coupling beam shear force (kN)	1107	1129	1091	1055	1065	1161	1067	1051	1314	1158	1100	0.057

^a The peak demand under this ground motion is closest to the mean demand

^b The peak demand under this ground motion is the largest demand

^c The peak demand under this ground motion is the smallest demand

The peak coupling beam shear force demands in Tables 15.30 and 15.31 always occur in the second floor beam. The mean peak beam shear force demand from the survival-level dynamic analyses in Table 15.30 is 1223 kN, which is considerably larger than the estimated demand of $Q_{b,max}=1.25V_{b,pty}=963$ kN from Chapter 12. Thus, the force used in Chapter 12 for the shear slip design of the coupling beam-to-wall interfaces does not appear to be valid for the second floor level. Note that the design approach does not require the estimation of the coupling shear force under the design-level earthquake; and thus, no design-level estimate is provided in Table 15.31.

As an example, Fig. 15.26 shows the shear force time histories for the eight coupling beams in Structure P1-CWUPT under the survival-level LA28 ground motion, for which the peak coupling shear force demand (occurring in the second floor beam) is closest to the mean demand from the twenty records (see Table 15.30). The dashed horizontal lines indicate the design estimate for the coupling beam shear force, $Q_{b,max}$ from Chapter 12, which is equal to $1.25V_{b,pty}$ for the second and third floor beams and $V_{b,pty}$ for the upper level beams. It is observed that the peak shear force demands in the upper level beams also exceed the design estimate. Since the coupling beam shear forces from the static analyses in Chapter 13 are estimated reasonably well by the proposed approximate procedures, the underestimation in the dynamic analysis results may be due to the effect of higher modes on the peak coupling beam shear force demands; however this was not investigated.

Fig. 15.27 plots the peak coupling beam shear force demands from Tables 15.30 and 15.31 (\square markers) against the maximum incremental velocity (MIV) of the ground

motion records (see Tables 14.2 and 14.1), where the dashed and solid horizontal lines represent the design estimate (from Chapter 12) and the mean peak coupling beam shear force demand, respectively for each data set. It is observed that there is considerable scatter in the peak coupling beam shear force demands under the survival-level ground motions but not so much scatter under the design-level ground motions.

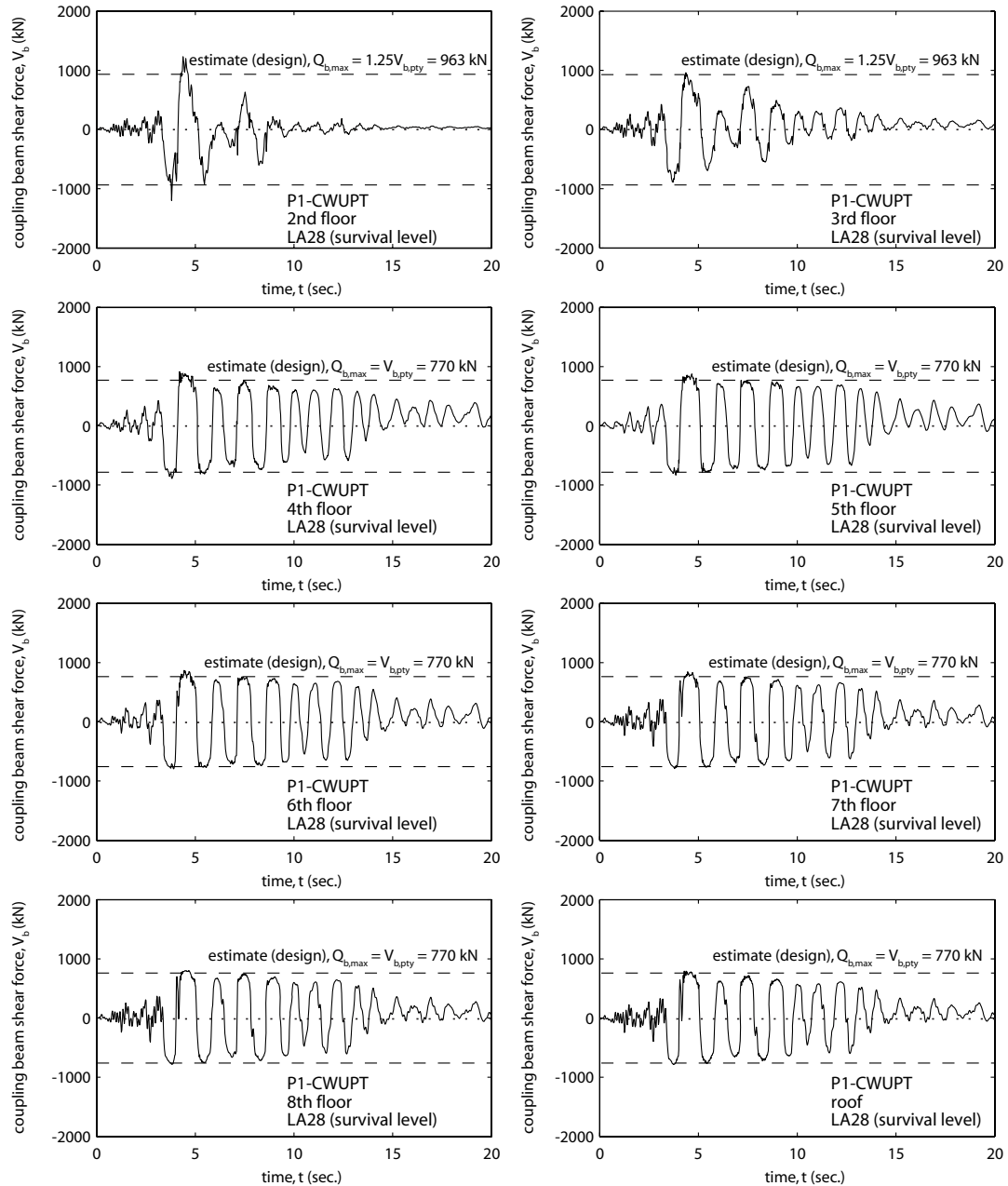
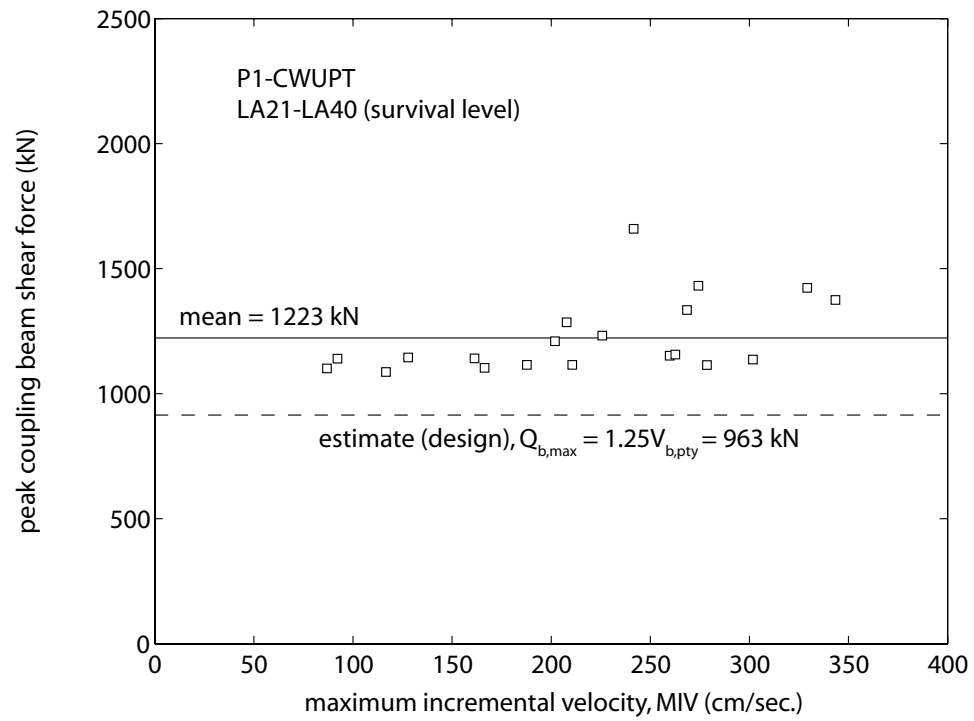
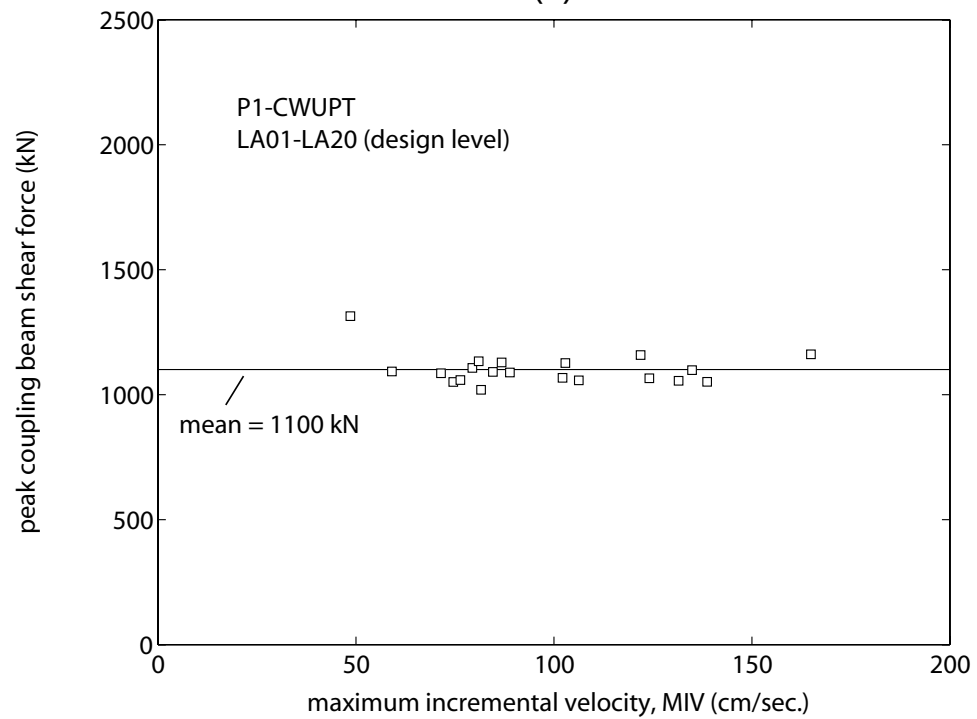


Fig. 15.26 Coupling beam shear force time histories for Structure P1-CWUPT



(a)



(b)

Fig. 15.27 Peak coupling beam shear force demands for Structure P1-CWUPT:
(a) survival level; (b) design level

15.2.13 Coupling Beam Shear Slip Failure

The minimum coupling beam shear slip capacity to shear force demand ratio from the dynamic analyses of Structure P1-CWUPT under the twenty survival-level SAC ground motion records (LA21-LA40) and twenty design-level records (LA01-LA20) are listed in Tables 15.32 and 15.33, respectively. The coupling beam shear slip capacity is computed as $V_{b,ss} = V_{p,ss} + V_{a,ss}$ where, $V_{a,ss}$ is the slip capacity from the top and seat angle-to-wall connections determined as described in Chapter 12 and $V_{p,ss}$ is the slip capacity due to the beam axial force calculated as the axial force at the beam end, C_b times the assumed coefficient of friction, $\mu_{bw} = 0.33$. Note that the axial force at the beam ends is larger than the axial force at the beam midspan as a result of the top and seat angle forces. The beam end axial forces are determined directly from the fiber beam-column elements at the beam ends in the analysis model. The coupling beam shear slip capacity, $V_{b,ss}$ varies with time during an earthquake since $V_{p,ss}$ due to the beam axial force varies. The slip capacity from the top and seat angle-to-wall connections, $V_{a,ss}$ is assumed to remain constant during an earthquake since the integrity of the angle-to-wall connections is assumed to be maintained.

The design estimate for the survival-level minimum coupling beam shear slip capacity to shear force demand ratio in Table 15.32 is determined as the ratio between the design estimates for the coupling beam shear slip capacity, $V_{b,ss}$ and the beam shear force demand, $Q_{b,max}$, from Chapter 12. It is observed that the mean ratio from the survival-level dynamic analysis results is smaller than the design estimate, and thus, the design procedure to prevent shear slip failure at the beam ends is not conservative. This is possibly because of the underestimated coupling beam shear force demands as described previously.

TABLE 15.32

MINIMUM COUPLING BEAM SHEAR SLIP CAPACITY-DEMAND RATIOS FOR
STRUCTURE P1-CWUPT UNDER SURVIVAL LEVEL GROUND MOTIONS

ground motion	LA21	LA22 ^c	LA23	LA24	LA25	LA26	LA27	LA28 ^a	LA29	LA30	estimate (design)	standard deviation
min. beam shear slip capacity-demand ratio	0.75	0.42	1.48	0.99	1.31	1.15	1.40	1.10	1.21	1.27	1.21	0.285
ground motion	LA31	LA32	LA33	LA34	LA35	LA36	LA37	LA38	LA39 ^b	LA40	mean	standard deviation/mean
min. beam shear slip capacity-demand ratio	1.00	0.79	1.12	1.13	0.96	0.85	1.54	1.17	1.55	0.94	1.11	0.26

^a The minimum ratio under this ground motion is closest to the mean ratio

^b The minimum ratio under this ground motion is the largest ratio

^c The minimum ratio under this ground motion is the smallest ratio

TABLE 15.33

MINIMUM COUPLING BEAM SLIP CAPACITY-DEMAND RATIOS FOR
STRUCTURE P1-CWUPT UNDER DESIGN LEVEL GROUND MOTIONS

ground motion	LA01	LA02 ^a	LA03	LA04	LA05	LA06	LA07	LA08	LA09	LA10	standard deviation	
min. beam shear slip capacity-demand ratio	1.17	1.17	1.18	1.18	1.18	1.18	1.18	1.18	1.18	1.18	0.018	
ground motion	LA11	LA12	LA13	LA14	LA15	LA16	LA17	LA18 ^b	LA19 ^c	LA20	mean	standard deviation/mean
min. beam shear slip capacity-demand ratio	1.18	1.16	1.18	1.19	1.18	1.18	1.18	1.19	1.10	1.16	1.17	0.0156

^a The minimum ratio under this ground motion is closest to the mean ratio

^b The minimum ratio under this ground motion is the largest ratio

^c The minimum ratio under this ground motion is the smallest ratio

The mean values of the minimum coupling beam shear slip capacity to shear force demand ratios in Tables 15.32 and 15.33 are both larger than 1.0. Thus, shear slip failure at the ends of the coupling beams in Structure P1-CWUPT, on average, does not occur, even though the design approach underestimates the peak coupling beam shear force demands from the dynamic analyses (see Fig. 15.27).

As an example, Fig. 15.28 shows comparisons between the shear slip capacity (solid lines) and shear force demand (dashed lines) time histories for the eight coupling beams in Structure P1-CWUPT under the survival-level LA28 ground motion, for which the minimum coupling beam shear slip capacity-demand ratio is closest to the mean ratio from the twenty records (see Table 15.32). For comparison, the solid and dashed horizontal lines indicate the design estimates for the coupling beam shear slip capacity, $V_{b,ss}$ and shear force demand, $Q_{b,max}=1.25V_{b,pty}$ (second and third floor level beams) or $Q_{b,max}=V_{b,pty}$ (upper level beams), respectively. As described in Chapter 12, the design estimate for the coupling beam shear slip capacity due to the beam end axial force, $V_{p,ss}$ is computed as the coupling beam initial post-tensioning force, P_{bi} times the assumed coefficient of friction at the beam ends, $\mu_{bw}=0.33$. In addition to the underestimated maximum shear force demands, the design approach seems to overestimate the minimum shear slip capacities from the dynamic analysis, also contributing to the unconservative design to prevent shear slip failure at the beam ends.

It is observed in Fig. 15.28 that the second floor coupling beam shear force demand exceeds the design estimate $Q_{b,max}$; however, shear slip does not occur during the earthquake. This is because, the times during the ground motion when the shear force

demand exceeds the design estimate also correspond to times when the shear slip capacity exceeds the design estimate $V_{b,ss}$ due to significant increases in the beam axial force (which are conservatively ignored in the design approach in Chapter 12). The results in Fig. 15.28 show that shear slip is not critical at the ends of the upper floor coupling beams.

Fig. 15.29 plots the minimum coupling beam shear slip capacity-demand ratios from Tables 15.32 and 15.33 (\square markers) against the maximum incremental velocity (MIV) of the ground motion records (see Tables 14.2 and 14.1), where the dashed and solid horizontal lines represent the design estimate (from Chapter 12) and the mean ratio, respectively, for each data set. Note that while shear slip at the ends of the coupling beams is not expected to occur under any of the design-level ground motion records, shear slip at the ends of the coupling beams (especially the second floor beams) may occur under some of the survival-level ground motion records. It is also interesting to note that there is little scatter or variation in the minimum coupling beam shear slip capacity-demand ratio under the design level ground motions and that the mean ratios under the design-level and survival-level ground motion sets are similar.

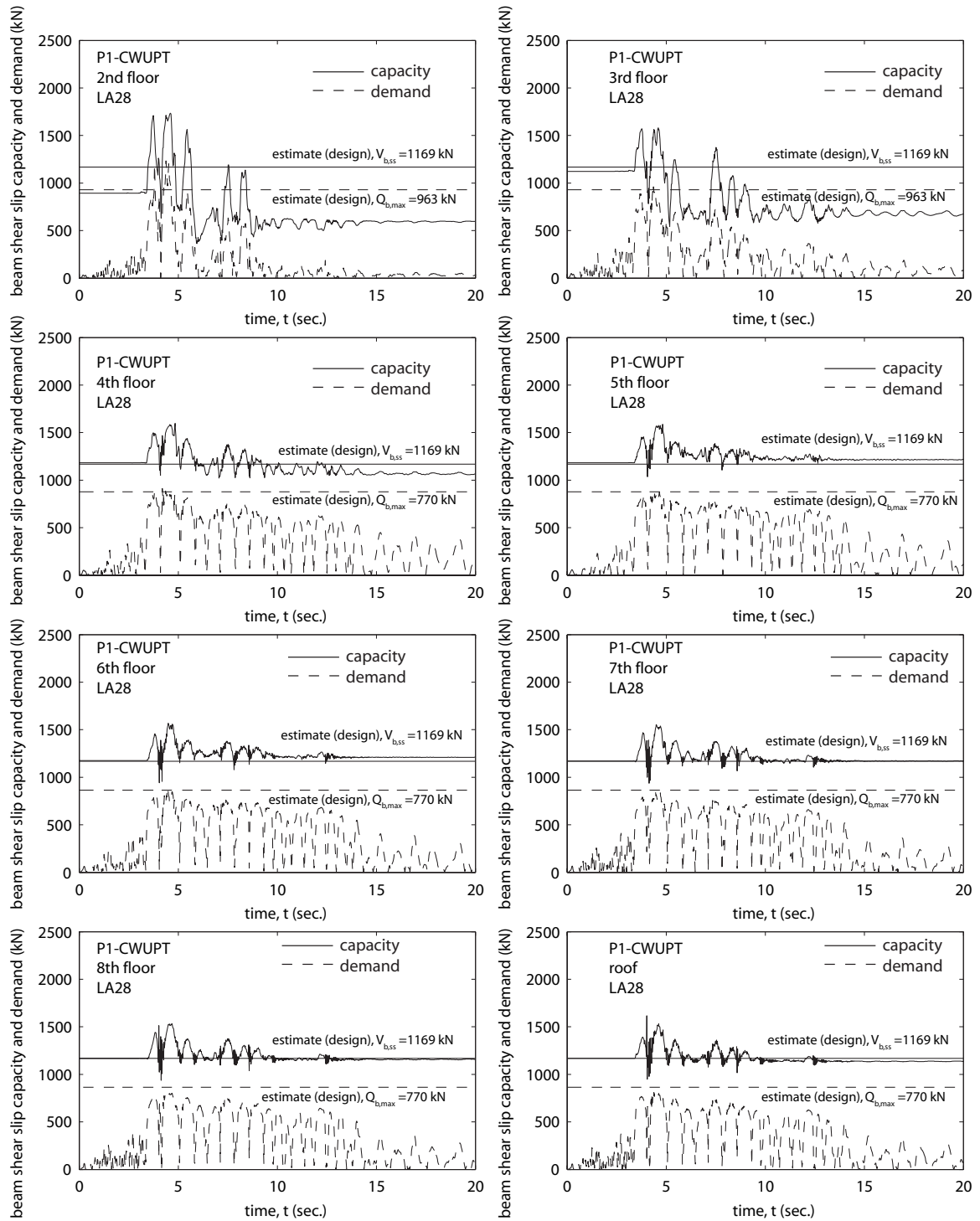
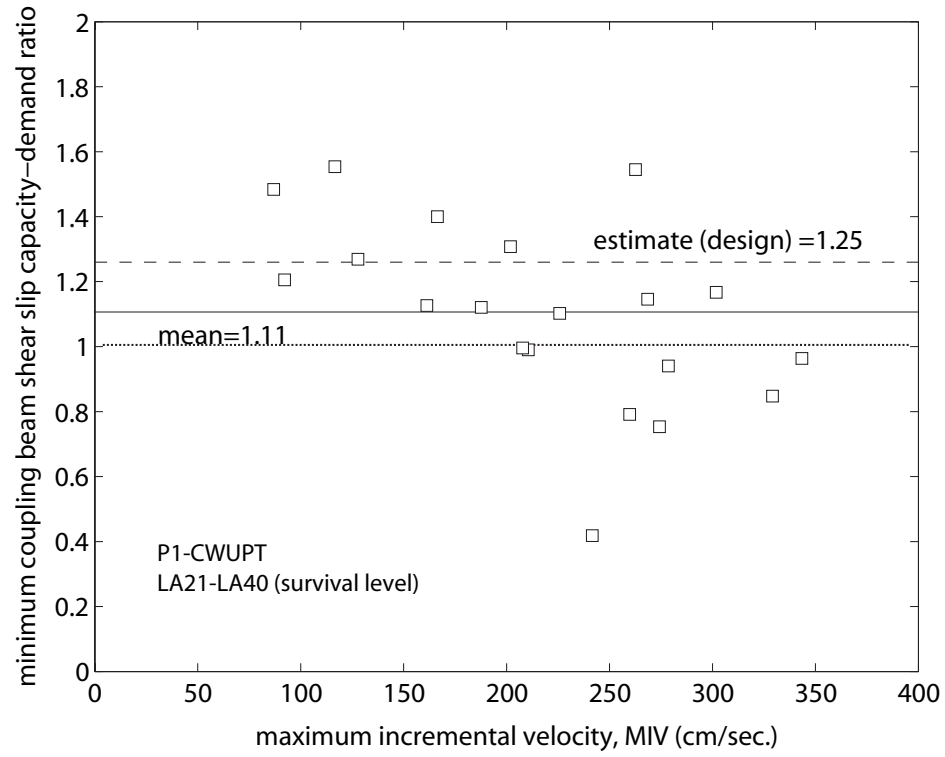
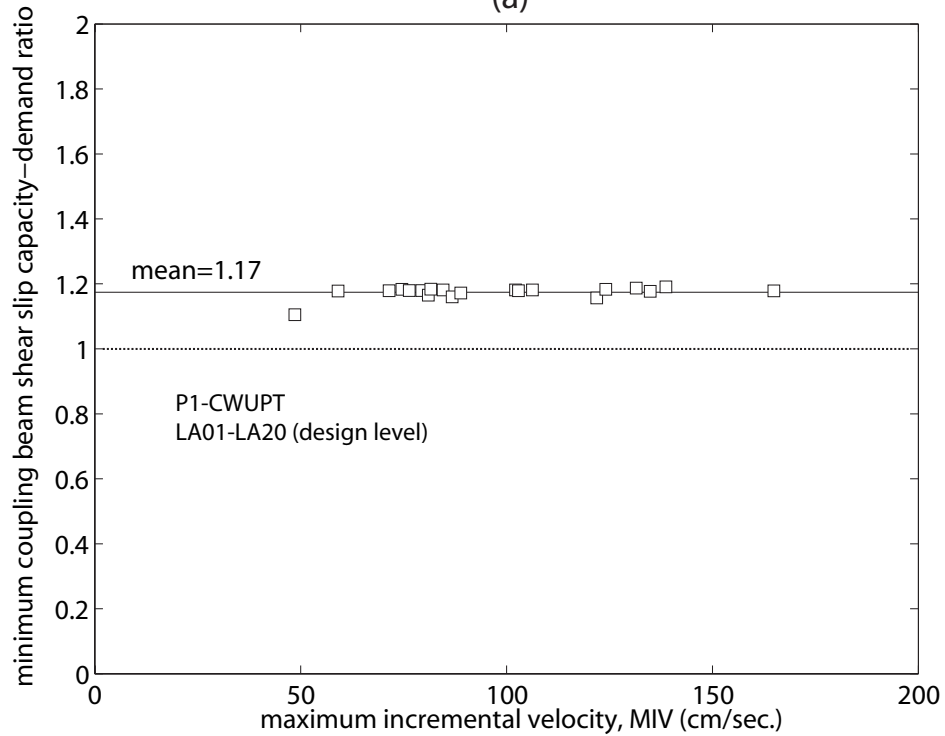


Fig. 15.28 Coupling beam shear slip capacity and shear force demand time histories for Structure P1-CWUPT



(a)



(b)

Fig. 15.29 Minimum coupling beam shear slip capacity to shear force demand ratios for Structure P1-CWUPT: (a) survival level; (b) design level

15.2.14 Angle Deformations

The peak tensile deformation demands in the top and seat connection angles of the coupling beams from the dynamic analyses of Structure P1-CWUPT under the twenty survival-level SAC ground motion records (LA21-LA40) and twenty design-level records (LA01-LA20) are listed in Tables 15.34 and 15.35. The angle deformations, δ_{ax} are determined directly from the horizontal angle elements in the analytical model as the deformations parallel to the coupling beams (i.e., horizontal displacement of angle heel from wall).

TABLE 15.34
PEAK ANGLE TENSILE DEFORMATION DEMANDS FOR STRUCTURE
P1-CWUPT UNDER SURVIVAL LEVEL GROUND MOTIONS

ground motion	LA21	LA22	LA23 ^c	LA24	LA25	LA26	LA27	LA28 ^a	LA29	LA30	estimate (design)	standard deviation
peak angle tensile deformation (mm)	35	26	12	25	34	46	26	33	14	19	30	15
ground motion	LA31	LA32	LA33	LA34	LA35 ^b	LA36	LA37	LA38	LA39	LA40	mean	standard deviation/mean
peak angle tensile deformation (mm)	33	36	21	24	68	65	43	49	14	33	33	0.47

^a The peak demand under this ground motion is closest to the mean demand

^b The peak demand under this ground motion is the largest demand

^c The peak demand under this ground motion is the smallest demand

TABLE 15.35

PEAK ANGLE TENSILE DEFORMATION DEMANDS FOR STRUCTURE

P1-CWUPT UNDER DESIGN LEVEL GROUND MOTIONS

ground motion	LA01	LA02	LA03	LA04	LA05	LA06 ^c	LA07	LA08 ^a	LA09	LA10	estimate (design)	standard deviation
peak angle tensile deformation (mm)	19	14	10	4	6	2	10	13	14	12	13	7
ground motion	LA11	LA12	LA13	LA14	LA15	LA16 ^b	LA17	LA18	LA19	LA20	mean	standard deviation/mean
peak angle tensile deformation (mm)	8	7	21	22	16	28	12	16	10	24	13	0.52

^a The peak demand under this ground motion is closest to the mean demand

^b The peak demand under this ground motion is the largest demand

^c The peak demand under this ground motion is the smallest demand

The mean peak angle tensile deformation demand from the survival-level dynamic analyses in Table 15.34 is 33 mm, which is larger than the estimated deformation of $u_{as}=30$ mm from Chapter 12, despite the over-estimated coupling beam chord rotation demands in Fig. 15.21. Thus, the method used in Chapter 12 to estimate the angle deformations needs to be improved.

As an example, Fig. 15.30 shows the deformation time histories, δ_{ax} for the bottom (i.e., seat) angles at the left ends of the eight coupling beams in Structure P1-CWUPT under the survival-level LA28 ground motion, for which the peak angle tensile deformation demand (occurring in the roof beam) is closest to the mean demand from the twenty records (see Table 15.34). The dashed horizontal lines indicate the design estimate for the peak angle tensile deformation, u_{as} , from Chapter 12.

Fig. 15.31 plots the peak angle tensile deformation demands from Tables 15.34 and 15.35 (\square markers) against the maximum incremental velocity (MIV) of the ground motion records (see Tables 14.2 and 14.1), where the dashed and solid horizontal lines represent the design estimate (from Chapter 12) and the mean peak angle tensile deformation demand, respectively, for each data set. It is observed that the peak angle tensile deformation demands tend to follow similar trends to the peak coupled wall roof drift demands in Fig. 15.2 and the peak coupling beam chord rotation demands in Fig. 15.21.

15.3 Structure P2-PWUPT

This section discusses the results from the nonlinear dynamic time-history analyses of Structure P2-PWUPT as follows: (1) floor/roof drifts; (2) inter-story drifts; (3) floor/roof accelerations; (4) wall post-tensioning forces; (5) wall base axial forces; (6) wall base shear forces; (7) wall base diagonal tension and shear slip failure; (8) wall base moments; (9) wall base strains; (10) coupling beam chord rotations; (11) coupling beam axial forces; (12) coupling beam post-tensioning forces; (13) coupling beam shear forces failure; (14) coupling beam shear slip failure; and (15) angle deformations.

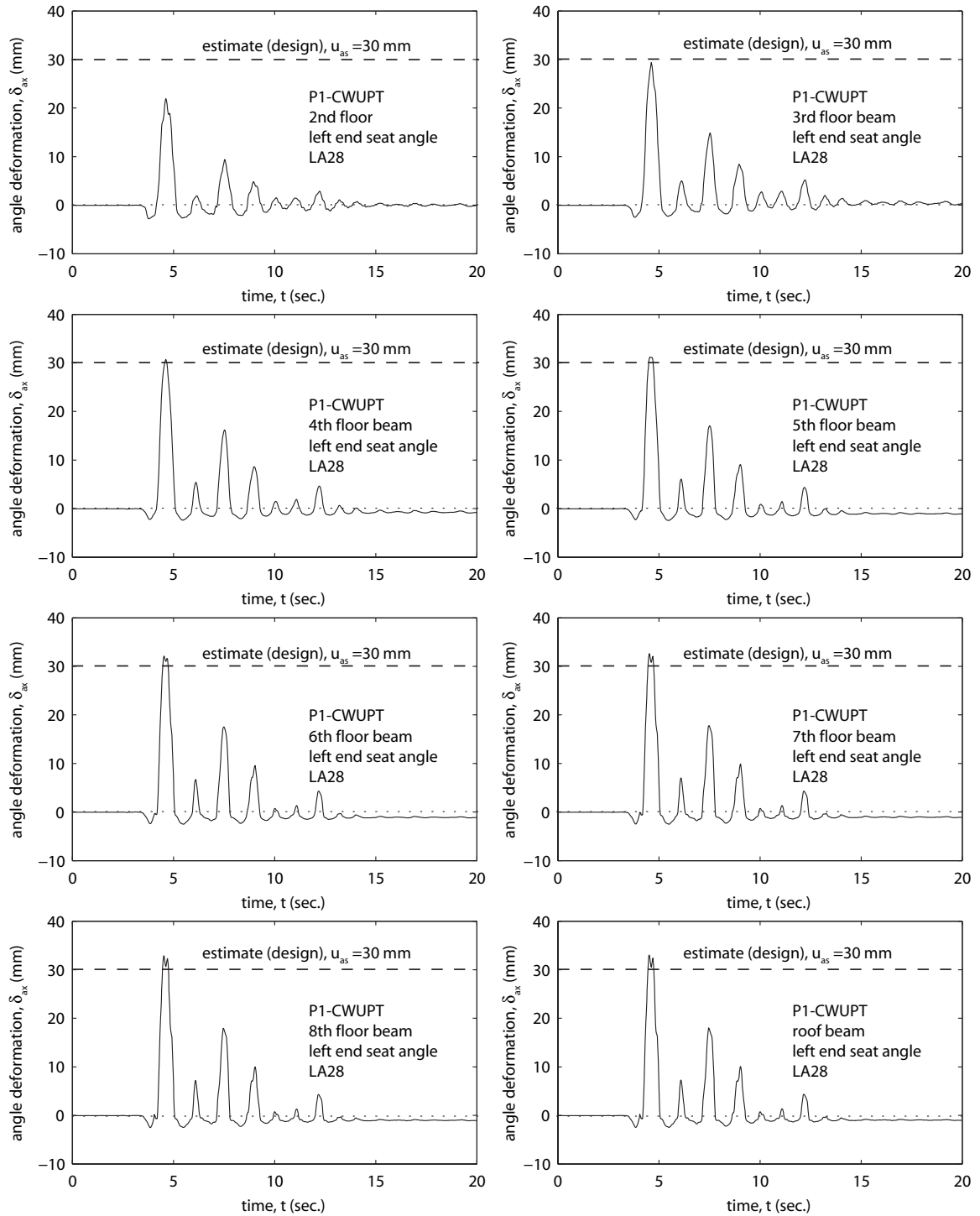
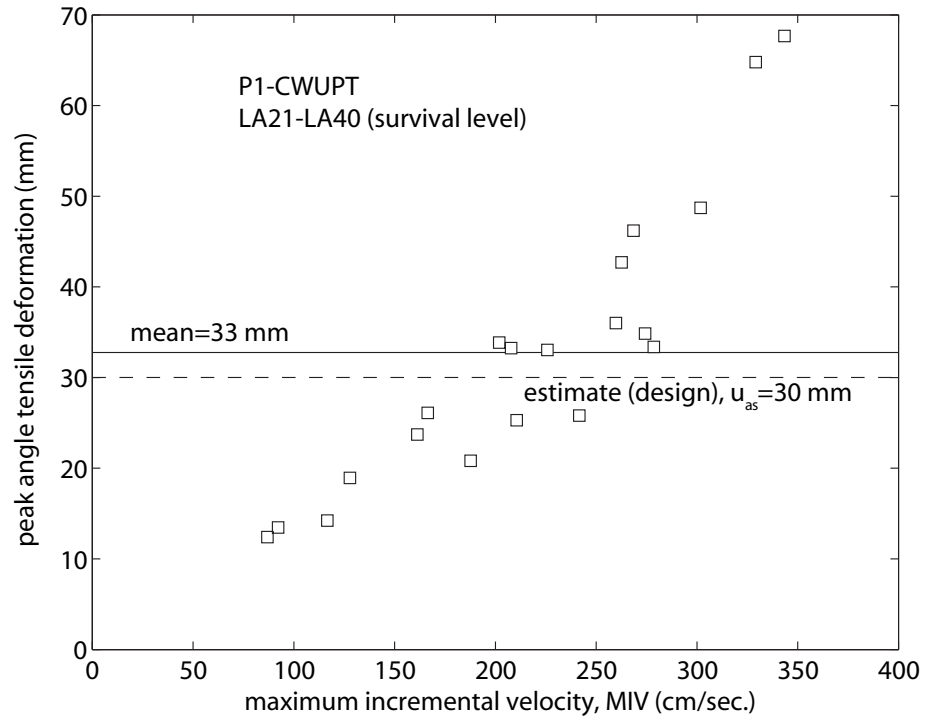
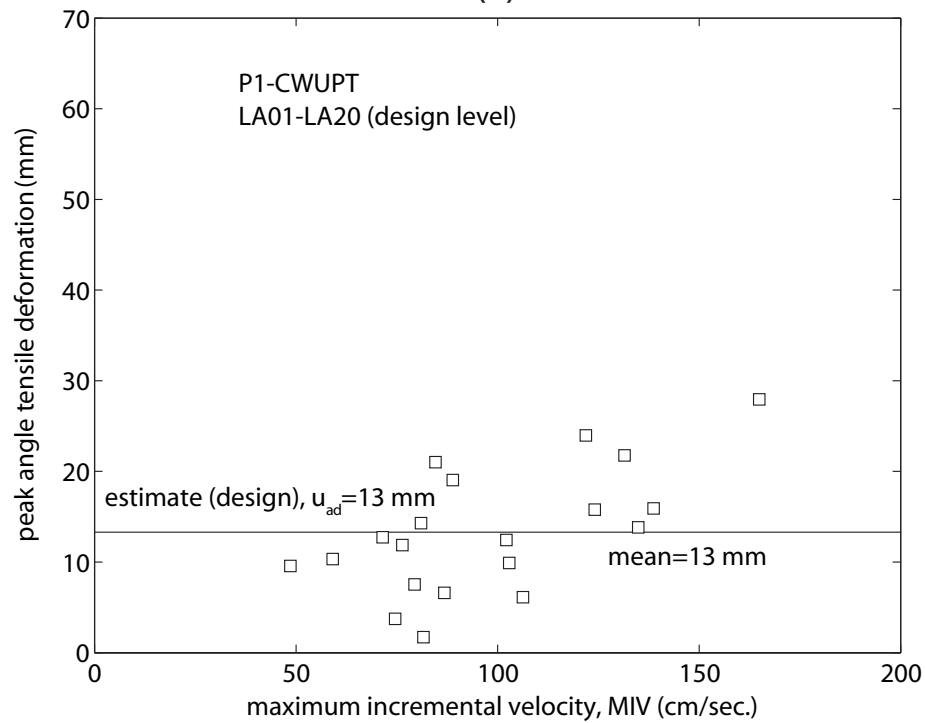


Fig. 15.30 Coupling beam connection angle deformation time histories for Structure P1-CWUPT



(a)



(b)

Fig. 15.31 Peak coupling beam connection angle tensile deformation demands for Structure P1-CWUPT: (a) survival level; (b) design level

15.3.1 Floor/Roof Drifts

The peak coupled wall roof drift demands from the dynamic analyses of Structure P2-PWUPT under the twenty survival-level SAC ground motion records (LA21-LA40) and twenty design-level records (LA01-LA20) are listed in Tables 15.36 and 15.37, respectively. As described before, the roof drift, Δ is calculated as the average lateral displacement of the left and right wall piers at the roof divided by the wall height to the base, h_w .

The mean peak roof drift demand from the survival-level dynamic analyses in Table 15.36 is 1.84%, which is close to the estimated survival-level roof drift demand of $\Delta_s=1.71\%$ and the allowable target roof drift demand of $\Delta_{ts}=1.75\%$ from Chapter 12. As an example, Fig. 15.32 shows the roof drift time-history of Structure P2-PWUPT under the LA24 ground motion, for which the peak roof drift demand is closest to the mean demand from the twenty records (see Table 15.37). The dashed horizontal lines indicate the design estimate for the peak roof drift demand, Δ_s from Chapter 12.

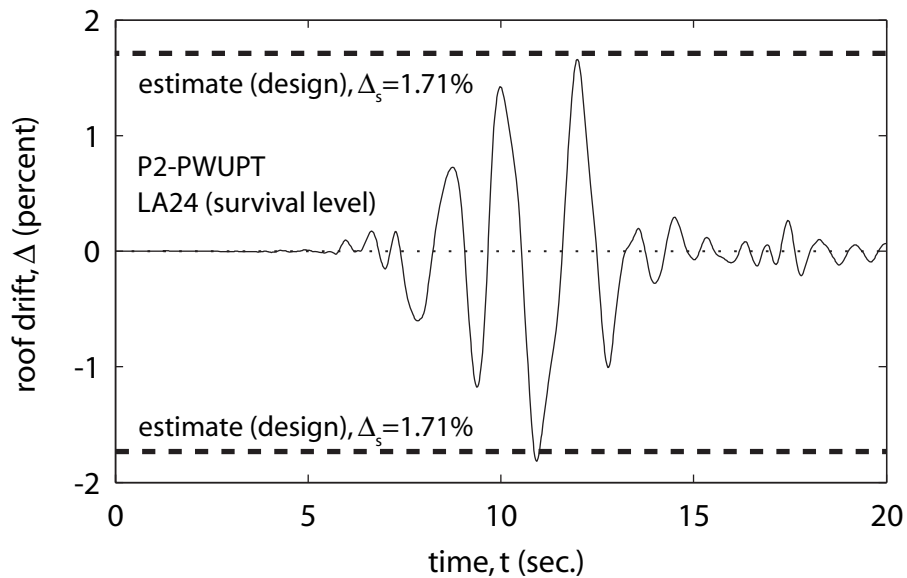


Fig. 15.32 Roof drift time history for Structure P2-PWUPT

TABLE 15.36

PEAK ROOF DRIFT DEMANDS FOR STRUCTURE P2-PWUPT

UNDER SURVIVAL LEVEL GROUND MOTIONS

ground motion	LA21	LA22	LA23	LA24 ^a	LA25	LA26	LA27	LA28	LA29	LA30	estimate (design)	standard deviation
peak roof drift (%)	2.80	1.47	0.73	1.81	1.72	2.53	1.31	2.16	0.84	0.97	1.71	0.84
ground motion	LA31	LA32	LA33	LA34	LA35	LA36 ^b	LA37	LA38	LA39 ^c	LA40	mean	standard deviation/mean
peak roof drift (%)	2.29	2.31	1.48	1.04	3.38	3.56	2.08	2.34	0.67	1.53	1.84	0.45

^a The peak demand under this ground motion is closest to the mean demand

^b The peak demand under this ground motion is the largest demand

^c The peak demand under this ground motion is the smallest demand

TABLE 15.37

PEAK ROOF DRIFT DEMANDS FOR STRUCTURE P2-PWUPT

UNDER DESIGN LEVEL GROUND MOTIONS

ground motion	LA01	LA02 ^a	LA03	LA04	LA05	LA06 ^c	LA07	LA08	LA09	LA10	estimate (design)	standard deviation
peak roof drift (%)	0.69	0.76	0.74	0.31	0.35	0.28	0.53	0.58	1.03	0.61	0.79	0.30
ground motion	LA11	LA12	LA13	LA14	LA15	LA16 ^b	LA17	LA18	LA19	LA20	mean	standard deviation/mean
peak roof drift (%)	0.62	0.55	1.03	1.16	0.85	1.46	0.88	0.84	0.61	1.07	0.75	0.40

^a The peak demand under this ground motion is closest to the mean demand

^b The peak demand under this ground motion is the largest demand

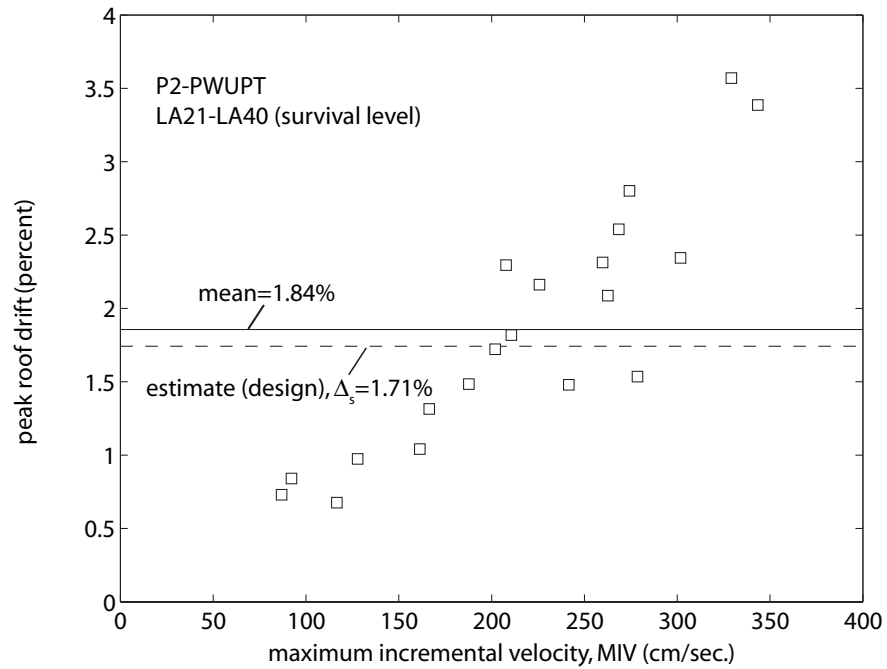
^c The peak demand under this ground motion is the smallest demand

Comparing Fig. 15.32 for Structure P2-PWUPT with Fig. 15.1 for Structure P1-CWUPT, it is observed that the oscillations of both structures are generally centered around the original zero-drift position; however, Structure P2-PWUPT appears to have a slightly larger self-centering capability than Structure P1-CWUPT. This is also true under

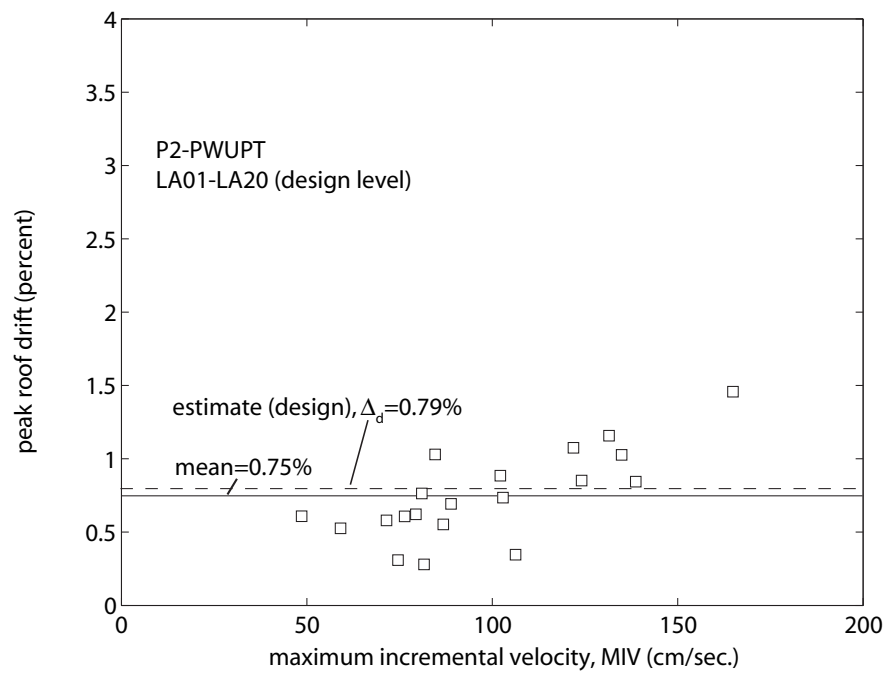
the other ground motion records included in the investigation. The increased self-centering capability in Structure P2-PWUPT occurs as a result of the post-tensioning steel used as flexural reinforcement in the precast concrete wall piers.

The mean peak roof drift demand from the design-level analyses of Structure P2-PWUPT in Table 15.37 is 0.75%, which is close to the estimated design-level roof drift demand of $\Delta_d=0.79\%$ and smaller than the allowable target roof drift demand of $\Delta_{td}=1.17\%$ from Chapter 12. As for Structure P1-CWUPT, it is concluded that the displacement-based design objectives for Structure P2-PWUPT under the survival-level and design-level ground motions are, on average, satisfied.

Fig. 15.33 plots the peak coupled wall roof drift demands from Tables 15.36 and 15.37 (\square markers) against the maximum incremental velocity (MIV) of the ground motion records (see Tables 14.2 and 14.1 for the MIV values of the LA21-LA40 and the LA01-LA20 records, respectively), where the dashed and solid horizontal lines represent the design estimate (from Chapter 12) and the mean peak roof drift demand, respectively, for each data set. Similar to Structure P1-CWUPT, it is observed that the peak roof drift demands for Structure P2-PWUPT tend to be larger under ground motions with larger MIV (i.e., there seems to be a correlation between MIV and the peak roof drift demand, especially for the survival-level records). Furthermore, there is a significant amount of scatter in the data indicating that, while the design objectives are satisfied on average, the peak roof drift demand may be significantly larger or significantly smaller than the design estimate, depending on the earthquake. This is investigated in more detail in Kurama and Farrow (2003).



(a)



(b)

Fig. 15.33 Peak roof drift demands for Structure P2-PWUPT:
(a) survival level; (b) design level

15.3.2 Inter-Story Drifts

The peak coupled wall inter-story drift demands from the dynamic analyses of Structure P2-PWUPT under the twenty survival-level SAC ground motion records (LA21-LA40) and twenty design-level records (LA01-LA20) are listed in Tables 15.38 and Table 15.39, respectively. The inter-story drift is defined as the relative lateral displacement between two adjacent floor/roof levels in a structure divided by the story height and is calculated as the average inter-story drift of the left and right wall piers.

TABLE 15.38
PEAK INTER-STORY DRIFT DEMANDS FOR STRUCTURE P2-PWUPT
UNDER SURVIVAL LEVEL GROUND MOTIONS

ground motion	LA21	LA22	LA23	LA24 ^a	LA25	LA26	LA27	LA28	LA29	LA30	estimate (design)	standard deviation
peak inter-story drift (%)	2.95	1.76	0.83	2.04	1.91	2.70	1.48	2.36	0.95	1.15	1.97	0.87
ground motion	LA31	LA32	LA33	LA34	LA35	LA36 ^b	LA37	LA38	LA39 ^c	LA40	mean	standard deviation/mean
peak inter-story drift (%)	2.63	2.50	1.64	1.17	3.62	3.80	2.25	2.52	0.81	1.71	2.04	0.43

^a The peak demand under this ground motion is closest to the mean demand

^b The peak demand under this ground motion is the largest demand

^c The peak demand under this ground motion is the smallest demand

TABLE 15.39

PEAK INTER-STORY DRIFT DEMANDS FOR STRUCTURE P2-PWUPT
UNDER DESIGN LEVEL GROUND MOTIONS

ground motion	LA01	LA02 ^a	LA03	LA04	LA05	LA06 ^c	LA07	LA08	LA09	LA10	estimate (design)	standard deviation
peak inter-story drift (%)	0.83	0.89	0.83	0.38	0.42	0.35	0.61	0.70	1.18	0.71	0.90	0.34
ground motion	LA11	LA12	LA13	LA14	LA15	LA16 ^b	LA17	LA18	LA19	LA20	mean	standard deviation/mean
peak inter-story drift (%)	0.74	0.78	1.28	1.35	0.99	1.66	1.03	0.95	0.70	1.26	0.88	0.39

^a The peak demand under this ground motion is closest to the mean demand

^b The peak demand under this ground motion is the largest demand

^c The peak demand under this ground motion is the smallest demand

The mean peak inter-story drift demand from the twenty survival-level analyses in Table 15.38 is 2.04%, which is close to the estimated survival-level inter-story drift demand of 1.97% (occurring in the eighth story) from Chapter 12. As an example, Fig. 15.34 shows the inter-story drift time histories of Structure P2-PWUPT under the LA24 ground motion, for which the peak inter-story drift demand is closest to the mean demand from the twenty records (see Table 15.38). It is observed that the drifts of all eight stories are in phase, and thus, the deflected shape of the structure is governed by the first vibration mode. As expected, the peak inter-story drift demand (2.04%) occurs in the eighth (top) story (indicating a flexure dominated deflected shape) and is larger than the corresponding peak roof drift demand of 1.81% from Table 15.36. The dashed horizontal lines show the design estimate for the peak inter-story drift demand in the eighth story from Chapter 12.

The mean peak inter-story drift demand from the twenty design-level analyses in Table 15.39 is 0.88%, which is close to the estimated design-level inter-story drift demand of 0.90% from Chapter 12. As discussed in Chapter 12, according to IBC 2000 (ICC 2000), the peak inter-story drift demand under the design-level ground motion should not exceed 2%. Because of the relatively small allowable target roof drift demands used in design ($\Delta_{ts}=1.75\%$ and $\Delta_{td}=1.17\%$), the peak inter-story drift demands in Tables 15.38 and 15.39 satisfy the 2% limit not only for the design-level ground motions, but also for many of the survival-level motions.

Note that, for both ground motion sets, the ratio between the mean and estimated peak inter-story drift demands is similar to the ratio between the mean and estimated peak roof drift demands. In general, the trends observed for the peak roof drift demands in the previous section are also valid for the peak inter-story drift demands.

Fig. 15.35 plots the peak coupled wall inter-story drift demands from Tables 15.38 and 15.39 (\square markers) against the maximum incremental velocity (MIV) of the ground motion records (see Tables 14.2 and 14.1), where the dashed and solid horizontal lines represent the design estimate (for the eighth story, from Chapter 12) and the mean peak inter-story drift demand, respectively, for each data set. Similar to the peak roof drift demands discussed in the previous section, there is a significant amount of scatter in the peak inter-story drift demands, and the demands tend to be larger under the ground motions with larger MIV (i.e., there seems to be a correlation between MIV and the peak inter-story drift demand, especially for the survival level records).

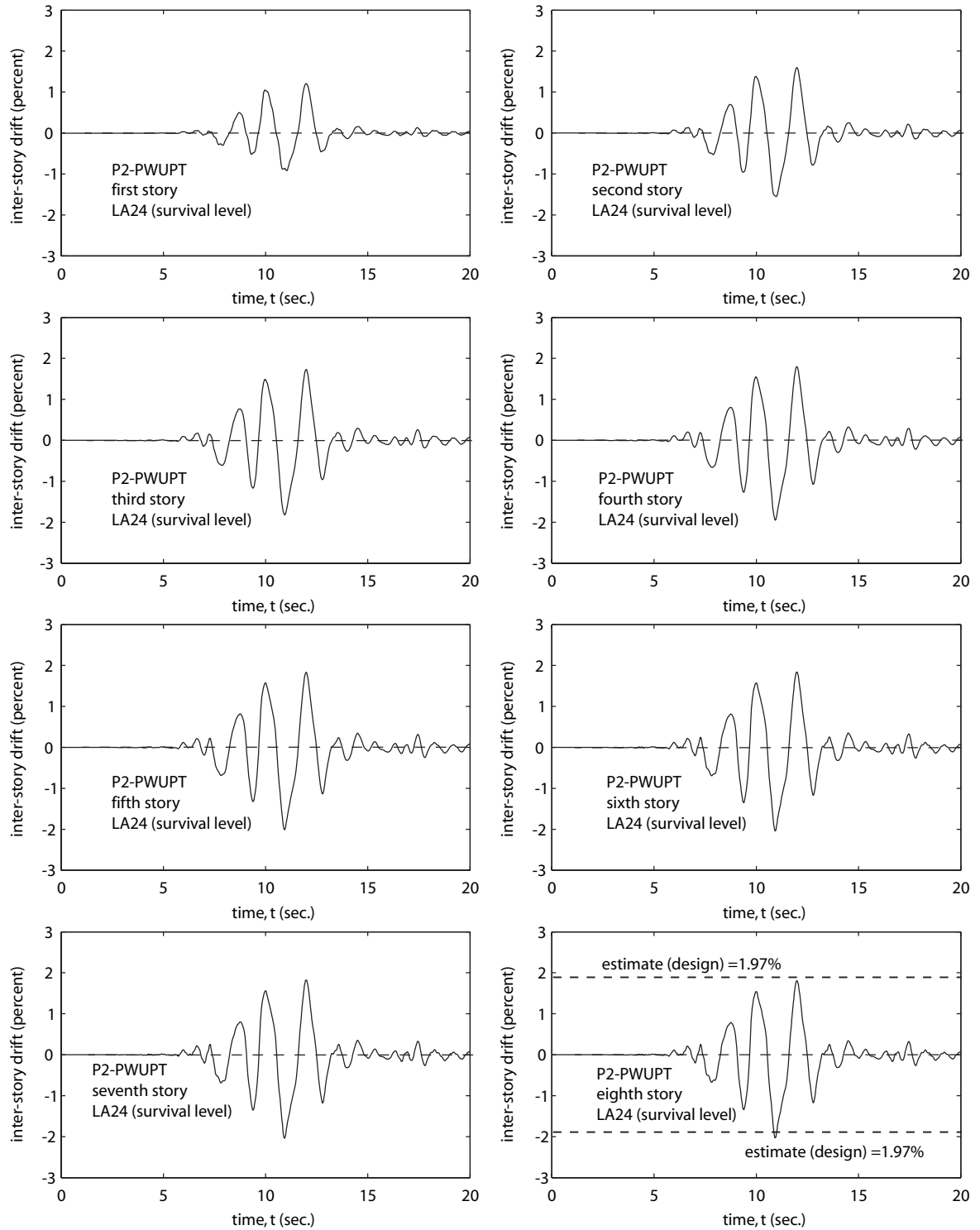
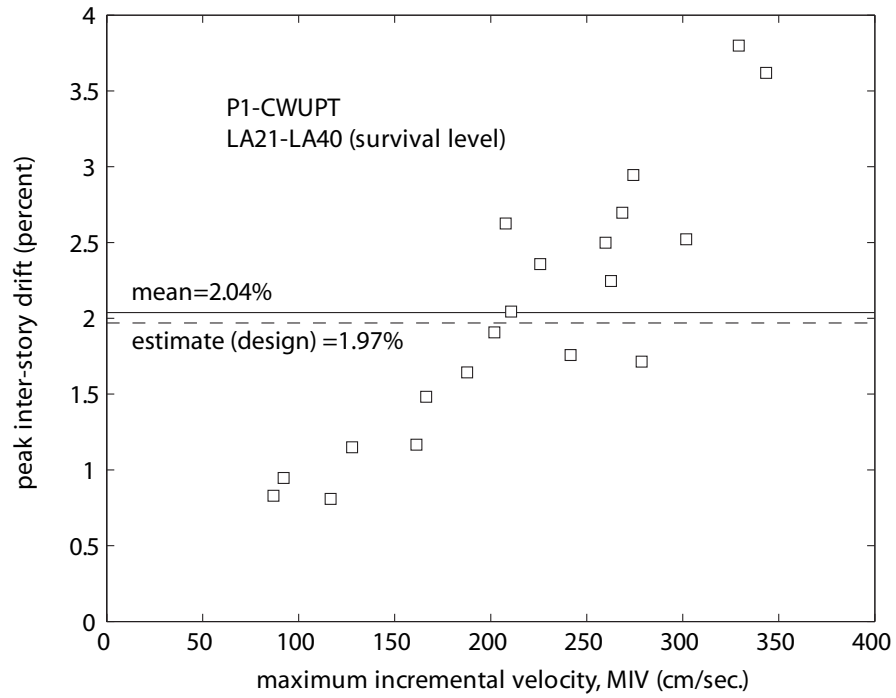
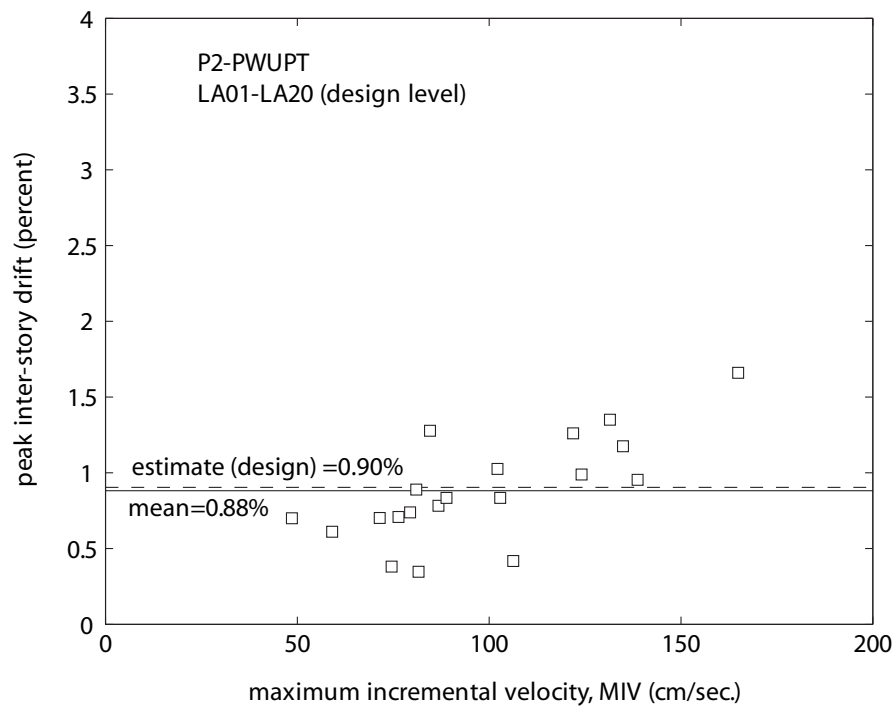


Fig. 15.34 Inter-story drift time histories for Structure P2-PWUPT



(a)



(b)

Fig. 15.35 Peak inter-story drift demands for Structure P2-PWUPT:
(a) survival level; (b) design level

15.3.3 Floor/Roof Accelerations

The peak absolute floor/roof acceleration demands from the dynamic analyses of Structure P2-PWUPT under the twenty survival-level SAC ground motion records (LA21-LA40) and twenty design-level records (LA01-LA20) are listed in Tables 15.40 and 15.41, respectively. The accelerations are calculated as the average total absolute lumped mass accelerations (i.e., relative accelerations with respect to the ground plus the ground acceleration) at the floor/roof levels of the left and right wall piers.

TABLE 15.40

PEAK FLOOR/ROOF ACCELERATION DEMANDS FOR STRUCTURE P2-PWUPT
UNDER SURVIVAL LEVEL GROUND MOTIONS

ground motion	LA21 ^b	LA22	LA23	LA24	LA25	LA26 ^a	LA27 ^c	LA28	LA29	LA30	standard deviation	
peak floor/roof acceleration (g)	2.59	2.28	1.36	1.88	1.78	1.98	1.17	2.25	2.42	2.57	0.48	
ground motion	LA31	LA32	LA33	LA34	LA35	LA36	LA37	LA38	LA39	LA40	mean	standard deviation/mean
peak floor/roof acceleration (g)	2.27	2.36	1.90	1.53	2.34	2.58	1.46	1.81	1.08	1.51	1.96	0.25

^a The peak demand under this ground motion is closest to the mean demand

^b The peak demand under this ground motion is the largest demand

^c The peak demand under this ground motion is the smallest demand

TABLE 15.41

PEAK FLOOR/ROOF ACCELERATION DEMANDS FOR STRUCTURE P2-PWUPT
UNDER DESIGN LEVEL GROUND MOTIONS

ground motion	LA01	LA02	LA03 ^a	LA04	LA05	LA06 ^c	LA07	LA08	LA09	LA10	standard Deviation	
peak floor/roof acceleration (g)	1.57	1.81	1.48	0.89	0.70	0.62	1.51	0.88	1.32	1.12	0.55	
ground motion	LA11	LA12	LA13	LA14	LA15	LA16	LA17	LA18	LA19	LA20 ^b	mean	standard deviation/mean
peak floor/roof acceleration (g)	1.63	2.30	1.67	1.21	1.30	1.31	1.01	1.68	2.09	2.88	1.45	0.38

^a The peak demand under this ground motion is closest to the mean demand

^b The peak demand under this ground motion is the largest demand

^c The peak demand under this ground motion is the smallest demand

As an example, Fig. 15.36 shows the floor/roof acceleration time histories of Structure P2-PWUPT under the survival-level LA22 ground motion, for which the peak acceleration demand (occurring at the roof level in this case) is closest to the mean demand from the twenty records (see Table 15.40). It is noted that the peak acceleration demand does not always occur at the roof level.

Fig. 15.37 plots the peak floor/roof acceleration demands (\square markers) from Tables 15.40 and 15.41 against the maximum incremental velocity (MIV) of the ground motion records, as well as the peak ground accelerations (PGA, \bullet markers) of the records (see Tables 14.2 and 14.1). The solid horizontal lines represent the mean peak floor/roof acceleration demand and the mean peak ground acceleration for each data set. As expected, the peak floor/roof acceleration demands are larger than the peak ground accelerations. There is a significant amount of scatter in the peak floor/roof acceleration

demands; however, unlike the peak roof drift and peak inter-story drift demands discussed in the previous sections, no significant correlation exists between the peak floor/roof acceleration demand and the MIV. It is also interesting to note that the design-level LA20 ground motion record results in a larger peak floor/roof acceleration demand than all of the other records, including the survival-level records. Comparing Figs. 15.37 and 15.6, it is observed that the peak floor/roof acceleration demands of Structure P2-PWUPT are, on average, larger than the peak acceleration demands of Structure P1-CWUPT.

15.3.4 Wall Post-Tensioning Forces

The minimum total coupled wall post-tensioning forces from the dynamic analyses of Structure P2-PWUPT under the twenty survival-level SAC ground motion records (LA21-LA40) and twenty design-level records (LA01-LA20) are listed in Tables 15.42 and 15.43, respectively. Similarly, the maximum total coupled wall post-tensioning forces from the dynamic analyses of the structure under the survival-level and design-level ground motion records are listed in Tables 15.44 and 15.45, respectively. The total coupled wall post-tensioning forces are calculated as the sum of the forces in the truss elements representing the left-side and right-side wall pier post-tensioning bars in the analytical model.

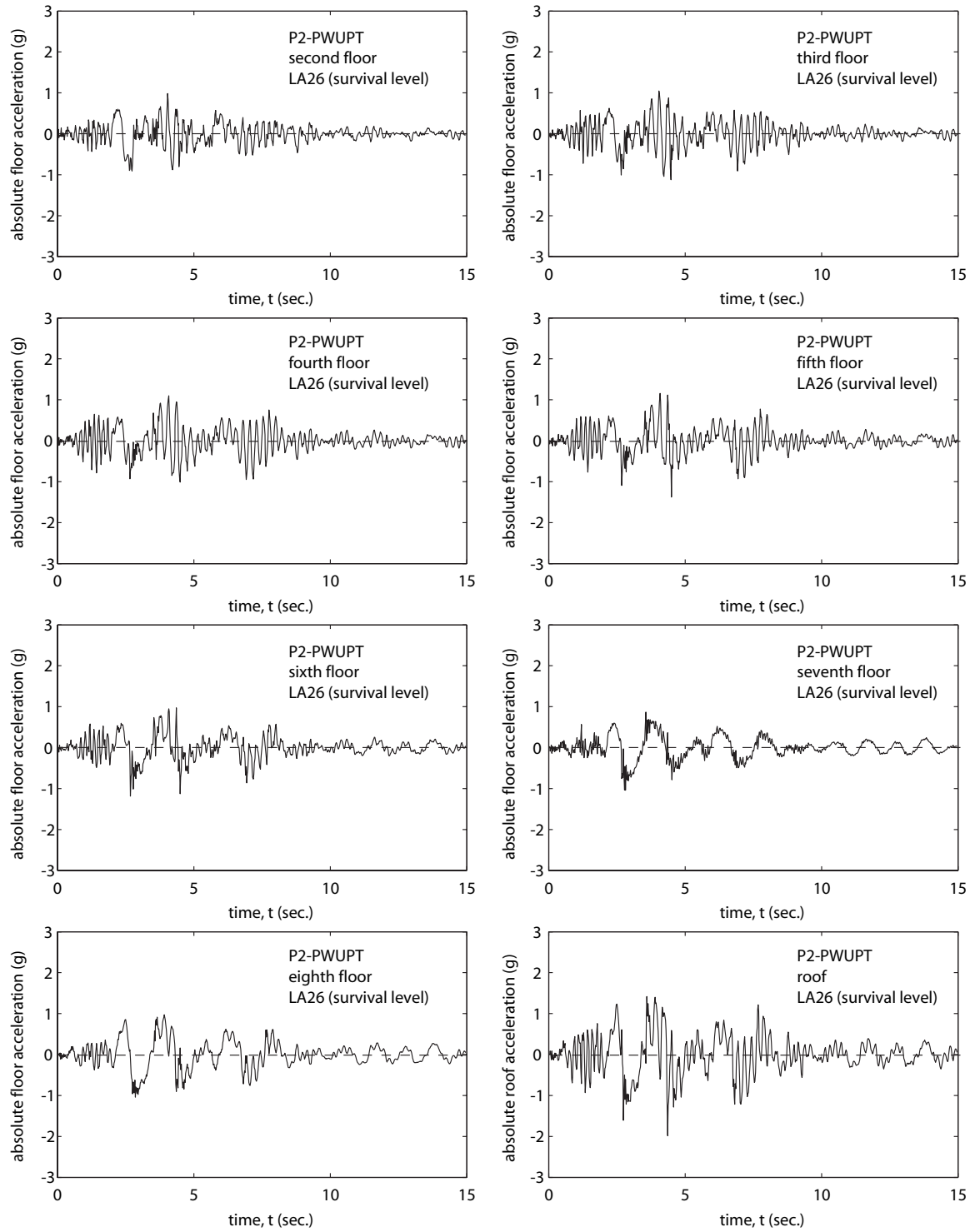
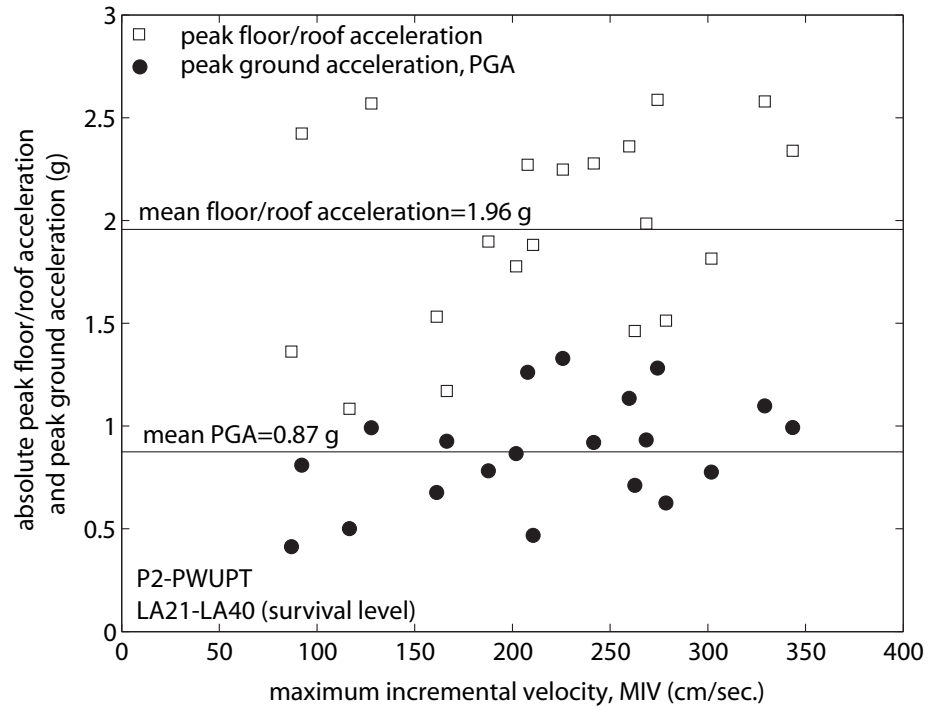
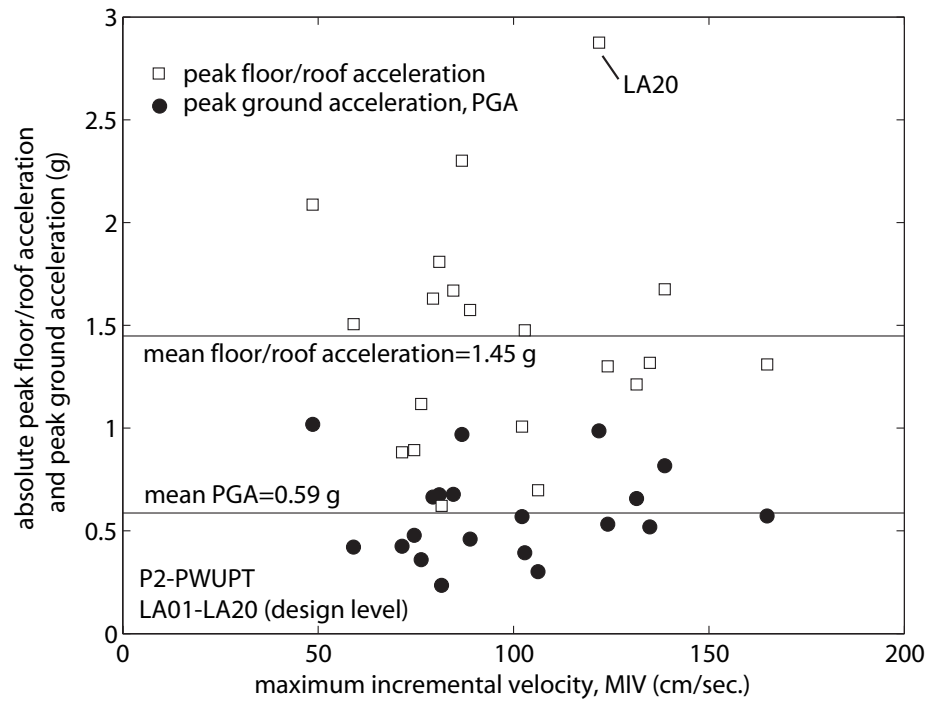


Fig. 15.36 Floor/roof acceleration time histories for Structure P2-PWUPT



(a)



(b)

Fig. 15.37 Peak floor/roof acceleration demands for Structure P2-PWUPT:
(a) survival level; (b) design level

TABLE 15.42

MINIMUM TOTAL COUPLED WALL POST-TENSIONING FORCES FOR
STRUCTURE P2-PWUPT UNDER SURVIVAL LEVEL GROUND MOTIONS

ground motion	LA21	LA22	LA23	LA24	LA25	LA26	LA27	LA28	LA29	LA30	estimate (design)	standard deviation
min. coupled wall post-tensioning force (kN)	29247	36167	37164	35136	36066	32258	36867	33147	37086	36988	33594	3791
ground motion	LA31	LA32	LA33	LA34	LA35	LA36 ^c	LA37	LA38 ^a	LA39 ^b	LA40	mean	standard deviation/mean
min. coupled wall post-tensioning force (kN)	32460	32972	36444	37096	26383	23662	34951	34049	37178	36223	34077	0.11

^a The force under this ground motion is closest to the mean force

^b The force under this ground motion is the largest force

^c The force under this ground motion is the smallest force

TABLE 15.43

MINIMUM TOTAL COUPLED WALL POST-TENSIONING FORCES FOR
STRUCTURE P2-PWUPT UNDER DESIGN LEVEL GROUND MOTIONS

ground motion	LA01	LA02	LA03	LA04	LA05	LA06 ^b	LA07	LA08	LA09	LA10	estimate (design)	standard deviation
min. coupled wall post-tensioning force (kN)	37178	37121	37202	37271	37267	37278	37221	37220	37132	37221	37758	143
ground motion	LA11	LA12	LA13	LA14	LA15 ^a	LA16 ^c	LA17	LA18	LA19	LA20	mean	standard deviation/mean
min. coupled wall post-tensioning force (kN)	37203	37133	37084	37034	37138	36629	37175	37132	37148	36965	37138	0.0039

^a The force under this ground motion is closest to the mean force

^b The force under this ground motion is the largest force

^c The force under this ground motion is the smallest force

TABLE 15.44

MAXIMUM TOTAL COUPLED WALL POST-TENSIONING FORCES FOR
STRUCTURE P2-PWUPT UNDER SURVIVAL LEVEL GROUND MOTIONS

ground motion	LA21	LA22	LA23	LA24	LA25	LA26	LA27	LA28	LA29	LA30	estimate (idealized)	standard deviation
max. coupled wall post-tensioning force (kN)	42498	41369	39116	41969	42280	43575	41196	43130	39465	40229	44782	1619
ground motion	LA31	LA32	LA33 ^a	LA34	LA35	LA36 ^b	LA37	LA38	LA39 ^c	LA40	mean	standard deviation/mean
max. wall post-tensioning force (kN)	42390	42428	41897	40335	44102	44183	43304	43473	38702	41680	41866	0.039

^a The peak force under this ground motion is closest to the mean force

^b The peak force under this ground motion is the largest force

^c The peak force under this ground motion is the smallest force

TABLE 15.45

MAXIMUM TOTAL COUPLED WALL POST-TENSIONING FORCES FOR
STRUCTURE P2-PWUPT UNDER DESIGN LEVEL GROUND MOTIONS

ground motion	LA01	LA02	LA03 ^a	LA04	LA05	LA06 ^c	LA07	LA08	LA09	LA10	estimate (idealized)	standard deviation
max. coupled wall post-tensioning force (kN)	38941	39370	39056	37600	37634	37427	38274	38300	40111	38487	41531	1087
ground motion	LA11	LA12	LA13	LA14	LA15	LA16 ^b	LA17	LA18	LA19	LA20	mean	standard deviation/mean
max wall post-tensioning force (kN)	38448	38046	40029	40403	39413	41453	39464	39399	38511	40576	39047	0.028

^a The force under this ground motion is closest to the mean force

^b The force under this ground motion is the largest force

^c The force under this ground motion is the smallest force

The mean minimum total coupled wall post-tensioning force from the survival-level dynamic analyses in Table 15.42 is 34077 kN, which is close to the estimated survival-level minimum total coupled wall post-tensioning force of 33594 kN from Chapter 12 (see Section 12.8.5 and Table 12.30). Thus, the design procedure to estimate the prestress losses in the wall pier post-tensioning bars appears to be valid. Under the design-level earthquake, the minimum total coupled wall post-tensioning force is assumed to be equal to the total initial post-tensioning force, $2P_{wi}=37758$ kN from Chapter 12, which is similar to the mean minimum coupled wall post-tensioning force from the design-level dynamic analyses in Table 15.43.

Since the proposed design approach in Chapter 12 does not require the estimation of the survival-level and design-level maximum total coupled wall post-tensioning forces, the results from the dynamic analyses in Tables 15.44 and 15.45 are compared with the results from the static idealized tri-linear pushover analysis of the structure in Chapter 13. The sum of the tension-side and compression-side wall pier post-tensioning forces, P_{tw} and P_{cw} , corresponding to the estimated coupled wall ultimate state and PT-yielding state are given in Tables 15.44 and 15.45, respectively (see also Table 13.2). The results show that the total coupled wall post-tensioning forces from the idealized pushover analysis provide reasonable estimates for the maximum post-tensioning forces from the dynamic analyses.

As an example, Fig. 15.38 shows the total coupled wall post-tensioning force time-histories of Structure P2-PWUPT under the survival level LA38 and LA33 ground motions, for which the minimum and maximum total coupled wall post-tensioning forces are closest to the corresponding mean forces from Tables 15.42 and 15.44, respectively. The dashed horizontal lines indicate the design estimate for the minimum post-tensioning force from Chapter 12 and the estimated idealized maximum post-tensioning force from the tri-linear static pushover analysis in Chapter 13.

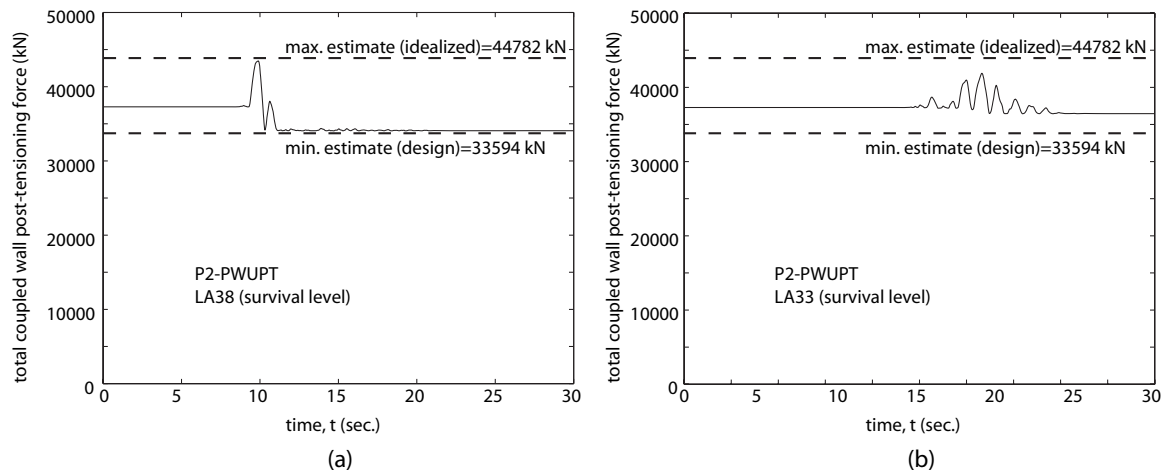


Fig. 15.38 Total coupled wall post-tensioning force time histories for Structure P2-PWUPT: (a) LA38; (b) LA33

Fig. 15.39 plots the minimum (\square markers) and maximum (\circ markers) total coupled wall post-tensioning forces from Tables 15.42-15.45 against the maximum incremental velocity (MIV) of the ground motion records (see Tables 14.2 and 14.1), where the dashed and solid horizontal lines represent the design/idealized estimate and the mean total coupled wall post-tensioning force, respectively, for each data set. It is observed that there is very little scatter or variation in the design-level minimum total

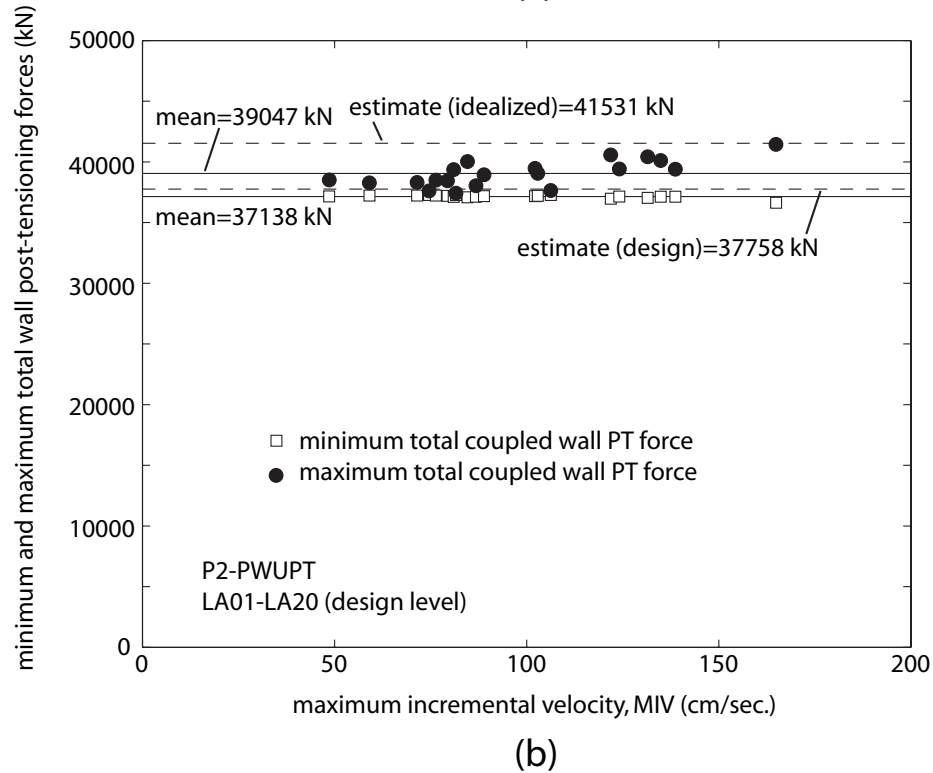
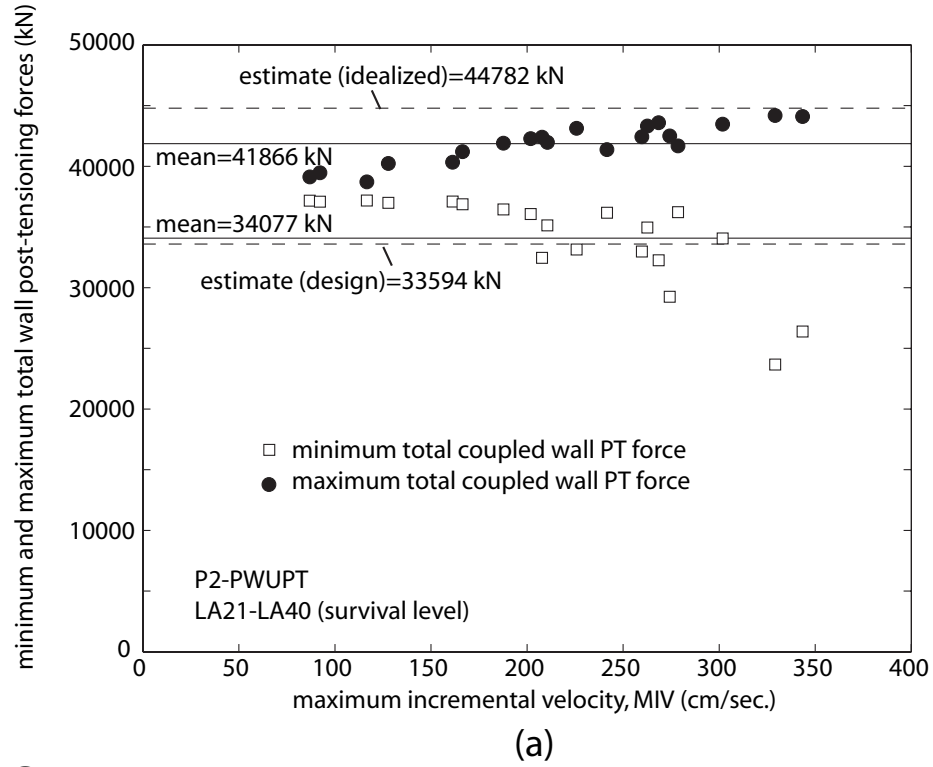


Fig. 15.39 Minimum and maximum total coupled wall post-tensioning forces for Structure P2-PWUPT: (a) survival level; (b) design level

coupled wall post-tensioning forces since yielding of the wall pier post-tensioning bars is prevented under the design level earthquake, and thus, the minimum post-tensioning force is equal to the initial force. In comparison, significant prestress losses occur in the wall pier post-tensioning bars under the survival-level ground motions, which should be considered in the design of the structure against shear slip failure at the base as discussed in more detail later.

15.3.5 Wall Base Axial Forces

As a result of the wall pier post-tensioning forces, the axial forces in both wall piers remain compressive during the dynamic analyses of Structure P2-PWUPT. The minimum wall pier base compressive axial force demands under the twenty survival-level SAC ground motion records (LA21-LA40) and twenty design-level records (LA01-LA20) are listed in Tables 15.46 and 15.47, respectively. Similarly, Tables 15.48 and 15.49 give the maximum wall pier base compressive axial force demands under the twenty survival-level and design-level records, respectively. The minimum wall pier base axial force demands are important in the design of the structure to prevent shear slip failure as described later. The wall pier base axial forces in Tables 15.46-15.49 are obtained directly from the fiber beam-column elements used for the wall piers in the analysis model, where a positive force indicates compression.

Since the proposed design approach does not require the estimation of the survival-level and design-level wall pier axial forces, the results from the dynamic analyses are compared with the results from the static idealized tri-linear pushover analysis of the structure in Chapter 13. The tension-side wall pier base axial forces, N_{twu} and N_{twy} , corresponding to the estimated coupled wall ultimate state and PT-yielding state are

given in Tables 15.46 and 15.47, respectively (see also Table 13.2). Similarly, the compression-side wall pier base axial forces, N_{cwu} and N_{cwy} , corresponding to the estimated coupled wall ultimate state and PT-yielding state are given in Tables 15.48 and 15.49, respectively. The results show that the N_{cwu} and N_{cwy} forces from the idealized pushover analysis are reasonably close to the maximum wall pier compressive axial force demands from the dynamic analyses; however, the N_{twu} and N_{twy} forces significantly overestimate the minimum wall pier compressive axial force demands. This is possibly because of the underestimated beam shear forces as described later in more detail.

TABLE 15.46

MINIMUM WALL PIER BASE COMPRESSION AXIAL FORCE DEMANDS FOR
STRUCTURE P2-PWUPT UNDER SURVIVAL LEVEL GROUND MOTIONS

ground motion	LA21	LA22	LA23 ^b	LA24	LA25	LA26	LA27	LA28 ^a	LA29	LA30	estimate (idealized)	standard deviation
min. wall pier base compression force (kN)	11142	12690	13237	12819	12890	12241	13139	12299	13006	12899	16489	912
ground motion	LA31	LA32	LA33	LA34	LA35	LA36 ^c	LA37 ^a	LA38	LA39	LA40	mean	standard deviation/mean
min. wall pier base compression force (kN)	11934	12018	12864	13219	10217	10141	12299	12245	13193	12695	12359	0.074

^a The peak demand under this ground motion is closest to the mean demand

^b The peak demand under this ground motion is the largest demand

^c The peak demand under this ground motion is the smallest demand

TABLE 15.47

MINIMUM WALL PIER BASE COMPRESSION AXIAL FORCE DEMANDS FOR
STRUCTURE P2-PWUPT UNDER DESIGN LEVEL GROUND MOTIONS

ground motion	LA01	LA02	LA03	LA04	LA05	LA06 ^b	LA07	LA08	LA09	LA10 ^a	estimate (idealized)	standard deviation
min. wall pier base compression force (kN)	13028	13113	13366	14701	14634	15123	13531	13184	13148	13393	16039	631
ground motion	LA11	LA12	LA13 ^c	LA14	LA15	LA16	LA17	LA18	LA19	LA20	mean	standard deviation/mean
min. wall pier base compression force (kN)	13486	13486	12828	13099	12975	13162	13068	13122	13322	12957	13436	0.047

^a The peak demand under this ground motion is closest to the mean demand

^b The peak demand under this ground motion is the largest demand

^c The peak demand under this ground motion is the smallest demand

TABLE 15.48

MAXIMUM WALL PIER BASE COMPRESSION AXIAL FORCE DEMANDS FOR
STRUCTURE P2-PWUPT UNDER SURVIVAL LEVEL GROUND MOTIONS

ground motion	LA21	LA22	LA23	LA24	LA25 ^a	LA26	LA27	LA28	LA29	LA30	estimate (idealized)	standard deviation
max. wall pier base compression force (kN)	36078	33885	31625	34868	35157	37581	33622	36411	32066	32132	32742	2447
ground motion	LA31	LA32	LA33	LA34	LA35	LA36 ^b	LA37	LA38	LA39 ^c	LA40	mean	standard deviation/mean
max wall pier base compression force (kN)	35686	36500	34579	32724	39440	39618	36652	37101	31025	34254	35050	0.070

^a The peak demand under this ground motion is closest to the mean demand

^b The peak demand under this ground motion is the largest demand

^c The peak demand under this ground motion is the smallest demand

TABLE 15.49

MAXIMUM WALL PIER BASE COMPRESSION AXIAL FORCE DEMANDS FOR
STRUCTURE P2-PWUPT UNDER DESIGN LEVEL GROUND MOTIONS

ground motion	LA01 ^a	LA02	LA03	LA04	LA05	LA06 ^c	LA07	LA08	LA09	LA10	estimate (idealized)	standard deviation
max. wall pier base compression force (kN)	31305	31603	31478	28325	28779	27982	30429	30816	32773	30785	31132	1599
ground motion	LA11	LA12	LA13	LA14	LA15	LA16 ^b	LA17	LA18	LA19	LA20	mean	standard deviation/mean
max. wall pier base compression force (kN)	30665	29597	32751	32777	31999	33867	32146	31839	30945	33098	31198	0.051

^a The peak demand under this ground motion is closest to the mean demand

^b The peak demand under this ground motion is the largest demand

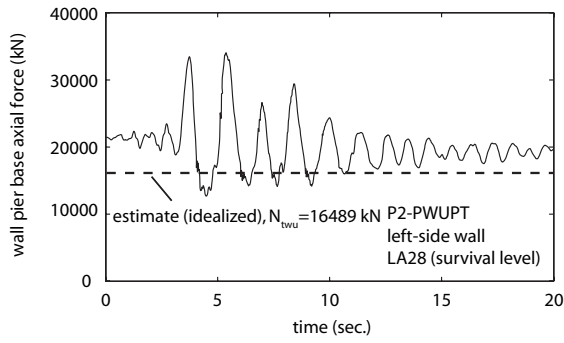
^c The peak demand under this ground motion is the smallest demand

As an example, Fig. 15.40 shows the axial force time histories at the bases of the left-side and right-side wall piers in Structure P2-PWUPT under the survival-level LA28 ground motion, for which the minimum wall pier base compressive axial force demand (occurring in the right-side wall pier) is closest to the mean demand from the twenty records (see Table 15.46). Similarly, Fig. 15.41 shows the axial force time histories at the bases of the left-side and right-side wall piers in Structure P2-PWUPT under the survival-level LA25 ground motion, for which the maximum wall pier base compressive axial force demand (occurring in the right-side wall pier) is closest to the mean demand from the twenty records (see Table 15.48). The dashed horizontal lines indicate the estimated idealized wall pier base axial forces, N_{twu} and N_{cwu} , from the tri-linear static pushover analysis in Chapter 13 at the coupled wall ultimate state.

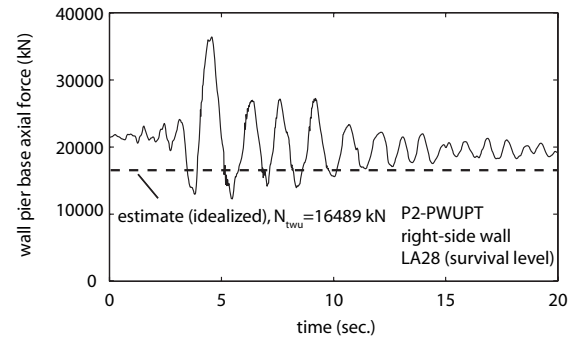
Fig. 15.42 plots the minimum (\circ markers) and maximum (\square markers) compressive wall pier base axial force demands from Tables 15.46-15.49 against the maximum incremental velocity (MIV) of the ground motion records (see Tables 14.2 and 14.1), where the dashed and solid horizontal lines represent the estimated idealized wall pier base axial force and the mean wall pier base axial force demand, respectively, for each data set. It is observed that there is very little scatter or variation in the wall pier base axial force demands in each data set, and that the wall pier base axial force demands under the survival-level and design-level ground motions are similar.

15.3.6 Wall Base Shear Forces

The peak total coupled wall base shear force demands from the dynamic analyses of Structure P2-PWUPT under the twenty survival-level SAC ground motion records (LA21-LA40) and twenty design-level records (LA01-LA20) are listed in Tables 15.50 and 15.51, respectively. The coupled wall base shear force, F is equal to the sum of the floor and roof level wall pier inertia forces, which are calculated as the lumped mass times the total absolute acceleration (i.e., relative acceleration with respect to the ground plus the ground acceleration) at each floor/roof level.

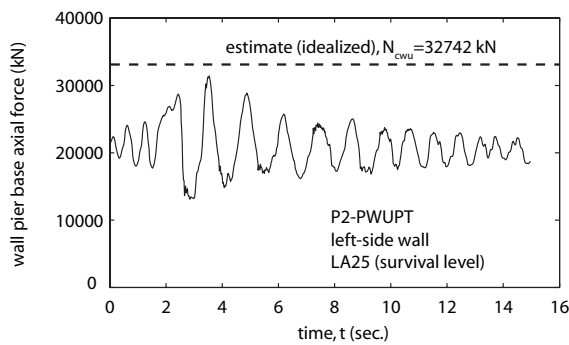


(a)

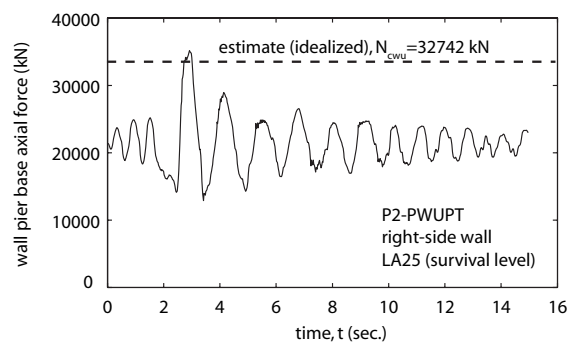


(b)

Fig. 15.40 Wall pier base axial force time histories for Structure P2-PWUPT:
(a) left-side wall; (b) right-side wall

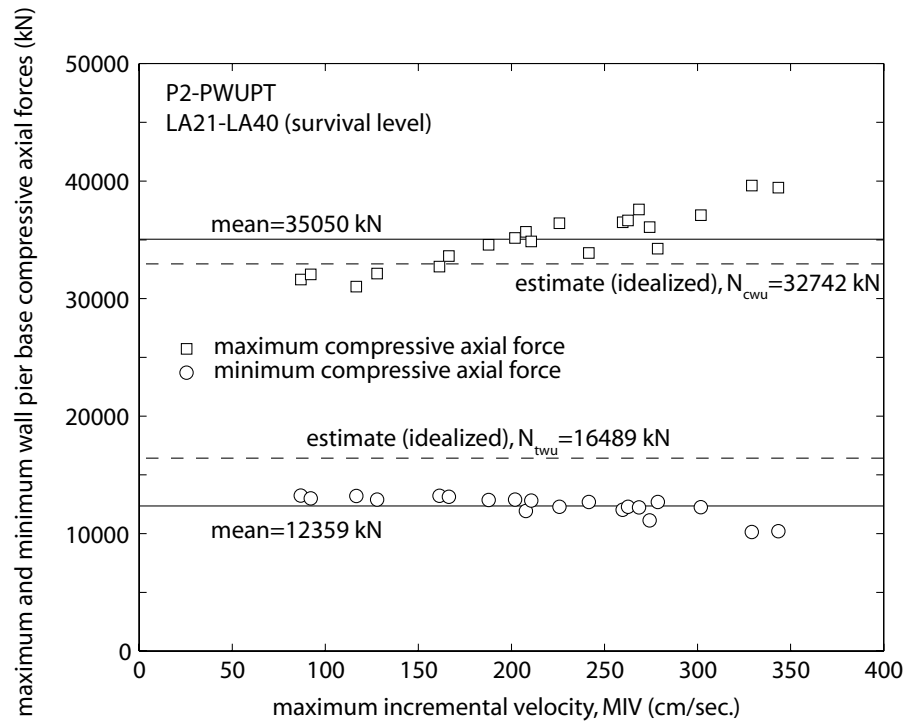


(a)

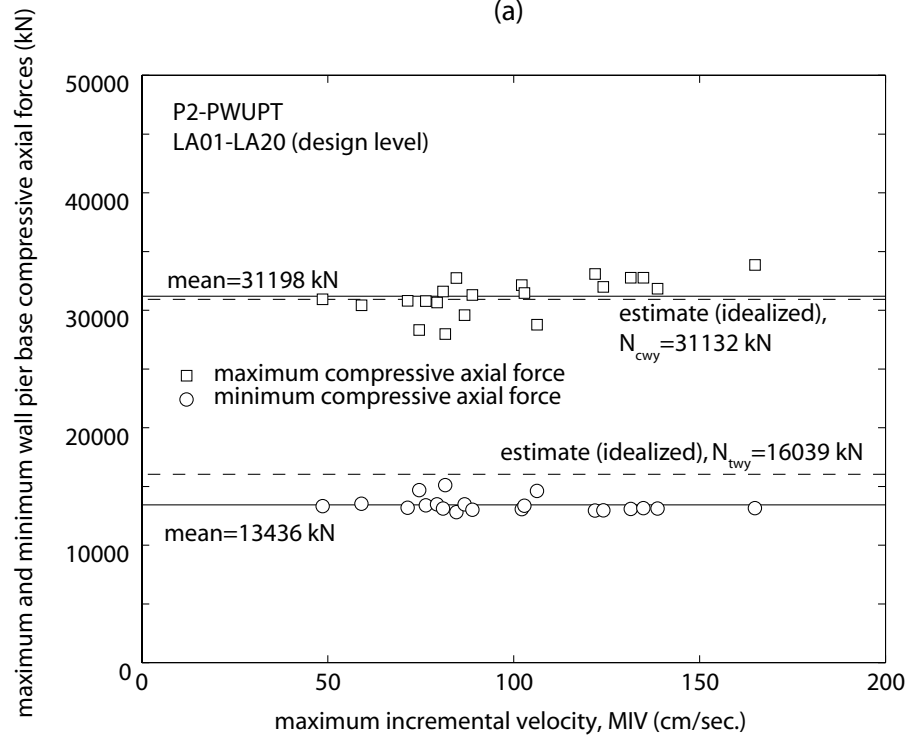


(b)

Fig. 15.41 Wall pier base axial force time histories for Structure P2-PWUPT:
(a) left-side wall; (b) right-side wall



(a)



(b)

Fig. 15.42 Peak wall pier base axial force demands for Structure P2-PWUPT:
(a) survival level; (b) design level

TABLE 15.50

PEAK COUPLED WALL BASE SHEAR FORCE DEMANDS FOR STRUCTURE

P2-PWUPT UNDER SURVIVAL LEVEL GROUND MOTIONS

ground motion	LA21	LA22	LA23 ^c	LA24	LA25	LA26 ^a	LA27	LA28 ^b	LA29	LA30	estimate (design)	standard deviation
peak coupled wall base shear force (kN)	13579	9632	8558	11283	11955	12477	10190	16350	12892	16139	13099	2315
ground motion	LA31	LA32	LA33	LA34	LA35	LA36	LA37	LA38	LA39	LA40	mean	standard deviation/mean
peak coupled wall base shear force (kN)	14246	15196	10869	10446	15416	13262	11346	11909	8990	11037	12289	0.19

^a The peak demand under this ground motion is closest to the mean demand

^b The peak demand under this ground motion is the largest demand

^c The peak demand under this ground motion is the smallest demand

TABLE 15.51

PEAK COUPLED WALL BASE SHEAR FORCE DEMANDS FOR STRUCTURE

P2-PWUPT UNDER DESIGN LEVEL GROUND MOTIONS

ground motion	LA01	LA02	LA03	LA04	LA05 ^c	LA06	LA07	LA08	LA09	LA10	standard deviation	
peak coupled wall base shear force (kN)	10043	10355	9280	7348	6264	6103	7351	7689	8953	7867	2625	
ground motion	LA11 ^a	LA12	LA13	LA14	LA15	LA16	LA17	LA18	LA19	LA20 ^b	mean	standard deviation/mean
peak coupled wall base shear force (kN)	9679	13892	10859	10507	9031	10114	8599	11683	14137	16152	9795	0.27

^a The peak demand under this ground motion is closest to the mean demand

^b The peak demand under this ground motion is the largest demand

^c The peak demand under this ground motion is the smallest demand

Comparisons of the peak coupled wall base shear force demands in Tables 15.50 and 15.51 with the coupled wall base shear forces reached during the static push-over analysis of the structure in Chapter 13 show that the forces from the dynamic analyses are significantly larger than the forces from the static analysis. As discussed in Chapter 11, the differences between the static and dynamic analysis forces are because of the contribution of higher modes of vibration to the dynamic response of the structure.

The mean peak coupled wall base shear force demand from the twenty survival-level ground motions is 12289 kN, which is close to and smaller than the estimated maximum coupled wall base shear force demand of $Q_{w,max}=13099$ kN from Chapter 12. Thus, the method used in Chapter 12 to estimate the coupled wall base shear force demand of the prototype structures including the effect of higher modes appears to be valid. Note that the design approach does not require the estimation of the maximum coupled wall base shear force demand under the design-level earthquake; and thus, no design-level estimate is provided in Table 15.51.

As an example, Fig. 15.43 shows the coupled wall base shear force time history of Structure P2-PWUPT under the survival-level LA26 ground motion, for which the peak coupled wall base shear force demand is closest to the mean demand from the twenty records (see Table 15.50). The dashed horizontal lines indicate the design estimate for the maximum coupled wall base shear force demand, $Q_{w,max}$ from Chapter 12.

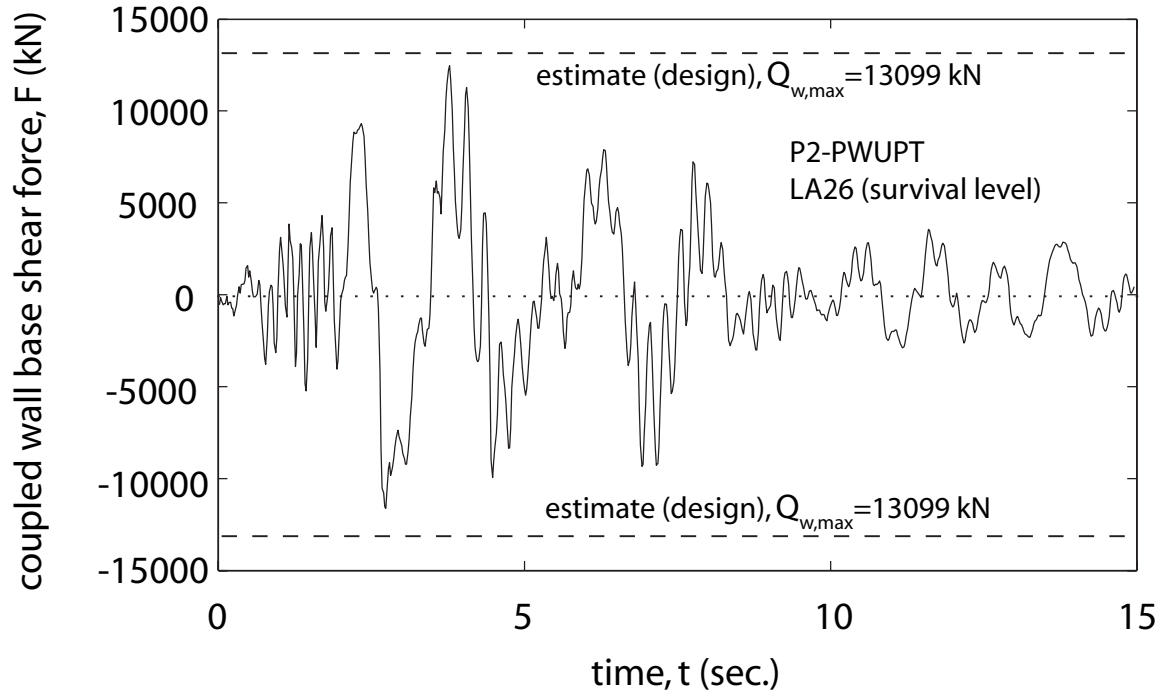


Fig. 15.43 Coupled wall base shear force time history for Structure P2-PWUPT

Fig. 15.44 plots the peak coupled wall base shear force demands from Tables 15.50 and 15.51 (\square markers) against the maximum incremental velocity (MIV) of the ground motion records (see Tables 14.2 and 14.1), where the dashed and solid horizontal lines represent the design estimate (from Chapter 12) and the mean peak coupled wall base shear force demand, respectively, for each data set. Significant scatter is observed in the data indicating that, while the survival-level design estimate matches the mean demand from the dynamic analyses quite well, the coupled wall base shear force demand may be considerably larger or smaller than the estimated demand, depending on the earthquake. It is also interesting to note that the design-level LA20 ground motion record results in a peak coupled wall base shear force demand that is similar to the largest demand from the survival-level records. Some correlation can be observed between the

peak coupled wall base shear force demands in Fig. 15.44 and the peak acceleration demands in Fig. 15.37.

The peak wall pier base shear force demands from the dynamic analyses of Structure P2-PWUPT under the twenty survival-level SAC ground motion records (LA21-LA40) and twenty design-level records (LA01-LA20) are listed in Tables 15.52 and 15.53, respectively. The wall pier base shear forces are calculated from the equilibrium of the floor/roof level wall pier inertia forces with the coupling beam axial forces and beam post-tensioning tendon forces from the analysis model (obtained from the fiber beam-column elements and the truss elements representing the coupling beams and the beam post-tensioning tendons, respectively).

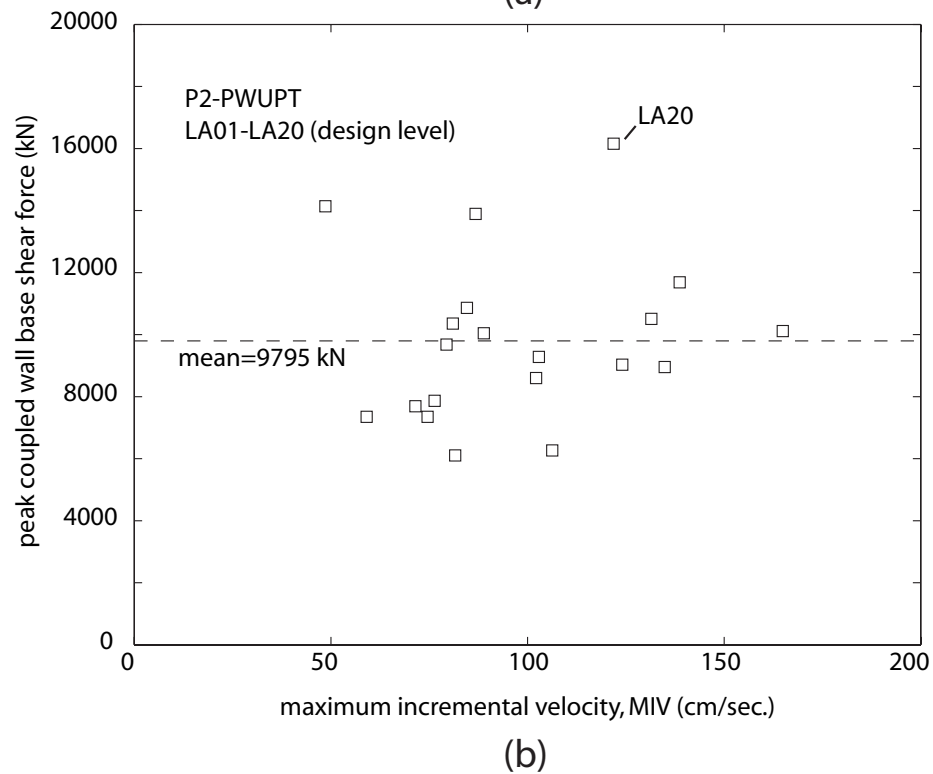
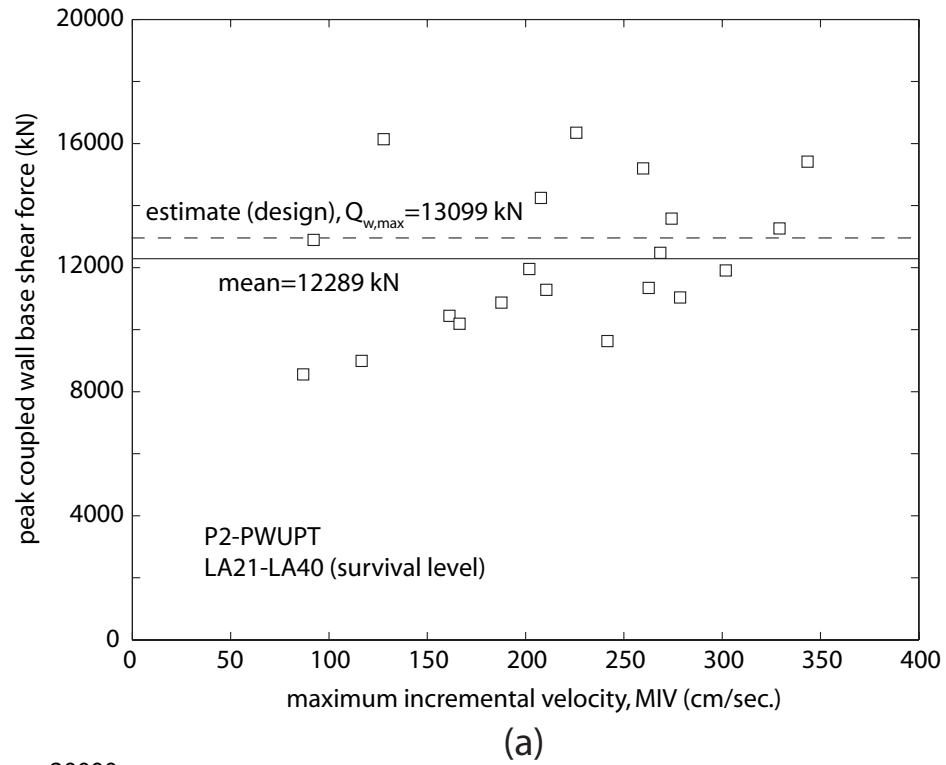


Fig. 15.44 Peak coupled wall base shear force demands for Structure P2-PWUPT:
(a) survival level; (b) design level

TABLE 15.52

PEAK WALL PIER BASE SHEAR FORCE DEMANDS FOR STRUCTURE

P2-PWUPT UNDER SURVIVAL LEVEL GROUND MOTIONS

ground motion	LA21	LA22	LA23 ^c	LA24	LA25	LA26	LA27	LA28 ^b	LA29	LA30	estimate (design)	standard deviation
peak wall pier base shear force (kN)	10379	7560	6824	8636	9361	9424	7812	11849	8781	10841	9955	1497
ground motion	LA31	LA32	LA33	LA34	LA35	LA36	LA37	LA38 ^a	LA39	LA40	mean	standard deviation/mean
peak wall pier base shear force (kN)	10182	11646	8353	8016	11487	10153	9079	9287	6904	8697	9264	0.16

^a The peak demand under this ground motion is closest to the mean demand

^b The peak demand under this ground motion is the largest demand

^c The peak demand under this ground motion is the smallest demand

TABLE 15.53

PEAK WALL PIER BASE SHEAR FORCE DEMANDS FOR STRUCTURE

P2-PWUPT UNDER DESIGN LEVEL GROUND MOTIONS

ground motion	LA01	LA02	LA03	LA04	LA05	LA06 ^c	LA07	LA08	LA09 ^a	LA10	standard deviation	
peak wall pier base shear force (kN)	7714	7944	6663	5178	4619	3802	5599	5723	7095	5878	1646	
ground motion	LA11	LA12	LA13	LA14	LA15	LA16	LA17	LA18	LA19	LA20 ^b	mean	standard deviation/mean
peak wall pier base shear force (kN)	6104	9323	8548	7189	7163	7967	6791	8729	8263	10415	7036	0.23

^a The peak demand under this ground motion is closest to the mean demand

^b The peak demand under this ground motion is the largest demand

^c The peak demand under this ground motion is the smallest demand

The mean peak wall pier base shear force demand from the twenty survival-level analyses is 9264 kN, which is close to and smaller than the estimated maximum wall pier base shear force demand of $Q_{w,dt}=9955$ kN from Chapter 12. Thus, the method used in Chapter 12 to estimate the maximum wall pier base shear force demand appears to be valid. Note that the design approach does not require the estimation of the maximum wall pier base shear force demand under the design-level earthquake; and thus, no design-level estimate is provided in Table 15.53.

As an example, Fig. 15.45 shows the shear force time histories at the bases of the left-side and right-side wall piers in Structure P2-PWUPT under the survival-level LA38 ground motion, for which the peak wall pier base shear force demand (occurring in the left-side wall pier) is closest to the mean demand from the twenty records (see Table 15.52). The dashed horizontal lines indicate the design estimate for the maximum wall pier base shear force demand, $Q_{w,dt}$ from Chapter 12. It is observed that there are residual base shear forces in the left-side and right-side wall piers at the end of the ground motion, even though the coupled wall base shear force is close to zero.

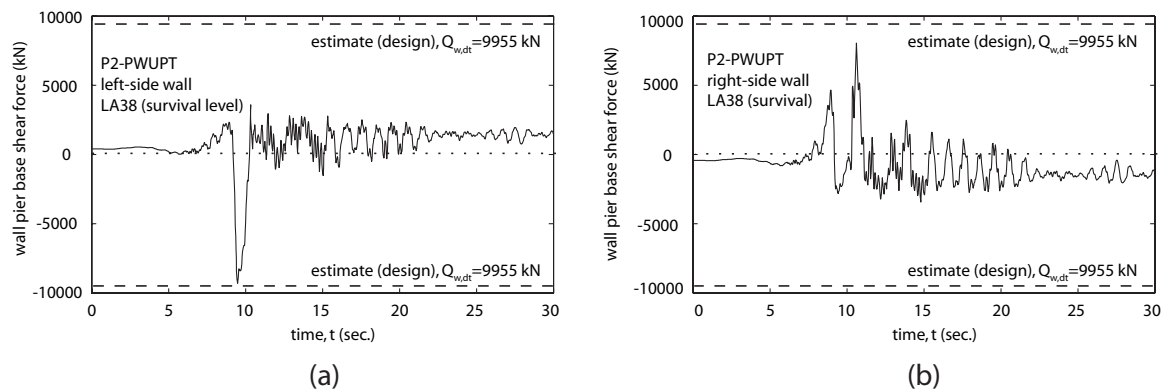
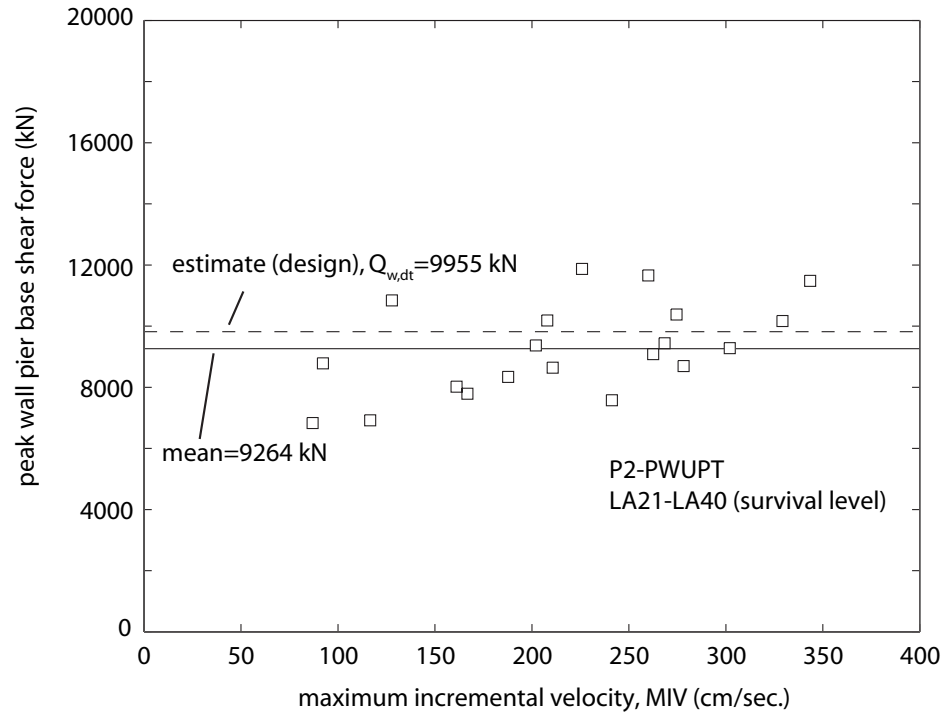


Fig. 15.45 Wall pier base shear force time histories for Structure P2-PWUPT:
(a) left-side wall; (b) right-side wall

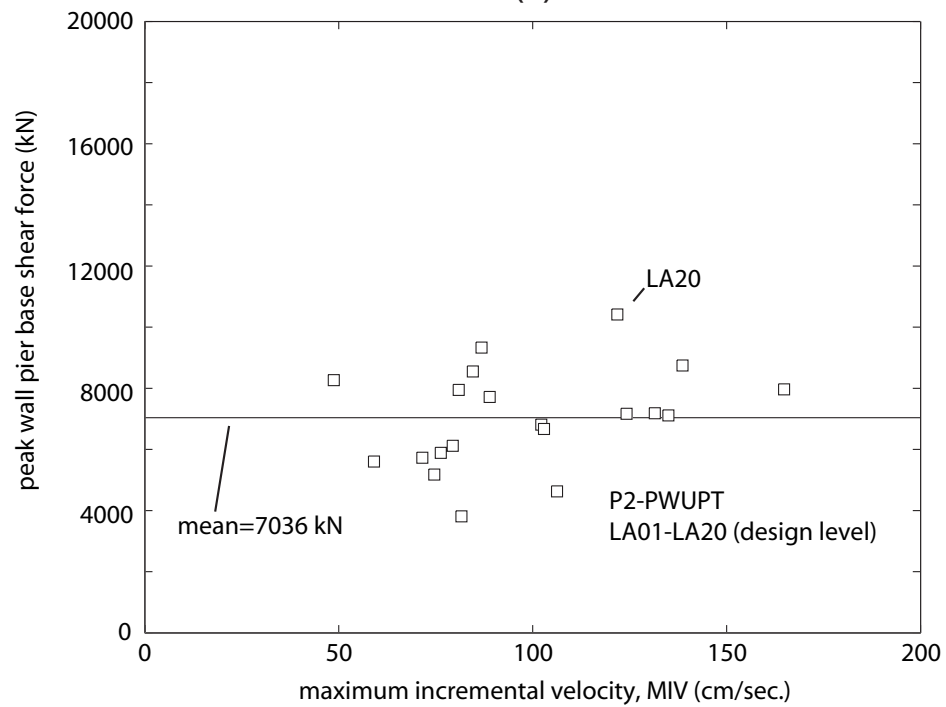
Fig. 15.46 plots the peak wall pier base shear force demands from Tables 15.52 and 15.53 (\square markers) against the maximum incremental velocity (MIV) of the ground motion records (see Tables 14.2 and 14.1), where the dashed and solid horizontal lines represent the design estimate (from Chapter 12) and the mean peak wall pier base shear force demand, respectively, for each data set. Similar to the peak coupled wall base shear force demands in Fig. 15.44, significant scatter is observed in the peak wall pier base shear force demands and the demand for the design-level LA20 ground motion record is similar to the largest demand from the survival-level records.

If the peak wall pier base shear force demands in Tables 15.52 and 15.53 are divided by the corresponding peak coupled wall base shear force demands in Tables 15.50 and 15.51, the wall pier base shear force distribution ratios are obtained. The mean wall pier base shear force distribution ratio from the twenty survival-level analyses is 0.75, which is close to the design ratio of $Q_{w,dt}/Q_{w,max}=0.76$ from Chapter 12.

Note that the peak wall pier base shear force demands in Tables 15.52 and 15.53 and the corresponding peak coupled wall base shear force demands in Tables 15.50 and 15.51 do not necessarily occur at the same time during each dynamic analysis. Thus, Tables 15.54 and 15.55 show the peak ratio of the wall pier base shear force to the corresponding coupled wall base shear force occurring at the same time during each analysis. The mean value of the peak wall pier base shear force distribution ratio from the twenty survival-level analyses in Table 15.54 is 0.76, which is the same as the value used in design and close to the value calculated from the peak wall pier and peak coupled wall base shear force demands above.



(a)



(b)

Fig. 15.46 Peak wall pier base shear force demands for Structure P2-PWUPT:
(a) survival level; (b) design level

TABLE 15.54

PEAK WALL PIER BASE SHEAR FORCE DISTRIBUTION RATIOS FOR
STRUCTURE P2-PWUPT UNDER SURVIVAL LEVEL GROUND MOTIONS

ground motion	LA21	LA22	LA23	LA24	LA25	LA26	LA27	LA28	LA29	LA30	estimate (design)	standard deviation
peak base shear force distribution ratio	0.76	0.78	0.82	0.79	0.78	0.75	0.79	0.72	0.69	0.67	0.76	0.037
ground motion	LA31	LA32	LA33	LA34	LA35	LA36	LA37	LA38	LA39	LA40	mean	standard deviation/mean
peak base shear force distribution ratio	0.74	0.77	0.77	0.78	0.76	0.77	0.80	0.78	0.78	0.81	0.76	0.049

TABLE 15.55

PEAK WALL PIER BASE SHEAR FORCE DISTRIBUTION RATIOS FOR
STRUCTURE P2-PWUPT UNDER DESIGN LEVEL GROUND MOTIONS

ground motion	LA01	LA02	LA03	LA04	LA05	LA06	LA07	LA08	LA09	LA10	standard deviation	
peak base shear force distribution ratio	0.77	0.77	0.72	0.70	0.74	0.62	0.77	0.77	0.79	0.76	0.061	
ground motion	LA11	LA12	LA13	LA14	LA15	LA16	LA17	LA18	LA19	LA20	mean	standard deviation/mean
peak base shear force distribution ratio	0.76	0.69	0.79	0.68	0.79	0.79	0.79	0.75	0.58	0.64	0.73	0.083

15.3.7 Wall Base Diagonal Tension and Shear Slip Failure

It is shown in the previous section that the mean peak wall pier base shear force demand under the twenty survival-level ground motion records in Table 15.52 is smaller than the estimated design maximum wall pier base shear force demand from Chapter 12. Thus, it is concluded that diagonal tension failure of the wall piers in Structure P2-PWUPT can be, on average, prevented as long as the design diagonal tension capacity $F_{w,dt}=9261$ kN from Chapter 12 is achieved and maintained.

Similarly, the mean peak coupled wall base shear force demand under the twenty survival-level ground motion records in Table 15.50 is smaller than the estimated design maximum coupled wall base shear force demand from Chapter 12. However, it cannot be simply concluded that shear slip failure of the structure is prevented since the shear slip capacity at the base of the structure, $F_{w,ss}$ varies during a ground motion. As described in Chapter 12, the coupled wall base shear slip capacity is computed as $F_{w,ss} = F_{g,ss} + F_{p,ss}$ where, $F_{g,ss}$ is the slip capacity due to the applied gravity loads and $F_{p,ss}$ is the shear friction capacity due to the wall pier post-tensioning forces. The coupled wall base shear slip capacity varies with time during an earthquake since $F_{p,ss}$ varies. The shear slip capacity from the gravity loads, $F_{g,ss}$ is assumed to remain constant during an earthquake.

The minimum coupled wall base shear slip capacity to base shear force demand ratios from the dynamic analyses of Structure P2-PWUPT under the twenty survival-level SAC ground motion records (LA21-LA40) and twenty design-level records (LA01-LA20) are listed in Tables 15.56 and 15.57, respectively. The coupled wall base shear slip capacity is calculated using an assumed coefficient of friction between the wall piers and the foundation of $\mu_{wf}=0.7$ (see Chapter 12). The design estimate for the survival-level minimum coupled wall base shear slip capacity to base shear force demand ratio in Table 15.56 is determined as the ratio between the design estimates for the coupled wall base shear slip capacity, $F_{w,ss}$ and base shear force demand, $Q_{w,max}$, from Chapter 12. It is observed that the mean ratio from the survival-level dynamic analysis results is larger than and reasonably close to the design estimate, and thus, the design procedure to prevent shear slip failure at the base of the structure seems to be valid.

The minimum coupled wall base shear slip capacity to base shear force demand ratios under all of the survival-level and design-level ground motion records in Tables 15.56 and 15.57 are larger than 1.0. Thus, shear slip failure at the base of Structure P2-PWUPT is prevented. As an example, Fig. 15.47 shows comparisons between the coupled wall base shear slip capacity (solid line) and base shear force demand (dashed line) time histories for the structure under the survival-level LA38 ground motion, for which the minimum coupled wall base shear slip capacity-demand ratio is closest to the mean ratio from the twenty records (see Table 15.56). For comparison, the solid and dashed horizontal lines indicate the design estimates for the coupled wall base shear slip capacity, $F_{w,ss}$ and base shear force demand, $Q_{w,max}$, respectively. As described in Chapter 12, the design estimate for the coupled wall base shear slip capacity due to the wall pier post-tensioning forces, $F_{p,ss}$ is computed from estimated residual stresses in the wall pier post-tensioning bars upon unloading the structure after displacing it laterally up to the survival-level roof drift demand Δ_s in the positive and negative directions.

Fig. 15.48 plots the minimum coupled wall base shear slip capacity-demand ratios from Tables 15.56 and 15.57 (\square markers) against the maximum incremental velocity (MIV) of the ground motion records (see Tables 14.2 and 14.1), where the dashed and solid horizontal lines represent the design estimate (from Chapter 12) and the mean ratio, respectively, for each data set. It is observed that there is significant scatter or variation in the minimum coupled wall base shear slip capacity-demand ratio; however, as stated previously, shear slip at the base of the structure is not expected to under any of the ground motion records.

TABLE 15.56

MINIMUM COUPLED WALL BASE SHEAR SLIP CAPACITY-DEMAND RATIOS
FOR STRUCTURE P2-PWUPT UNDER SURVIVAL LEVEL GROUND MOTIONS

ground motion	LA21	LA22	LA23 ^b	LA24	LA25	LA26	LA27	LA28 ^c	LA29	LA30	estimate (design)	standard deviation
min. wall shear slip capacity-demand ratio	2.38	3.33	3.70	3.00	2.82	2.59	3.02	1.96	2.43	1.97	2.10	0.51
ground motion	LA31	LA32	LA33	LA34	LA35	LA36	LA37	LA38 ^a	LA39	LA40	mean	standard deviation/mean
min. wall shear slip capacity-demand ratio	2.23	2.28	2.87	2.94	2.21	1.99	3.04	2.75	3.47	3.07	2.70	0.19

^a The peak ratio under this ground motion is closest to the mean ratio

^b The peak ratio under this ground motion is the largest ratio

^c The peak ratio under this ground motion is the smallest ratio

TABLE 15.57

MINIMUM COUPLED WALL BASE SHEAR SLIP CAPACITY-DEMAND RATIOS
FOR STRUCTURE P2-PWUPT UNDER DESIGN LEVEL GROUND MOTIONS

ground motion	LA01	LA02	LA03 ^a	LA04	LA05	LA06 ^b	LA07	LA08	LA09	LA10	standard deviation	
min. wall shear slip capacity-demand ratio	3.15	3.01	3.32	4.13	4.83	4.94	4.17	4.02	3.56	3.86	0.81	
ground motion	LA11	LA12	LA13	LA14	LA15	LA16	LA17	LA18	LA19 ^c	LA20	mean	standard deviation/mean
min. wall shear slip capacity-demand ratio	3.15	2.25	2.96	2.93	3.49	3.27	3.70	2.69	2.17	1.92	3.38	0.24

^a The peak ratio under this ground motion is closest to the mean ratio

^b The peak ratio under this ground motion is the largest ratio

^c The peak ratio under this ground motion is the smallest ratio

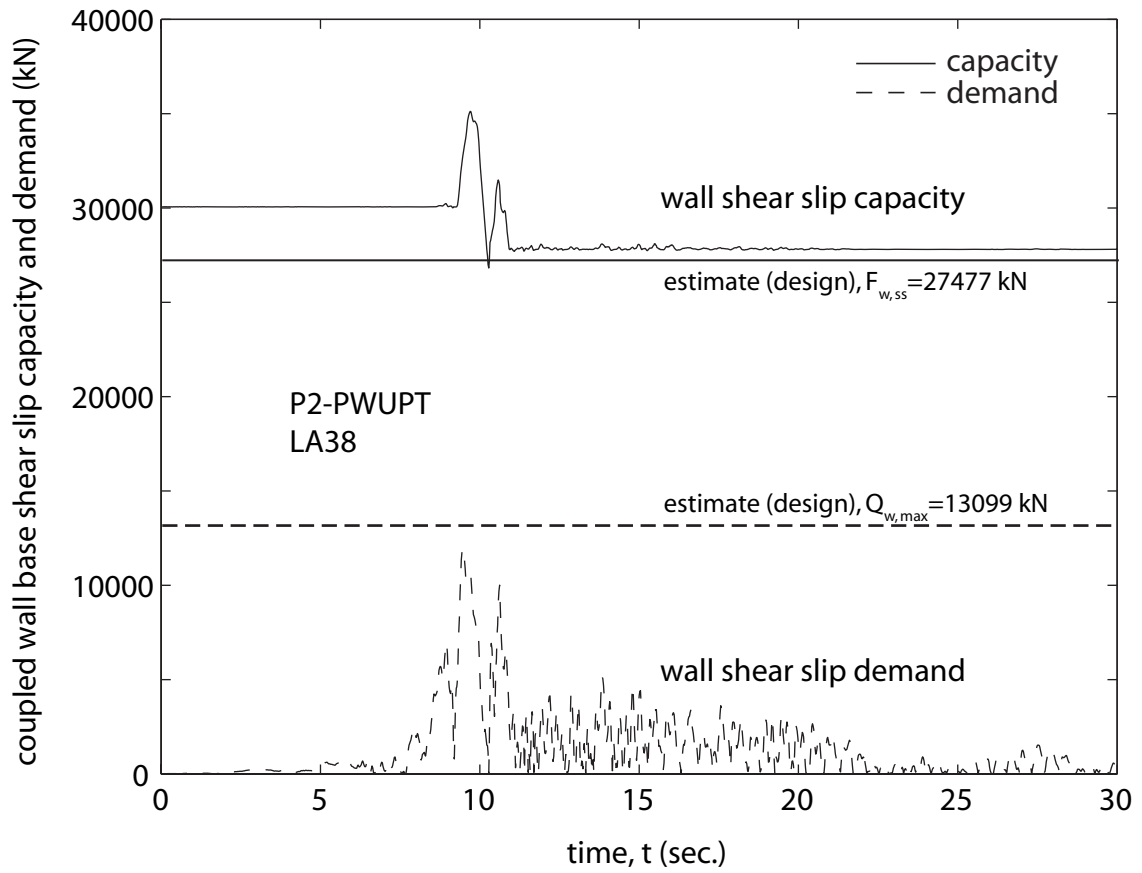


Fig. 15.47 Coupled wall base shear slip capacity and base shear force demand time histories for Structure P2-PWUPT

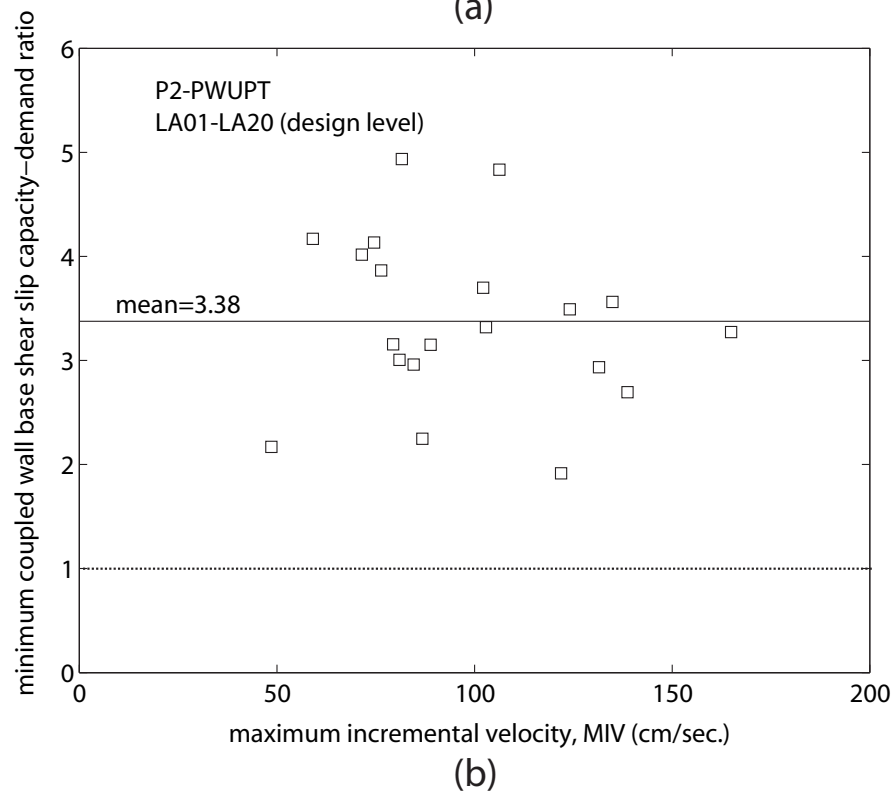
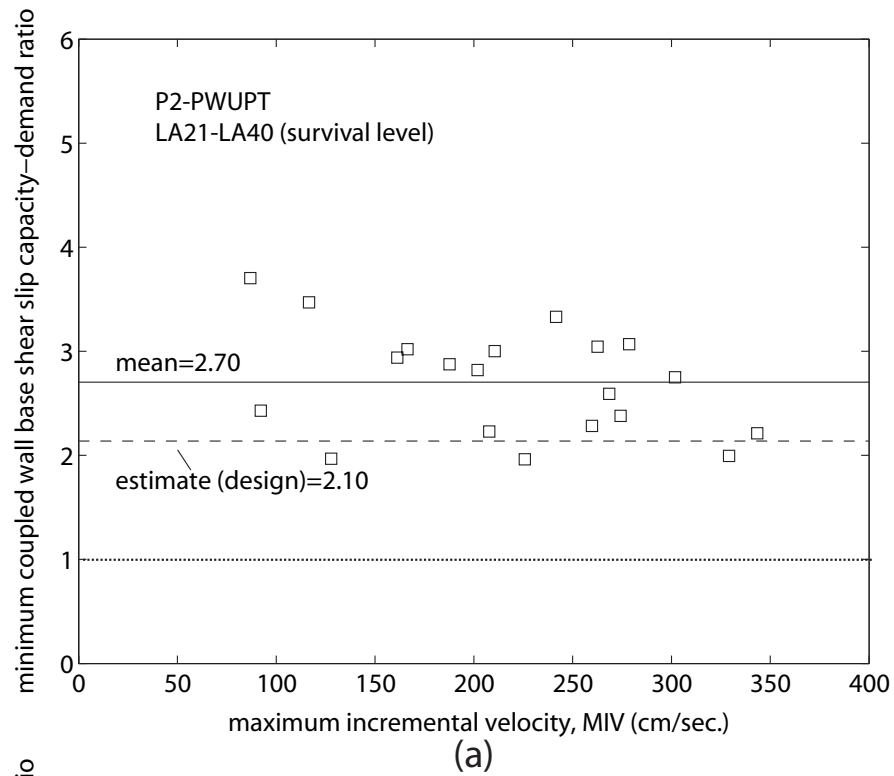


Fig. 15.48 Minimum coupled wall base shear slip capacity to base shear force demand ratio for Structure P2-PWUPT: (a) survival level; (b) design level

15.3.8 Wall Base Moments

The peak wall pier base moment demands from the dynamic analyses of Structure P2-PWUPT under the twenty survival-level SAC ground motion records (LA21-LA40) and twenty design-level records (LA01-LA20) are listed in Tables 15.58 and 15.59, respectively. The wall pier base moments are calculated from the equilibrium of the floor/roof level wall pier inertia forces with the coupling beam midspan axial forces and beam post-tensioning tendon forces from the analysis model (obtained from the fiber beam-column elements and the truss elements representing the coupling beams and the beam post-tensioning tendons, respectively).

TABLE 15.58
PEAK WALL PIER BASE MOMENT DEMANDS FOR STRUCTURE P2-PWUPT
UNDER SURVIVAL LEVEL GROUND MOTIONS

ground motion	LA21	LA22	LA23	LA24	LA25	LA26	LA27	LA28	LA29	LA30	estimate (idealized)	standard deviation
peak wall pier base moment (kN.m)	68533	64929	59484	66816	66692	70284	64455	68737	59924	62613	61800	4242
ground motion	LA31	LA32	LA33 ^a	LA34	LA35	LA36 ^b	LA37	LA38	LA39 ^c	LA40	mean	standard deviation/mean
peak wall pier base moment (kN.m)	67991	68759	66511	62568	72826	72973	69494	69708	57540	66002	66342	0.064

^a The peak demand under this ground motion is closest to the mean demand

^b The peak demand under this ground motion is the largest demand

^c The peak demand under this ground motion is the smallest demand

TABLE 15.59

PEAK WALL PIER BASE MOMENT DEMANDS FOR STRUCTURE P2-PWUPT
UNDER DESIGN LEVEL GROUND MOTIONS

ground motion	LA01	LA02	LA03	LA04	LA05	LA06 ^c	LA07	LA08	LA09	LA10	estimate (idealized)	standard deviation
peak wall pier base moment (kN.m)	59212	60071	59009	46988	47191	39803	54750	54592	62579	55371	58235	6351
ground motion	LA11	LA12	LA13	LA14	LA15	LA16 ^b	LA17	LA18	LA19 ^a	LA20	mean	standard deviation/mean
peak wall pier base moment (kN.m)	54885	53270	63054	61461	60139	64771	60365	59845	56501	63833	56884	0.11

^a The peak demand under this ground motion is closest to the mean demand

^b The peak demand under this ground motion is the largest demand

^c The peak demand under this ground motion is the smallest demand

Since the proposed design approach does not require the estimation of the survival-level and design-level wall pier base moments, the results from the dynamic analyses are compared with the results from the static idealized tri-linear pushover analysis of the structure in Chapter 13. The bending moments at the base of the compression-side wall pier (which has a larger base moment than the tension-side wall pier), M_{cwu} and M_{cwy} , corresponding to the estimated coupled wall ultimate state and coupled wall PT-yielding state are given in Tables 15.58 and 15.59, respectively (see also Table 13.2). The results show that the wall pier base moments, M_{cwu} and M_{cwy} , from the idealized pushover analysis provide good estimates of the peak wall pier base moment demands from the dynamic analyses.

As an example, Fig. 15.49 shows the bending moment time histories at the bases of the left-side and right-side wall piers in Structure P2-PWUPT under the survival-level

LA33 ground motion, for which the peak wall pier base moment demand (occurring in the left-side wall pier) is closest to the mean demand from the twenty records (see Table 15.54). The dashed horizontal lines indicate the estimated idealized compression-side wall pier base moment, M_{cwu} from the tri-linear static pushover analysis in Chapter 13 at the coupled wall ultimate state.

Fig. 15.50 plots the peak wall pier base moment demands from Tables 15.54 and 15.55 (\square markers) against the maximum incremental velocity (MIV) of the ground motion records (see Tables 14.2 and 14.1), where the dashed and solid horizontal lines represent the estimated idealized wall pier base moment (from Chapter 13) and the mean peak wall pier base moment demand, respectively, for each data set. A considerable amount of scatter is observed in the peak wall pier base moment demands in each data set.

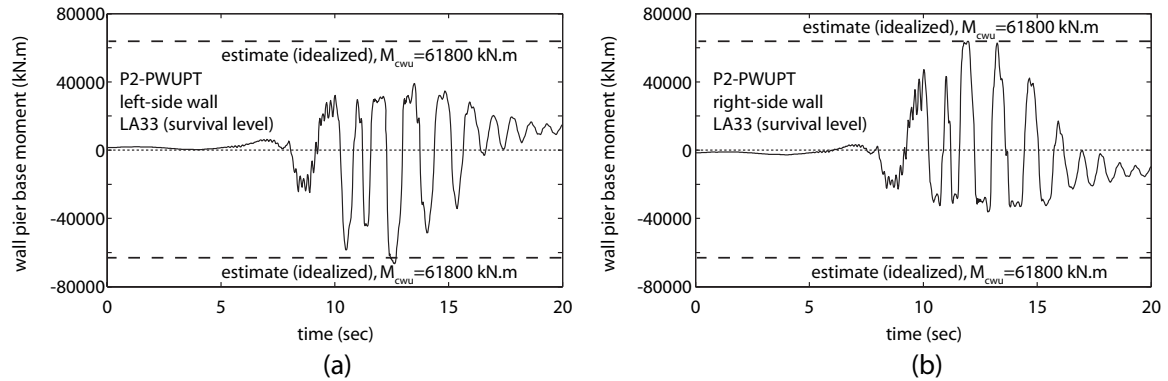
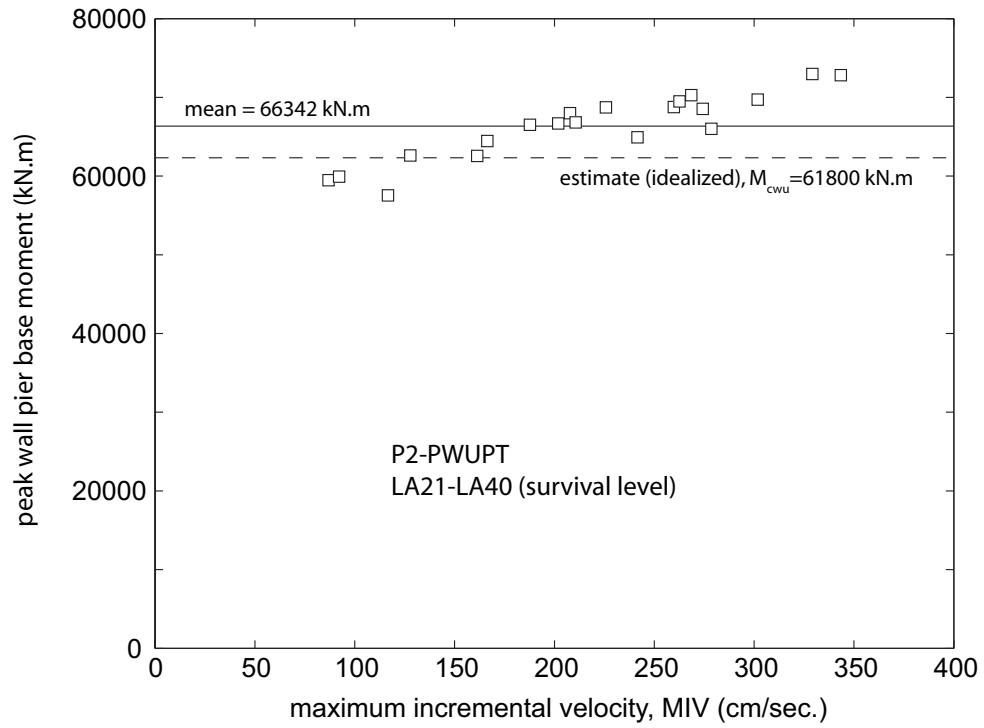


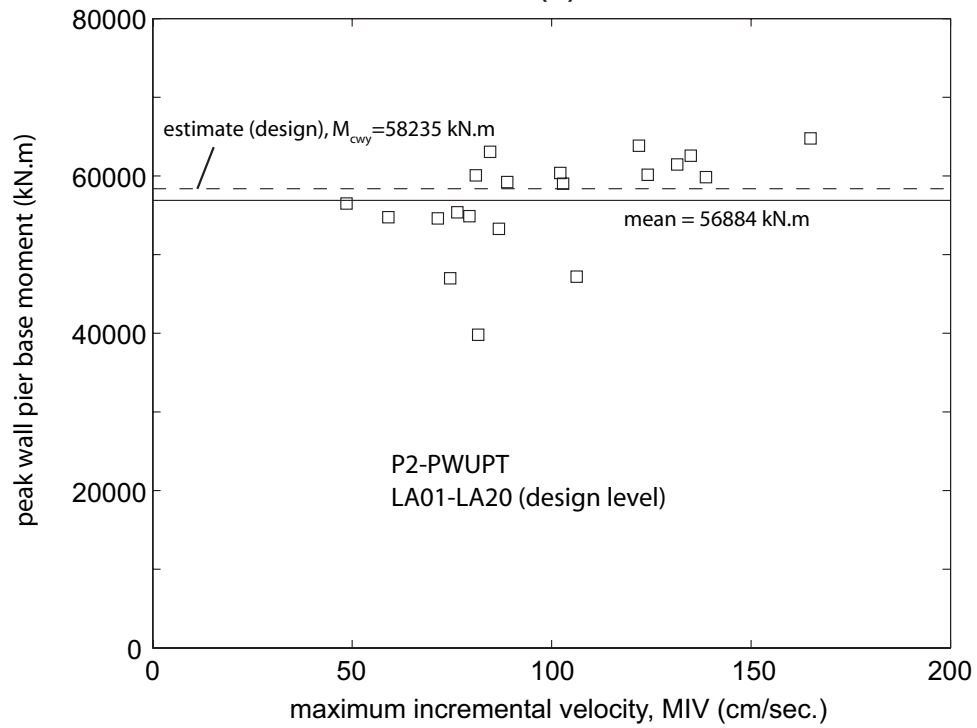
Fig. 15.49 Wall pier base moment time histories for Structure P2-PWUPT:
(a) left-side wall; (b) right-side wall

The peak total coupled wall base moment demands from the dynamic analyses of Structure P2-PWUPT under the twenty survival-level SAC ground motion records (LA21-LA40) and twenty design-level records (LA01-LA20) are listed in Tables 15.60 and 15.61, respectively. The coupled wall base moment, M_w is calculated from the equilibrium of the floor and roof level wall pier inertia forces.

Similar to the wall pier base moments, the peak coupled wall base moment demands from the dynamic analyses are compared with the results from the static idealized tri-linear pushover analysis of the structure in Chapter 13. The coupled wall base moments, M_{wu} and M_{wy} , corresponding to the estimated coupled wall ultimate state and PT-yielding state are given in Tables 15.60 and 15.61, respectively (see also Table 13.2). The results show that the coupled wall base moments, M_{wu} and M_{wy} , from the idealized pushover analysis underestimate the peak coupled wall base moment demands from the dynamic analyses even though the wall pier base moment demands are estimated reasonably well. This is possibly because of the underestimated coupling beam shear forces as described later in more detail.



(a)



(b)

Fig. 15.50 Peak wall pier base moment demands for Structure P2-PWUPT:
(a) survival level; (b) design level

TABLE 15.60

PEAK COUPLED WALL BASE MOMENT DEMANDS FOR STRUCTURE

P2-PWUPT UNDER SURVIVAL LEVEL GROUND MOTIONS

ground motion	LA21 ^b	LA22	LA23	LA24	LA25 ^a	LA26	LA27	LA28	LA29	LA30	estimate (idealized)	standard deviation
peak coupled wall base moment (kN.m)	249711	193240	172936	201761	200660	221160	188434	211976	169190	168147	154844	23852
ground motion	LA31	LA32	LA33	LA34	LA35	LA36	LA37	LA38	LA39 ^c	LA40	mean	standard deviation/mean
peak coupled wall base moment (kN.m)	213558	217696	187010	172921	224774	233441	203306	206712	159868	191164	199380	0.12

^a The peak demand under this ground motion is closest to the mean demand^b The peak demand under this ground motion is the largest demand^c The peak demand under this ground motion is the smallest demand

TABLE 15.61

PEAK COUPLED WALL BASE MOMENT DEMANDS FOR STRUCTURE

P2-PWUPT UNDER DESIGN LEVEL GROUND MOTIONS

ground motion	LA01 ^a	LA02	LA03	LA04	LA05	LA06 ^c	LA07	LA08	LA09	LA10	estimate (idealized)	standard deviation
peak coupled wall base moment (kN.m)	162830	162900	172330	126050	126930	112440	149330	155540	177680	153920	144019	20633
ground motion	LA11	LA12	LA13	LA14	LA15	LA16 ^b	LA17	LA18	LA19	LA20	mean	standard deviation/mean
peak coupled wall base moment (kN.m)	155490	141440	181900	181390	169780	192600	171880	163410	155460	177350	159530	0.13

^a The peak demand under this ground motion is closest to the mean demand^b The peak demand under this ground motion is the largest demand^c The peak demand under this ground motion is the smallest demand

As an example, Fig. 15.51 shows the coupled wall base moment time history of Structure P2-PWUPT under the survival-level LA25 ground motion, for which the peak coupled wall base moment demand is closest to the mean demand from the twenty records (see Table 15.60). The dashed horizontal lines indicate the estimated idealized coupled wall base moment, M_{wu} from the tri-linear static pushover analysis in Chapter 13 at the coupled wall ultimate state.

Fig. 15.52 plots the peak coupled wall base moment demands from Table 15.60 and 15.61 (\square markers) against the maximum incremental velocity (MIV) of the ground motion records (see Tables 14.2 and 14.1), where the dashed and solid horizontal lines represent the estimated idealized coupled wall base moment (from Chapter 13) and the mean peak coupled wall base moment demand, respectively, for each data set. Similar to the peak wall pier base moment demands, a considerable amount of scatter is observed in the peak coupled wall base moment demands in each data set.

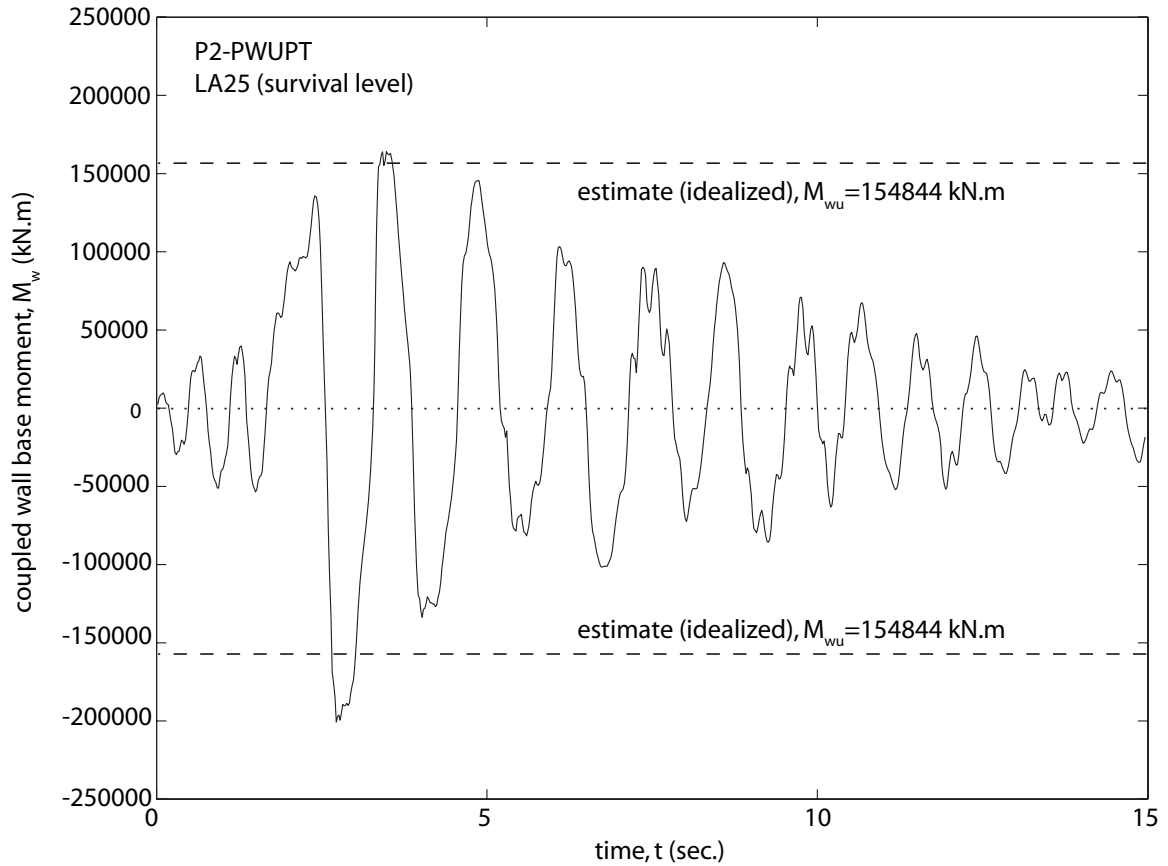
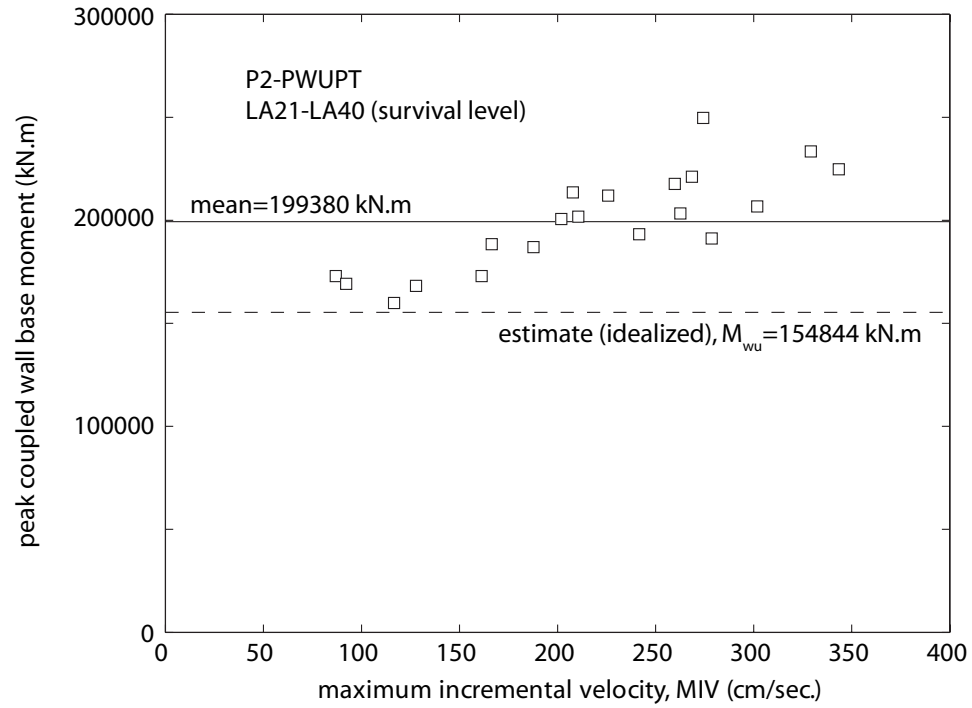


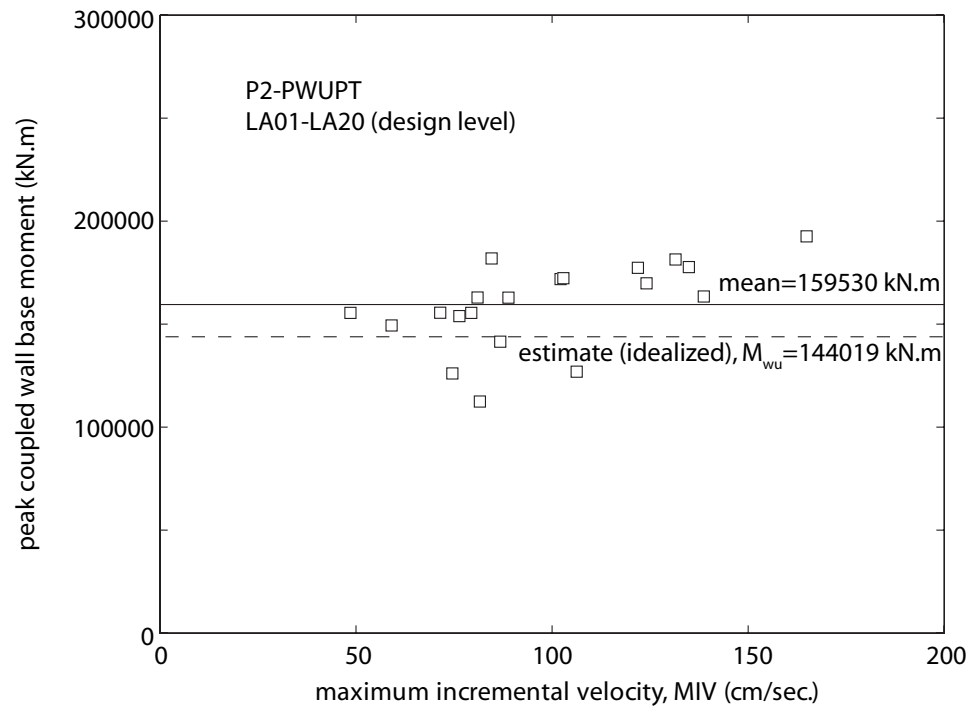
Fig. 15.51 Coupled wall base moment time history for Structure P2-PWUPT

15.3.9 Wall Base Strains

The peak confined concrete compression strain demands at the bases of the wall piers from the dynamic analyses of Structure P2-PWUPT under the twenty survival-level SAC ground motion records (LA21-LA40) and twenty design-level records (LA01-LA20) are listed in Tables 15.62 and 15.63, respectively. The concrete compression strains are determined directly from the fiber beam-column elements used for the wall piers in the analysis model.



(a)



(b)

Fig. 15.52 Peak coupled wall base moment demands for Structure P2-PWUPT:
(a) survival level; (b) design level

TABLE 15.62

PEAK WALL PIER BASE CONFINED CONCRETE COMPRESSION STRAIN
DEMANDS FOR STRUCTURE P2-PWUPT UNDER SURVIVAL LEVEL GROUND
MOTIONS

ground motion	LA21	LA22	LA23	LA24	LA25	LA26	LA27	LA28	LA29	LA30	estimate (design)	standard deviation
peak confined concrete strain (10^{-3})	-7.5	-2.1	-0.82	-3.1	-2.5	-6.1	-1.9	-5.0	-0.86	-1.7	-3.2	0.029
ground motion	LA31	LA32 ^a	LA33	LA34	LA35	LA36 ^b	LA37	LA38	LA39 ^c	LA40	mean	standard deviation/mean
peak confined concrete strain (10^{-3})	-5.5	-4.9	-2.9	-1.3	-10.0	-10.7	-5.2	-5.6	-0.65	-2.8	-4.0	0.73

^a The peak demand under this ground motion is closest to the mean demand

^b The peak demand under this ground motion is the largest demand

^c The peak demand under this ground motion is the smallest demand

TABLE 15.63

PEAK WALL PIER BASE CONFINED CONCRETE COMPRESSION STRAIN
DEMANDS FOR STRUCTURE P2-PWUPT UNDER DESIGN LEVEL GROUND
MOTIONS

ground motion	LA01	LA02	LA03	LA04	LA05	LA06 ^c	LA07	LA08	LA09	LA10	standard deviation	
peak confined concrete strain (10^{-3})	-8.1	-10.0	-7.5	-2.5	-2.6	-1.7	-5.1	-4.9	-12.2	-5.5	0.0046	
ground motion	LA11	LA12	LA13	LA14	LA15	LA16 ^b	LA17 ^a	LA18	LA19	LA20	mean	standard deviation/mean
peak confined concrete strain (10^{-3})	-5.7	-5.9	-12.6	-12.3	-8.3	-20.0	-8.2	-8.9	-6.0	-15.6	-8.2	0.56

^a The peak demand under this ground motion is closest to the mean demand

^b The peak demand under this ground motion is the largest demand

^c The peak demand under this ground motion is the smallest demand

The mean peak wall pier base confined concrete compression strain demand from the survival-level dynamic analyses in Table 15.62 is -0.040, which is considerably larger than the estimated wall pier base confined concrete strain demand of -0.032 from Chapter 12. Thus, the method used in Chapter 12 to estimate the wall pier base confined concrete compression strain demand needs to be improved. Note that the design approach does not require the estimation of the confined concrete compression strain demand under the design-level earthquake; and thus, no design-level estimate is provided in Table 15.63.

As an example, Fig. 15.53 shows the extreme confined concrete compression strain time histories at the base of Structure P2-PWUPT under the survival-level LA32 ground motion, for which the peak wall pier base confined concrete compression strain demand (occurring at the left end of the left-side wall pier) is closest to the mean demand from the twenty records (see Table 15.62). A total of four strain time histories are shown for the left and right ends of the left-side and right-side wall piers, where the dashed horizontal lines indicate the design estimate for the wall pier base confined concrete compression strain demand from Chapter 12.

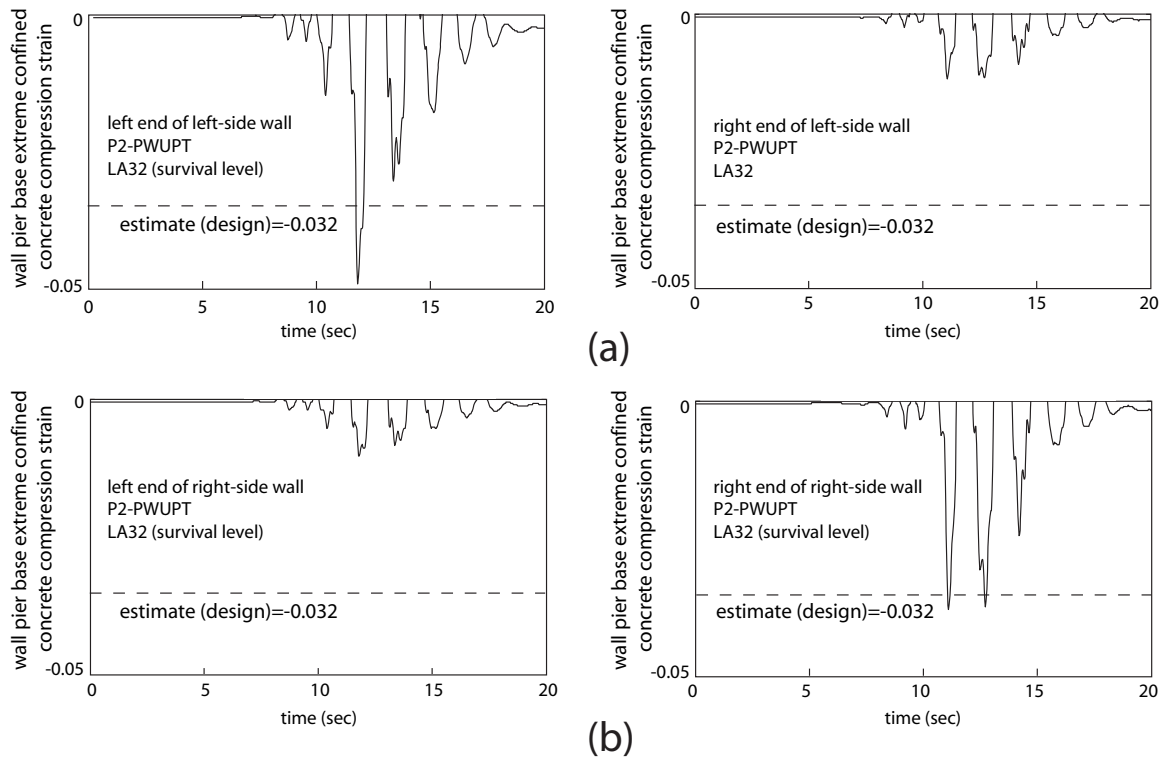
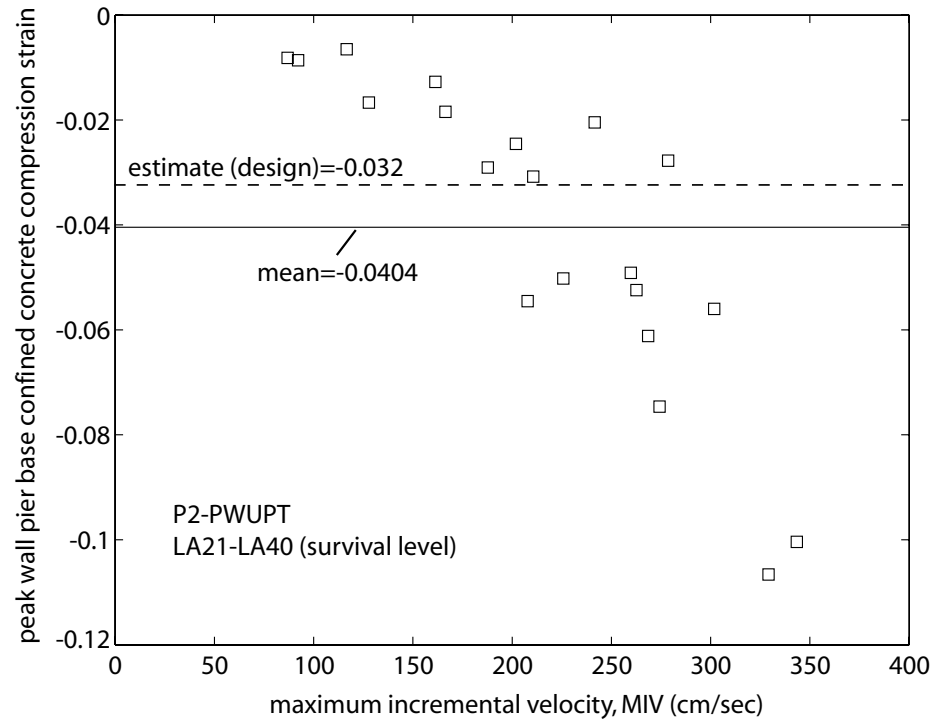
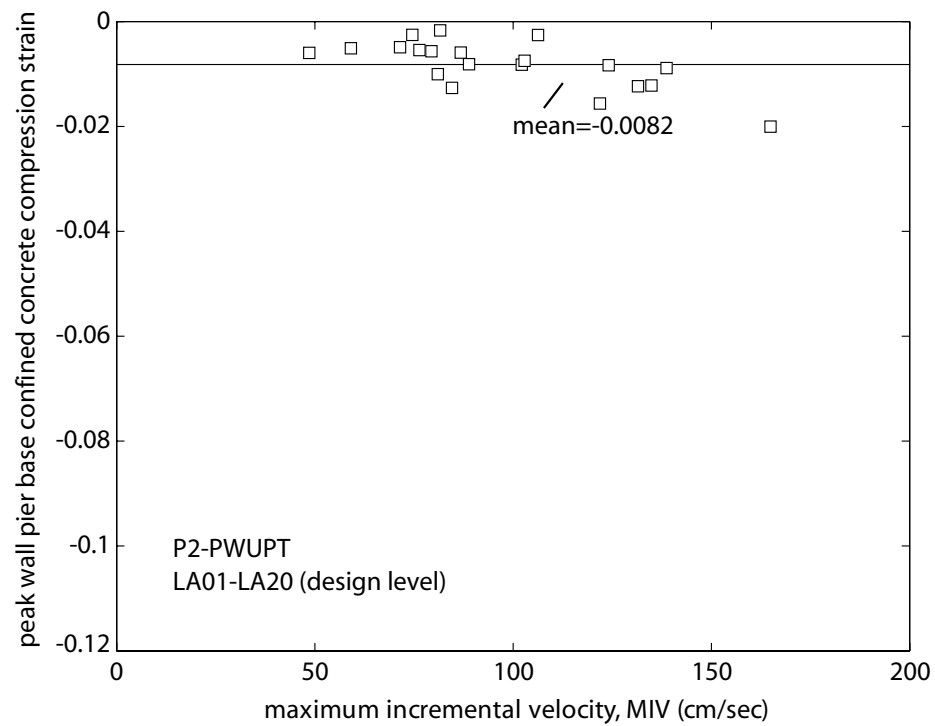


Fig. 15.53 Wall pier base extreme confined concrete compression strain time histories for Structure P2-PWUPT: (a) left-side wall; (b) right-side wall

Fig. 15.54 plots the peak wall pier base confined concrete compression strain demands from Tables 15.62 and 15.63 (\square markers) against the maximum incremental velocity (MIV) of the ground motion records (see Tables 14.2 and 14.1), where the dashed and solid horizontal lines represent the design estimate and mean peak wall pier base confined concrete compression strain demand, respectively, for each data set. The trends for the peak wall pier base confined concrete compression strain demands in Fig. 15.54 are similar to the trends for the peak coupled wall roof drift demands in Fig. 15.33.



(a)



(b)

Fig. 15.54 Peak wall pier base confined concrete compression strain demands for Structure P2-PWUPT: (a) survival level; (b) design level

15.3.10 Coupling Beam Chord Rotations

The peak coupling beam chord rotation demands from the dynamic analyses of Structure P2-PWUPT under the twenty survival-level SAC ground motion records (LA21-LA40) and twenty design-level records (LA01-LA20) are listed in Tables 15.64 and 15.65, respectively. As described in Chapter 7, the coupling beam chord rotation, θ_b , is measured from a tangent drawn at the left end of each beam.

TABLE 15.64

PEAK COUPLING BEAM CHORD ROTATION DEMANDS FOR STRUCTURE P2-PWUPT UNDER SURVIVAL LEVEL GROUND MOTIONS

ground motion	LA21	LA22	LA23	LA24 ^a	LA25	LA26	LA27	LA28	LA29	LA30	estimate (design)	standard deviation
peak coupling beam chord rotation (%)	4.70	2.63	1.24	3.18	2.98	4.31	2.28	3.71	1.42	1.69	5.62	1.41
ground motion	LA31	LA32	LA33	LA34	LA35	LA36 ^b	LA37	LA38	LA39 ^c	LA40	mean	standard deviation/mean
peak coupling beam chord rotation (%)	3.97	3.94	2.56	1.79	5.77	6.09	3.58	4.03	1.16	2.68	3.19	0.44

^a The peak demand under this ground motion is closest to the mean demand

^b The peak demand under this ground motion is the largest demand

^c The peak demand under this ground motion is the smallest demand

TABLE 15.65

PEAK COUPLING BEAM CHORD ROTATION DEMANDS FOR STRUCTURE
P2-PWUPT UNDER DESIGN LEVEL GROUND MOTIONS

ground motion	LA01 ^a	LA02	LA03	LA04	LA05	LA06 ^c	LA07	LA08	LA09	LA10	estimate (design)	standard deviation
peak coupling beam chord rotation (%)	1.13	1.24	0.70	0.43	0.49	0.27	0.79	0.93	1.36	0.94	2.59	0.58
ground motion	LA11	LA12	LA13	LA14	LA15	LA16 ^b	LA17	LA18	LA19	LA20	mean	standard deviation/mean
peak coupling beam chord rotation (%)	0.61	0.62	1.84	1.97	1.38	2.44	1.46	1.33	0.85	1.83	1.13	0.51

^a The peak demand under this ground motion is closest to the mean demand

^b The peak demand under this ground motion is the largest demand

^c The peak demand under this ground motion is the smallest demand

The mean peak coupling beam chord rotation demand from the survival-level dynamic analyses in Table 15.64 is 3.19%, which is significantly smaller than the estimated survival-level coupling beam chord rotation demand of $\theta_s=5.62\%$ from Chapter 12. As an example, Fig. 15.55 shows the chord rotation time histories for the eight coupling beams in Structure P2-PWUPT under the survival-level LA24 ground motion, for which the peak coupling beam chord rotation demand (occurring in the roof beam) is closest to the mean demand from the twenty records (see Table 15.64). The design estimate for the peak coupling beam chord rotation demand, θ_s from Chapter 12 is indicated in the figure.

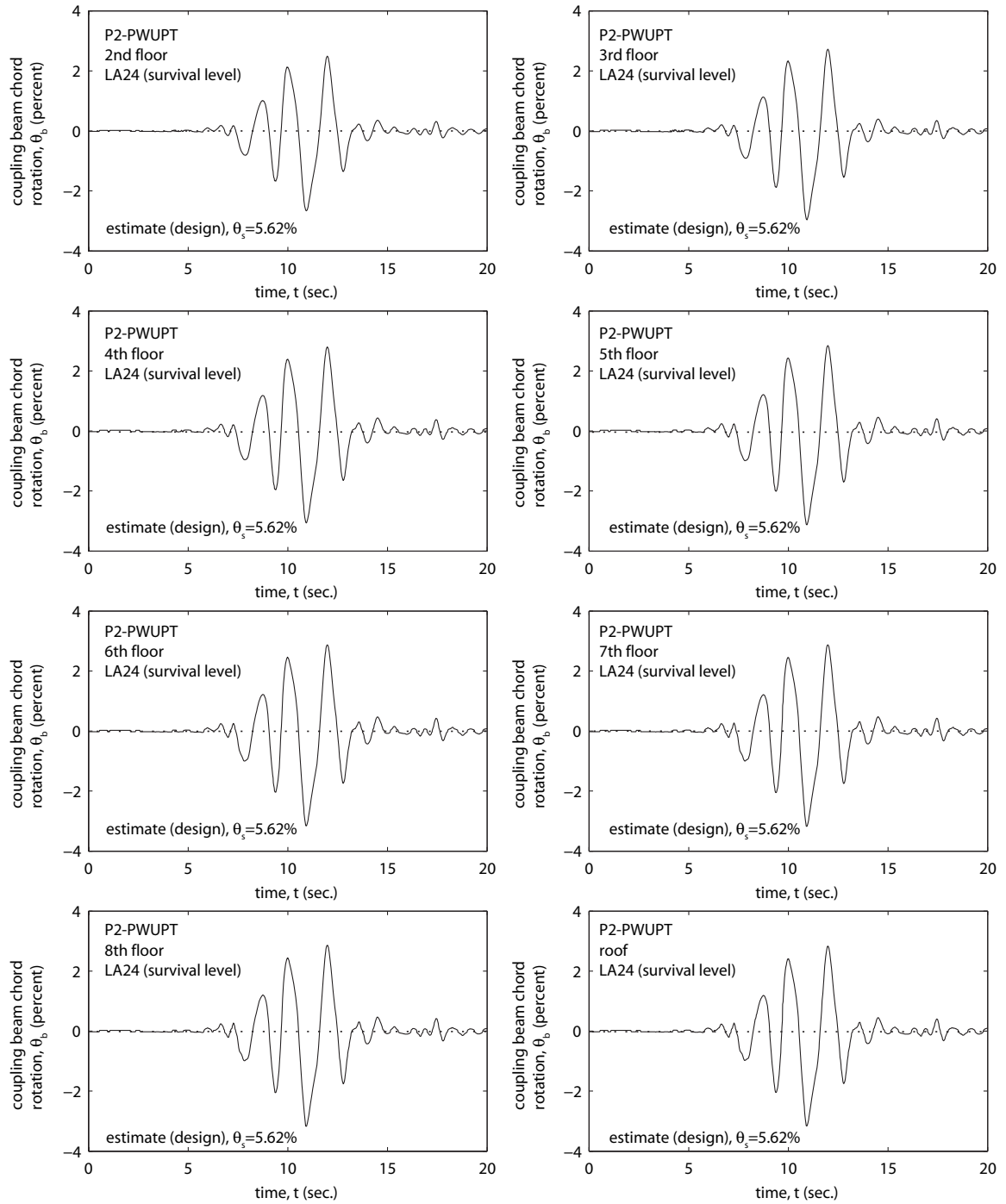


Fig. 15.55 Coupling beam chord rotation time histories for Structure P2-PWUPT

Similarly, the mean peak coupling beam chord rotation demand from the design-level analyses in Table 15.65 is 1.13%, which is smaller than the estimated design-level coupling beam chord rotation demand of $\theta_d=2.59\%$ from Chapter 12. It is concluded that the displacement-based design objectives under the survival-level and design-level ground motions are satisfied; however, the procedure to estimate the coupling beam chord rotation demands may need to be improved to prevent an overly-conservative design.

Fig. 15.56 plots the peak coupling beam chord rotation demands from Tables 15.64 and 15.65 (\square markers) against the maximum incremental velocity (MIV) of the ground motion records (see Tables 14.2 and 14.1), where the dashed and solid horizontal lines represent the design estimate (from Chapter 12) and the mean peak coupling beam chord rotation demand, respectively, for each data set. It is observed that the coupling beam chord rotation demands tend to follow similar trends to the coupled wall roof drift demands in Fig. 15.33.

15.3.11 Coupling Beam Axial Forces

The peak axial force demands at the midspan of the coupling beams from the dynamic analyses of Structure P2-PWUPT under the twenty survival-level SAC ground motion records (LA21-LA40) and twenty design-level records (LA01-LA20) are listed in Tables 15.66 and 15.67, respectively. The coupling beam midspan axial forces, N_b are determined directly from the fiber beam-column elements at the beam midspan locations in the analysis model.

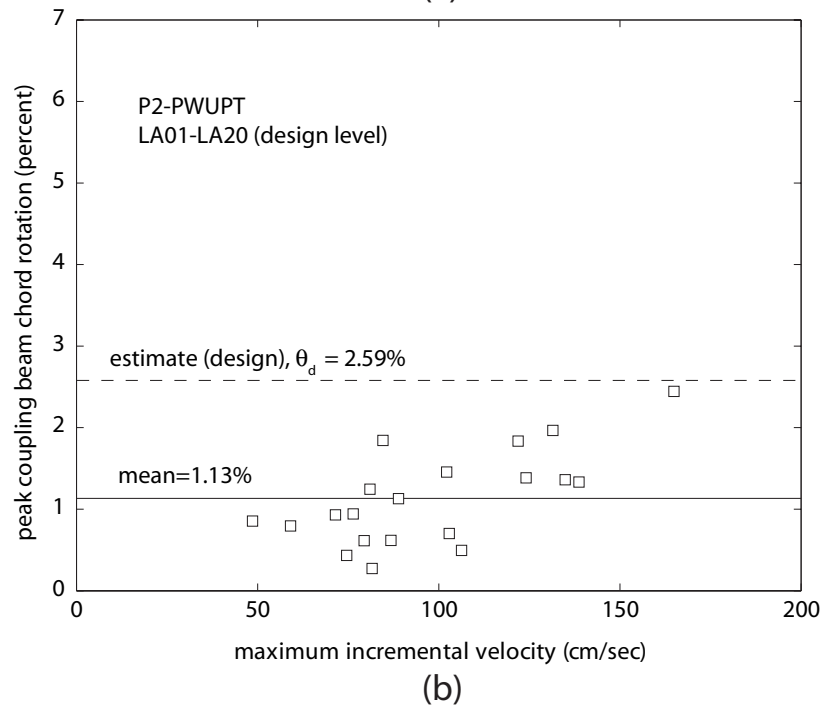
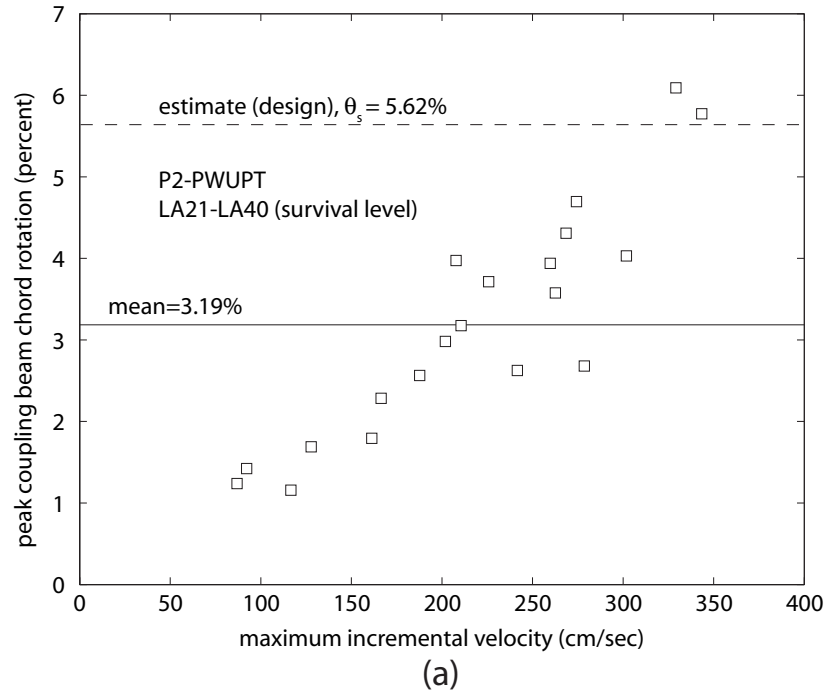


Fig. 15.56 Peak coupling beam chord rotation demands for Structure P2-PWUPT:
(a) survival level; (b) design level

TABLE 15.66

PEAK COUPLING BEAM MIDSPAN AXIAL FORCE DEMANDS FOR
STRUCTURE P2-PWUPT UNDER SURVIVAL LEVEL GROUND MOTIONS

ground motion	LA21	LA22	LA23	LA24 ^a	LA25	LA26	LA27	LA28	LA29	LA30	estimate (design)	standard deviation
peak coupling beam midspan axial force (kN)	4519	3708	3082	3719	4047	3718	3408	4016	3513	3891	2365	497
ground motion	LA31 ^b	LA32	LA33	LA34	LA35	LA36	LA37	LA38	LA39 ^c	LA40	mean	standard deviation/mean
peak coupling beam midspan axial force (kN)	4750	4351	3486	3346	4330	4355	3619	3503	2809	3507	3784	0.13

^a The peak demand under this ground motion is closest to the mean demand

^b The peak demand under this ground motion is the largest demand

^c The peak demand under this ground motion is the smallest demand

TABLE 15.67

PEAK COUPLING BEAM MIDSPAN AXIAL FORCE DEMANDS FOR
STRUCTURE P2-PWUPT UNDER DESIGN LEVEL GROUND MOTIONS

ground motion	LA01	LA02	LA03	LA04	LA05	LA06 ^c	LA07	LA08	LA09	LA10	standard deviation	
peak coupling beam midspan axial force (kN)	3199	3404	2825	2160	1972	1835	2585	2444	3212	2611	578	
ground motion	LA11	LA12	LA13	LA14	LA15	LA16	LA17 ^a	LA18	LA19	LA20 ^b	mean	standard deviation/mean
peak coupling beam midspan axial force (kN)	2628	3403	3439	3375	3439	3389	2993	3450	3071	4069	2975	0.19

^a The peak demand under this ground motion is closest to the mean demand

^b The peak demand under this ground motion is the largest demand

^c The peak demand under this ground motion is the smallest demand

As discussed in Chapter 13, the largest coupling beam axial forces develop in the lowest beam at the second floor level as a result of the fixed boundary conditions assumed at the wall pier bases. The mean peak coupling beam midspan axial force demand from the survival-level dynamic analyses in Table 15.66 is 3784 kN, which is much larger than the design force of, approximately, $1.25P_{by}=2365$ kN from Chapter 12. Thus, the axial force used in Chapter 12 for the design of the coupling beams appears unconservative and need to be improved. Note that the design approach does not require the estimation of the coupling beam axial force under the design-level earthquake; and thus, no design-level estimate is provided in Table 15.67.

As an example, Fig. 15.57 shows the midspan axial force time histories for the eight coupling beams in Structure P2-PWUPT under the survival-level LA24 ground motion, for which the peak coupling beam midspan axial force demand (always occurring in the second floor beam) is closest to the mean demand from the twenty records (see Table 15.66). The dashed horizontal lines indicate the design estimate for the peak coupling beam midspan axial force, which is equal to $1.25P_{by}$ for the second and third floor beams and P_{by} for the upper level beams. It is observed that the peak midspan axial force demands in the upper level beams also exceed the design estimate. Looking at the coupling beam midspan axial force time histories in Fig. 15.57 and since the coupling beam axial forces from the static analyses in Chapter 13 are estimated reasonably well by the proposed approximate procedures, the large peak axial force demands from the dynamic analyses may be due to the effect of higher modes during the response of the structure; however, this was not investigated. Note that there is a considerable loss in the

second floor beam axial force as discussed in Chapter 13, resulting in a smaller axial force in this beam at the end of the earthquake as compared with the upper level beams.

Fig. 15.58 plots the peak coupling beam midspan axial force demands from Tables 15.66 and 15.67 (\square markers) against the maximum incremental velocity (MIV) of the ground motion records (see Tables 14.2 and 14.1), where the dashed and solid horizontal lines represent the design estimate (from Chapter 12) and the mean peak coupling beam midspan axial force demand, respectively, for each data set. A significant amount of scatter is observed in the dynamic analysis results.

15.3.12 Coupling Beam Post-Tensioning Forces

The peak coupling beam post-tensioning force demands from the dynamic analyses of Structure P2-PWUPT under the twenty survival-level SAC ground motion records (LA21-LA40) and twenty design-level records (LA01-LA20) are listed in Tables 15.68 and 15.69, respectively. The beam post-tensioning forces, P_b are calculated as the sum of the forces in the truss elements representing the beam post-tensioning tendons at each floor/roof level in the analytical model.

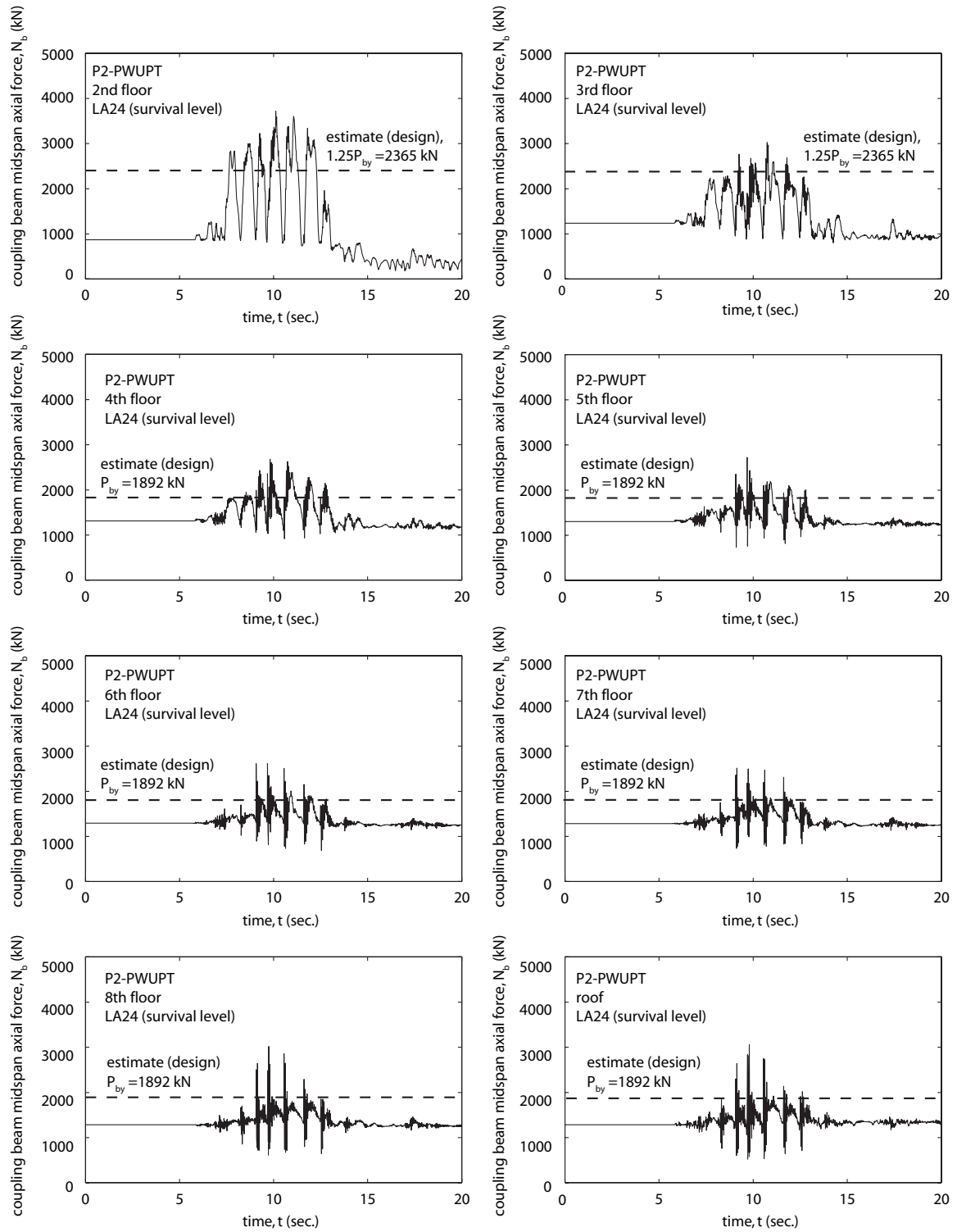
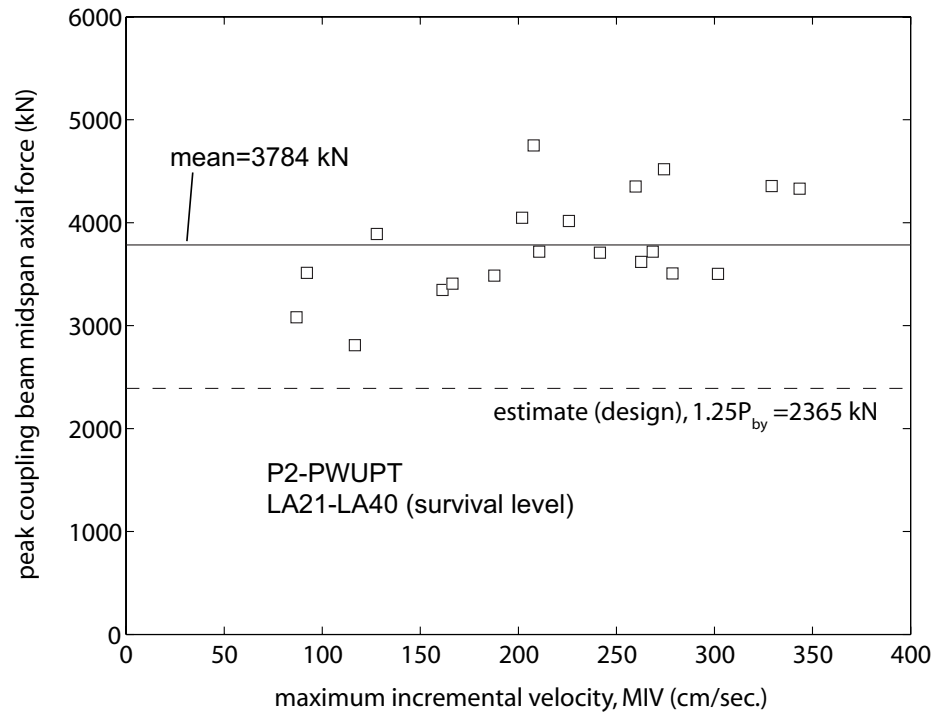
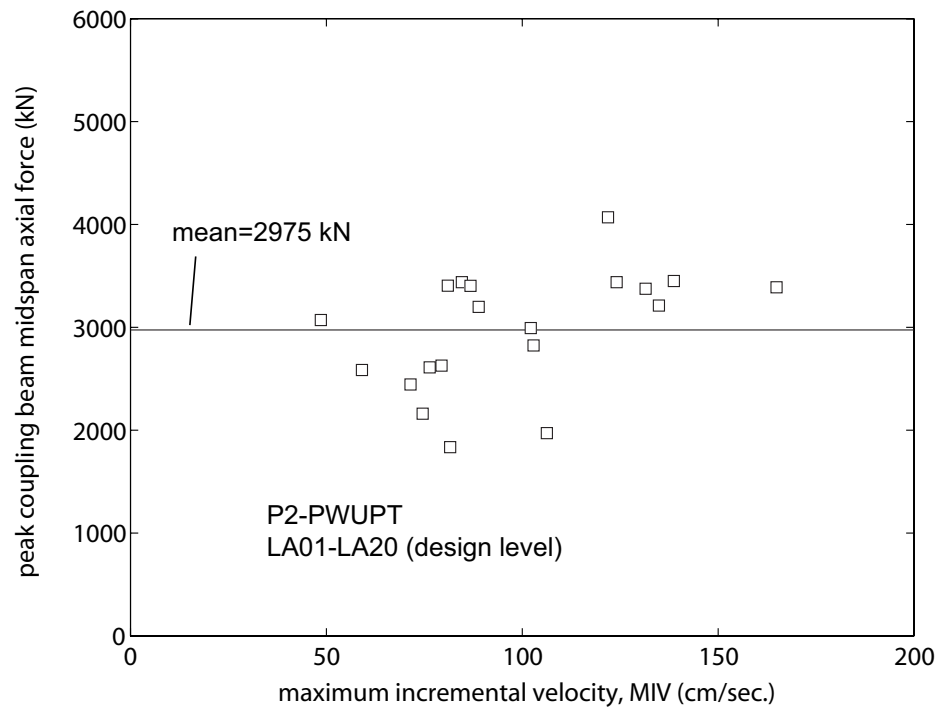


Fig. 15.57 Coupling beam midspan axial force time histories for Structure P2-PWUPT



(a)



(b)

Fig. 15.58 Peak coupling beam midspan axial force demands for Structure P2-PWUPT: (a) survival level; (b) design level

TABLE 15.68

PEAK COUPLING BEAM POST-TENSIONING FORCE DEMANDS FOR
STRUCTURE P2-PWUPT UNDER SURVIVAL LEVEL GROUND MOTIONS

ground motion	LA21	LA22	LA23	LA24	LA25 ^a	LA26	LA27	LA28	LA29	LA30	estimate (design)	standard deviation
peak coupling beam post-tensioning force (kN)	1937	1748	1496	1831	1793	1922	1678	1898	1528	1586	1892	169
round motion	LA31	LA32	LA33	LA34	LA35	LA36 ^b	LA37	LA38	LA39 ^c	LA40	mean	standard deviation/mean
peak coupling beam post-tensioning force (kN)	1912	1908	1726	1592	1993	2009	1887	1912	1486	1748	1780	0.095

^a The peak demand under this ground motion is closest to the mean demand

^b The peak demand under this ground motion is the largest demand

^c The peak demand under this ground motion is the smallest demand

TABLE 15.69

PEAK COUPLING BEAM POST-TENSIONING FORCE DEMANDS FOR
STRUCTURE P2-PWUPT UNDER DESIGN LEVEL GROUND MOTIONS

ground motion	LA01	LA02 ^a	LA03	LA04	LA05	LA06 ^c	LA07	LA08	LA09	LA10	standard deviation	
peak coupling beam post-tensioning force (kN)	1493	1516	1494	1367	1376	1356	1432	1456	1591	1458	97	
ground motion	LA11	LA12	LA13	LA14	LA15	LA16 ^b	LA17	LA18	LA19	LA20	mean	standard deviation/mean
peak coupling beam post-tensioning force (kN)	1465	1486	1621	1643	1538	1728	1552	1528	1456	1620	1509	0.064

^a The peak demand under this ground motion is closest to the mean demand

^b The peak demand under this ground motion is the largest demand

^c The peak demand under this ground motion is the smallest demand

The mean peak coupling beam post-tensioning force demand from the survival-level dynamic analyses in Table 15.68 is smaller than the total yield force of the coupling beam post-tensioning tendons, $P_{by}=1892$ kN from Chapter 12; and thus, the yielding of the beam post-tensioning tendons is prevented as required by design. As an example, Fig. 15.59 shows the post-tensioning force time-histories for the eight coupling beams in Structure P2-PWUPT under the survival-level ground motion LA25, for which the peak coupling beam post-tensioning force demand (occurring in the 6th floor beam) is closest to the mean demand from the twenty records (see Table 15.68). The dashed horizontal lines indicate the total yield force of the coupling beam post-tensioning tendons, P_{by} . It is observed that there is almost no loss in the coupling beam post-tensioning forces during the ground motion since the tendons do not yield. The smallest post-tensioning force develops in the second floor coupling beam, since the fixed foundation conditions at the bases of the wall piers restrain the opening of gaps at the beam ends, and thus, limit the elongation of the post-tensioning tendons during the ground motion.

Fig. 15.60 plots the peak coupling beam post-tensioning force demands from Tables 15.68 and 15.69 (\square markers) against the maximum incremental velocity (MIV) of the ground motion records (see Tables 14.2 and 14.1), where the dashed and solid horizontal lines represent the design estimate (from Chapter 12) and the mean peak coupling beam post-tensioning force demand, respectively, for each data set. It is observed that yielding of the coupling beam post-tensioning tendons occurs under some of the survival-level ground motion records, since the design roof drift from Chapter 12 is exceeded (see Fig. 15.2).

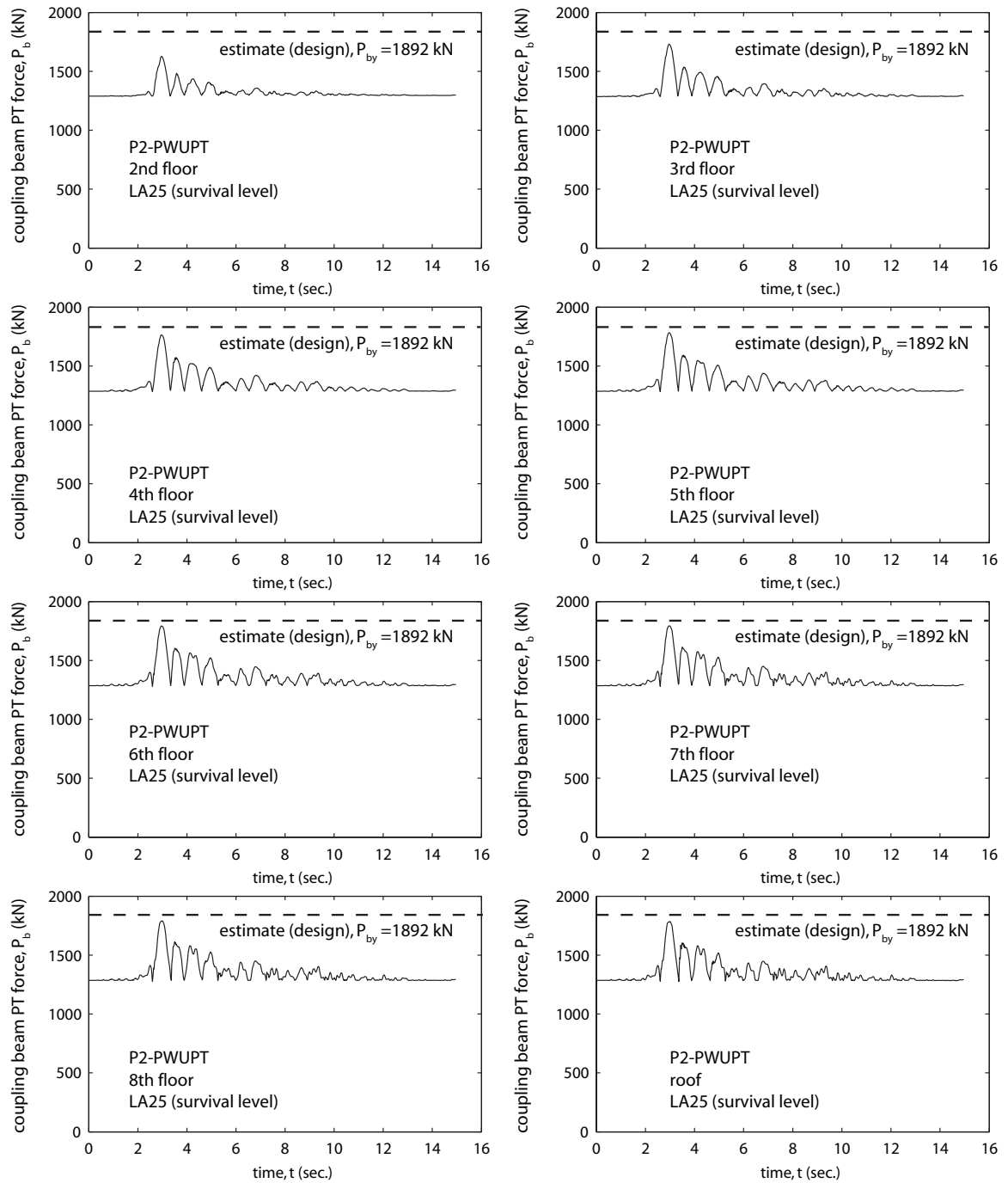


Fig. 15.59 Coupling beam post-tensioning force time histories for Structure P2-PWUPT

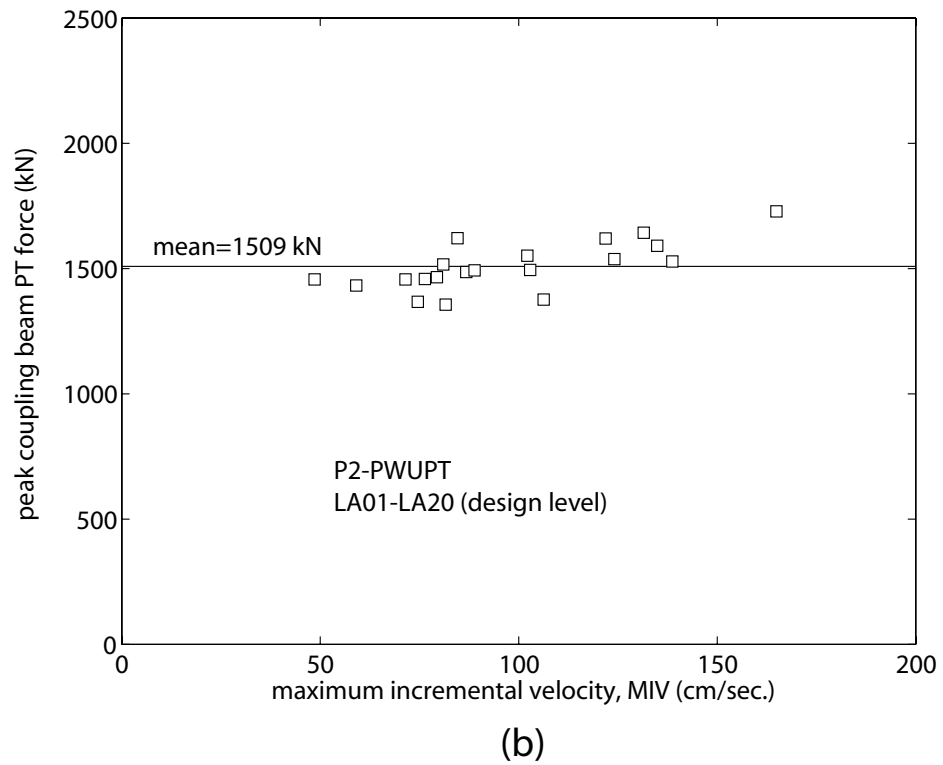
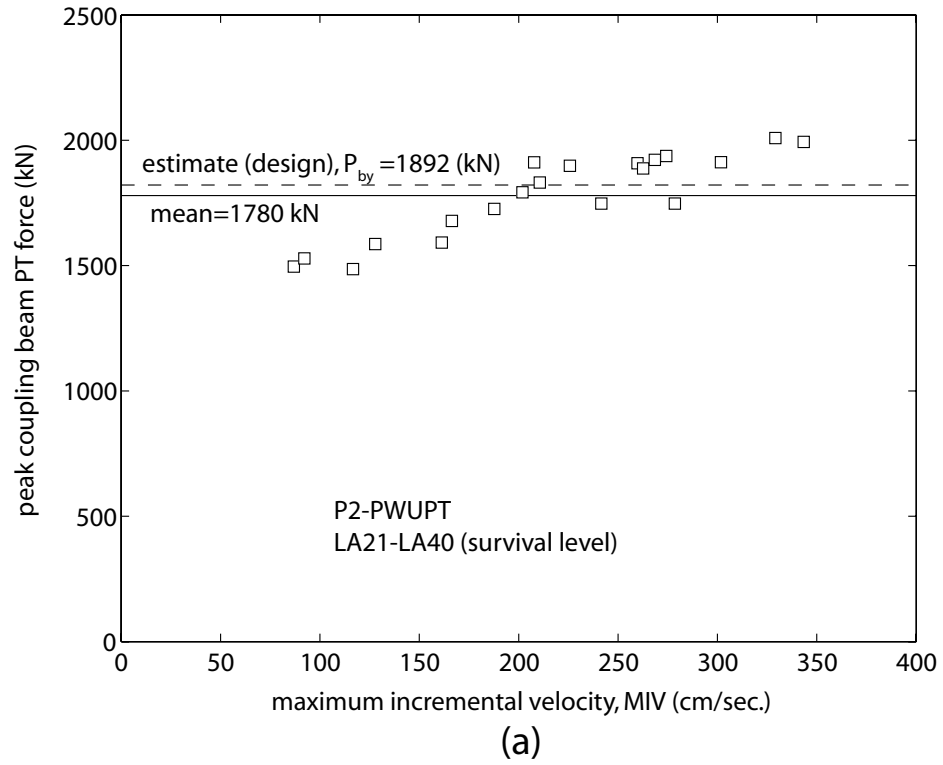


Fig. 15.60 Peak coupling beam post-tensioning force demands for Structure P2-PWUPT: (a) survival level; (b) design level

15.3.13 Coupling Beam Shear Forces

The peak coupling beam shear force demands from the dynamic analyses of Structure P2-PWUPT under the twenty survival-level SAC ground motion records (LA21-LA40) and twenty design-level records (LA01-LA20) are listed in Tables 15.70 and 15.71, respectively. The coupling beam shear forces, V_b are calculated based on the equilibrium of the wall pier floor/roof level applied gravity loads and the wall pier axial forces above and below each floor/roof level as determined from the fiber beam-column elements used for the wall piers in the analytical model.

TABLE 15.70
PEAK COUPLING BEAM SHEAR FORCE DEMANDS FOR STRUCTURE
P2-PWUPT UNDER SURVIVAL LEVEL GROUND MOTIONS

ground motion	LA21 ^b	LA22	LA23	LA24	LA25	LA26	LA27	LA28	LA29	LA30	estimate (design)	standard deviation
peak coupling beam shear force (kN)	2473	1730	1623	1832	1983	2082	1655	2073	1690	1708	1184	266
ground motion	LA31	LA32	LA33	LA34	LA35	LA36	LA37	LA38	LA39 ^c	LA40 ^a	mean	standard deviation/mean
peak coupling beam shear force (kN)	2166	2108	1877	1712	2388	2317	2184	1988	1583	1930	1955	0.17

^a The peak demand under this ground motion is closest to the mean demand

^b The peak demand under this ground motion is the largest demand

^c The peak demand under this ground motion is the smallest demand

TABLE 15.71

PEAK COUPLING BEAM SHEAR FORCE DEMANDS FOR STRUCTURE

P2-PWUPT UNDER DESIGN LEVEL GROUND MOTIONS

ground motion	LA01 ^a	LA02	LA03	LA04	LA05	LA06 ^c	LA07	LA08	LA09	LA10	standard deviation	
peak coupling beam shear force (kN)	1517	1645	1561	1245	1263	1183	1396	1392	1695	1418	157	
ground motion	LA11	LA12	LA13	LA14	LA15	LA16	LA17	LA18	LA19	LA20 ^b	mean	standard deviation/mean
peak coupling beam shear force (kN)	1436	1525	1668	1628	1570	1681	1495	1584	1481	1748	1507	0.10

^a The peak demand under this ground motion is closest to the mean demand

^b The peak demand under this ground motion is the largest demand

^c The peak demand under this ground motion is the smallest demand

The peak coupling beam shear force demands in Tables 15.70 and 15.71 always occur in the second floor beam. The mean peak beam shear force demand from the survival-level dynamic analyses in Table 15.70 is 1955 kN, which is considerably larger than the estimated demand of $Q_{b,max}=1.25V_{b,pty}=1184$ kN from Chapter 12. Thus, the force used in Chapter 12 for the shear slip design of the coupling beam-to-wall interfaces does not appear to be valid for the second floor level. Note that the design approach does not require the estimation of the coupling beam shear force under the design-level earthquake; and thus, no design-level estimate is provided in Table 15.71.

As an example, Fig. 15.61 shows the shear force time histories for the eight coupling beams in Structure P2-PWUPT under the survival-level LA40 ground motion, for which the peak coupling shear force demand (occurring in the second floor beam) is closest to the mean demand from the twenty records (see Table 15.70). The dashed horizontal lines indicate the design estimate for the coupling beam shear force, $Q_{b,max}$

from Chapter 12, which is equal to $1.25V_{b,pty}$ for the second and third floor beams and $V_{b,pty}$ for the upper level beams. It is observed that the peak shear force demands in the upper level beams also exceed the design estimate. Since the coupling beam shear forces from the static analyses in Chapter 13 are estimated reasonably well by the proposed approximate procedures, the underestimation in the dynamic analysis results may be due to the effect of higher modes on the peak coupling beam shear force demands; however, this was not investigated.

Fig. 15.62 plots the peak coupling beam shear force demands from Tables 15.70 and 15.11 (\square markers) against the maximum incremental velocity (MIV) of the ground motion records (see Tables 14.2 and 14.1), where the dashed and solid horizontal lines represent the design estimate (from Chapter 12) and the mean peak coupling beam shear force demand, respectively for each data set. It is observed that there is considerable scatter in the peak coupling beam shear force demands under the survival-level and design-level ground motions.

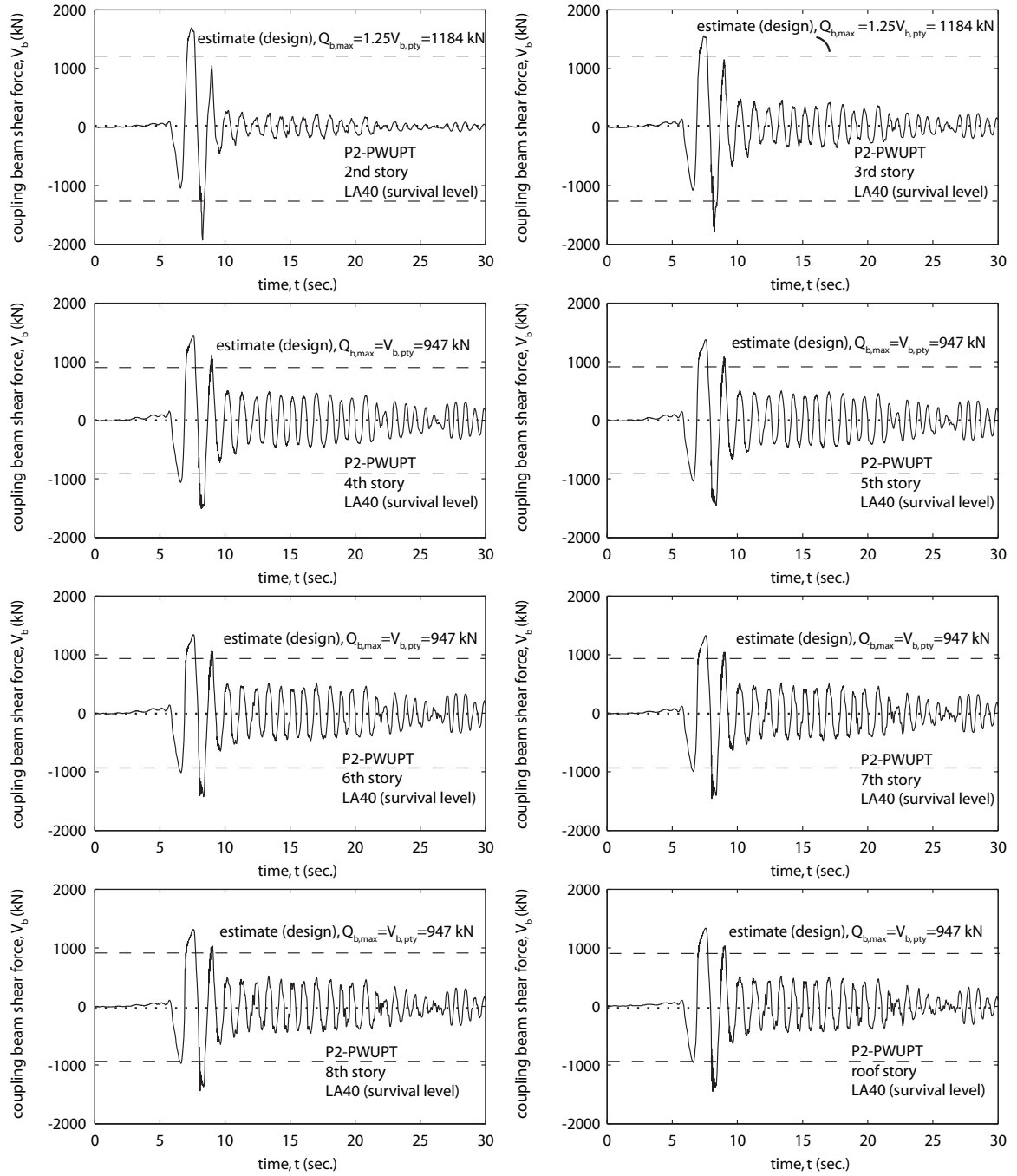
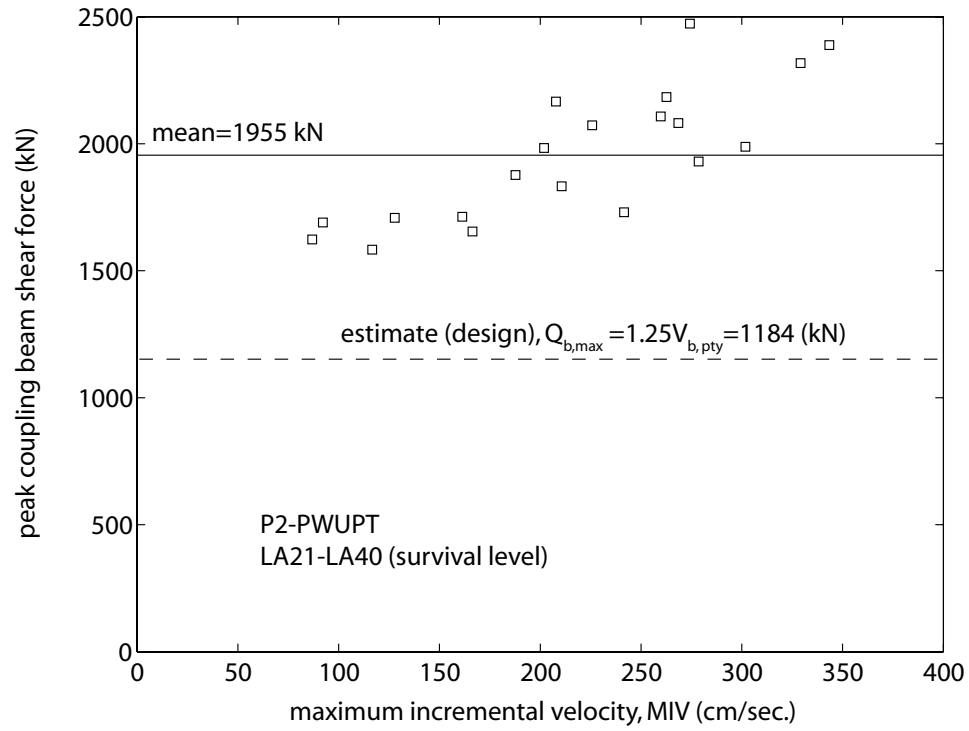
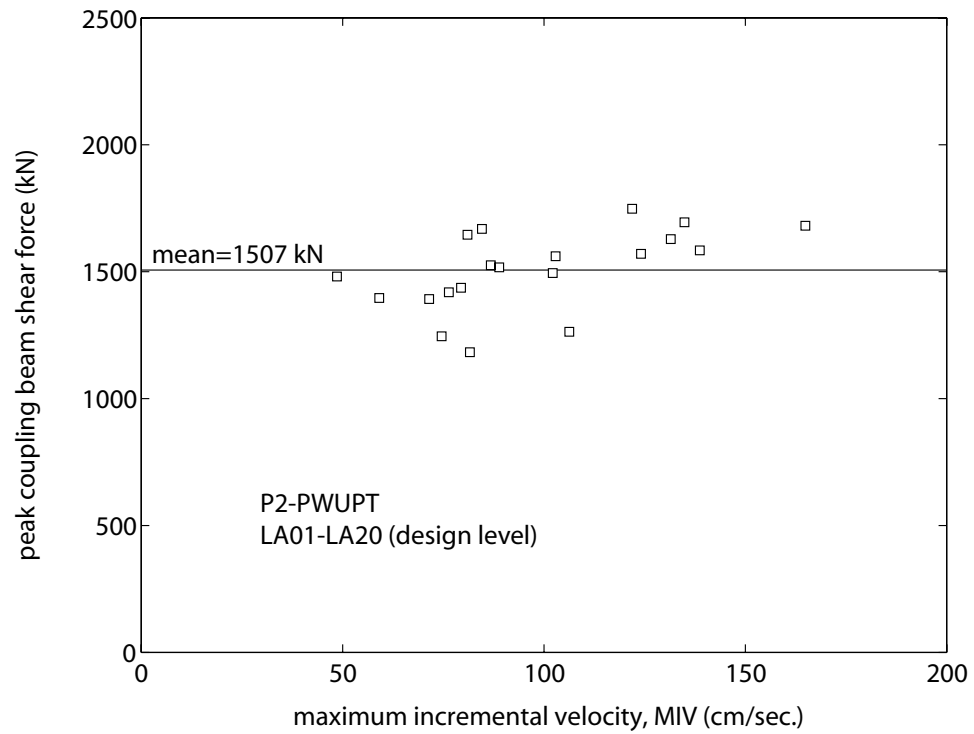


Fig. 15.61 Coupling beam shear force time histories for Structure P2-PWUPT



(a)



(b)

Fig. 15.62 Peak coupling beam shear force demands for Structure P2-PWUPT:
(a) survival level; (b) design level

15.3.14 Coupling Beam Shear Slip Failure

The minimum coupling beam shear slip capacity to shear force demand ratio from the dynamic analyses of Structure P2-CWUPT under the twenty survival-level SAC ground motion records (LA21-LA40) and twenty design-level records (LA01-LA20) are listed in Tables 15.72 and 15.73, respectively. The coupling beam shear slip capacity is computed as $V_{b,ss} = V_{p,ss} + V_{a,ss}$ where, $V_{a,ss}$ is the slip capacity from the top and seat angle-to-wall connections determined as described in Chapter 12 and $V_{p,ss}$ is the slip capacity due to the beam axial force calculated as the axial force at the beam end, C_b times the assumed coefficient of friction, $\mu_{bw}=0.33$. Note that the axial force at the beam ends is larger than the axial force at the beam midspan as a result of the top and seat angle forces. The beam end axial forces are determined directly from the fiber beam-column elements at the beam ends in the analysis model. The coupling beam shear slip capacity, $V_{b,ss}$ varies with time during an earthquake since $V_{p,ss}$ due to the beam axial force varies. The slip capacity from the top and seat angle-to-wall connections, $V_{a,ss}$ is assumed to remain constant during an earthquake since the integrity of the angle-to-wall connections is assumed to be maintained.

TABLE 15.72

MINIMUM COUPLING BEAM SHEAR SLIP CAPACITY-DEMAND RATIOS FOR
STRUCTURE P2-PWUPT UNDER SURVIVAL LEVEL GROUND MOTIONS

ground motion	LA21	LA22	LA23	LA24	LA25	LA26	LA27 ^b	LA28	LA29	LA30	estimate (design)	standard deviation
min. beam shear slip capacity-demand ratio	0.61	0.82	0.79	0.79	0.64	0.78	0.85	0.76	0.80	0.82	1.08	0.103
ground motion	LA31	LA32	LA33	LA34	LA35	LA36 ^c	LA37 ^a	LA38	LA39	LA40	mean	standard deviation/mean
min. beam shear slip capacity-demand ratio	0.60	0.69	0.81	0.83	0.59	0.48	0.74	0.77	0.84	0.78	0.74	0.139

^a The peak ratio under this ground motion is closest to the mean ratio

^b The peak ratio under this ground motion is the largest ratio

^c The peak ratio under this ground motion is the smallest ratio

TABLE 15.73

MINIMUM COUPLING BEAM SLIP CAPACITY-DEMAND RATIOS FOR
STRUCTURE P2-PWUPT UNDER DESIGN LEVEL GROUND MOTIONS

ground motion	LA01	LA02	LA03 ^a	LA04	LA05	LA06 ^b	LA07	LA08	LA09 ^c	LA10	standard deviation	
min. beam shear slip capacity-demand ratio	0.90	0.78	0.87	1.05	1.03	1.09	0.93	0.94	0.74	0.93	0.0921	
ground motion	LA11	LA12	LA13	LA14	LA15	LA16	LA17	LA18	LA19	LA20	mean	standard deviation/mean
min. beam shear slip capacity-demand ratio	0.91	0.84	0.87	0.86	0.87	0.81	0.91	0.91	0.83	0.75	0.89	0.104

^a The peak ratio under this ground motion is closest to the mean ratio

^b The peak ratio under this ground motion is the largest ratio

^c The peak ratio under this ground motion is the smallest ratio

The design estimate for the survival-level minimum coupling beam shear slip capacity to shear force demand ratio in Table 15.72 is determined as the ratio between the design estimates for the coupling beam shear slip capacity, $V_{b,ss}$ and the beam shear force demand, $Q_{b,max}$, from Chapter 12. It is observed that the mean ratio from the survival-level dynamic analysis results is smaller than the design estimate, and thus, the design procedure to prevent shear slip failure at the beam ends is not conservative. This is possibly because of the underestimated coupling beam shear force demands as described previously.

The mean values of the minimum coupling beam shear slip capacity to shear force demand ratios in Tables 15.72 and 15.73 are both less than 1.0. Thus, shear slip failure at the ends of the coupling beams in Structure P2-PWUPT, on average, might occur. As an example, Fig. 15.63 shows comparisons between the shear slip capacity (solid lines) and shear force demand (dashed lines) time histories for the eight coupling beams in Structure P2-PWUPT under the survival-level LA37 ground motion, for which the minimum coupling beam shear slip capacity-demand ratio is closest to the mean ratio from the twenty records (see Table 15.72). For comparison, the solid and dashed horizontal lines indicate the design estimates for the coupling beam shear slip capacity, $V_{b,ss}$ and shear force demand, $Q_{b,max}=1.25V_{b,pty}$ (second and third floor level beams) or $Q_{b,max}=V_{b,pty}$ (upper level beams), respectively. As described in Chapter 12, the design estimate for the coupling beam shear slip capacity due to the beam end axial force, $V_{p,ss}$ is computed as the coupling beam initial post-tensioning force, P_{bi} times the assumed coefficient of friction at the beam ends, $\mu_{bw}=0.33$. In addition to the underestimated maximum shear force demands, the design approach seems to overestimate the minimum

shear slip capacities from the dynamic analysis, also contributing to the unconservative design to prevent shear slip failure at the beam ends. As a result, it is observed from Fig. 15.63 that shear slip can occur not only at the ends of the lower floor level coupling beams but also the upper level beams.

Fig. 15.64 plots the minimum coupling beam shear slip capacity-demand ratios from Tables 15.72 and 15.73 (\square markers) against the maximum incremental velocity (MIV) of the ground motion records (see Tables 14.2 and 14.1), where the dashed and solid horizontal lines represent the design estimate (from Chapter 12) and the mean ratio, respectively, for each data set. The results clearly point to the need for improvement in the design approach to prevent shear slip failure at the ends of the coupling beams.

15.3.15 Angle Deformations

The peak tensile deformation demands in the top and seat connection angles of the coupling beams from the dynamic analyses of Structure P2-PWUPT under the twenty survival-level SAC ground motion records (LA21-LA40) and twenty design-level records (LA01-LA20) are listed in Tables 15.74 and 15.75. The angle deformations, δ_{ax} are determined directly from the horizontal angle elements in the analytical model as the deformations parallel to the coupling beams (i.e., horizontal displacement of angle heel from wall).

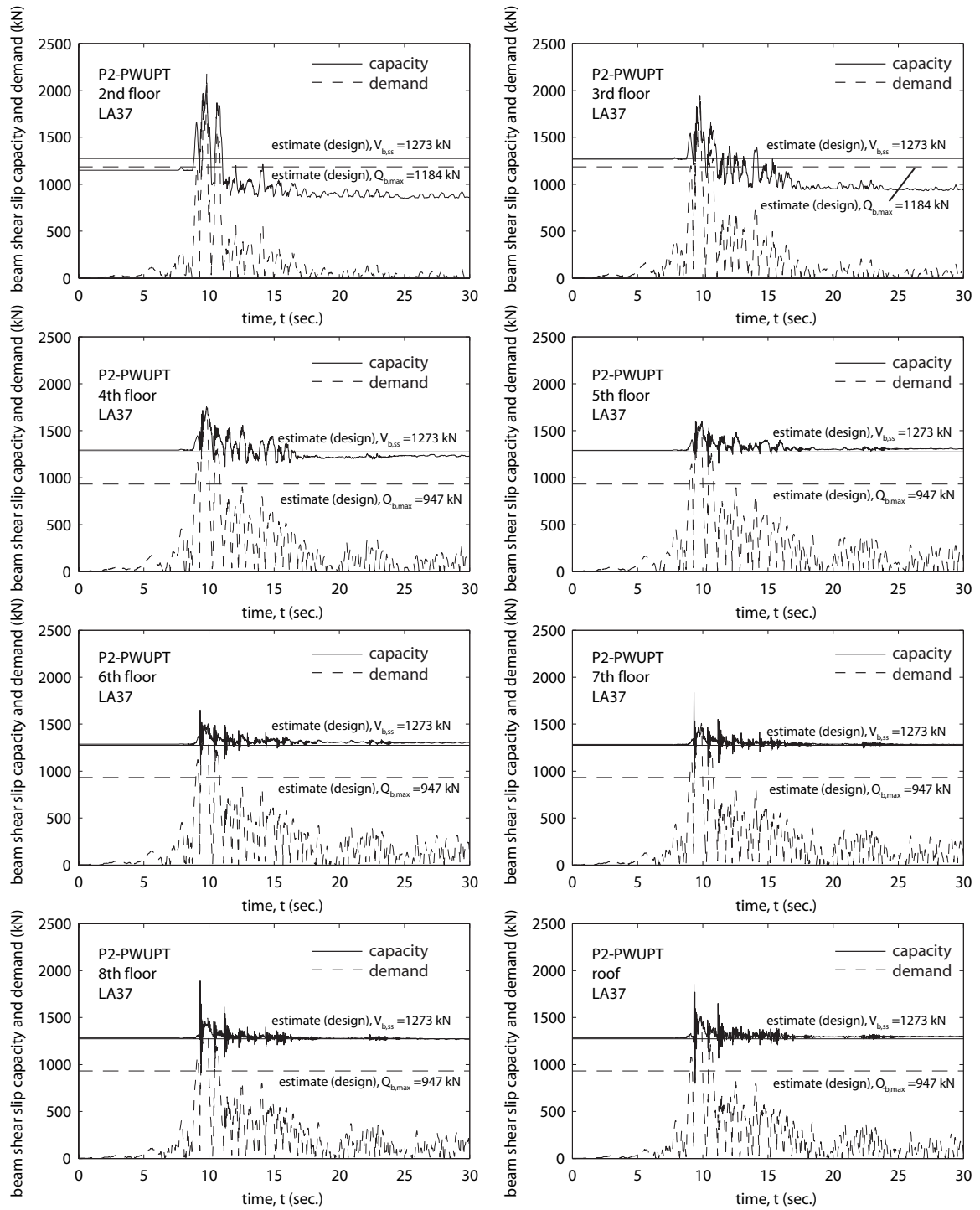
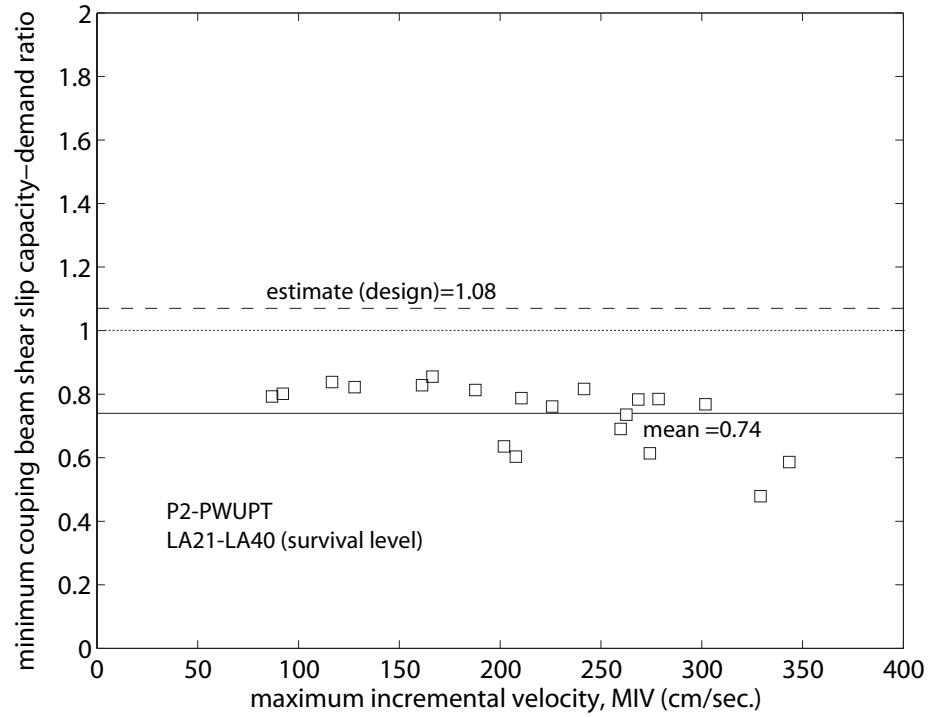
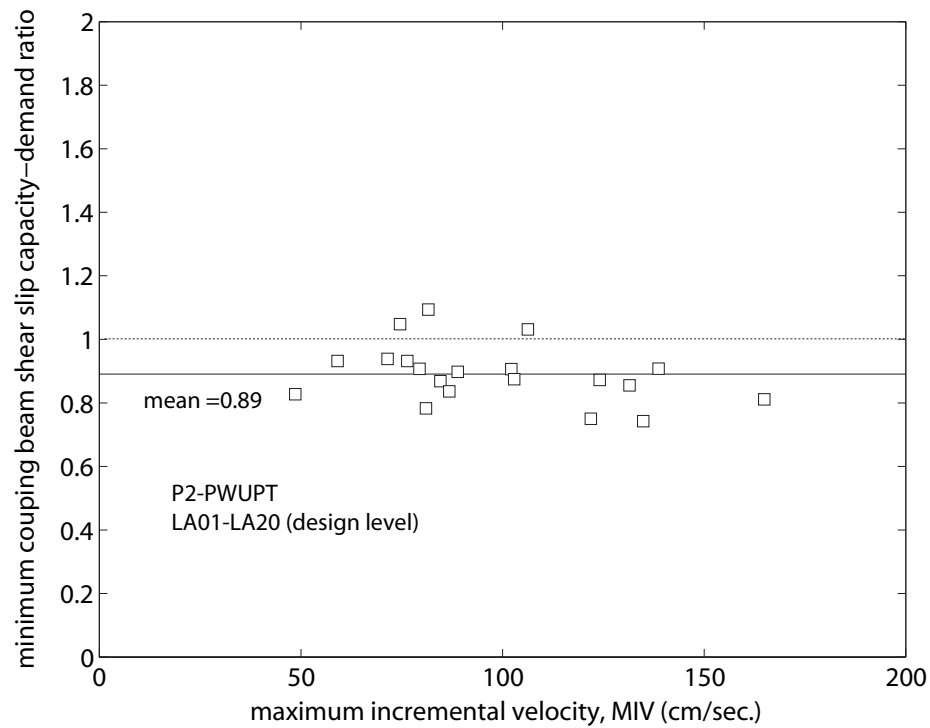


Fig. 15.63 Coupling beam shear slip capacity and shear force demand time histories for Structure P2-PWUPT



(a)



(b)

Fig. 15.64 Minimum coupling beam shear slip capacity to shear force demand ratios for Structure P2-PWUPT: (a) survival level; (b) design level

TABLE 15.74

PEAK ANGLE TENSILE DEFORMATION DEMANDS FOR STRUCTURE
P2-PWUPT UNDER SURVIVAL LEVEL GROUND MOTIONS

ground motion	LA21	LA22	LA23	LA24 ^a	LA25	LA26	LA27	LA28	LA29	LA30	estimate (design)	standard deviation
peak angle tensile deformation (mm)	46	26	12	31	29	42	22	36	14	17	31	14
ground motion	LA31	LA32	LA33	LA34	LA35	LA36 ^b	LA37	LA38	LA39 ^c	LA40	mean	standard deviation/mean
peak angle tensile deformation (mm)	39	39	25	18	57	60	35	40	11	26	31	0.45

^a The peak demand under this ground motion is closest to the mean demand

^b The peak demand under this ground motion is the largest demand

^c The peak demand under this ground motion is the smallest demand

TABLE 15.75

PEAK ANGLE TENSILE DEFORMATION DEMANDS FOR STRUCTURE
P2-PWUPT UNDER DESIGN LEVEL GROUND MOTIONS

ground motion	LA01	LA02	LA03	LA04	LA05 ^c	LA06	LA07	LA08 ^a	LA09	LA10	estimate (design)	standard deviation
peak angle tensile deformation (mm)	12	13	7	5	5	3	8	10	15	10	14	6
ground motion	LA11	LA12	LA13	LA14	LA15	LA16 ^b	LA17	LA18	LA19	LA20	mean	standard deviation/mean
peak angle tensile deformation (mm)	7	7	20	21	15	26	16	14	9	20	12	0.51

^a The peak demand under this ground motion is closest to the mean demand

^b The peak demand under this ground motion is the largest demand

^c The peak demand under this ground motion is the smallest demand

The mean peak angle tensile deformation demand from the survival-level dynamic analyses in Table 15.74 is 31 mm, which is equal to the estimated deformation of $u_{as}=31$ mm from Chapter 12. However, the estimated angle deformations are based on over-estimated coupling beam rotation demands (see Fig. 15.56). Thus, it is concluded that the method used in Chapter 12 to estimate the angle deformations needs to be improved.

As an example, Fig. 15.65 shows the deformation time histories, δ_{ax} for the bottom (i.e., seat) angles at the left ends of the eight coupling beams in Structure P2-PWUPT under the survival-level LA24 ground motion, for which the peak angle tensile deformation demand (occurring in the roof beam) is closest to the mean demand from the twenty records (see Table 15.74). The dashed horizontal lines indicate the design estimate for the peak angle tensile deformation, u_{as} , from Chapter 12.

Fig. 15.66 plots the peak angle tensile deformation demands from Tables 15.74 and 15.75 (\square markers) against the maximum incremental velocity (MIV) of the ground motion records (see Tables 14.2 and 14.1), where the dashed and solid horizontal lines represent the design estimate (from Chapter 12) and the mean peak angle tensile deformation demand, respectively, for each data set. It is observed that the peak angle tensile deformation demands tend to follow similar trends to the peak coupled wall roof drift demands in Fig. 15.33 and the peak coupling beam chord rotation demands in Fig. 15.56.

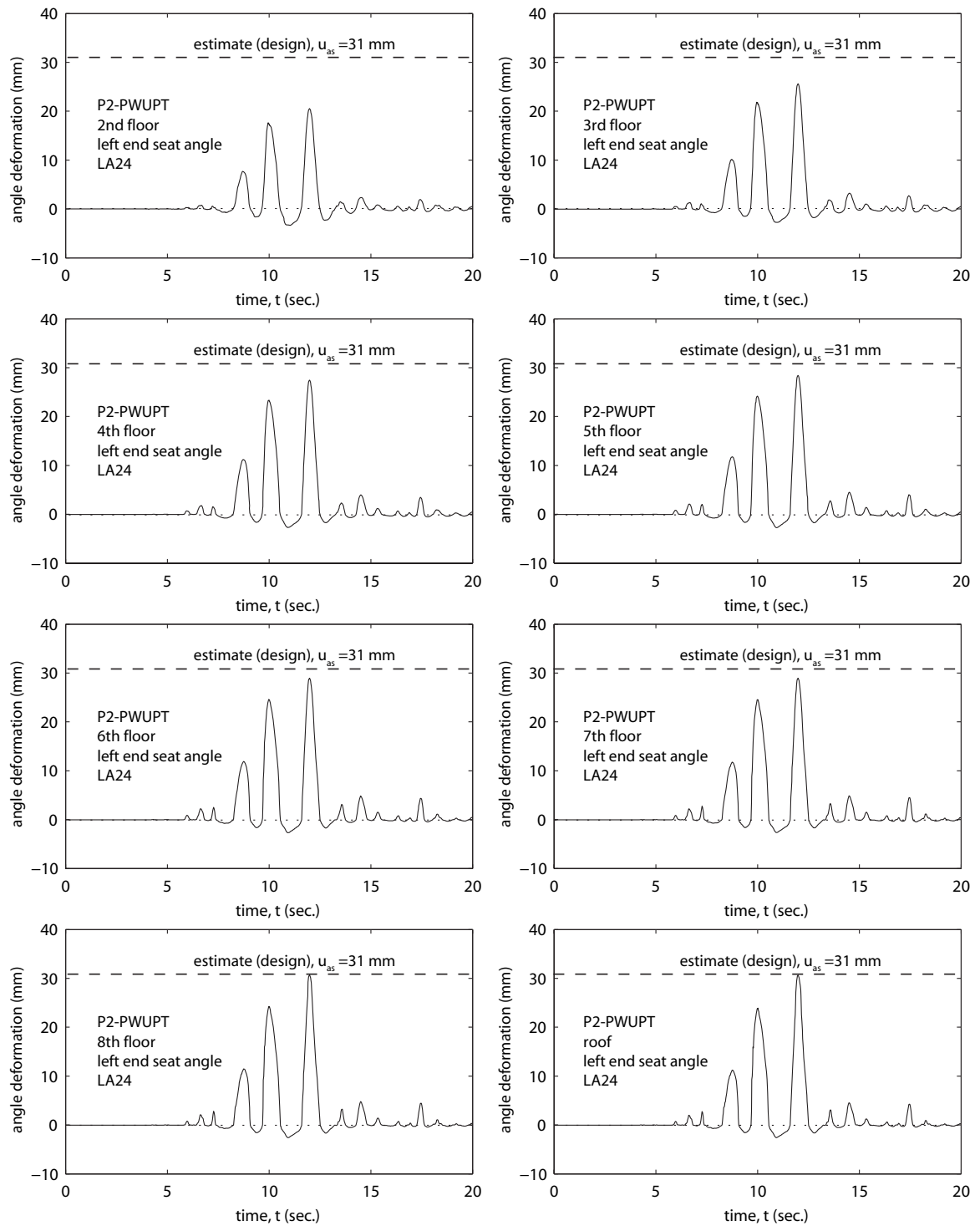
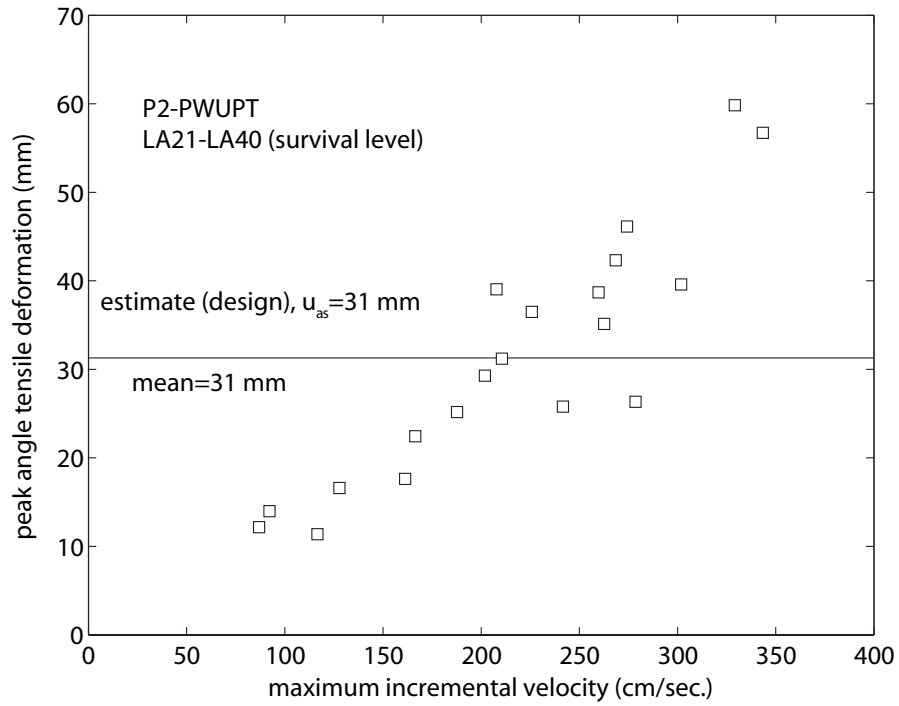
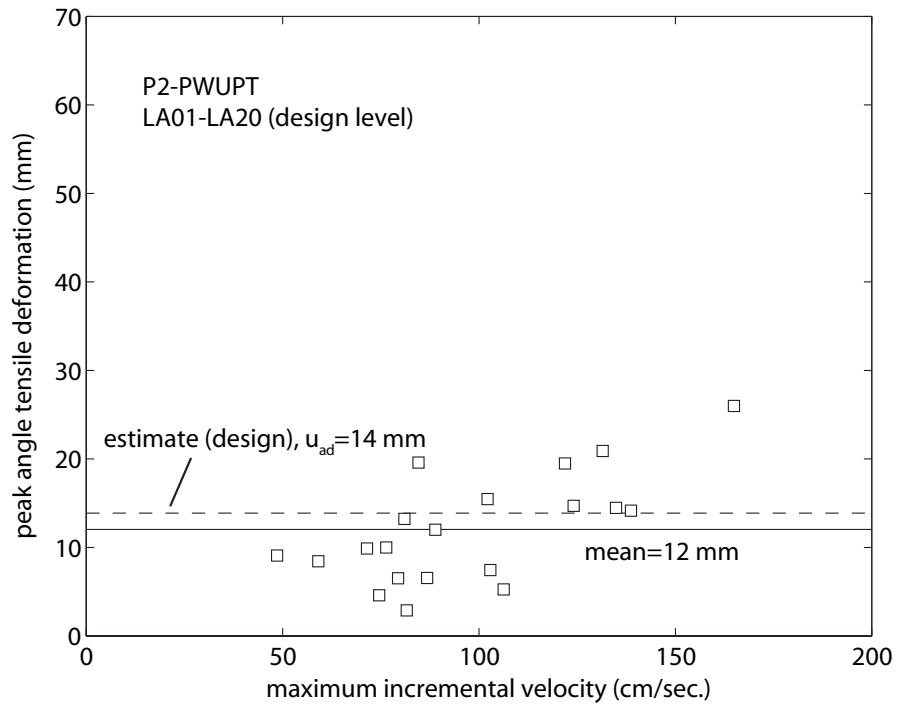


Fig. 15.65 Coupling beam connection angle deformation time histories for Structure P2-PWUPT



(a)



(b)

Fig. 15.66 Peak coupling beam connection angle tensile deformation demands for Structure P2-PWUPT: (a) survival level; (b) design level

15.4 Uncoupled Concrete Wall Systems

This section discusses the dynamic peak roof drift response of uncoupled wall pier systems (two wall piers with no coupling beams in between), referred to as Structures P4-CWUNC and P5-PWUNC corresponding to the prototype coupled wall Structures P1-CWUPT and P2-PWUPT, respectively. The analytical models for the uncoupled systems are created by removing the coupling beams in Structures P1-CWUPT and P2-PWUPT.

The behavior of the uncoupled wall systems under static monotonic lateral loading can be found in Chapter 13. For dynamic analysis, it is assumed that the building masses for the uncoupled systems are the same as those for the corresponding coupled wall structures. As a result of the reduced lateral stiffness, the fundamental periods for Structures P4-CWUNC and P5-PWUNC are 0.95 sec. and 1.02 sec., respectively, which are significantly longer than the fundamental periods of the coupled wall systems in Chapter 12.

The peak roof drift demands for Structures P4-CWUNC and P5-PWUNC under the twenty survival-level SAC ground motion records (LA21-LA40) are listed in Tables 15.76 and 15.77, respectively.

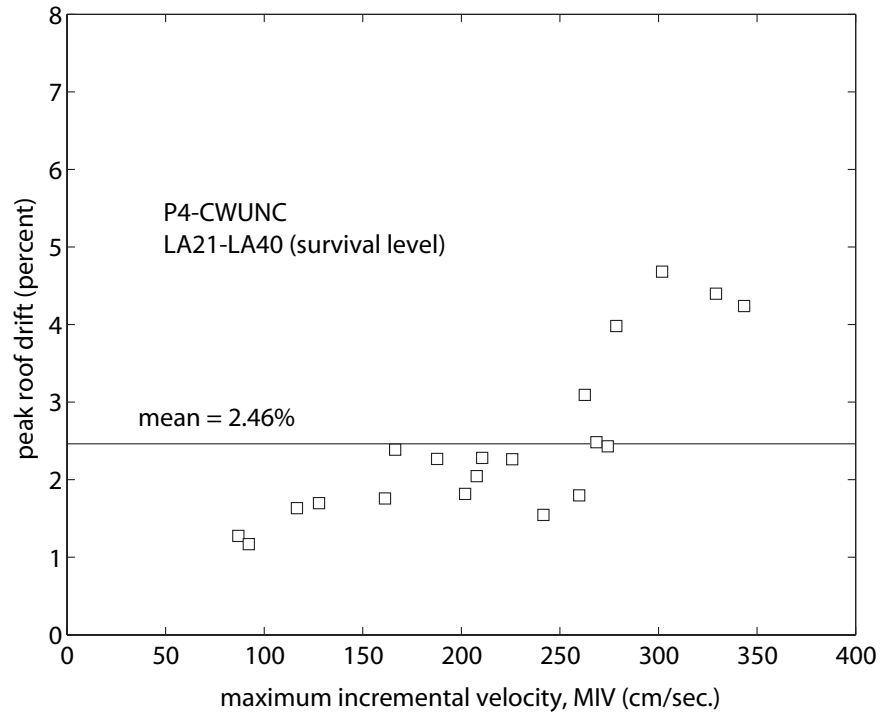
TABLE 15.76
PEAK ROOF DRIFT DEMANDS FOR STRUCTURE P4-CWUNC
UNDER SURVIVAL LEVEL GROUND MOTIONS

ground motion	LA21	LA22	LA23	LA24	LA25	LA26	LA27	LA28	LA29	LA30	standard deviation	
peak roof drift (%)	2.43	1.55	1.28	2.28	1.82	2.48	2.39	2.26	1.17	1.70	1.06	
ground motion	LA31	LA32	LA33	LA34	LA35	LA36	LA37	LA38	LA39	LA40	mean	standard deviation/mean
peak roof drift (%)	2.04	1.80	2.27	1.76	4.24	4.40	3.09	4.68	1.63	3.98	2.46	0.43

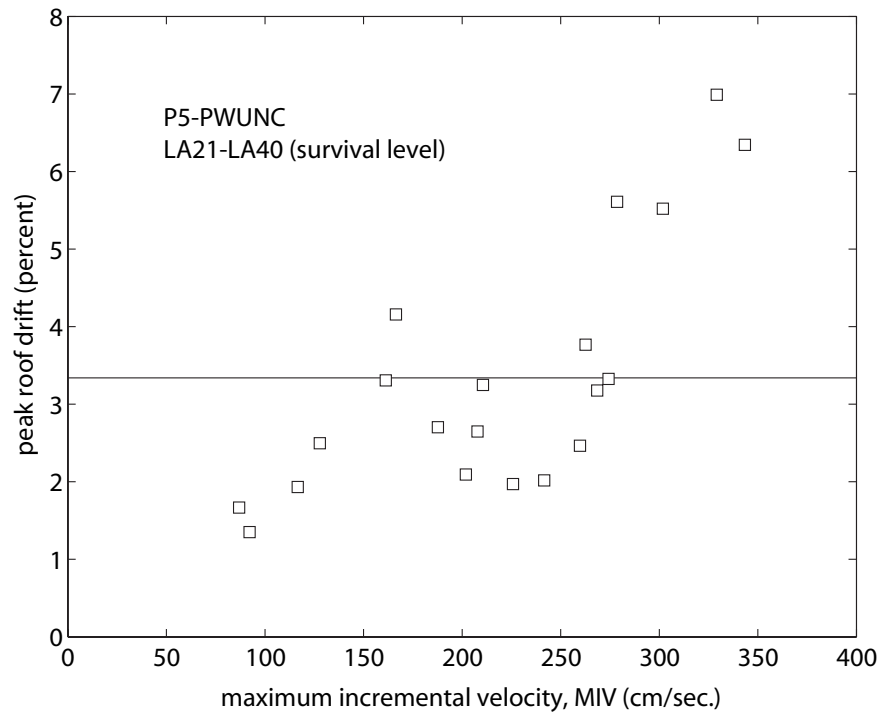
TABLE 15.77
PEAK ROOF DRIFT DEMANDS FOR STRUCTURE P5-PWUNC
UNDER SURVIVAL LEVEL GROUND MOTIONS

ground motion	LA21	LA22	LA23	LA24	LA25	LA26	LA27	LA28	LA29	LA30	standard deviation	
peak roof drift (%)	3.33	2.02	1.67	3.25	2.09	3.18	4.16	1.97	1.35	2.50	1.61	
ground motion	LA31	LA32	LA33	LA34	LA35	LA36	LA37	LA38	LA39	LA40	mean	standard deviation/mean
peak roof drift (%)	2.65	2.47	2.70	3.31	6.34	6.99	3.77	5.52	1.93	5.61	3.34	0.48

Figs. 15.67a and 15.67b plot the peak roof drift demands of Structures P4-CWUNC and P5-PWUNC from Tables 15.76 and 15.77, respectively, against the maximum incremental velocity (MIV) of the 20 survival level ground motion records (LA21-LA40). It is observed that the peak roof drift demands of the uncoupled wall pier systems are significantly larger than the peak roof drift demands of the corresponding coupled wall systems (see Figs. 15.2a and 15.33a). The ratio between the mean peak roof drift demands of the coupled and uncoupled wall systems is equal to 0.72 and 0.55 for the cast-in-place and precast concrete wall systems, respectively.



(a)



(b)

Fig. 15.67 Peak roof drift demands for uncoupled wall systems:
(a) Structure P4-CWUNC; (b) Structure P5-PWUNC

15.5 Chapter Summary

This chapter discusses the response of prototype Structures P1-CWUPT and P2-PWUPT from Chapter 12 under earthquake loading. A series of nonlinear dynamic time-history analyses of the structures are conducted using the twenty survival-level and twenty design-level ground motion records from Chapter 14. Evaluations of the global behavior of the structures as well as the local behavior of the wall piers and the coupling beams are provided. The results of the dynamic analyses indicate that the design approach and procedures presented in Chapters 11 and 12 are mostly valid.

The following components of the proposed design approach provide, on average, good correlation with the dynamic analysis results: (1) estimation of peak floor/roof drift demands; (2) estimation of peak inter-story drift demands; (3) estimation of peak coupled wall base shear forces; (4) estimation of coupling beam post-tensioning forces; and (5) estimation of wall pier post-tensioning forces.

The following components of the design approach need further improvement: (1) estimation of peak coupling beam chord rotations; (2) estimation of peak coupling beam axial forces; (3) estimation of peak coupling beam shear forces; and (4) estimation of peak top and seat angle deformations. The deficiencies of the proposed procedures in providing satisfactory designs for the performance of the coupling beams may be due to the development of significant higher mode effects under dynamic loading; however, this is not investigated in the dissertation.

Significant scatter is observed in the response of the prototype structures under the ground motion records used in the dynamic analyses. This is possibly due to a large variation in the intensity of the ground motion records. The large scatter in the dynamic

analysis results indicate that the seismic demands under some of the ground motions (especially survival-level motions) can be significantly larger than the estimated design demands.

Effective ground motion scaling methods are needed to reduce the scatter in the dynamic analysis results. It may be possible to obtain more uniform levels of seismic demands for the structures by scaling the ground motion records to a constant maximum incremental velocity (MIV).

CHAPTER 16

SUMMARY, CONCLUSIONS, AND FUTURE WORK

16.1 Summary

This dissertation investigates a new method to couple concrete walls using unbonded post-tensioned steel beams, without embedding the beams into the walls. The dissertation includes analytical investigations on the nonlinear behavior of floor-level coupled wall subassemblages as well as multi-story coupled wall structures under lateral loads, experimental investigations of half-scale coupled wall subassemblage test specimens, performance-based seismic design, and nonlinear dynamic time-history response evaluations of prototype coupled wall structures under earthquake loading.

An introduction and overview of the dissertation can be found in Chapter 1. Then, Chapter 2 provides a summary of previous research related to the dissertation as follows: (1) coupled wall structural systems; (2) concrete coupled wall structures; (3) hybrid structures with embedded steel coupling beams; (4) wall shear force demands in coupled wall structures; (5) unbonded post-tensioning in building construction; and (6) behavior of top and seat angles.

Chapter 3 describes a fiber element analytical model to investigate the nonlinear behavior of floor-level hybrid coupled wall subassemblages. The details of a prototype coupled wall subassemblage are also presented. The purpose of the analytical model is to provide a basis for comparisons with subassemblage experimental results as described

later in the dissertation and to provide a basis for the modeling of multi-story coupled wall structures. A preliminary verification of the fiber element subassembly model is done based on comparisons with finite element models. An analytical model for embedded steel coupling beam subassemblies is also developed to investigate the differences in the seismic behaviors of coupled wall structures with unbonded post-tensioned and embedded steel beams later in the dissertation.

Chapter 4 presents an analytical investigation on the nonlinear behavior of unbonded post-tensioned hybrid coupled wall subassemblies under lateral loads. The effects of structural design parameters such as the amount of post-tensioning, beam properties, and angle properties on the behavior of the subassemblies, including the lateral resistance and energy dissipation are investigated. These subassembly analyses form a foundation for the investigation of multi-story coupled wall behavior later in the dissertation. The prototype subassembly and the fiber element model presented in Chapter 3 are used to conduct the analyses.

Chapter 5 presents an idealized beam end moment versus chord rotation relationship for unbonded post-tensioned hybrid coupled wall subassemblies under monotonic lateral loading. Procedures are developed to estimate the structure behavior using basic principles of equilibrium, compatibility, and constitutive relationships. These procedures, which are verified based on comparisons with the analytical model from Chapter 3, can be used to conduct approximate, simplified analyses of coupled wall subassemblies with different structural properties. The proposed procedures are used later in the dissertation as design tools and to develop idealized lateral load versus displacement relationships for multi-story coupled wall structures.

Chapter 6 describes fiber element analytical models to investigate the nonlinear behavior of multi-story unbonded post-tensioned hybrid coupled wall systems. The details of two prototype coupled wall structures are also presented. The analytical models are constructed by joining subassemblage models at the floor and roof levels. Systems with monolithic cast-in-place reinforced concrete wall piers as well as with precast concrete wall piers are considered. Verification of the cast-in-place reinforced concrete wall pier model is presented based on comparisons with previous experiments of isolated (i.e., uncoupled) wall specimens.

Chapter 7 presents an analytical investigation on the nonlinear behavior of multi-story unbonded post-tensioned hybrid coupled wall structures under lateral loading. The effects of structural design parameters such as the amount of post-tensioning, beam properties, and wall properties on the behavior of the structures, including the degree of coupling, energy dissipation, and lateral displacement capacity are investigated. Systems with precast concrete wall piers as well as monolithic cast-in-place reinforced concrete wall piers are considered. The lateral load behavior of unbonded post-tensioned hybrid coupled wall structures is compared with the behavior of structures that use embedded steel coupling beams and structures without coupling.

Chapter 8 presents idealized base shear force versus roof drift relationships for unbonded post-tensioned hybrid coupled wall structures under monotonic lateral loading. Procedures are developed to estimate the structure behavior using basic principles of equilibrium, compatibility, and constitutive relationships. These procedures, which are verified based on comparisons with the analytical models from Chapter 6, can be used to conduct approximate, simplified analyses of coupled wall systems with cast-in-place reinforced concrete and precast concrete wall piers. The proposed procedures are used

later in the dissertation as design tools for unbonded post-tensioned hybrid coupled wall structures.

Chapter 9 describes the results from eleven half-scale experiments to investigate the nonlinear behavior of unbonded post-tensioned hybrid coupled wall subassemblages. Each test specimen includes a steel coupling beam and the adjacent concrete wall regions at a floor level. The experiments were conducted in the Structural Systems Laboratory at the University of Notre Dame by two other graduate students, Michael A. May and Brad D. Weldon, as part of their research towards a Master of Science Degree in Civil Engineering. A large portion of the material presented in this chapter is based on their work (May et al. 2006).

Chapter 10 uses the experimental results from Chapter 9 to make necessary modifications to the fiber element subassemblage analytical model described in Chapter 3. The revised analytical model is critically evaluated by comparing the analytical estimations with the experimental measurements. The idealized coupling beam end moment versus chord rotation relationship developed in Chapter 5 is also modified based on the experimental results. These revised models are used in the remainder of the dissertation for the modeling, design, and analysis of coupled wall structures.

Chapter 11 proposes a two-level performance-based seismic design approach for unbonded post-tensioned hybrid coupled wall structures. The objectives of the design approach are to achieve the “Collapse Prevention” performance level under the “survival” demand level and to achieve the “Life Safety” performance level under the “design” demand level. The chapter describes a set of design criteria to achieve these objectives by limiting the peak displacement demands of a structure to allowable target design-level and survival-level displacements. In addition, design tools and procedures

are developed to estimate the seismic demands and capacities for unbonded post-tensioned hybrid coupled wall structures.

Chapter 12 describes the seismic design of two prototype unbonded post-tensioned hybrid coupled wall structures based on the performance-based design approach introduced in Chapter 11.

Chapter 13 discusses the expected behavior of the prototype structures from Chapter 12 under static lateral loading, including comparisons with the behavior of a similar structure with embedded steel coupling beams. The analyses are conducted using the model described in Chapter 6 including the modifications recommended in Chapter 10. Evaluations of the global behavior of the structures as well as the local behavior of the wall piers and the coupling beams are provided.

Chapter 14 describes twenty design-level ground motion records and twenty survival-level ground motion records used in the nonlinear dynamic time-history analyses of the prototype structures from Chapter 12. These ground motion records are considered to be representative of the seismic conditions used in the design of the structures.

Finally, Chapter 15 investigates the response of the prototype structures from Chapter 12 under earthquake loading. A series of nonlinear dynamic time-history analyses of the structures are conducted using the survival-level and design-level ground motion records from Chapter 14. Evaluations of the global behavior of the structures as well as the local behavior of the wall piers and the coupling beams are provided. The effect of coupling is investigated by comparing the dynamic analysis results for the prototype coupled wall systems with results obtained from dynamic analyses of the structures with the coupling beams removed.

16.2 Conclusions

The research presented in this dissertation has produced a number of conclusions. The most important conclusion is that unbonded post-tensioned steel beams provide an effective and feasible system to couple reinforced concrete wall piers in seismic regions. Other important conclusions from this work are listed below.

Behavior of Unbonded Post-Tensioned Hybrid Coupling Systems

(1) As a result of post-tensioning, the initial lateral stiffness of an unbonded post-tensioned coupling beam system is similar to the initial stiffness of a comparable system with embedded steel coupling beams.

(2) In the nonlinear range, the lateral displacements of unbonded post-tensioned coupling beams occur primarily as a result of the opening of gaps at the beam ends.

(3) The effect of gap opening on the lateral stiffness of the structure is small until the gaps extend over a significant portion of the beam depth.

(4) In the proposed coupling system, top and seat angles are used at the beam-to-wall interfaces to provide energy dissipation during an earthquake. The angles also provide a part of the coupling force of the structure, prevent sliding of the beam at the beam-to-wall interfaces (together with friction resistance against sliding as induced by post-tensioning), and can serve as temporary beam supports during construction.

(5) In a properly-designed unbonded post-tensioned hybrid coupling system, the desired behavior under lateral loads is yielding of the top and seat angles due to the opening of gaps at the beam ends, with little yielding and damage in the beam and the wall piers. The yielded angles can be replaced after an earthquake.

(6) The behavior of properly-designed and detailed unbonded post-tensioned hybrid coupling systems under lateral loads can be characterized by the following five states: (i) decompression; (ii) yielding of the connection angles in tension; (iii) yielding of the beam flange cover plates (if used) in compression; (iv) yielding of the beam flanges in compression; and (v) yielding of the post-tensioning tendons. The yielding of the angles in tension, accompanied by increased gap opening at the beam ends, corresponds to a significant reduction in the lateral stiffness of the structure, which is referred to as the “softening state.”

(7) The total beam post-tensioning force remains relatively constant until the softening state is reached.

(8) The contact depth at the beam-to-wall interfaces remains relatively constant after the softening state is reached.

(9) The hysteretic behavior of unbonded post-tensioned hybrid coupling systems without yielding components (i.e., without the top and seat angles at the beam-to-wall interfaces of the proposed system) is similar to a nonlinear-elastic type of behavior with little energy dissipation.

(10) Unbonded post-tensioned hybrid coupling systems dissipate less energy per displacement cycle than systems with embedded coupling beams. This is because, a significant portion of the strength of the structure is provided by the post-tensioning steel, which is designed to remain mostly linear elastic.

(11) Upon unloading from a large nonlinear lateral displacement, the post-tensioning force provides a restoring effect that yields the tension angles back in compression, closes the gaps, and pulls the wall piers and the beams back towards their undisplaced position, reducing the residual lateral displacements. This results in a large

self-centering capability in unbonded post-tensioned coupling systems as compared with systems using conventional embedded steel or monolithic concrete coupling beams.

(12) The use of unbonded tendons delays the yielding (i.e., nonlinear straining) of the post-tensioning steel and reduces the tensile stresses transferred to the wall concrete. Upon unloading from a large nonlinear lateral displacement of the structure, the initial post-tensioning force is maintained as long as the yielding of the tendons is prevented. The yielding of the post-tensioning steel can be controlled by the initial stress and unbonded length of the post-tensioning tendons.

(13) The strength of an unbonded post-tensioned hybrid coupling system can be controlled by the area of post-tensioning steel as well as the beam depth, the angle thickness, and the angle vertical leg gage length.

(14) As a result of the opening of gaps at the beam-to-wall interfaces, the lateral strength of an unbonded post-tensioned steel coupling beam is smaller than the strength of a properly-designed and detailed embedded steel coupling beam with the same cross section. This loss in strength is somewhat compensated by the top and seat angles used at the beam ends.

(15) Experiments of floor-level coupled wall subassemblages demonstrate that properly-designed unbonded post-tensioned hybrid coupling systems have excellent stiffness, ductility, energy dissipation, and self-centering characteristics under large nonlinear reversed cyclic lateral displacements. Little damage occurs in the coupling beams and in the coupling regions of the wall piers, with most of the damage being concentrated in the sacrificial top and seat angles. Corresponding to a given nonlinear lateral displacement level, the amount of damage in the wall piers and beams of an

unbonded post-tensioned system is much smaller than the corresponding damage in conventional systems with embedded steel or monolithic concrete beams.

(16) The post-tensioning anchors are critical components that can adversely affect the performance of these structures. Premature fracture of single wires inside the anchors of the unbonded post-tensioning strands was observed during the subassembly experiments. Anchor types other than the steel wedge/barrel system used in this experimental program may improve the performance of the post-tensioning strands. It may also be possible to grout a short length of the post-tensioning tendons near the anchors to prevent premature fracture of the strands inside the anchors.

(17) Kinking of the post-tensioning strands at the beam-to-wall interfaces during the experiments did not have any adverse effects on the performance of the strands.

(18) The angle-to-wall and angle-to-beam connections are also critical components of unbonded post-tensioned hybrid coupling systems. Slip at these connections can adversely affect the performance of these structures.

(19) The slip critical angle-to-beam connections used in the test specimens worked well. If the required slip capacity cannot be achieved using a bolted angle-to-beam connection, it may also be possible to weld the angles to the beam flanges.

(20) The post-tensioned angle-to-wall connections used in the test specimens performed well, with no yielding in the connection strands and no damage in the wall concrete.

(21) Significant loss of the beam post-tensioning force can result in a loss of the friction resistance against slip of the beam with respect to the wall piers. It may be possible to increase the contribution of the top and seat angles to prevent slip at the beam

ends by fillet welding the vertical legs of the angles to the walls. It is important that this weld does not prevent the development of a ductile yield mechanism in the angle.

(22) The experimental results showed that the use of cover plates on the coupling beam flanges is not necessary for nominal flange initial stress values of up to 75% of the steel yield strength, as long as compact sections are used for the beams.

(23) The use of confinement reinforcement inside the wall-contact regions and steel plates at the beam-to-wall interfaces is necessary to prevent damage to the wall concrete. Shim plates used in the experiments ensured contact between the beam flanges and the wall piers, and maintained the initial lateral stiffness of the structure under cyclic loading. Thus, the use of shim plates in practice is recommended.

Behavior of Multi-Story Coupled Wall Structures

(1) Unbonded post-tensioned steel beams can provide stable levels of coupling, similar to the levels of coupling that can be developed using conventional embedded steel or monolithic concrete beams, between concrete walls over large nonlinear cyclic lateral displacements.

(2) In order to achieve the same lateral strength, coupled wall structures with unbonded post-tensioned steel coupling beams require beams of larger cross section than walls with embedded steel coupling beams.

(3) The lateral strength of unbonded post-tensioned hybrid coupled walls can be controlled by the area of the beam post-tensioning steel, as well as other parameters such as the wall length, beam depth, and thickness and vertical leg gage length of the beam-to-wall connection angles.

(4) As compared with embedded steel and monolithic concrete coupling beams, unbonded post-tensioned beams can provide a large restoring force to the wall piers, reducing the residual lateral displacements upon unloading from a nonlinear displacement. This results in a large self-centering capability of the coupled wall structure. Thus, corresponding to a given peak nonlinear lateral displacement level during an earthquake, the amount of residual displacement (i.e., permanent drift after the earthquake) in an unbonded post-tensioned system is expected to be smaller than the residual displacement in a system with embedded steel or monolithic concrete beams.

(5) Unbonded post-tensioned hybrid coupled walls dissipate less energy than walls with embedded steel coupling beams. Most of the energy dissipation is provided by the yielding of the top and seat angles at the beam-to-wall interfaces and the inelastic behavior of the wall piers near the base.

(6) Unbonded post-tensioned coupled wall structures with cast-in-place reinforced concrete wall piers have larger energy dissipation and a somewhat reduced but still large self-centering capability as compared with structures that use post-tensioned precast concrete wall piers.

(7) The lateral displacements and rotations of the tension-side and compression-side wall piers in a coupled wall structure under lateral loading are similar.

(8) The degree of coupling remains relatively constant as a coupled wall structure is displaced laterally into the nonlinear range.

(9) A significant portion of the total initial force in the 2nd floor coupling beam post-tensioning tendons is not transferred into the 2nd floor coupling beam as a result of the fixed base conditions assumed for the wall piers. The initial axial forces in the upper

level coupling beams are close to the total initial post-tensioning forces, indicating that the effect of the foundation/wall pier stiffness quickly diminishes above the base. The wall pier length has the largest influence on the amount of initial post-tensioning force transferred into the 2nd floor beam, since it results in the largest effect on the lateral stiffness of the wall piers.

(10) Upon lateral displacements of the structure, the fixed foundation conditions restrain the opening of gaps at the ends of the 2nd floor coupling beam, resulting in the development of additional axial compression forces in the beam as the walls displace.

(11) During large nonlinear cyclic lateral displacements of an unbonded post-tensioned hybrid coupled wall system, the 2nd floor coupling beam can lose most of its initial compression even if the total force in the post-tensioning tendons remains close to the initial force. This behavior is not observed in the upper level coupling beams, which maintain most of their initial axial compression levels.

(12) The initial axial forces that develop in the coupling beams are not significantly affected by the sequence of post-tensioning over the height of the structure.

Analytical Modeling and Procedures

(1) Comparisons between experimental results and analytical predictions of floor-level unbonded post-tensioned hybrid coupled wall subassemblages show that the analytical models provide good representations of not only the global load-deformation behavior, but also the local behavior (e.g., gap opening behavior) of the proposed coupling system.

(2) The test results indicate that the method developed by Kishi and Chen (1990) provides reasonable estimates for the initial stiffness and yield strength of the top and seat angles in tension.

(3) The subassemblage analytical models can be combined at the floor and roof levels to develop models of multi-story coupled wall structures.

(4) In addition to the analytical models, relatively simple procedures are developed to estimate the nonlinear lateral load-deformation behavior of unbonded post-tensioned hybrid coupled wall structures. These procedures, which are verified with results from the analytical models, can be used as design tools to conduct approximate analyses of structures with different properties.

Seismic Design and Response Evaluation

(1) The proposed seismic design procedures and tools can be used to determine the properties of the wall piers, coupling beams, post-tensioning tendons, top and seat angles, angle-to-beam and angle-to-wall connections, and beam-to-wall connections and contact regions in an unbonded post-tensioned hybrid coupled wall structure.

(2) Since the coupling beams in an unbonded post-tensioned hybrid coupled wall structure are not embedded into the wall piers, the selection of the beam shape and dimensions is not affected by the reinforcing steel details in the walls, and the use of widely available rolled cross sections is recommended. In comparison, the wall reinforcement inside the embedment regions and the seismic detailing requirements in the form of stiffener and cover plates often result in the use of fabricated beam cross sections in embedded systems.

(3) Large levels of coupling can lead to large tension forces in the tension-side wall pier and large compressive and shear forces in the compression-side wall pier, and thus, should be avoided in design.

(4) Monotonic and cyclic static lateral load analyses of prototype unbonded post-tensioned hybrid coupled wall structures indicate that the proposed design procedures are valid. The design estimations of the various design parameters and structure capacities match reasonably well with the static analysis results.

(5) Nonlinear dynamic time-history analyses of the prototype structures under design-level and survival-level ground motions indicate that the following components of the design approach provide, on average, good correlation with the analysis results: (1) estimation of peak floor/roof drift demands; (2) estimation of peak inter-story drift demands; (3) estimation of peak coupled wall base shear forces; (4) estimation of coupling beam post-tensioning forces; and (5) estimation of wall pier post-tensioning forces (in systems with precast concrete wall piers).

(6) Similarly, the following components of the design approach need further improvement: (1) estimation of peak coupling beam chord rotations; (2) estimation of peak coupling beam axial forces; (3) estimation of peak coupling beam shear forces; and (4) estimation of peak top and seat angle deformations. The deficiencies of the proposed procedures in providing satisfactory designs for the performance of the coupling beams may be due to the development of significant higher mode effects under dynamic loading.

(7) Significant scatter is observed in the response of the prototype structures under the ground motion records used in the dynamic analyses of the structures. This is possibly due to a large variation in the intensity of the ground motion records. The large scatter in

the dynamic analysis results indicate that the seismic demands under some of the ground motions (especially survival-level motions) can be significantly larger than the estimated design demands. Effective ground motion scaling methods are needed to reduce the scatter in the seismic demands.

(8) The dynamic analysis results indicate that it may be possible to obtain more uniform levels of seismic demands for the walls by scaling the ground motion records to a constant maximum incremental velocity (MIV).

(9) Nonlinear dynamic time-history analyses indicate that the proposed BP-type equivalent nonlinear single-degree-of-freedom system provides an effective tool to estimate the lateral displacement response of unbonded post-tensioned hybrid coupled wall structures under earthquake loading.

(10) The roof displacement time-history results demonstrate the self-centering capability of the prototype structures as indicated by the oscillations about close to the zero-displacement position, with little residual (i.e., permanent) displacements at the end of a ground motion.

(11) The dynamic analysis results also show that the lateral displacement responses of the prototype structures decay (i.e., decrease) at a reasonable rate. This indicates the presence of an adequate level of energy dissipation in the structures.

(12) The peak lateral displacement demands of the prototype coupled wall structures are smaller than the displacement demands of the wall piers with the coupling beams removed.

(13) The peak absolute roof accelerations of the prototype structures do not seem to have a strong correlation with the ground motion intensity.

16.3 Future Work

The following areas of future work are recommended based on the research described in this dissertation:

(1) Experiments of multi-story unbonded post-tensioned hybrid coupled wall structures, especially substructures near the base.

(2) Investigation of low cycle fatigue fracture of the top and seat angles.

(3) Investigation of wire fracture inside the post-tensioning strand anchors.

(4) More detailed investigations of the angle-to-beam and angle-to-wall connections, including welded connection configurations.

(5) Investigation of other energy dissipation systems that utilize the gap opening displacements at the beam-to-wall interfaces.

(6) Investigation of higher mode effects on the response of the coupling beams.

(7) Investigation of high-rise (i.e., twenty stories and more) unbonded post-tensioned hybrid coupled wall structures.

(8) Investigation of unbonded post-tensioning as a possible method for the seismic retrofit and strengthening of existing concrete walls. The post-tensioning tendons can be placed outside the walls and above and below the slab for this purpose.

REFERENCES

ACI Committee 318, "Building Code Requirements for Structural Concrete (ACI 318-99) and Commentary (ACI 318R-99)," American Concrete Institute, Farmington Hills, MI, 1999.

ACI Committee 318, "Building Code Requirements for Structural Concrete (ACI 318M-02) and Commentary (ACI 318RM-02)," American Concrete Institute, Farmington Hills, MI, 2002.

ACI Innovation Task Group 1 and Collaborators, "Acceptance Criteria for Moment Frames Based on Structural Testing (T1.1-01) and Commentary (T1.1R-01)," American Concrete Institute, Farmington Hills, MI, 2001, 11 pp.

ACI Innovation Task Group and Collaborators, "Acceptance Criteria for Special Precast Structural Walls Based on Validation Testing and Commentary," DRAFT, ITG T5.1, 2004.

ACI Innovation Task Group 1 and Collaborators, "Special Hybrid Moment Frames Composed of Discretely Jointed Precast and Post-Tensioned Concrete Members," ACI Proposed Standard T1.2-03 and Commentary ACI T1.2R-03, American Concrete Institute, Farmington Hills, MI, 2003.

AISC, "Load and Resistance Factor Design Manual of Steel Construction," Vol. I and Vol. II, Second Edition, American Institute of Steel Construction, Chicago, IL, 1998.

Ajrab, J., Pekcan, G., and Mander, J., "Rocking Wall-Frame Structures with Supplemental Tendon Systems," *Journal of Structural Engineering*, American Society of Civil Engineers, Vol. 130, No. 6, June 2004, pp. 895-903.

Aktan, A. and Bertero, V., "Seismic Response of R/C Frame-Wall Structures," *Journal of Structural Engineering*, American Society of Civil Engineers, Vol. 110, No. 8, August 1984, pp. 1803-1821.

Aktan, A. and Bertero, V., "RC Structural Walls: Seismic Design for Shear," *Journal of Structural Engineering*, American Society of Civil Engineers, Vol. 111, No. 8, August 1985, pp. 1775-1791.

Aktan, A. and Bertero, V., "Evaluation of Seismic Response of RC Buildings Loaded to Failure," *Journal of Structural Engineering*, American Society of Civil Engineers, Vol. 113, No. 5, May 1987, pp. 1092-1108.

Aktan, A., Bertero, V., and Piazza, M. "Prediction of the Seismic Responses of R/C Frame-Coupled Wall Structures," Earthquake Engineering Research Center, Report No. UCB/EERC-82/12, Berkeley, CA, 1982, 182 pp.

Aktan, H., Yousef-Agha, W., and Olowokere, O., "Seismic Response of Low-Rise Steel Frames," *Journal of Structural Engineering*, American Society of Civil Engineers, Vol. 115, March 1989, pp. 594-607.

Al-Sulaimani, G. and Roessett, J., "Design Spectra for Degrading Systems," *Journal of Structural Engineering*, Vol. 111, No. 12, December 1985, pp. 2611-2623.

ANSYS, Release 5.4, Swanson Analysis Systems IP, Inc., Canonsburg, PA, 1997.

Aoyama, H., "Earthquake Resistant Design of Reinforced Concrete Frame Buildings with 'Flexural' Walls," in "Earthquake Resistance of Reinforced Concrete Structures, A Volume Honoring Hiroyuki Aoyama," Editor: T. Okada, Department of Architecture, Faculty of Engineering, University of Tokyo, Japan, November 1993, pp. 78-100.

Aristizabal-Ochoa, J., "Seismic Behavior of Slender Coupled Wall Systems," *Journal of Structural Engineering*, American Society of Civil Engineers, Vol. 113, No. 10, October 1987, pp. 2221-2234.

ASCE, "Minimum Design Loads for Buildings and Other Structures," ASCE 7-02, American Society of Civil Engineers, 2003, 376 pp.

ASCE, "Prestandard and Commentary for the Seismic Rehabilitation of Buildings," FEMA-356, American Society of Civil Engineers, Reston, Virginia, and Federal Emergency Management Agency (FEMA), Washington, D.C., November 2000.

Azizinamini, A., "Cyclic Characteristics of Bolted Semi-Rigid Steel Beam-to-Column Connections," Ph.D. Dissertation, University of South Carolina, 1985.

Borzi, B. and Elnashai, A., "Refined Force Reduction Factors for Seismic Design," *Engineering Structures*, Vol. 22, No. 10, October 2000, pp. 1244-1260.

BSSC, "NEHRP Guidelines for the Seismic Rehabilitation of Buildings," FEMA-273, Building Seismic Safety Council, Federal Emergency Management Agency (FEMA), Washington, D.C., October 1997.

BSSC, "NEHRP Recommended Provisions for Seismic Regulations for New Buildings and Other Structures," Part 1 and Part 2, FEMA-302 and FEMA-303, Building Seismic Safety Council, Federal Emergency Management Agency (FEMA), Washington, D.C., February 1998.

Chaallal, O., "Finite Element Model for Seismic RC Coupled Walls Having Slender Coupling Beams," *Journal of Structural Engineering*, American Society of Civil Engineers, Vol. 118, No. 10, October 1992, pp. 2936-2943.

Chaallal, O. and Gauthier, D., "Seismic Shear Demand on Wall Segments of Ductile Coupled Shear Walls," *Canadian Journal of Civil Engineering*, Vol. 27, No. 3, 2000, pp. 506-522.

Chaallal, O., Gauthier, D., and Malenfant, P., "Classification Methodology for Coupled Shear Walls," *Journal of Structural Engineering*, American Society of Civil Engineers, Vol. 122, No. 12, December 1996, pp. 1453-1458.

Chaallal, O., Guizani, L., and Malenfant, P., "Drift-Based Methodology for Seismic Proportioning of Coupled Shear Walls," *Canadian Journal of Civil Engineering*, Vol. 23, No. 5, October 1996, pp. 1030-1040.

Cheok, G. and Lew, H., "Model Precast Concrete Beam-to-Column Connections Subject to Cyclic Loading," *PCI Journal*, Precast/Prestressed Concrete Institute, Vol. 38, No. 4, July-August 1993, pp. 80-92.

Cheok, G. and Stone, W., "Performance of 1/3 Scale Model Precast Concrete Beam-Column Connections Subjected to Cyclic Inelastic Loads — Report No. 4," Report NISTIR 5436, National Institute of Standards and Technology, Gaithersburg, MD, 1994, 59 pp.

Cheok, G., Stone, W., and Lew, H., "Performance of 1/3-Scale Model Precast Concrete Beam-Column Connections Subjected to Cyclic Inelastic Loads - Report No. 3," NISTIR 5246, National Institute of Standards and Technology, Gaithersburg, MD, August 1993.

Cheok, G., Stone, W., Kunnath, S., "Seismic Response of Precast Concrete Frames with Hybrid Connections," *ACI Structural Journal*, American Concrete Institute, Vol. 95, No. 5, September-October 1998, pp. 527-539.

Cheok, G., Stone, W., and Nakaki, S., "Simplified Design Procedure for Hybrid Precast Concrete Connections," NISTIR 5765, National Institute of Standards and Technology, Gaithersburg, MD, 1996, 81 pp.

Chopra, A., Dynamics of Structures: Theory and Applications to Earthquake Engineering, Prentice Hall, Inc., Englewood Cliffs, New Jersey, 1995, 729 pp.

Christopoulos, C., Filiatrault, A., and Folz, B., "Seismic Response of Self-Centering Hysteretic SDOF Systems," *Earthquake Engineering and Structural Dynamics*, Vol. 31, No. 5, May 2002, pp. 1131-1150.

Christopoulos, C., Filiatrault, A., Uang, C., and Folz, B., "Posttensioned Energy Dissipating Connections for Moment-Resisting Steel Frames," *Journal of Structural Engineering*, American Society of Civil Engineers, Vol. 128, No. 9, September 2002, pp. 1111-1120.

Clough, R. and Penzien, J., Dynamics of Structures, McGraw-Hill, New York, 1993.

Cosenza, E. and Pecce, M., "Shear and Normal Stresses Interaction in Coupled Structural Systems," *Journal of Structural Engineering*, American Society of Civil Engineers, Vol. 127, No. 1, January 2001, pp. 84-88.

CSI, SAP2000-Integrated Finite Element Analysis and Design of Structures, Computers and Structures, Inc., Berkeley, CA, 1999.

Deierlein, G., "Proposed Ground Motions for Dynamic Analyses," 4th *Joint Technical Coordinating Committee Meeting*, U.S.-Japan Cooperative Earthquake Research Program on Composite and Hybrid Structures, October 1997, Monterey, CA, 12 pp.

Dywidag[®] Systems International http://www.dywidag-systems.com/download/us/DSI_Bar_Post_Tensioning.pdf, 2002

Eberhard, M. and Sozen, M., "Behavior-Based Method to Determine Design Shear in Earthquake-Resistant Walls," *Journal of Structural Engineering*, American Society of Civil Engineers, Vol. 119, No. 2, February 1993, pp. 619-640.

Elghadamsi, F. and Mohraz, B., "Inelastic Earthquake Spectra," *Earthquake Engineering and Structural Dynamics*, Vol. 15, 1987, pp. 91-104.

El-Sheikh, M., Sause, R., Pessiki, S., and Lu, L.W., "Seismic Analysis, Behavior, and Design of Unbonded Post-Tensioned Precast Frames," Research Report No. EQ-97-02, Department of Civil and Environmental Engineering, Lehigh University, Bethlehem, PA 18015, November 1997, 316 pp.

El-Sheikh, M., Sause, R., Pessiki, S., and Lu, L.W., "Seismic Behavior, and Design of Unbonded Post-Tensioned Precast Concrete Frames," *PCI Journal*, Precast/Prestressed Concrete Institute, Vol. 44, No. 3, May-June 1999, pp. 54-71.

El-Tawil, S., Kuenzli, C., and Hassan, M., "Pushover of Hybrid Coupled Walls I: Design and Modeling," *Journal of Structural Engineering*, Vol. 128, No. 10, 2002, pp. 1271-1281.

El-Tawil, S. and Kuenzli, C., "Pushover of Hybrid Coupled Walls II: Analysis and Behavior," *Journal of Structural Engineering*, Vol. 128, No. 10, 2002, pp. 1282-1289.

Fajfar, P. and Fischinger, M., "N2-A Method for Non-Linear Seismic Analysis of Regular Structures," *9th World Conference on Earthquake Engineering*, 1988, Tokyo-Kyoto, Japan.

Farrow, K. and Kurama, Y., "Capacity-Demand Index Relationships for Performance-Based Seismic Design," Structural Engineering Research Report #NDSE-01-02, Department of Civil Engineering and Geological Sciences, University of Notre Dame, Notre Dame, IN, November 2001, (available for download at <http://www.nd.edu/~concrete>).

Farrow, K. and Kurama, Y., "CDSPEC (Capacity-Demand SPECtra) Program," Department of Civil Engineering and Geological Sciences, University of Notre Dame, Notre Dame, IN, November 2001, (available for download at <http://www.nd.edu/~concrete>)

Farrow, K. and Kurama, Y., "SDOF Demand Index Relationships for Performance-Based Seismic Design," *Earthquake Spectra*, Vol. 19, No. 4, November 2003, pp. 799-838.

Farrow, K. and Kurama, Y., "SDOF Displacement Ductility Demands Based on Smooth Ground Motion Response Spectra," *Engineering Structures*, Elsevier, Vol. 26, No. 12, October 2004, pp. 1713-1733.

FEMA, "NEHRP Recommended Provisions for Seismic Regulations for New Buildings and Other Structures," Federal Emergency Management Agency, 1997.

Fintel, M. and Ghosh, S., "Seismic Resistance of a 31 Storey Frame-Wall Building Using Dynamic Inelastic Response History Analysis," *7th World Conference on Earthquake Engineering*, Istanbul, 1980, pp. 379-386.

Fintel, M. and Ghosh, S., "Case Study of Aseismic Design of a 16 Storey Coupled Wall Structure Using Inelastic Dynamic Analysis," *ACI Structural Journal*, American Concrete Institute, Vol. 79, No. 3, May-June 1982, pp. 171-179.

Garlock, M., Ricles, J., and Sause, R., "Cyclic Load Tests and Analysis of Bolted Top-and-Seat Angle Connections," *Journal of Structural Engineering*, Vol. 129, No. 12, December 2003, pp. 1615-1625.

Ghosh, S. and Markevicius, V., "Design of Earthquake Resistant Shearwalls to Prevent Shear Failure," *4th U.S. National Conference on Earthquake Engineering*, Earthquake Engineering Research Institute, Palm Springs, CA, Vol. 2, May 1990, pp. 905-913.

Gong, B. and Shahrooz, B., "Steel/Composite Coupling Beams-Behavior and Design," *4th Joint Technical Coordinating Committee Meeting*, U.S.-Japan Cooperative Earthquake Research Program on Composite and Hybrid Structures, October 1997, Monterey, CA, 20 pp.

Gong, B., Shahrooz, B., and Gillum, A., "Seismic Behavior and Design of Composite Coupling Beams," in "Composite Construction in Steel and Concrete III," New York: American Society of Civil Engineers, 1997, pp. 258-271.

Gong, B. and Shahrooz, B., "Seismic Behavior of Composite Coupled Wall Systems," University of Cincinnati, College of Engineering, Report No. UC-CII 98/01, June 1998, 274 pp.

Gong, B. and Shahrooz, B., "Concrete-Steel Composite Coupling Beams. I: Component Testing," *Journal of Structural Engineering*, American Society of Civil Engineers, Vol. 127, No. 6, June, 2001a, pp. 625-631.

Gong, B. and Shahrooz, B., "Concrete-Steel Composite Coupling Beams. II: Subassembly Testing and Design Verification," *Journal of Structural Engineering*, American Society of Civil Engineers, Vol. 127, No. 6, June, 2001b, pp. 632-638.

Goto, Y., Suzuki, S., and Chen, W., "Analysis of Critical Behavior of Semi-Rigid Frames With or Without Load History in Connection," *Journal of Solid Structures*, Vol. 27, 1991, pp. 467-483.

Hall, J., Heaton, T., Halling, M., and Wald, D., "Near-Source Ground Motion and Its Effects on Flexible Buildings," *Earthquake Spectra*, Vol. 11, No. 4, 1995, pp. 569-605.
Harries, K. "Seismic Response of Steel Beams Coupling Concrete Walls," M.S. Thesis, McGill University, May 1992, 95 pp.

Harries, K., "Seismic Design and Retrofit of Coupled Walls Using Structural Steel," Ph.D. Dissertation, McGill University, Canada, 1995, 229 pp.

Harries, K., "Design and Analysis of Four Prototype Eighteen Story Coupled Wall Structures," McGill University, Structural Engineering Series Report No. 96-01, 1996, 122 pp.

Harries, K., "Ductility and Deformability of Coupling Beams in Reinforced Concrete Coupled Walls," *Earthquake Spectra*, Vol. 17, No. 3, August 2001, pp. 457-478.

Harries, K. and McNeice, D., "Performance-Based Design of High-Rise Coupled Wall Systems," *The Structural Design of Tall and Special Structures*, Vol. 15 No. 3, 2006, pp. 289-306.

Harries, K. and Shahrooz, B., "Hybrid Coupled Wall Systems," *Concrete International*, American Concrete Institute, Vol. 27, No. 5, May 2005, pp. 45-51.

Harries, K., Cook, W., Redwood, R., and Mitchell, D., "Concrete Walls Coupled by Ductile Steel Link Beams," *10th World Conference on Earthquake Engineering*, Vol. 6, Madrid, July 1992, pp. 3205-3211.

Harries, K., Mitchell, D., Cook, W., and Redwood, R., "Seismic Response of Steel Beams Coupling Concrete Walls," *Journal of Structural Engineering*, American Society of Civil Engineers, Vol. 119, No. 12, December 1993, pp. 3611-3629.

Harries, K., Cook, W., Mitchell, D., and Redwood, R., "The Use of Steel Beams to Couple Reinforced Concrete Walls," *7th Canadian Conference on Earthquake Engineering*, Montreal, June 1994, pp. 509-516.

Harries, K., Mitchell, D., Redwood, R., and Cook, W., "Seismic Design of Coupled Walls-A Case for Mixed Construction," *Canadian Journal of Civil Engineering*, Vol. 24, 1997, pp. 448-459.

Harries, K., Mitchell, D., Redwood, R., and Cook, W., "Nonlinear Seismic Response Predictions of Walls Coupled with Steel and Concrete Beams," *Canadian Journal of Civil Engineering*, Vol. 25, No. 5, October 1998, pp. 803-818.

Harries, K., Gong, B., and Shahrooz, B., "Behavior and Design of Reinforced Concrete, Steel, and Steel-Concrete Coupling Beams," *Earthquake Spectra*, Vol. 16, No. 4, November 2000, pp. 775-799.

Harries, K., Fortney, P., Shahrooz, B., and Brien, P., "Design of Practical Diagonally Reinforced Concrete Coupling Beams – A Critical Review of ACI 318 Requirements," *ACI Structures Journal*, American Concrete Institute, Vol. 102, No. 6, 2005, pp. 876-882.

Hassan, M. and El-Tawil, S., "Inelastic Dynamic Behavior of Hybrid Coupled Walls," *Journal of Structural Engineering*, American Society of Civil Engineers, Vol. 130, No. 2, February 2004, pp. 285-296.

Hibbitt, Karlsson, and Sorensen, "ABAQUS User's Manual," Hibbitt, Karlsson, & Sorensen, Inc., Version 5.8, 1998.

Holden T., Restrepo J., and Mander J., "Seismic Performance of Precast Reinforced and Prestressed Concrete Walls," *Journal of Structural Engineering*, American Society of Civil Engineers, Vol. 129, No. 3, March 2003, pp. 286-296.

Holden, T., Restrepo, J., and Mander, J., "A Comparison of the Seismic Performance of Precast Wall Construction: Emulation and Hybrid Approaches," Rep. No. 2001-4, Dept. of Civil Engineering, Univ. of Canterbury, Christchurch, New Zealand, 2001.

ICBO, "Uniform Building Code," International Conference of Building Officials, Whittier, CA, 1997.

ICC, "2000 International Building Code (2000 IBC)," International Code Council, Falls Church, VA, December 2000.

Kabeyasawa, T., "Ultimate-State Design of Wall-Frame Structures," in "Earthquake Resistance of Reinforced Concrete Structures, A Volume Honoring Hiroyuki Aoyama," Editor: T. Okada, Department of Architecture, Faculty of Engineering, University of Tokyo, Japan, November 1993, pp. 431-440.

Keintzel, E., "Seismic Design Shear Forces in RC Cantilever Shear Wall Structures," *European Earthquake Engineering*, Vol. IV, No. 3, 1990, pp. 7-16.

Kishi, N. and Chen, W., "Moment-Rotation Relations of Semirigid Connections with Angles," *Journal of Structural Engineering*, American Society of Civil Engineers, Vol. 116, No. 7, July 1990, pp. 1813-1834.

Kurama, Y., "Seismic Analysis, Behavior, and Design of Unbonded Post-Tensioned Precast Concrete Walls," Ph.D. Dissertation, Department of Civil and Environmental Engineering, Lehigh University, Bethlehem, PA 18015, May 1997, 491 pp.

Kurama, Y., "Seismic Design of Unbonded Post-Tensioned Precast Walls with Supplemental Viscous Damping," *ACI Structural Journal*, American Concrete Institute, Vol. 97, No. 4, July-August 2000, pp. 648-658.

Kurama, Y., "Simplified Seismic Design Approach for Friction-Damped Unbonded Post-Tensioned Precast Walls," *ACI Structural Journal*, American Concrete Institute, Vol. 98, No. 5, September-October 2001, pp. 705-716.

Kurama, Y., "Hybrid Post-Tensioned Precast Concrete Walls for Use in Seismic Regions," *PCI Journal*, Precast/Prestressed Concrete Institute, Vol. 47, No. 5, September-October 2002, pp. 36-59.

Kurama, Y., "Seismic Design of Partially Post-Tensioned Precast Concrete Walls," *PCI Journal*, Precast/Prestressed Concrete Institute, Vol. 50, No. 4, July-August 2005, pp. 100-125.

Kurama, Y. and Farrow, K., "Ground Motion Scaling Methods for Different Site Conditions and Structure Characteristics," *Earthquake Engineering and Structural Dynamics*, Vol. 32, No. 15, 2003, pp. 2425-2450.

Kurama, Y., Pessiki, S., Sause, R., Lu, L., and El-Sheikh, M., "Analytical Modeling and Lateral Load Behavior of Unbonded Post-Tensioned Precast Concrete Walls," Research Report No. EQ-96-02, Department of Civil and Environmental Engineering, Lehigh University, Bethlehem, PA 18015, November 1996, 190 pp.

Kurama, Y., Sause, R., Pessiki, S., Lu, L., and El-Sheikh, M., "Seismic Design and Response Evaluation of Unbonded Post-Tensioned Precast Concrete Walls," Research Report No. EQ-97-01, Department of Civil and Environmental Engineering, Lehigh University, Bethlehem, PA 18015, November 1997, 184 pp.

Kurama, Y., Sause, R., Pessiki, S., and Lu, L., "Seismic Behavior and Design of Unbonded Post-Tensioned Precast Concrete Walls," *6th U.S. National Conference on Earthquake Engineering*, Earthquake Engineering Research Institute, Seattle, WA, May 31-June 4, 1998a, 12 pp.

Kurama, Y., Sause, R., Pessiki, S., and Lu, L., "Seismic Design of Unbonded Post-Tensioned Precast Concrete Walls," *Structural Engineers World Congress*, San Francisco, CA, July 19-23, 1998b, 8 pp.

Kurama, Y., Sause, R., Pessiki, S., and Lu, L., "Lateral Load Behavior and Seismic Design of Unbonded Post-Tensioned Precast Concrete Walls," *ACI Structural Journal*, American Concrete Institute, Vol. 96, No. 4, July-August 1999a, pp. 622-632.

Kurama, Y., Pessiki, S., Sause, R., and Lu, L., "Seismic Behavior and Design of Unbonded Post-Tensioned Precast Concrete Walls," *PCI Journal*, Precast/Prestressed Concrete Institute, Vol. 44, No. 3, May-June 1999b, pp. 72-89.

Kurama, Y., Sause, R., Pessiki, S., and Lu, L., "Seismic Response Evaluation of Unbonded Post-Tensioned Precast Walls," *ACI Structural Journal*, American Concrete Institute, Vol. 99, No. 5, September-October 2002, pp. 641-651.

Kwan, W. and Billington, S., "Seismic Behavior of Precast Concrete Pier Cap-Beam-to-Column Joints with Horizontal and Vertical Prestressing," *Earthquake Engineering: the 8th Canadian Conference*, 1999, pp. 439-444.

Lawson, R., Vance, V., and Krawinkler, H., "Nonlinear Static Push-Over Analysis - Why, When, and How?" *5th US Conference in Earthquake Engineering*, Earthquake Engineering Research Institute, Oakland, California, Vol. 1, 1994.

Lin, J. and Mahin, S., "Effect of Inelastic Behavior on the Analysis and Design of Earthquake Resistant Structures," Report No. UCB/EERC-85/08, Earthquake Engineering Research Center, University of California, Berkeley, CA, June 1985.

Lorenz, R., Kato, B., and Chen, W., "Semi-Rigid Connections in Steel Frames," Council on Tall Buildings and Urban Habitat, Committee 43, McGraw-Hill, Inc., 1993.

MacRae, G. and Priestley, M., "Precast Post-Tensioned UngROUTED Concrete Beam-Column Subassemblage Tests," Report No. PRESS-94/01, Department of Applied Mechanics and Engineering Sciences, Structural Systems, University of California, San Diego, CA, March 1994, 124 pp.

Mander, J., Priestley, M., and Park, R., "Theoretical Stress-Strain Model for Confined Concrete," *Journal of Structural Engineering*, American Society of Civil Engineers, Vol. 114, No. 8, August 1988, pp. 1804-1826.

Mander, J., Chen, S., and Pekcan, G., "Low-Cycle Fatigue Behavior of Semi-Rigid Top-and-Seat Angle Connections," *Engineering Journal*, Vol. 31, No. 3, 1994, pp. 111-121.

Marcakis, K. and Mitchell, D., "Precast Concrete Connections with Embedded Steel Members," *PCI Journal*, Precast/Prestressed Concrete Institute, July-August 1980, pp. 88-116.

MATLAB, 2000, The Math Works, Inc., Natick, MA.

Matsuoka, K., Kishi, N., Chen, W., and Goto, Y., "Analysis Program for the Design of Flexibly Jointed Frames," *Computers and Structures*, Vol. 49, Nov. 1993, pp. 705-713.

Mattock, A. and Gaafar, G., "Strength of Embedded Steel Sections as Brackets," *ACI Structural Journal*, American Concrete Institute, Vol. 79, No. 2, March-April 1982, pp. 83-93.

May, M., Kurama, Y. and Shen, Q., "Experimental Evaluation of Unbonded Post-Tensioned Hybrid Coupled Wall Subassemblages," Structural Engineering Research Report, Civil Engineering and Geological Sciences, University of Notre Dame, Notre Dame, Indiana, April 2006.

Miranda, E., "Site-Dependent Strength-Reduction Factors," *Journal of Structural Engineering*, Amer. Soc. of Civil Eng., Vol. 119, No. 12, December 1993, pp. 3503-3519.

Miranda, E., "Seismic Evaluation and Upgrading of Existing Buildings," Ph.D. Dissertation, Department of Civil Engineering, University of California, Berkeley, California, 1991.

Morgen, B. and Kurama, Y., "A Cast-Steel Friction Damper for Post-Tensioned Precast Concrete Beam-to-Column Joints," *National Technical and Operating Conference, Session on Castings for Building*, Steel Founders' Society of America, Chicago, IL, November 6-8, 2003.

Morgen, B. and Kurama, Y., "A Friction Damper for Post-Tensioned Precast Concrete Beam-to-Column Joints," *PCI Journal*, Precast/Prestressed Concrete Institute, Vol. 49, No. 4, July-August 2004a, pp. 112-133.

Morgen, B. and Kurama, Y., "A Friction Damper for Post-Tensioned Precast Concrete Beam-to-Column Joints," *13th World Conference on Earthquake Engineering*, Vancouver, BC, Canada, August 1-6, 2004b, 15 pp. (CD-ROM)

Morgen, B. and Kurama, Y., "An Innovative Friction-Damped Precast Concrete Frame Structure for Seismic Regions," *ASCE Structures Congress*, American Society of Civil Engineers, New York, NY, April 20-24, 2005, 12 pp.

Munshi, J. and Ghosh, S., "Displacement-Based Seismic Design for Coupled Wall Systems," *Earthquake Spectra*, Vol. 16, No.3, August 2000, pp. 621-642.

Naeim, F., "On Seismic Design Implications of the 1994 Northridge Earthquake Records," *Earthquake Spectra*, Vol. 11, No. 1, 1995, pp. 91-109.

Nassar, A. and Krawinkler, H., "Seismic Demands for SDOF and MDOF Systems," Report No. 95, Department of Civil Engineering, Stanford University, June 1991, 204 pp.

Newmark, N. and Hall, W., "Procedures and Criteria for Earthquake Resistant Design," *Building Science Series*, No. 46, 1973, National Bureau of Standards, U.S. Department of Commerce, Washington, D.C.

Newmark, N. and Riddell, R., "Inelastic Spectra for Seismic Design," *7th World Conference on Earthquake Engineering*, Vol. 4, 1980, Ankara, pp. 129-136.

Otani, S., Teshigawara, M., Hayashi, M., Ishii, T., Kawabata, I., and Kani, N., "Earthquake Response Characteristics of Reinforced Concrete Structural Walls," *4th Meeting of the U.S.-Japan Joint Technical Coordinating Committee on Precast Seismic Structural Systems*, Tsukuba, Japan, May 1994.

Paulay, T., "Ductility of Reinforced Concrete Shear Walls for Seismic Areas," in *"Reinforced Concrete Structures in Seismic Zones,"* American Concrete Institute, SP-53, 1977, pp. 127-147.

Paulay, T., "A Displacement-Focused Seismic Design of Mixed Building Systems," *Earthquake Spectra*, Vol. 18, No.4, November 2002, pp. 689-718.

Paulay, T. and Priestley, M., "Seismic Design of Reinforced Concrete and Masonry Buildings," John Wiley & Sons, Inc., 1992, 744 pp.

Paulay, T. and Santhakumar, A., "Ductile Behavior of Coupled Shear Walls," *Journal of Structural Engineering*, American Society of Civil Engineers, Vol. 102, No. ST1, January 1976, pp. 93-108.

PCI, PCI Design Handbook, Precast/Prestressed Concrete Institute, Sixth Edition, 2004.

Pekau, O. and Cistra, V., "Behavior of Nonlinear Coupled Shear Walls with Flexible Bases," *Canadian Journal of Civil Engineering*, Vol. 18, February 1989, pp. 45-54.

Peng, S., Ricles, J., Sause, R., and Lu, L., "Experimental Evaluation of a Post-Tensioned Moment Connection for Steel and Composite Frames in Seismic Zones," *6th ASCCS International Conference on Steel-Concrete Composite Structure*, Los Angeles, March 22-24, 2000, pp. 721-728.

Perez, F., "Lateral Load Behavior of Precast Concrete Walls with Ductile Vertical Joint Connectors," M.S. Thesis, Department of Civil and Environmental Engineering, Lehigh University, Bethlehem, PA, December 1998.

Perez, F., Pessiki, S., and Sause, R., "Seismic Design of Unbonded Post-Tensioned Precast Concrete Walls with Vertical Joint Connectors," *PCI Journal*, Precast/Prestressed Concrete Institute, Vol. 49, No.1, January-February, 2004a, pp. 58-79.

Perez, F., Pessiki, S., and Sause, R., "Lateral Load Behavior of Unbonded Post-Tensioned Precast Concrete Walls with Vertical Joints," *PCI Journal*, Precast/Prestressed Concrete Institute, Vol. 49, No.2, March-April, 2004b, pp. 48-64.

Prakash, V., Powell, G., and Campbell, S., "DRAIN-2DX Base Program Description and User Guide; Version 1.10," Rep. No. UCB/SEMM-93/17, Department of Civil Engineering, University of California, Berkeley, CA, 1993.

Priestley, M., "The PRESSS Program: Current Status and Proposed Plans for Phase III," *PCI Journal*, Precast/Prestressed Concrete Institute, Vol. 41, No. 2, March-April 1996, pp. 22-40.

Priestley, M. and MacRae, G., "Seismic Tests of Precast Beam-to-Column Joint Subassemblages With Unbonded Tendons," *PCI Journal*, Precast/Prestressed Concrete Institute, Vol. 41, No. 1, January-February 1996, pp. 64-81.

Priestley, M. and Tao, J., "Seismic Response of Precast Prestressed Concrete Frames with Partially Debonded Tendons," *PCI Journal*, Precast/Prestressed Concrete Institute, Vol. 38, No.1, January-February 1993, pp. 58-69.

Priestley, M., Sritharan S., Conley J., and Pampanin S., "Preliminary Results and Conclusions from the PRESSS Five-Story Precast Concrete Test Building," *PCI Journal*, Precast/Prestressed Concrete Institute, Vol. 44, No.6, November-December 1999, pp. 42-67.

Qi, X. and Moehle, J., "Displacement Design Approach for Reinforced Concrete Structures Subjected to Earthquakes," Report No. EERC 91/02, Earthquake Engineering Research Center, University of California, Berkeley, California, 1991.

Rahman, A. and Restrepo, J., "Earthquake Resistant Precast Concrete Buildings: Seismic Performance of Cantilever Walls Prestressed Using Unbonded Tendons," Rep. No. 2000-5, Dept. of Civil Engineering, Univ. of Canterbury, Christchurch, New Zealand, 2000.

Rahnama, M. and Krawinkler, H., "Effects of Soft Soil and Hysteresis Model on Seismic Demands," John A. Blume Earthquake Engineering Center, Report No. 108, Department of Civil Engineering, Stanford University, July 1993.

Raths, C., "Embedded Structural Steel Connections," *PCI Journal*, Precast/Prestressed Concrete Institute, Vol. 19, No. 3, May-June 1974, pp. 104-112.

Remmetter, M., Qin, F., and Shahrooz, B., "Seismic Resistance of Coupled Structural Walls," Cincinnati Infrastructure Institute, University of Cincinnati, College of Engineering, Report No. UC-CII 92/01, Cincinnati, Ohio, October 1992, 174 pp.

Restrepo, J., "Self-Centering Precast Post-Tensioned Cantilever Walls – Theory and Experimental Work," *Structures Congress*, American Society of Civil Engineers, Seattle, May 29-31, 2003.

Ricles, J., Sause, R., Garlock, M., and Zhao, C., "Posttensioned Seismic-Resistant Connections for Steel Frames," *Journal of Structural Engineering*, American Society of Civil Engineers, Vol. 127, No. 2, February, 2001, pp. 113-121.

Ricles, J., Sause, R., Peng, S., and Lu, L., "Experimental Evaluation of Earthquake Resistant Posttensioned Steel Connections," *Journal of Structural Engineering*, American Society of Civil Engineers, Vol. 128, No.7, 2002, pp. 850-859.

Saatcioglu, M., Derecho, A., and Corley, W., "Parametric Study of Earthquake-Resistant Coupled Walls," *Journal of Structural Engineering*, American Society of Civil Engineers, Vol. 113, No. 1, January 1987, pp. 141-157.

Saiidi, M. and Sozen, M., "Simple Nonlinear Seismic Analysis of R/C Structures," *Journal of the Structural Engineering Division*, American Society of Civil Engineers, Vol. 107, No. ST5, 1981, pp. 937-951.

Sarraf, M. and Bruneau, M., "Cyclic Testing of Existing and Retrofitted Riveted Stiffened Seat Angle Connections," *Journal of Structural Engineering*, American Society of Civil Engineers, Vol. 122, No. 7, July, 1996, pp. 762-775.

SEAOC, Recommended Lateral Force Requirements and Commentary, Sixth Edition, Structural Engineers Association of California, Seismology Committee, Sacramento, CA, 1996.

Shahrooz, B., Remmetter, M., and Qin, F., "Seismic Design and Performance of Composite Coupled Walls," *Journal of Structural Engineering*, American Society of Civil Engineers, Vol. 119, No. 11, November 1993a, pp. 3291-3309.

Shahrooz, B., Remmetter, M., and Qin, F., "Seismic Response of Composite Coupled Walls," in "Composite Construction in Steel and Concrete II," edited by W. Easterling and W. Roddis, American Society of Civil Engineers, 1993b, pp. 429-441.

Shahrooz, B., Fortney, P., and Rassati, G., "Seismic Performance of Hybrid Corewall Buildings," *International Workshop on Steel and Concrete Composite Construction*, National Center for Research on Earthquake Engineering (NCEE) of Taiwan, Taipei, Oct. 2003, pp. 79-88.

Shen, J. and Astaneh-Asl, A., "Hysteretic Behavior of Bolted Angle Connections," *Journal of Construction Steel Research*, Vol. 51, No. 3, July, 1999, pp. 201-218.

Shen, J. and Astaneh-Asl, A., "Hysteretic Model of Bolted Angle Connections," *Journal of Construction Steel Research*, Vol. 54, No. 3, April, 2000, pp. 317-343.

Shome, N., Cornell, C., Bazzurro, P., and Carballo, J., "Earthquakes, Records, and Nonlinear Responses," *Earthquake Spectra*, Vol. 14, No. 3, 1998, pp. 469-500.

Sims, J., "Flange Angle Behavior in Semi-Rigid Connections for Steel PR Frames," M.S. Thesis, Department of Civil Engineering and Geological Sciences, University of Notre Dame, IN, April 2000, 187 pp.

Srichatrapimuk, T., "Earthquake Responses of Coupled Shear Wall Buildings," Earthquake Engineering Research Center, Report No. UCB/EERC-76/27, 1976, 117 pp.

Stanton, J. and Nakaki, S., "Design Guidelines for Precast Concrete Seismic Structural Systems," PRESSS Report No. 01/03-09, UW Report No. SM 02-02, Department of Civil Engineering, University of Washington, Seattle, WA, February 2002.

Stanton, J., Stone, W., and Cheok, G., "A Hybrid Reinforced Precast Frame for Seismic Regions," *PCI Journal*, Precast/Prestressed Concrete Institute, Vol. 42, No. 2, March-April 1997, pp. 20-32.

Stone, W., Cheok, G., and Stanton, J., "Performance of Hybrid Moment-Resisting Precast Beam-Column Concrete Connections Subjected to Cyclic Loading," *ACI Structural Journal*, American Concrete Institute, Vol. 91, No. 2, March-April 1995, pp. 229-249.

Subedi, N., "RC-Coupled Shear Wall Structures. I: Analysis of Coupling Beams," *Journal of Structural Engineering*, American Society of Civil Engineers, Vol. 117, No. 3, March 1991a, pp. 667-680.

Subedi, N., "RC-Coupled Shear Wall Structures. II: Ultimate Strength Calculations," *Journal of Structural Engineering*, American Society of Civil Engineers, Vol. 117, No. 3, March 1991b, pp. 681-698.

Sugaya, K., Teshigawara, M., Kato, M. and Matsushima, Y., "Experimental Study on Carrying Shear Force Ratio of 12-Story Coupled Shear Wall," *12th World Conference on Earthquake Engineering*, paper 2152, 2000.

Swanson, J. and Leon, R., "SAC Steel Project," <http://www.ce.gatech.edu/~sac/>, School of Civil and Environmental Engineering, Georgia Institute of Technology, GA, 1999.

Tassios, T., Moretti, M., and Bezas A., "On the Behavior and Ductility of Reinforced Concrete Coupling Beams of Shear Walls," *ACI Structural Journal*, American Concrete Institute, Vol. 93, No. 6, November-December 1996, pp. 711-720.

Teshigawara, M., Sugaya, K., Kato, M., and Matsushima, Y., "Seismic Test on 12-Story Coupled Shear Wall with Flange Walls," reprinted in *List of Technical Papers Written in English Authored by Japan-Side Researchers*, U.S.-Japan Cooperative Earthquake Research Program on Composite and Hybrid Structures, December 2000.

University of Michigan, "Recommendations for U.S. Japan Cooperative Earthquake Research Program Phase 5 - Composite and Hybrid Structures," Report No. UMCEE 92-29, Department of Civil and Environmental Engineering, University of Michigan, Ann Arbor, MI, 48109, September 10-12, 1992.

USGS, USGS National Seismic Hazard Mapping Project, U.S. Geological Survey, WWW Document, <http://eqhazmaps.usgs.gov/>, 1996.